MODELLING OF FIRE SPREAD AND THE GROWTH OF FIRE IN BUILDINGS USING COMPUTATIONAL FLUID DYNAMICS

ANTHONY ERNEST FERNANDO

A research thesis completed as fulfilment of the requirements of the degree

Doctor of Philosophy

undertaken at the

Centre for Environmental Safety and Risk Engineering
Victoria University of Technology

2000

for Denise

ACKNOWLEDGMENTS

Five and a half years ago, I undertook a life altering journey, the culmination of which is the substantial wad of processed wood pulp the reader is presently either holding in their hand or (more likely) lain prone upon a sturdy surface. Like most such pieces of work, there are many forces at work in its creation other than the author's quill (or in this case, mouse and keyboard), and I would like to acknowledge these persons or organisations here.

The research presented in this thesis was financially supported by an Australian Research Council (ARC) Infrastructure Grant which was conducted in association with BHP and the National Association of Forest Industries. My gratitude to these organisations for making this research possible.

I would like to thank my principal supervisor, Professor Vaughan Beck, Director of the Centre for Environmental Safety and Risk Engineering, for taking me on as a student and choosing the area of research. He was a source of good advice on the writing of conference papers and this thesis, although his pen had a seemingly endless supply of red ink. I would also like to thank my co-supervisor, Associate Professor Graham Thorpe, for helping to explain some of the more technical and numerical aspects of the work in this project, and for likewise being adept with the crimson writing fluid. My gratitude to my other co-supervisor, Dr. Mingchun Luo, who was the resident expert on the field model CESARE-CFD, and helped to explain some of the quirks of this most complex beast. This thesis would also not have been possible without the clear-headed advice of Dr. Özden Turan, who was also a great help in unravelling the mysteries (for me, anyway) of the k-epsilon turbulence model. My thanks also to Dr. Yaping He, Mr. Paul Clancy, and Mr. Mahesh Prakash, who have helped with other technical aspects of this thesis.

There was a substantial amount of work involved in the preparation and execution of experiments at the Experimental Building Fire Facility. My gratitude to Mr. Scott Stewart for setting up the instrumentation and doing all the hard work in preparing the facility for testing. He was assisted by Messrs. Eddie Szmalko and Ben White for the propane burner tests, and Martin Coles for the polyurethane foam tests. My thanks to all these persons.

Experiments were also carried out at the Division of Building, Construction and Engineering at CSIRO, Highett. My thanks to Dr. G. Caird Ramsay and Mr. Vince Dowling for organising the cone calorimeter tests, and to Mr. Justin Leonard for carrying out the tests and other technical advice about the cone, and numerous other diversions. Thanks also to Mr. Paul Bowditch for

completing the second round of cone calorimeter tests. Vince was also responsible for organising the furniture calorimeter tests which were ably carried out by Messrs. Neville Macarthur and Alex Webb.

On a personal note, I would like to thank family and friends who have been so sympathetic and supportive the last four years. In particular, I wish to express my gratitude to my "-in-laws" Derrick and Rita Fernando for their encouragement, generosity, and weekly curries, and Rosie Fernando and Trevor Plant for their support and friendship. I would also like to thank Trevor for his "expertise" in setting up my home computer, for frequent loans of his zip drive, and for insisting I upgrade my home computer (a worthwhile investment as it transpires, although the result is that I now own the PC equivalent of the Millennium Falcon). My thanks to Evan Linwood for musical distractions on nights off, and also for providing the frame-grabber technology and producing the video stills for the thesis. My thanks also to my friends Grant Armstrong, who started his PhD six months before me, and Iain and Luisa Cook, who completed theirs several years ago, for their sympathy, wisdom and advice, having been through it all themselves.

I would dearly like to thank my grandmother, Lilian Leitch (1/7/13 – 16/6/98) who provided me with companionship and a home during my undergraduate years, and also frequently provided a nice hot cuppa and a stress-free zone during my postgraduate years. "Gran" is still missed by all.

Most of all, my most heartfelt gratitude goes to my wife, Denise, whose patience, dedication, support and love has sustained me throughout the project, and to whom I shall be forever indebted.

ABSTRACT

The motivation for undertaking this research is to contribute to the development of a model of fire spread over a surface, and to integrate this model with a computational fluid dynamics (CFD) model that is capable of making predictions of the environment associated with full-scale fires in enclosures. The research focuses on the growth and spread stage of such fires, where a small, localised flame spreads across a single fuel item, increasing the heat release rate. In particular, the phenomenon of opposed flow flame spread across flat, non-charring, thermally thick fuel surfaces is examined.

Thermal radiation, which is an important mechanism of heat transfer in most combustion scenarios including building-fires, has a strong effect on the rate of flame spread over, and heat release rate of, a burning fuel item. The basic CFD model used throughout this project originally employed overly simplified radiation transfer equations, consequently producing unsatisfactory results. Modifications were made to the radiation model, improving the radiation predictions, as well as the overall performance of the CFD model. Comparisons have been made with a steady-state fire conducted in a full-scale multi-room fire facility, and a good correlation is shown between experimental data and model predictions.

A numerical model for flame spread over flat surfaces has been developed by the author. The surface of the fuel is discretised with a regular square array. Flame spread occurs as a series of ignitions of surface elements. Ignition of an element is determined by a combination of critical surface ignition temperature and cellular automata techniques. Three dimensional heat conduction within the fuel is considered, and temperatures within the fuel are determined by calculating the heat balance equation on an appropriately constructed grid. The grid is finely spaced near the burning surface, where the temperature gradient is highest. Regression of the surface due to combustion of the fuel is modelled, and the fine grid is retained by allowing the grid to "collapse" locally with the fuel surface. A grid transformation is applied to restore orthogonality of the collapsed grid, which allows computation of the heat equation.

The flame spread model has been designed to be independent of geometry, although experiments were only carried out for radial spread over horizontal surfaces. The model was initially developed as a stand-alone model, with empirical equations and assumptions used to describe the properties of the flame region for a horizontal geometry. The experiments were performed with cushion sized polyurethane foam slabs in a furniture calorimeter. The experimental results compare reasonably

well with the modelled results, with the discrepancies largely attributable to the assumptions made about the flame and other gas phase phenomena.

The fuel used for the flame spread experiments was standard polyurethane flexible foam. Material properties for the foam were obtained mainly from the literature. Attempts were made to extract combustion data from cone calorimeter experiments. However, due to the transient nature of the phenomena associated with small samples of foam burning in a cone calorimeter configuration, it was difficult to extract fundamental data from the experiments. This result emphasises the care required in the interpretation of cone calorimeter data for polyurethane foams and similar materials.

The flame spread model has also been incorporated as a working submodel of a larger CFD model, so that the gas phase assumptions of the stand-alone model were replaced with CFD calculations. The calculations for the flame spread submodel were performed on a finer grid than the flow region for the main CFD model, in order to resolve the small-scale detail important to flame spread while not burdening computer resources with an excessive amount of calculations in the flow region. Predictions were made for the burning of a slab of polyurethane foam in a full-scale multi-room experimental building-fire facility. The predictions compare favourably with the experiments, indicating the validity of the methods used in flame spread model. Discrepancies still exist, and proposed remedies are suggested as future work.

The research undertaken in this thesis resulted in two refereed and one non-refereed conference papers. The refereed papers are included in the Appendix to this thesis. "A Numerical Model for Horizontal Flame Spread over Solid Combustible Fuels" was presented at the Sixth Australasian Heat and Mass Transfer Conference, University of New South Wales, Sydney, Australia, 1996, and was co-written with Associate Professor Graham Thorpe. "A Cellular Automata Approach to CFD Flame Spread Modelling" was presented at the Sixth International Symposium on Fire Safety Science", Poitiers, France, 1999.

TABLE OF CONTENTS

LIST OF FIGURES

LIST OF TABLES

NOMENCLATURE

ROMAN

a_g	Acceleration due to gravity
a_k, b_k, c_k, d_k	Intermediates in Thomas algorithm
A, dA, A_b	Area, area element, bounding surface area
A	Pre-exponential constant
c_m, c_v	Mass concentration, volume concentration
c_p	Thermal capacity
d	Particle diameter
D	Characteristic dimension
D	Distance from flame base
E	Activation energy
E	Wall roughness constant
E_b, $E_{b,\lambda}$	Energy radiated by black body, by black body at wavelength λ
f	Fuel mixture fraction
F	Configuration factor
F	Fraction fuel remaining
g	Fuel fraction fluctuation
h, Δh	Enthalpy, change in enthalpy
h	Heat transfer coefficient
H	Flame height
ΔH_c	Heat of combustion
I	Intensity
i, j, k	Cartesian indicies
k	Turbulence kinetic energy
k	Thermal conductivity
k, K	Extinction coefficient
L, L_m	Pathlength, mean beam length
L_v	Heat of volatilisation
$\dot{m}''$	Mass flux
M	Mass
M_X	Molar mass of species X
n	Neighbourhood number
n	Refractive index
p	Pressure field
p	Partial pressure
ΔP	Pressure difference
q	Heat
$\dot{q}''$, $\dot{Q}''$	Heat flux
r	Radius
r_o	Fuel/oxygen stoichiometric ratio
R	Universal gas constant
R	Flame radius
R_s	Decomposition rate of solid
s	Distance
S, S_ϕ	Source term of flow variable ϕ
S_v	Surface area per unit volume
t	Time
T	Temperature
u, v, w	Velocity components
v	Velocity
V, V_f	Volume, flame volume
x	Wall thickness
x, y, z	Cartesian coordinates*
Y_X	Concentration of species X

* Note that the convention used throughout this thesis for modelling results etc. is that x denotes the east/west direction, y denotes the north/south direction, and z denotes the vertical direction

GREEK

α	Thermal diffusivity
α	Absorption
β_k, δ_k	Intermediates in Thomas algorithm
Γ, Γ_ϕ	Exchange coefficient
ε, ε_λ	Emissivity, emissivity at wavelength λ
θ, ϕ	Spherical coordinates
κ	Absorption constant
κ	von Karman's constant
λ	Wavelength
μ_t	Turbulence viscosity
ν	Kinematic viscosity
ξ, η, ζ	Transformed coordinates
ρ	Density
σ	Stefan-Boltzmann constant
σ_ϕ	Prandtl/Schmidt number of flow variable ϕ
τ	Thermal thickness
τ	Transmission fraction
ϕ	Flow variable
ϕ_e	Equivalence ratio
Ω, $d\Omega$	Solid angle, increment of solid angle

ABBREVIATIONS AND ACRONYMS

1D	One Dimensional
3D	Three Dimensional
ADI	Alternating Direction Implicit (method)
CESARE	Centre for Environmental Safety and Risk Engineering
CESARE-CFD	CFD model developed by researchers at CESARE
CFD	Computational Fluid Dynamics
CSIRO	Commonwealth Scientific and Industrial Research Organisation
EBBF	Experimental Building-Fire Facility
EHC	Effective Heat of Combustion
FDM	Finite Difference Method
MIMS	Mineral Insulated Metal Sheathed (thermocouple)
PMMA	Polymethylmethacrylate
PUF	Polyurethane Foam
RAM	Risk Assessment Model
RHR	Rate of Heat Release
VUT	Victoria University of Technology

1. OVERVIEW

1.1. INTRODUCTION

1.1.1. Fire Safety

Fire may be described as the chemical process by which a fuel reacts in the gaseous phase with an oxidant to produce heat and reaction products. If properly controlled and harnessed, such as in a coal fired power plant or a domestic cooking appliance, this reaction may be greatly beneficial. However, an accidental or uncontrolled fire is often hazardous, and may pose a serious threat to both life and property. The magnitude of the hazard depends on the nature of the fuel, the speed of the reaction, the amount of heat released, the toxicity of the products, the location and situation of the fire, and so forth. A particularly hazardous situation arises when the fire occurs in an enclosure, such as any building structure with a ceiling and walls to prevent or restrict the escape of the combustion products. In such an instance, the fire may deplete the enclosure of oxygen, replacing it with toxic combustion products. Conversely, if there is sufficient ventilation to maintain a steady supply of oxygen to the fire, the buildup of hot products close to the ceiling will increase the amount of heat feeding back to the fire source and surroundings. This will cause the fire to grow and in turn heat the combustion products further in a runaway reaction, a phenomenon called flashover. In a flashover fire, all combustible objects in the vicinity of the original fire become involved in the combustion reaction, and there is a significant release of heat and toxic gases which rapidly spread the fire to other parts of the building or enclosure. Regardless of whether flashover occurs or not, it is the replacement of oxygen with asphyxiating and toxic gases which is responsible for the majority of casualties in building-fires.

It is desirable, therefore, that measures be taken to prevent fires in buildings, or at least to minimise their impact, as well as allowing occupants of the buildings every opportunity to make a swift and safe egress should such a fire occur. These factors in essence comprise the discipline of fire safety, and many building regulations for fire safety and protection have arisen. Fire science is an integral component of fire safety, as the understanding of the physical and chemical properties of fires is vital in both explaining fires which have occurred, and in predicting the possible outcomes of future fires. Traditionally, building-fire regulations tend to reflect the former; that is to say, when a major fire occurs, the causes are identified, and (often arbitrary) regulations are enforced in an attempt to prevent a similar fire occurring in the same or other buildings of a similar design. However, there is a move in many countries to replace such "prescriptive" style fire codes with "performance-based"

codes, as often the prescriptive regulations may in some situations be excessive, or lead to levels of redundancy, and therefore add unnecessary costs and restrictions to building design[1]. Development of a performance based code may be accomplished with the aid of an efficient Risk Assessment Model (RAM), which is able to assess the level of protection afforded to occupants and property against a fire, and aims to minimise both the risk, and the cost of providing that protection over the lifetime of the building in question[1]. Amongst the many components required in a RAM is a comprehensive fire model capable of making accurate predictions of possible fire scenarios in the building or enclosure under consideration, and the time of occurrence of key events within the scenario.

Developing a fire model capable of making the predictions required of a RAM requires a thorough understanding of the physical and chemical processes of fire, in particular those aspects which contribute the most to the overall hazard. Since the RAM needs to be provided with the response times of fire detection and suppression subsystems, and the time available for occupants to make a safe egress before conditions in the building become untenable, the factors relating to fire growth and spread are of particular importance. Babrauskas and Peacock[2] have identified four main constituent phenomena comprising a typical* fire growth and spread scenario, namely ignition, flame spread, heat release rate, and the release rate of smoke and toxic gases. While the heat release rate was identified as the most important variable contributing to the fire hazard, the factors are related and all need to be considered in the development of an accurate fire growth and spread model.

1.1.2. Fire Models

The scope of fire modelling goes beyond just providing data for a RAM, which is merely one of many practical applications of fire models. Fire modelling is also a tool for understanding the nature of fire itself; indeed, a model is a mathematical and physical representation of the modeller's understanding of the physical process.

There have been many approaches in the past to constructing fire models. These approaches have been categorised in several ways. Luo and Beck[3] categorise enclosure models into stochastic, scale, zone, and field. Galea[4] describes scale modelling as experimental rather than mathematical, and divides mathematical models into probabilistic (stochastic) and deterministic, which Weber[5] further

* Only fires where casualties occur remotely from the ignition source were considered, hence excluding instances such as explosions or direct contact with the flammable item.

categorises* into empirical, and physical. The main distinction between deterministic models and probabilistic models is that given a set of initial conditions, only one final result will be forthcoming from a deterministic model, whereas probabilistic models will generally produce a spread of results. This project is concerned with deterministic models, which incorporate the underlying physics of the scenarios they model. The two main types of deterministic enclosure fire models are zone models and field models.

Zone models fall into the "empirical" category of deterministic models. Their initial development precedes the widespread availability of powerful computers, as their relative simplicity allowed the possibility of a solution to the problem in question, which did not require excessive amounts of computation. The models are based on the observation that a flaming fire in an enclosure tends to develop a clear stratification; that is, the smoke and hot gases from the fire rise due to buoyancy to the upper portion of the enclosure, where they spread out forming a layer whose boundary is at a fairly uniform height. At the same time, the cooler "fresh" air remains at the bottom, forming a second distinct layer. Most zone models consist of these two layers, although some also include the fire plume as an additional zone, and possibly one or two other prominent phenomena as extra zones, while some even consider the entire enclosure as a single zone. Whatever the case, the physical properties within each zone are assumed to be constant and homogeneous, and the conservation of energy and mass is observed for each zone, and for the interaction between zones.

The main weakness of zone models is they have been validated against a particular class of enclosure fire, that being mainly domestic style single enclosures. They have not generally been validated for enclosures of a large area, or with large open spaces such as atria, or those possessing complex geometries. Also, they provide limited information about movement of smoke between compartments within an enclosure, as well as many other physical phenomena. However, their relative simplicity means that, running on a typical modern personal computer, they can yield satisfactory solutions to a particular fire problem in a matter of minutes[4.6].

Because of the great increase in computing power over the past decade or so, it is becoming less easy to justify the simplifications of zone models solely on the basis of lack of computational power. Hence, the other main type of enclosure fire model, namely the field model, is finding increasing application in the study of fire science[4]. Field models fall into the "physical" category of deterministic models, meaning that in principle, they try to avoid making assumptions of an empirical nature, where possible. The internal workings of the model are based on a branch of physics known as computational fluid dynamics (CFD), hence their other common name, CFD

* In this case, pertaining to fire spread rather than fires in general, but the principal still holds.

models. The model is formulated by examining the fundamental physical and physiochemical behaviour of the fire scenario. In fact, due to the plethora of phenomena which contribute to the fire scenario, most field models contain empirical assumptions somewhere in their subroutines, so that in some ways they may be thought of as being just complex zone models. However, these "zone models" contain typically tens of thousands of cells rather than two or three (or a dozen or so if multiple compartments are considered), and can calculate a much wider range of variables, in particular the velocity components of the moving fluids (air and combustion products), and distributions of temperature and heat fluxes. Thus, it is possible to compute in some detail the movement of smoke throughout the enclosure, and the temperature and species distribution within the smoke layer itself. This thesis makes considerable use of CFD modelling: in particular, the model hereafter referred to as CESARE-CFD is widely used, its name derived from having been developed by researchers at the Centre for Environmental Safety and Risk Engineering (CESARE). A more detailed description of this and other models will be given later.

The main drawback of field models is that, in spite of the advances in modern computers, they are still very computationally intensive and require a great deal of time and computer resources to execute. In addition, many of the phenomena they attempt to model are not fully understood; examples include turbulence, chemical reaction kinetics, and the combination of the two, turbulent combustion. Nevertheless, improved computing power and further research into key areas will progressively diminish these problems.

A deterministic model is valuable if it can make reasonably accurate predictions of fire scenarios. If a model can predict well the phenomena it is modelling for a variety of scenarios, then it may be considered to be validated. It should be noted, however, that the term "validated" is somewhat contentious, and should therefore be used with caution. This applies in particular to field models, which often make literally millions of predictions about the scenario being modelled; that is, predictions of ten or twenty flow quantities, at tens or hundreds of thousands of points. However, it is not possible to experimentally verify every point in the flow region for even the simplest of test cases. So, what constitutes validation of a field model? A possible definition is that a field model must be able to successfully describe *qualitatively* the behaviour of the flow region as a whole, while *quantitatively* making successful descriptions about the flow at key locations, for a variety of flow scenarios. In such a definition, the key locations and scenarios will be dependent on the nature of the model being validated, and what sort of information the model will be required to produce. The degree of tolerance in qualitative and quantitative predictions will likewise depend on the nature of the problem (and will ultimately depend inversely with the degree of cynicism of the scrutiniser of the model).

Validation of a field model requires that its predictions be compared with some other quantitative data. For some very simple fire scenarios, this may be in the form of an analytical solution. Zone models also offer a limited number of data points for comparison, although they themselves require validation. However, a CFD model attempting to make full-scale predictions will, in the majority of cases, require that full-scale experiments be performed for comparison, particularly when complex geometries are involved. Full-scale tests by their nature are more dangerous and more expensive than models, but they are necessary to provide the data needed for validation of the models. Because of their cost, it is necessary that full-scale experiments be well devised, constrained to avoid variable effects, and that the maximum amount of data should be extracted from each experiment.

1.1.3. Flame Spread Modelling

Given that deterministic enclosure fire models have been in use for some time, the question to be asked is, to what extent have they been used to address the factors contributing to fire hazard? Namely, ignition, fire spread, rate of heat release, and rate of product release, as mentioned earlier. Certainly, the rate of heat release is an integral factor of most models, since if there is no heat source, there is no fire, and the modelling becomes a nihilistic exercise. Often, though, this heat "input" into the system is either constant or is specified as a predetermined history. Even for a complex scenario such as the field modelling of the Kings Cross Underground Station fire[7], an assumed heat release history was used.* Of course, this need not always be the case, as many models attempt to determine the heat release rate as well as the effect that the heat release has on the enclosure. Heat release may be determined by size of the burning area and hence the combustion rate, which may increase due to flame spread. These models usually take into account the radiant feedback effect that the enclosure has on the combustion rate and rate of spread as well. Typically, the spread rate is an empirical function of the externally applied heat flux and local oxygen concentration[8,9]. Similarly, empirical relationships are often used for the combustion behaviour, and the release of smoke and other combustion products[9].

That is not to say that there are not fundamental, sophisticated flame spread and heat release models in existence; there are. Analytical or numerical approaches to flame spread modelling date back at least to the work of de Ris[10], and much work has been done since. However, these models are

* The authors were, however, working to tight deadlines imposed by the official investigation, so a more detailed analysis of the heat release was not feasible.

largely self contained. Even if they employ CFD techniques to calculate the gas phase behaviour, the region modelled is in the vicinity of the flame only. If ambient or environmental factors are considered, they are usually assumed, and there is generally no feedback between the burning region and the surroundings. Often these models assume a geometrical configuration, so that they apply only to upward flame spread, or horizontal radial spread, or some other geometry which reduces the complexity of the problem.

A reason that there is a separation between full-scale CFD models, used to model the environment associated with fires in full scale enclosures, and detailed flame spread models is possibly one of scale. In modelling a full-scale enclosure using CFD, it is unlikely that grid cells smaller than, say, 50 mm will be used. A typical "standard" room measures 2.4×2.4×3.6 m, so unless a choice is made to discretise the modelled enclosure with literally millions of control cells (a number which is still prohibitively large for all but the most powerful supercomputers), the grid will be necessarily coarse. Of course, that is ignoring the possibility of modelling additional compartments adjoining the room of fire origin. On the other hand, in modelling flame spread, particularly spread in the direction opposite the local fluid flow direction, important phenomena occur at scales of the order of a few millimetres. While future computers may be powerful enough to use a very fine mesh in the vicinity of the burning region, or even for the entire enclosure of interest, for the present it is necessary to develop other techniques to resolve the different scale requirements.

1.2. AIMS OF THE PROJECT

1.2.1. General Requirements

The primary aim of the research reported in this thesis is to construct a flame spread model, and then incorporate it in an interactive mode with a CFD model, to accurately predict full-scale fires involving flame spread across solid fuel objects. The flame spread model will be used to predict the contribution of heat and fuel volatiles to the gas phase, whereby the CFD model will be used to calculate the combustion of the fuel and the distribution of heat and products of combustion. At the same time, the CFD model will be used to calculate the heat feedback to the fuel surface within the flame spread model, in turn affecting the flame spread rate and rate of volatilisation of the fuel.

There are several requirements of such a flame spread submodel, which need to be taken into account if it is to be generally compatible with a CFD model. Naturally, these requirements will subsequently affect the form of the eventual model. For compatibility, the flame spread model will

operate on a discrete grid, with the properties being uniform over each control cell, as is the case with CFD models. This means that unlike most analytical models of flame spread, the flame front will be characterised as advancing by a series of discrete jumps rather than continuously.

The requirements of the flame spread model as identified previously by the author[11] are basically threefold. Firstly, in keeping with the spirit of CFD models, the flame spread model must be based as much as possible on first principles. Secondly, it must be geometrically flexible, so that it is capable of modelling a wide variety of flame spread scenarios. These scenarios include horizontal radial spread, horizontal planar, vertical upwards, vertical downwards, and even arbitrary shapes, angles, and orientations. Thirdly, the fundamental material properties required for the model must be experimentally derivable[12].

In addressing the first requirement, the natural question to ask is: what are the "first principles" involved in flame spread modelling? At a fundamental level, flame spread is an ignition and combustion problem. Evidence of this may be seen in the fact that flame spread properties are closely linked to the heat release rate properties of the fuel in question[13]. This is logical, as preheating of the fuel ahead of the flame front will be in proportion to the amount of heat released from the burning region. It would be expected that as more heat is released, the faster the preheating of the unburnt fuel, and the faster the rate of spread. In light of the discrete nature of numerical modelling, this research will investigate whether the modelling of flame spread may be represented as a series of ignitions of discrete fuel elements, the combustion of which is determined by fundamental material properties.

This approach will help greatly with the geometric flexibility aspect of the second requirement. If the amount of heat received by a fuel element can be determined, it is possible to calculate its ignition and combustion properties, presuming of course that the fundamental material properties are themselves independent of the geometry. However, there are phenomena associated with heat transfer which are significant only close to the flame front. Thus, it will be necessary to develop a method of determining the arrival of a flame front of arbitrary shape. In this research the feasibility of one such technique, developed by the author, based on the methods of cellular automata will be investigated.

Finally, if the model is to depend on fundamental material properties, experimental techniques to determine these properties must be available. Fortunately, many such methods are in existence and are becoming widespread. This research will investigate whether bench scale methods such as Cone Calorimetry and Thermo-Gravimetric Analysis (TGA), given that they are properly executed

and interpreted, can yield fundamental data required for the flame spread model. The data includes the time to, and surface temperature of, ignition as a function of applied radiant heat, heat of volatilisation, chemical kinetics of thermal decomposition, effective heat of combustion of the decomposition products, and so on.

1.2.2. Specific Aims

To summarise, the aims of the project may be expressed as follows

- Identify which submodels encoded in CESARE-CFD, if any, yield inadequate predictions of physical quantities occurring in fire environments, and if possible to rectify these submodels.
- Perform appropriate full-scale experiments to acquire data for comparison with model predictions, and investigate whether changes to the model result in improved predictions.
- Develop an ignition and combustion model that requires fundamental, experimentally derivable material properties. Acquire the required data for a selection of materials by a combination of bench-scale experiments and established literature values.
- Develop a stand-alone flame spread model by combining the ignition and combustion model for an array of fuel cells in conjunction with spread criteria. Use empirical models and assumptions for the gas phase phenomena.
- Perform furniture calorimeter experiments to investigate the validity of the stand-alone flame spread model.
- Incorporate the flame spread model as a submodel of the field model CESARE-CFD.
- Investigate the validity of the combined CFD-flame spread model by comparing the predicted results with results obtained from a series of realistic full-scale experiments.

1.3. THESIS OVERVIEW

The research presented in this thesis is divided into five main chapters. Chapter 2 gives an overview of the methods of CFD and their application to enclosure fire modelling. It comprises a review of CFD modelling of enclosure fires, and a description of the numerical methods encoded in CFD models, both in general, and specifically the methods used in CESARE-CFD, the model used to produce the predicted results in this research.

The remaining chapters of this thesis reflect the stages which needed to be fulfilled in order to achieve the goal of an integrated CFD model and compatible flame spread model. The first stage, described in Chapter 3, is to modify the radiation submodel of CESARE-CFD in order to produce more accurate predictions of radiant heat flux incident at the bounding surfaces of the enclosure (including possible combustible surfaces). As flame spread is sensitive to the heat flux received by the fuel element, and radiation is an important component of this flux, accurate predictions are necessary.

The second stage, described in Chapter 4, deals with the determination of the fundamental combustion properties of solid fuels. While efforts were made to keep the methods general, only two fuels were investigated; namely a standard polyurethane foam and a fire retarded polyurethane foam. These fuels were chosen as they are materials commonly encountered in domestic and commercial occupancies, and have the advantage of being homogenous and isotropic in composition with relatively simple combustion behaviour. They were chosen in favour of materials such as wood which, although one of the most common building materials, is generally non-uniform in composition and directional properties and burns in a complex fashion, and polymethylmethacrylate (PMMA) which, while it has simple uniform combustion properties and has been used extensively in previous combustion and flame spread research[14,15,16,17], is a somewhat uncommon building and furnishing material.

Chapter 5 deals with the development of a numerical flame spread model, which combines the ignition and combustion methods developed in Chapter 4 with criteria that are used to predict the flame spread. The model was initially developed as a "stand-alone" model, using empirical models for the flame shape and temperature. This is because the cumbersome and time consuming process of encoding, executing, and the inevitable debugging of any model would be further exacerbated by the complexity and lengthy execution time of CFD models.

Once these other requirements have been met, the eventual encoding of the flame spread model into the CFD model can take place. A description of the method of encoding the flame spread model is presented in Chapter 6, and the behaviour of the interface between the flame spread model and the CFD model is examined in detail. This is to ensure that the interface methods are robust and do not introduce unwanted behaviour to the model.

2. FIELD MODELLING

In this chapter a more detailed description of CFD models is presented, both in general terms, and in particular details are given of the model CESARE-CFD which is the basis of the CFD modelling for the research reported throughout this thesis. The aim of this chapter is to establish the methods involved in constructing a CFD model, and how these methods are incorporated within CESARE-CFD. A description of some of the boundary conditions and convergence criteria which apply to the modelling work throughout the thesis are also included. A review is also presented here, to identify similar modelling work which appears in the literature.

2.1. REVIEW

Although the fundamental equations describing fluid flow have been established for over a century, field modelling became a prominent fire modelling tool around twenty years ago, when computer technology had advanced to the point at which it became feasible to numerically calculate the equations which govern the behaviour of fires. The development of numerical methods suited to computation occurred in tandem with the development of computing power, as the methods became feasible, and could be tested. There was considerable research by workers such as Launder and Spalding (see reference 18 for example) in improving the computational accuracy of turbulence calculations, and by Patankar and others in developing methods for numerically solving the coupling between pressure and velocity fields. Patankar's classic secondary text[19], first published in 1980, describes the methods, particularly the finite volume techniques, which form the basis of many field models today. It was only another year or two before fire field models were regularly being used and validated[20].

A number of general purpose field models emerged at this time in response to the development of the numerical methods. One of the first fire field models to emerge[21] was JASMINE, itself based on the commercially available general purpose code PHOENICS, and this remains a widely used commercial package. It has since been joined by FLOW3D, used in the modelling of conditions in the Kings Cross Underground fire[7], as a commonly used commercial fire field model. Other available fire models have been reviewed by Galea[4] and Friedman[6], although the properties of each model and some of their capabilities were described only in general terms. A quantitative comparison of FLOW3D and JASMINE, both with each other, and as they compare to experimental results, has been performed by Kerrison et al[22]. This is important work, as the licence fees for even

a single commercial package stretch the resources of many institutions, and indeed concern has been raised about the availability of such models for the purposes comparative scrutiny[23]. Comparisons showed that both models overall made good predictions of the flow in a simple compartment fire, but that discrepancies occurred close to the boundaries of the enclosure, possibly as a result of the different formulations of the boundary conditions in the models.

The use of CFD models for modelling combustion and fire scenarios comprises only a portion of the overall field of applications for such models. Fluid dynamics encompasses a broad range of topics, including classic problems such as air flowing over an aircraft wing or water flow through a pipe. Combustion modelling is a particular class of fluid flow problem, the difficulty of which is compounded by the fact that the fluid being modelled is undergoing a change of composition and specific volume as it flows. Furthermore, heat transfer to and from the fluid is an important component of modelling combustion processes. CFD combustion modelling itself covers a broad range of subjects, with CFD models finding applications such as modelling the gasification of biomass[24] or coal[25], the operation of incinerators[26] and furnaces[27], or small scale phenomena such as the combustion of wood samples in a cone calorimeter[28]. Of interest in this thesis, though, is the enclosure fire, which as the name suggests is a fire which takes place in a confined region, with a limited number of openings (or possibly none) to the surroundings.

What is the role of field models in the modelling of enclosure fires? Much has been written about both the merits and shortcomings of zone and field models[3,4,6], although the usual consensus is that there is, and probably always will be, a need and a use for both. The role of the field model is to provide the detail which the zone model cannot, which in some cases may even provide insights into the nature of the fire itself. A good illustration of this is demonstrated in the modelling of the King's Cross Underground fire[7]. Field modelling was undertaken to determine if there were any aerodynamic effects which may have contributed to the rapid spread of the fire. This modelling led to the discovery of the so called "trench effect", whereby a flame in an inclined trench such as an escalator will tend to "adhere" to the floor of the trench. This effect was later verified experimentally.

This result perhaps encapsulates the philosophy of field models, in that it is the hope of the modeller that such results will be forthcoming, independently of what the modeller may be expecting to find. To use the trench effect as an example, if such an effect were known *before* the modelling was undertaken, then the temptation to the modeller may have been to ensure, by specification of input and boundary conditions, that such an effect was forthcoming, or even make the assumption *a priori*, as in the manner of zone models. On the other hand, results obtained from

modelling should not be accepted in blind faith. All modelling must be held up to scrutiny, and the cycle of model prediction and experimental verification, or experimental contradiction and model readjustment will inevitably continue, as it does with any scientific process.

It is perhaps the vision of present-day modellers that there will ultimately be a model capable of accurate, detailed, and comprehensive predictions of any arbitrary fire scenario; a "perfect" model. Such a model, as well as providing a detailed description of fluid phase phenomena, such as the concentration and composition of the products of combustion and their movement throughout the enclosure, would also include a physical description of the fuel, including the combustion behaviour of its constituent components. Also included would be the ignition characteristics, growth and spread behaviour of the flame, as well as the heat feedback from the products back to the burning fuel, and even the interaction of the fire environment with fire suppression systems such as sprinklers. Indeed, in a comprehensive model, the presence of walls or a ceiling would be optional, making them just as applicable to open fires as enclosure fires. Such a model does not yet exist*, and research continues in attempting to bring it about (including the development of the computing power required for its execution).

Most work currently undertaken in enclosure fire models does not attempt to include all the phenomena required in the "perfect" model, as many aspects are still unknown or untested. Rather, attention is normally focused in a particular study on one or a few aspects at a time. Since enclosure geometry is a variable factor, many modelling exercises, and the experiments undertaken to validate the models, are performed with a simple geometry, usually a rectangular enclosure[20,29,30,31], and often with a door placed centrally in one wall, creating a plane of symmetry[21,32,33]. The simplicity of the geometry makes independent experimental reproducability more likely, and therefore more open to scrutiny and critical assessment. The simplicity of the geometry also minimises the effects of the geometry itself, so that other phenomena can be investigated in a controlled fashion.

There are many examples of the specific modelling aspects studied with simplified geometry. Chow and Leung[32] have examined the effect of solid-wall boundaries, in order to compare two different treatments of near wall phenomena, namely the use of wall functions, and low Reynolds number turbulence models. It was concluded that the low Reynolds model produced a closer fit to available data, but that the method was more computationally expensive due to the fine spacing of the grid in the vicinity of the wall. Chow[34] also examined the effect of including combustion in the model, rather than specifying the fire as simply a heat source. It was found that while both

approaches produced similar temperature distributions, inclusion of the combustion model produced a more realistic flow profile through the compartment opening. This is to be expected, as the flow pattern depends on the volume change associated with the chemical reaction. It does highlight, however, that if ventilation flow rates are important to the application of the fire model, then combustion should be considered. Both modelling exercises by Chow were compared with data produced by Steckler et al[35], although it was noted that there were insufficient data acquired in the test to provide confidence in the validation of the model. Other issues raised included whether the absence of an adequate radiation model might also be a source of discrepancies.

The effect of thermal radiation on the flow field in a fire has been investigated by Kumar et al[20] for a simple rectangular enclosure. The study likewise used the flow data of Steckler et al[35], and investigated the effect the presence or absence of a radiation model has on the predictions of the flow rate. As might be expected, the inclusion of a radiation model improved the modelled predictions. The reason that it should be expected is the nature of thermal radiation. The radiant heat output of a hot body is proportional to the fourth power of the absolute temperature, so that radiant heat temperature becomes increasingly dominant as temperature increases. A fire plume is typically at a very high temperature (around 1000°C or higher), which renders radiation heat transfer a significant component of total heat transfer within the enclosure containing the fire plume. Lewis et al[36] also investigated the effect the inclusion of a radiation model has on the computed upper layer temperature in a compartment, also making comparisons with the experimental data of Steckler et al[35]. It was found that the inclusion of a radiation model improved the prediction of the flow temperatures in the upper region of the enclosure. The importance of accurate radiation heat transfer modelling has been touched upon here. As it forms a significant portion of the work presented in this thesis, a more detailed investigation of radiation heat transfer, and its role in CFD modelling, is left for Chapter 3.

Another feature of the study by Kumar et al. is the prediction of a "warm" layer sandwiched between the upper hot layer and lower cool layer, which accounted for anything up to 25% of the total outflow, when radiation was accounted for[20]. The layer was associated in the predictions with a relatively low fuel mixture fraction (and hence product concentration), although higher than the cool layer, and it was absorption of radiation by the products in this layer which was the mechanism attributed to its heating. A similar "smearing" of the hot and cold layers was also observed by Kerrison et al[22], although this was interpreted as a discrepancy rather than a feature. In this case, a *lack* of a radiation model was proposed as a possible source of the discrepancy. This appears to be

---

• nor, some may suspect, will it ever, at least to the satisfaction of all modellers.

borne out in the work of Lewis et al[36] who found that the inclusion of a radiation model improved the layer definition. Other mechanisms proposed by Kerrison et al for the layer smearing were inadequacies in the turbulence model, or false diffusion due to the upwind discretisation scheme[22]. The upwind scheme is a numerical mechanism employed to reduce numerical instability in flows which are strongly one-directional, and is described in detail by Isenberg and de Vahl Davis[37]. While it is unconditionally stable (i.e. the method will converge, regardless of the grid size and time step chosen), it does lead to a diffusion-like term ("false diffusion") which could feasibly produce the discrepancies observed by Kerrison et al. This effect is noted here, as it will be encountered again later in this thesis.

Another relatively simple geometry which has been investigated is the flow generated by a pool fire in a large wind tunnel[38,39]. Full scale experimental and modelling tests were undertaken to provide an understanding of the behaviour of fires in elongated enclosures, such as a ventilated mine roadway, or vehicular tunnel. The study yielded useful information regarding the flow rates required to prevent the buoyant backflow of products, as well as providing further validation opportunity for the code. The findings emphasise the importance of accurate radiation modelling of the smoke products, and of the critical role of buoyancy terms in k-ε turbulence equations, in successfully predicting the backflow phenomenon. This has similar implications for any model which attempts to make predictions of smoke spread in ventilated enclosures.

While simplified geometry is useful for validation exercises, the geometry of practical applications is often quite complex. Geometry is an important aspect of a fire scenario, and field modelling of more realistic enclosure geometries is undertaken both as further validation exercises of field models[3], and as a practical exercise in determining fire safety of a given enclosure. Whilst experimental data for complex geometries are useful, and efforts to continue their acquisition should be made, modelling exercises are not, and should not, be limited to cases for which experimental data are available. Validation for simple geometries should attribute confidence in a model's ability to make at least qualitative predictions of more complex geometries. For instance, Hadjisophocleous and Cacambouras[21] again use the data of Steckler et al.[35] to validate their code, then with the confidence of validation, explore the effect of several factors including opening size, location of the fire within the enclosure, and the presence of large internal objects in the enclosure. The predictions thus issue a challenge to the experimentalist for verification.

For complex geometries, the issue of constructing a grid for the calculation of the fire scenario becomes important. If the enclosure is a typical office or residential building, the geometry is likely to be rectilinear. Apart from removing walls and other obstructions from the flow region,

construction of the grid is otherwise straightforward. The flow equations in the model are typically discretised using a finite difference method[40], and take their simplest form in such co-ordinates, so that computational effort is minimised. On the other hand, enclosures which include walls not meeting at right angles, or that have curved surfaces, are more difficult to model. If a rectilinear grid is established for the finite difference method, then such surfaces will manifest themselves as step-like boundaries of the flow region. One remedy is to mathematically transform the non-rectilinear space into one that is rectilinear. The transformation results in additional terms appearing in the discretised equations. Another remedy is to fit the grid to the geometry, and to apply the finite element method to derive the governing equations of the flow. However, the equations are in a more complex form than for finite difference, so are computationally more demanding to solve. Ravichandran and Gouldin[26] performed a comparison of finite element and finite difference methods for an incinerator of complex shape. It was found that the finite element method produced more accurate results, and the solution showed less variation with mesh refinement, than the finite difference. However, the method was far more computationally intensive, especially when full combustion and turbulence was considered in the equations.

One of the greatest challenges still facing the development of field models is their so-called "validation". Kerrison et al[33] describe "validation" (with quotation marks) as the systematic comparison of predictions with experimental results. Hence, a model is presumably deemed to be "valid" if the comparisons are favourable. However, comparison is by no means a trivial exercise, as field models make predictions about thousands (even millions) of data points, whereas only a limited number of data points can be measured in an experiment (perhaps a thousand in an extensively instrumented steady state experiment where measuring devices are movable, and one or two hundred in unsteady fires where devices are likely to be fixed). Since comparison at every point is not feasible, agreement is usually sought at key locations, such as the centreline of the room of fire origin, or profiles of variables across the enclosure opening. If agreement between model and experiment is good at these key locations, then some confidence may be expressed about the modelling results at other locations.

The work presented in this thesis includes experiments conducted in a full-scale, multi room building, which was equipped with a large array of measuring instruments. It has been previously identified that such comprehensive full scale data are somewhat sparse, and that the emphasis on existing data has been for the validation of zone models[3,20]. Since the tests performed for this thesis were undertaken for the specific purpose of comparison with field models, a favourable comparison of modelling results with this experimental data should indicate a comparatively strong case for validation of the model. A useful exercise would be to repeat the modelling work with a

commercial fire field model such as JASMINE or FLOW3D for comparison, although such work is beyond the scope of this thesis.

2.2. COMPONENTS OF FIELD MODELLING

This section outlines the methodology used to formulate a fire field model. The description begins with the conservation equations which govern heat, mass and momentum transfer within a fluid. Following this is a description of additional components of a field model which are required for fire modelling applications, such as turbulence models and combustion models. Finally, a description is given of the numerical methods required to solve the basic conservation equations.

2.2.1. Conservation Equations

At the heart of field models lie the general conservation equations, the prototypal form of which is

$$\frac{\partial \phi}{\partial t} + \nabla \cdot \rho \boldsymbol{u} \phi = \nabla \cdot \Gamma_{\phi} \nabla \phi + S_{\phi} \qquad (2.1)$$

where ρ is the fluid density, $\boldsymbol{u}$ is the local fluid velocity, and $\phi(x,y,z,t)$ is the quantity which is being conserved. This quantity may be fluid momentum, temperature, concentration of a chemical species, or turbulence kinetic energy, amongst other properties, and in its general form is a function in three dimensions with time dependence.

As can be seen, there are four terms in Equation 2.1. Left to right, they are respectively the unsteady term, the advection term, the dispersion term, and the source term. The unsteady term involves the partial derivative with respect to the time variable, t, and describes the local rate of change of the species ϕ. When the system is invariant in time, or steady state, this term is zero. Such cases are often easier to solve than unsteady state problems. The advection term arises when the fluid is in motion, characterised by a local velocity vector $\boldsymbol{u}$. If the fluid is stagnant, this term disappears (as it also does when considering cases such as heat flow through solids). The third term in the equation is the dispersion term. This arises from a spatial gradient, $\nabla\phi$, of the quantity in question. When a non-zero gradient exists, the quantity will be transferred in the direction of the gradient, by an amount determined by the term Γ_{ϕ}. For instance, when considering heat transfer by conduction, this term is the thermal conductivity of the fluid. Γ_{ϕ} may be a constant, or it may be a

function of ϕ itself, or it may have spatial and temporal dependencies. If it is a constant, the third term may be rewritten

$$\nabla \cdot \Gamma_\phi \nabla \phi = \Gamma_\phi \nabla^2 \phi \tag{2.2}$$

The source or sink term, S_ϕ, corresponds to the amount of the quantity being produced or removed in situ, rather than being transported into or away from the point in question. Such terms may arise, for instance, with thermal energy conservation, where radiant heat is being absorbed or emitted, or in a species mass conservation equation when a particular chemical species is being produced or consumed by a chemical reaction.

In the special case when ϕ is the local momentum of the fluid, Equation 2.1 is known as the Navier-Stokes equation, developed over 150 years ago[4]. The Navier-Stokes equation may be expressed in suffix notation by the equation

$$\rho \frac{\partial u_i}{\partial t} + \rho u_j \frac{\partial u_i}{\partial x_j} = -\frac{\partial p}{\partial x_i} + \frac{\partial t_{ji}}{\partial x_j} + \frac{1}{3}\frac{\partial t_{jj}}{\partial x_i} \tag{2.3}$$

where p is the pressure, and t_{ij} is the viscous stress tensor, given by

$$t_{ij} = 2\mu s_{ij} \tag{2.4}$$

where μ is the molecular viscosity, and s_{ij} is the strain-rate tensor, given by

$$s_{ij} = \frac{1}{2}\left(\frac{\partial u_i}{\partial x_j} + \frac{\partial u_j}{\partial x_i}\right) \tag{2.5}$$

There are four unknown quantities appearing in the Navier-Stokes equation, namely the three velocity components and pressure. However, there are only three equations in Equation 2.3, one for each value of i, so there are only three equations for four unknowns. An additional equation is required, namely the continuity equation, given by

$$\frac{\partial \rho}{\partial t} + \nabla \cdot (\rho \boldsymbol{u}) = 0 \tag{2.6}$$

If the flow is incompressible, the density is constant, and Equation 2.6 simplifies to

$$\nabla \cdot \boldsymbol{u} = 0 \tag{2.7}$$

Also for incompressible flows, the term at the far right of Equation 2.3 vanishes.

2.2.2. Turbulence

Solving Equation 2.1 is reasonably straightforward when the velocity is laminar throughout the control volume. However, in many flow problems, such as those involving extensive buoyancy driven flows which occur in building-fires, turbulent flow is almost always present. Turbulent flow is disorderly and chaotic in nature, with the fluid flowing in a dynamic, ever-changing pattern of whorls and eddies, which are present on scales down to a microscopic level at which the viscosity of the fluid dominates the smallest eddies[41]. With the current computer technology, CFD models cannot resolve down to this small scale, especially when dealing with generic full-scale building-fires.

The random nature of turbulence may be dealt with in a statistical manner, using the methods first developed by Reynolds in 1895. The velocity (hence its momentum) of a fluid flowing turbulently at a given point may be divided into two components; the mean velocity, and the variation about the mean, due to the random fluctuations in velocity resulting from the turbulence. This is expressed in the following notation

$$u_i = U_i + u_i' \tag{2.8}$$

where u_i is the instantaneous velocity, U_i is the time-averaged velocity, and u_i' the fluctuating velocity. The corresponding fluctuations in pressure, p, can be expressed in a similar fashion. Since it is the time-averaged conditions which are of concern in fluid modelling, Equation 2.8 is substituted into the Navier-Stokes equation (Equation 2.3), and the time average is taken, to yield the Reynolds-averaged Navier-Stokes equation. This is best illustrated for incompressible fluids. In this case, the Reynolds-averaged Navier-Stokes equation is given by

$$\rho\frac{\partial U_i}{\partial t} + \rho U_j\frac{\partial U_i}{\partial x_j} + \overline{\rho u_j'\frac{\partial u_i'}{\partial x_j}} = -\frac{\partial P}{\partial x_i} + \frac{\partial T_{ji}}{\partial x_j} \tag{2.9}$$

where T_{ij} is similar to the corresponding tensor, t_{ij}, in Equation 2.3, except that it involves the mean velocity U_i in place of the instantaneous velocity, u_i. The bar above the third term denotes that it has been time-averaged. It can be seen that Equation 2.9 is very similar to Equation 2.3, except for the term involving u_i'. If the continuity equation for incompressible fluids (Equation 2.7) is taken into account, and terms are rearranged, then Equation 2.9 may be expressed in conservation form, as given by

$$\rho\frac{\partial U_i}{\partial t} + \rho U_j\frac{\partial U_i}{\partial x_j} = -\frac{\partial P}{\partial x_i} + \frac{\partial T_{ji}}{\partial x_j} - \overline{\rho u_i' u_j'} \tag{2.10}$$

The last term is known as the Reynolds stress tensor, denoted τ_{ij}. As it is symmetric, there are 6 independent terms, all of which are unknown. These unknowns are in addition to the four time averaged unknowns, without any increase in the number of equations; in other words, there are now more unknowns than equations. The system of equations is said to be unclosed.

In order to close the system of equations, it is necessary to make some approximations for the unknown quantities, based on known flow properties. Some of these approximations have an empirical basis, while others are based principally on a dimensional argument. The first step in this procedure is to introduce the quantity *k*, the turbulence kinetic energy, defined by

$$k = \frac{1}{2}\overline{u_i' u_i'} = -\frac{1}{2\rho}\tau_{ii} \tag{2.11}$$

Algebraic manipulation of products of fluctuating quantities with the Reynolds-averaged equation yield the following transport equation for the turbulence kinetic energy[42]

$$\rho\frac{\partial k}{\partial t} + \rho U_j \frac{\partial k}{\partial x_j} = \tau_{ij}\frac{\partial U_i}{\partial x_j} - \rho\varepsilon + \frac{\partial}{\partial x_j}\left[\mu\frac{\partial k}{\partial x_j} - \frac{1}{2}\overline{\rho u_i' u_i' u_j'} - \overline{p' u_j'}\right] \tag{2.12}$$

where ε is the rate of dissipation of turbulence kinetic energy per unit mass, defined by

$$\varepsilon = \nu\overline{\frac{\partial u_i'}{\partial x_k}\frac{\partial u_i'}{\partial x_k}} \tag{2.13}$$

However, there are still several unknowns in Equation 2.12, although there are physical interpretations which can be attributed to these terms. It is a common practice to assume that the Boussinesq approximation holds for the Reynolds stress tensor[42], i.e.

$$\tau_{ij} = 2\mu_T S_{ij} - \frac{2}{3}\rho k\delta_{ij} \tag{2.14}$$

where μ_T is the eddy viscosity. A further approximation is made for the last two terms in the brackets of Equation 2.12, namely that the sum of the two terms behaves as a gradient-transport process[42], described by

$$\frac{1}{2}\overline{\rho u_i' u_i' u_j'} + \overline{p' u_j'} = -\frac{\mu_T}{\sigma_k}\frac{\partial k}{\partial x_j} \tag{2.15}$$

where σ_k is the Prandtl number for turbulence, which in most instances is chosen to be a constant. With these approximations, Equation 2.12 can be written in the form

$$\rho\frac{\partial k}{\partial t} + \rho U_j \frac{\partial k}{\partial x_j} = \tau_{ij}\frac{\partial U_i}{\partial x_j} - \rho\varepsilon + \frac{\partial}{\partial x_j}\left[\left(\mu + \frac{\mu_T}{\sigma_k}\right)\frac{\partial k}{\partial x_j}\right] \tag{2.16}$$

This turbulence transport equation is common to many closure methods. There are two remaining unknowns in the system of equations which need to be accounted for to complete closure. They are the dissipation, ε and turbulence length scale, l. Dimensional arguments suggest that these terms are related to turbulence kinetic energy by

$$\varepsilon \propto \frac{k^{\frac{3}{2}}}{l} \tag{2.17}$$

One equation models are so called because they use only the turbulence transport equation. Closure is completed by taking Equation 2.17 and multiplying the right hand side by a constant of proportionality, which is another closure coefficient. The remaining unknown in the turbulence transport equation, turbulence length scale, must be specified by some means. This usually requires some knowledge of the behaviour of the turbulence in the problem of interest.

Two equation models, on the other hand, introduce a second equation which calculates either the turbulence length scale, or an equivalent. The most commonly used of the two-equation models is the k-ε model. In this model, an equation for the transport of dissipation, ε, is derived by a similar methodology to the turbulence transport equation. In doing so, a plethora of additional terms is generated, for which further closure approximations must be made[42]. In summary, the transport equation for the dissipation rate is given by

$$\rho\frac{\partial \varepsilon}{\partial t}+\rho U_j\frac{\partial \varepsilon}{\partial x_j}=C_{\varepsilon 1}\frac{\varepsilon}{k}\tau_{ij}\frac{\partial U_i}{\partial x_j}-C_{\varepsilon 2}\rho\frac{\varepsilon^2}{k}+\frac{\partial}{\partial x_j}\left[\left(\mu+\frac{\mu_T}{\sigma_\varepsilon}\right)\frac{\partial \varepsilon}{\partial x_j}\right] \tag{2.18}$$

and the eddy viscosity given by

$$\mu_T=\rho C_\mu\frac{k^2}{\varepsilon} \tag{2.19}$$

where σ_ε, $C_{\varepsilon 1}$, $C_{\varepsilon 2}$, and C_μ are closure coefficients.

The k-ε model in the form given closes the system of equations, and provides a complete description of the turbulent flow; complete in this context meaning that the turbulence length scale is calculated rather than specified. It should be noted, however, that it is difficult to experimentally measure some of the properties appearing in the dissipation transport equation, nor is there a great deal of certainty in the closure approximations[42]. Additionally, the model assumes isotropy in the properties of the turbulence. This assumption of isotropy is not particularly valid in flow near walls or in regions where turbulent transport is dominated by large eddies, for instance. Consequently, attempts are made to produce more sophisticated k-ε models which deal with anisotropy in certain situations[43]. Other models attempt to avoid some or all of the closure assumptions and develop

further equations to achieve closure. Nevertheless, the k-ε model presented here is a widely-used all-purpose model which is relatively straightforward to incorporate in CFD computer models.

2.2.3. Combustion

In building-fires, most combustion occurs in turbulent diffusion flames. In other words, the volatiles leaving a burning fuel surface will not be pre-mixed with oxygen, so combustion of the volatiles cannot occur until the two species in the flame region are mixed. Here diffusion refers to the mixing which occurs by turbulence induced by entrainment in the existing flame, rather than by molecular diffusion. Since the time scales involved in turbulent mixing are much longer than those involved in the actual reaction, combustion rates are dominated by the mixing rate rather than by chemical kinetics. This mechanism is encapsulated in several different combustion models, which interface with the k-ε model, or other models for turbulence.

Before combustion models are considered, the distribution of fuel and oxidant needs to be determined. This is achieved by considering the time-mean fuel mixture fraction, f, which takes the value 1 for pure fuel, and 0 for pure oxidant. The oxidant is typically the oxygen in air, which is approximately 23% oxygen by mass; the remaining component being considered as an inert diluent. The distribution of fuel mixture fraction is determined using the conservation equation (Equation 2.1). A calculation is then performed to determine whether some or all of the fuel is consumed, according to reactions described below. The reaction will release thermal energy, which appears as a source term in the conservation equation for enthalpy, as well as create product gases. Since mass is conserved in a chemical reaction, the only change in distribution as far as the model is concerned is a change in the number of mole of gaseous species, which affects the density distribution.

While some applications may be concerned with the production of a particular species (such as the oxides of nitrogen or sulphur), and may be following the progress of many intermediate species involved in several reactions, in enclosure fires the primary interest, from a fire safety point of view, is in the carbonaceous products, namely carbon dioxide, carbon monoxide, and solid carbon. There are several reasons for this; carbonaceous products, in the form of smoke, are the main cause of casualties in fire, so their overall distribution is of interest to the modeller. Also, solid carbon, or soot, is the main source of visual obscuration which impedes the egress of occupants in a real fire situation, as well as being very important in radiant heat exchange. The combustion is usually modelled with a simple one step reaction, as this reduces the complexity of attempting to keep track

of intermediate radical species and so forth. This requires an empirical expression to determine the relative proportions of the products of the reaction.

For a generic organic fuel with the empirical formula $C_mH_nO_pN_q$, the stoichiometric reaction is written

$$C_mH_nO_pN_q + (\frac{n}{4} - \frac{p}{2})O_2 \xrightarrow{\Delta H_c} mCO_2 + \frac{n}{2}H_2O + \frac{q}{2}N_2 \qquad (2.20)$$

where ΔH_c is the heat of combustion. Stoichiometric in this context means that the products are in their most stable form[44]. For most common fuels (with the generic formula given above) these are carbon dioxide, water, and elemental nitrogen. However, depending on the local temperature and the relative concentrations of oxygen and fuel, the combustion of the carbonaceous component of the fuel may not be complete. More generally, the equation can be written

$$C_mH_nO_pN_q + (a + \frac{b}{2} + \frac{n}{4} - \frac{p}{2})O_2 \xrightarrow{\Delta H_c} aCO_2 + bCO + (m - a - b)C + \frac{n}{2}H_2O + \frac{q}{2}N_2 \qquad (2.21)$$

where ΔH_c is the effective heat of combustion. In many instances, the carbon monoxide to carbon dioxide ratio is of primary interest, which in this case is given by

$$\frac{Y_{CO}}{Y_{CO_2}} = \frac{bM_{CO}}{aM_{CO_2}} = \frac{28b}{44a} \qquad (2.22)$$

where Y_X is the mass concentration of the species in question. For convenience, the equivalence ratio, ϕ_e, is defined as the fuel to oxygen mass ratio, normalised by dividing by the stoichiometric fuel to oxygen ratio. Thus, for fuel-rich fires, ϕ_e will be greater than 1, and between 0 and 1 for fuel-lean fires. Tsuchiya[45] has noted that the CO/CO_2 ratio for wood fires in large compartments varies approximately linearly with ϕ_e. In other words, the more fuel rich the fire, the more incomplete the combustion will be. Gottuk et al[46] point out that the ratio is case sensitive; the reactions which create and oxidise carbon monoxide occur mainly in the hot region of the fire plume, so the carbon monoxide may be quenched upon entering a cooler upper layer and not react further. If there is a well developed hot layer present, this will increase the combustion efficiency in the flame, and allow further post-flame reaction of carbon monoxide, resulting in lower yields.

Based on observations of polyurethane fires, Takeda and Yung[9] make the assumption that the CO/CO_2 ratio is dependent only on the local oxygen concentration, given by

$$\frac{28b}{44a} = \frac{23}{60Y_{O_2}} \qquad (2.23)$$

Implicit in this equation is that oxygen displacement may be due to either fuel enrichment, which results in a high equivalence ratio, or the combustion products, as for example in a fire in a sealed room.

The other major combustion product of concern in building-fires is soot. There are two main sources of carbonaceous particles in combustion products. The first is the charred residue of particulate solid or aspirated liquid fuels, which retain to some extent the size and structure of the original unburnt particles. The second, which is more prevalent in building-fires where the fuel source is usually not deliberately pulverised or aspirated, is the high temperature formation of large aromatic hydrocarbon molecules under conditions of low oxidant concentration. The chemical composition of these large molecules is mostly carbon with smaller amounts of hydrogen, so it can be effectively treated as solid carbon in an amorphous form. The mechanism appears to be the formation of acetylene by dissociation and dehydrogenation of the fuel, followed by polymerisation of the acetylene into polyacetylenes and finally aromatic compounds which build up into graphite-like layers.[47] Solid carbon should form by this mechanism when $m>2y$ in the following equation

$$C_mH_n + yO_2 = 2yCO + \frac{n}{2}H_2 + (m-2y)C \qquad \textbf{(2.24)}$$

The production of soot, and its combustion within a turbulent diffusion flame, may also be modelled by the eddy dissipation model[48], described below. Soot particles form in a turbulent diffusion flame from radical nuclei in fuel-rich eddies, and combustion of the soot and radical nuclei is controlled more by eddy dissipation than by reaction kinetics. The "radical nuclei" are presumably analogous to the polyacetylene compounds mentioned by Goldberg[47].

The time-mean fuel mixture fraction and a one-step reaction equation are alone not sufficient to fully describe the combustion taking place in a turbulent diffusion flame. In a turbulent fluid, the velocity is not the only property exhibiting fluctuating behaviour. The fuel concentration itself fluctuates about the mean value. The fluctuations in turn affect the extent of the reaction zone, radiation transport, and composition of reaction products[49]. There are two main ways of modelling the consequences of the fluctuations, which are described here.

The first is the eddy dissipation model of combustion[48], which is a version of the eddy break up model[50]. It is based on the premise that the mixing of the fuel and oxygen by turbulence is much slower than the chemical kinetics associated with the reaction itself. The fuel and oxygen are constrained within eddies, and it is the dissipation of both these collections of eddies which allows mixing of the two species. When the local oxygen concentration is high, the combustion rate will be limited by the dissipation of fuel eddies, which may be given by the equation

$$R = Ac_f \frac{\varepsilon}{k} \tag{2.25}$$

where A is a constant related to the flame structure and chemical reaction rate, and c_f is the local time-mean fuel concentration. A similar equation may be written for the case where the local fuel concentration is high, and dissipation of oxygen eddies limits the reaction. The equation in this case is

$$R = A\frac{c_{O_2}}{r_0}\frac{\varepsilon}{k} \tag{2.26}$$

where r_0 is the stoichiometric oxygen requirement to react with a unit mass of fuel.

There is a third limiting factor to the combustion reaction. The combined oxygen and fuel requires energy to initiate the reaction, provided by the hot reaction products. The hot products are themselves initially constrained within eddies, so the dissipation of hot product eddies also drives the reaction. The equation for the dissipation rate of eddies is given by

$$R = A \cdot B\frac{c_p}{(1+r_0)}\frac{\varepsilon}{k} \tag{2.27}$$

where B is a constant associated with the reaction. Whichever of these three dissipation rates is proceeding the slowest will dominate the local combustion rate.

The second method of modelling the fluctuations is to use the method of variance of fluctuations in mixture fraction, or the g-equation. In a fashion analogous to the fluctuating velocity for turbulence modelling, the concentration fluctuation, g, is defined by

$$g \equiv \left(f - \overline{f}\right)^2 \tag{2.28}$$

Transport of the variance of fluctuations is calculated using Equation 2.1, which in this case has the form

$$\rho\frac{\partial g}{\partial t} + \rho U_i \frac{\partial g}{\partial x_i} = \frac{\partial}{\partial x_i}\frac{\mu_T}{\sigma_g}\frac{\partial g}{\partial x_i} + C_{g1}\left(\frac{\partial f_i}{\partial x_i}\right)^2 - C_{g2}\rho a_g \frac{\varepsilon}{k} \tag{2.29}$$

where σ_g is the Prandtl-Schmidt number for g, C_{g1} and C_{g2} are constants of closure, f is the time mean fuel concentration, and a_g is the acceleration due to gravity. Hence, the fluctuating concentrations are distributed about the time-mean value; a Gaussian distribution is assumed in most cases[38,49]. Given the time-mean value and variance, a probability density function for the fuel mixture fraction, f, may be specified. A particular value of f leads to a particular composition of

products and amount of heat release. The overall product and heat release is found by integrating over the whole distribution. Since integration is computationally expensive, especially if it must be performed at every point in the region being modelled, the Gaussian distribution is typically sampled at selected points, and the product and heat outcomes averaged.

2.3. NUMERICAL HEAT AND MASS TRANSFER SOLUTION METHOD

The general conservation equations have been formulated for functions that are continuous in both time and space. Except for a few special cases, the equations cannot be solved analytically, and numerical methods must be resorted to in order to compute a solution. Numerical methods solve the equations at discrete points in space and time rather than continuously. In other words, the equation for the flow variable ϕ is not solved; rather, the continuous equations are approximated and solved at selected locations. The region of interest is divided into a number of "control volumes", and the quantities of interest follow an assumed profile between one control volume and the next. The discrete version of Equation 2.1 may be determined in one of two ways; either the general conservation equations are derived again using finite volumes rather than infinitesimal volumes, or Equation 2.1 is expanded via a Taylor series about the point of interest, using the discrete grid size for the interval of expansion (see Equation 5.41). Overall, it is the practical computer solution of the general conservation equations by this or similar numerical methods which constitutes the study of computational fluid dynamics.

The key elements of CFD are outlined in a text written by Patankar[19], and indeed, the encoding of the methods of Patankar and other collaborators forms the basis of many CFD models. As the methods incorporated in the CFD model used throughout the work presented in this thesis closely follow the general method outlined by Patankar, a summarised description is presented in this section.

The first step in a numerical solution is to establish the domain over which the equations will be solved; that is, the distribution of discrete points at which the equations will be evaluated, and the control cell surrounding each point. The choice of grid will depend on the problem and any symmetries involved in the geometry. However, since the equations are in a simple and familiar form when expressed in Cartesian co-ordinates, and the terms appearing in the numerical methods are likewise simple in this situation, a rectilinear grid will be considered here. Fortunately, since much enclosure architecture is rectilinear, particularly that associated with domestic and office buildings, a rectilinear grid is usually quite adequate for modelling purposes. It also has the added

advantage that encoding of the conservation equations is simpler, and therefore less time and resources is required for computation, when the equations are expressed in Cartesian coordinates.

In the case of a rectilinear grid, the control volumes are simply an array of cuboids arranged in an orthogonal fashion. The points where the equations are evaluated lie within each control volume, and lie along lines parallel to the Cartesian axes. To illustrate this, a point and its six neighbours, and some of the dimensions associated with the geometry, are shown in Figure 2.1, along with the "half-cell" associated with the boundary. Once the grid is defined, the conservation equation is integrated over each control volume.

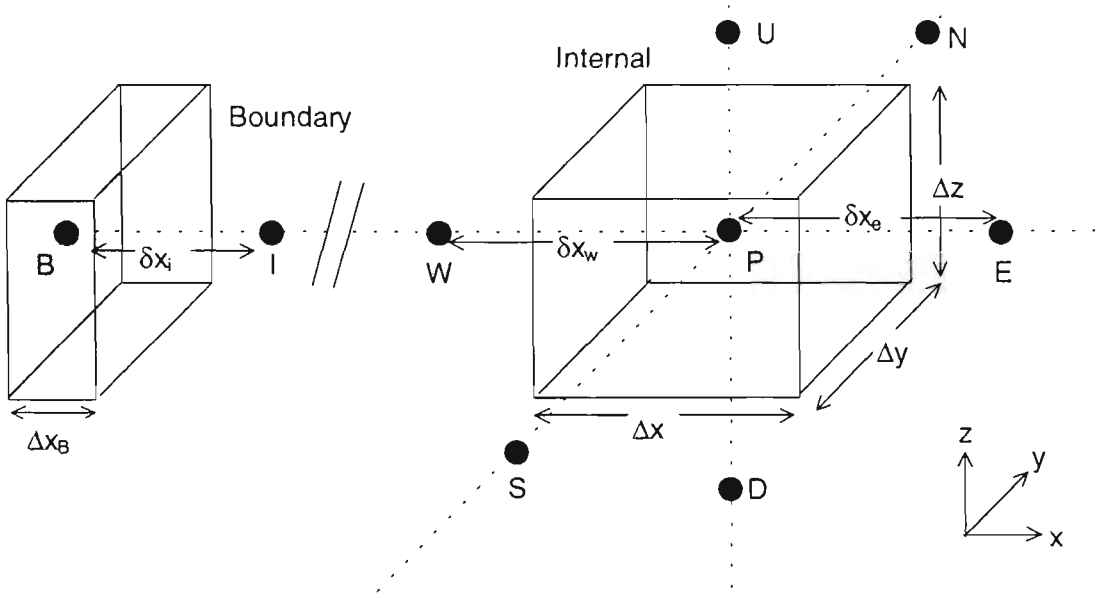

Figure 2.1 Control cell in Cartesian co-ordinates

2.3.1. Steady One-Dimensional Heat Conduction

As a simple example, consider the equation for one-dimensional steady conduction in a solid. Since there is no unsteady term, nor any convection, the equation is given by

$$\frac{d}{dx}\left(k\frac{dT}{dx}\right)+S=0 \qquad (2.30)$$

where k is the thermal conductivity of the solid. If the (internal) control volume in Figure 2.1 is taken to be of unit length in the y and z directions, then integrating Equation 2.30 over this control volume gives the equation

$$\left(k\frac{dT}{dx}\right)_e-\left(k\frac{dT}{dx}\right)_w+\int_w^e S\,dx=0 \qquad (2.31)$$

where h is the heat transfer coefficient. If the temperature is known or given, further calculations are obviously not required. When the temperature is not given, it is necessary to consider an additional discretised equation at the boundary. This is done by considering the half-control cell as shown in Figure 2.1. If the heat flux from the boundary is given by q_B, and the heat flux from the internal cell I to the half-cell as calculated above for internal cells, then integrating Equation 2.30 over the half cell gives the discretised equation

$$q_B - \frac{k_i(T_B - T_I)}{\delta x_i} + (S_C + S_P T_B)\Delta x_B = 0 \tag{2.37}$$

Since a prescribed flux is not used in any of the modelling in this thesis, only the heat transfer coefficient case is given here. Substituting Equation 2.36 into Equation 2.37 and gathering terms, the discretised equations for the boundary may be written

$$a_B T_B = a_I T_I + b \tag{2.38}$$

where

$$\begin{aligned} a_I &= \frac{k_i}{\delta x_i} \\ a_B &= a_I - S_P \Delta x_B + h \\ b &= S_C \Delta x_B + h T_{solid} \end{aligned} \tag{2.39}$$

2.3.2. Unsteady Heat Conduction

Consider now the inclusion of the unsteady term in the heat conduction equation, given by

$$\rho c \frac{\partial T}{\partial t} = \frac{\partial}{\partial x}\left(k \frac{\partial T}{\partial x}\right) + S \tag{2.40}$$

Integration of the equation must be performed over the time interval t to $t+\Delta t$, as well as over the control volume. This introduces additional unknowns into the discretised equations, namely the new temperatures at time $t+\Delta t$. As with the spatial variation of T, an assumption of how T varies from t to $t+\Delta t$ must be made. If the assumption that the (known) old temperatures prevail up until time $t+\Delta t$, the temperature T_P may be expressed in terms of the old temperatures, and no new unknowns are generated. This is known as the explicit scheme; the new temperatures are given explicitly in terms of known values. However, the explicit scheme may lead to numerical instabilities if certain conditions are violated, particularly if the time step is not sufficiently small (this is discussed in further detail in Chapter 4). As a consequence, it is customary to include the (unknown) new temperatures in some form in the discretised equation. One such scheme is the

Crank-Nicholson scheme, which assumes a linear variation between old and new temperatures. This scheme is quite accurate for small time steps, but loses accuracy and possibly stability if a larger time step is used[19]. The other scheme widely used is the fully implicit scheme, whereby the new temperature is assumed to prevail over the entire time step. The implicit scheme has the advantage of unconditional stability for any time step, so that relatively large time steps can be used, which is useful for simulations of long timespans.

The fully implicit discretised equation for unsteady one-dimensional heat conduction is identical to Equation 2.34, and the coefficients a_E and a_W are likewise identical. The difference is in the other terms, which are given by

$$\begin{aligned} a_P^0 &= \frac{\rho c \Delta x}{\Delta t} \\ a_P &= a_E + a_W + a_P^0 - S_P \Delta x \\ b &= S_C \Delta x + a_P^0 T_P^0 \end{aligned} \qquad (2.41)$$

where the superscript '0' refers to the old value. The system of equations is solved using the Thomas algorithm with appropriate boundary conditions. The discretised equation is readily generalised to three dimensions thus:

$$a_P T_P = \sum_I a_I T_I + b \qquad (2.42)$$

where I in this case refers to a general co-ordinate, and is summed over the six directions E, W, N, S, U and D, and

$$\begin{aligned} a_I &= \frac{k_i}{\delta x_i} \Delta x_j \Delta x_k \\ a_P^0 &= \frac{\rho c \Delta x \Delta y \Delta z}{\Delta t} \\ a_P &= \sum_I a_I - S_P \Delta x \Delta y \Delta z \\ b &= S_C \Delta x \Delta y \Delta z + a_P^0 T_P^0 \end{aligned} \qquad (2.43)$$

where the j and k subscripts refer to the two directions perpendicular to I. For example, when I is east, x_j and x_k are y and z respectively.

However, the Thomas algorithm is not so readily adapted to three dimensions. In order to solve the implicit equations in three dimensions, the old values of temperature need to be used, at least at an interim step. The Gauss-Seidel point-by-point method is perhaps the simplest way of doing this; each point is visited in a certain order, and the new temperature calculated from 2.42 using whatever values of the neighbouring temperatures T_I are in computer storage. One full sweep of the

region under consideration represents one iteration. However, this method is slow to converge, considering that boundary information is only transmitted to the centre one grid point per iteration.

The next level of complexity is represented by the line-by-line method. This method combines the Gauss-Seidel method and the Thomas algorithm. A line is chosen in a particular direction, and the temperatures along the line solved using the Thomas algorithm, using the current values from the neighbouring lines. The process may be repeated for lines in the other directions. This method has the advantage that boundary conditions are transmitted to the interior in a single timestep. As this is the method used in CESARE-CFD, this will be described in more detail in Section 2.4.4.

Another line-by-line method which uses implicit methods is the Alternating Direction Implicit (ADI) method[51]. This differs from the conventional line-by-line method in that the timestep is divided into three intervals (or two for the two dimensional case), and the intermediate values apply to the intermediate interval, rather than to the beginning or the end of the time interval. The additional complexity and the need to store intermediate values makes this method somewhat more computationally intensive than the more conventional line-by-line method.

2.3.3. Steady Convection and Diffusion

Returning to the steady one-dimensional case, but now considering now a general flow variable ϕ in the presence of a given flow field, u. Since the velocity field is now being considered, the continuity equation (Equation 2.6) must also be considered. As the flow is steady, this is given by

$$\frac{d}{dx}(\rho u) = 0 \tag{2.44}$$

Taking continuity into account, the conservation equation may be written

$$\rho u \frac{d\phi}{dx} = \frac{d}{dx}\left(\Gamma \frac{d\phi}{dx}\right) \tag{2.45}$$

By the same process as discussed earlier, Equation 2.45 is integrated over the control volume, and the discretised equation obtained. If the following definitions are made;

$$F \equiv \rho u, \qquad D \equiv \frac{\Gamma}{\delta x} \tag{2.46}$$

then the terms in the discretised equation (Equation 2.34 without the source term) are given by

$$a_E = D_e - \frac{F_e}{2}$$
$$a_W = D_w + \frac{F_w}{2} \qquad (2.47)$$
$$a_P = a_E + a_W - (F_e - F_w)$$

However, since the velocities u_e and u_w can be either negative or positive, the terms a_E and a_W may become negative for some values, which can lead to numerical instability. Thus, various methods have been proposed to overcome potential instabilities, including the upwind, exponential, hybrid, and power-law schemes, which are described in Patankar[19]. Patankar recommends the power-law scheme, and indeed this method is used in CESARE-CFD, so it will be described here. An optional alternative in CESARE-CFD is to use a quadratic upwind (QUICK) scheme[40], although this scheme was not used in any of the simulations presented in this thesis, so it is not described here. The QUICK scheme results in less numerical dispersion than the power-law scheme, but at the expense of increased computational intensity.

The power-law scheme is based on the fact that Equation 2.45 has an exact solution for a constant diffusion gradient term Γ. The exact solution contains exponential terms, which are computationally intensive, so instead a power-law curve is used, which follows the exponential curve very closely, but which uses algebraic terms which are less computationally intensive. To compute the terms in the discretisation equation, it is first useful to define the Peclet number, P, which is given by

$$P = \frac{F}{D} \qquad (2.48)$$

which may be considered as the ratio of the strengths of convection and diffusion. The power-law scheme is then embodied in the following function

$$A(|P|) = \max\left[0, (1 - 0.1|P|)^5\right] \qquad (2.49)$$

The coefficients of the discretisation are then given by

$$a_E = D_e A(|P_e|) + \max(-F_e, 0)$$
$$a_W = D_w A(|P_w|) + \max(F_w, 0) \qquad (2.50)$$
$$a_P = a_E + a_W - (F_e - F_w)$$

Including the source and unsteady terms, the terms of the discretisation equation in three dimensions (Equation 2.42) for a given velocity field may finally be expressed as

$$
\begin{aligned}
a_I &= D_i A\left(|P_i|\right) + \max\left(-1^n F_i, 0\right) \\
a_P^0 &= \frac{\rho_P^0 \Delta x \Delta y \Delta z}{\Delta t} \\
b &= S_C \Delta x \Delta y \Delta z + a_P^0 \phi_P^0 \\
a_P &= \sum_I a_I + a_P^0 - S_P \Delta x \Delta y \Delta z
\end{aligned}
\tag{2.51}
$$

where n is any odd integer for the E, N and U directions, and any even integer for the others, and the convective and diffusive terms are given by

$$
F_i = (\rho u)_i \Delta x_j \Delta x_k, \qquad D_i = \frac{\Gamma_i}{\delta x_i} \Delta x_j \Delta x_k \tag{2.52}
$$

where the indices j and k are defined above.

2.3.4. Variable Flow Field

The terms in the discretised equation have been derived for the specified flow field. However, the point of most field modelling work is to determine the flow field itself, as the field is seldom known. In fact, the techniques and equations presented so far are almost in a form which can be used to solve the momentum equation. Even the convective term which contains the momentum explicitly is analogous to the heat equation with a temperature dependent conduction coefficient, which the techniques deal with. The problem arises from the presence of the pressure field, p. The methods can solve the momentum equations for a given pressure field, but like the flow field, the pressure field is seldom known, and must likewise be solved.

Discretisation of the pressure field about the same points as the other flow variables leads to other problems. The usual central difference discretisation of the pressure term $\partial p/\partial x_i$ for the case where the control volume faces lie halfway between points leads to an expression for the momentum which contains the pressure difference between alternate points rather than between adjacent points. Thus, if the pressure is the same at alternate points and much higher or lower in the middle, there will be no net calculated pressure driving the flow, whereas in actuality there should be a significant driving force either into or out of the control volume. The remedy is to calculate the three velocity components, u, v, w, on a grid which is staggered with respect to the rest of the flow variables, including pressure. A typical control volume for the u component is the shaded region shown in Figure 2.2. As can be seen in the diagram, the velocity cell boundaries coincide with the control cell for the other flow variables in the y (and z) direction, but are staggered in the x direction.

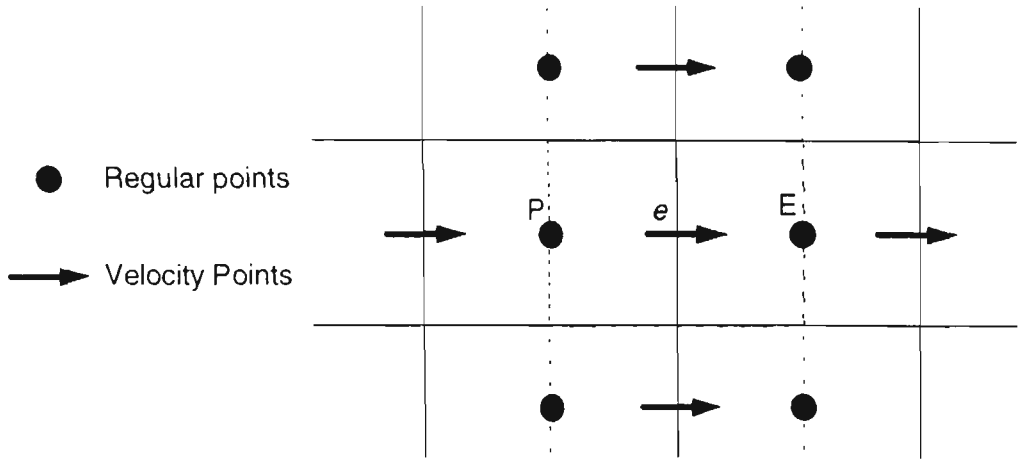

Figure 2.2 Control volume for velocity component u

A similar principle can be applied for the v and w components of the velocity; control cell centres are located at the centre of the north and south faces in the case of the v component, and in the centre of the top and bottom faces in the case of the w component. The advantage of the staggered grid is that the velocities are driven by pressure difference at adjacent grid points rather than alternate points. The staggered grid also helps overcome similar problems with the velocity components in the discretisation of the continuity equation.

With the staggered grid established, the discretised equation for the u velocity component is given by

$$a_e u_e = \sum_I a_I u_I + b + (p_P - p_E)A_e \tag{2.53}$$

where I refers to the six neighbouring velocity points (four of the points in the x-y plane are represented by the arrows in Figure 2.2) and A_e is the area of the east face of the control cell, which in the three-dimensional case is $\Delta y \Delta z$. Similar equations may be written for the other two velocity components, i.e.

$$\begin{aligned} a_n v_n &= \sum_I a_I v_I + b + (p_P - p_N)A_n \\ a_u w_u &= \sum_I a_I w_I + b + (p_P - p_U)A_u \end{aligned} \tag{2.54}$$

The coefficients a_I are calculated from the terms given in Equation 2.51, where the diffusion term Γ for momentum is the viscosity of the fluid. The coefficients are dependent on quantities such as density which are calculated at the main grid points. In order to use Equation 2.53 the quantities must be interpolated with an appropriate weighting between the two main grid cells which the velocity control cell overlaps.

As mentioned already, the momentum equations can only be solved if the pressure field is given or guessed. If an incorrect field is used, the resulting velocity field will not satisfy continuity. However, an initial estimate may be improved upon by using iterative methods. Before proceeding with numerical detail, an algorithm for solving the momentum equations will be described qualitatively. The algorithm is known as the SIMPLE algorithm, which is an acronym for Semi-Implicit Method for Pressure-Linked Equations (significance of the term semi-explicit is discussed below).

The SIMPLE algorithm begins with a guessed pressure field. From this, the momentum equations are solved to produce an "interim" velocity field, which as noted will not in general satisfy the continuity equation. A correction of the pressure field is performed, so that corresponding corrected velocities do satisfy continuity. If this corrected pressure turns out to be sufficiently close to zero at all points in the calculation domain, then convergence has been achieved. Otherwise, other flow variables which affect the velocity field are calculated. Then, using the corrected pressure field as a new guess, the process is repeated until convergence is achieved. Once convergence is achieved, the remaining flow variables are calculated.

The SIMPLE algorithm is quite adequate for solving the pressure-velocity equations. However, since it is up to the pressure correction equation to likewise correct the velocities, the correction can be severe and lead to overshoot or even divergence. Convergence, when it occurs, can take a large number of iterations. The practice of guessing the pressure field leads to problems also. If the velocity field happens to be the correct one, but the pressure field is incorrect, then initial iterations would actually move away from the correct velocity field.

To remedy this situation, the SIMPLER algorithm (an acronym for SIMPLE Revised) has been devised. This method differs from SIMPLE in that a pressure equation is extracted from a guessed velocity field, rather than the other way around. Thus, if the velocity field is initially correct, the correct pressure field will immediately result. The algorithm proceeds as follows.

First, a guessed velocity field is obtained, either from an initialisation or a previous iteration. Then, rearranging the equation for momentum (Equation 2.53) yields

$$u_e = \frac{\sum_l a_l u_l + b}{a_e} + d_e\left(p_P - p_E\right) \qquad \textbf{(2.55)}$$

where

$$d_e = \frac{A_e}{a_e} \tag{2.56}$$

Next, a "pseudovelocity[19]" $\hat{u}_e$ is defined by

$$\hat{u}_e = \frac{\sum_l a_l u_l + b}{a_e} \tag{2.57}$$

Similar expressions may be written for the other two pseudovelocity components, $\hat{v}_n$ and $\hat{w}_u$. Thus, the three velocity components can be written as

$$\begin{aligned} u_e &= \hat{u}_e + d_e(p_P - p_E) \\ v_n &= \hat{v}_n + d_n(p_P - p_N) \\ w_u &= \hat{w}_u + d_u(p_P - p_U) \end{aligned} \tag{2.58}$$

These pseudovelocities are used to calculate the pressure field as follows. First, the continuity equation (Equation 2.6) is integrated, to give

$$\frac{(\rho_P - \rho_P^0)\Delta x\Delta y\Delta z}{\Delta t} + \left[(\rho u)_e - (\rho u)_w\right]\Delta y\Delta z + \left[(\rho v)_n - (\rho v)_s\right]\Delta x\Delta z + \left[(\rho w)_u - (\rho w)_d\right]\Delta x\Delta y = 0 \tag{2.59}$$

The velocities in Equation 2.58 are substituted into Equation 2.59, which, after gathering terms, gives the equation for the pressure field

$$a_P p_P = \sum_l a_l p_l + b \tag{2.60}$$

where

$$\begin{aligned} a_l &= \rho_i d_i \Delta x_j \Delta x_k \\ a_P &= \sum_l a_l \\ b &= \frac{(\rho_P - \rho_P^0)\Delta x\Delta y\Delta z}{\Delta t} + \left[(\rho\hat{u})_e - (\rho\hat{u})_w\right]\Delta y\Delta z + \left[(\rho\hat{v})_n - (\rho\hat{v})_s\right]\Delta x\Delta z + \left[(\rho\hat{w})_u - (\rho\hat{w})_d\right]\Delta x\Delta y \end{aligned} \tag{2.61}$$

These equations are then solved to find the pressure field. This pressure field is considered as an interim or "guessed" pressure field, denoted p^*, and plays a similar role to the guessed pressure field in the SIMPLE algorithm discussed above. Using the guessed pressure field, the momentum equations (Equations 2.53 and 2.54) are solved to give guessed velocities, u^*, v^*, and w^*. In essence, the equations being solved are

$$
\begin{aligned}
a_e u_e^* &= \sum_l a_l u_l^* + b + \left(p_P^* - p_E^*\right) A_e \\
a_n v_n^* &= \sum_l a_l v_l^* + b + \left(p_P^* - p_N^*\right) A_n \\
a_u w_u^* &= \sum_l a_l w_l^* + b + \left(p_P^* - p_U^*\right) A_u
\end{aligned}
\tag{2.62}
$$

If these velocities satisfy the continuity equation, then convergence has been achieved, as in the SIMPLE algorithm. At this point, the velocities are used to calculate the other flow variables in the calculation domain, and the iteration may move on to the next time step (or exit, in the steady-state case). If convergence has not been achieved, these velocities need to be corrected using the pressure correction equation. This is done by presuming that the correct pressure field may be obtained from the equation

$$p = p^* + p' \tag{2.63}$$

where p' is the pressure correction, and that the velocities respond to the pressure correction according to

$$u = u^* + u' \qquad v = v^* + v' \qquad w = w^* + w' \tag{2.64}$$

Subtracting Equation 2.62 from Equations 2.53 and 2.54 gives the velocity correction equations

$$
\begin{aligned}
a_e u_e' &= \sum_l a_l u_l' + \left(p_P' - p_E'\right) A_e \\
a_n v_n' &= \sum_l a_l v_l' + \left(p_P' - p_N'\right) A_n \\
a_u w_e' &= \sum_l a_l w_l' + \left(p_P' - p_U'\right) A_u
\end{aligned}
\tag{2.65}
$$

At this point, the term $\Sigma a_l u'_l$ is dropped (as is the corresponding term for the other two velocity components). This term contains an implicit dependence of the pressure correction on velocity, and is influenced by neighbouring velocities; ultimately, solution of the equation would involve all points in the flow region. However, omission of the term for the benefit of the calculation is justified on the basis that at convergence, no velocity correction is required, and no error has resulted from removing the term[19]. The omission of this term, and its implicit influence on velocity, leads to "semi-implicit" appearing in the SIMPLER acronym.

With the terms dropped, the corrected velocities are given by the equations

$$
\begin{aligned}
u_e &= u_e^* + d_e\left(p_P' - p_E'\right) \\
v_n &= v_n^* + d_n\left(p_P' - p_N'\right) \\
w_u &= w_u^* + d_u\left(p_P' - p_U'\right)
\end{aligned}
\tag{2.66}
$$

As can be seen, these equations are in the same form as Equation 2.58. Thus, the pressure correction can be extracted in the same manner as the original pressure equation, to yield

$$a_P p'_P = \sum_l a_l p'_l + b \tag{2.67}$$

where

$$\begin{aligned} a_l &= \rho_i d_i \Delta x_j \Delta x_k \\ a_P &= \sum_l a_l \\ b &= \frac{\left(\rho_P - \rho_P^0\right)\Delta x \Delta y \Delta z}{\Delta t} \\ &\quad + \left[\left(\rho u^*\right)_e - \left(\rho u^*\right)_w\right]\Delta y \Delta z + \left[\left(\rho v^*\right)_n - \left(\rho v^*\right)_s\right]\Delta x \Delta z + \left[\left(\rho w^*\right)_u - \left(\rho w^*\right)_d\right]\Delta x \Delta y \end{aligned} \tag{2.68}$$

The pressure correction equation is solved, and used to calculate the corrected velocities. This corrected velocity field is used to calculate other flow variables. The corrected velocity field is then used as the starting point in the next iteration, whereby a new pressure field is calculated, and so on until convergence.

2.3.5. Iteration and Convergence

An iterative method for solving the flow variable equations culminating in the SIMPLER algorithm has been outlined in the preceding sections. However, the methodology should not be taken at face value, as there are other factors which contribute to the efficiency, computational economy, and indeed the convergence of the solution. The equations governing the flow variables are generally non-linear, and usually depend on one or more other flow variables. The methods developed to ensure convergence, such as the particular linearisation of the source term, apply to a fixed set of coefficients in the discretisation equations. However, the SIMPLE algorithm calculates one variable at a time, using nominally linear algebraic equations. Thus, once the coefficients have been calculated, it is not wise to spend a great deal of computational effort in attaining convergence for values of coefficients which are only interim values. On the other hand, if the coefficients themselves change slowly, then it is reasonable to suppose that convergence may still be attained.

A powerful tool which helps to ensure that coefficients, and the flow variables themselves, do not change too rapidly from iteration to iteration is under-relaxation. This simple technique may be described as follows. Given a quantity, X, which has the value X_0 at the previous iteration, and a

calculated value of X_{calc} at the next iteration, the actual value this quantity will take at the next iteration is

$$X = \alpha X_{calc} + (1-\alpha) X_0 \tag{2.69}$$

where α is the under-relaxation factor, which can take any value between 0 and 1. Lower values of α will result in X changing by a small amount per iteration (or not at all if α=0), while higher values will result in larger changes, with α=1 corresponding to no relaxation at all. Choice of the magnitude of under-relaxation factors, and which variables to apply them to, are dependent on the problem being modelled. A further discussion of under-relaxation will be encountered in the next section, which deals with its use in the field model CESARE-CFD.

Perhaps the most important aspect of the iteration process is deciding when a satisfactory level of convergence has been attained. Like under-relaxation, this decision may be problem dependent. A simple method may be to monitor dominant quantities in the flow, and if there is no significant change in the variable between iterations, then convergence has been achieved. However, this may be misleading if heavy under-relaxation is being exercised, as the aim of under-relaxation is to prevent large changes from occurring. An alternative approach is to examine how well the discretisation equations are satisfied by the calculated flow variables. A quantity known as the residual, R, can be computed for a given flow variable ϕ at a particular point in the calculation domain by the equation

$$R = \sum_I a_I \phi_I + b - a_P \phi_P \tag{2.70}$$

When the flow variable satisfies the discretisation equation, the residual is zero. This principle is somewhat similar to the construction of the pressure correction term in the SIMPLER algorithm. Convergence is then assumed to occur when the residuals become sufficiently small, either the maximum magnitude from all points, or the summation over all points in the domain.

The fundamental principles of numerical fluid flow and combustion have been outlined in this section. The next section will contain a description of the field model CESARE-CFD, and how the equations presented in this section have been encoded and applied in this model.

2.4. THE FIELD MODEL CESARE-CFD

The field model CESARE-CFD has been developed in recent years at the Centre for Environmental Safety and Risk Engineering (CESARE) to model a number of fire experiments which have been performed at the Centre's Experimental Building-Fire Facility (EBFF)[3,8,52]. It is a modified version of the field model FURNACE, originally developed by Boyd and Kent[27] to model coal fired furnaces and pool fires. FURNACE itself was developed from the field model TEACH[27], with the addition, amongst other features, of Lagrangian particle tracking procedures to calculate the trajectories of coal particles*. The main modifications to FURNACE to produce CESARE-CFD include the incorporation of submodels to simulate multiple enclosure openings, multiple burning objects, an oxygen limitation model, CO generation[3], and a soot generation submodel. A full description is presented here, as further references to the model, as well as further modifications, will be encountered throughout this thesis. Also, some of the parameters and boundary conditions apply to all CFD modelling work throughout the thesis, so they will be described here, rather than repeated later. Many of the recommendations encountered throughout the following description stem from the users' guide supplied by Kent with the original version of the code acquired by CESARE[53].

2.4.1. Overview

CESARE-CFD solves the general conservation equation, Equation 2.1, in three dimensions for nine quantities, with the pressure-momentum equations being solved by the SIMPLER algorithm[19]. A two-equation turbulence model, the k-ε model, is used to calculate turbulence in the fluid flow, incorporating additional equations to account for turbulence induced by buoyant flows. The equation for mass continuity is solved using $\phi=1$, as well as the three velocity components (u,v,w), enthalpy (h), fuel mixture fraction (f), fuel fraction fluctuation (g), turbulence kinetic energy (k), and turbulence dissipation rate (ε). The turbulence viscosity is given by the equation $\mu_t = C_\mu \rho k^2/\varepsilon$. The values of the exchange coefficients, Γ_Φ, and the source terms, S_Φ, are given in Table 2.1. Other constants and variables appearing in Table 2.1 are the pressure field, p, the density distribution, ρ, the gravitational constant, a_g, and the enthalpy source term due to thermal radiation, Q_R.

* Particle tracking is a feature not used in the modelling presented in this thesis, although it remains a feature of CESARE-CFD, and may find future use in soot and smoke tracking and combustion.

Φ	Γ_Φ	S_Φ
1	0	0
u	μ_t	$-\frac{\partial p}{\partial x}+\frac{\partial}{\partial x}\left(\mu_t\frac{\partial u}{\partial x}\right)+\frac{\partial}{\partial y}\left(\mu_t\frac{\partial v}{\partial x}\right)+\frac{\partial}{\partial z}\left(\mu_t\frac{\partial w}{\partial x}\right)$
v	μ_t	$-\frac{\partial p}{\partial y}+\frac{\partial}{\partial x}\left(\mu_t\frac{\partial u}{\partial y}\right)+\frac{\partial}{\partial y}\left(\mu_t\frac{\partial v}{\partial y}\right)+\frac{\partial}{\partial z}\left(\mu_t\frac{\partial w}{\partial y}\right)$
w	μ_t	$-\frac{\partial p}{\partial z}+\frac{\partial}{\partial x}\left(\mu_t\frac{\partial u}{\partial z}\right)+\frac{\partial}{\partial y}\left(\mu_t\frac{\partial v}{\partial z}\right)+\frac{\partial}{\partial z}\left(\mu_t\frac{\partial w}{\partial z}\right)+a_g\left(\rho_{ref}-\rho\right)$
h	μ_t/σ_h	$-Q_R$
f	μ_t/σ_f	0
g	μ_t/σ_g	$C_{g1}\left[\left(\frac{\partial f}{\partial x}\right)^2+\left(\frac{\partial f}{\partial y}\right)^2+\left(\frac{\partial f}{\partial z}\right)^2\right]-C_{g2}\rho g\frac{\varepsilon}{k}$
k	μ_t/σ_k	$G_k-\rho\varepsilon+a_g\mu_t\frac{1}{\rho}\frac{\partial\rho}{\partial z}$
ε	μ_t/σ_ε	$\frac{\varepsilon}{k}\left[C_1\left(G_k+C_3a_g\mu_t\frac{1}{\rho}\frac{\partial\rho}{\partial z}\right)-C_2\rho\varepsilon\right]$

$$\mu_t = C_\mu\rho\frac{k^2}{\varepsilon}$$

$$G_k = \mu_t\left[2\left(\left(\frac{\partial u}{\partial x}\right)^2+\left(\frac{\partial v}{\partial y}\right)^2+\left(\frac{\partial w}{\partial z}\right)^2\right)+\left(\frac{\partial u}{\partial y}+\frac{\partial v}{\partial x}\right)^2+\left(\frac{\partial v}{\partial z}+\frac{\partial w}{\partial y}\right)^2+\left(\frac{\partial u}{\partial z}+\frac{\partial w}{\partial x}\right)^2\right]$$

$C_{g1} = 2.8$	$\sigma_k = 0.9$
$C_{g2} = 2.0$	$\sigma_\varepsilon = 1.22$
$C_1 = 1.44$	$\sigma_f = 0.7$
$C_2 = 1.92$	$\sigma_g = 0.7$
$C_3 = 0.8$	$\sigma_h = 0.7$
$C_\mu = 0.09$	

Table 2.1. Values of exchance coefficients and source terms used in CESARE-CFD

The combustion of the fuel is modelled by computing the local fuel mixture fraction, then reacting the fuel with the air. The combustion method used is the fluctuation of mixture fraction method, as described in Section 2.2.3. When the local oxygen concentration falls below a specified value (normally chosen in the region of 5-10%), combustion is assumed not to occur. The equation for gas phase combustion is given by Equations 2.21 and 2.22, where, in the absence of other data, the

CO/CO_2 ratio for the combustion of polyurethane is taken to be fairly typical of most fuels. This assumption needs to be qualified somewhat. The empirical calculation of CO is for reporting purposes only; it does not take part in the calculations of product density in the model itself (fuel combustion, when it occurs, it assumed to occur stoichiometrically). Since CO is usually produced in small quantities compared to CO_2 and water vapour, its omission from calculations is not expected to create any serious error. The work of Beyler[54] suggests that since the CO yield is calculated for an oxygenated hydrocarbon (polyurethane is an oxygen and nitrogen containing hydrocarbon), the CO yield will be overestimated for hydrocarbon and aromatic fuels when conditions are fuel rich, and underestimated when conditions are fuel lean.

Radiation heat transfer is calculated using the discrete transfer method[55], which will be described in greater detail in the next chapter. An option exists in the program for the radiation to be calculated on a separate grid to that used for the rest of the flow variables. This is because the radiation calculations are particularly time consuming, which may be minimised by performing the calculations on a coarser grid than that used for the remaining flow variables.

2.4.2. Computational Grid

The choice of grid mesh is important if the details of the distribution of flow variables throughout the computational domain are to be accurately captured. In regions where the gradient of flow variables is steep, the mesh should be sufficiently fine to ensure that the discretisation errors are so small that the numerical solution approaches the solution of the continuous equations. Where the gradients are less steep, it is not necessary for the grid to be as fine, particularly if computational resources are limited. Determining which regions to refine the grid requires some insight into the problem, and it is likely that there will be a process of simulation and readjustment to improve the choice of construction of the grid mesh.

The computation grid, both in the flow subroutine and in the radiation subroutine, is rectilinear, with cell boundaries perpendicular to one of the three Cartesian axes. Each control cell is therefore cuboid in shape. The model does have the capacity to include planes which are skewed to the primary axes, and conical or hemispherical regions. In such regions, the boundary of the flow grid is defined in a stepwise fashion; that is, if a cell lies mostly within the skew boundary, it is wholly included in the flow region, and if it lies mostly without, it is wholly excluded. This retains the rectilinearity of the grid. The flow along a stepped boundary will produce different behaviour to

that along a smooth plane. However, since the modelling work in this thesis is all performed in rectilinear enclosures, inaccuracies due to stepped boundaries do not arise.

The flow grid for the enclosure of interest is constructed by initially defining a single cuboid which encompasses the entire region of interest, which is done by specifying the maximum and minimum values in each of the three co-ordinate axes. Blocks of cells which are not part of the flow domain are then removed from the large cuboid. The program automatically locates the removed regions and identifies them as boundaries. The radiation grid on the other hand is constructed by defining the location of the boundary surfaces. Normally these will be chosen to coincide with the boundaries of the flow region, although this need not necessarily be the case. For example, it may be chosen to model the radiation in only a portion of the flow region, and openings to the rest of the flow region may be replaced with an ideal black surface of prescribed temperature.

A total number of grid divisions in each direction is specified. The grid spacing in each of the three directions may be specified in regions, or over the whole domain. In this research, the grid is specified to be uniformly fine in specified regions of high gradients. However, this fine spacing prevails throughout the flow domain, so that other regions of relatively uniform distributions of flow quantities are discretised finely by default (see Figure 3.62 for example, where the fine region specified for the fire plume extends to adjoining rooms). In the specified regions, the grid spacing is uniform. In the remaining regions, the program automatically fills the grid with either uniformly increasing or decreasing size divisions, until the total specified number of divisions is reached. The automatic filling is done in such a way that, if possible, the size ratio of all pairs of adjacent divisions is between 1.01 and 2.

To express this mathematically, suppose a region of width s is to be filled, and that the width of the specified grid cells bounding this region are a_1 and a_2. For simplicity, it can be assumed without loss of generality that $a_1 < a_2$. The region is to be filled with n cells whose width increases geometrically with ratio r. Thus, the first cell will have width $r \cdot a_1$, while the last will have width $r^n \cdot a_1$. This situation is illustrated in Figure 2.3.

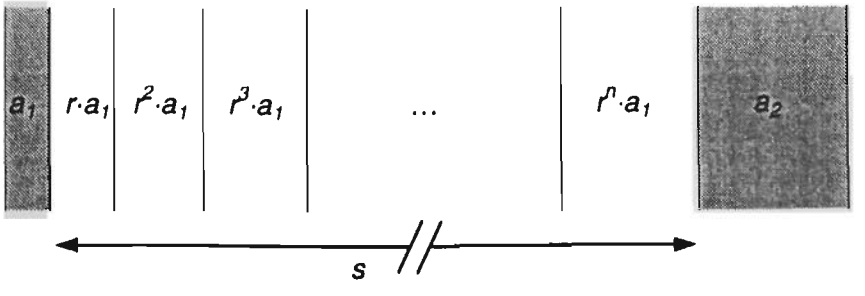

Figure 2.3 Automatic filling of grid points

The distance s is the sum of a geometric series, which can be written

$$s = a_1 \sum_{i=1}^{n} r^i = a_1 r \frac{1 - r^n}{1 - r} \tag{2.71}$$

Equation 2.71 contains two unknowns, namely r and n. Rearranging for n gives the equation

$$n = \frac{\log\left[(r-1)\frac{s}{a_1 r} + 1\right]}{\log(r)} \tag{2.72}$$

If the cell at a_2 happens to be a boundary rather than an internal node, there is no size constraint on the size of the adjacent cell having width $r^n \cdot a_1$. The cell sizes are calculated by substituting the minimum ratio r=1.01 into Equation 2.72 to yield a value of n. This value is then truncated down to the nearest integer, and substituted back into Equation 2.72 and solved numerically to yield the exact value of the ratio r. If r is not greater than 2, the width of each cell is calculated accordingly, otherwise an error is reported by the automatic grid generation program.

If the width of the cell at a_2 is specified, there is a constraint on the size of the adjacent cell with width $r^n \cdot a_1$. In this instance, a_2 completes the geometric series, so that its width is given by

$$a_2 = a_1 r^{n+1} \tag{2.73}$$

Rearranging for n gives the equation

$$n = \frac{\log\left(\frac{a_2}{a_1}\right)}{\log(r)} - 1 \tag{2.74}$$

Equation 2.72 and Equation 2.74 are equated and solved for r, which after some manipulation yields the expression

$$r = \frac{(s + a_2)}{(s + a_1)} \tag{2.75}$$

Of course, the values of s, a_1 and a_2 may be such that the value of r does not lie between 1.01 and 2. To avoid this, the grid generation routine does not begin with the value given in Equation 2.75. Instead, it begins with a value of r=1.01. Two values of n are calculated, using Equation 2.74 and Equation 2.72. The latter is the number of cells in the series which would be used to fill up the interval given the value of r, while the former is based on the number of times a_1 is multiplied by r to increase the size to a_2. If the number of cells required to span the interval (Equation 2.72) is smaller, then Equation 2.75 is then used as a better estimate of r, and a uniformly expanding grid is

used to fill the interval between a_1 and a_2. The grid generation routine adjusts the ratio r so that the sum of the cell widths is the length of the interval.

If the number of cells required to span the interval is the larger of the two values of n, then the grid is allowed to expand from both ends of the interval to fill the remaining space. The number of cells is thus increased, and the equation for the sum of the cells in the interval is

$$s = a_1 \sum_{i=1}^{n_1} r^i + a_2 \sum_{j=1}^{n_2} r^j = a_1 r \frac{1 - r^{n_1}}{1 - r} + a_2 r \frac{1 - r^{n_2}}{1 - r} \qquad (2.76)$$

Again, the ratio r is adjusted so that the two series meet at a point in the interval. In the case where $a_1 = a_2$, the adjustment results in the two series meeting in the centre of the interval.

When an interval is filled with two series, there is flexibility in the number of cells that can fill the interval. A number of values of r may exist which fill the interval precisely, with larger values filling the interval with less cells. This is likewise true of the intervals adjacent to the boundary, where there is no constraint on the size of the cell adjacent to the boundary. Consequently, the grid generation routine will attempt to use the smallest possible ratio (r = 1.01) and adjust upwards until the cells fill the interval. However, if the grid generation routine exceeds the specified maximum number of cells in the course of calculations, then the ratio r will be increased in these intervals in an attempt to reduce the number of cells used. If a value of r = 2 is exceeded and the number of cells required is still in excess of the maximum, then the routine fails, and the user must specify a higher maximum (computer memory permitting) or increase the size of the cells in the specified refined regions bounding the intervals.

Each control cell will now have been assigned a unique Cartesian index (i,j,k), each component of which lies in the range 1-*imax*, 1-*jmax*, and 1-*kmax* respectively, where the maxima are the specified totals. Once the location of the grid divisions is established, the scalar locations* are defined to lie midway between divisions. The scalar locations then form the boundaries of the velocity control cells. The velocity location points themselves coincide with the original grid divisions. This method of staggering the velocity cells is called the Marker and Cell method (MAC). Its merit over other possible staggering methods has been espoused by Zhao[56], who also notes that the method of placing scalar nodes in the centre of grid cells, as used here, has advantages in terms of accuracy and convenience in calculating source terms and the flux terms at control volume interfaces.

2.4.3. Model Structure

The structure of the model CESARE-CFD is outlined in Figure 2.4. This shows the sequence of procedures which occur before and after the main calculation loop, and the sequence of calculations within the loop itself. The iteration loop essentially encompasses the SIMPLER algorithm. In terms of the model structure, this algorithm may again be described as follows.

First, the old density and fluid properties such as turbulence viscosity are calculated from the state of the previous iteration (or initialised in the case of the first iteration). Then the coefficients of the velocity discretisation equations are calculated. These are required to calculate the pressure field, which is done in the next step. The pressure field is then "anchored" relative to a fixed point. This is done by subtracting the pressure at the reference point from all points. This can be done because the flow is driven by pressure differences; thus, p and p + *constant* are both solutions to the pressure equation. Since floating point subtractions are most accurate when the two numbers are close to zero (rather than around 101,325 Pa, for instance, where roundoff errors may arise because the first five or six significant digits of the two numbers are identical), setting one arbitrary reference point to zero improves accuracy, while not otherwise affecting the solution.

Once the pressure field is established, the coefficients of each velocity component are calculated and the velocity solved in turn. The pressure correction coefficients are calculated (using the same subroutine as the pressure equation, but using a different "scratch" variable), the pressure correction equation solved, and the velocities subsequently corrected. The remaining scalar variable coefficients are determined and the variables solved, in the following order: turbulence kinetic energy, turbulence dissipation rate, fuel mixture fraction, fuel fraction fluctuation, and enthalpy. The subroutine SCALARCOEFFS serves as a generic subroutine to calculate the coefficients of the discretisation equation for the given variable, once the boundary conditions and source terms are determined.

This completes one iteration of the SIMPLER algorithm. Other operations which are performed before the end of the loop, where applicable, are calculation of flame spread and radiation heat transfer (which is not necessarily calculated every iteration. In the work presented in this thesis, it is calculated every fifth iteration).

---

* Scalars are all the non-velocity flow variables e.g. enthalpy, pressure, density, turbulence kinetic energy etc.

2.4.4. Line-by-Line Solution Method

In Figure 2.4, an operation which appears often is the command "Call LISOLV(*var*,...)". The subroutine being called is that responsible for the solution of the discretised equation of the flow variable *var*. The coefficients a_e, a_w, etc. from the discretised equation of the variable in question are first determined by another subroutine, then passed down to the LISOLV subroutine, along with the source terms, boundary conditions, and grid information pertinent to the variable. The distribution of the variable and its residual are passed back to the main program.

The solution method is the line-by-line method, where the value of the flow for a line of cells in one Cartesian direction is solved using the Thomas algorithm, and the co-ordinate of this line in the other two directions is altered in a systematic manner. More specifically, the procedure in CESARE-CFD is as follows.

The lines in the *y* direction are solved first, sweeping row by row in the *x* direction from 1 to *imax*, the rows themselves incrementing in the *z* direction from *kmax* to 1. Lines in the *x* direction are then solved, sweeping row by row in the *y* direction from *jmax* to 1, each row incrementing from 1 to *kmax* in the *z* direction. Finally, lines in the *z* direction are solved, sweeping in rows from *imax* to 1 in the *x* direction, the rows incrementing from 1 to *jmax* in the *y* direction. This solving of lines in each of the three directions counts as one overall sweep of the solution. This may be repeated a specified number of times. In the work in this thesis, all variables are swept twice, except pressure, which is swept four times.

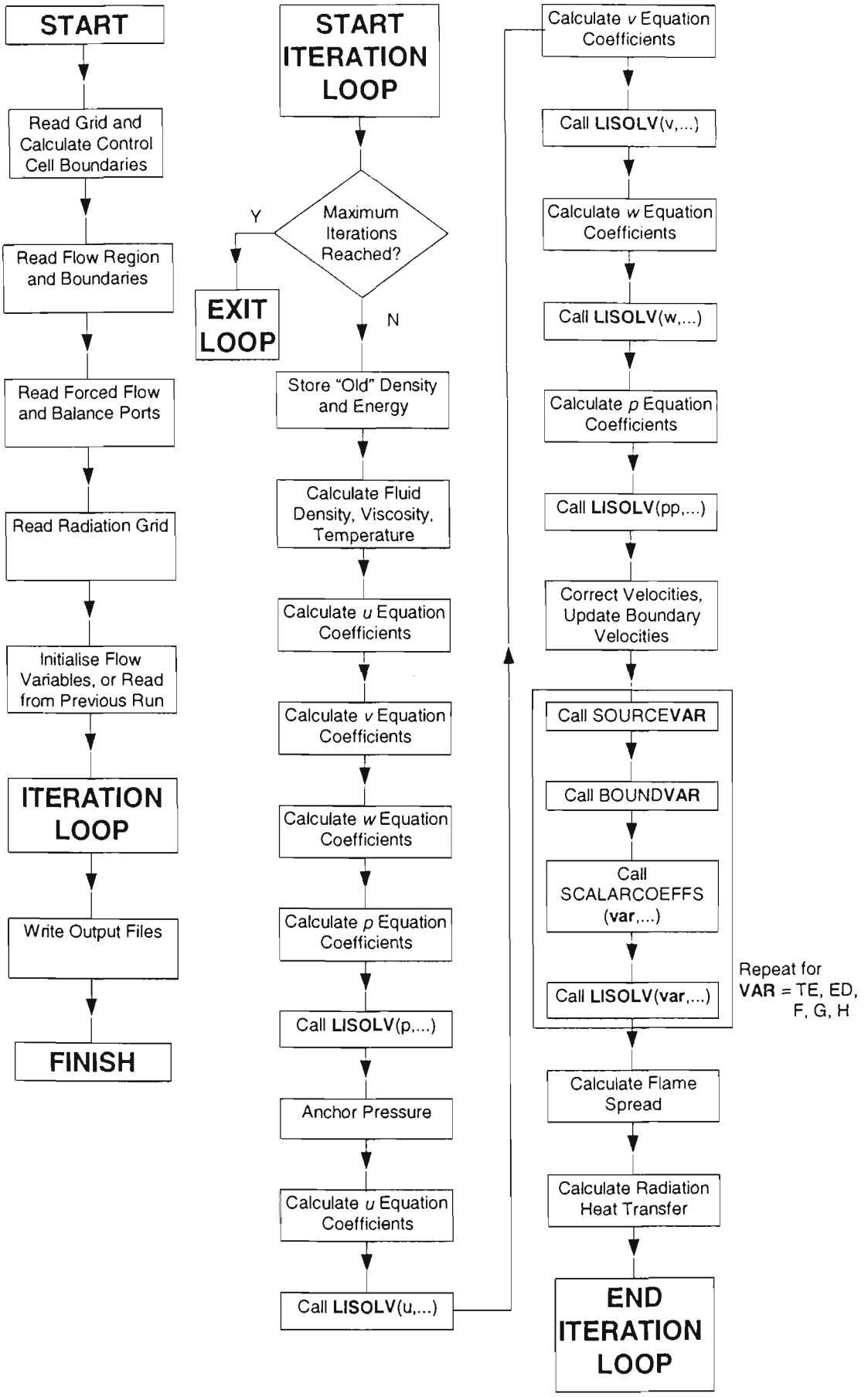

Figure 2.4 Flow diagram for CESARE-CFD

2.4.5. Source Terms

The source terms for each of the calculated flow variables are outlined in Table 2.1. The method of linearising the source term, as given by Equation 2.33, for variables where the source term is not dependent on the variable itself is simply to assign the source term in Table 2.1 to the S_C component. This is true for the fuel mixture fraction, f, where there is in fact no source term, due to conservation of mass in a chemical reaction. Fuel is introduced to the flow region via fuel ports, which are treated as boundary conditions in the model rather than source terms. The enthalpy, h, comprises the heat of combustion, assumed to be proportional to the fuel mass only, and the radiant heat transfer, which is decoupled from the enthalpy calculations, so it too is linearised using only the term S_C.

The source term is more complex when solving for the velocity components, although again linearisation is straightforward as there is no explicit dependence on the velocity component. Source terms in the momentum conservation equation arise due to shear stresses in the fluid. In addition, there is a source due to buoyancy in the vertical, or w, component of velocity.

On the other hand, the source terms for turbulence kinetic energy, k, rate of eddy dissipation, ε, and fluctuation of mixture fraction, g, do depend on the variable in question. The source term for k includes both k and ε. However, ε is not passed down to the calculation subroutine; instead, the turbulent viscosity is used. Transforming the equation for turbulent viscosity, Equation 2.19, gives the expression

$$\varepsilon = \frac{C_\mu \rho k^2}{\mu_T} \tag{2.77}$$

The substitution is made because the resulting form of the source terms is numerically more stable. Using the above substitution, the source term for k is expressed by the linearisation

$$\begin{aligned} S_C &= G_k + a_g \mu_T \frac{1}{\rho}\frac{\partial \rho}{\partial z} \\ S_P &= \frac{C_\mu \rho^2 k}{\mu_T} \end{aligned} \tag{2.78}$$

where G_k is as given in Table 2.1. The substitution for ε is also made in the source term for ε itself. The linearisation in this instance is

$$S_C = C_1\left(G_k + C_3 a_g \mu_T \frac{1}{\rho}\frac{\partial \rho}{\partial z}\right)\frac{C_\mu \rho k}{\mu_T}$$
$$S_P = \frac{C_2 \rho \varepsilon}{k} \qquad (2.79)$$

The inclusion of the second term in the brackets, with the closure coefficient C_3, of the expression for S_C is optional. If the flow is mainly horizontally stratified, inclusion of the term is recommended, whereas if the flow is mainly vertical buoyant flow, omission is recommended[53]. Since the flows encountered in building fires are typically stratified in two layers (as assumed in zone models), the buoyancy term is included in all the work presented in this thesis. An alternative to this global approach is offered by Henkes[57], who considers the local behaviour of the fluid instead. The term C_3 is multiplied by the factor $\tanh(v/u)$, where v is the vertical component of velocity, and u is the horizontal component.

The final variable, the fluctuation in fuel mixture fraction, g, is linearised as follows

$$S_C = C_{g1}\mu_T\left[\left(\frac{\partial f}{\partial x}\right)^2 + \left(\frac{\partial f}{\partial y}\right)^2 + \left(\frac{\partial f}{\partial z}\right)^2\right]$$
$$S_P = \frac{C_{g2}\rho \varepsilon}{k} \qquad (2.80)$$

The linearised source term is also used in some instances to introduce boundary conditions to the flow regions. The value of the flow cell adjacent to the boundary, ϕ_B, is determined from the boundary subroutine (described in the next section). The source term linearisation for that cell is given by

$$S_C = C_{BIG}\phi_B$$
$$S_P = -C_{BIG} \qquad (2.81)$$

where C_{BIG} is a constant large enough to make the other coefficients in the discretisation equation negligible (10^{20} is used in CESARE-CFD). The discretisation equation then becomes

$$S_P\phi_P + S_C \approx 0 \qquad (2.82)$$

so that solving the equation at the boundary gives

$$\phi_P = -\frac{S_C}{S_P} = \phi_B \qquad (2.83)$$

2.4.6. Boundary Conditions

There are five types of boundary recognised by the field model CESARE-CFD. They are forced flow ports, balance ports, free stream planes, symmetry planes, and solid boundaries. Free stream boundaries (i.e. where the flow region adjoins a region of fluid flowing with uniform velocity) were not used in this study, nor were symmetry planes, so only the other three boundary types will be considered here in detail.

2.4.6.1. Solid Boundary

The first boundary type considered here is the solid boundary. A solid boundary is one which does not allow any transfer of fluid across it. As a consequence, the component of velocity normal to the plane of the surface must be zero, and is set accordingly. The pressure calculations are skipped in this case. As a result of the no-slip condition at the surface, the tangential components of velocity at the surface are also zero. However, since the centre of the control cells for the tangential velocity components do not coincide with the boundary, the velocity in this case cannot simply be set to zero. Instead, the behaviour of the flow at a small distance from the wall must be considered.

The presence of a solid boundary affects the behaviour of a turbulent flow field close to the wall, creating what is referred to as the boundary layer. Perturbation analysis at the boundary layer yields information about the structure and behaviour of the layer as predicted by the fluid models, and leads to the formulation of the so-called "wall functions"[42]. At very small distances from the boundary, turbulence is negligible, and flow is dominated by viscous forces. This region is called the viscous sublayer. In this region, the (dimensionless) tangential velocity increases linearly with (dimensionless) distance from the solid surface. Beyond this sublayer, there is a transition to a second layer known as the log-layer. In this region, the tangential velocity increases as the logarithm of the distance from the surface, and turbulence effects become significant. Beyond this region, full turbulence is in effect, and the flow is described by the k-ε model. The assumption which has been used in the construction of FURNACE and ultimately CESARE-CFD is that control cells immediately adjacent to the solid boundary are always subject to boundary layer effects, and only these cells.

When determining the value of a flow variable at a solid boundary, the location of the variable lies at point P within the control cell adjacent to the boundary. It must be determined whether this point is within the viscous sublayer or the log layer. Now, the thickness of the subregions within the

boundary layer may be quantified in terms of flow variables. A dimensionless length, y^+, is defined in terms of the distance from the wall, y, by the expression

$$y^+ = \frac{\rho k^{\frac{1}{2}} C_\mu^{\frac{1}{4}} y}{\mu} \tag{2.84}$$

where μ is the laminar viscosity of the fluid, and k the turbulence kinetic energy. If $y^+>11.63$, then the point in question is deemed to lie within the log layer. The momentum flux to this point from the boundary is then taken to obey the expression given by Launder and Spalding[18]

$$\frac{U_p}{(\tau/\rho)_w} C_\mu^{\frac{1}{4}} k_p^{\frac{1}{2}} = \frac{1}{\kappa} \log\left(\frac{E y C_\mu^{\frac{1}{4}} k_p^{\frac{1}{2}}}{\mu}\right) \tag{2.85}$$

where U_P is the time average velocity at P tangential to the wall, κ is the von Karman constant, which has a value of 0.41, E is a constant which is a function of the wall roughness, τ is the shear stress in the fluid, k_P is the turbulence kinetic energy at P, y_P is the distance of P from the wall, and the other parameters are the closure coefficients as described earlier. The shear stress in Equation 2.85 appears as a source term at the boundary in the momentum conservation equations, the form given by rearranging Equation 2.85 thus:

$$\tau = \frac{C_\mu^{\frac{1}{4}} k^{\frac{1}{2}} \rho \kappa}{\log\left(\frac{E y C_\mu^{\frac{1}{4}} k^{\frac{1}{2}}}{\mu}\right)} U \equiv S_P U \tag{2.86}$$

If, on the other hand, $y^+<11.63$, then the point P lies within the viscous sublayer, and the shear stress is given by the simpler expression

$$\tau = \frac{\mu}{y} U \equiv S_P U \tag{2.87}$$

The source term is calculated in two halves, with each part corresponding to the overlap with the scalar grid, as the source term also appears in the boundary source for turbulence kinetic energy, k. The source term for k takes the form

$$S_C = \tau \frac{U^2}{y} \tag{2.88}$$

where all terms are as described above. In addition to this term, there is the normal component of shear stress and the term due to buoyancy as given in Equation 2.78, which still apply in the cell adjacent to the boundary. Like the normal velocity, the turbulence kinetic energy k is also zero at the wall itself. On the other hand, the rate of dissipation ε does not vanish at the wall; it must

remain at a finite value as the distance from the wall approaches zero. In CESARE-CFD, the value is set at the first grid point inside the wall by the equation

$$\varepsilon = \frac{C_\mu^{\frac{1}{4}} k^{\frac{1}{2}}}{\kappa y} \tag{2.89}$$

which is in agreement with the value given for other natural convection computations[57].

There are several factors to consider when calculating the heat transfer at the boundary, since heat, unlike fluid, can be transported across the solid boundary. Despite this permeability, the boundary nevertheless marks a convenient reference for calculating the heat flux. There are three conditions in CESARE-CFD which can be applied to the solid boundary. Either the heat flux is specified, the boundary is specified as adiabatic (no heat transfer across the boundary), or the heat transfer may be calculated. In the latter case, the heat flux from the boundary to a point in the log-layer follows the formulation given by Launder and Spalding[18]

$$\frac{(T_P - T_w) C_p \rho C_\mu^{\frac{1}{4}} k_P^{\frac{1}{2}}}{\dot{Q}''_w} = \frac{\sigma_h}{\kappa} \log\left(\frac{E y_P C_\mu^{\frac{1}{4}} k_P^{\frac{1}{2}}}{\mu}\right) + \sigma_h \frac{\frac{\pi}{4}}{\sin(\frac{\pi}{4})} \left(\frac{A}{k}\right)^{\frac{1}{2}} \left(\frac{\sigma_{h,l}}{\sigma_h} - 1\right) \left(\frac{\sigma_{h,l}}{\sigma_h}\right)^{\frac{1}{4}} \tag{2.90}$$

Here, as before, the subscript P refers to the node located in the centre of the flow cell above the surface, except in the case of C_p, the constant-pressure specific heat of the fluid, and the subscript w refers to the wall, or solid boundary. The variables are as given in the equation for the boundary momentum flux, Equation 2.85. Other variables appearing in the equation are the temperature, T, the heat flux $\dot{Q}''$, and Prandtl numbers, σ_h, $\sigma_{h,l}$ for, respectively, fully turbulent and wholly laminar fluid[18]. If the assumption $\sigma_h \approx \sigma_{h,l}$ is made, the second term on the right hand side of Equation 2.90 effectively vanishes. Rearranging the remaining terms, the equation may be written

$$\dot{Q}''_w = \frac{C_p \rho C_\mu^{\frac{1}{4}} k_P^{\frac{1}{2}}}{\frac{\sigma_h}{\kappa} \log\left(\frac{E y_P C_\mu^{\frac{1}{4}} k_P^{\frac{1}{2}}}{\mu}\right)} (T_P - T_w) \equiv h(T_P - T_w) \tag{2.91}$$

where h is the convective heat transfer coefficient. This value of the coefficient is then incorporated into calculations using the formulation given in Equation 2.39. If the point in question is in the viscous sublayer, then the heat transfer is given by

$$\dot{Q}''_w = \frac{\mu}{\sigma_{h,l}} (T_P - T_w) \equiv h(T_P - T_w) \tag{2.92}$$

Use of the wall function requires knowledge of the boundary temperature itself. Formerly, the temperature was simply specified in the model. Since this requires some foreknowledge of the problem being modelled, CESARE-CFD has been modified so that wall temperatures are calculated rather than specified. Calculation of the wall temperature uses a simplified flux balance approach. Heat is assumed to be received by convection, and by radiation (as calculated by the thermal radiation model), while it is lost by surface re-radiation and conduction through the wall, either to the surface behind or to the outside. Assuming a global constant for the heat transfer coefficient (h = 10 W/m^{2}K), and blackbody emissive properties, the heat balance can be expressed by the following equation

$$h(T_g - T) + \dot{Q}''_{rad} = \frac{k}{x}(T - T_{opp}) + \sigma T^4 \tag{2.93}$$

where T is the temperature of the wall which is to be calculated, T_g is the temperature of the fluid adjacent to the wall, T_{opp} is the temperature of the opposite wall surface (ambient if it is an external boundary), k is the conductivity of the wall and x the wall thickness, $\dot{Q}''_{rad}$ is the incident radiant flux, and σ is the Stefan-Boltzmann constant. Rearranging Equation 2.93 gives

$$\begin{aligned} &T^4 + aT - b = 0 \\ &a = \frac{1}{\sigma}\left(h + \frac{k}{x}\right) \\ &b = \frac{1}{\sigma}\left(hT_g + \frac{k}{x}T_{opp} + \dot{Q}''_{rad}\right) \end{aligned} \tag{2.94}$$

Since all terms in a and b are positive, so are a and b themselves, and the resulting quartic equation in T has two real roots, one positive and one negative. The positive root is the desired temperature, and is given by

$$\begin{aligned} &z = \left(27a^2 + \sqrt{729a^4 + 6912b^3}\right)^{\frac{1}{3}} \\ &y = \left(-\frac{2^{\frac{2}{3}}b}{z} + \frac{z}{3\cdot 2^{\frac{1}{3}}}\right) \\ &T = \frac{1}{2}\left(-\sqrt{y} + \sqrt{-y + \frac{2a}{\sqrt{y}}}\right) \end{aligned} \tag{2.95}$$

This equation for the wall temperature makes the assumption that conduction through the wall is uniform, and has reached steady conditions, namely that a linear temperature profile exists between the two wall surfaces. While this may be reasonable for a steady-state simulation, for transient or unsteady conditions it will produce discrepancies. In terms of fire modelling, in the fire growth stage, the wall in reality will not have had sufficient time to reach a linear temperature profile; the

temperature gradient will be relatively high, so that heat losses will be greater than the modelled losses, resulting in higher predicted temperatures. The opposite may be true in the decay phase of the fire, where the predicted wall temperature may drop too quickly in response to dropping fluid temperatures, whereas there may in reality be substantial heat stored in the wall, keeping temperatures higher. Real behaviour may be even more complex than this. However, for the sake of simplicity, the assumption of a steady-state temperature profile in the wall serves as a first approximation.

There are no special boundary conditions for the f and g equations, apart from those "inherited" from the momentum and turbulence equations. Naturally, since the fuel, like the fluid, cannot cross the solid boundary, the mixture fraction flux at the boundary is zero.

2.4.6.2. Forced Flow Port

A forced flow port, as the name suggests, is a region of the flow grid where mass is introduced at a fixed rate. Normally this occurs at a plane which corresponds to an opening in a solid surface. There are several options in CESARE-CFD available to the modeller, which control how the port interacts with the flow region. The mass flow rate may be positive or negative. If it is negative, then the only effect the port has is to remove mass at the specified rate from the layer of cells immediately adjacent to the flow port. If the flow rate is positive, then it introduces other quantities to the layer of boundary cells as well as the mass source. These quantities will be in proportion to the mass flow rate, so that a source will appear in the conservation equations for all variables at the forced flow port. In the source term linearisation equation, the mass flow is incorporated into the S_P component, and the actual quantity being introduced into the flow (multiplied by the flow rate) appears in the S_C component.

The mass flow rate at a forced flow port leads to a non-zero velocity component at this boundary. The mass flow rate is assumed to be uniform across the port, so that the normal velocity is readily calculated by dividing the mass flow rate by the product of the fluid density and port area. The model also allows tangential components of velocity to be present in the port flow. If these components differ from the corresponding component in the flow region adjacent to the port (as they will in general be) then shear stresses will result from the velocity difference, and these are included in the source term for the momentum conservation equations for the tangential velocity components.

There will in general be turbulence associated with the incoming flow. The incoming turbulence is specified in terms of turbulence intensity and turbulence length scale, normalised by the normal flow velocity and the area of the port respectively. If v_{norm} is the normal velocity at the port, and I the specified turbulence intensity, then the turbulence energy of the incoming flow is given by

$$k = 1.5\left(I \cdot v_{norm}\right)^2 \tag{2.96}$$

This incoming turbulence dissipation, ε, is based on the turbulence length scale as given in Equation 2.17. If the port area is A, the specified ratio of turbulence length scale to the square root of the port area is r, and k is the port flow turbulence kinetic energy given in Equation 2.96, then the turbulence dissipation rate of the incoming flow is given by

$$\varepsilon = C_\mu \frac{k^{\frac{3}{2}}}{r\sqrt{A}} \tag{2.97}$$

Investigation into suitable values for turbulence intensity and length scales was not included in the scope of this thesis. The values used throughout the modelling presented in this thesis were 0.01 for turbulence intensity, and 0.004 for length scale factor, as these were used in previous modelling work[3,8,52]. While the choice is somewhat arbitrary, Ravichandran and Gouldin[26] investigated a range of (likewise arbitrarily chosen) values for inflow turbulence intensity and length scale for a numerical simulation of an incinerator, and found the values to have little influence on the overall flow patterns within the incinerator.

The fuel mixture fraction of the incoming fluid also needs to be specified. The fraction is zero for air flow, and unity for pure fuel. The fluctuation of mixture fraction, g, of the incoming fluid is assumed to be zero, so that the only term appearing in the g equation is the introduced mass itself. The temperature of the incoming fluid can be specified, and this appears as an enthalpy source in the conservation of enthalpy equation.

2.4.6.3. Balance Port

The balance port is handled in essentially the same manner as a forced flow port in terms of introducing flow quantities to the flow region, or removing them from, as the case may be. The crucial difference is that the fluid flow rate is not fixed at the balance port, and indeed may, if specified, be non-uniform across the port. If non-uniform flow is allowed, then it is possible for reverse flow to be present, and the properties of this reverse flow must then be specified. As with the forced flow port, the temperature, mixture fraction, turbulence intensity, and turbulence length scale for the incoming flow are specified. Since the port flow may be non-uniform, a reference

velocity is also specified to scale the turbulence intensity. The incoming turbulence is in fact calculated based on the actual velocity at an individual port cell. All these specifications for the incoming flow are optional; they only apply if the inflow is selected to be "fresh". Otherwise, the program will ignore the specifications for the incoming flow, and no source terms other than the mass flow are present in the equations. Thus, the properties of the incoming flow are effectively set equal to those of the flow immediately adjacent to the flow port.

The flow rate at the balance port is calculated by considering the mass balance over the entire flow region. The net mass flow at the balance port is the difference between the flow rates of all forced flow ports and the mass source throughout the flow region, as expressed by the equation

$$\dot{m}_{balance} = \sum_{n} \dot{m}_{port(n)} - \sum_{i,j,k} \left(\rho_{i,j,k} - \rho^{0}_{i,j,k}\right) \frac{\Delta x_i \Delta y_j \Delta z_k}{\Delta t} \qquad (2.98)$$

For steady state calculations, the mass source term does not appear in the calculations, so that the balance port mass flow in this case equals the total flow through the forced flow ports. If the balance port is set to uniform flow, then the net mass flux is simply the mass flow divided by the area of the port. The velocity at each cell within the balance port is the mass flux divided by the density of the fluid adjacent to the port cell.

If non-uniform flow is allowed, then the flow at the port must be matched to the flow region in order to determine the local flow at regions within the balance port. This is done by imposing a zero normal velocity gradient at the balance port. Now, the port boundary coincides with the nodes of the velocity component normal to the port. Thus, the mass flux for a given port cell is initially set equal to the mass flux of the first adjacent velocity cell inside the boundary. This is simply the product of the normal velocity and fluid density at the first inner velocity cell. The row of cells around the periphery of the balance port are then assigned an additional mass flux due to fluid flow tangential to the port plane. Once the mass flux for all port cells has been established, the balance in Equation 2.98 is then reassessed. If the balance is non-zero, then a flow correction is applied uniformly to all cells in the balance port so that Equation 2.98 is satisfied.

This method of coupling of the flow and the balance port has a tendency to become unstable. Indeed, in all the CFD modelling work presented in this thesis, divergence of the flow at the balance port would occur if allowed. To prevent divergence from occurring, the reference velocity for normalising the turbulence energy was also used to specify the maximum allowable flow rate in the direction normal to the port. The value chosen in the modelling work presented in this thesis was

typically of the order of 1-2 m/s. This is approximately in the range of maximum velocities observed in experiments relating to the scenarios being modelled[1].

2.4.7. Convergence and Under-Relaxation

With any numerical method that involves iteration, a decision must be made at some stage as to what point the iterations will be terminated. Typically, this is when iteration produces only very small variations in the quantities being calculated, with the trend being that the differences between the values at successive iterations are progressively getting smaller as iteration continues*. Naturally, before the decision to terminate a converging sequence of numbers is made, a converging sequence of numbers must first be produced. Under-relaxation of quantities to produce convergence, and calculation of residuals as a means of quantifying convergence, were discussed in Section 2.3.5.

Under-relaxation is employed throughout CESARE-CFD to prevent divergence of a number of variables - three velocity components, pressure equation (mass continuity), turbulence energy, turbulence dissipation rate, fuel mixture fraction, fluctuation of mixture fraction, enthalpy, fluid viscosity, fluid density, fuel source, enthalpy source, radiative heat source, and balance port flow - a total of thirteen, plus another five associated with particle trajectories, and two for fuel and enthalpy correction, not used in this study. Many of the values used in this study followed recommendations due to Kent[53], although experimentation by the author refined values to make them more suitable to the particular problems being modelled.

For steady state simulations, it is recommended[53] that the under-relaxation factor for the pressure equation should be 1 if possible, while the factors for enthalpy and mixture fraction should be high (0.8-1.0). The factors for the velocity components should be low (0.2-0.3) for flows controlled by buoyancy (as is the case for the work presented in this thesis). The turbulence equations are also sensitive, so the factors are likewise suggested to be kept low[53]. These guidelines were indeed found by the author to be effective in achieving convergence. It was found that a value of 0.7 for enthalpy and mixture fraction factors were necessary to help stabilise the initial stages of the solution, but that they could be raised to 1.0 as the solution was approached. The factors for the three velocity components were usually kept at 0.3. It was noted that when they ware set at 0.7 the solution was likely to diverge and numerical overflow errors occurred. Values of around 0.3 for the

* The concept here is that numbers hopefully form a Cauchy sequence; if terms are getting sufficiently closer together, then the sequence is converging to a fixed point which is likewise close to the current values.

three source terms were found to be effective for maintaining stability. Values for turbulence energy and dissipation, and fluid viscosity and density assumed the suggested[53] typical values of 0.3, 0.3, 0.5 and 0.5 respectively.

For unsteady simulations, all under-relaxation factors should, if possible, be set to unity. However, it was found that not under-relaxing velocity and turbulence, even for unsteady state, resulted in instabilities in the solution. Values of 0.8 for velocity, and 0.5 for turbulence, were found to stabilise the solution. In the early stages of an unsteady simulation, some instabilities usually occur due to the sudden changes in conditions, from ambient to a full fire situation for instance. However, if the instabilities persisted after, say, 100 time steps, then the under-relaxation values would need to be reassessed and the simulation re-started.

Refinement of the under-relaxation factors was achieved by monitoring the values of the residuals as the solution progressed. The values whose residuals were monitored were the three velocity components, mass, and enthalpy. The residual for the flow variable in question at a particular cell is given by Equation 2.70, with the variation that the right-hand side of the equation is divided by a_P. The monitored value of the residual is the sum over all flow cells divided by the number of flow cells i.e the average residual of the flow region. The residuals have not been normalised, so they have the same units as the flow variable to which they apply. Thus, the magnitude of the residuals needs to be assessed in context to the magnitude of the variable itself. For instance, since the heat release rate is of the order of 10^4 kJ/kg, while flow rates are of the order of 1 m/s, it is expected that velocity residuals will be several orders of magnitude less that the enthalpy residuals.

Convergence of the solution is characterised by the residuals gradually getting smaller. For coarse grids, the residuals appeared to decrease comparatively steadily and rapidly, whilst for finer grids, the residuals reduce to a particular level, and further iterations do not reduce the residuals by any appreciable amount. The residuals at this point were typically of the order of 10^{-6} kg for mass, 10^{-3} m/s for velocity, and 0.5 kW for enthalpy, which are sufficiently small for convergence to have occurred.

No specific convergence criteria were encoded in the model itself. For steady-state simulations, a number of iterations was specified at the outset (usually a round number, like 1000 or 2000) and the model left to execute, where it would be checked at completion (occasionally, intervention was required during execution to adjust under-relaxation factors). If the residuals were sufficiently small (of the order of the figures quoted above), then the solution was accepted, otherwise the simulation was continued, with adjustments made to under-relaxation factors, if appropriate. For

unsteady-state simulations, a steady-state simulation needed to be performed to initiate the calculations, with the same constraints on convergence as described above. However, since the unsteady-state calculation occurs over a specified number of iterations (each iteration corresponding to a single timestep; there are no iterations within timesteps), the convergence of the solution can only be assessed by examining the entire simulation. If residuals have remained low throughout the simulation (less than, say, 10^{-2} m/s for velocity and 1.0 kW for enthalpy), then convergence of the solution can be accepted with confidence. If divergence has occurred at any stage, then there is little option but to adjust the appropriate under-relaxation factors or the time step, and re-run the simulation.

Another quantity which is useful to examine in order to assess the convergence of a simulation is the global energy balance. For a steady state simulation, the energy contributed to the flow region must balance the energy lost from the flow region. For an unsteady state simulation, the difference between the energy gains and energy losses must equal the change in energy of the flow region. This may be expressed by the equation

$$E_{in} = E_{out} + \frac{dE}{dt} \tag{2.99}$$

where E_{in} is the energy entering the flow region, E_{out} is the energy leaving the flow region, and dE/dt is the change in energy of the flow region, which is zero for a steady state solution. The balance should ideally be achieved at every iteration.

In CESARE-CFD, E_{in} is the sum of the enthalpy contributed by all port flows entering the flow region. This includes all forced flow ports, plus the inflowing component of the balance port. The latter will in general contribute only a small amount of enthalpy to the flow region, as the inflow at a balance port is usually designated as air at ambient temperature. The majority of the enthalpy originates from the forced flow ports designated as fuel ports.

The term E_{out} comprises several terms. It is the sum of the enthalpy leaving via all outflowing ports, energy lost by convection to the boundaries, and radiant energy lost to the walls. The latter two terms may be of either sign (i.e. they may be energy sources or energy sinks), but for the purposes of calculating the energy balance, they are always treated as terms contributing to the energy losses.

2.5. CONCLUSION

A review has been performed of recent work into CFD modelling of enclosure fires, and a comprehensive overview of the CFD model used in the modelling work in this thesis has been presented. The model has many fundamental features in common with other CFD models widely used in fire modelling, so the findings and conclusions presented throughout the thesis should, in general, also apply to other CFD models.

Validation was identified as a continuing concern to CFD modellers of enclosure fires, with the availability (or lack thereof) of suitable and adequate experimental data for validation purposes contributing to the demand for further validation exercises, particularly for complex enclosure geometries. This thesis will contribute to the further development and validation of CFD models in general by making comparisons with data acquired from full-scale experiments performed in a realistic apartment-style enclosure.

3. ENCLOSURE FIRE MODELLING

3.1. INTRODUCTION

In past work, the radiation submodel of the original CESARE-CFD model has not provided sufficiently accurate predictions of radiant heat transfer associated with a particular full-scale fire scenario[3]. In particular, the CFD model predicted levels of radiant heat flux to floor level in a full-scale fire experiment that were in some cases only half the measured level. The underestimation carries implications not only for the predicted heat flux to floor level, but the fire plume and upper layer temperatures as well. It is important to remedy these discrepancies, as the phenomenon of flame spread over a fuel surface is sensitive to the level of radiant flux, as will be elaborated upon in later chapters.

The broad scope of the research reported in this chapter is to undertake further experimental and modelling work, with a particular aim of developing an improved radiation model to rectify the discrepancies in the distribution of radiant heat flux. The first step is to review the theory of radiative heat transfer, and the methods, both analytical and numerical, for solving the resulting equations, in order to identify the cause of the discrepancies in the radiation heat transfer predictions of CESARE-CFD, and to propose an improved mathematical formulation of the problem. Comparisons of the predictions from the modified model need to be compared with experimental results and predictions from the unmodified model, to investigate whether the modifications made result in improved predictions.

A further aim of the research reported in this chapter is to scrutinise the numerical behaviour of the CFD model. This includes examining issues such as the grid independence and convergence of the solution, to ensure that errors due to numerical artefacts are minimised. Additionally, the sensitivity of the solution to changes of the value for some model parameters, for which the exact value is not precisely known, are also examined, to determine whether the choice of values for the parameters has a significant effect on the solution.

3.2. THERMAL RADIATION

Radiant heat may be defined as the energy transferred by electromagnetic waves emitted by a system due to the temperature of the system. Radiation is one of three basic mechanisms of heat

transfer which occur in physical systems, the other two being convection and conduction. The relative contributions of the three mechanisms to the total heat transferred depends on the situation being considered. Radiation becomes important when considering heat exchange between isolated items, since unlike convection and conduction, it does not require a medium through which to propagate, and it is also the dominant factor in situations of high temperatures, such as those leading to flashover fires in buildings. This is due to the rapid increase in radiant output of an emitting body as its temperature increases.

Because it is one of the major heat transfer mechanisms, a numerical simulation of a combustion scenario must take radiation into account. However, there are many variables involved in solving the radiation transfer equations, since every solid surface, fire plume, smoke particle, or volume of gas is a potential emitter and absorber of radiant heat. The extent of emittance or absorbance depends on the substance, and its temperature, density, orientation, and position relative to other emitters, and many other variable factors. An exact solution of radiation distribution in real cases is out of the question, and even numerical solutions must make many assumptions and approximations if the computation time is to be kept reasonably short.

The accurate prediction of radiation in a combustion situation is important for several reasons. Radiation itself is a hazard to persons in the vicinity of a blaze, so predictions of the radiation levels in a building-fire will identify possible risks to both occupants of the building and fire fighters. There are also many phenomena occurring in fire situations which are sensitive to the level of radiant heat present, such as the ignition of an object either remote from the fire source or in contact with it[58], the rate of combustion of a material[59], and the spread of flame across an item[60,61,62]. Accurate prediction of these phenomena therefore relies on the ability to accurately model radiation heat transfer.

Because it is a significant heat transfer mechanism, radiation should also be considered in CFD models which attempt to simulate situations where combustion and heat release is occurring, such as enclosure fires. Radiation heat transfer affects the temperature of the flow regions, as well as the temperature of boundaries. The temperature distribution will in turn affect buoyancy driven flows and the convective heat transfer at boundaries. Several authors have investigated the interaction between fluid flow and radiation in enclosures[20,36,56,63,64,65], with some reporting the benefits of including even basic radiation transfer calculations in CFD simulations compared with using no calculations at all[20,36].

3.3. THEORY OF RADIATIVE HEAT TRANSFER

3.3.1. Fundamentals

Since thermal radiation is a form of electromagnetic radiation, its behaviour can be described by the equations of electromagnetic wave theory and quantum mechanics. Radiation from a surface is emitted as photons, with each photon possessing an energy that is dependent on its frequency (or equivalently, its wavelength). The main thermal radiation spectrum lies in the wavelength band between 0.1μm and 100μm. The shorter wavelengths correspond to the visible spectrum, so that bodies hotter than about 500°C emit sufficient light to be visible to the human eye. Like visible light, thermal radiation travels in straight lines, and large opaque objects in the path of a radiation source will cast shadows. Thus, a body cannot directly receive radiation from another body unless it can "see" it.

Any object which is hotter than absolute zero radiates energy. An ideal body, or "black body" absorbs all radiant energy incident upon it, and emits the maximum possible amount of thermal radiation at a particular temperature. This amount is given by the formula

$$E_b = \sigma T^4 \tag{3.1}$$

where E_b is the rate of energy radiated per unit area of the surface of the black body into the hemisphere of space above it, T is the absolute temperature, and $\sigma = 5.67\times10^{-8}$ W/m^{2}K^4 is the Stefan-Boltzmann constant. The emissive power at a given wavelength, $E_{b\lambda}$, for a black body is given by Planck's distribution law

$$E_{b\lambda} = \frac{c_1 \lambda^{-5}}{e^{c_2/\lambda T} - 1} \tag{3.2}$$

where λ is the wavelength, T is the absolute temperature, and c_1 and c_2 are the Planck constants with values 3.742×10^{-16} Wm^2 and 0.001439 m·K respectively. Integration over all wavelengths yields Equation 3.1.

Real objects typically absorb only a fraction of the thermal radiation incident on them. The fraction of radiation at wavelength λ absorbed is called the monochromatic emissivity, and is denoted by ε_λ. According to Kirchoff's Law[66], the emissivity of opaque bodies also describes the fraction of radiant energy emitted at a given wavelength from the surface, compared with a black body at the same temperature. The function ε_λ is often averaged over the entire spectrum to yield the so called grey body approximation, given by

$$\varepsilon = \frac{\int_0^\infty \varepsilon_\lambda E_{b\lambda} d\lambda}{\int_0^\infty E_{b\lambda} d\lambda} = \frac{\int_0^\infty \varepsilon_\lambda E_{b\lambda} d\lambda}{\sigma T^4} \tag{3.3}$$

so that the total energy emitted at the surface of the body per unit area is given by

$$E = \varepsilon \sigma T^4 \tag{3.4}$$

The intensity of a beam of radiant energy is defined as the energy per unit area per unit solid angle, and is related to E by the equation

$$I = \frac{E}{\pi} = \frac{\varepsilon \sigma T^4}{\pi} \tag{3.5}$$

3.3.2. Direct Transfer Between Surfaces

The exchange of radiation between two surfaces depends on two factors; the view the surfaces have of each other, and the emitting and absorbing characteristics of each surface. There are a few cases for which the situation can be simplified. An example is a black body completely surrounded by black surfaces. If the temperature of the body is T_1, and the temperature of the surrounding surfaces is T_2, then the body emits radiation at a rate of σT_1^4 while receiving radiation at a rate of σT_2^4, so that the net heat transferred to the body is

$$q = \sigma(T_2^4 - T_1^4) \tag{3.6}$$

A similar situation exists when considering a grey body with emissivity ε, again completely surrounded by black surfaces. In this case, the body emits $\varepsilon \sigma T_1^4$, while receiving σT_2^4 from its surroundings. However, it only absorbs a fraction ε of this energy, the rest being reflected, so that the net heat transferred to the body is

$$q = \varepsilon \sigma(T_2^4 - T_1^4) \tag{3.7}$$

The situation becomes a little more complicated when a grey body is surrounded by grey surfaces, because some of the radiation emitted by the body will be reflected back to it by the grey surfaces. However, if the body is small compared with the surroundings, then Equation 3.7 may be used (substituting $\varepsilon_2 T_2^4$ for T_2^4), since the body will intercept a negligible portion of the reflected radiation.

Consider now the radiation transferred between two surfaces. The view factor or configuration factor, F_{12}, between the surfaces is defined as the fraction of the total radiation emitted by one surface which is directly incident on the other. Since radiation from the first surface is emitted into the hemisphere above it, the view factor is the fraction of the hemisphere obscured by the second surface, as viewed from the first. To calculate this mathematically, the two surfaces are taken to have areas A_1 and A_2 respectively, with the temperature being uniform over each surface. The radiation emitted from an elemental area dA_1 at an angle ϕ_1 to the surface normal, and transmitted through the incremental solid angle $d\Omega$ is given by

$$dq = \frac{E}{\pi} dA_1 \cos(\phi_1) d\Omega \tag{3.8}$$

where E is the energy emitted by surface 1 as given by Equation 3.4 and q is the heat released per unit area. Integrating this expression over the whole of A_1 and the solid angle Ω (the angle subtended by A_2 at dA_1) gives the total energy transferred from A_1 to A_2. i.e.

$$q = \frac{E}{\pi A_1} \int_{\Omega} \int_{A_1} dA_1 \cos(\phi_1) d\Omega \tag{3.9}$$

Now, $d\Omega$ intercepts surface 2 at the area element dA_2. The relationship between $d\Omega$ and dA_2 is given by

$$d\Omega = \frac{dA_2 \cos(\phi_2)}{r^2} \tag{3.10}$$

where r is the distance between the two surface elements, and ϕ_2 is the angle which the line joining the two elements makes with the normal of surface 2. Equation 3.9 can now be rewritten as

$$q = \frac{E}{A_1} \int_{A_2} \int_{A_1} \frac{\cos(\phi_1)\cos(\phi_2)}{\pi r^2} dA_1 dA_2 = E F_{12} \tag{3.11}$$

and hence, the configuration factor can be expressed as

$$F_{12} = \frac{1}{A_1} \int_{A_2} \int_{A_1} \frac{\cos(\phi_1)\cos(\phi_2)}{\pi r^2} dA_1 dA_2 \tag{3.12}$$

The subscripts may be interchanged to yield a similar expression for F_{21}, and comparison with Equation 3.11 gives the useful result

$$A_1 F_{12} = A_2 F_{21} \tag{3.13}$$

Equation 3.12 may be integrated directly, although for simple geometries the factors have been solved and tabulated in many basic texts.

For heat transfer between grey surfaces of significant size, it is necessary to take into account the reflected radiation, which requires more complicated computational procedures. One such method of calculating the transfer is Hottel's zone method[67]. In this method, the surfaces (usually comprising an enclosure) are divided into n cells, and the configuration factor between each cell and every other cell is calculated. Rather than just the emitted radiation intensity from a surface cell being considered, the sum of the emitted and reflected radiation, known as the radiosity is considered. Because the reflected intensity is dependent on the radiosity from all the other cells, considering the radiosity from each cell results in n equations with n unknowns, which may be solved simultaneously.

3.4. RADIATION FROM AN ABSORBING MEDIUM

Consider a beam of radiation with intensity I emitted from a diffuse radiating surface. The intensity of the beam is independent of the angle of emission, and if it is propagating through a non-absorbing medium it will retain this intensity until it encounters another surface, at which point some portion may be absorbed and the rest reflected, depending on the emissivity of the surface encountered. However, if the medium is an absorbing one, then a beam with intensity I will be attenuated by an incremental amount $-\mathrm{d}I$ on passage through an incremental length $\mathrm{d}L$. The attenuation is proportional to the intensity of the incident beam, and is given by

$$-\mathrm{d}I = KI\mathrm{d}L \tag{3.14}$$

where K is the attenuation or extinction coefficient. The radiation removed from the beam may be dispersed in all directions, a process known as scatter, or dissipated into other forms of energy, otherwise known as absorption. The relative contributions of absorption and scatter to the total extinction of the beam vary depending on the nature of the absorbing medium. Equation 3.14 is integrated over a length L to determine the intensity of the beam at any point on this length, to give

$$I = I_0 e^{-\int_0^L K\mathrm{d}L} \tag{3.15}$$

or if K is independent of position,

$$I = I_0 e^{-KL} \tag{3.16}$$

Now, the fraction of radiation transmitted through the medium, τ, is given by

$$\tau = \frac{I}{I_0} = e^{-KL} \tag{3.17}$$

If it is assumed that the remainder is absorbed by the medium, and that the medium behaves as a grey radiator, then the absorption, α, and hence the emissivity (by Kirchoff's Law) of the medium is given by

$$\varepsilon = \alpha = 1 - \tau = 1 - e^{-KL} \tag{3.18}$$

and hence the radiant energy emitted by the medium is

$$q = \varepsilon\sigma T^4 = (1 - e^{-KL})\sigma T^4 \tag{3.19}$$

It is seen that the emissivity of the medium is a function of the pathlength, L. When calculating the emissivity of a volume of radiating medium of arbitrary shape, it is useful to consider the mean beam length, L_m, of the medium. This is generally expressed as a function of the extinction coefficient, K, and the characteristic dimension, D, of the volume i.e.

$$L_m = f(KD) \tag{3.20}$$

Calculations involving the exchange of radiant heat between an absorbing medium and its enclosing surface are much simplified by using the mean beam length. The standard emissivity of a gas is defined as the emissivity corresponding to a fixed path length L_m. It can be expressed as the fraction of radiation from a hemisphere of gas of radius L_m to a point in the centre of the base, compared with hemispherical black body radiation.

3.4.1. Absorbing Gases

A vacuum is a perfectly non-absorbing medium, while homonuclear gases such as N_2, O_2, or H_2 are very nearly non-absorbing in the thermal spectral region. Media which do absorb and emit thermal radiation include heteronuclear gases (i.e. gases whose component molecules comprise two or more different elements; for example H_2O, CO, CO_2, HCN, HCl), and gases that contain a suspension of fine particles such as soot, pulverised coal, or oil droplets. Absorbing gases will be dealt with first.

The most important radiating gases encountered in engineering applications are water vapour (H_2O) and carbon dioxide (CO_2), since these are the gases evolved in the greatest quantities in the combustion of most common materials. These gases do not emit over the whole thermal spectrum, but rather in bands within the spectrum[67]. However, the gases may be treated as grey gases by

averaging the monochromic emissivities of these bands over the whole spectrum, as in Equation 3.3.

The emissivity of a radiating gas, as given by Equation 3.18, is a function of the absorption coefficient and the mean beam length. The absorption coefficient itself is dependent on the temperature of the gas, the partial pressure of the gas (or equivalently its concentration), and the total pressure of the medium containing the radiating gas. If more than one radiating species is present in a medium, a correction factor for the overlap of the radiating bands of the species is often included. For a mixture of carbon dioxide and water vapour, the emissivity may be expressed as

$$\begin{aligned}\varepsilon &= \varepsilon_{CO_2} + \varepsilon_{H_2O} - \Delta\varepsilon \\ &= \varepsilon^*_{CO_2} C_{CO_2} + \varepsilon^*_{H_2O} C_{H_2O} - \Delta\varepsilon\end{aligned} \tag{3.21}$$

where $\varepsilon^*_{CO_2}$ and $\varepsilon^*_{H_2O}$ are respectively the emissivities of carbon dioxide and water vapour for a total pressure of 1 atmosphere and in the limit as the partial pressure of each approaches zero, C_{CO_2} and C_{H_2O} are the correction factors for partial pressures different from zero, and $\Delta\varepsilon$ is the correction factor for the overlapping of the carbon dioxide and water bands. These values have been tabulated for varying temperatures and partial pressures by Hottel and Sarofim[67].

Since the emissivity of a gas depends on many variables, and the dependence is not always a simple one, it is often necessary to make approximations in order to perform engineering calculations. A suggestion[67] for the combined emissivity of carbon dioxide, ε, is approximately inversely proportional to the gas temperature, T_g, so that the quantity εT_g is a function of the pathlength, L, and the sum of the partial pressures, $(p_{CO_2} + p_{H_2O})$. The function only changes slightly as the ratio of the partial pressures changes. However, the relationship is valid for temperatures in a range encountered in furnace operating conditions, so that its usage is limited for applications outside of furnace modelling[67].

The simplest approximation for estimating gas emissivity is to assume that the absorption coefficient depends only on the partial pressure of the gas (or gases), so that the emissivity may be written

$$\varepsilon = (1 - e^{k_p pL}) \tag{3.22}$$

where p is the partial pressure of the emitting gas, and L is the pathlength.

3.4.2. Absorbing Particles

In addition to absorbing gases, an absorbing medium may contain a suspension of particles which also interact with thermal radiation. These particles may be either fuel particles, such as pulverised coal or aspirated liquid droplets, or combustion products such as ash or soot. The diameters of these particles are all of the order of 200μm downwards, with the exception of soot particles which are small agglomerations ranging from 5nm to 150nm in diameter, composed of carbon or high molecular weight hydrocarbon crystals[68]. It is the presence of soot which causes the yellow-orange colour emitted by luminous flames.

Radiation incident on a suspension of particles is partly transmitted, partly absorbed, and partly scattered. Absorbed radiation may be re-emitted diffusely at other wavelengths, depending on the temperature of the particles, while scattering is a combination of diffraction and reflection at the particle surface, and refraction and internal reflection within the particle. A complete description of the interaction of spherical particles with electromagnetic radiation involves the solving of Maxwell's equations. The analysis involves the parameter $\pi d/\lambda$ (where d is the diameter of the particle, and λ is the wavelength of radiation under consideration) and the complex refractive index $n\text{-}ik$. Such an approach, while accurate, is unnecessarily complicated and difficult for most engineering applications. A simpler approach is usually employed in such situations. Two approaches described here relate to the particular size range of the particles relative to the wavelength of radiation, namely "large" particles and "small" particles.

Large particles[66] are those for which $d > 5\lambda/\pi \approx 2\lambda$. Since the wavelengths important to thermal radiation are in the range 1-1000μm, fuel particles, ash, and smoke from smouldering combustion fall into this category. Provided that the particles are present in the medium in low concentrations, the absorption coefficient is proportional to the area intercepted by the particles. This can be written

$$A = c_n A_n \tag{3.23}$$

where c_n is the number of particles per unit volume of the suspension, and A_n is the projected area per particle in the direction of the radiation. Similar expressions can be written for the volume and mass concentrations ($c_v A_v$ and $c_m A_m$, noting that $c_m = \rho c_v$, where ρ is the density of the particle). It can be shown[66] that for randomly distributed particles, $A_v = S_v/4$, where S_v is the surface area per unit volume of particles. For spherical particles, this quantity is $6/d$. Hence, the absorption coefficient can be written

$$K = c_v A_v = \frac{c_v S_v}{4} = \frac{6 c_m}{4 \rho d} \tag{3.24}$$

Small particles are those for which $d < 3\lambda/5\pi \approx \lambda/5$,[66] which for real fires applies mainly to soot particles. Since the particles are much smaller than the wavelengths of radiation, obscuration cannot be described by simple geometric optics. An alternative analysis is possible if it assumed that the particle is composed of a dielectric material, and is small enough so that the field produced by a passing electromagnetic ray is approximately uniform across it. This approach leads to the Rayleigh equation, which in turn describes the apparent scattering and absorption cross sections of the particle. A full description of the analysis is described elsewhere[67,68]. An important result obtained from this analysis is that the scattering term is negligible in comparison to the absorption term. The monochromatic absorption coefficient is given by

$$K_\lambda = \frac{36\pi\phi c_v}{\lambda} \equiv \frac{\kappa c_v}{\lambda} = \frac{\kappa c_m}{\rho\lambda} \tag{3.25}$$

where ρ is the density and c_m the mass concentration of the particles, λ is the wavelength, and

$$\phi = \frac{nk}{(n^2 - k^2 + 2)^2 + 4n^2k^2} \tag{3.26}$$

is a function of the complex refractive index, n-ik, of the particles. The density of soot is taken to be that of lampblack carbon, which is given[47] as 1900 kg/m^3 (compared with single crystal graphite, 2250 kg/m^3).

Since the absorption coefficient is inversely proportional to the wavelength, a cloud of soot particles is markedly non-grey. It is nevertheless possible to obtain a grey body emissivity of the soot cloud by substituting $\varepsilon_\lambda = (1 - e^{-K_\lambda L})$ into Equation 3.3. After appropriate manipulations and cancellations, the following equation is obtained

$$\varepsilon = 1 - \frac{1}{\left(1 + \frac{\kappa c_v L T}{c_2}\right)^4} \tag{3.27}$$

where c_2 is the constant in Planck's formula 3.2. Several values of κ for soot have been quoted in the literature. The value also varies as the composition of the soot varies from pure carbon to heavy hydrocarbons. For propane flames, a value of κ=4.9 is often quoted as the best estimate based on current measurements.

Equation 3.27 gives the grey body emissivity of a cloud of soot particles. However, some applications require the mean absorption coefficient so that Equation 3.16 may be employed. Tien et al[69] suggest a value of

$$K_{soot} = 3.72\frac{\kappa c_m T}{\rho c_2} \tag{3.28}$$

which is the average of the mean absorption coefficients in the optically thin and optically thick limits.

When radiating gas and soot are both present in a medium, the simplest way of estimating the emissivity is to add the absorption coefficients and substitute this sum into Equation 3.18. A suggestion for better approximation is given by[69]

$$\varepsilon_{total} = (1 - e^{-K_s L}) + \varepsilon_g e^{-K_s L} \tag{3.29}$$

This emissivity may then substituted into Equation 3.18 to find the equivalent "pseudo-grey" absorption coefficient[29].

3.5. NUMERICAL SOLUTIONS

Thermal radiation appears in Equation 2.1 for conservation of heat energy, as the source term, *S*. This quantity must be calculated for each cell in the region of interest, and the calculation requires its own subroutine within a field model.

There are three main features which are required of a computational procedure. Firstly, it must possess a satisfactory degree of accuracy, otherwise the results produced will be meaningless. Secondly, it must be computationally economical; in other words, the number of calculations and hence the time taken to perform them needs to kept to a minimum. There is often a balance which needs to be made between accuracy and economy, since it generally requires a greater number calculations to achieve better accuracy. Thirdly, the method requires geometric flexibility, so that it may be applied in a variety of situations.

Hottel's zone method works well in simple situations, and in such cases is computationally economical since the solution requires solving an *n*-by-*n* matrix, for which efficient algorithms exist (provided *n* is not too large). However, its main draw back is that it lacks geometric flexibility, since the configuration factors need to be calculated in advance, and are unique for each situation. Even for a simple rectangular enclosure, the configuration factors are quite complicated. In

addition to this, greater accuracy requires a larger number or cells, so that computational economy is severely compromised.

3.5.1. Monte Carlo Method

A way of avoiding the lengthy procedure of calculating configuration factors of the zone method is to use the Monte Carlo method. This is a procedure by which the nature of a physical process is determined by its effect or action upon a selection of a series of physical quantities with a random spread of values. In this sense it may be applied to any process where certain events can be assigned probabilities. To calculate the configuration factor between two surfaces using the Monte Carlo method, the first step is to choose a point at random on the first surface. The probability weighting is assigned in such a way so that every point on the surface has equal probability of being chosen. The second step is to choose a direction for a ray to be emitted from this point on the surface. Every direction in the hemisphere above this point must have equal probability of being chosen. The third step is to determine whether this ray strikes the second surface. These three steps are then repeated many times, until the desired level of statistical accuracy is achieved. The configuration factor is then the number of rays which strike the second surface divided by the total number of rays emitted.

This method can be extended to include other aspects of radiative heat transfer. A ray incident at a surface has a probability ε of being absorbed, and hence a probability of $(1-\varepsilon)$ of being reflected. Similarly, a ray traversing a characteristic length L through an absorbing medium has a probability $1-e^{-KL}$ of being absorbed completely. A ray which is not absorbed is assumed to continue unattenuated. If the emissivity of the surface or the absorbing medium varies with wavelength, then the wavelength of the emitted ray may be chosen from

$$\text{prob}[x \le \lambda] = \frac{\int_0^{\lambda} \varepsilon_\lambda E_{b\lambda} d\lambda}{\int_0^{\infty} \varepsilon_\lambda E_{b\lambda} d\lambda} \qquad (3.30)$$

where x is a randomly generated number between 0 and 1.

When the Monte Carlo method is employed to model the radiation exchange in an enclosure, a ray is emitted from a random point in the enclosure, and tracked to extinction, which may involve many reflections from surfaces. The method offers a high degree of geometric flexibility, since the method determines the configuration factors rather than requiring them as inputs. However the method is limited by the fact that a large number of random rays needs to be generated in order to

minimise statistical deviations from the true solution. Such a large number of calculations makes this method slow, and is further limited by the imperfections of computer random number generation routines.

3.5.2. Six-Flux Method

The six-flux method was widely used in early field models, and is still used today due to its relative simplicity and computational efficiency. The method is based on the radiation transfer equation, obtained by considering the balance of monochromatic radiant energy of a pencil of rays passing through a control cell filled with a participating medium. The equation is given by[55,63]

$$\frac{dI}{ds} = -(k_a + k_s)I + k_a\frac{E_g}{\pi} + k_s\int_{4\pi} p(\bar{\Omega},\bar{\Omega}')I(\bar{\Omega}')d\Omega' \qquad (3.31)$$

where I is the radiant intensity in the direction of $\bar{\Omega}$, s is the distance traversed by the ray, $E_g = \sigma T_g^4$ is the black body emissive power of the gas, k_a and k_s are the absorbing and scattering coefficients, and $p(\bar{\Omega},\bar{\Omega}')$ is the probability that incident radiation in the direction $\bar{\Omega}'$ will be scattered into the increment of solid angle $d\Omega$ about $\bar{\Omega}$.

As the name suggests, the six-flux method considers the six rays passing through a control cell normal to each face. If F_i^+ and F_i^- are the forward and backward fluxes passing through the cell in the i direction, then the generalised six-flux model equations are of the form[63]

$$\frac{d}{dx_i}\left(2\Gamma_R\frac{dR}{dx_i}\right) + S_i = 0 \qquad (3.32)$$

where

$$\Gamma_R = \frac{1}{(k_a + k_s)}$$

$$S_i = \frac{dq_i''}{dx_i} = -2(k_a + k_s)R_i + 2k_aE_g + 2\frac{k_s}{3}\sum_{i=1}^{3}R_i$$

$$R_i = \frac{F_i^+ + F_i^-}{2}$$

$$\dot{q}_i'' = F_i^+ - F_i^-$$

Equation 3.32 is in the same form as the general conservation equation, Equation 2.1. Its solution is therefore a simple extension of the methods presented in Chapter 2. The source term, S_i, in the radiation equation appears as a sink term in the enthalpy equation. The conditions at the boundary

will depend on the emissivity and temperature at the boundary, and whether the boundary is solid, or an opening in the enclosure. Assuming a solid surface which is grey, if the flux incident on the surface is F_i^+, the returning flux is

$$F_i^- = (1-\varepsilon_w)F_i^+ + \varepsilon_w \sigma T_w^4 \tag{3.33}$$

so that the net radiation flux leaving the gas phase is

$$\dot{q}_i'' = \frac{2\varepsilon_w}{2-\varepsilon_w}\left(R_i - \varepsilon_w \sigma T_w^4\right) \tag{3.34}$$

where the subscript w refers to the wall. If the boundary is at an opening, then the net flux leaving the enclosure is

$$\dot{q}_i'' = 2\left(R_i - \varepsilon_{op}\sigma T_{op}^4\right) \tag{3.35}$$

where the subscript *op* refers to the cell adjacent to the opening. The leaving fluxes are sink terms in the radiation equation.

The advantage of the six-flux method is that the numerical methods required to solve the equations already exist in a standard CFD model. However, its main disadvantage is the small number of directions in which radiation transfer is calculated (six), and its geometrical limitations. The method is designed to operate on an orthogonal, rectilinear grid, and while it can be generalised to non-regular grids, the resulting formulation is often exceedingly complicated[55]. Because the radiation transfer is only calculated in the Cartesian directions, inaccuracies may arise due to the small number of directions sampled. As a result of these shortcomings, Kumar and Cox[63] have suggested that while the six-flux method may be acceptable for calculating radiant heat transfer from stratified layers, it is unsuitable for the detail required to model flame spread.

3.5.3. The Discrete Transfer Method

The discrete transfer method was developed by Lockwood and Shah[55] to avoid the shortcomings of Hottel's zone method, the Monte Carlo method, and the six-flux method, while retaining the advantages, to produce a fast, accurate, and geometrically flexible model. The discrete transfer method was developed in such a way that it could be incorporated into a general field model. The basis of the method is again the solution of the general equation for radiant intensity, Equation 3.31. Defining the extinction coefficient $k_e \equiv k_a + k_s$, the elemental optical depth $ds^* \equiv k_e\, ds$, and the

modified emissive power $E^* \equiv 1/k_e[k_a E_g + (k_s/4)\int_{4\pi} p(\bar{\Omega},\bar{\Omega}')I(\bar{\Omega}')d\Omega']$, Equation 3.31 may be rewritten as

$$\frac{dI}{ds^*} = -I + \frac{E^*}{\pi} \tag{3.36}$$

Equation 3.36 is solved for a number of representative rays within the region of interest. Unlike the Monte Carlo method, however, the direction of these rays is specified rather than selected at random, and each ray is tracked from surface to surface only, rather than being partially reflected and tracked to extinction. The representative rays are presumed to emanate from the centre of a given surface cell, in a regularly spaced pattern into the hemisphere above the surface. As each ray is tracked across the enclosure, it will pass through a number of control volume cells and will be attenuated by an amount specified by Equation 3.36 in each cell. The net loss or gain in intensity of the ray corresponds respectively to a gain or loss of heat energy from the control cell. When the rays from all surface cells have been calculated, a total radiative source term can be determined.

Since the temperature within a control cell is presumed to be constant, Equation 3.36 may be integrated to yield

$$Ie^{s^*} = \frac{E^*}{\pi}e^{s^*} + C \tag{3.37}$$

where C is the constant of integration. If E^* is also presumed constant over the cell, the following recurrence relation is obtained

$$I_{n+1} = I_n e^{-\delta s^*} + \frac{E^*}{\pi}(1 - e^{-\delta s^*}) \tag{3.38}$$

where I_{n+1} and I_n are respectively the leaving and entering intensities of the ray passing through the control cell, and δs^* is the length of the ray segment which intersects the control volume.

It is now necessary to specify the initial intensity of the emitted rays. If the surface is black, then the intensity of the leaving ray is simply

$$I_w = \frac{E_w}{\pi} = \frac{\sigma T_w^4}{\pi} \tag{3.39}$$

and each I_n can be calculated using a once through application of Equation 3.38. The heat received by a surface element is the sum of all the rays emitted from other elements which happen to be incident on the surface element. If the surface is grey, however, then it is necessary to use

$$I_w = \frac{q_+}{\pi} = (1 - \varepsilon_w)\frac{q_-}{\pi} + \varepsilon_w \frac{E_w}{\pi} \tag{3.40}$$

where q_+ and q_- are respectively the leaving and incident energy fluxes. However, in order to calculate the leaving flux at a given surface element, it is necessary to know the leaving flux from all the other points whose rays are incident on the element. This is a similar problem to that which gives rise to Hottel's method. However, with Hottel's method, the leaving fluxes, or radiosities, are solved simultaneously, whereas with the discrete transfer method, the values of the radiosities are solved by iteration, with the initial values being the grey body emissions of the surfaces. Since solution procedure for the fluid flow equations is itself iterative by nature, this presents no problem.

As indicated by Equation 3.31, the discrete transfer method is capable of including the "in-scattering" term in the calculation of the intensities. Naturally, the inclusion of this term significantly increases the computation time. Fortunately, the scattering term is negligible for radiant gases and soot particles, so scattering can be safely ignored if these are the only radiating species present in the region of interest. Nevertheless, if a situation exists where scattering is significant, its inclusion poses no extra difficulty to the method. If scattering is ignored, then Equation 3.31 can be rewritten as

$$\frac{dI}{ds} = -k_a I + k_a \frac{E}{\pi} \tag{3.41}$$

which is already in the same form as Equation 3.36.

The discrete transfer method has been shown to be a fast, accurate, and geometrically flexible radiation model. It is now widely used as the standard calculation procedure for predicting the radiation distribution in most modern field models.

3.6. RADIATION MODELLING IN CESARE-CFD

The field model FURNACE was originally developed to model pulverised coal fired furnaces and pool fires[27]. The modified version of FURNACE, now referred to as CESARE-CFD, has been used to successfully predict the fluid flows and temperature distributions of building-fires[3,8]. However, the predicted radiation fluxes to the floor level were in some instances approximately half the value of the measured levels[3]. This is most likely a consequence of the fact that little attention was paid to the radiation submodel in previous modifications[3]. This neglect has been recognised in light of the information presented above, and this section describes the modifications of the original code which have to a large extent rectified the discrepancies.

The radiation submodel of CESARE-CFD, as indicated earlier, uses the discrete transfer method, and the bulk of the submodel code deals with the manipulation and formatting of variables required to make the method compatible with the general fluid flow calculation procedure. Since the method has been shown to be accurate[55], particularly for the number of grid divisions used previously[3], the discrepancy is most likely due to the input variables rather than the method itself.

The radiation submodel used for earlier modelling was basically unaltered from the original version developed for a coal fired furnace[27]. This version allows for several variables to be user specified. These are the particle absorption and particle scattering coefficients (constants), an additional absorption coefficient and the subregion for which it is to be included (also a constant), and the number of representative rays to be tracked from each surface element. The number of rays is determined by specifying the number of theta and phi divisions, with theta and phi being the spherical polar coordinates of the hemisphere above the surface element. The gas absorption coefficient is written directly into the source code, and applies throughout the modelled region. The gas absorption coefficient used does assume a temperature dependence, but there is no dependence on the local partial pressures of the radiating gas. This relationship is given by

$$K_{gas} = 0.28e^{-T/1135} \qquad (3.42)$$

This value presumably corresponds to a uniform radiative gas distribution typically encountered in coal fired furnaces. It corresponds roughly to the mean absorption coefficient of a mixture of carbon dioxide and water vapour at a partial pressure in the order of 0.1 atmospheres. The temperature dependence implies that the gas absorption coefficient will highest in regions of highest temperature. Since the hottest region in an enclosure fire is the fire plume, and this is also the region with the highest concentration of species which interact with radiation, the equation is expected to model with some success the fire plume, as well as cooler regions with low concentrations of interacting species. However, some doubt must arise in the equation's ability to predict the absorption coefficient for a cooler interacting region, such as the smoke layer at some distance from the fire plume.

The temperature and concentration of both gas and particles in each control volume cell is calculated by the main fluid flow subroutine. Because the radiation subroutine is computationally intensive, there is an option built into CESARE-CFD which allows the subroutine to use a coarser grid than the flow region, in order to lessen the computation time somewhat. This requires an additional set of computations to convert variables from one grid system to another, although the net result is nevertheless to reduce computation time. Zhao[56] found in a study of radiation and

convection in enclosures that radiation was less sensitive than convection to grid refinement, so that fortunately the radiation grid can be made coarser than the flow grid without significant loss of accuracy. However, certain regions, notably those of high temperature gradient, should not be made too coarse, as the averaging involved in converting from the flow grid to the radiation grid will "smear" the temperatures. As the averaging is linear, while the temperature dependence of radiant heat is quartic, smearing may lead to significant errors in strongly emitting areas such as the fire plume.

Because the gas temperature was the only spatially varying quantity in the original radiation equation, this was the only variable which required conversion from flow grid to radiation grid. The modifications presented in this chapter required that the distributions of soot and CO_2 be calculated also, so these quantities are now also converted to the radiation grid. The net radiant heat transfer in each cell is the only variable which requires conversion back again, so that it may provide a heat source term in the flow region.

The particles considered by the FURNACE program were originally intended to be pulverised coal, or other particles of a similar size, due to its furnace combustion modelling origins. These particles fall into the "large" particle category referred to previously. However, the particles most likely to have an effect on the radiation level in a building-fire are soot particles produced at the fire source. FURNACE and the original version of CESARE-CFD[3] did not include a soot production subroutine, so a soot radiation term could be included in the model only as an additional (constant) absorption coefficient. Accordingly, instead of the soot distribution being calculated by the fluid flow subroutine, the subregion where soot radiation is to be included needed to be specified by the user.

In order to rectify the lack of a soot distribution, a soot formation submodel formulated by Magnussen and Hjertager[48] was included in CESARE-CFD[8]. This submodel should generate a soot source term in the appropriate volume control cells, with the conservation equation (Equation 2.1) calculating the soot mass concentration in each cell in a similar manner to the other scalar quantities. However, at the time of writing this thesis, the soot formation model requires further refinement, and is not used in this work. For the purposes of the work presented in this thesis, soot is assumed to be produced as a constant fraction of the fuel mixture fraction, Y_F before combustion. A figure of 0.02 Y_F is used, which is in accordance with values used by Novozhilov et al[16]. This only appears as a term in the radiation heat transfer equations, and hence in the enthalpy source term, but does not affect the flow computations or the composition of the products.

Perhaps the most serious shortcoming of the original version is that the wall temperatures were user-specified. It was found through a few numerical experiments that the radiant fluxes to the floor level were quite sensitive to the specified ceiling temperature, as would be expected from Equation 3.40. Worse than that, however, is that it runs contrary to the whole deterministic, predictive nature of CFD models. It is possible that the original application of the model was in a situation where these temperatures could be measured, and where a few measurements could be taken as being representative (not an unreasonable assumption in a furnace whose gases are well mixed). However, for a general purpose predictive tool, the wall temperatures must likewise be calculated rather than defined. In a typical building-fire, upper wall temperatures will be higher than lower wall temperatures, and the division is not likely to be sharply defined since the gas temperatures themselves vary continuously. Similarly, the ceiling temperature will be high at the point directly above the fire plume, and decrease radially to the walls as the ceiling jet progressively loses heat to the ceiling.

3.6.1. Particle and Gas Absorption Coefficients

Several modifications of the radiation submodel were performed by the author to rectify these shortcomings. The single value of the particle absorption coefficient was replaced with one that is dependent on the mass concentration in each cell, as given by Equation 3.28. The particle concentration distribution had to be converted from the flow grid to the radiation grid, which added to the computation time.

Another variable addressed was the gas absorption coefficient. The carbon dioxide production and concentration in each cell is included in CESARE-CFD, and is determined from a mass balance of carbon between the unburnt fuel and the products. The CO_2 concentration distribution is now included in the variables converted from the flow grid to the radiation grid. The water vapour production can be determined in two ways; either by a mass balance of hydrogen, or by assuming a fixed ratio between water vapour and carbon dioxide which is determined by the carbon-hydrogen ratio in the fuel. Since the mass balance of hydrogen involves creating another variable (water vapour concentration), the distribution of which must be solved by solution of the general conservation equation, the latter approach was used in this research.

The grey absorption coefficients of these two gases depend not only on the gas temperature, but on the partial pressures of the relevant species. From the values of the mean absorption coefficients given by Tien et al[69], $\log(k_{CO_2})$ decreases almost linearly with temperature for temperatures above

about 800K, while $\log(k_{H_2O})$ decreases somewhat more rapidly with temperature, although the values are of a similar magnitude to $\log(k_{CO_2})$. Since both carbon dioxide and water vapour will typically be present in approximately equal concentrations*, an average value for $\log(k_{CO_2})$ and $\log(k_{H_2O})$ can be used which decreases linearly with temperature, as shown in Figure 3.1. This "average" grey gas absorption coefficient may be approximately expressed as

$$k_{gas} = k_{CO_2} + k_{H_2O} \approx (p_{CO_2} + p_{H_2O})(75e^{-T_g/650}) \qquad (3.43)$$

where p_{CO_2} and p_{H_2O} are the partial pressures of carbon dioxide and water vapour respectively, and T_g is the gas temperature. Carbon monoxide is also included in Figure 3.1 for illustration purposes. It is a less radiantly absorbent gas than either carbon dioxide or water vapour at the same partial pressure. Since it is also typically produced in far less quantities than either of these two gases, its contribution to the overall radiant heat transfer will be negligible, and therefore may be ignored. The accuracy gained by its inclusion would only be negated by the accuracy loss of the average grey gas assumption.

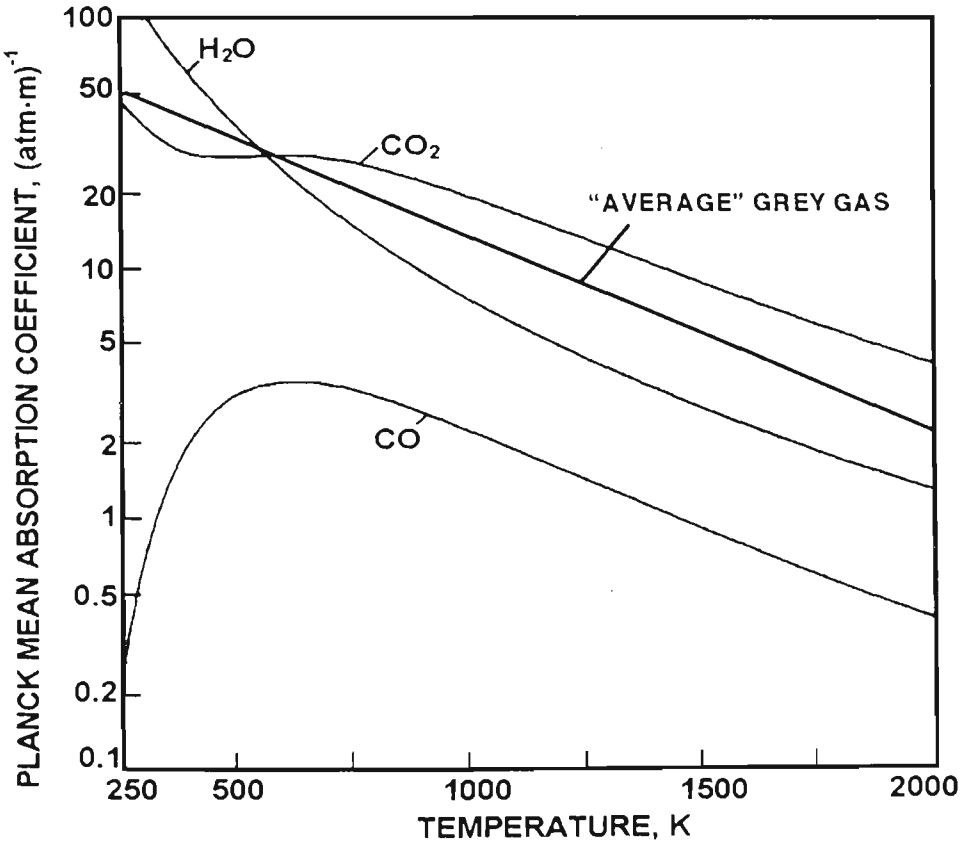

Figure 3.1 Planck mean absorption coefficient (Tien et al[69])

* For most solid organic fuels, the carbon/hydrogen ratio is roughly 1:2. Since most of the carbon ends up as CO_2 after combustion, and most of the hydrogen as H_2O, the CO_2/H_2O ratio will be roughly 1:1

Even though the hydrogen mass balance is not calculated in the flow region, the combined grey gas partial pressure is readily calculated from the carbon mass balance and the respective mass fraction of each element in the fuel. The carbon dioxide concentration is calculated from a mass balance of carbon and has units of kg/kg. It is necessary to convert this to value to partial pressure. Firstly, the volume of 1kg of gas at local temperature, T, is calculated from the local gas density ρ_{gas} (which takes the local temperature into account), and is simply given by

$$\mathrm{Vol}_{gas} = \frac{1}{\rho_{gas}} \tag{3.44}$$

Likewise, the volume of C_{CO2} kg at temperature T is given by

$$\mathrm{Vol}_{CO_2} = \frac{C_{CO_2} \cdot 1000}{M_{CO_2}} \cdot V_m \cdot \frac{T}{273.15} \tag{3.45}$$

where M_{CO2} is the molar weight of carbon dioxide, 44.01 g/mol, and V_m is the molar volume of an ideal gas, 0.02241 m^3/mol. The volume percent of carbon dioxide is found by dividing Equation 3.45 by Equation 3.44, to give

$$\mathrm{Vol\%\ CO_2} = \frac{C_{CO_2} \cdot 22.41 \cdot T_{gas}}{44.01 \cdot 273.15} \Big/ \frac{1}{\rho_{gas}} = C_{CO_2} \cdot T_{gas} \cdot \rho_{gas} \cdot 1.864 \times 10^{-3} \tag{3.46}$$

The volume percent of water vapour can be found by noting that for every gram of fuel burnt

$$\frac{\mathrm{Vol\%\ CO_2}}{\mathrm{Vol\%\ H_2O}} = \frac{n_{CO_2}}{n_{H_2O}} = \frac{n_C}{\frac{1}{2} n_H} = \frac{frac_C}{12.01} \cdot \frac{2 \times 1.00}{frac_H} \Rightarrow \mathrm{Vol\%\ H_2O} = 6.005 \cdot \frac{frac_H}{frac_C} \cdot \mathrm{Vol\%\ CO_2} \tag{3.47}$$

where n_X is the number of mole of species X, and $frac_X$ is the mass fraction of the element X in the fuel. Finally, Equation 3.46 and Equation 3.47 are added to get the partial pressure of the average grey gas

$$\begin{aligned} \mathrm{Vol\%\ GreyGas} &= \left(1 + 6.005 \cdot \frac{frac_H}{frac_C}\right) \mathrm{Vol\%\ CO_2} \\ &= \left(1 + 6.005 \cdot \frac{frac_H}{frac_C}\right) C_{CO_2} \cdot T_{gas} \cdot \rho_{gas} \cdot 1.864 \times 10^{-3} \end{aligned} \tag{3.48}$$

3.6.2. Wall Temperatures

The initial intensity of a given ray is a function of the temperature of the boundary, T_{wall}, as given by Equation 3.40. The wall temperature itself is a function of Q''_{net}, the net radiant flux to the

boundary. Since the solution procedure for the discrete transfer method is iterative, the wall temperature is calculated from the old net radiant flux (which is zero for the first iteration), and is used to calculate the new flux. Taking into account convection and conduction, the wall temperature is given by the simple heat flux balance equation

$$Q''_{net} = h(T_{wall} - T_{gas}) + \frac{k}{x}(T_{wall} - T'_{wall}) \Rightarrow T_{wall} = \frac{Q''_{net} + hT_{gas} + \frac{k}{x}T'_{wall}}{h + \frac{k}{x}} \qquad (3.49)$$

Here, T'_{wall} is the temperature of the opposite face of the wall, which is the calculated temperature in the case of internal walls (the current value in computer memory), and is taken to be ambient temperature in the case of external walls (i.e. walls bounding the enclosure). The heat transfer coefficient, h, is taken to be a constant for all surfaces. This assumption is made as a first approximation: it is consistent with the method used in the flow region calculations, and is considerably more convenient to implement owing to the way the CFD model has been constructed. The wall conduction coefficient is the quotient of the effective wall conductivity, k, and its thickness x.

It should be noted that the heat conduction through the walls assumes a "quasi-steady" situation, that is, there are no transient effects. The temperature profile through the wall is therefore a linear one, regardless of the heating history. This is a reasonable supposition when modelling steady-state scenarios, but it will be a source of error for unsteady cases, particularly if the temperature change is rapid. For instance, in a real situation, if the temperature rise on one or both sides of the wall is rapid, there will be a time lag in heating up the wall to a linear temperature profile. In the interim, there will be a greater heat loss to the wall than would be predicted by assuming an instantaneous attainment of the steady state. The net result in this case is that the predicted wall temperatures will rise more rapidly than in the actual situation.

The previously described changes to the radiation submodel of CESARE-CFD were implemented, and used to make predictions for comparison with full-scale experimental data. The following section describes a full-scale near-steady-state fire test which was performed in a multi-room fire test facility, and the subsequent section describing a corresponding simulation performed with CESARE-CFD with the modified version of the radiation submodel.

3.7. EXPERIMENTS

3.7.1. Aims

Full-scale experiments were undertaken to acquire experimental data for making comparisons with modelled results, with the aim of validating the alterations to the radiation submodel described in the previous section. The immediate priority was the acquisition of radiation heat flux data, to make direct comparison with the fluxes predicted by the radiation submodel. Temperature and species concentration readings were also acquired, as these quantities influence the radiation heat transfer, and hence the fluxes themselves. They are also helpful in verifying the overall CFD model, with which the radiation submodel interacts.

3.7.2. Instrumentation and Methodology

Experiments were conducted at the Centre for Environmental Safety and Risk Engineering's Experimental Building-Fire Facility, which is a prototype full-scale, multi-room, multi-storey building. The facility was fitted out to resemble an apartment building. This series of experiments took place on the ground floor only, in the section shown in Figure 3.2. Dimensions and positions of features within the enclosure are included, as frequent reference is made to them throughout the remainder of the chapter.

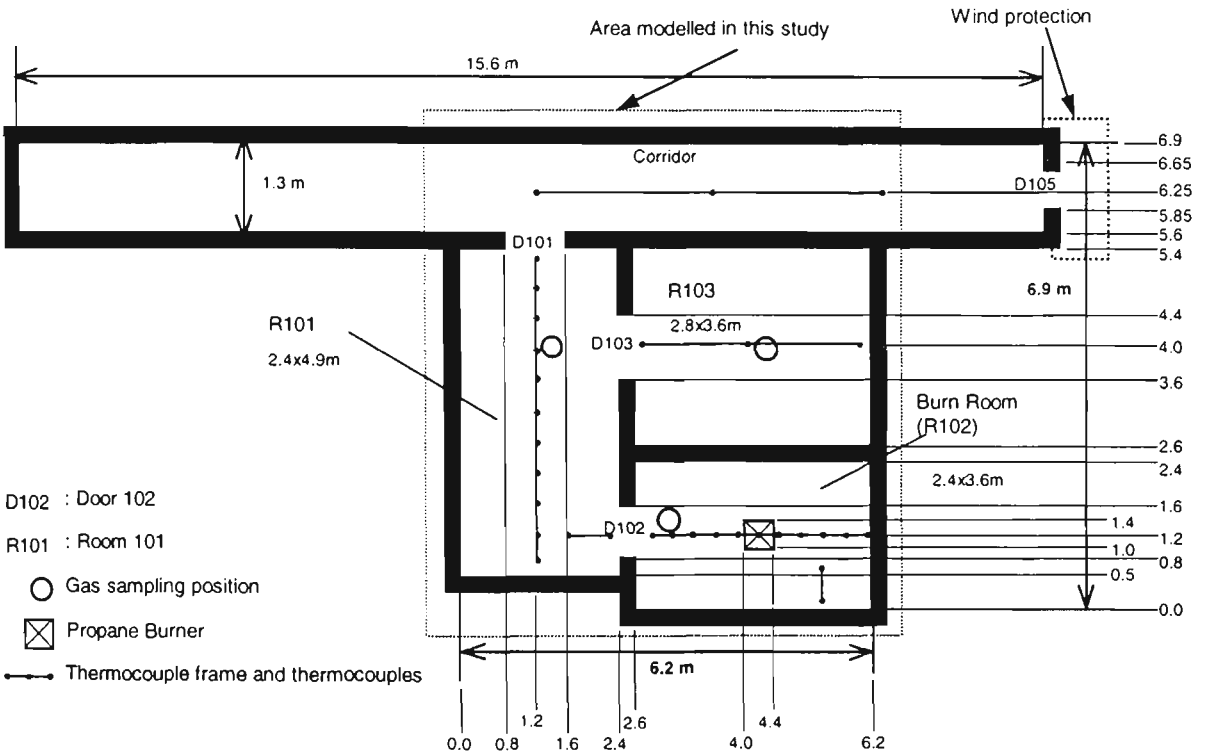

Figure 3.2 The portion of the Experimental Building-Fire Facility used in this study

The walls and ceiling were lined with 16mm fire-rated plasterboard. An additional layer was added for the burn room walls, and two extra layers for the burn room ceiling. A propane burner was placed on the floor of the Burn Room (R102), and the propane gas regulated to produce a steady flow of 0.004 kg/s, corresponding to a stoichiometric burning rate of 200kW, assuming stoichiometric heat release of 50kJ/kg for propane[3]. The burner was run initially for 20 minutes (to preheat the building), and then for a further 40 minutes; during this latter period the internal environmental conditions remained approximately steady. Tests were not run for any longer than 1 hour to prevent excessive cracking of the plasterboard. The temperature history of a number of representative thermocouples is shown in Figure 3.3, where it can be seen that temperatures do not change significantly after about 1200 seconds (20 min) into the test.

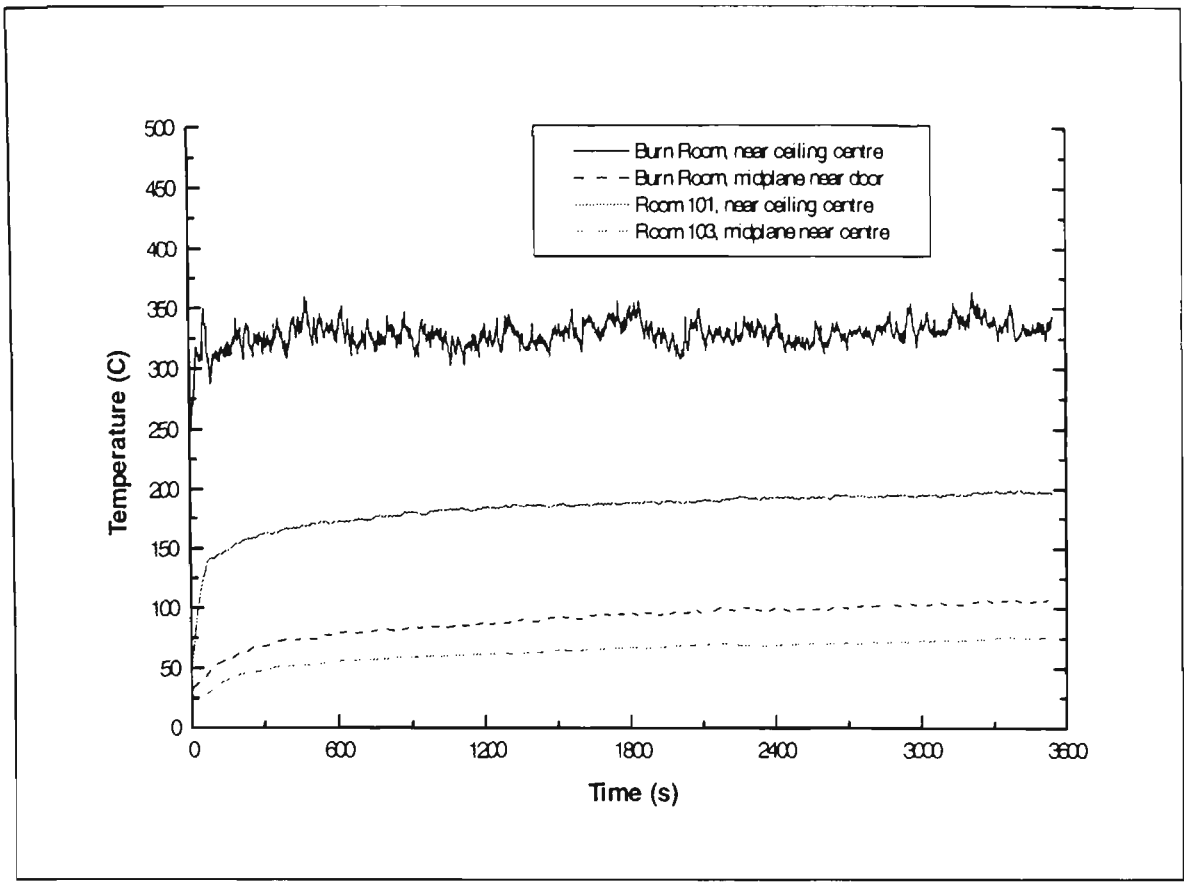

Figure 3.3 Temperature histories of a few points throughout the test facility

Thermocouples were mounted throughout the building on fixed racks at four heights above floor level, namely at 2.15, 1.65, 1.20 and 1.00 m (see Figure 3.2). The thermocouples were all K-type (nickel-chromium/nickel-aluminium) mineral insulated metal sheathed (MIMS), with a diameter of 1.5mm. In total, 116 thermocouples were used in the tests, all of which were unshielded.

A water-cooled heat flux meter was attached to a moveable stainless steel pole, and was shifted throughout the test to measure the radiant heat flux at 14 different locations at floor level, along the centrelines of both the Burn Room and Room 101. The radiant flux was measured continuously for two minutes before moving to the next location. A reference location, the floor of the door to the burnroom (at x=2.6m), was returned to several times during the course of the experiment to check for any "drift" in the overall radiant flux levels over the duration of the test. The measurements at the start of readings, at the end, and at two intermediate times are shown in Table 3.1

Table 3.1 Heat flux measurement

Time (min)	Reading (kW/m^2)
20	3.4
30	3.4
40	3.2
60	3.7

Two gas sampling tubes were attached to cables, so that they could be raised or lowered. Gas samples were taken at varying heights throughout the duration of the test, these being 0.2, 0.5, 0.8,

1.0, 1.2, 1.7, and 2.2 m. The sample tubes were passed through cooling coils to a custom built Anri® chemical gas analysis unit, where the CO, CO_2, and O_2 concentrations were measured. Each height was sampled for a duration of five minutes, partly because there were less points to sample than the heat flux, and also because there was a significant lag in gas entering the tube, and reaching the analyser via the cooling coils before being sampled. A gas sampling tube was fixed at height 1.9m in Room 103 throughout the experiment. The CO_2 concentration was recorded, and is shown in Figure 3.4. The concentration shows a peak just before commencement of measurements at 1200s, followed by a steady decline to about 80% of the peak value. This profile was also observed in the initial stages of CO_2 measurements at the other two locations, before the sampling location was shifted to varying heights. The implication is that the measurements may differ from true steady-state values by as much as 20%

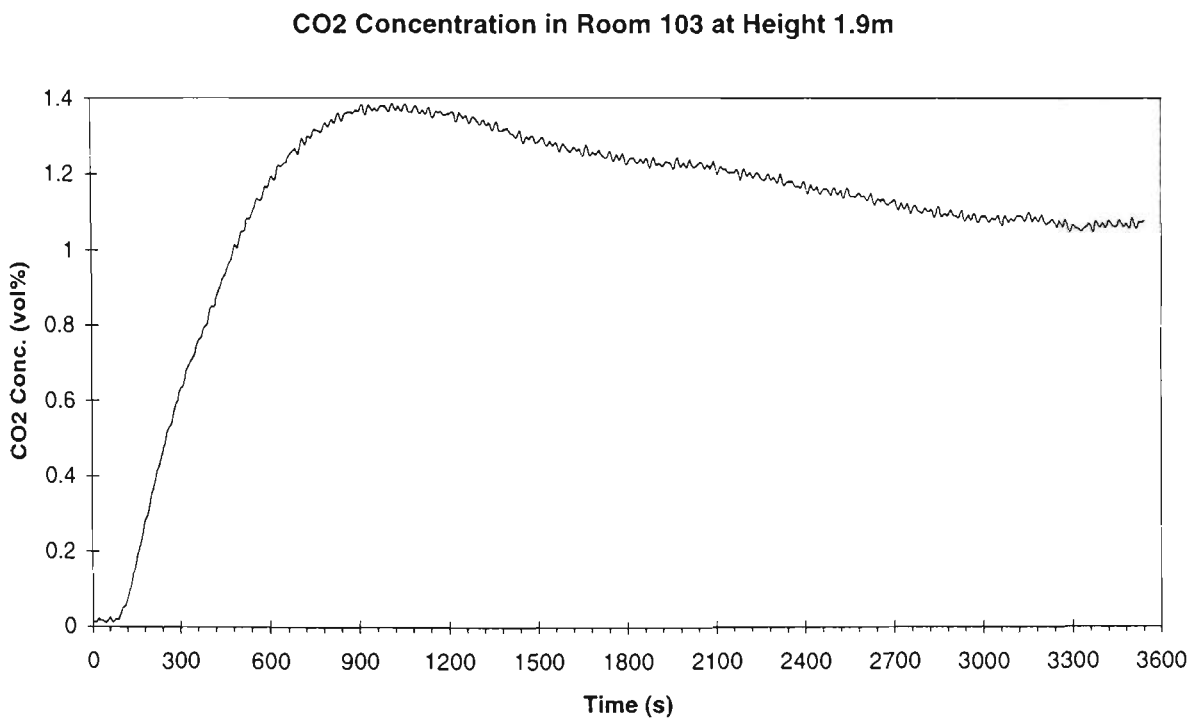

Figure 3.4 Carbon dioxide concentration history for Room 103

A custom-built optical density meter, comprising an infrared emitter and receiver mounted on a piece of timber and separated by a distance of 0.5m, was used to measure smoke obscuration. The emitter and receiver were each located at the end of a short narrow tube. The meter was attached to cables so that, like the gas sampling tubes, it too could be raised and lowered. The electronics of the instrument are not designed to withstand high temperatures for extended periods. To mitigate temperature extremes, the electronic components of the meter were swaddled in an insulating layer of glass wool, and a thermocouple attached to the meter to monitor the temperature beneath the insulation. During the experiment, the meter was raised to its measurement height, and left to record the smoke density until such time as the temperature within the insulation layer exceeded 50°C, at which point the meter was lowered to floor level.

All measurement devices were sampled at a rate of 1 Hz, and the voltage data recorded in binary form with a data logger set up on a 486 DX-4/100 PC. The voltage data were then converted to the appropriate physical quantities, and averaged over 25 points before analysis to filter out experimental noise.

The floor plan of the facility, and the location of the thermocouple racks, were specified for a previous series of experiments not related to the research reported here. As the thermocouple locations were chosen to provide optimal data for CFD model calculations, it was convenient to leave the thermocouples in these locations for the series of experiments reported here. The author specified the locations for the gas analysis tubes, radiant heat flux measurements, and optical density measurements, and the rate at which propane fuel was to be supplied to the burner.

The instrumentation that was to be moved throughout the test, namely the heat flux meter, the gas collection tubes, and the optical density meter, needed to be left in place for sufficient duration to establish a measurement of the quantity at a given location. This was to account for any lag in measurement (as noted above for the gas analysis), and to provide sufficient points to perform time averaging and other data analysis techniques. This limited the number of heights and locations at which measurements could be made. The heights for gas analysis were chosen to be 0.2, 0.5, 0.8, 1.0, 1.2, 1.7, and 2.2 m. The intention of this choice was to check for any smoke and combustion products in the lower layer, and to concentrate measurements around the transition point between upper and lower layers, expected to occur at around half door height (1.0m). The location of two tubes was chosen based on points of interest identified in preliminary modelling work, and previous experimental and modelling work[8]. The tube in the burnroom was located between the burner and the door, to best capture the layering in the burnroom and to provide data to compliment the heat flux measurements. The tube in Room 101 was placed in line with the doorway to Room 103, as this was a region in which a particular anomaly was identified in preliminary modelling work (see Section 3.11.1).

Placement of the optical density meter in Room 101, and the measurements heights, were intended to complement the measurements of the gas analysis tube placed in a similar location in Room 101. The sensitivity of the instrument to extreme heat precluded location in the burnroom. Even the location in Room 101 was subject to high temperatures in the upper layer, as noted above.

The heat flux was measured at floor level, along the centreline of the burnroom, and the centreline of Room 101. The centrelines were chosen as being "representative", given the limited number of

points which could be measured. Accessibility issues rendered wall measurements impractical, and there were also doubts about the accuracy of measurements of heat flux in the smoke layer, if soot were to be deposited on the surface of the measuring device.

The heat release rate of 200kW was chosen as an optimal value to produce a realistic fire. Higher release rates would place stress on structural elements of the EBFF and the plasterboard linings, which would preferably be avoided. Also, flashover was observed to occur in preliminary tests not related to this thesis for heat release rates above 400kW. Earlier experiments without automatic data logging showed that the measured heat fluxes were typically around the middle of the measurement range of the heat flux meter. Hence, heat release rates lower than 200kW would produce heat fluxes at the lower end of the measurement scale, resulting in less accurate measurements.

Experiments were conducted with the assistance of technical staff responsible for the operation of the EBFF, under supervision of the author.

3.7.3. Results

A selection of results has already been presented in Section 3.7.2, to help illustrate the methodology. The following tables present the key data that are used for comparison with the modelling results presented in the following sections. As noted in Section 3.7.2, the temperatures were measured at four heights, 2.35m, 1.85m, 1.4m, and 1.2m. These heights correspond to the four data rows in each of the temperature tables. The columns correspond to horizontal positions of the thermocouples, as measured relative to the lower left corner of the "modelled region" shown in Figure 3.2. For example, the western wall of Room 101 corresponds to x=0m. Room 101 is 2.4m wide, the wall between Room 101 and the burnroom 0.2m, and the burnroom 3.6m in length. Hence, the thermocouple rack in the burnroom lies just within the walls of the burnroom, between the positions x=2.7m and x=6.1m.

A feature of note in these temperature data is the clear decrease in temperature from the upper region to the lower region. Also notable is the relative uniformity of temperatures across a given height. The presence of the fire plume in the burnroom is quite obvious, with the hottest part of the plume in the lower region, close to the fuel source, as would be expected.

Table 3.2 Temperatures (°C) measured in the Burn Room, at y=1.2m

Burn Room	x=2.7	3.04	3.38	3.72	4.06	4.4	4.74	5.08	5.42	5.76	6.1
z=2.35	301	281	275	292	347	339	295	286	286	283	274
1.85	261	262	264	268	359	412	291	276	273	274	269
1.4	110	130	139	177	309	579	289	184	163	111	106
1.2	106	118	126	140	279	671	203	123	98	93	93

Table 3.3 Temperatures (°C) measured in Room 101, at x=1.2m

Room 101	y=0.75	1.19	1.63	2.07	2.51	2.95	3.39	3.83	4.27	4.71	5.15
z=2.35	227	234	233	202	205	197	194	198	190	187	186
1.85	179	177	172	164	168	166	168	169	173	173	180
1.4	89	90	93	91	97	98	94	90	91	90	86
1.2	69	68	70	66	74	74	69	64	61	60	57

Table 3.4 Temperatures (°C) measured in Room 103, at y=4.2m

Room 103	x=3.5	4.4	5.3
z=2.35	121	126	121
1.85	109	110	108
1.4	95	92	92
1.2	75	76	72

Table 3.5 Temperatures (°C) measured in the corridor, at y=6.25m

Corridor	x=1.2	3.7	6.2
z=2.35	127	136	179
1.85	100	102	120
1.4	68	59	68
1.2	37	35	35

Table 3.6 Heat Fluxes (kW/m^2) measured at floor level

Burnroom	y=1.2m	Room 101	x=1.2m
x=2.6	3.4	y=0.8	2.3
3.0	3.6	1.2	2.5
3.4	4.5	1.6	2.5
3.8	6.6	2.0	2.4
4.2	5.7	2.4	2.4
4.6	7		
5.0	5.8		
5.4	5.2		
5.8	4.3		

Table 3.7 Carbon dioxide concentrations (kg/kg) measured at various heights

Height (m)	Burnroom	Room 101
z=2.2	0.0310	0.0230
1.7	0.0255	0.0210
1.2	0.0110	0.0025
1.0	0.0025	0.0020
0.8	0.0020	0.0020
0.5	0.0020	0.0015
0.2	0.0020	0.0015

Measured heat fluxes to floor level are given in Table 3.6. It can be seen that the values decrease with distance from the burner at x=4.4m in the burnroom. The relatively lower value at x=4.2m corresponds to a measurement tucked in close to the edge of burner facing the doorway. The burner itself would therefore be providing shielding of the heat flux meter from a significant portion of the fire plume. The location on the other side of the burner, at x=4.6m, was not as close to the burner, so the heat flux meter was therefore more exposed to the fire plume. This is borne out by the fact that the highest heat flux reading was recorded at this point. Heat flux readings in Room 101 are highest at the point in line with the burnroom door, at y=1.2m, and decrease with distance from this point.

The carbon dioxide data show the clear stratification of the products of combustion. The lower layer contains only a very small amount of carbon dioxide, up to a height of 1.0m. At 1.2m, some carbon dioxide is present in the burnroom, while the air in Room 101 is still essentially fresh at this height. However, at a height of 1.7m, there is an obvious increase in the amount of carbon dioxide. It is apparent, therefore, that the interface between the hot and cool layers occurs at around 1.2m in the burnroom, and somewhere between 1.2m and 1.7m in Room 101.

A time history of the raw data measurements is shown in Figure 3.5. As can be seen, there was significant drift in baseline reading, in spite of precautions against exposure to elevated temperature. The five downward peaks correspond to five instances where the smoke obscuration meter was within the hot layer, but was returned to the cool layer after a minute or so. After each excursion to the hot layer, the baseline reading was somewhat lower. There are two mechanisms which may have caused this anomaly. Firstly, the elevated temperatures may have affected the electronics, causing a drift in the baseline voltage. Secondly, deposition of soot on the optical

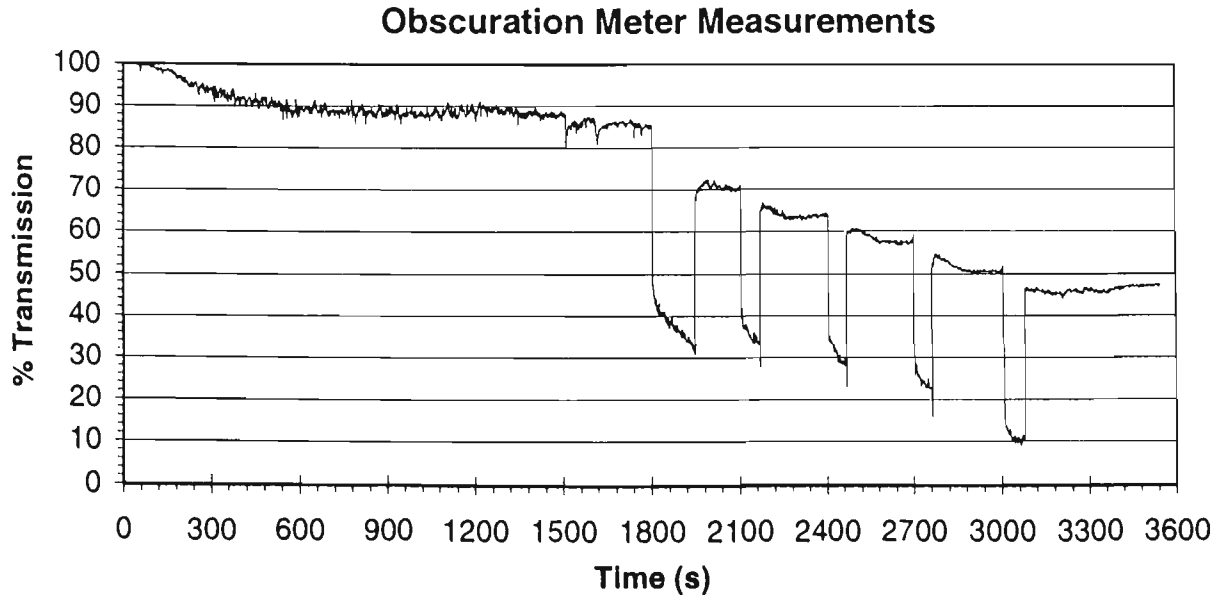

Figure 3.5 Time history of obscuration meter measurements

instruments may have occurred, resulting in a similar reduction in baseline voltage. The latter is quite likely, as there was no fresh air purging of the tubes in front of the emitter or receiver. As the relative contribution of each factor is uncertain, it is very difficult to extract meaningful or accurate smoke obscuration data from Figure 3.5. However, taking the results at "face value", an order of magnitude estimate may be made for the soot concentration. The inverted peaks in Figure 3.5 appear to indicate that transmission may be reduced to as low as one third. As the emitter and receiver are 0.5m apart, the optical density, K, may be as high as $2.2m^{-1}$. Taking the density of soot as $2000kg/m^3$, the wavelength of the obscuration meter emitter as 950nm, and an absorption constant of $\kappa=4.9$ for propane soot, Equation 3.25 yields a value of 8.5×10^{-4} kg/m^3 as the maximum soot concentration.

3.8. MODELLING

3.8.1. Modelling Method

The region of the EBFF shown in Figure 3.2 was the subject of a series of modelling exercises. The fire scenario is that of a 200kW propane burner fire located in a 2.4×3.6×2.4m enclosure, connected to the outside by a larger room and a corridor. Some earlier results and findings were obtained; these are presented later in Section 3.11. The work presented in this section represents the culmination of a process of refinement of the CFD model. In this study, the flow region in four interconnecting rooms was divided into 43×48×34 cells, while the radiation grid was divided into 24×26×16 cells. A horizontal cross section of the flow grid is shown in Figure 3.6(a), while the corresponding cross section of the radiation grid is shown in Figure 3.6(b). To prevent numerical smearing of quantities, finer grid spacing was used in regions of expected high species gradients, namely the plume region in the burn room, and the boundary between the hot and cool layers which is expected to occur somewhere in the height interval 0.8m-1.4m. Refinement of the grid was also made in the region of the walls, to reduce errors in the implementation of the wall function method at the boundaries. Further refinement was not practical, given the full-scale nature and complex geometry of the problem, and the computational resources available to the author; the additional grid points generated by a further refined grid would place a burden on computational resources and time constraints. The current refinement was found in previous work to yield acceptably accurate results[3.8]. In the model, fuel was supplied to the flow region via an inlet port at floor level, at a rate of 0.004 kg/s, and was treated as a forced flow port. The opening at the end of the corridor was designated a balance port, with maximum flow rate of 2 m/s. A full description of these boundary conditions is given in Section 2.4.6.

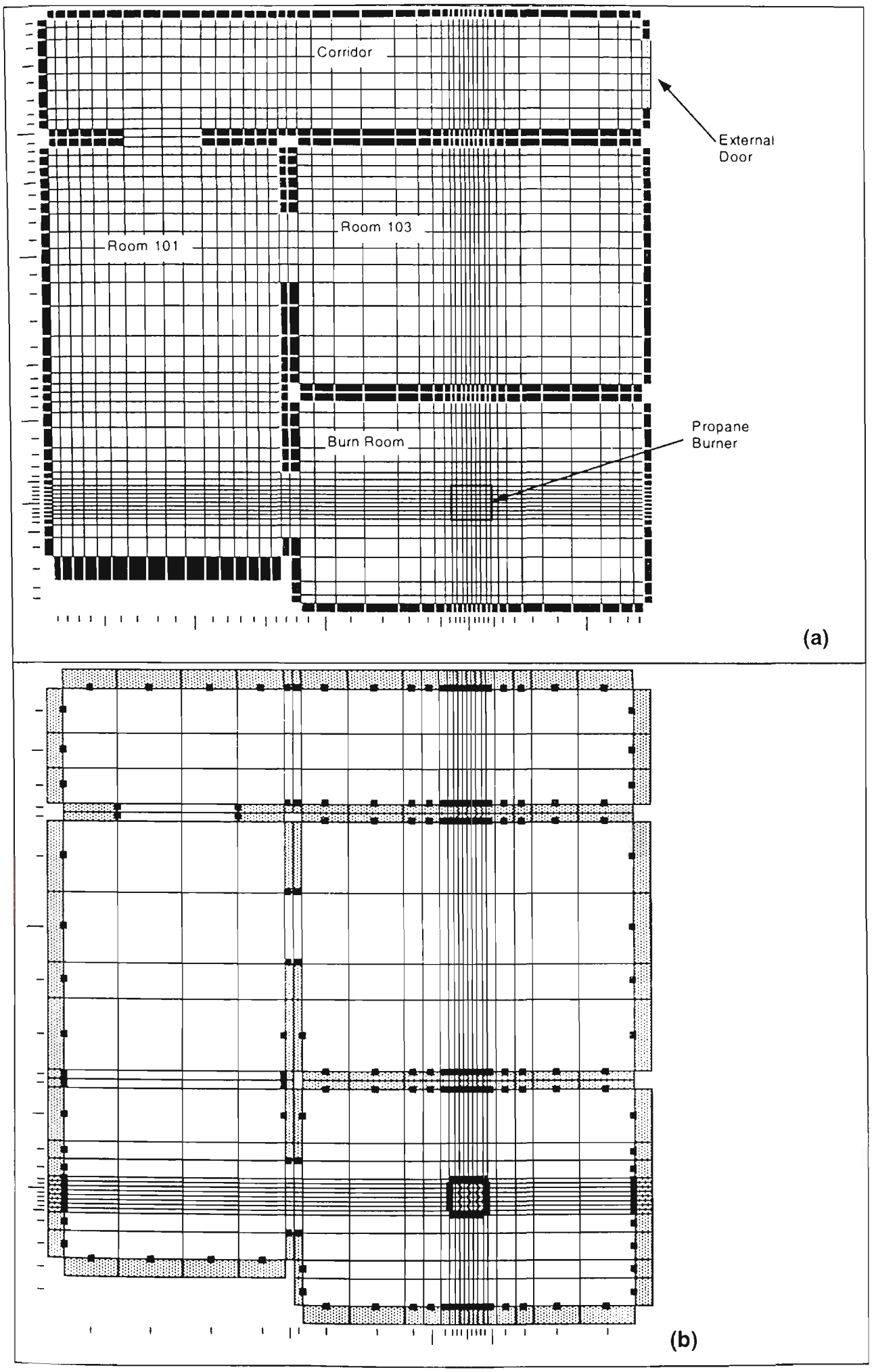

Figure 3.6 The flow grid (a) and radiation grid (b) used in this study

In the discrete transfer method for radiation calculations, a specified number of representative rays per boundary element was tracked through the flow region. In this study, the hemisphere above each boundary element was divided into 192 regularly arranged solid angle units. This corresponds to 24 rays in the ϕ-direction (ϕ being measured around the base of the hemisphere) and 8 in the θ-direction (measured between the base of the hemisphere and its apex). One ray passes through the centre of each solid angle unit, making a total of 192 representative rays per boundary element.

The radiation grid was specified coarser than the flow grid (see Figure 3.6), but matched the refinement in the region of the fire plume. The reason for matching the grids in the region of the plume is that the flow properties in the radiation grid are determined by a weighted average of the flow grid values in the cells that the radiation grid cells overlap. In the region of the plume, high temperature regions are in contact with low temperature regions outside the plume. Since the radiation emitted by the plume is proportional to the fourth power of absolute temperature, if the plume temperatures are averaged with the surrounding temperatures, the resulting mean temperature will produce significantly less heat output than if the true plume temperature were used.

Wall temperatures were calculated using Equation 3.49. Composition of the walls, and their corresponding emissivities, ε, are given in Table 3.8. The emissivity of plaster and concrete are as given by Drysdale[70], while the value for the soot coated plaster takes the value of carbon black, as given by Goldberg[47]. The values of the other coefficients used throughout the calculation are given in Table 3.9. Ambient temperature for this simulation was set at 20°C.

Table 3.8. Emissivities of surfaces

Location	Material Type	Emissivity ε
Ceiling & upper walls	Soot coated plaster	0.96
Lower Walls	Clean plaster	0.91
Floor	Concrete	0.63

Table 3.9. Values of constants used in Equation 3.49

Convection coefficient, h (W/m^2.K)	10
Conductivity, k (W/m· K)	0.134
Wall Thickness, x (m)	0.2

The combustion reaction for propane is given by the reaction

$$C_3H_8 + (2 + 2a + b)O_2 \xrightarrow{\Delta H_{comb}} aCO_2 + bCO + 4H_2O \qquad (3.50)$$

where ΔH_{comb} for this reaction is taken to be 46 MJ/kg. This figure will vary slightly depending on the local combustion efficiency[3]. The values of a and b are as given in Equations 2.21 and 2.22, noting that $m = a + b = 3$ in this equation.

A coarse grid with dimensions 25×29×18 was used to initialise the flow patterns as a starting base for finer grid predictions. Convergence for the coarse grid after 1800 iterations was very satisfactory, with residuals typically being two or three orders of magnitude less than the "typical" figures quoted in Section 2.4.7. These figures were around 10^{-4} m/s for velocity residuals, 10^{-7} kg for mass, 10^{-20} for mixture fraction, and 0.01 m^2/s^2 for enthalpy. The 43×48×34 grid used in this study was computed for an additional 3000 iterations, using the coarse grid solution as a starting point. Residuals initially increased as the solution adjusted to the new grid, then settled back to a level somewhat higher than the coarse grid, but nevertheless quite steady. The residuals for the velocity components were around 1.5×10^{-2} m/s, mass around 10^{-5} kg, and enthalpy around 0.5 kJ/kg. These were deemed to be sufficiently small to indicate convergence.

3.8.2. Comparison of Modelling with Experimental Results

The main physical quantity of interest in this section is the radiant heat flux. A comparison of modelled versus experimental heat flux measured along the centreline of the burnroom at floor level is shown in Figure 3.7. The positions of measurement relate to the calculation grid: the doorway is at 2.6m, the burner at 4.4m, and the far wall at 6.2m. The overall match is quite satisfactory, particularly in the region closest the burnroom door. The dip in the predicted levels where there is a peak in the measurements, at 4.6m, corresponds to the heat flux at the floor, immediately adjacent to the edge of the burner opposite the door. This may be due to a combination of "shadowing" of the plume by the burner base, and an artefact of the radiation grid*. Overall, the match of the predicted values and the experimental measurements is a significant improvement on previously reported values[3], where the model significantly underestimated the measured values, by as much as one half.

* Information regarding the surface elements in the radiation grid is stored in the cell adjacent to the flow region in the grid. On a convex corner, two surface elements on adjacent edges of the corner share the same cell. On assigning the information to the cell, one will overwrite the other. What has occurred here is that the cell on the far edge of the burner has been overwritten, so that no heat flux emanates from this cell. This may be an important local effect with regards the measured point in question.

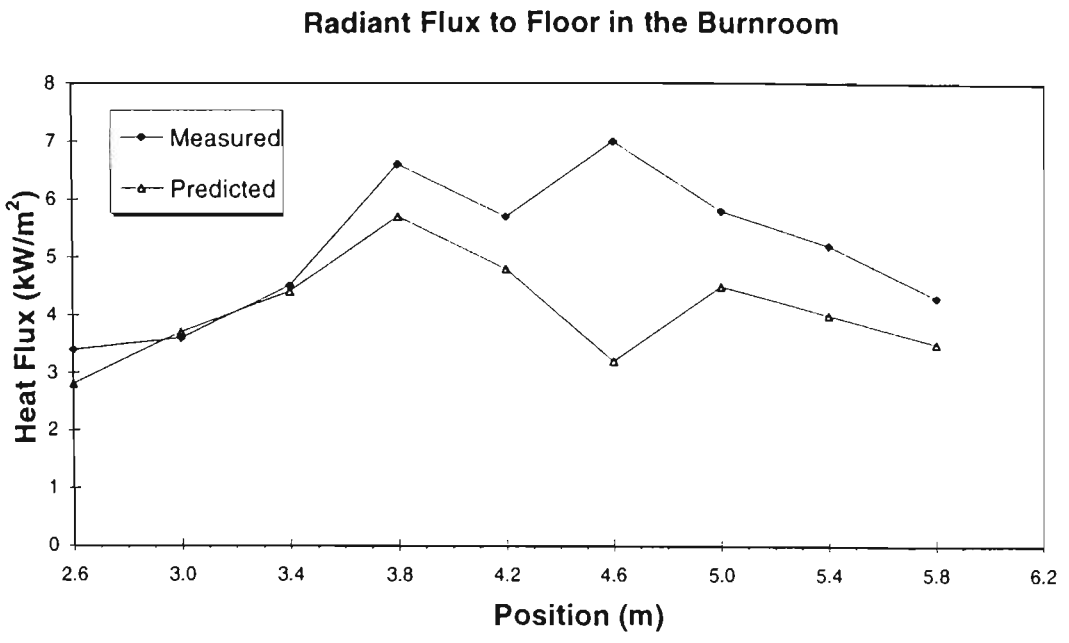

Figure 3.7 Predicted and measured heat fluxes to floor level

Predicted temperatures in the Burnroom and Room 101 are given in Figure 3.8 and Figure 3.9 respectively. The overall trends are quite good; however, the values appear to be consistently overestimated, particularly in the upper region of the fire plume, which manifests itself in the peak around the position x=4.2m in the Burnroom, shown in Figure 3.8. In addition, in Room 101, the predicted temperatures at 1.2m are approximately double measured temperatures. As the heat flux to floor level is underestimated and the predicted temperatures are overestimated, this is of concern. This could indicate that the predicted hot layer is not a sufficiently efficient radiant emitter. Alternatively, it could indicate an overestimation of ceiling temperatures, which heats the upper layers, but that the resultant increased radiant heat output is absorbed before reaching floor level. This latter postulate is a possible explanation for the high predicted temperatures around a height of 1.2m in Room 101. These trends are further discussed in Section 3.8.3.

A comparison of the predicted and measured CO_2 concentrations is shown in Figure 3.10. The measured values clearly show a layering effect, with the concentrations being very low in the lower cool layer, then increasing sharply in the transition to the upper hot layer at around 1.2m above the floor. However, the results show that this sharp transition is not modelled very well. The predictions for the burn room show a gradual rise in concentration with height (Figure 3.10.a). There is a region of high concentration gradient in the predictions of Room 101 (Figure 3.10.b) marking the transition from one layer to another. The problem is that there appears, in fact, to be two regions of high gradient instead of one, as shown by the two jumps in the chart shown (one near the floor and one at 1.2m). This appears to be caused by mixing and diffusion of the hot layer with the cool layer in the model, and appears to occur to an even greater extent in the relatively still space of Room 103.

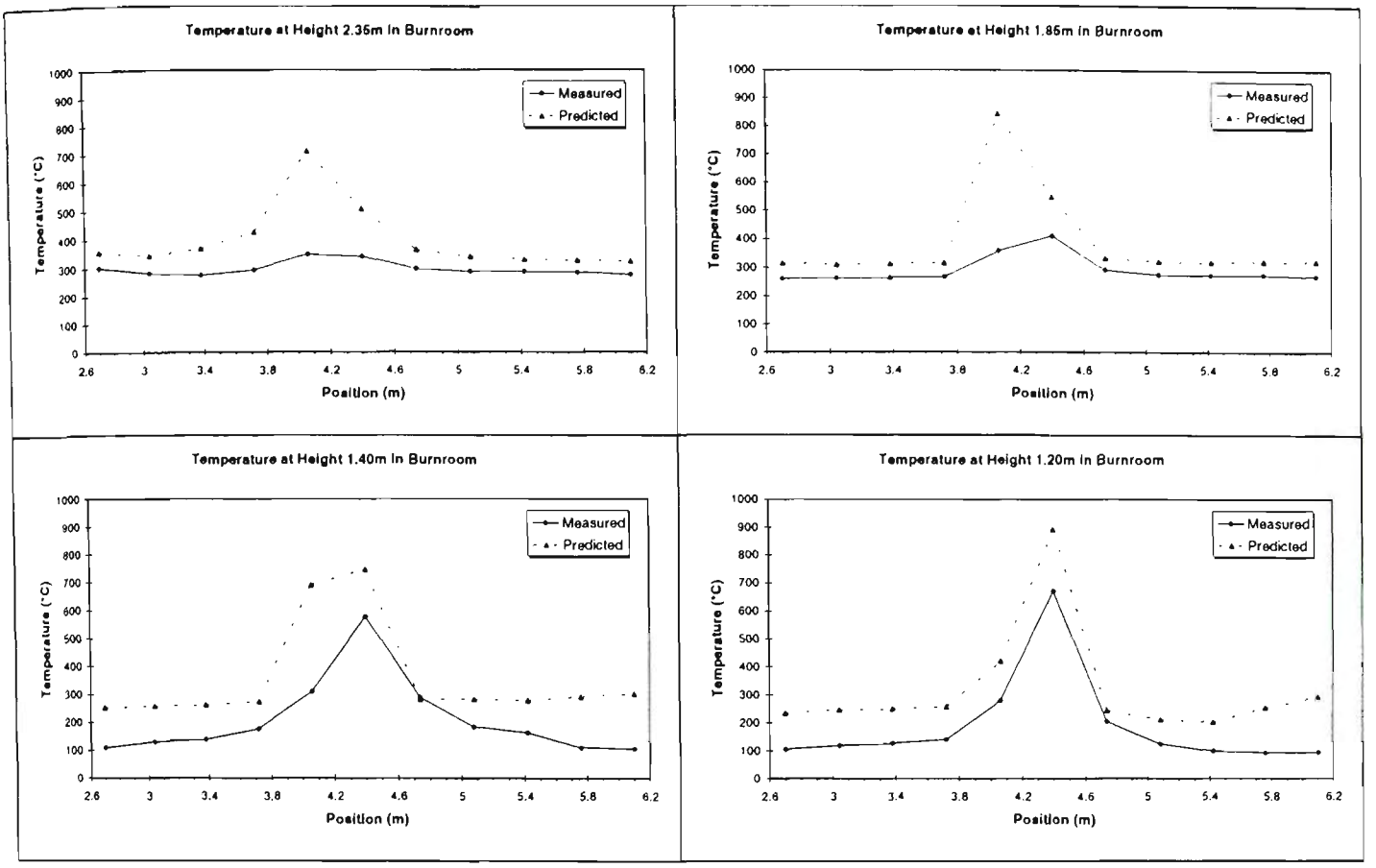

Figure 3.8 Predicted and measured temperatures along the centreline of the burn room

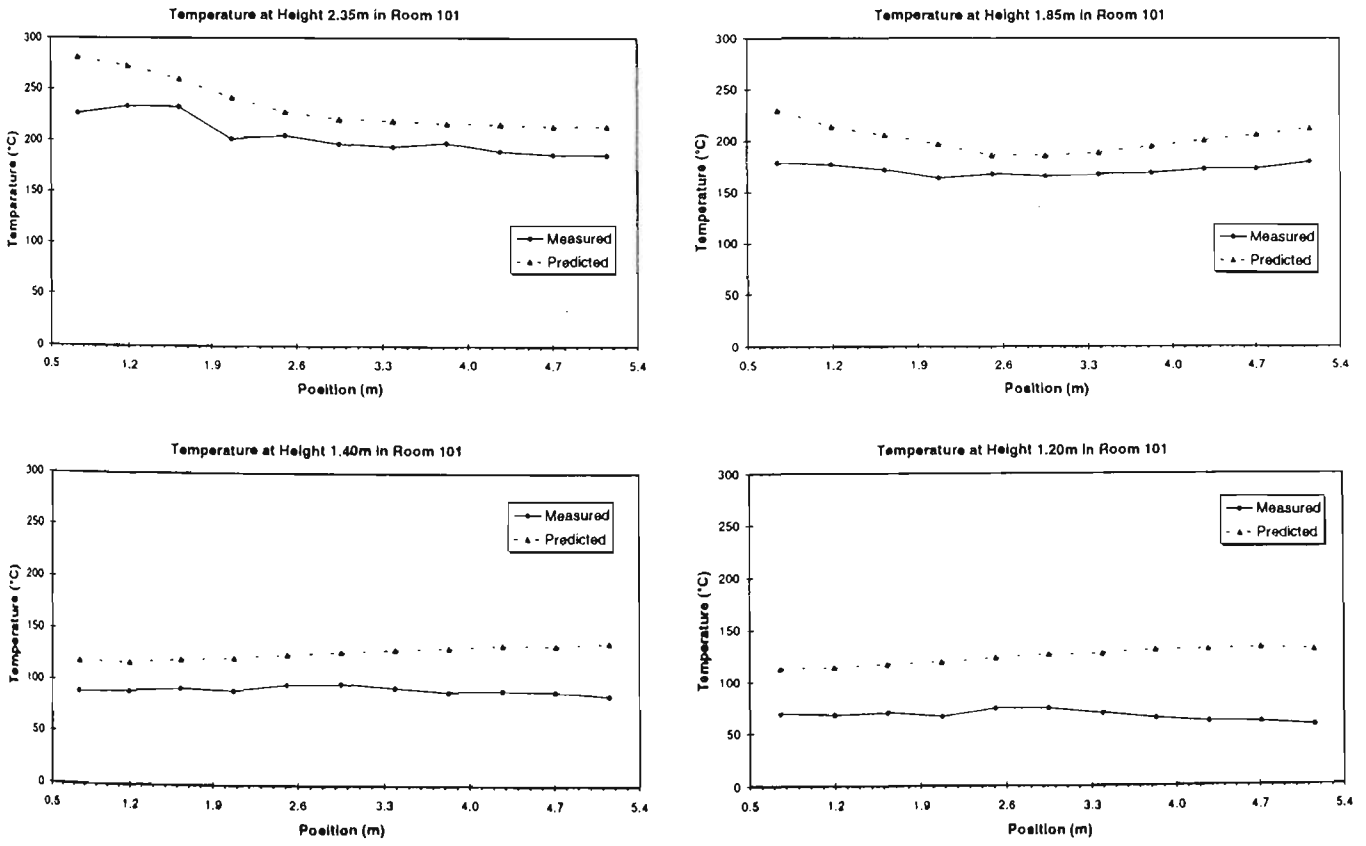

Figure 3.9 Predicted and measured temperatures in Room 101

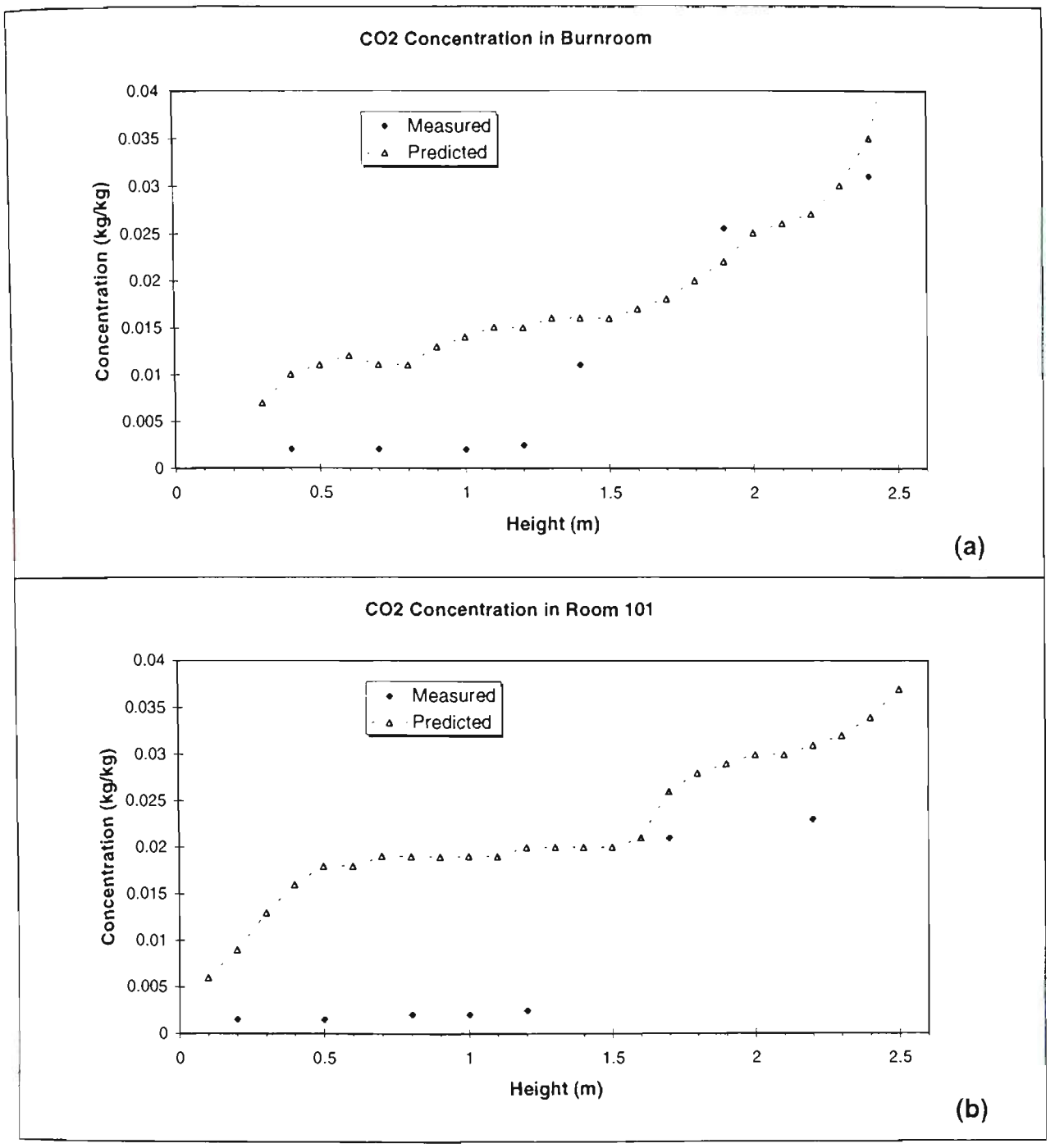

Figure 3.10 Predicted and measured CO_2 concentrations in (a) Burnroom (b) Room 101

The reason that the model was unable to predict sharp layering is not entirely clear, although it appears to be related to the predicted flow pattern. The region between the upper and lower layers corresponds to a region of very low velocity in the flow region. It is possible that the model predicts diffusion of the mixture fraction from the hot layer to the cool layer at the interface, some of which is converted by the combustion routine to products, which are then not cleared by any bulk movement or convection of the flow. The diffusion may also be due to "false diffusion" which was discussed in Chapter 2, and was proposed as a mechanism for explaining why another CFD model predicted an intermediate layer[22].

This effect is even more pronounced in the relatively still region of Room 103*, where the predicted species concentration gradient is even more uniform, and overall composition of products throughout this room is predicted by the simulation to be somewhere between that of combustion products and fresh air. The predicted flow regime in the doorway D103 comprises an inflow of hot products in the upper portion of the doorway, an inflow of fresh air in the bottom portion of the doorway, and an outflow of intermediate composition gases through the central portion of the doorway. While the flow profile has not been measured for this doorway, it has previously been done so for doorways D101 and D102, and found to be in excellent agreement with the simulated flow field[3]. It therefore seems reasonable to presume that the simulation of the flow regime in doorway D103 is at least qualitatively accurate. Regardless of the accuracy, the model predicted an "injection" from Room 103 of combustion products into the region between the hot and cold layers, which only exacerbates the problem of the lack of prediction of clearly delineated layers.

The reason attention is drawn to this phenomenon is that according to Equation 3.43, a relatively small amount of cool absorbing gas in the lower layer will absorb a significant amount of radiation while emitting little, thus reducing the predictions of the radiation flux to floor level. Figure 3.11 shows that the model tended to underestimate the radiant fluxes to floor level in the burn room and Room 101 despite the fact that upper layer temperatures were overestimated, as shown in Figure 3.12. As can be seen in Figure 3.10, the predicted levels of CO_2 were not present in the experiments.

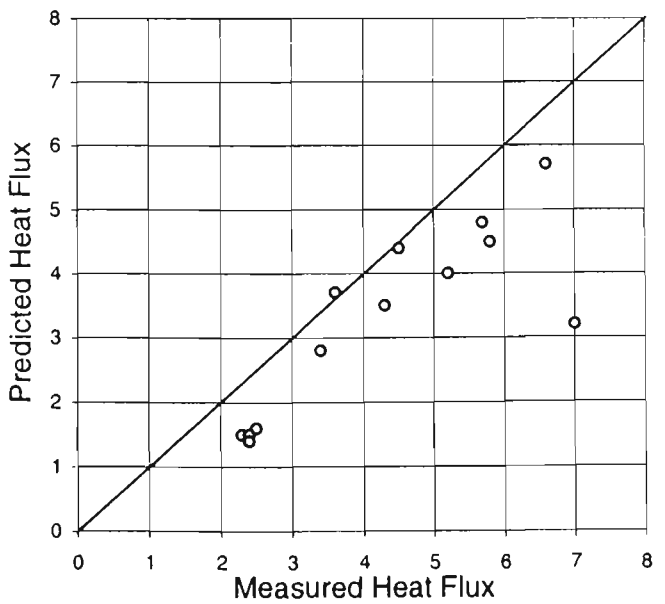

Figure 3.11 Measured versus predicted heat fluxes (kW/m^2)

* It has been suggested by an examiner of this thesis that mixing of the layers may be a consequence of using the k-ε turbulence model, which does not predict well the flow in quiescent spaces.

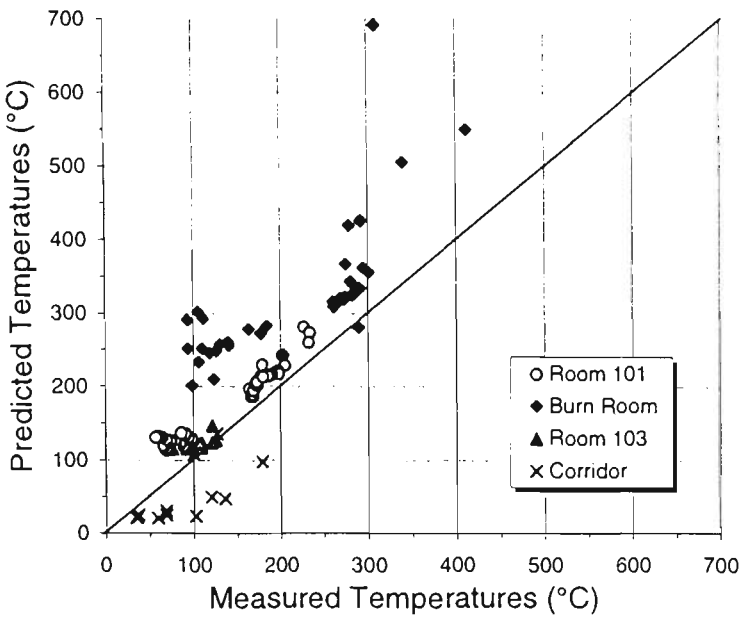

Figure 3.12 Measured versus predicted temperatures (°C)

As a demonstration as to how significant this effect is, the results of an approximate calculation are given here. Note that this calculation is not intended to be rigorously quantitative, but serves to illustrate the radiatively interactive nature of the contaminated lower layer. From Figure 3.10, it can be seen that the lower layer in the burnroom, as predicted by CESARE-CFD, occupies the region at least between the heights 0.75m and 1.25m. Thus, the pathlength of a beam of radiation passing through this layer from the ceiling layer or the fire plume is therefore at least 0.5m. The predicted concentration of carbon dioxide in this region is about 0.010 kg/kg, corresponding to a combined partial pressure of the order of 0.02 atm for carbon dioxide and water vapour. The predicted temperature in the middle layer averages about 450K. According to Equation 3.43, these values correspond to an absorption coefficient of k_{gas}=0.75. If this value is used in Equation 3.17 with a pathlength of 0.5m, the transmission is 0.68 i.e. the ray is attenuated by over 30%. Now, this approximate calculation ignores the effect of emission by the layer itself, which would reduce the attenuation, but it likewise ignores the contribution of particle absorption, and the fact that rays from the fire plume will pass diagonally through the layer, thus increasing the pathlength. Both of these effects would increase the attenuation of a ray.

Inconsistencies may also be introduced due to the assumption of Kirchoff's Law when dealing with the emissivities of absorbing media along a traced path in the discrete transfer method (as given by Equation 3.18). The temperature dependence of emissivity as given by Equations 3.28 and 3.43 refer to the spectrally averaged value of *emitted* radiation for that gas. The emissivity at a particular wavelength does not change at all with temperature; the temperature dependence arises because of the peak intensity region of the black body spectrum changes with temperature. Therefore, in general, the emissivity of a sample of gas will equal the absorptivity only if the "temperature" of the

incoming ray being absorbed is the same temperature as the gas. To clarify the situation a little, consider the contaminated lower layer which has a reasonable quantity of absorbing medium that is relatively cool. According to the grey emissivity, it is a good emitter at low temperatures and a poor emitter at high temperatures, due to high emissivity in the infra-red region of the spectrum. Thus, by the assumption of Kirchoff's Law, any incoming radiation from the hot plume or upper layer will be significantly attenuated. However, the plume region in particular is emitting at a high temperature, with much of the heat being emitted in the near infra-red and visible wavelengths. It should, in theory, pass through this absorbing layer relatively unattenuated. However, in the model it is not, because the absorption is calculated from the temperature of the gas, not the temperature of the ray.

The situation may be remedied to some extent by considering a number of spectral bands rather than a single full spectrum monochromatic band. The variation between absorption and emission does not vary much within a band, so this should minimise this phenomenon. However, the discrete transfer method must be solved for each band, with the number of calculations increasing linearly with the number of bands. Even increasing from one to two bands will double the calculation time*.

Another possibility is to keep track of the "effective temperature" as well as the total intensity of a monochromatic ray. This would enable absorption and emission to be kept separate. However, when a ray has been partly absorbed and then augmented by radiation at a different temperature after passing through a cell, it is not immediately obvious how a new "effective temperature" would be calculated.

As for the upper layer gas temperatures, the model tended to overestimate them, as shown in Figure 3.12. This overprediction of temperatures is partly due to the steady state approximation of a quasi-steady experiment. A true steady state was not reached in the experiments; rather, the temperatures were slowly rising. For this reason, the measured temperatures shown in Table 3.2-Table 3.5 were calculated from the last five minutes of the test, when the readings were at their highest.

* This is not necessarily so for the discrete transfer method, where a large portion of the calculation time is the initial tracing of the rays, which is a once off overhead, unlike the Monte Carlo method. However, FURNACE has been constructed in such a way that the rays are not stored in any way, thus requiring a retracing of the rays every iteration, as with the Monte Carlo method. This is likely deliberate though: storage of the large number of paths requires a great deal of computer memory, so speed was traded for storage space.

Despite the shortcomings mentioned previously, the predicted and measured data presented here are nevertheless in reasonable agreement, considering the simplifications which have been made in the radiation model. Based on the results described here, it seems possible that some additional improvement can be made. In particular, the grid should be refined further to test whether the problem contaminated lower layer is an artefact of the grid spacing. This will also be a useful exercise in determining whether grid independence has been attained. Grid refinement exercises may be useful in elucidation of the mechanism causing excessive blurring of the two layers. Grid refinement is indeed addressed in this thesis, but was undertaken historically later than the work presented here, so it is described later in Section 3.9.

3.8.3. Comparison of Original and Modified Radiation Models

This section is intended to demonstrate the improvements in the radiation predictions due to the changes to the radiation submodel outlined in this chapter. All calculations were performed with the grid described in the previous section. Two models were used; the "Original" model which was compiled with the original version of the radiation subroutine, and the "Modified" model which was compiled with the version of the radiation submodel modified by the author. Each model was executed with the same number of iterations, each resulting in essentially the same degree of convergence, comparable to the convergence described in the previous section. The wall temperatures are calculated for the flow grid in both the Original and Modified models, taking into account the incident radiation calculated by the radiation submodel. All other boundary conditions in the flow region are identical.

It is worth reiterating here the improvements of the Modified over the Original radiation submodels, as discussed in Section 3.6. The Original model uses prescribed wall temperatures in the radiation submodel. The temperatures were set to 40°C for floor surfaces, 90°C for the lower half of walls and door frames, and 150°C for the upper half of walls and ceilings apart from the burn room. It was found from preliminary numerical experiments that the burn room ceiling temperature has a strong effect on the radiant flux to the floor level. With the inclusion of radiation in the wall temperature calculations in the flow region, this effect has lessened somewhat. However, its significance remains, and is illustrated by the modelling examples presented here. Three prescribed burn room ceiling temperatures were modelled: 200°C, 300°C, and 400°C. The absorption of the gas is given by Equation 3.42, the particle absorption coefficient throughout the enclosure is 0.4, and the scattering coefficient 0.005.

The Modified model calculates all wall temperatures using Equation 3.49, calculates the local gas absorption coefficient using Equation 3.43, and calculates the local particle absorption coefficient using 3.28. The scattering coefficient is likewise set to 0.005 throughout the enclosure.

Comparisons of the predicted upper layer temperatures in Room 101 of the Original and Modified models with experiment are shown in Figure 3.13, while the upper layer temperatures in the burn room are shown in Figure 3.14. The legend key refers to the ceiling temperature in the predictions, which is either calculated for the Modified model, or prescribed for the Original model (either 200, 300, or 400 °C). Predicted curves are presented along with the curve for the measured temperatures (listed first in the legend). The comparison shows that the Modified model predicts similar temperatures to the Original, except in the plume region (Figure 3.14), in which it predicts lower temperatures (although the Modified model results are still considerably higher than those measured). Overall, the Modified model most closely resembles the Original model with a ceiling temperature of 300°C. The temperature trends observed in the burn room for the Original model, particularly away from the plume, persist outside in Room 101 (see Figure 3.13) even though ceiling temperatures have only been set differently in the burn room itself.

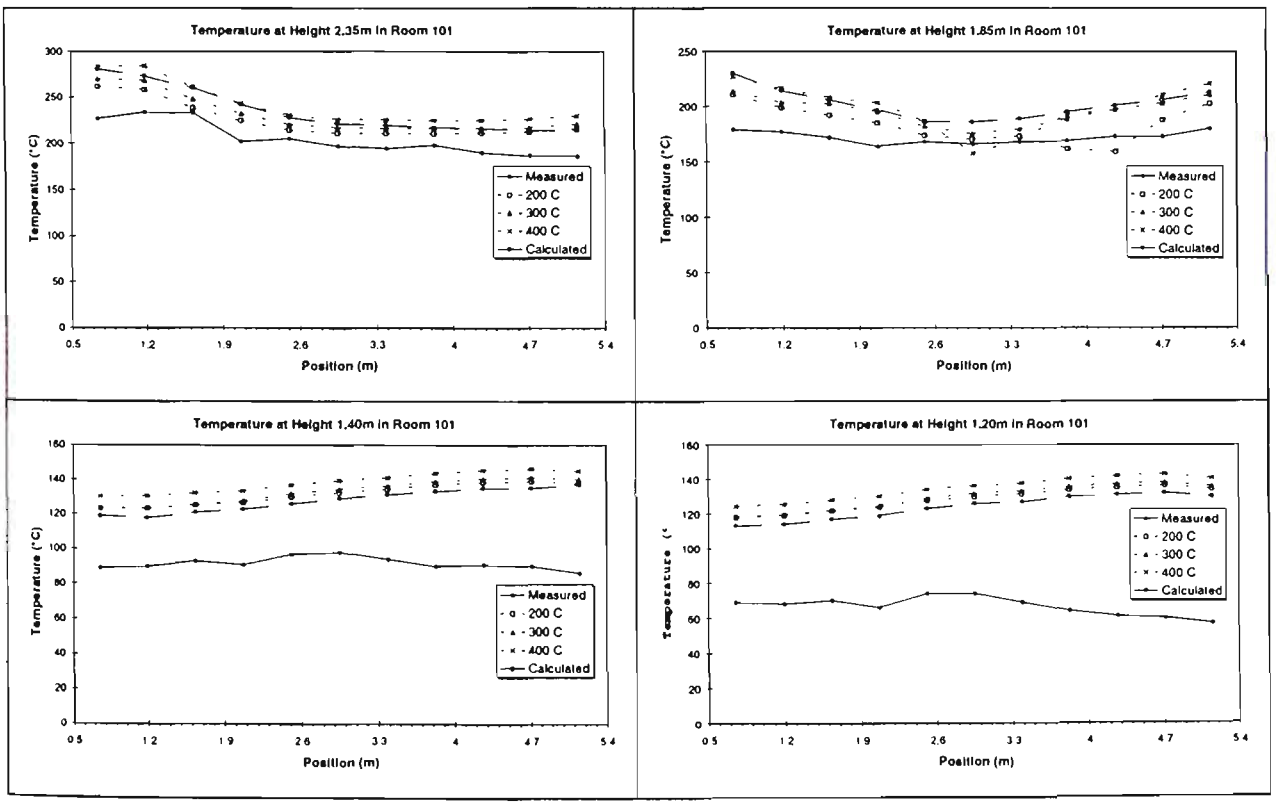

Figure 3.13 Comparison of predicted temperatures in Room 101

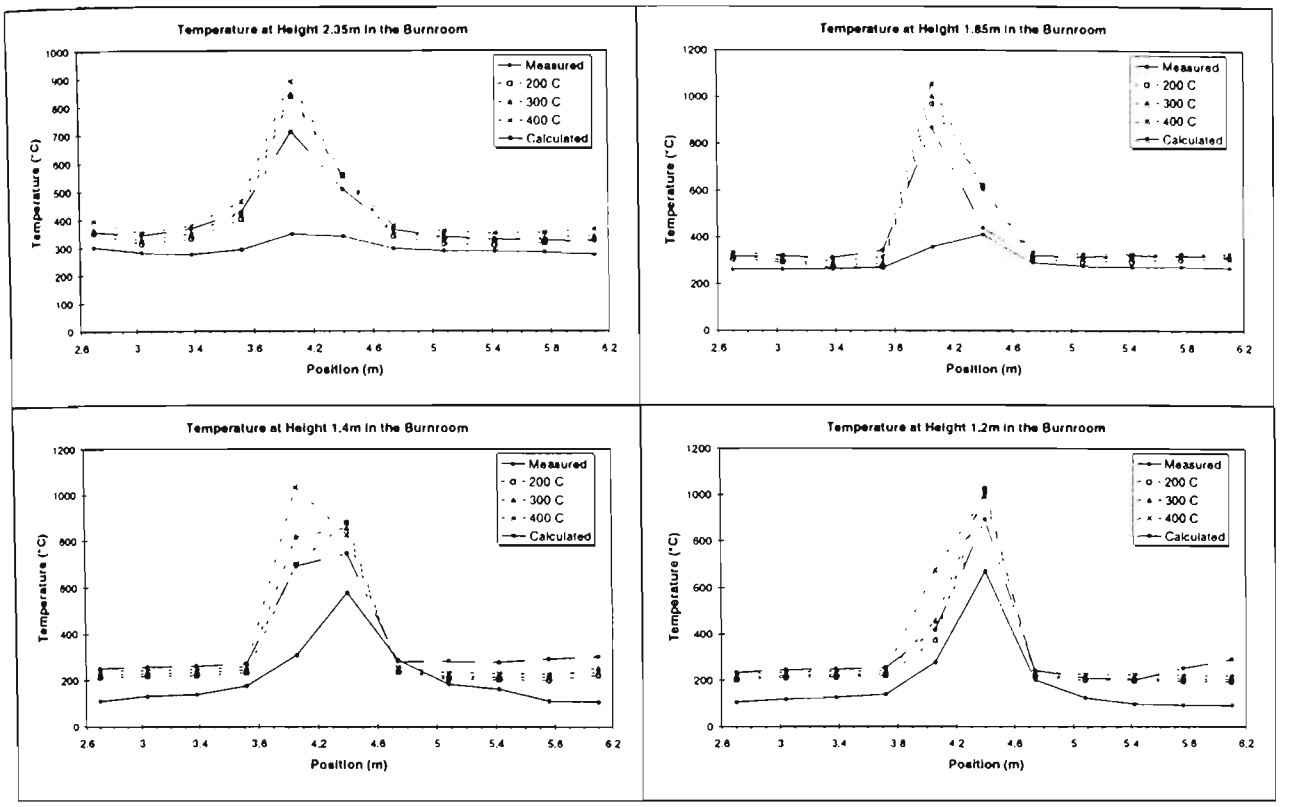

Figure 3.14 Comparison of predicted temperatures in the Burn Room

The predictions for the radiant flux to floor level are shown in Figure 3.15. The trend is much more pronounced than for temperature measurements, with the Modified model predicting higher heat fluxes for comparable ceiling temperatures and lower plume temperatures than the Original model. The over-prediction of plume temperatures and the under-prediction of radiant heat flux to the floor imply that the Modified model still does not predict enough radiant heat loss from the plume region, particularly in the upper regions (although Modified model predictions are nevertheless an improvement over predictions by the Original model).

Optical density in the plume region is quite large due to the presence of fuel and combustion products, so the emissivity is close to unity in this region. Increasing optical density, artificially or otherwise, would have minimal effect in increasing emissivity, which is already close to unity. Even if the model were modified by some means to make the plume a more effective emitter, the resulting cooler temperatures would result in even lower predictions of radiant heat flux to the floor. Accordingly, more detailed investigations are required in order to identify where rectifications can be made.

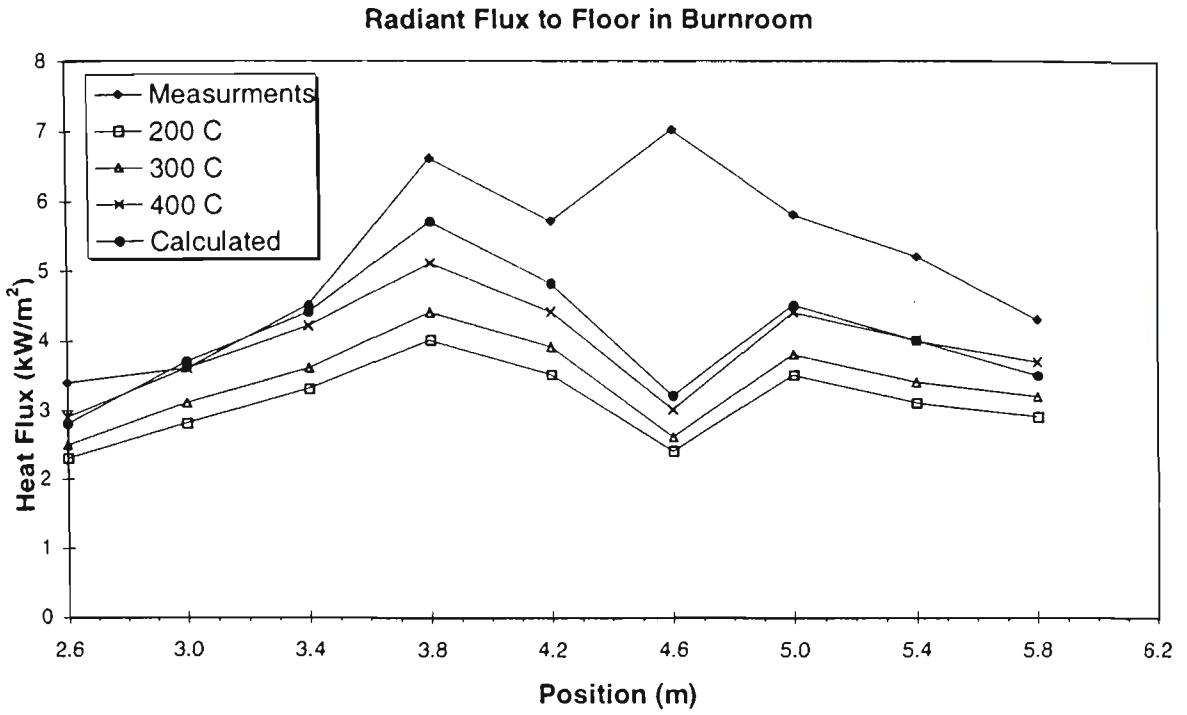

Figure 3.15 Comparison of predicted radiant fluxes to floor level in Burn Room

The predictions for the CO_2 concentrations in both the burn room and Room 101 are given in Figure 3.16. The three cases for the Original model were found to be practically indistinguishable, so only the 200°C case is shown. The distributions are largely similar for the Original and Modified models, although the Modified model made improved predictions particularly in upper

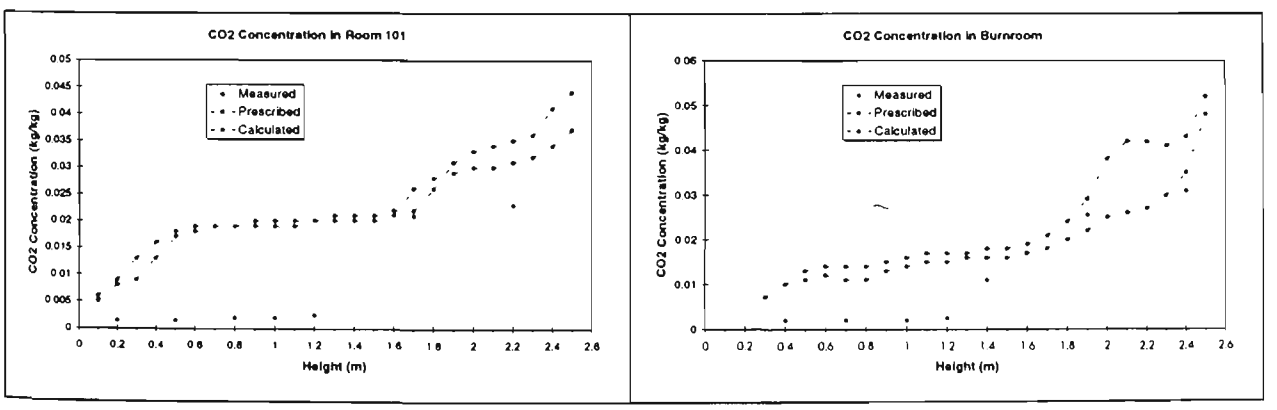

Figure 3.16 Comparison of predicted CO_2 concentrations

layers of the burn room.

Overall, the results presented here show that the model which included the modified radiation submodel made improved predictions over the Original model when compared to experimental results, particularly in the key areas of radiant flux to the floor and plume temperature. While the temperature predictions throughout the rest of the enclosure were comparable for both the Original and Modified models, the Modified model predicted higher heat fluxes to floor level, while simultaneously predicting lower temperatures in the fire plume, the main source of radiant heat.

3.9. NUMERICAL INVESTIGATION OF THE MODEL

It is essential that the numerical solution of the governing discretised differential equations closely approximates the solution of the continuous equations. This concordance is warranted by ensuring that the solution is independent of the grid on which the equations are discretised. It is also important that the solution has converged to the point at which errors in the solution are less than pre-determined values. This section investigates in detail the numerical behaviour of CESARE-CFD for the modelled scenario presented in the previous section. A grid refinement exercise is undertaken to determine the degree of dependence of the solution to the choice of grid size. The convergence of the solution for each of the grid sizes is examined also, to ensure that each solution has converged. In addition, the solution is obtained using two methods – a steady-state solution and a transient solution – to determine the effect of the method used on the solution. The aim is to investigate whether the predicted results presented in this chapter are sufficiently accurate, with numerical errors introduced by choice of grid or lack of convergence minimised. This will ensure that the results can be presented with confidence.

The modelling scenario described in the previous section was undertaken with coarse, medium, and fine grids, to determine whether grid independence of the solution was attained. A grid that is too coarse may introduce errors due to smoothing of the distribution of flow variables, particularly in high gradient regions. A grid independent solution is one in which further refinement of the grid has negligible effect on the solution.

Also considered in this analysis is a solution obtained for an unsteady state simulation. The unsteady simulation is included to test the independence of the solution from the method employed to achieve a steady state. By definition, a steady state simulation makes an assumption of steadiness, and approaches the solution by iteration, whereas an unsteady simulation begins from an initial state, and time-marches the solution until additional timesteps do not alter the solution. The unsteady state simulation employed the medium grid for computational purposes.

3.9.1. Grid Generation

The 200 kilowatt steady-state propane fire described above was again simulated with CESARE-CFD, using the same input values and boundary conditions as described in the previous section. On this occasion, the fire was simulated using three different grids. A coarse grid with a mesh of

26×33×13 was used to initialise the flow patterns as a starting base for finer grid predictions. The grid was constructed systematically: all boundary cells had a thickness of 0.2m, and the number of cells was specified for the burner and door regions. The grid was divided uniformly throughout the entire vertical region, with each cell being 0.2m thick. The automatic grid generation routine then filled the remaining spaces, as described in Section 2.4.2. An analysis of the coarse grid predictions is included for comparison with the finer grids.

A medium grid with dimensions 44×59×26 was constructed systematically from the coarse grid by halving the size of the boundary cells to 0.1m, and doubling the number of grids in the specified refined regions. The number of divisions in the vertical direction was also doubled. The remaining regions were again filled using the automatic grid generation routine. The process was repeated to produce a third, fine, grid with dimensions 86×99×52. The boundary cell thickness in this case was 0.05m, as were the vertical spacings. The three grid arrangements are shown in Figure 3.17. The left column consists of the plan views (in the x-y plane) while the right column consists of the vertical cross-sections through the centre of the burnroom (in the x-z plane).

The program for the coarse and medium simulations was compiled and executed on a Pentium II 350MHz PC with 64MB RAM. The execution time was comparable, if not superior, to SPARC-10 execution times*. However, the limited storage prevented execution of the fine refinement of the grid mesh. The fine grid was executed on a computer with a greater memory capacity, namely a Pentium II with 384MB of RAM and a 450MHz processor.

* A remarkable feat, compared to only 10 years ago. With 500MHz Pentium III computers now readily available on the market, and even more powerful computers always on the horizon, CFD modelling is rapidly shifting from the mainframe to the desktop.

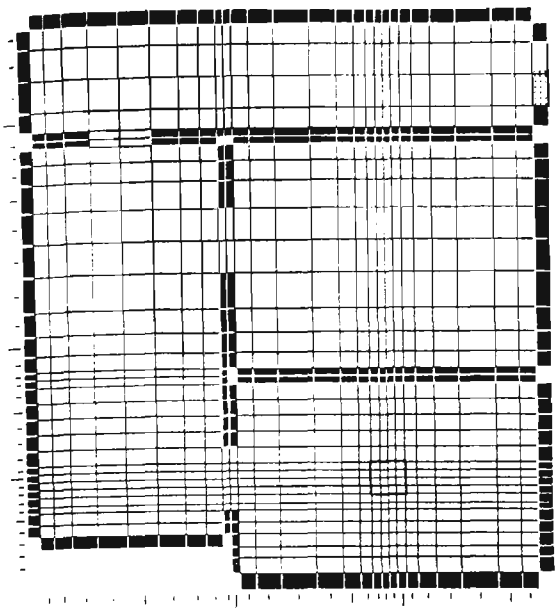

(a)

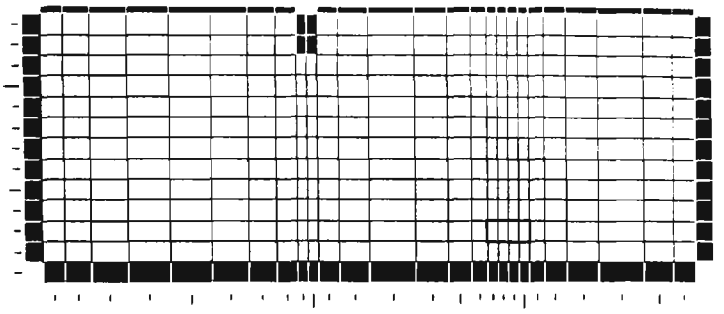

(b)

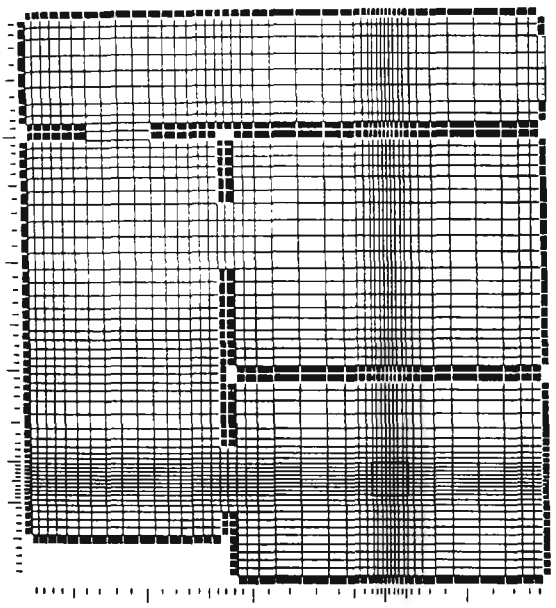

(c)

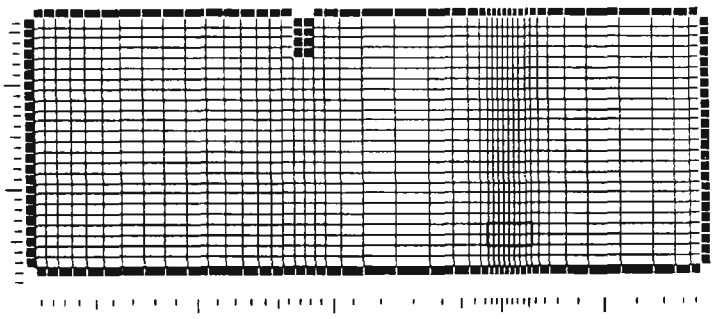

(d)

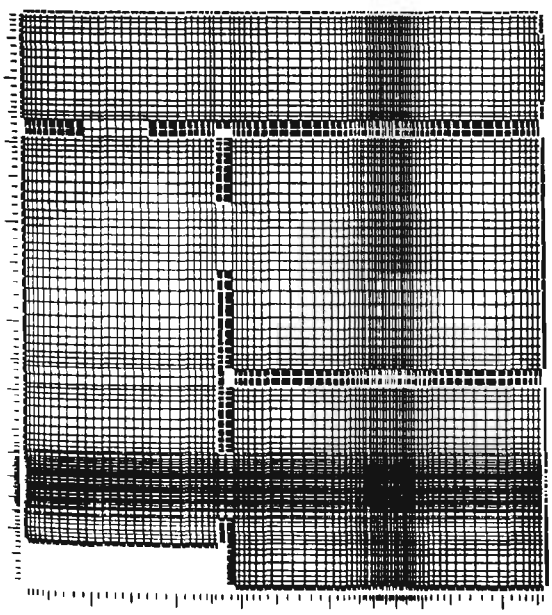

(e)

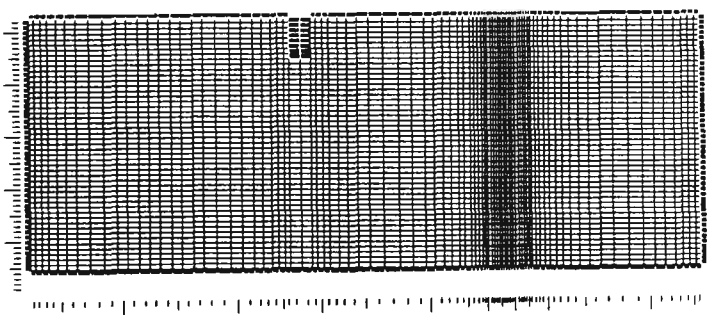

(f)

Figure 3.17 Flow grids (a,b) Coarse (c,d) Medium (e,f) Fine

3.9.2. Modelling Results

Comparisons of modelled values for the fine, medium, and coarse grids are made with the experimental results presented in Section 3.7. A comparison of the predictions along the centreline of the burnroom of the upper layer temperatures are shown in Figure 3.19, while the radiant flux to floor level is shown in Figure 3.20. The positions of measurement relate to the calculation grid: the doorway is at 2.6m, the burner at 4.4m, and the far wall at 6.2m. The predictions indicate that all three grids tend generally to overestimate the temperature, particularly in the region of the fire plume, as shown by the spike in Figure 3.19. The fine grid demonstrates the best prediction of the fire plume region close to ceiling level, but predicts higher temperatures and a forward leaning behaviour closer to the seat of the flame. Away from the fire plume, the temperature profiles for the three grids are in close agreement. This is particularly evident in Figure 3.18, which shows the temperature predictions for Room 101.

The predicted results for all grids agree well for the heat flux to the floor level between the burner and the doorway (Figure 3.20). The predictions marginally overestimate the experimental values in this region. This may be a product of the high temperature predictions in the plume region by all models. Between the burner and the wall opposite the door, there is a greater variation between modelled and predicted results. There is a gradual decrease in predicted heat flux with increasing grid refinement (i.e coarse to fine). Examination of the results reveal that this is matched with an increasing concentration of product gases on that side of the fire plume with increasing grid refinement (see Figure 3.22). As no measurements of concentration were made in this region, the accuracy of the predictions cannot be assessed. However, as the discussion in the previous section points out, the effect is consistent with the hypothesis that the increased concentration of products absorbs the radiation from the plume and ceiling regions.

Comparisons of the CO_2 concentrations are shown in Figure 3.21 for the burnroom and for Room 101. In all instances, the predicted CO_2 concentrations are quite high all the way down to floor level. This is due in part to the mixing effect produced at the doorway to Room 103. Overall, grid refinements are in agreement, particularly in Room 101. The burnroom profiles show the greatest variation, with the fine grid showing the lowest CO_2 levels near floor level, and the highest close to the ceiling. This indicates that the fine grid is capable of resolving features of the flow which are smoothed by the coarser grids.

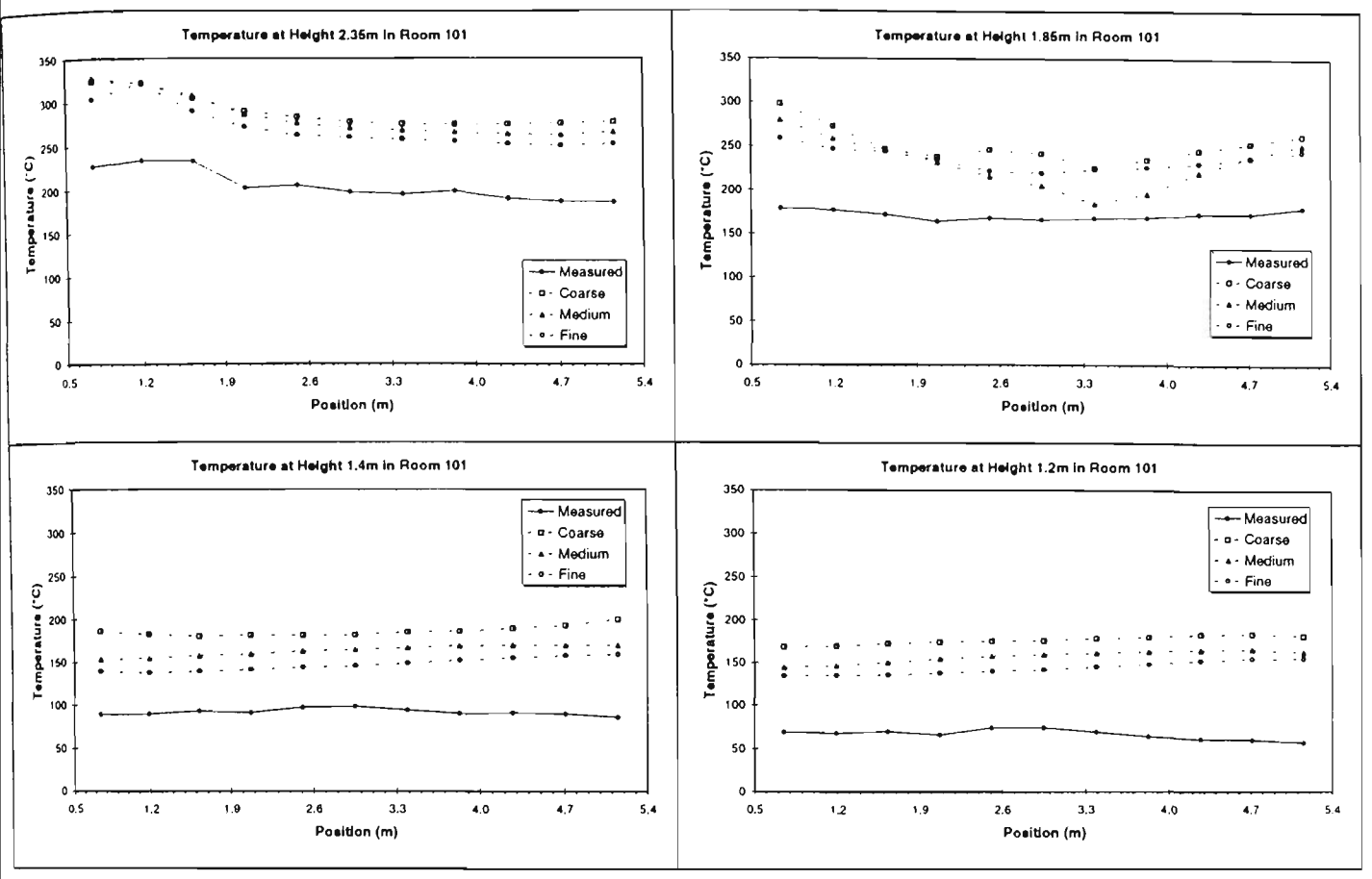

Figure 3.18 Comparison of predicted temperatures in Room 101

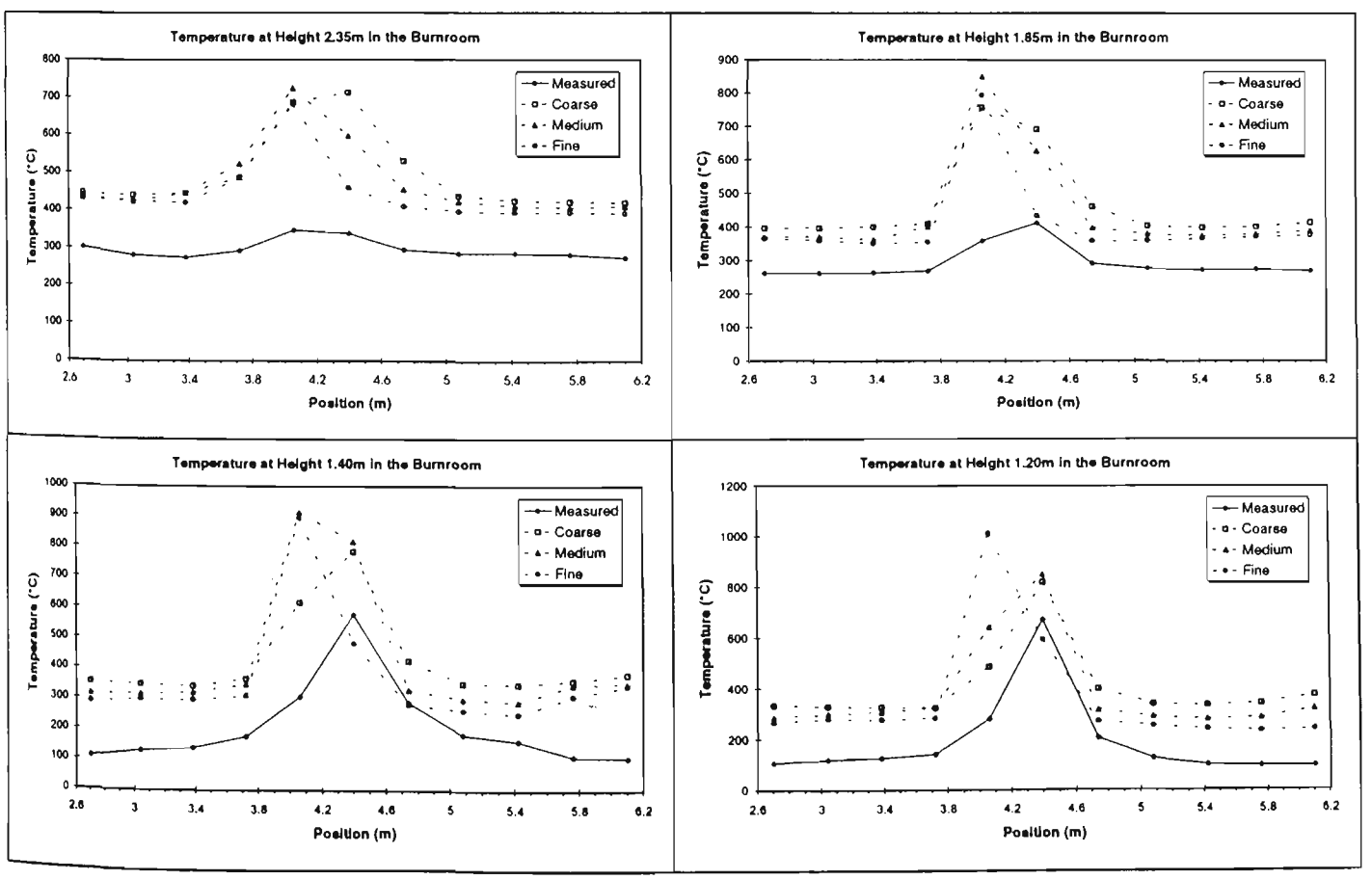

Figure 3.19 Comparison of predicted temperatures in the Burn Room

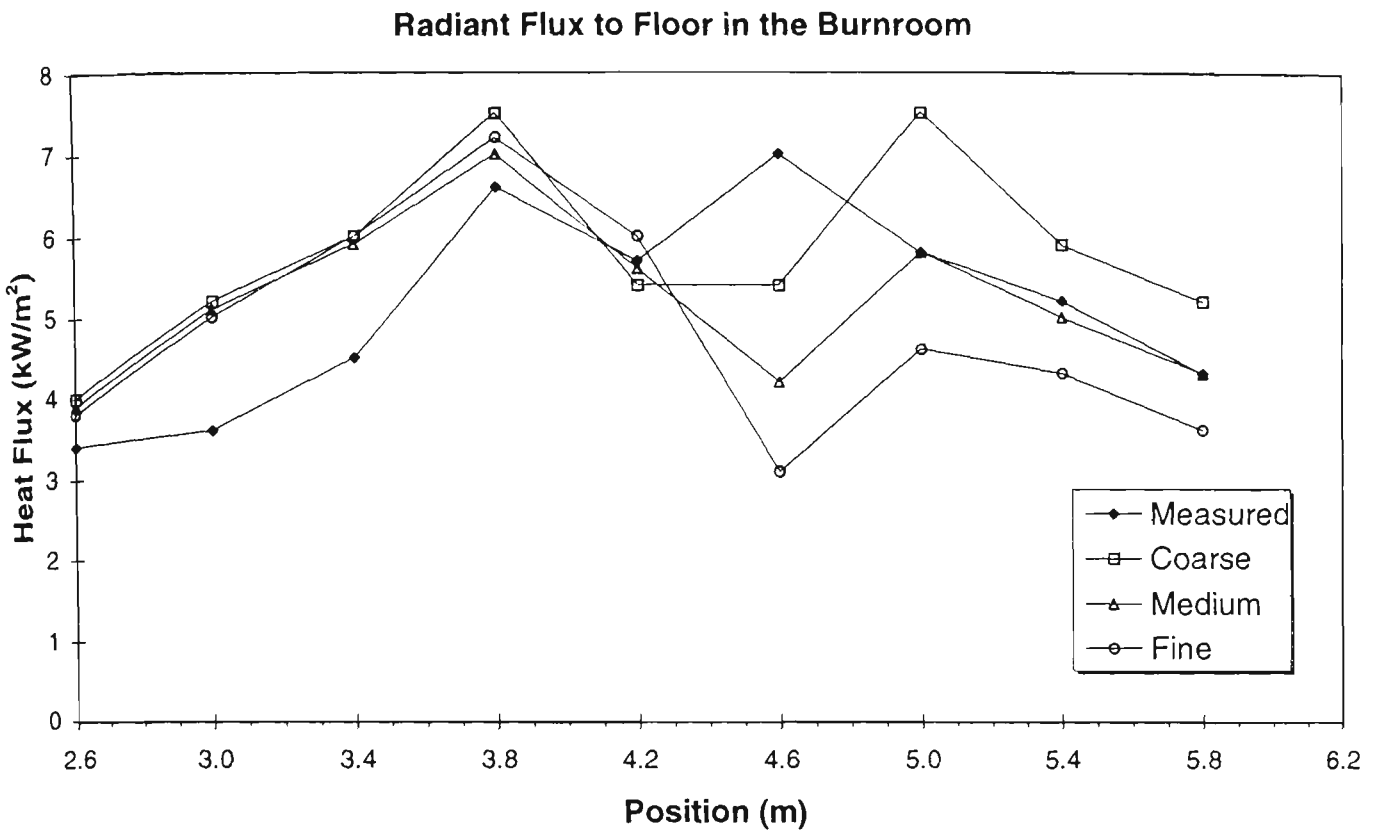

Figure 3.20 Comparison of predicted radiant fluxes to floor level in Burn Room

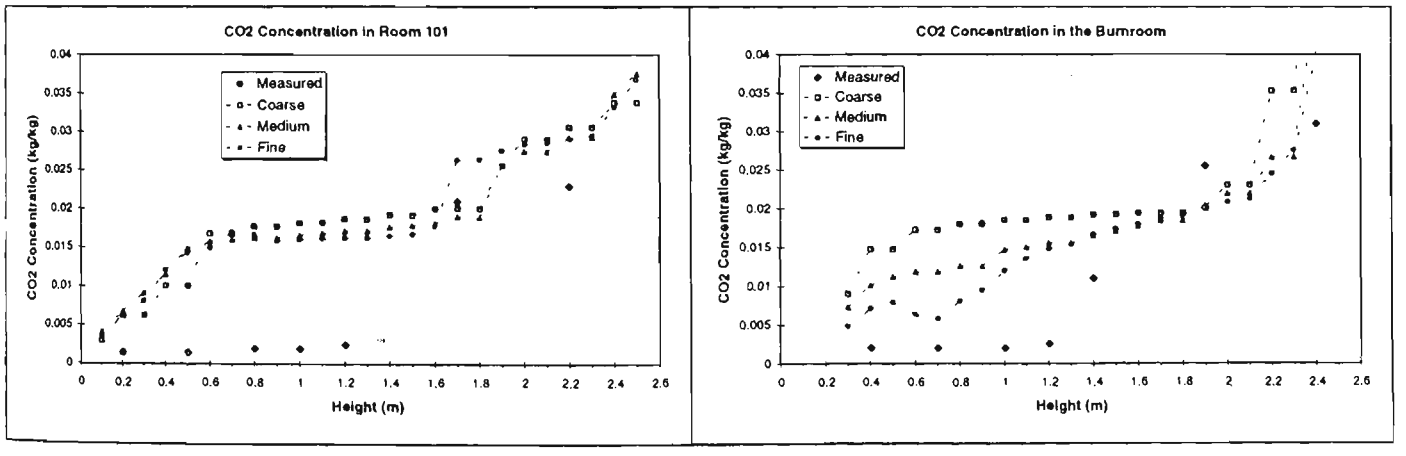

Figure 3.21 Comparison of predicted CO_2 concentrations

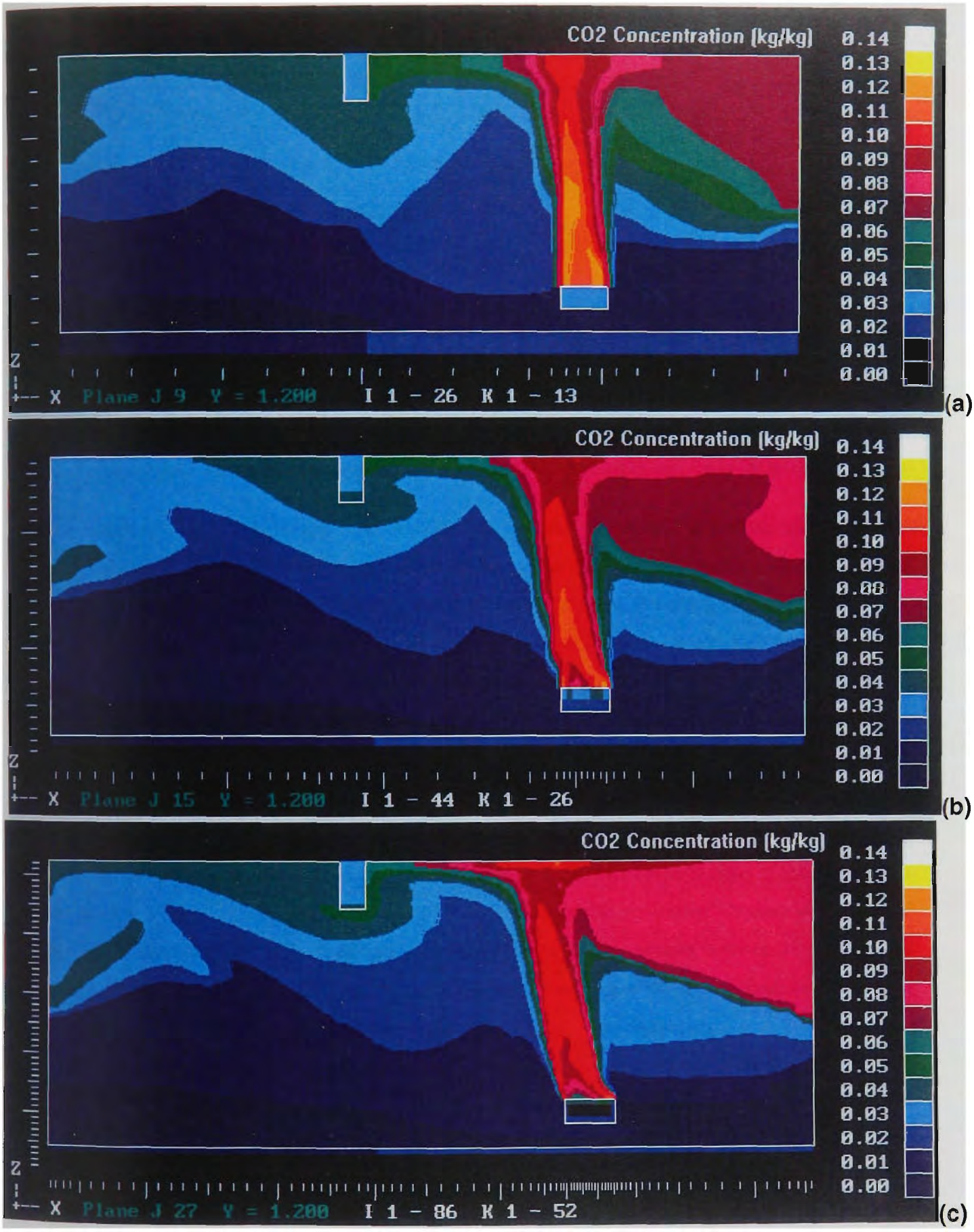

Figure 3.22 Predicted carbon dioxide concentration distributions for (a) coarse (b) medium and (c) fine grids

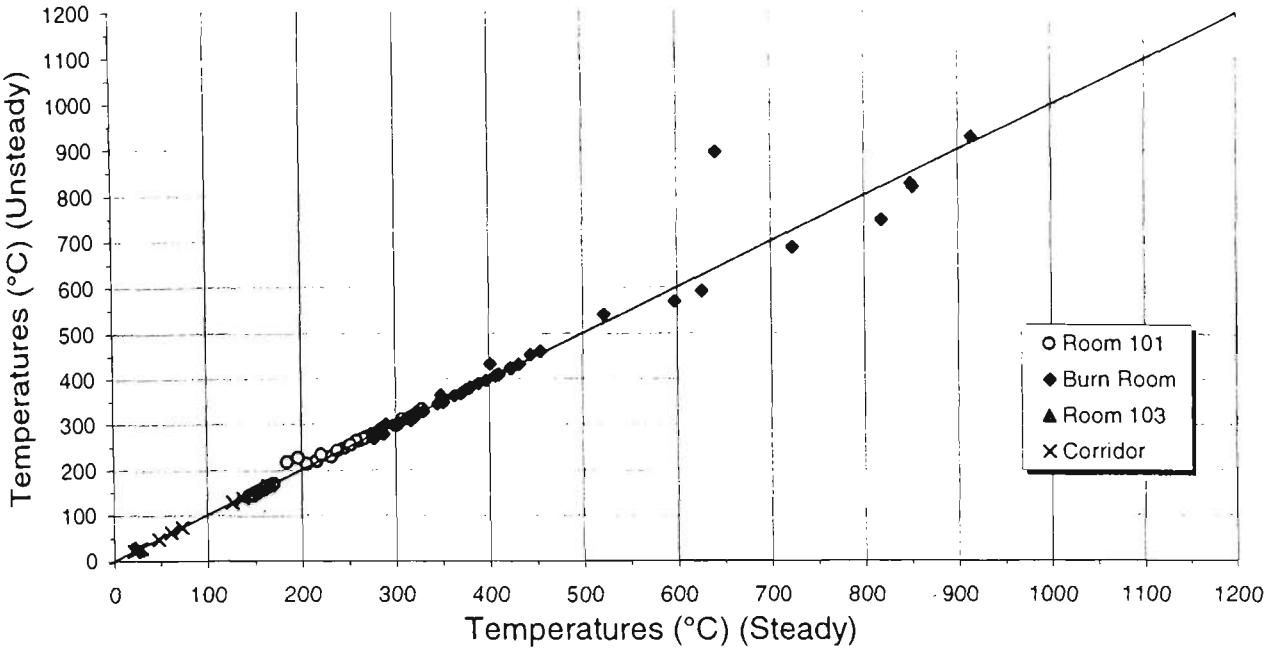

Figure 3.23 Comparison of predicted temperatures for the steady and unsteady solutions

The unsteady simulation results were not included in the preceding figures for clarity, as the unsteady results were very close to the steady results for the medium grid. Instead, a comparison of the predicted temperatures for the steady and unsteady solutions is shown in Figure 3.23. This shows that apart from some variation in the plume region, as indicated in the high temperatures in the burn room, the temperature predictions are coincident with the line of equality. That is, predicted temperatures for both methods at the given points are nearly equal. The implications of this result is that the solution is independent of the method used to achieve it, where the method is either a steady-state iterative solution, or an extended duration time-marching unsteady solution.

There were two points raised in Section 3.8 which were to be addressed in light of the findings in this section. The first was whether the high CO_2 levels observed in Section 3.8 were an artefact of the grid refinement. A feature of the predictions of the CO_2 concentrations in Room 101 is that grid refinement does not appear to reduce the problem of the mixing of layers. Indeed, the three grid refinements show little variation in this particular region. The discrepancy is either due to the model's inability to predict well the behaviour of the flow in quiescent spaces such as Room 103, which are not part of the main flow of fresh air and combustion products, or due to experimental factors, such as the enclosure not reaching true steady-state conditions (see also the footnote on page 98). "Smoke logging" of Room 103, the loss of buoyancy of the combustion products, and subsequent mixing with the inflowing cold layer, may be effects which will not be observed in the first 60 minutes of the experimental test, but nevertheless may eventually occur. This phenomenon is explored further in Section 3.11.

Further experiments involving measurement of the flows in the doorway to Room 103, and predictions involving other CFD models, are necessary to resolve the issue of the layer mixing. Experiments will help determine what the true situation is with regard to the flow pattern in the doorway to Room 103, and within the room itself, as well as species and temperature distribution. Predictions made with other CFD models will determine whether the poor prediction of quiescent spaces is a consequence of CFD methods in general, or a particular deficiency of the implementation of the methods in CESARE-CFD.

The second point raised in Section 3.8 was whether a grid independent solution had been attained. From the results presented here, it would appear that the answer is "almost". The temperatures and product concentrations are close for each refinement, but there is still a change in progressing from coarse to fine grid. As noted earlier, grid refinement seems to bring out features not resolved in the coarser grids, particularly in the region of the fire plume. This is to be expected to some degree. It seems that finding a grid independent solution is a problematic exercise for a complex, full-scale geometry such as examined here. For example, a further doubling of the grid nodes of the "fine" grid considered here would require a computer with at least 1GB of RAM to store all the data points in memory (the fine grid considered here required 140MB. A further doubling of nodes increases this number eightfold.) This alone increases the computation time; added to this is the trend noted above that the greater the refinement, the more iterations are required for convergence. For the fine grid presented here, 3 weeks were required to compute 35000 iterations. If the refinement were to be doubled, and the number of iterations increased, it would take months to attain convergence. However, even 3 weeks is impractical if development of the CFD model or investigation of its parameters is to be undertaken. Thus, grid refinements comparable to the "medium grid" were used throughout the work presented in the remainder of this thesis. They were coarse enough to minimise computation time and hence be of practical use from an engineering viewpoint, while exhibiting a sufficient resolution and accuracy to represent the details of the flow important to the fire scenarios under investigation. Since it is of some concern that a grid independent solution has not been achieved, then as computing resources improve further, further work should be undertaken utilising improved methods of convergence and finer grids.

3.9.3. Convergence Analysis

To gain a greater insight into the behaviour of the model, the convergence of the model for three different grid refinements and the results reported were examined in detail in this section. A selection of graphs of residuals as a function of the number of iterations is presented, and the main

features highlighted by the graphs are described. These features help to identify the factors that hamper or contribute to the successful convergence of the model to a solution. The analysis also demonstrates that the results presented in the previous section have reached a maximum degree of convergence.

The solutions for the three grid refinements were obtained sequentially, with subsequent simulations taking advantage of a previously obtained solution as a starting point. The fine grid solution was obtained first. Initially 3000 iterations were performed, with the residuals falling to levels deemed acceptable based on previous modelling exercises. While this was sufficient to reveal the overall pattern of the solution, the qualitative nature of the results indicated that full convergence was not obtained. What was revealed in this exercise was that the residuals alone are not sufficient to determine convergence. The magnitude of the residuals for the fine grid appeared to be much the same at 2000 iterations as they were at 20000 iterations. The key indicator was determined to be the global energy balance of the solution; that is, the energy entering the system should equal the sum of the energy leaving plus the change in energy.

The behaviour of the residuals for the three grid refinements is examined in the following subsections, as well as the unsteady simulation for the medium grid. The graphs display the iteration number along the x-axis, with the iteration number being cumulative as successive simulations were continued from the previous simulations. Thus, the fine grid iterations are numbered 500-34700, the unsteady simulation 34700-38300, the medium grid 38300-43300, and the coarse grid 43300-48300.

3.9.3.1. Fine Grid

The fine grid is examined first. A total of almost 35000 iterations were performed with this grid in three stages, with runs of 2500, 10000, and 22500 iterations in each stage respectively. The under-relaxation factors are as described above, except for the mixture fraction factor which was set to 1.0 throughout the simulation, and the enthalpy factor which was set to 0.5 for most of the simulation, but adjusted to 1.0 at certain stages.

The velocity residuals are shown in Figure 3.24. For most of the simulation, the residuals appear to be variable and chaotic. This corresponds to the section where the enthalpy under-relaxation factor was set to 0.5. There are two sections at around 18000 and 20000 iterations where the residuals decreased, and again after 22000 iterations where the residuals decreased to a fairly steady (non-

decreasing) value. These correspond to intervals where the enthalpy under-relaxation factor was set to 1.0. The author was attempting to speed up convergence by raising the under-relaxation factor, then reduce numerical oscillations by decreasing the factors. Indeed, the general rule is that a higher under-relaxation factor is more likely to lead to instability, which is the main reason that under-relaxation is used at all. What is notable in these results is that the opposite seems to hold, namely increased instability appears to occur with a lower under-relaxation factor.

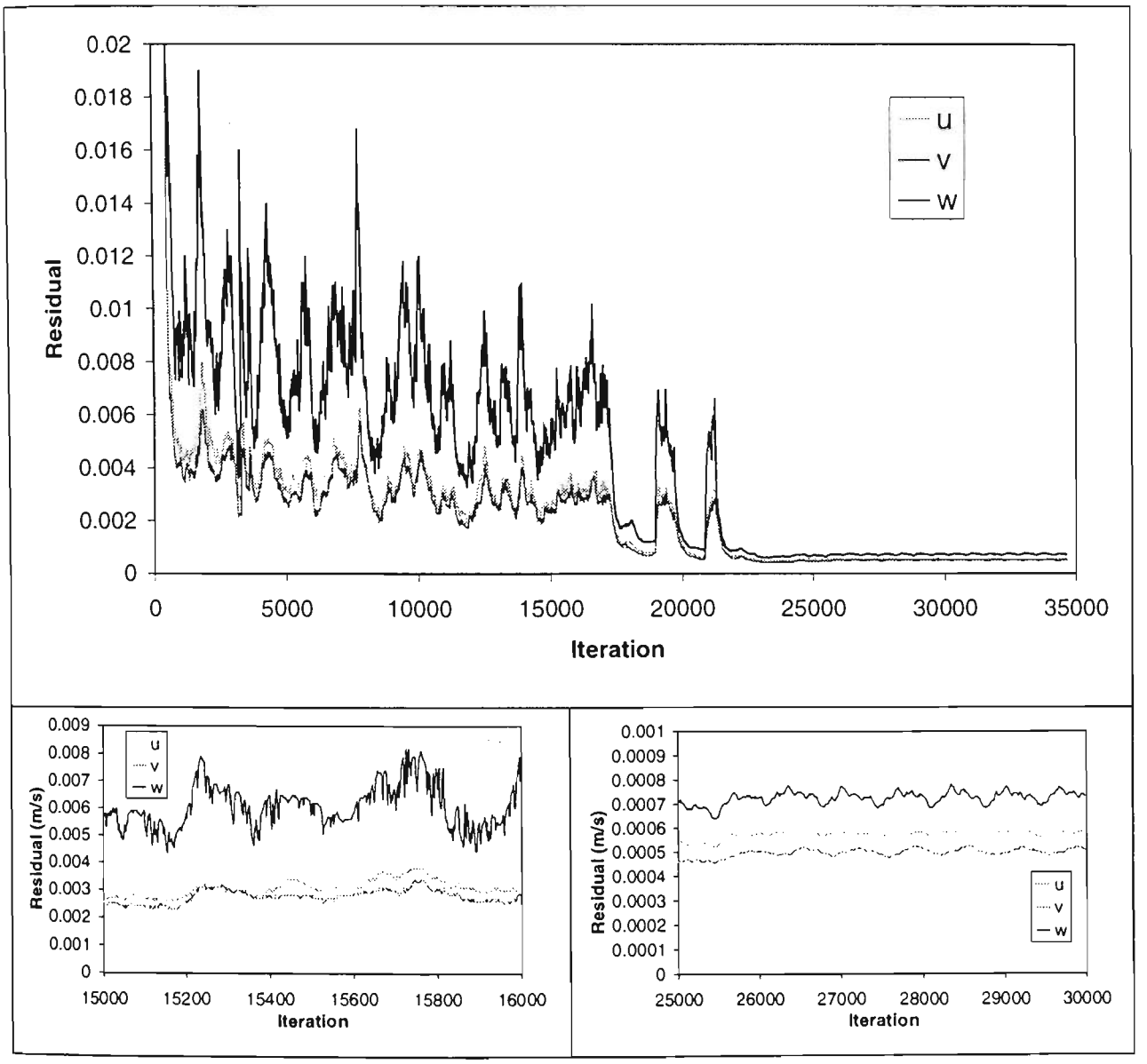

Figure 3.24 Velocity residuals for the fine grid 200kW steady state fire simulation

Several features are highlighted in the detailed frames of Figure 3.24. Earlier in the simulation (as highlighted at 15000 iterations) when instabilities are higher, the residuals of the *w* component of velocity (in the vertical direction) are approximately double those of the *u* and *v* components. This higher residual is most likely due to terms associated with buoyancy, which appear in the vertical component only of velocity, as well as in turbulence source terms. Towards the end of the simulation when the residuals have decreased to some extent, the residuals of the vertical component of velocity are still greater than those of the horizontal components, but not to such a

prominent a degree. What is also significant about this stage of the simulation is that the residuals are fairly steady, rather than gradually decreasing. This suggests that no matter how many more iterations are performed, the solution is not going to converge any further. Another interesting feature of this phase of the solution is a semi-regular oscillatory pattern in the residuals with a period of approximately 650 iterations. There is no obvious mechanism for such periodicity, although its presence and persistence is a further indication that there may be some inherent instability in the solution preventing complete convergence.

These features are apparent in the residuals of other flow quantities, as shown in Figure 3.25. The exception is the residuals for the fuel mixture fraction (Figure 3.25 d), which does in fact appear to be steadily converging towards the end of the simulation. The latter graph is plotted with a logarithmic scale in the vertical axis, so that the nearly linearly decreasing line indicates that the residuals are decreasing geometrically, roughly at a rate of one order of magnitude per 2000 iterations. Another feature of this graph is the sudden jumps at 2500 and 12500 iterations, which correspond to the point at which the simulation was restarted after completion of the previous specified number of iterations.

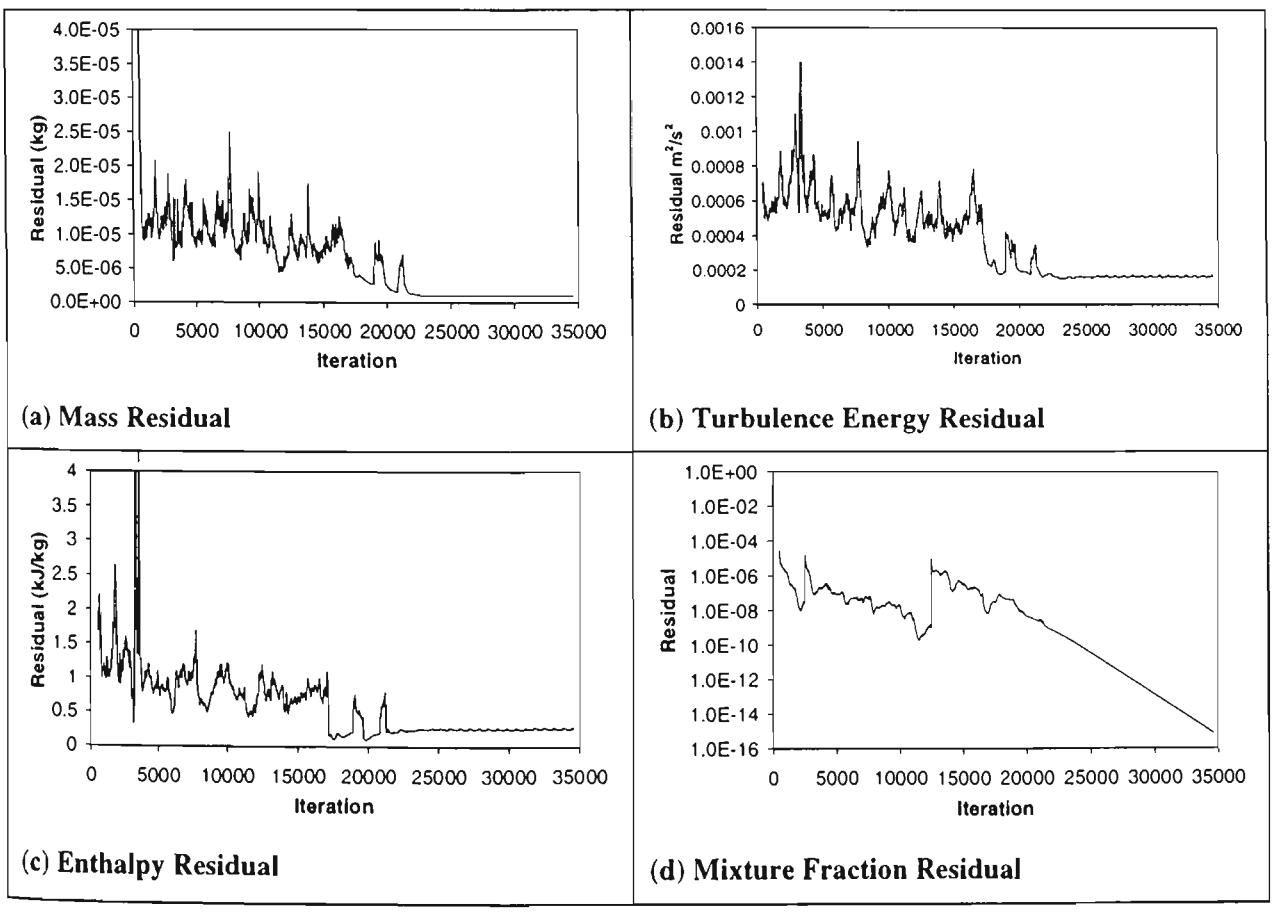

Figure 3.25 Residuals for the fine grid 200kW steady state fire simulation

Another factor which was found to be important in deciding the degree of convergence of the iteration procedure was the energy balance in the flow region. The energy balance comprises two

components, E_{in} and $E_{out}+dE/dt$, as described in Section 2.4.7. A graph of these two quantities is shown in Figure 3.26.

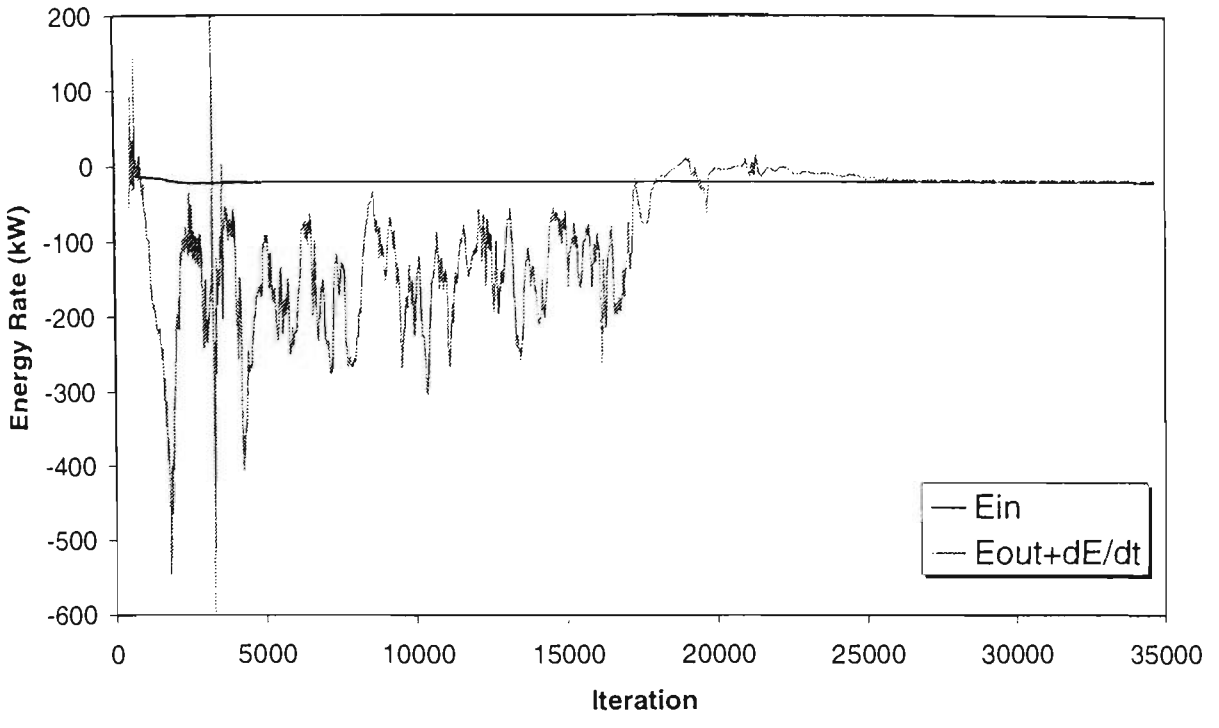

(a) **Full simulation**

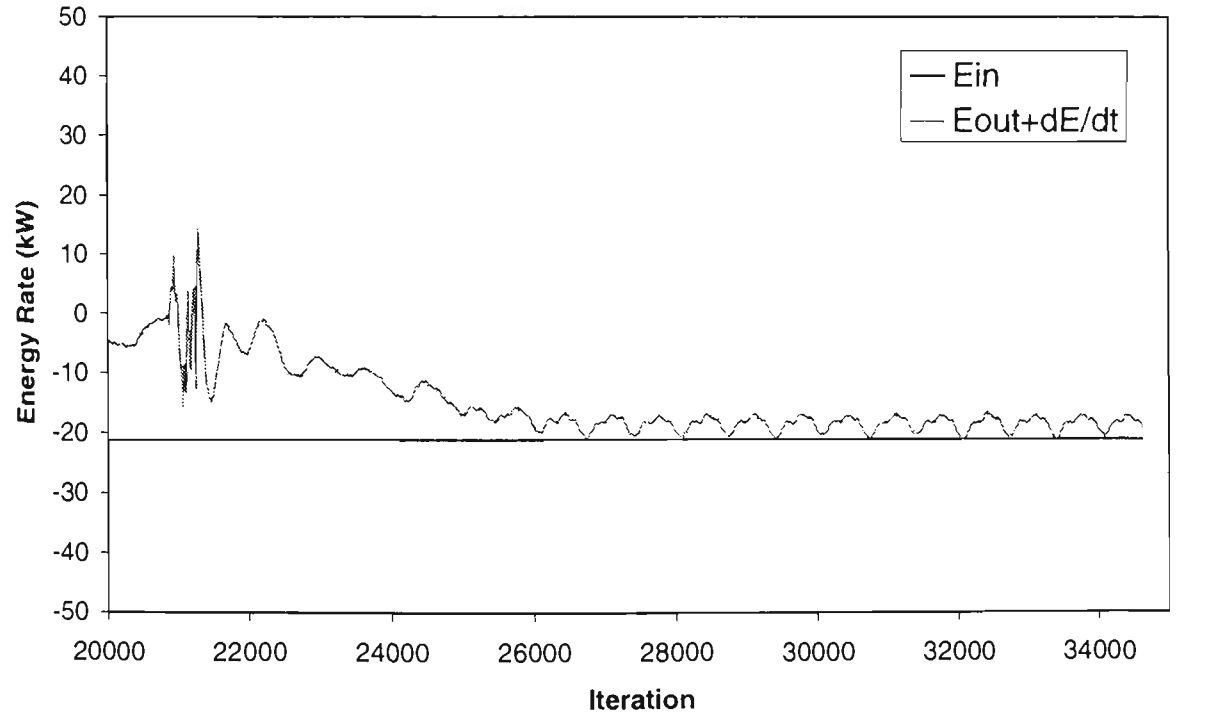

(b) **Detail of final stages of simulation**

Figure 3.26 Energy balance for the fine grid 200kW steady state fire simulation

The graphs show that there is a high degree of instability in the sum of the output and change in energy in the earlier stages of the simulation, while the input energy is very steady overall. The output enthalpy peaks at –800 and 600 kW (not shown on the scale in Figure 3.26), which is an

order of magnitude greater than the input enthalpy which remains around –20 kW. At convergence, the two quantities should be in balance. The reason that these quantities are a good indicator of convergence is because the energy balance appears to converge slower than the residuals. After the implementation of an under-relaxation factor of 1.0 for the enthalpy equation after iteration 20000, the residuals decrease to their steady value by about iteration 23000, while the energy balance does not reach a steady value until around 26000. The energy balance shows the same periodic oscillations late in the simulation as was noted above in the residuals, again suggesting that the solution has reached the limit of convergence.

3.9.3.2. Medium Grid

Presented here are results of a simulation for a medium refinement grid, which was a continuation of the fine grid simulation described previously. The distribution of flow variables over the coarser grid is calculated by a weighted average of the values in the finer grid. The under-relaxation factors were the same as for the fine grid, with the enthalpy factor initially set to 0.5, and increased to 1.0 after about 2500 iterations. As can be seen in Figure 3.27, the adjusting of the enthalpy under-relaxation factor has a similar effect on the residuals to that observed in the fine grid simulations, as seen in Figure 3.24. The residuals are also non-vanishing for the medium grid, which indicates that the solution has reached the limit of convergence.

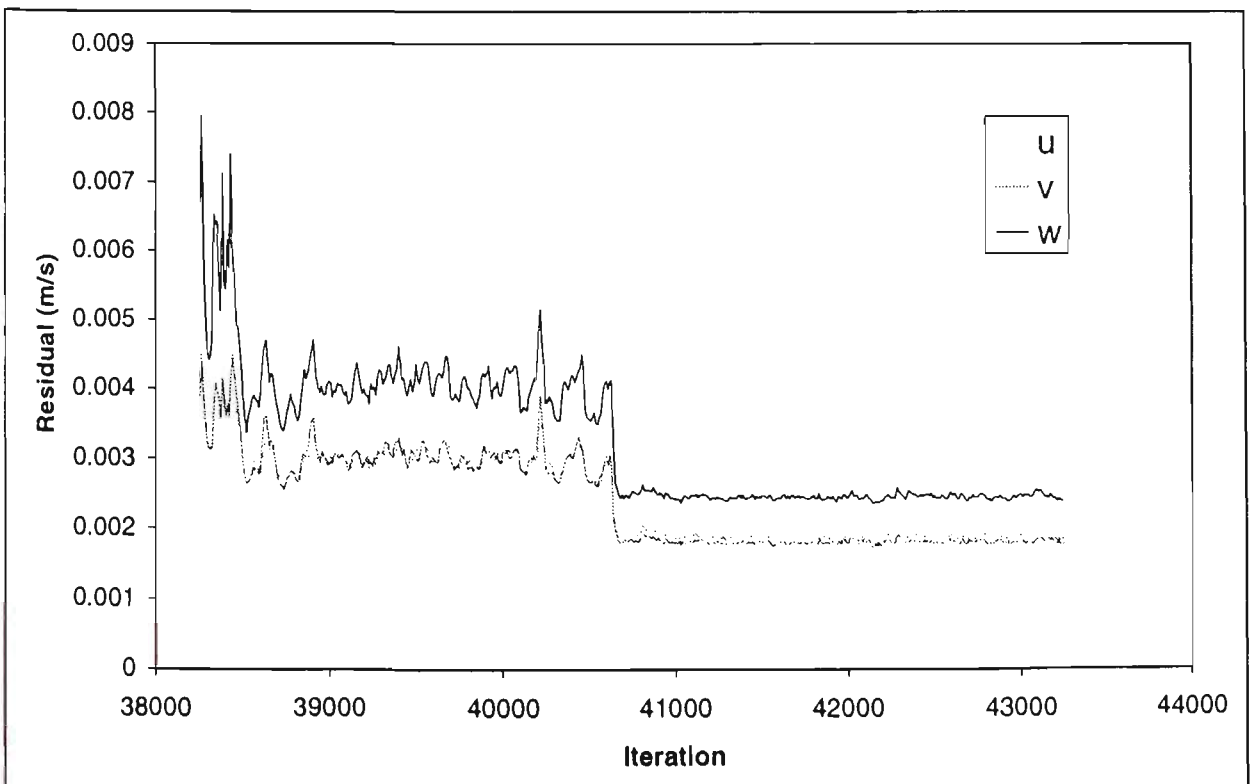

Figure 3.27 Velocity residuals for the medium grid 200kW steady state fire simulation

The residuals of the other flow quantities are shown in Figure 3.28. The overall trends are similar the velocity residuals, as was the case for the fine grid. As with the fine grid, the mixture fraction residual is steadily decreasing. The rate is most rapid when the enthalpy under-relaxation factor is 0.5, decreasing by one order of magnitude every 600 iterations. The rate decreases to one order of magnitude every 2500 iterations when the factor is increased to 1.0. There are a few notable differences to the fine grid trends. Overall, the limits of the residuals are higher than the fine grid case, but unlike the latter they do not show a regular oscillation. Also, the mass residual actually increases when the enthalpy under-relaxation factor is increased from 0.5 to 1.0.

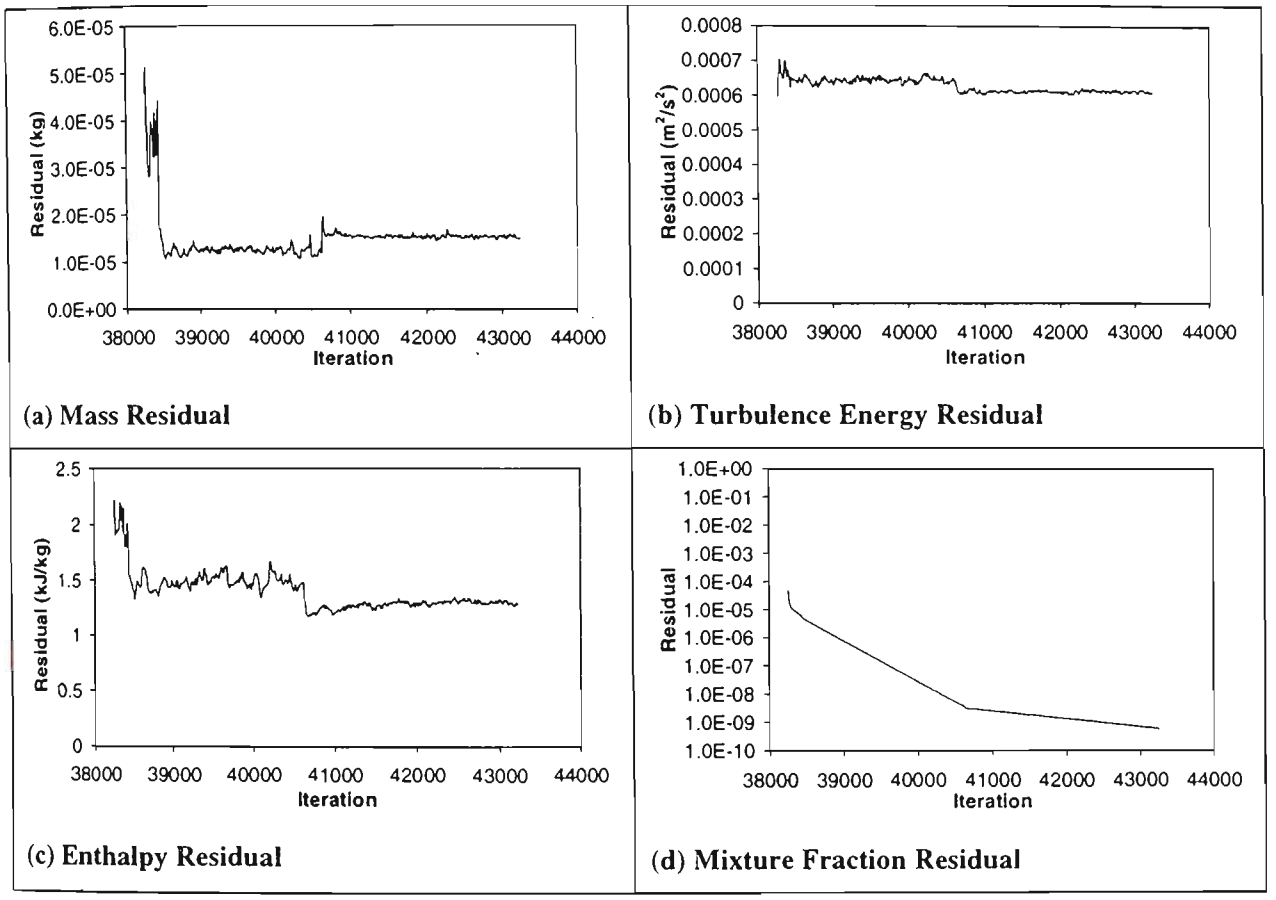

Figure 3.28 Residuals for the medium grid 200kW steady state fire simulation

The energy balance is shown in Figure 3.29. The earlier stage of the simulation is characterised by significant instability in the energy balance, which also shows a semi-regular oscillation with a period of around 100 to 110 iterations. This is a shorter period than the oscillations observed with the fine grid. This is consistent with a grid propagation related mechanism contributing to the instabilities, as a coarser grid will propagate a localised instability to its surroundings more rapidly. After adjustment of the enthalpy under-relaxation factor, the imbalance in energy decreases, although not to the extent of the fine grid.

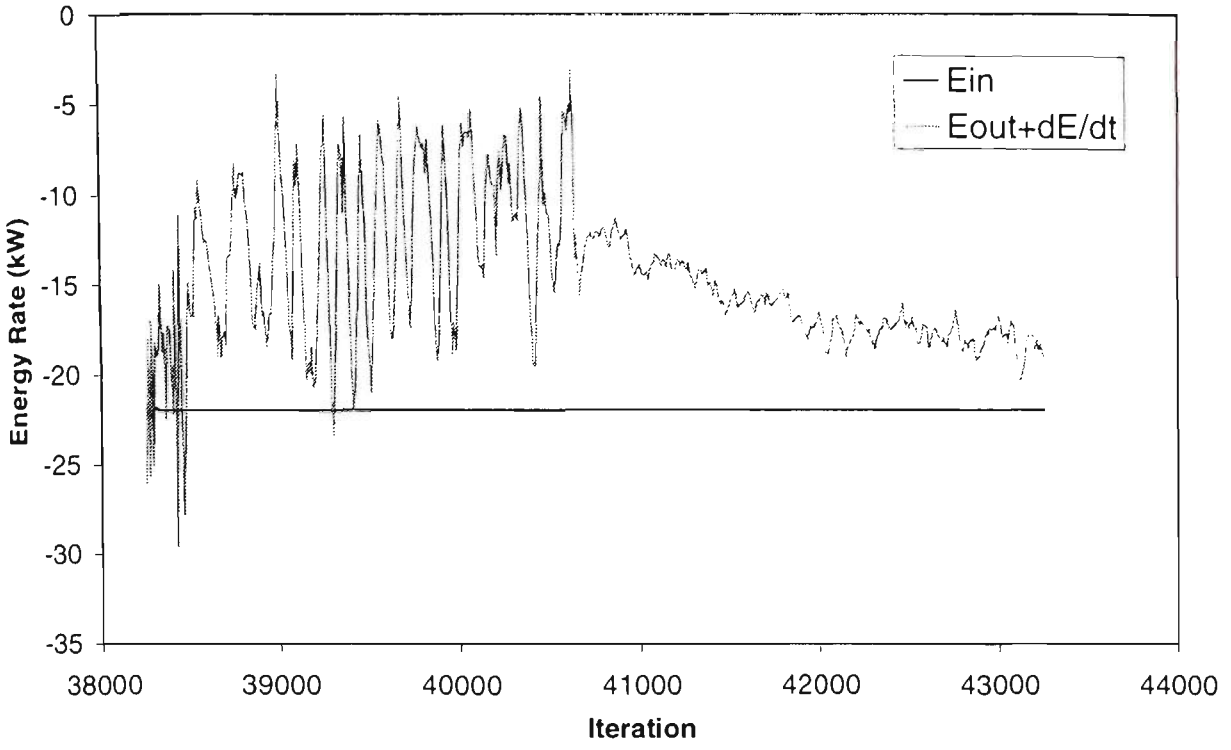

Figure 3.29 Energy balance for the medium grid 200kW steady state fire simulation

3.9.3.3. Coarse Grid

The simulation for the coarse grid was carried out using the medium grid results as a starting point in the calculations. Previous experience suggested that coarse grids are generally quite stable (see results in the next section), so that under-relaxation factors of 0.5 were used for the three velocity components, and a factor of 1.0 was used for the enthalpy, throughout the simulation. The results for the velocity residuals are shown in Figure 3.30, which shows that after the initial adjustment, the residuals reduce very quickly to a steady, but non-vanishing level. The magnitude of the average residual and the size of the oscillations is slightly higher than for the medium grid.

Similar trends are observed for the residuals of the other variables, as shown in Figure 3.31. Of particular interest is the residuals of the mixture fraction (Figure 3.31d), not only for the rapid rate of convergence (one order of magnitude every 200 iterations), but in that the magnitude of the residuals does not decrease indefinitely. The residuals stop decreasing at a value of around 10^{-22}, which is a significant reduction from the initial values of around 10^{-4}. This may in fact be the limit of numerical accuracy of the computer, with roundoff errors preventing further convergence.

The energy balance is shown in Figure 3.32. Once again, the balance shows some instability which is neither increasing nor decreasing, suggesting a limit to the degree of convergence has been reached. The limit has been reached rapidly in comparison to the finer grids.

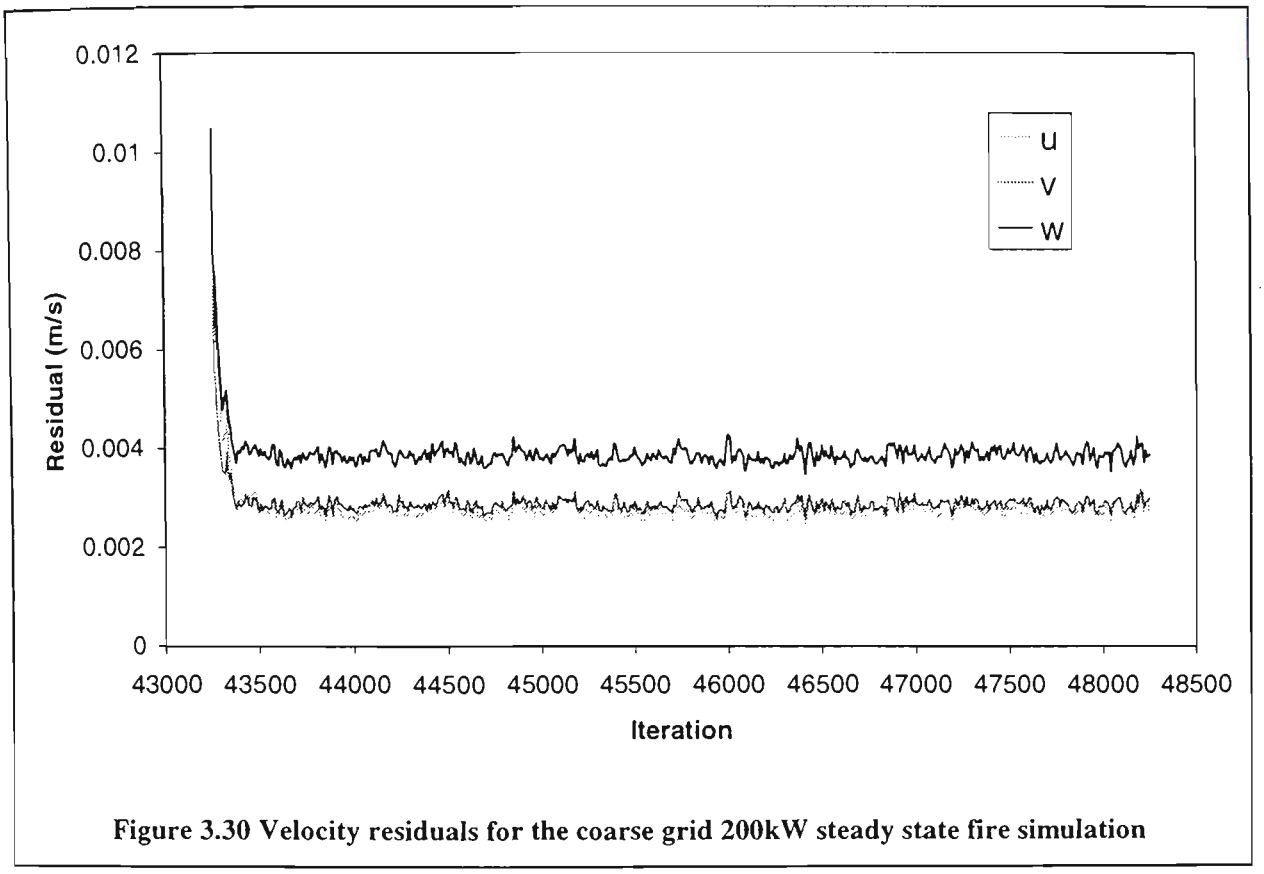

Figure 3.30 Velocity residuals for the coarse grid 200kW steady state fire simulation

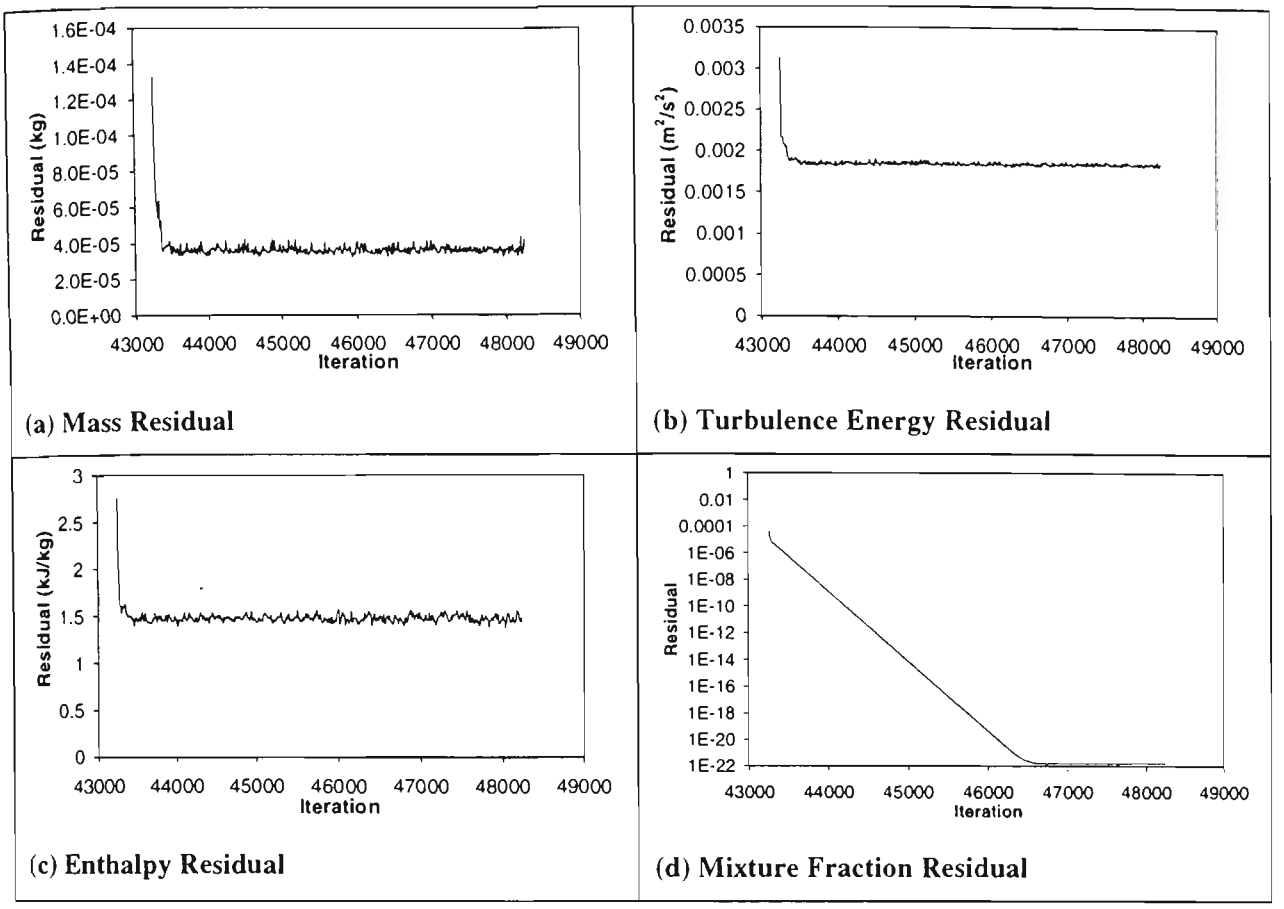

Figure 3.31 Residuals for the coarse grid 200kW steady state fire simulation

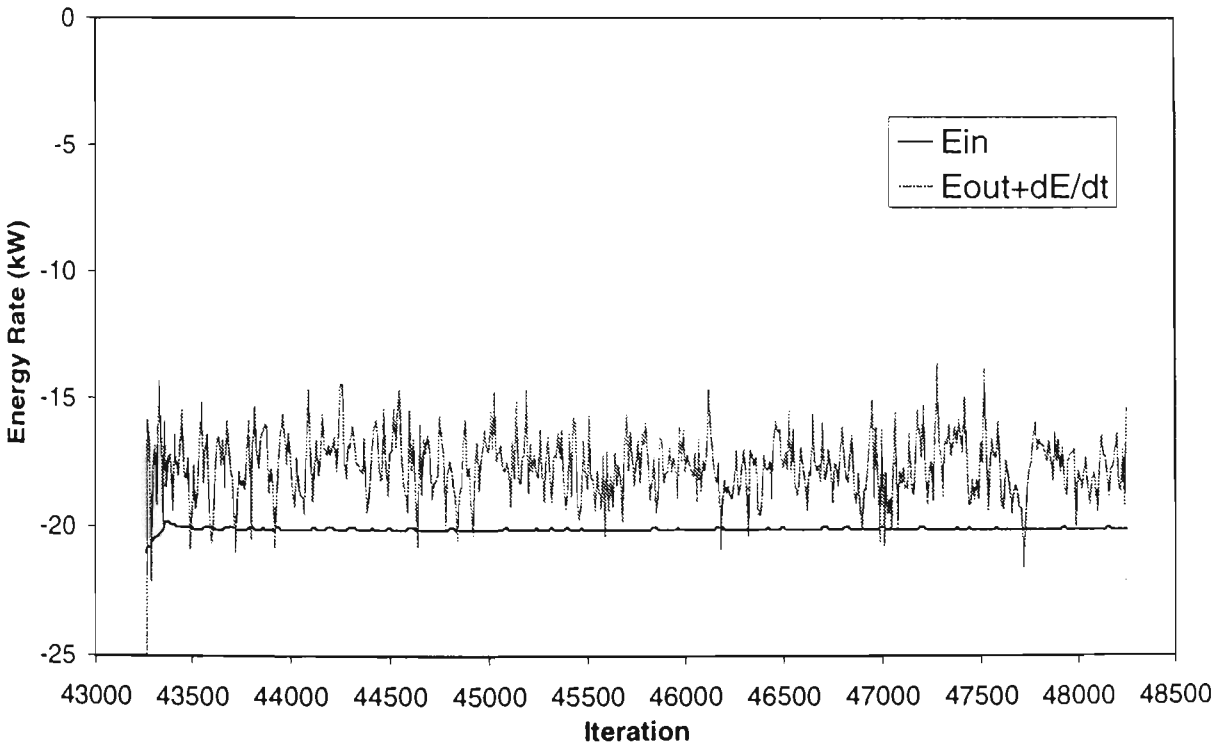

Figure 3.32 Energy balance for the coarse grid 200kW steady state fire simulation

3.9.3.4. Medium Grid Unsteady State

Finally, the medium refinement grid is again considered, although in this instance, the simulation is unsteady state rather than steady state. It is recommended[53] that an unsteady simulation is initialised with a steady state simulation to avoid instabilities in the first few iterations. In this instance, the fine grid simulation described above was used as a starting point. A medium grid steady state simulation was then run for 500 iterations to allow the solution to adjust to the new grid. The unsteady state simulation with the medium grid was then started using this last solution as a starting point. As the unsteady simulation is a time marching solution, each iteration in this instance corresponds to 1 second.

The velocity residuals are shown in Figure 3.33, where it can be seen that there appears to be an initial adjustment period of about 300 iterations, after which the residuals remain at a steady level. This pattern is likewise observed in the other residuals, shown in Figure 3.34, with the exception again being the fuel mixture fraction, which is steadily decreasing.

The energy balance is shown in Figure 3.35. Instability is again present in the balance, which may be due to the high under-relaxation factors used in the unsteady simulation. The magnitude of the unstable oscillations is comparable to the steady medium and coarse grid simulations presented above. The pattern of convergence suggests, as is has for the steady simulations presented above, that the limit of convergence has been reached for the simulation parameters used.

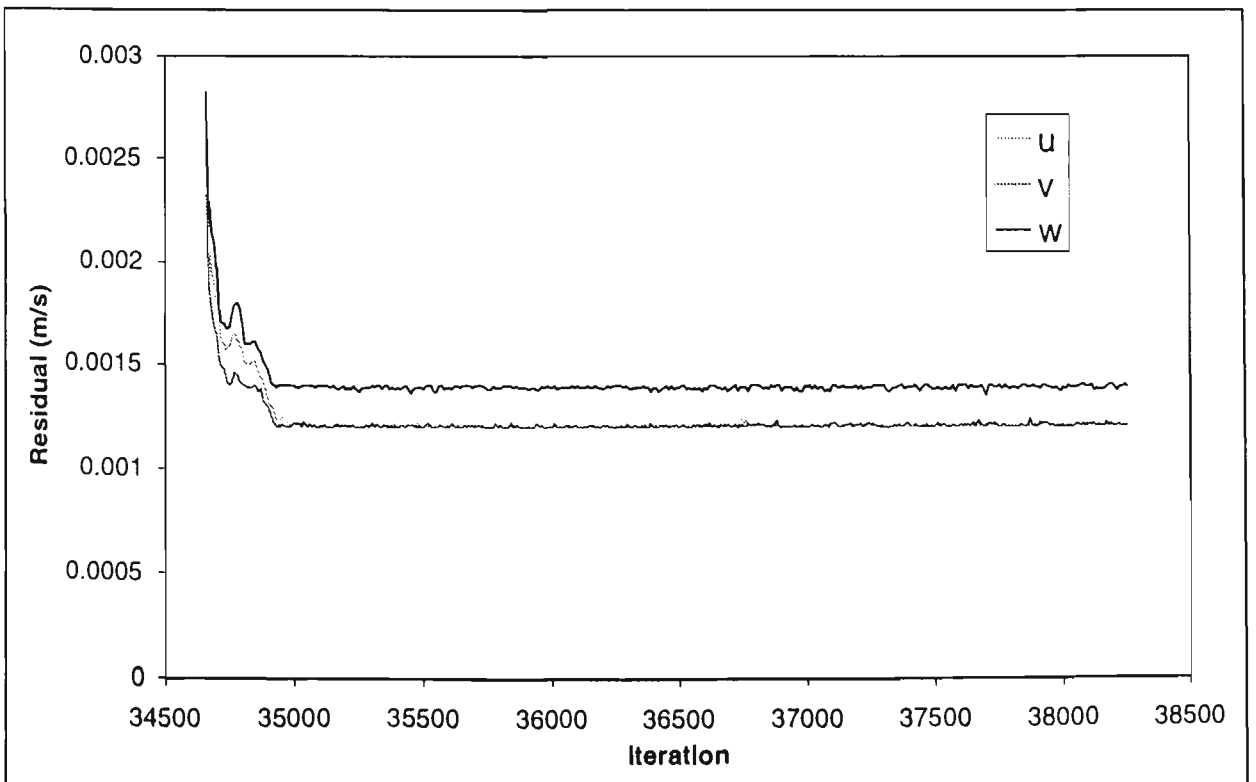

Figure 3.33 Velocity residuals for the medium grid 200kW unsteady state fire simulation

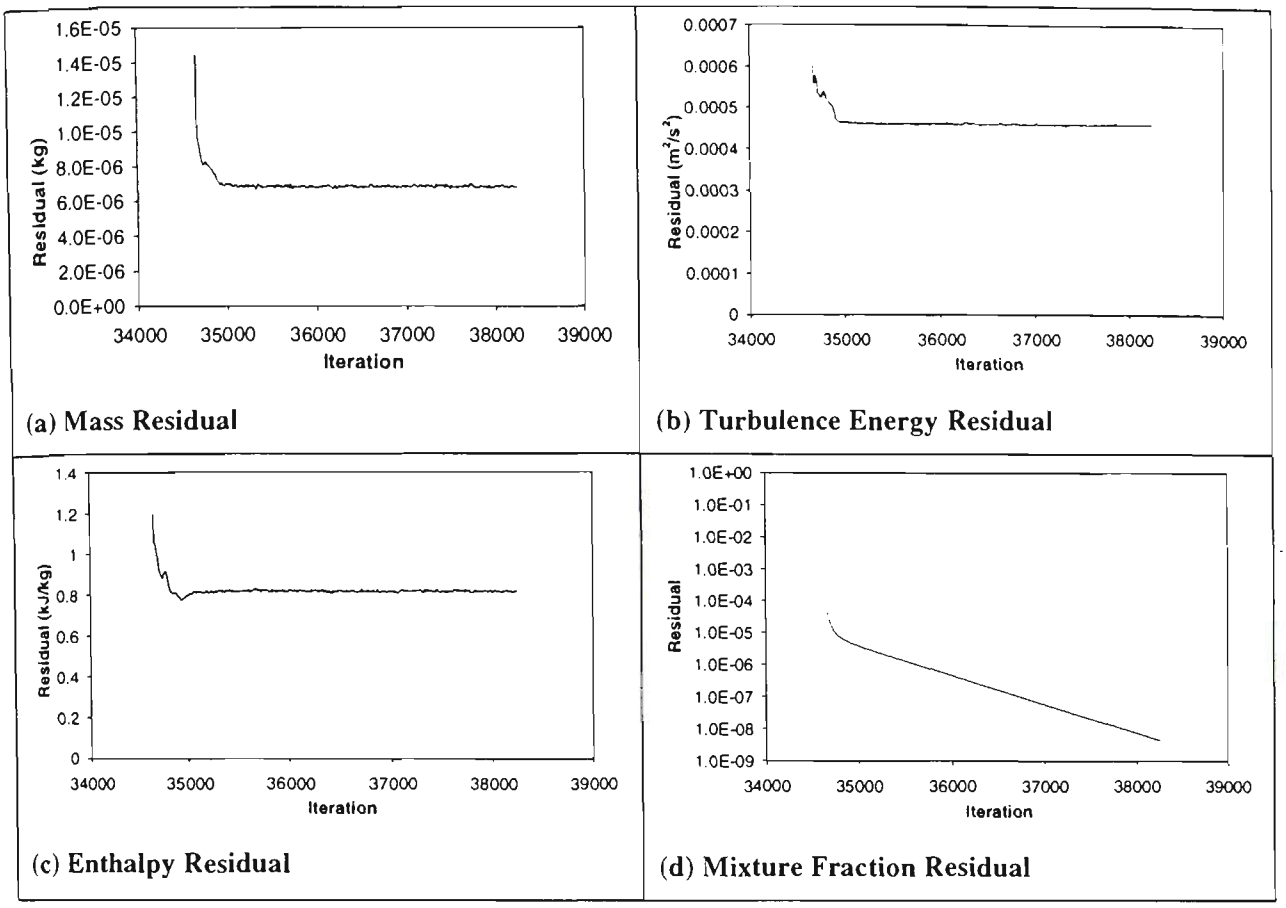

Figure 3.34 Residuals for the medium grid 200kW unsteady state fire simulation

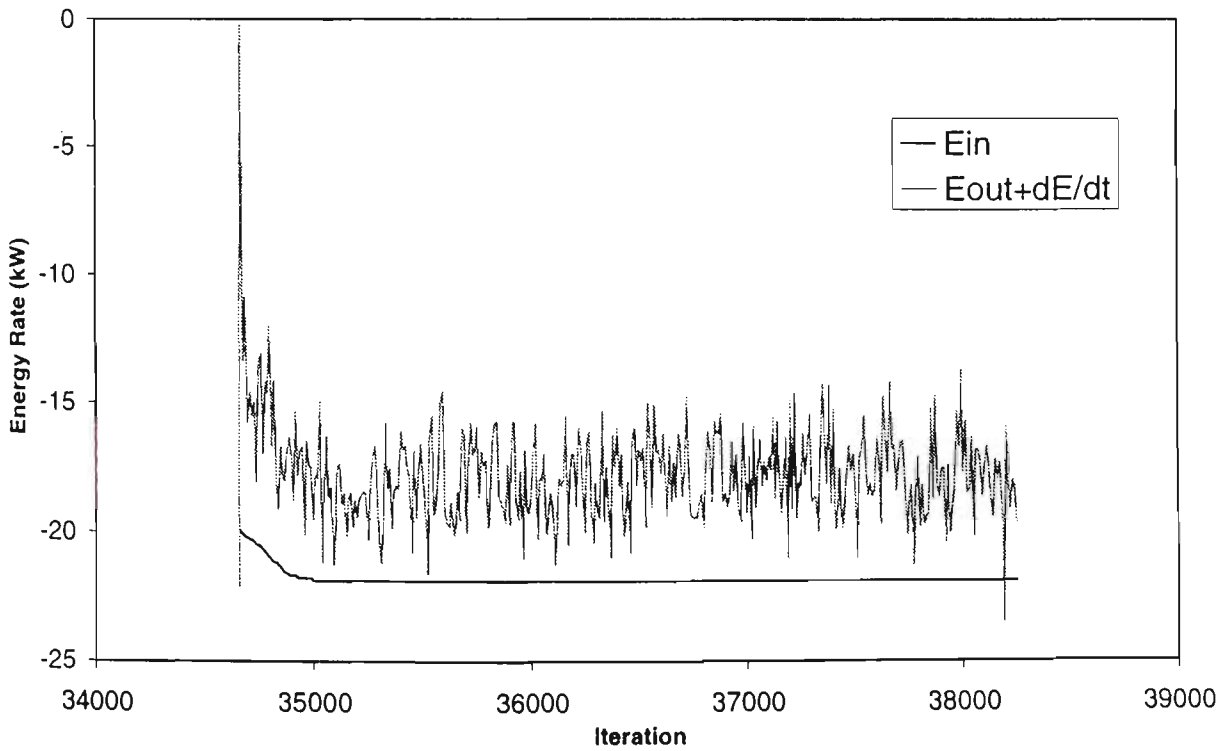

Figure 3.35 Energy balance for the medium grid 200kW unsteady state fire simulation

3.10. SENSITIVITY ANALYSIS

In this section, a sensitivity analysis of several parameters of the CFD model is performed, to ascertain the influence of the parameters on the outcome of the simulations. The parameters investigated are those which are of uncertain or variable value. It is important to ascertain the influence of these variables on the outcome of the solution. If changing the value of variable within its range has little impact on the solution, then the choice of value is not important. The converse is true, so that if the solution is sensitive to changes of a particular variable, then the choice of value becomes important and must be justified. A sensitivity analysis also reveals the behaviour not only of the variable being altered, but of the system as a whole.

The variables that are investigated are:

- The fraction conversion of fuel to soot
- The oxygen limit of combustion
- The maximum velocity at the balance port
- The heat transfer coefficient at the walls
- The heat of combustion

Each of these parameters, along with the results of the simulations, are described individually in the following subsections. The scenario modelled is the 200kW steady-state fire described in Section 3.8, using the coarse grid described in Section 3.9. The coarse grid was used for rapidity of execution and convergence, as a large number of simulations needed to be performed for the sensitivity analysis. The results in Section 3.9 suggest that the coarse grid solution is sufficiently accurate for the exercise to be undertaken here, as it reproduces all the major features of the fire scenario. It is reasonable to suppose that the coarse grid solution will respond in a very similar fashion to the alteration of a parameter as will a finer grid. Of the parameters under investigation, each will take a default value, apart from the single parameter that is being altered. The parameters investigated, their default values used, and their range is listed in Table 3.10.

Table 3.10. Parameters considered in the sensitivity analysis

Parameter	Default Value	Range
Fuel to soot conversion (%)	2	0, 2, 4
O_2 combustion limit (%)	10	0, 4, 7, 10
Maximum balance port velocity (m/s)	2	1, 2, 4
Heat transfer coefficient ($W/m^2 \cdot K$)	10	5, 10, 30
Heat of combustion (kJ/kg)	46000	40000, 46000, 50000

3.10.1. Fuel to Soot Conversion

The fraction of fuel converted to soot is used to estimate the concentration of soot throughout the modelled enclosure, as outlined in Section 3.6. A default value of 2% was chosen as it is in agreement with previously used values[16]. The soot concentration is used in Equation 3.28 to determine the local absorption coefficient, for use in the radiation heat transfer equations. There are two other constants in Equation 3.28 which affect the absorption coefficient, and whose values are also not known with great precision. These two values are the absorption constant, κ, and the particle density, ρ. As it is ultimately the absorption coefficient that is of interest in the equations, altering the fraction of fuel converted to soot is equivalent to altering either of the other two constants in the context of performing a sensitivity analysis.

In this analysis, two other values of the conversion factor were investigated. For the first value, the conversion factor was doubled to 4%, while for the second, it was reduced to 0%, to simulate no soot at all. The charts of all three parameters are plotted in the following figures for comparison.

Figure 3.36 shows the temperature distributions for the three values in Room 101. It is quite apparent that altering the conversion fraction has a negligible effect on the temperature distribution. This trend is likewise observed in Room 103 and the Corridor, shown in Figure 3.38 and Figure 3.39 respectively. In the burnroom, altering the conversion factor has little effect on the predicted temperature distribution on the periphery of the room, as shown in Figure 3.37. It is only in the region of the plume, where the fuel concentration is particularly high, that altering the conversion factor has any significant effect. In the plume region, using a conversion factor of 4% results in the lowest predicted temperatures. This is most likely due to the fact that increasing the absorption coefficient in the plume region results in increased radiant emission (as the plume region is hotter than the surroundings, it is emission which is increased, resulting in lower temperatures). The results for a conversion factor of 4% also show the best match with experimentally measured temperatures. This alone does not necessarily support adjusting the default conversion factor to 4%, as it does not rectify the temperature discrepancies beyond the plume region. However, it does suggest that improving the soot production model so that it predicts higher soot yields in the plume region will improve temperature predictions therein.

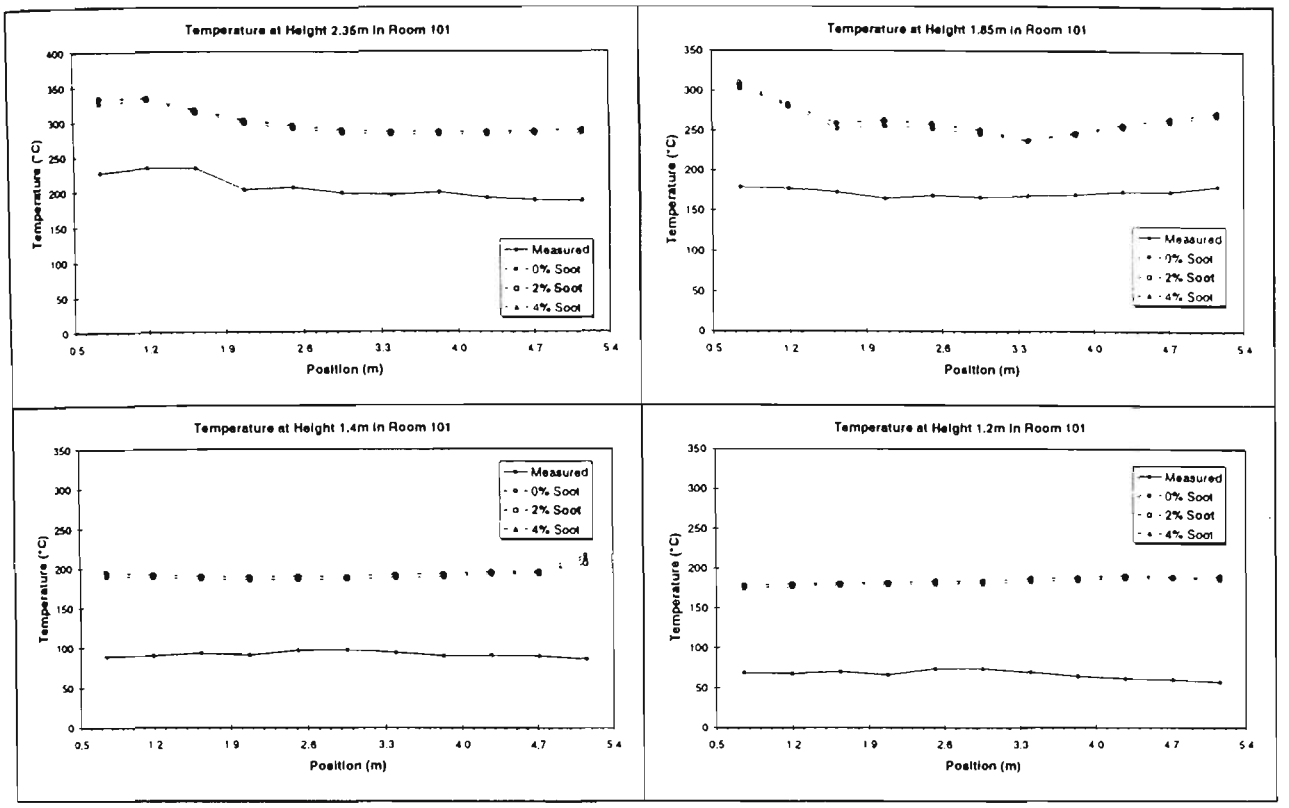

Figure 3.36 Comparison of predicted temperatures in Room 101

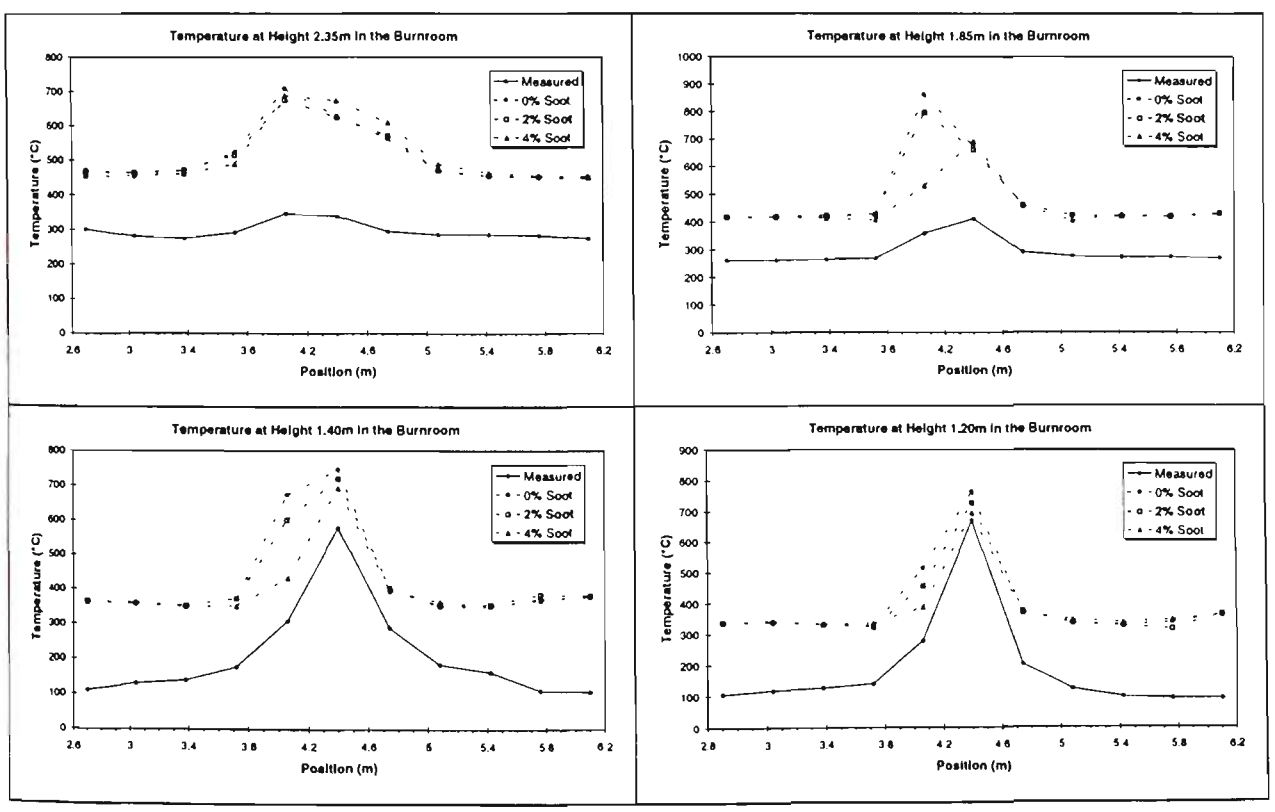

Figure 3.37 Comparison of predicted temperatures in the Burn Room

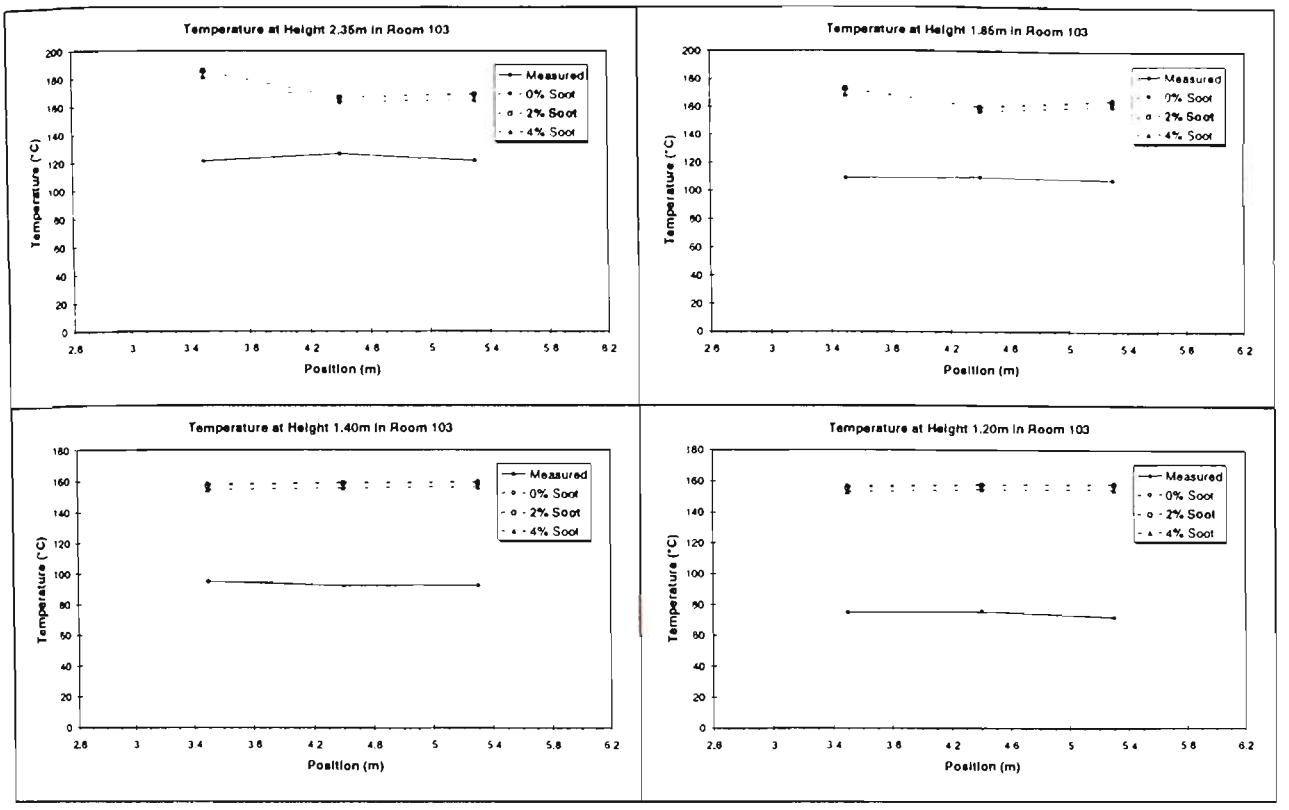

Figure 3.38 Comparison of predicted temperatures in Room 103

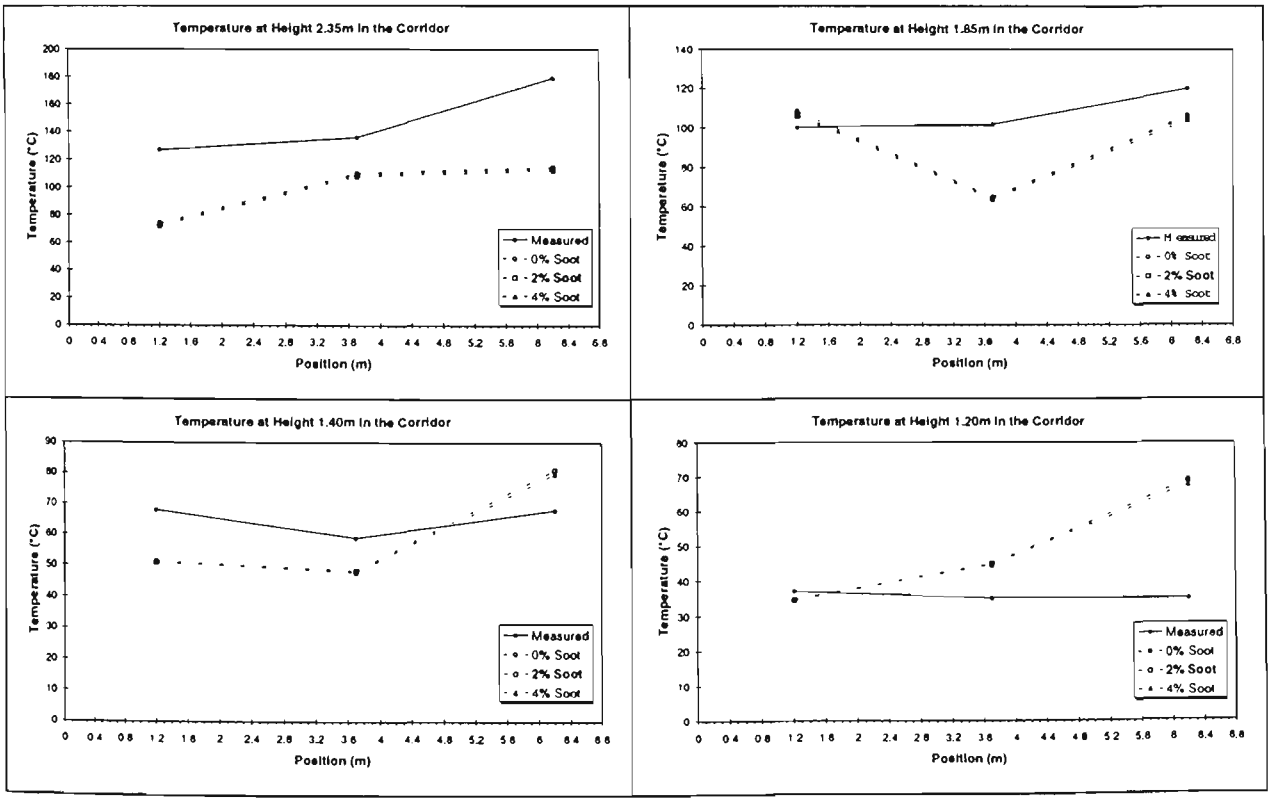

Figure 3.39 Comparison of predicted temperatures in the corridor

The CO_2 concentrations for Room 101 and the burnroom are shown Figure 3.40. The results show, as with the temperature distributions, that adjusting the conversion factor has little effect on the distribution of CO_2 within the enclosure. The only noticeable variation is the 4% curve in the burnroom. It is marginally higher up to within 0.4m of the ceiling, after which it is marginally lower in the vicinity of the ceiling. A possible mechanism for this variation is the increased soot concentration causing increased emissivity and hence lower temperatures in the plume region, resulting in reduced buoyancy. The reduced buoyancy would carry less combustion products into the ceiling layer, instead distributing them in the region below.

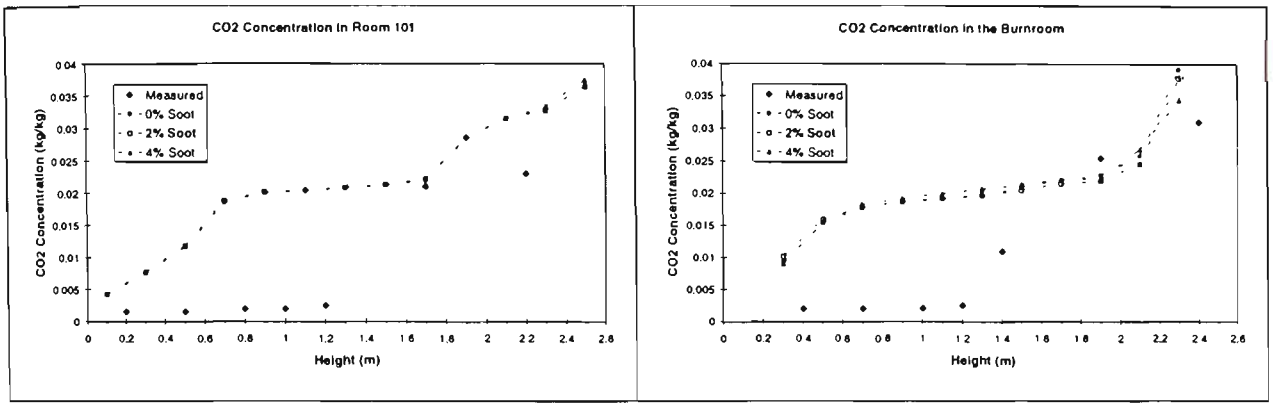

Figure 3.40 Comparison of predicted CO_2 concentrations

3.10.2. Oxygen Limit for Combustion

In this subsection, the effect of altering the oxygen concentration combustion limit on the temperature and species distributions is investigated. The model uses the variation in fuel mixture fraction model described in Section 2.2.3, with the addition of an oxygen limitation criterion. If the oxygen concentration in a given control cell is below the limit, then no combustion occurs in that cell. The default value* used in this analysis is 10%, which is close to values used elsewhere[9]. The exact value varies depending on the composition of the gas displacing oxygen, which may be fuel, nitrogen, combustion products, or more typically, a combination of all three. The main reason for choosing a value of 10% is that the model produces a physically realistic solution when a value close to this figure is used. This reason is clarified in the analysis that follows. The other values chosen for the analysis were 0%, 4% and 7%. The former was chosen to investigate the effects of no limit, while the latter two are intermediate values. The reason small limits were investigated is that it feasible that combustion may be possible in regions of low oxygen concentration, particularly in extreme conditions such as flashover.

* The value of 10% was mistakenly used as a default value in this analysis, as a value of 7% was used elsewhere in this chapter. The small difference between 7% and 10% limits should be considered when comparing results here with those elsewhere in the chapter.

The effect of altering the limit on the distribution of temperatures in Room 101 is shown in Figure 3.41. It can be seen that there is little difference between the limits 0% and 4%, both of which are the furthest removed from the experimentally measured values. Increasing the limit to 7% produces a very different curve, which is closest to the measured values, while the default value of 10% is in between the 7% curve and the 0% curve, but resembles the 7% curve in overall shape. These trends are also observed in the temperature distributions for Room 103, shown in Figure 3.43, and for the corridor, shown in Figure 3.44, although in the latter the temperatures for the 7% and 10% cases are closer to the measured temperatures.

These trends are even more pronounced in temperature distributions for the burnroom, shown in Figure 3.42. What is most notable in the temperatures for the 0% and 4% cases is the conspicuous absence of a well defined plume. What was observed qualitatively in these results is that a spherical temperature distribution forms around a "hotspot" close to the fuel inlet port, with temperatures decreasing radially (see Figure 3.46a). There is only a nominal vertical flow pattern above this hotspot, and a reduced flow in the upper and lower layers in both the burnroom and Room 101. The flow pattern is difficult to interpret physically, and indeed the conclusion reached by the author is that the solution is physically unrealistic. The results indicate that the transition from unrealistic to realistic occurs somewhere between a combustion oxygen limit of 4% and 7%.

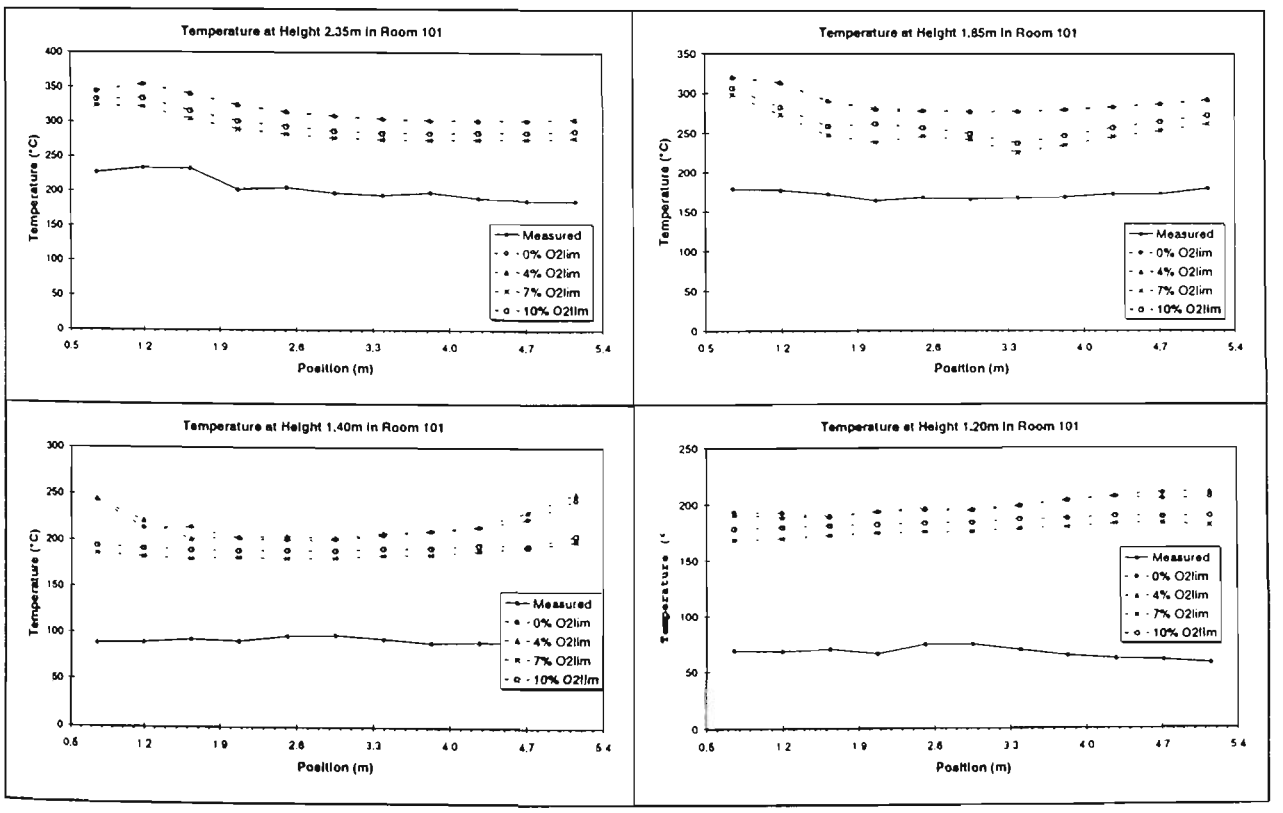

Figure 3.41 Comparison of predicted temperatures in Room 101

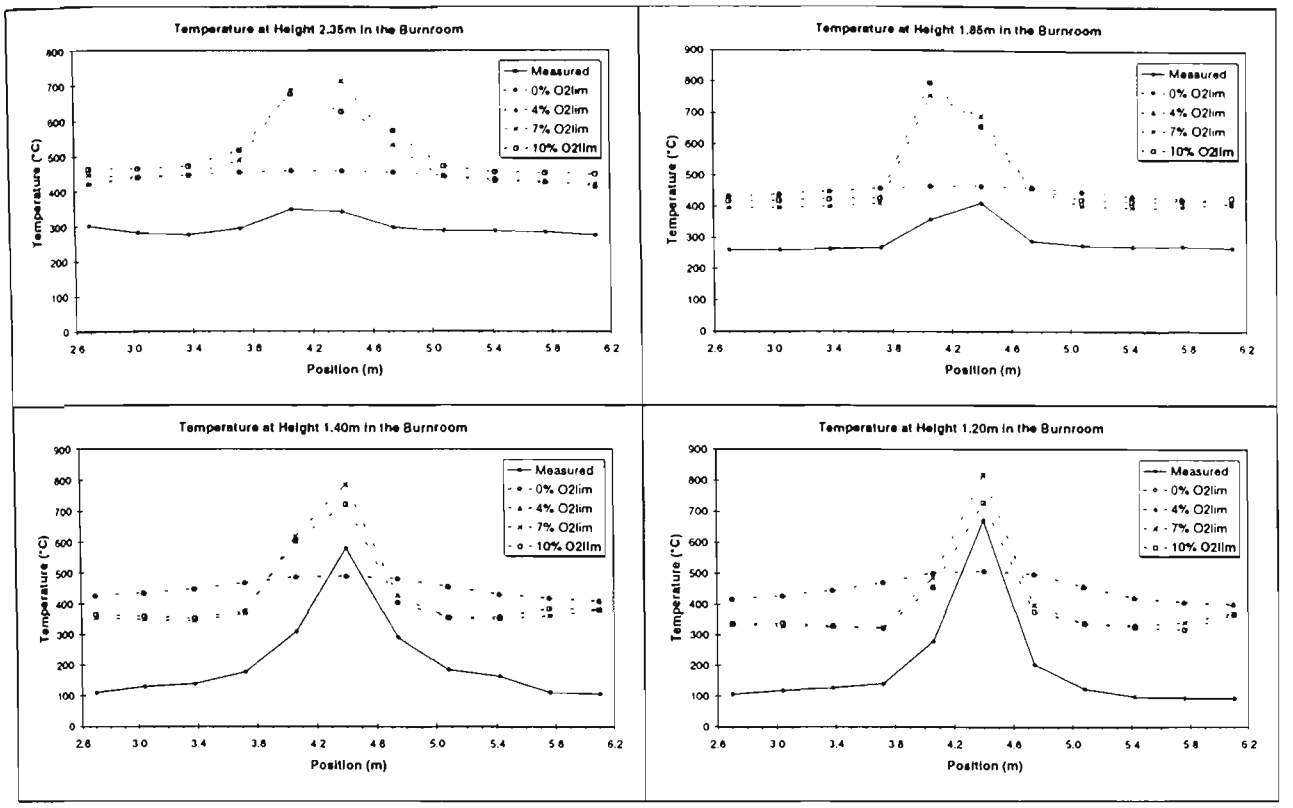

Figure 3.42 Comparison of predicted temperatures in the Burn Room

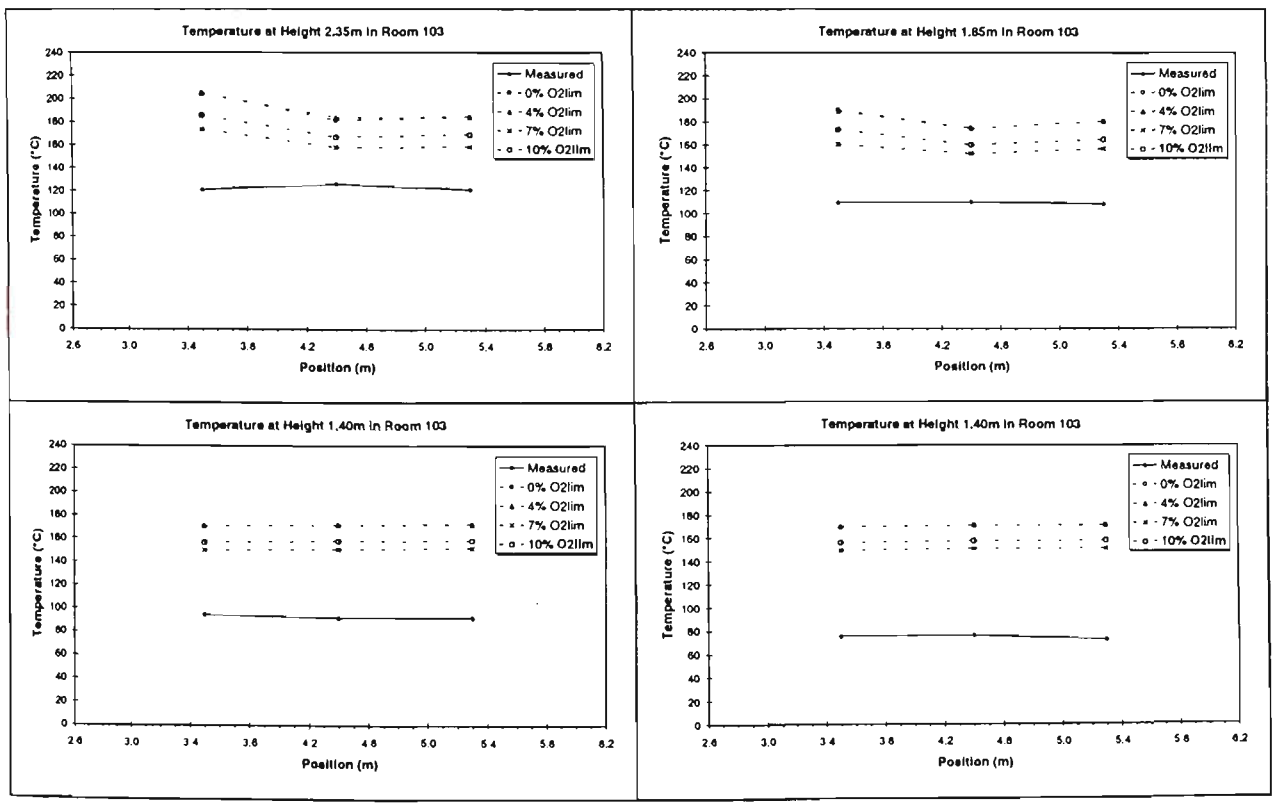

Figure 3.43 Comparison of predicted temperatures in Room 103

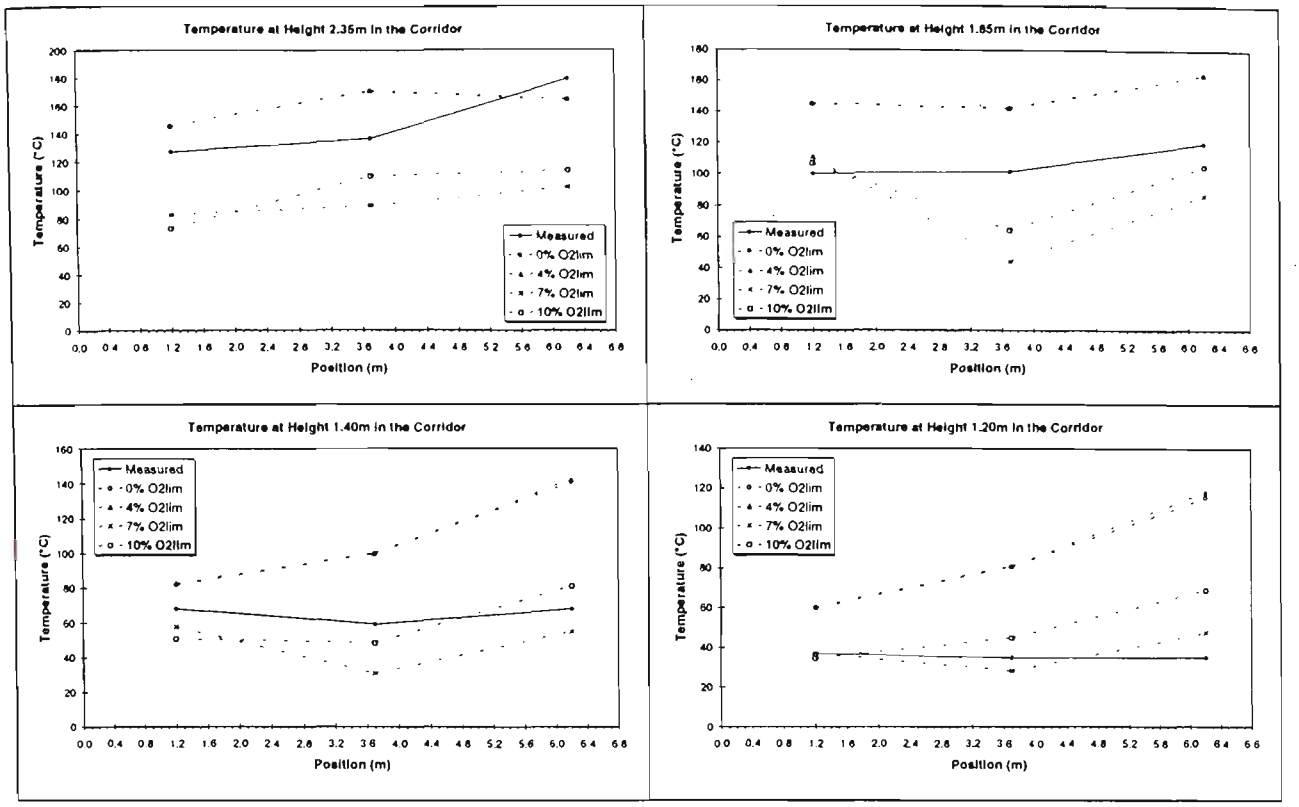

Figure 3.44 Comparison of predicted temperatures in the corridor

The CO_2 concentration distributions shown in Figure 3.45 are further evidence of the physically unrealistic nature of the solution for low combustion oxygen limits. While the Room 101 results show similar trends to the temperatures, the results for the burnroom show overall greatly elevated levels of CO_2 for the 0% and 4% values, and which are nearly uniform from close to the floor all the way to the ceiling. As with the temperatures, it is the 7% value which produces predicted results nearest the measured results.

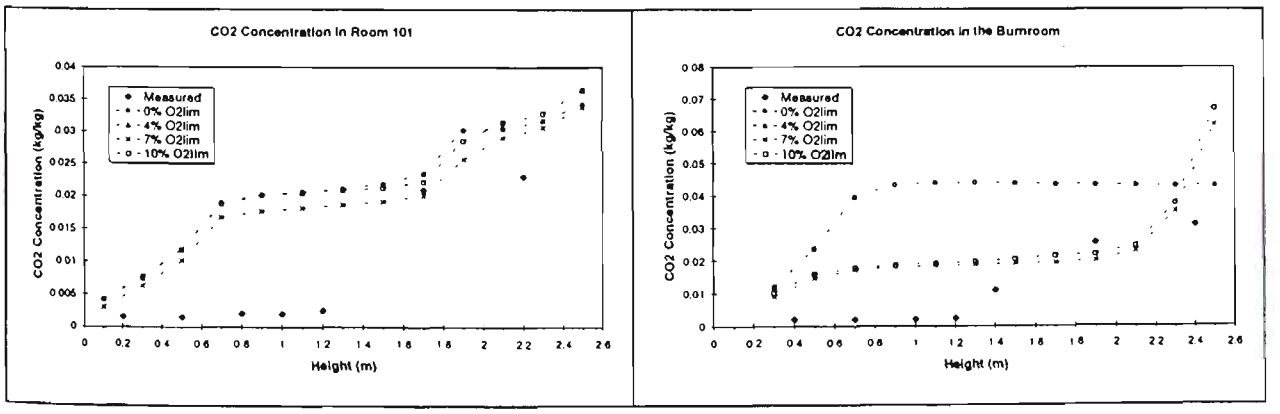

Figure 3.45 Comparison of predicted CO_2 concentrations

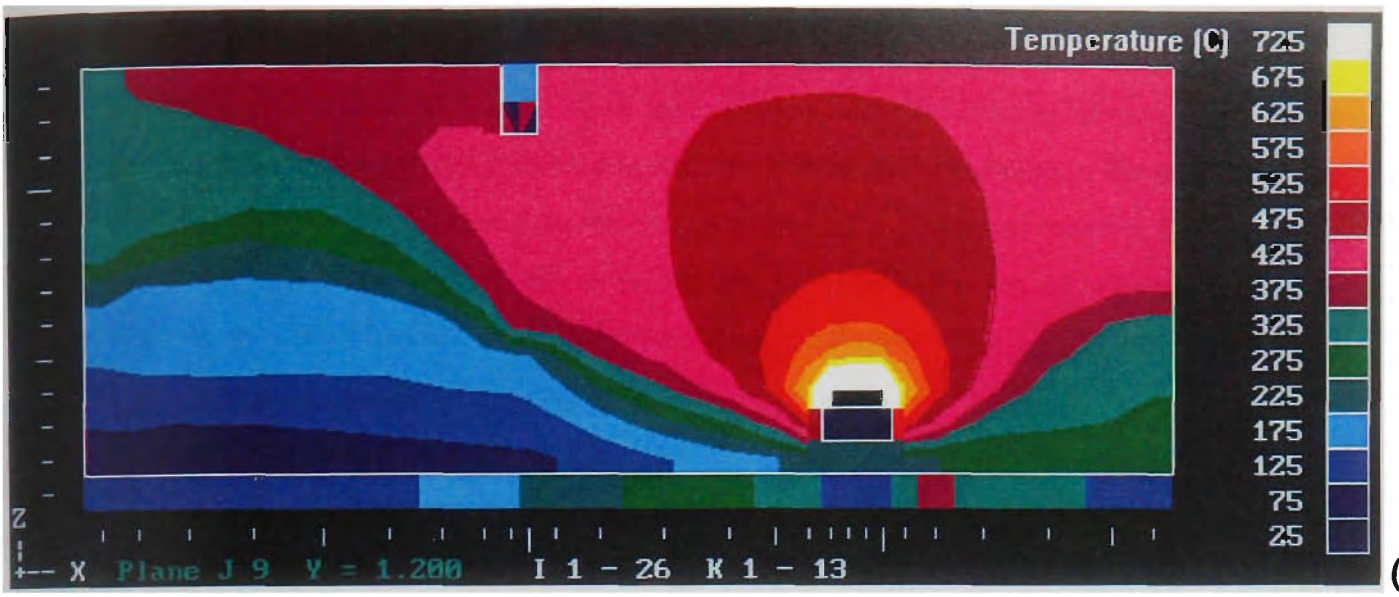

(a)

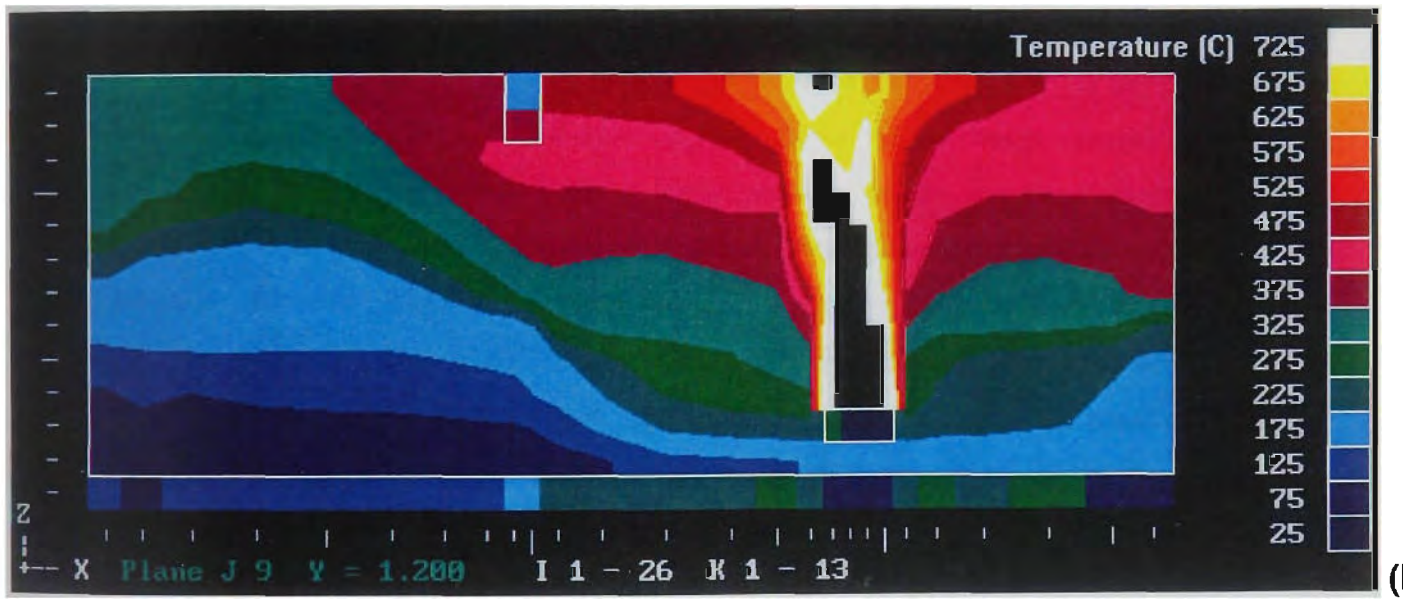

(b)

Figure 3.46 Predicted temperature distribution for oxgygen combustion limits of (a) 4% and (b) 7%

3.10.3. Balance Port Velocity Limit

Given in this section are the results of an investigation into the effect of altering the limiting velocity at the balance port. As described in Section 2.4.6.3, the formulation of the pressure at the balance port has a strong tendency to become unstable, so a maximum velocity limit is set to prevent divergence of the flow velocity at the balance port. As maximum velocity was previously observed[3] to be in the range of 1-2m/s, the default limit value was chosen to be 2m/s, with 1m/s and 4m/s investigated as bounds for the range of choice.

The results for the temperatures in Room 101 are shown in Figure 3.47. The results show that there is only a small difference between a limit of 2m/s and a limit of 4m/s, particularly in the upper regions, but that setting a limit of 1m/s results overall in elevated temperatures. This trend is also observed in the temperatures for the burnroom (Figure 3.48), Room 103 (Figure 3.49), and the corridor (Figure 3.50). The most likely explanation for such a uniform trend is the cooling effect produced by an enhanced flow at the balance port. Since the maximum velocity is invariably reached at some cell in the balance port, a higher velocity results in greater cooling due to an increased flow of air at ambient temperature, and greater heat losses due to the increased outflow of hot products. However, from the relatively small difference between the 2m/s and 4m/s limits, it appears that there is a limit to this effect. Increasing the velocity limit will affect the room immediately connected to the balance port, namely the corridor in this instance, but the effect of the induced flow will be diminished for every obstruction to the flow, such as a doorway perpendicular to the flow, of which there are two in this geometry. Hence, the difference between 2m/s and 4m/s is negligible in the burnroom (Figure 3.48), but still noticeable in the corridor (Figure 3.50).

Just as an increased flow produces a cooling effect on the temperatures, so too does it have a ventilating effect on the combustion products, as shown in the CO_2 concentrations in Figure 3.51. Thus, the highest product concentrations occur for the 1m/s limit, which induces the least ventilation. Again, there is little variation between 2m/s and 4m/s, with the only noticeable variation occurring in the middle layer of the room closest the balance port, namely Room 101.

The results overall indicate that it is acceptable to use 2m/s as the default value, as it does not lead to accumulation of products throughout the enclosure, while minimising induced ventilation effects in the room containing the balance port.

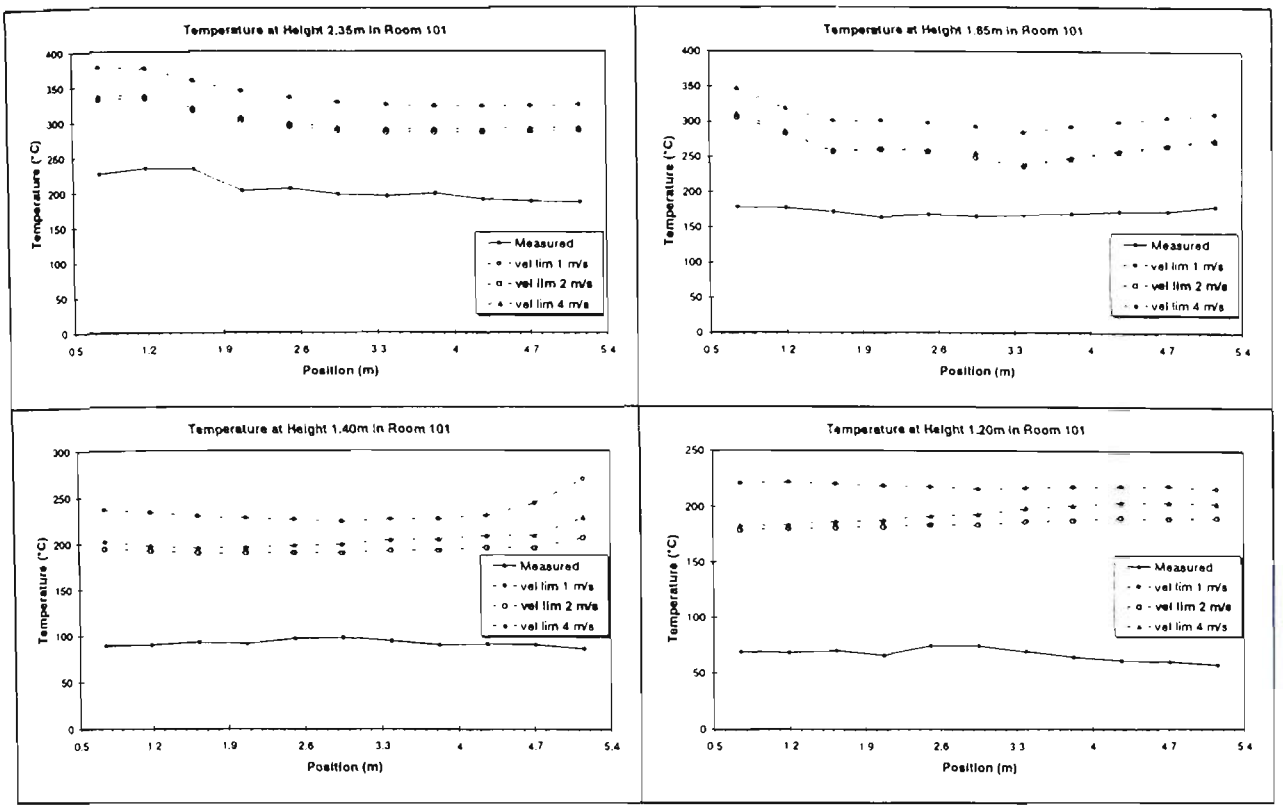

Figure 3.47 Comparison of predicted temperatures in Room 101

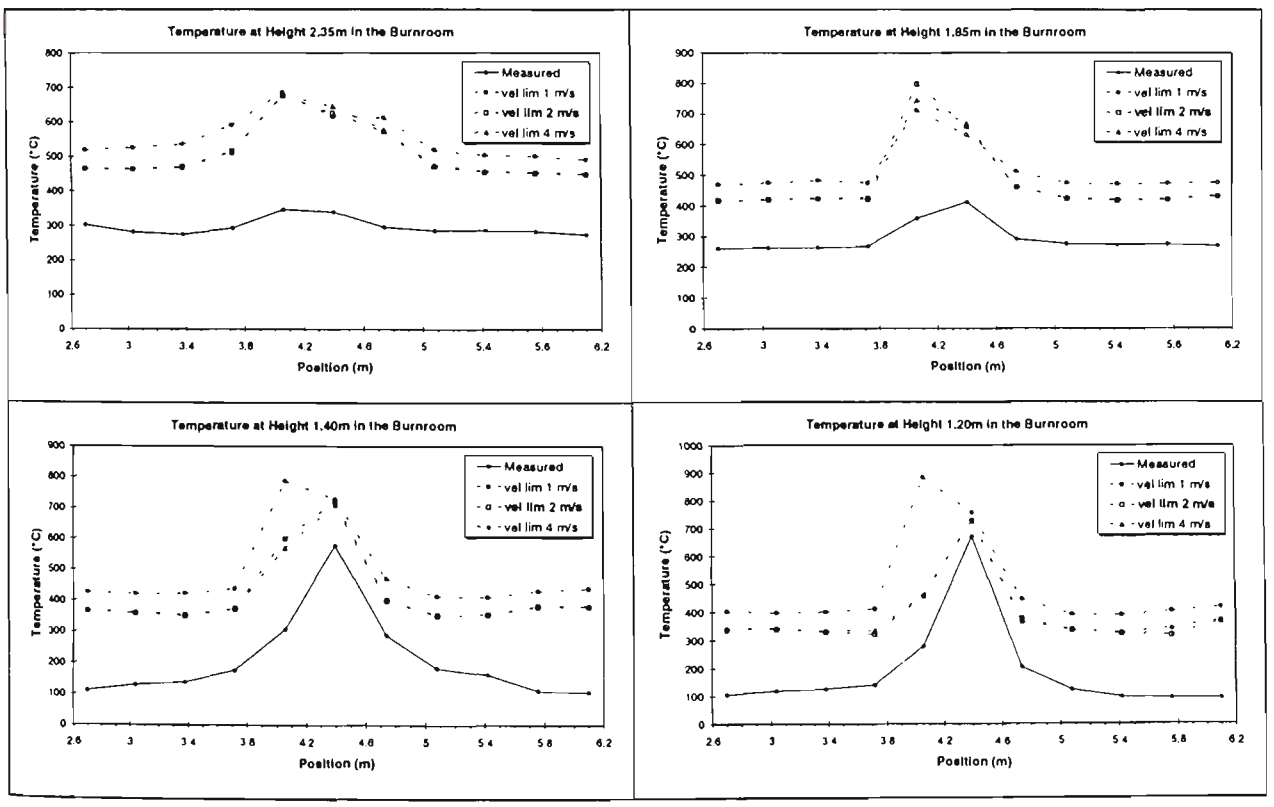

Figure 3.48 Comparison of predicted temperatures in the Burn Room

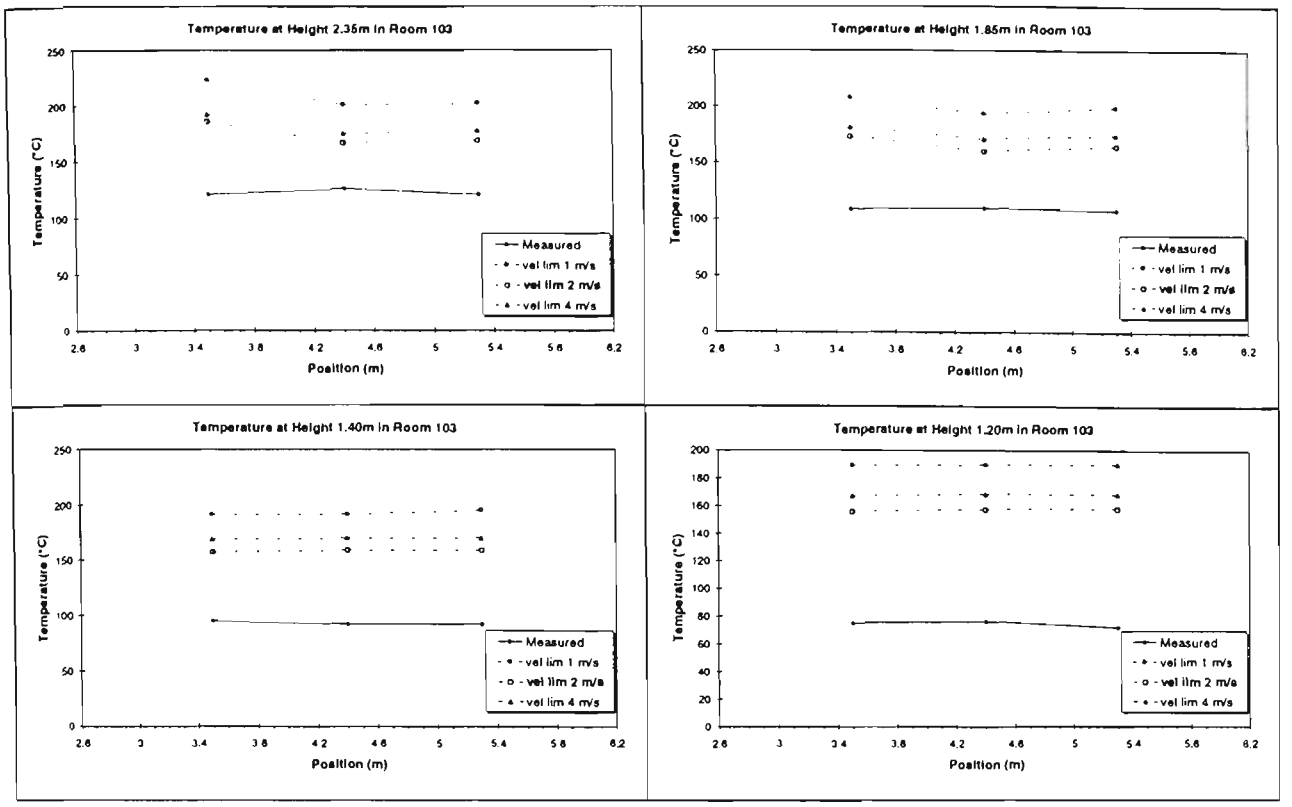

Figure 3.49 Comparison of predicted temperatures in Room 103

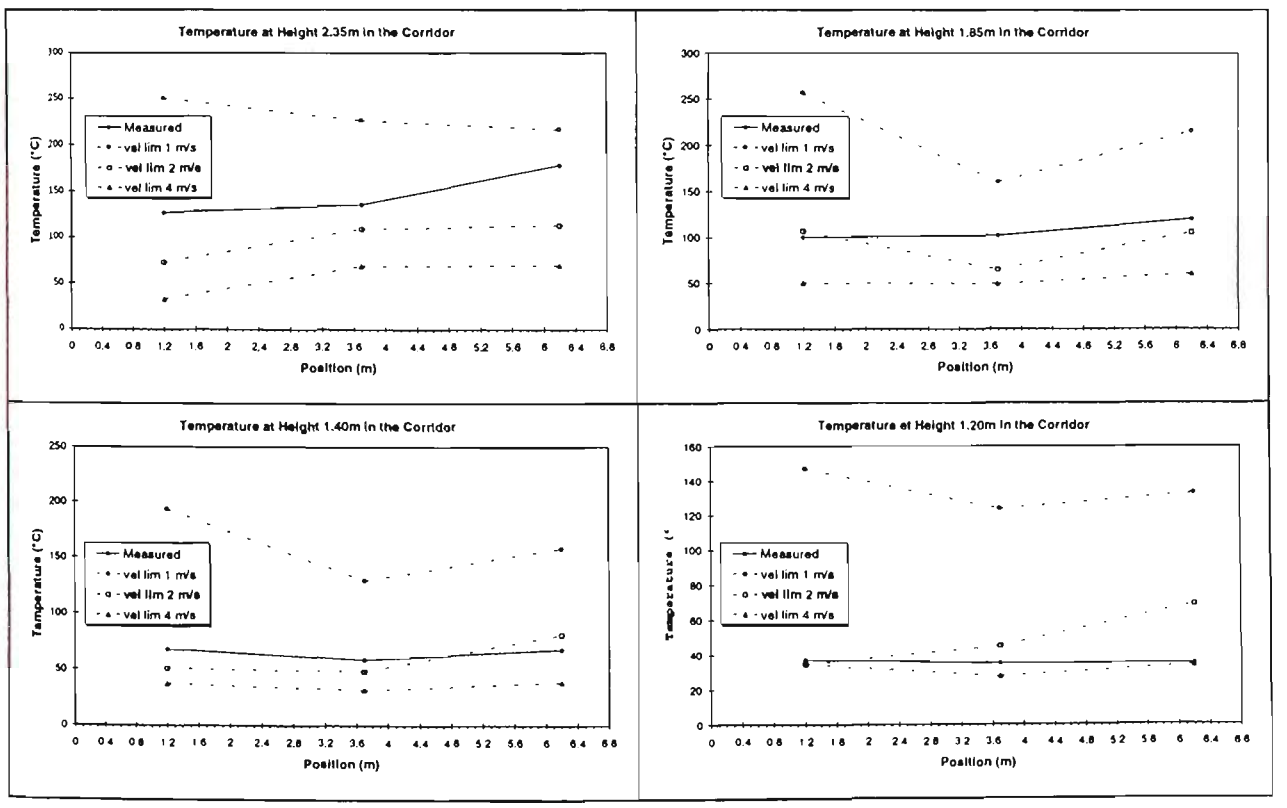

Figure 3.50 Comparison of predicted temperatures in the corridor

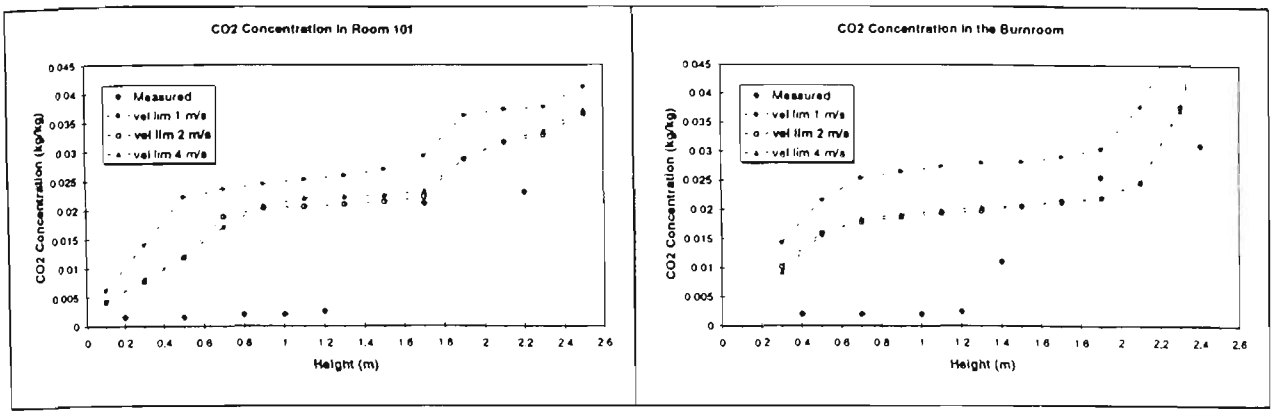

Figure 3.51 Comparison of predicted CO_2 concentrations

3.10.4. Heat Transfer Coefficient

The parameter investigated in this subsection is the heat transfer coefficient. This is the constant h which appears in the wall temperature calculation given by Equation 3.49. The default value of $10W/m^2 \cdot K$ was taken as a typical value for naturally ventilated enclosures and is comparable to values used elsewhere[71]. However, as the value can vary considerably depending on the local geometry and flow conditions, higher and lower values of $30W/m^2 \cdot K$ and $5W/m^2 \cdot K$ respectively were also investigated.

Temperature predictions are shown for Room 101 (Figure 3.52), the burnroom (Figure 3.53), Room 103 (Figure 3.54) and the corridor (Figure 3.55), while the CO_2 concentrations are shown in Figure 3.56. The charts show consistent trends throughout all rooms and heights, and in the CO_2 concentrations. However, a value of $10W/m^2 \cdot K$ produces higher temperatures and CO_2 concentrations than either the higher or lower value, rather than there being a progression from lowest to highest. A mechanism which produces a maximum for a particular value, rather than a monotonic progression, is not readily explainable. Consequently, the results are presented here without further hypothesis. Suffice to say, altering the heat transfer coefficient has a significant effect on the temperature distribution throughout the enclosure, so that further investigation of its effect, or of alternative models which consider local variation rather than a global constant, comprises important future investigation.

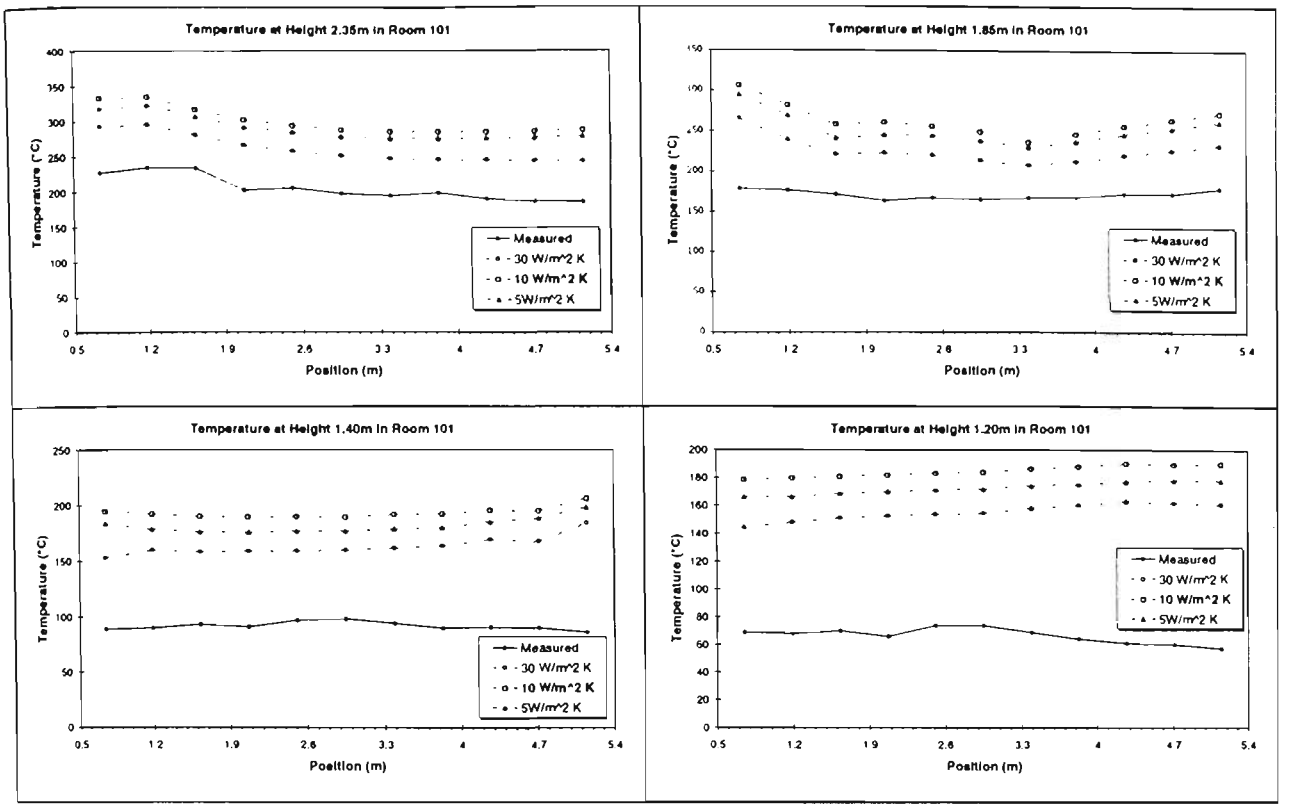

Figure 3.52 Comparison of predicted temperatures in Room 101

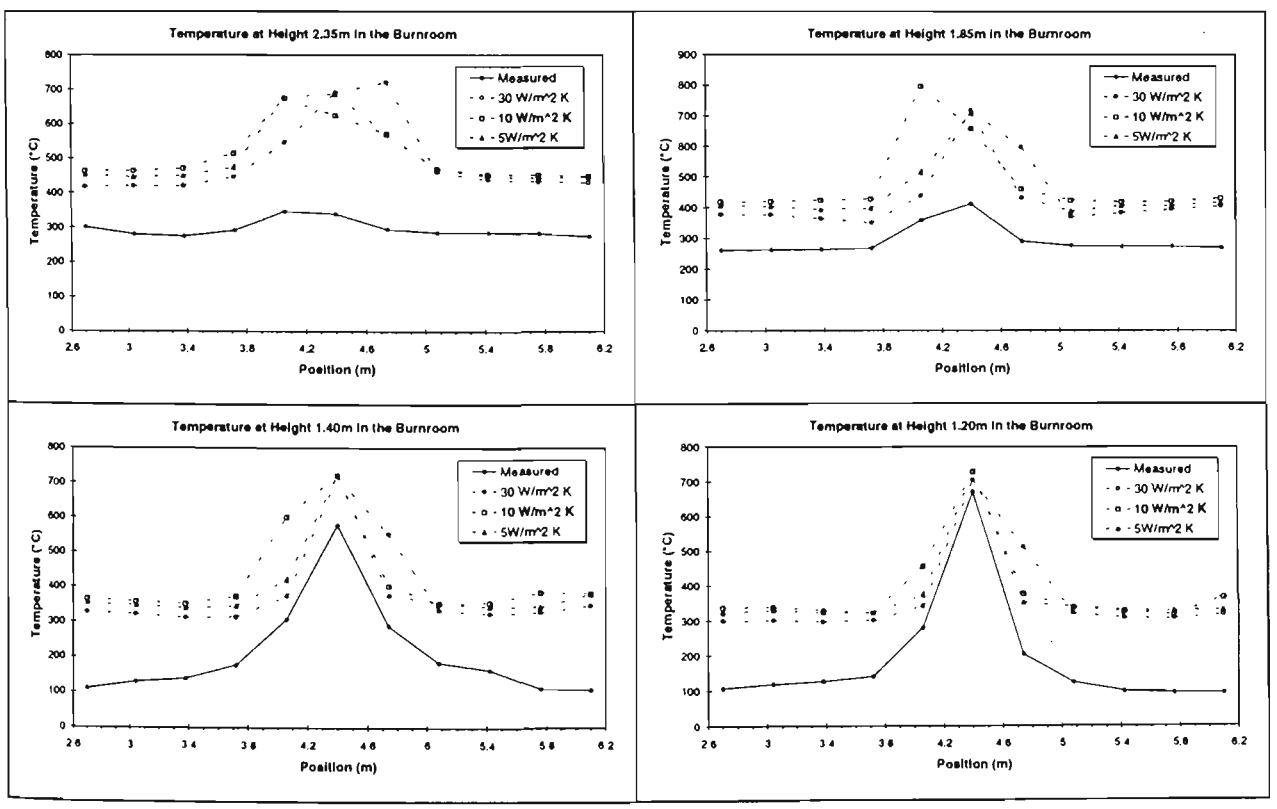

Figure 3.53 Comparison of predicted temperatures in the Burn Room

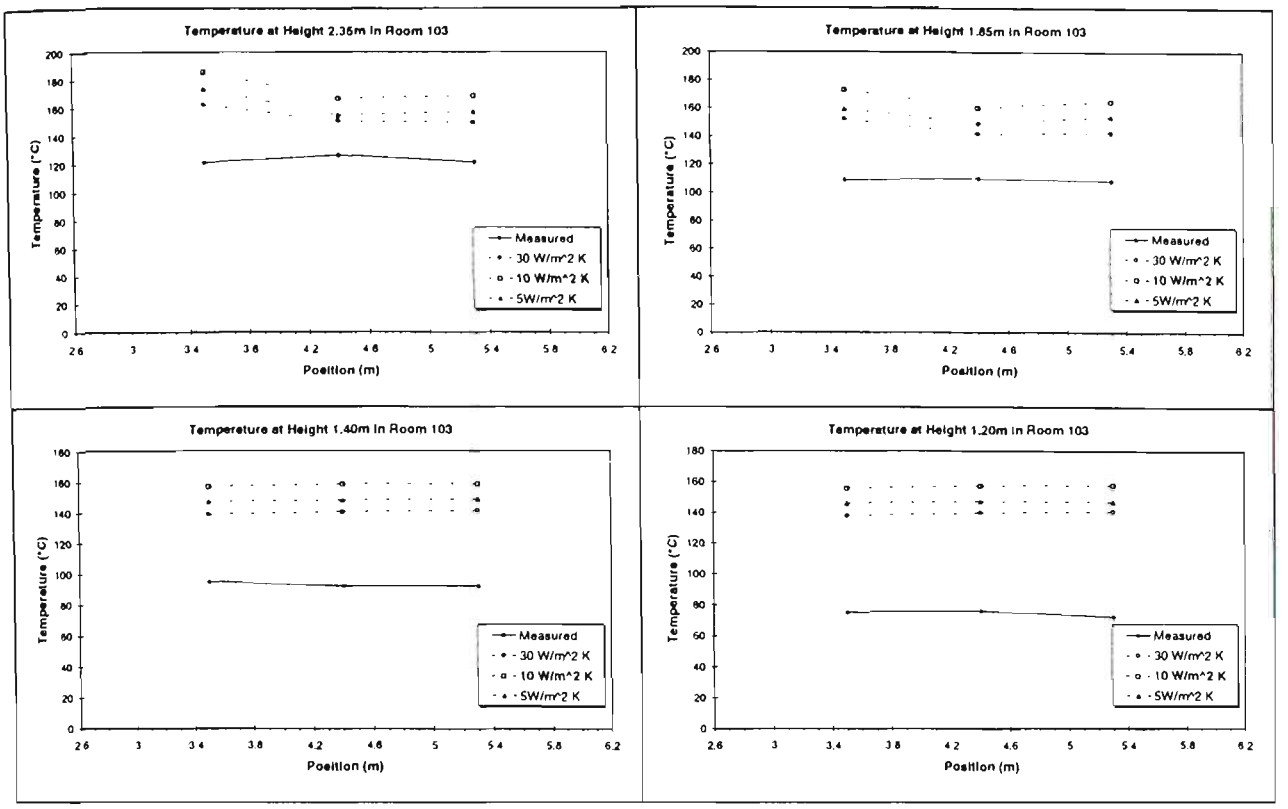

Figure 3.54 Comparison of predicted temperatures in Room 103

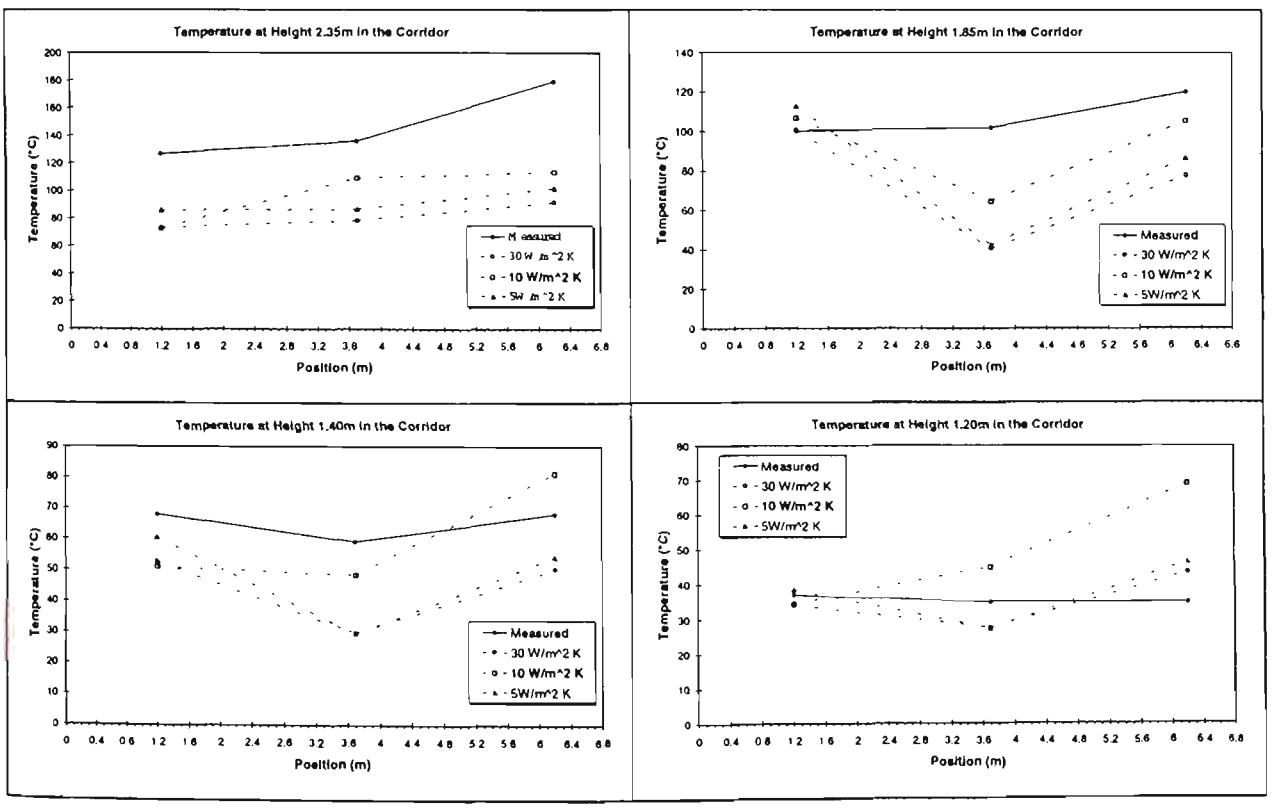

Figure 3.55 Comparison of predicted temperatures in the corridor

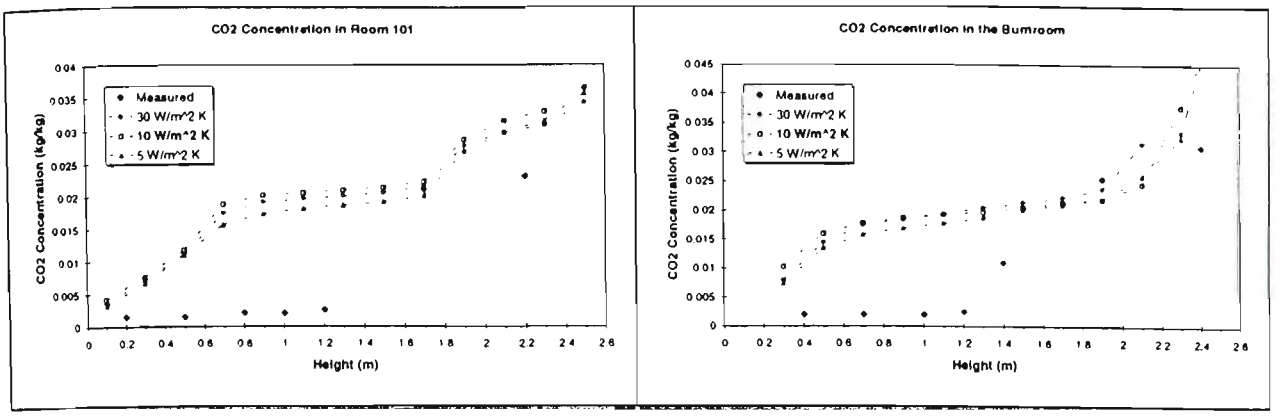

Figure 3.56 Comparison of predicted CO_2 concentrations

3.10.5. Heat of Combustion

The final variable considered in this analysis is the heat of combustion. The fuel used in this modelling analysis is propane, which reacts with oxygen according to Equation 3.50. When combustion is complete, that is, only carbon dioxide and water vapour are produced, with no carbon monoxide or soot formed, the enthalpy change for the reaction is 46 MJ per kilogram of propane. This figure is the default value, and is used throughout this chapter. However, if the final product is taken to be liquid water rather than water vapour, then the enthalpy change is 50 MJ/kg. Although the enthalpy equations in the model assume the properties of water vapour, this latter figure is investigated as an upper limit for the reaction, and to test the sensitivity of the model to higher values. Conversely, if the reaction is incomplete, then the enthalpy change will be somewhat less than the default value. How much less depends on the actual yield of incomplete combustion products, which varies with ventilation and ambient conditions. However, in all but the most severe of ventilation restrictions, the yield of products such as soot and carbon monoxide will be relatively low compared with carbon dioxide. Consequently, a figure of 40 MJ/kg is taken as a reasonable lower limit, and is the other value investigated here.

The temperature comparisons are shown for Room 101 (Figure 3.57), the burnroom (Figure 3.58), Room 103 (Figure 3.59) and the corridor (Figure 3.60). The trends are very much as expected, with the higher heat of combustion producing the higher temperatures. The lowest heat of combustion produces temperatures closest to the measured value, although a further reduction of temperatures is required for a better match. As the effect of changing the heat of combustion is significant, it suggests that improvements in modelling the reaction would be beneficial in terms of better predictions. Such improvements could include incorporating the products of incomplete combustion in the flow density calculations, and a locally calculated heat of combustion based on the energy of formation of the products.

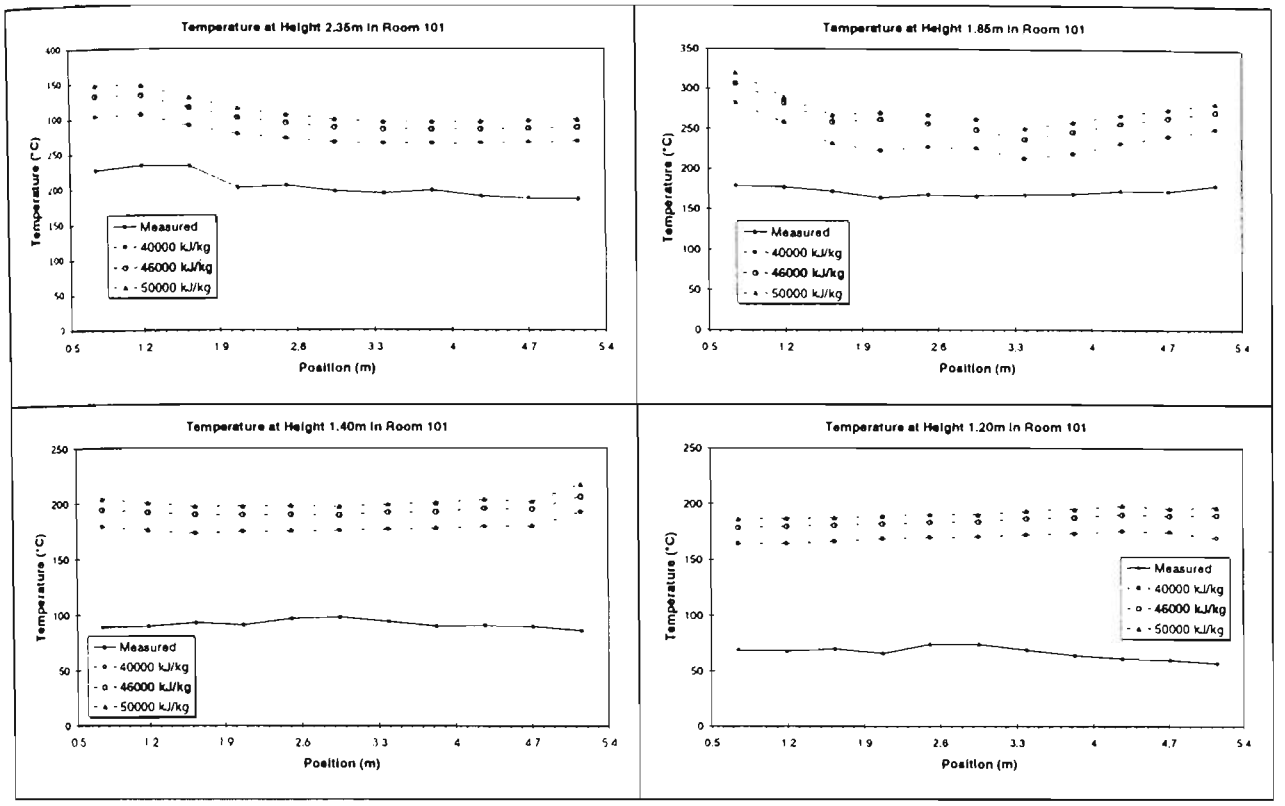

Figure 3.57 Comparison of predicted temperatures in Room 101

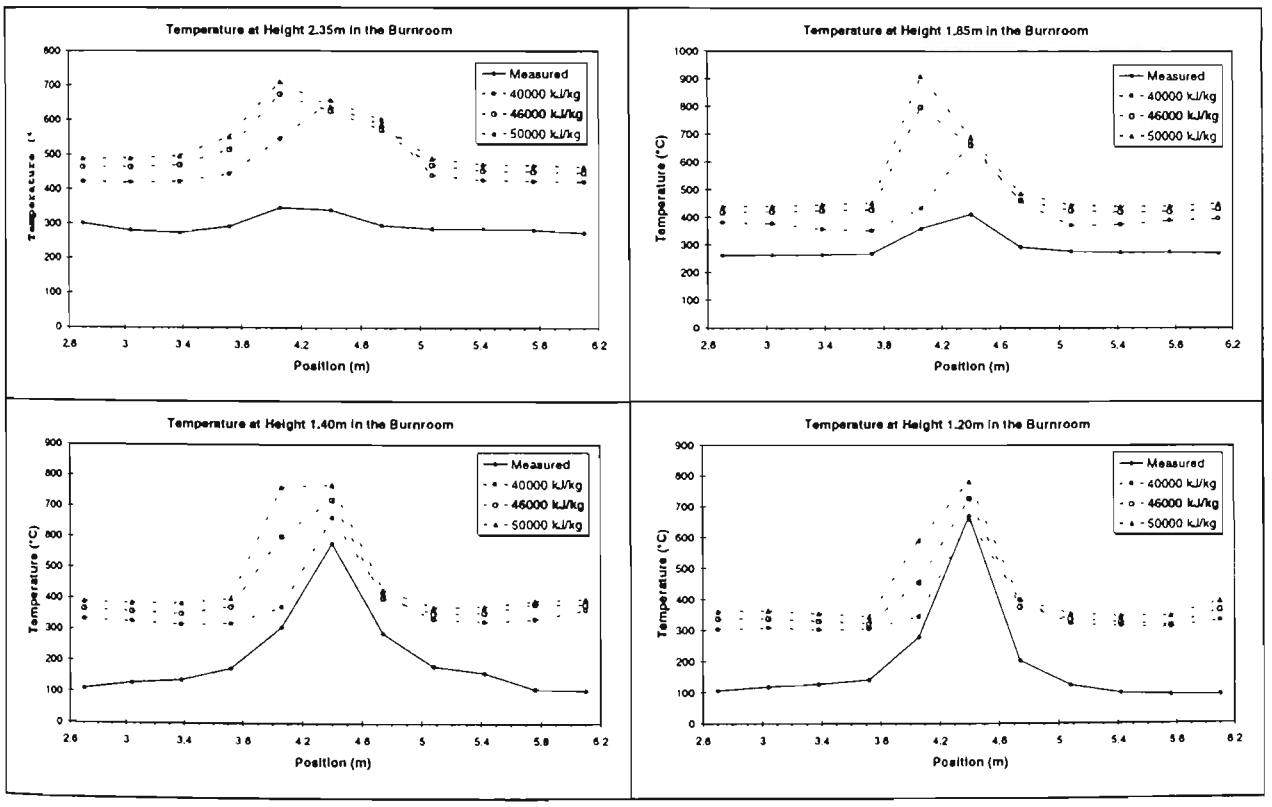

Figure 3.58 Comparison of predicted temperatures in the Burn Room

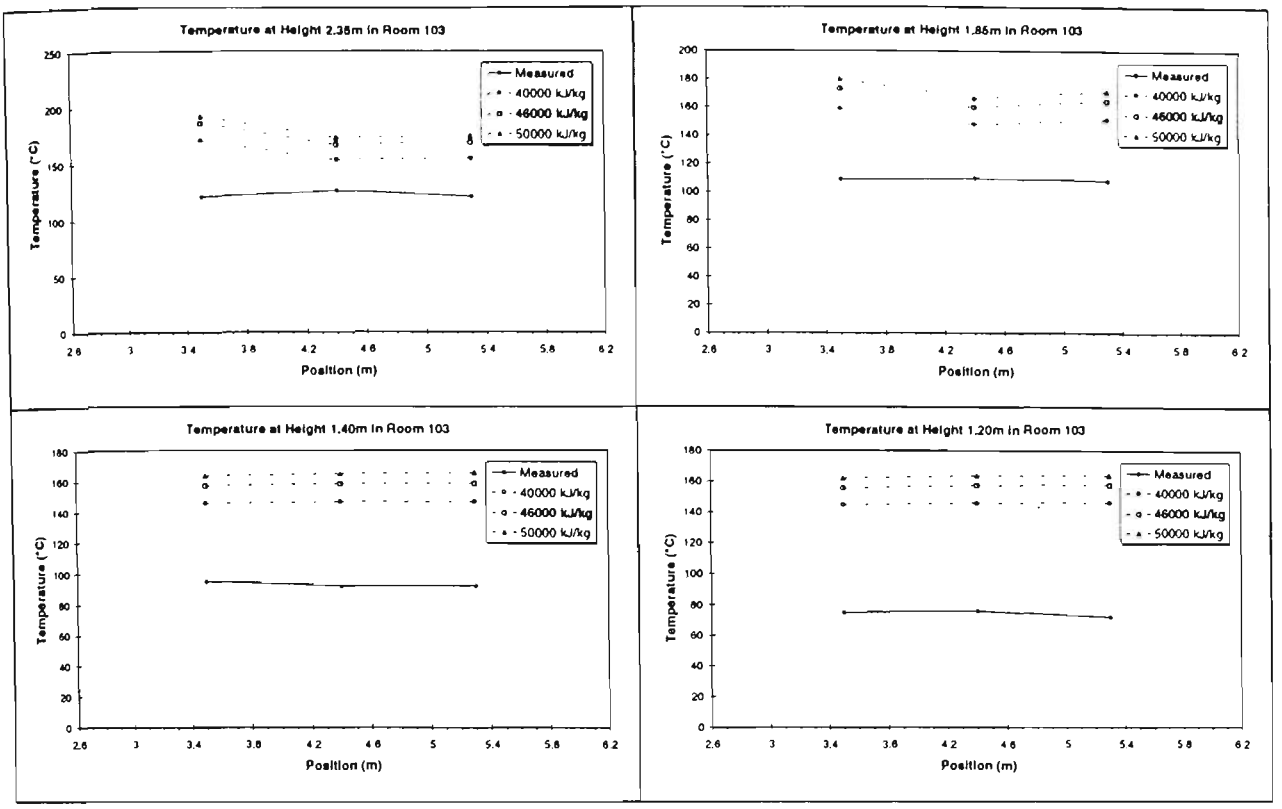

Figure 3.59 Comparison of predicted temperatures in Room 103

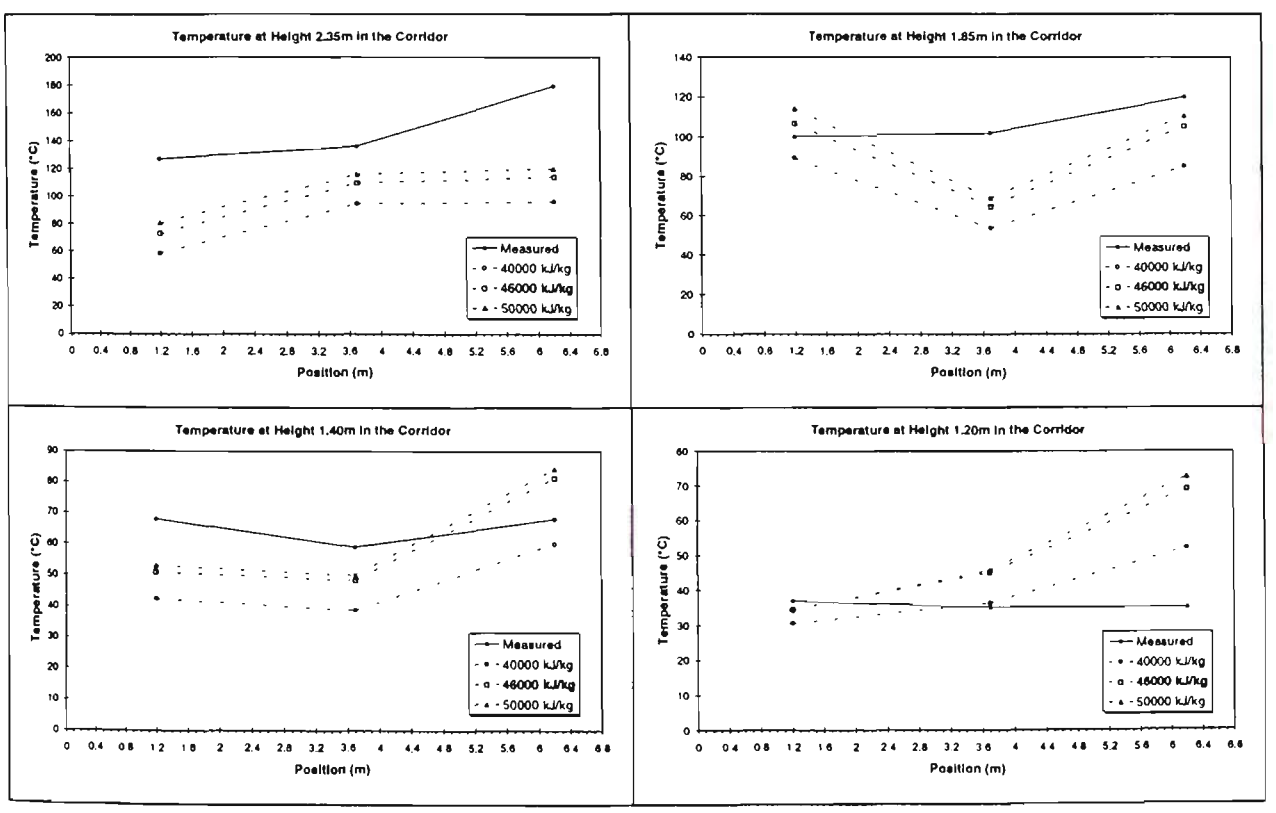

Figure 3.60 Comparison of predicted temperatures in the corridor

The concentration of CO_2 for Room 101 and the burnroom are shown in Figure 3.61. There is a small but regular trend in the results for Room 101, with the lowest heat of combustion showing the highest concentration of CO_2. This is more noticeable in the burnroom, where the 40MJ/kg curve is significantly higher than the other two. A possible cause for this trend is the higher temperatures increase buoyant flow and expansion, resulting in a greater flow of products from the enclosure (which in turn increases the diluting effect of inflowing cool air).

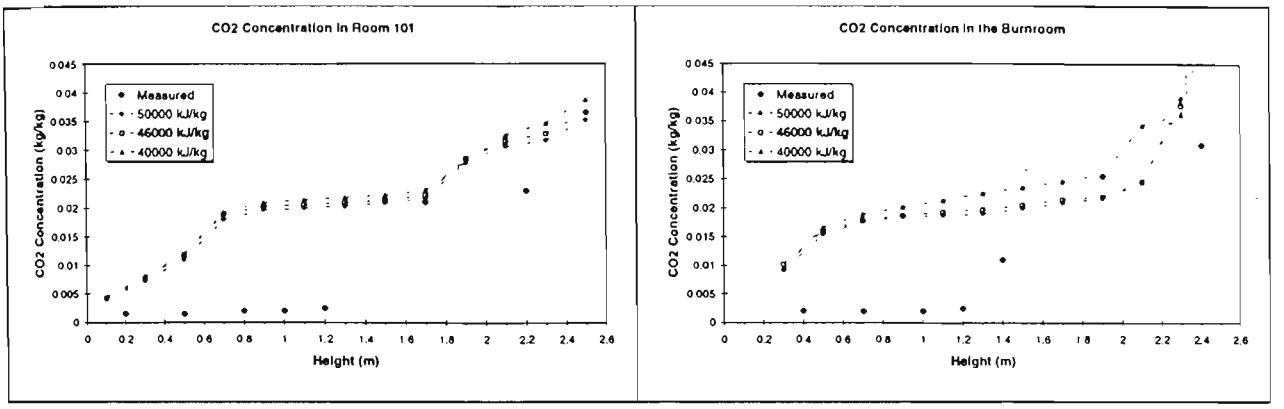

Figure 3.61 Comparison of predicted CO_2 concentrations

3.10.6. Summary

Five parameters identified as being user specified, and of uncertain value, were investigated in the sensitivity analysis as presented in the preceding sections. Overall, the solution was not found to be excessively sensitive to alteration of the parameters, and the default values chosen for the parameters were found to be acceptable in all cases.

Altering the fuel to soot conversion factor was found to have little effect on the predicted temperature and species distributions throughout the enclosure, except in the localised region of the fire plume. The results in this region indicated that a choice of value higher than the default value used throughout this chapter may improve plume temperature predictions. Overall, the choice of value for this parameter does not appear critical.

The oxygen limit for combustion was found to have a significant impact on the predicted results. Choosing a value of 4% or less produced a physically unrealistic solution. Consequently, a value of 7% or higher is recommended. A value of 7% was found to produce marginally better results than a value of 10%, but the value does not appear critical provided it is in the range of these two values.

The limiting velocity for the balance port appears to have an optimal value of around 2m/s, which was the chosen default value. A value of 1 m/s leads to elevated temperatures and product

concentrations throughout the enclosure, while a value of 4m/s leads to significant depletion of products in the room containing the balance port, although the effect is largely restricted to this room and does not significantly affect adjoining rooms.

The heat transfer coefficient at the flow boundaries was found to have a noticeable effect on temperatures and to a lesser extent on product concentration. However, no consistent trend on predictions was observed with changing values of this parameter, so no conclusions on the effect of changing the value can be drawn, other than further investigation of this parameter and the nature of the boundary equations in the model is recommended.

Altering the heat of combustion was found to have an intuitively expected effect on temperatures; namely, higher values lead to higher predicted temperatures. A value less than the default stoichiometric value improved overall temperature predictions. This suggests that future modifications to the model which take into account the local combustion efficiency in the enthalpy calculations may be beneficial to temperature predictions.

3.11. PREVIOUS MODELLING WORK

3.11.1. A Preliminary Modelling Exercise

Much of the work described in this section has been summarised previously by Fernando and Luo[72], and is elaborated here for clarity. The modelling work is the result of a certain amount of trial and error, although naturally this will not be reproduced here except where relevant. It should be pointed out that the work presented in this section has subsequently been updated, using finer grid spacing at the boundary and a CFD model with minor improvements, and the results of this work were presented in Section 3.8. The work presented in this section is included merely for completeness, and because it also highlights points of interest not demonstrated in Section 3.8 alone.

In this study, the flow region in three interconnecting rooms was divided into 30x32x25 cells. A horizontal cross section of the flow grid is shown in Figure 3.62. The construction of the grid, and aspects of the modelling, are as described in Section 3.8

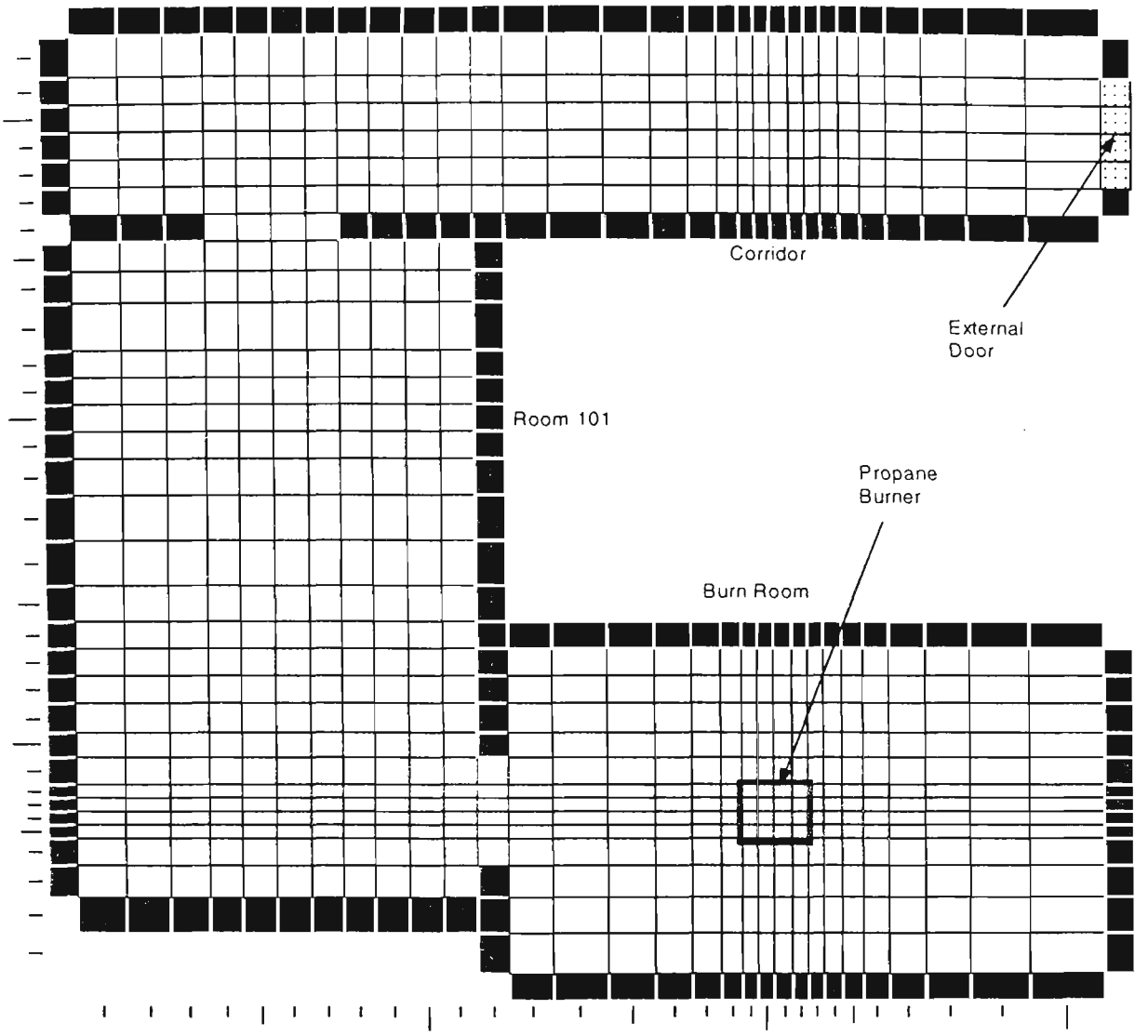

Figure 3.62 The flow grid used in original study

Comparing Figure 3.62 with the experimental layout shown in Figure 3.2, it is apparent that Room 103 is not included in the computational region, even though it was included in the fire tests. The doorway to Room 103 was replaced with a solid boundary of emissivity 1. The motivation for removing Room 103 is explained in detail below; it was done mainly to reproduce the sharp layering of hot products and cool fresh air observed in the experiments. The presence of Room 103 was found in initial modelling exercises to cause significant contamination of the lower layer, along with associated blurring of the two layers, which in turn affected predictions of radiation flux and product concentrations. This contamination was observed in the results presented in Section 3.8.

The number of rays traced per radiation grid element was the same as used in Section 3.8, namely 192 points. The radiation grid itself was coarser than the flow grid and incorporated only Rooms 101 and 102, although the grid refinement in the region of the plume matched that of the flow grid, for the reasons given in Section 3.8.

The model was compiled and executed on a SPARC-10 Sun Workstation. A total of 3000 iterations was required to reach convergence of the steady state solution to a level deemed to be satisfactory, by the criteria outlined in Section 2.4.7. The residuals for the velocity components were around 1.5×10^{-2} m/s, fuel mixture fraction around 10^{-5}, and enthalpy around 0.5 kJ/kg. This required around 36 hours of computing time. The radiation heat balance was performed only after every fifth flow region iteration, but was nevertheless responsible for approximately half the calculation time.

3.11.2. Comparison of Experimental and Modelled Results

An examination of the comparison of the predicted and measured CO_2 concentrations given in Section 3.8 helps to explain the motivation for omitting Room 103 from the calculations. The measured values clearly show a layering effect, with the concentrations being very low in the lower cool layer, then increasing sharply in the transition to the upper hot layer at around 1.2m above the floor. However, initial modelling exercises with CESARE-CFD did not model this sharp transition very well, and the results presented here, while better, still show discrepancies. The predictions for the burn room show a more gradual rise in concentration with height (Figure 3.63.a). There is a region of high concentration gradient in the predictions of Room 101 (Figure 3.63.b) marking the transition from one layer to another. The problem is that there are in fact two regions of high gradient instead of one, as shown by the two jumps in the graph (one at 0.7m and one at 1.2m), producing a "middle layer" as well as the upper hot layer and lower cold layer. This appeared to be caused by mixing and diffusion of the hot layer with the cool layer in the model, and was found to occur to an even greater extent when the relatively still space of Room 103 was included (see Figure 3.64). When Room 103 was removed from the calculation region, more realistic modelled results were obtained for the other rooms, and a closer reproduction of the experimentally observed sharp layering effect, thus allowing better comparisons of the overall scenario conditions to be made. The omission of Room 103 from the calculation had only a minor effect on other predicted data such as the temperature distribution, except for that which was effected by the "blurring" of the hot and cold layer interface.

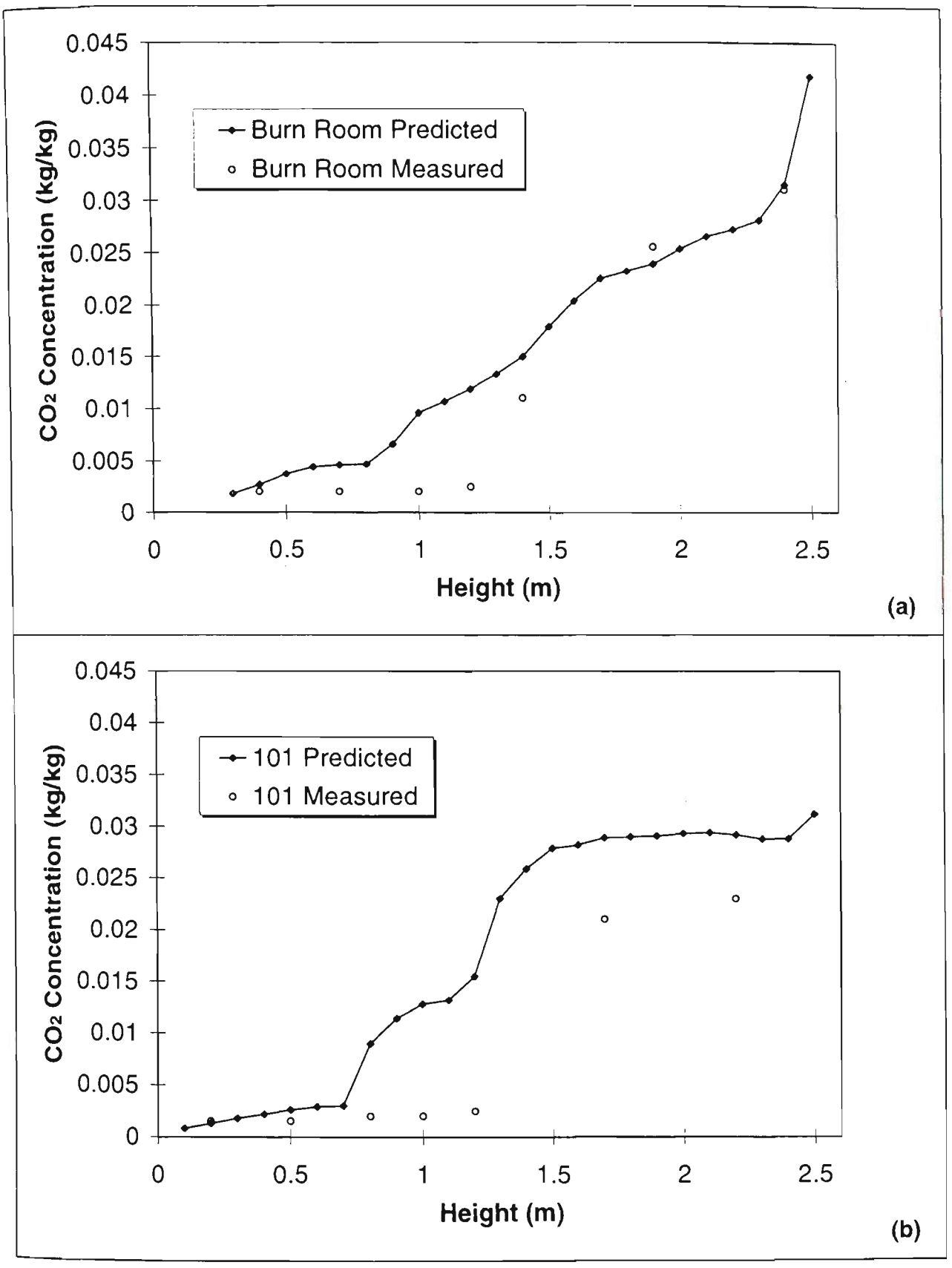

Figure 3.63 Predicted and measured CO_2 concentrations in (a) Burnroom (b) Room 101

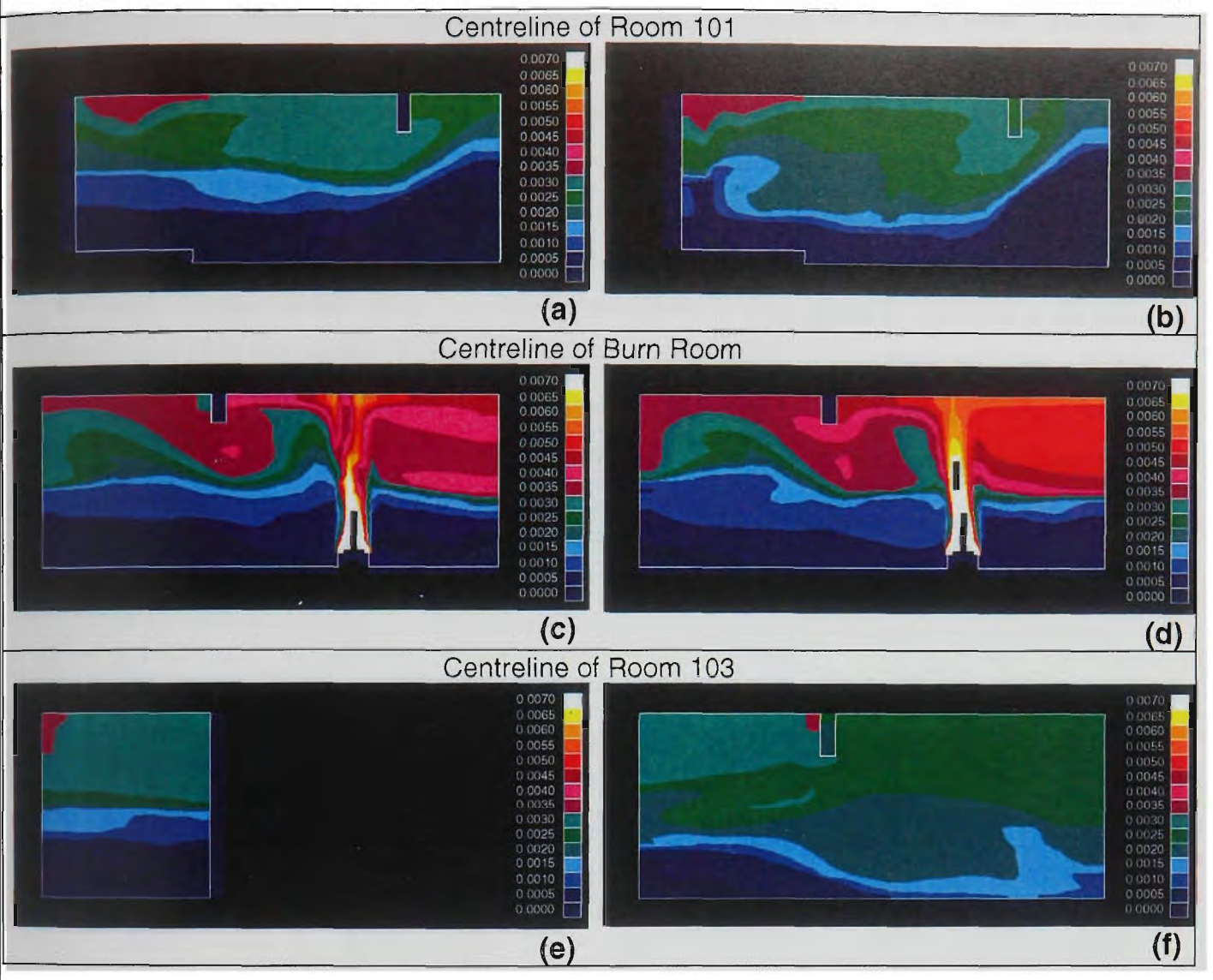

Figure 3.64 Predicted CO_2 concentrations without Room 103 (a,c,e) and with Room 103 (b,d,e)

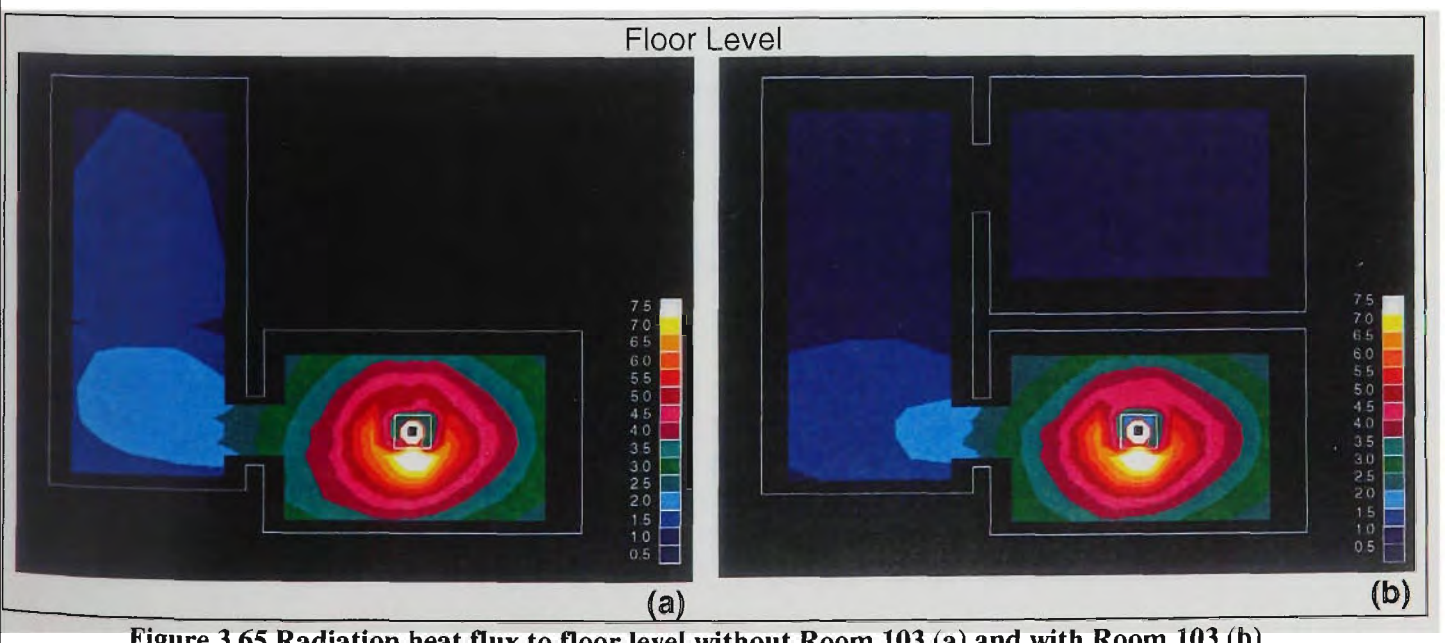

Figure 3.65 Radiation heat flux to floor level without Room 103 (a) and with Room 103 (b)

The reason that the model was unable to predict sharp layering is not entirely clear. The extra "middle layer" corresponds to a region of very low velocity in the flow region, and some mechanisms were proposed earlier to try to explain this phenomenon. In spite of the removal of Room 103 from the calculations, Figure 3.66 shows that the model still tended to underestimate the radiant fluxes to floor level in the burn room and Room 101 despite the fact that upper layer temperatures were overestimated. With the flow region in Room 103 included, predicted fluxes were up to a further 30-40% lower, even though the predicted temperature distributions in the other three rooms were very similar (Figure 3.65). This was mostly due to the model predicting a higher concentration of absorbing gases in the cool layer (up to 0.02 kg/kg), originating from the outflow of Room 103 (Figure 3.64 e,f). As can be seen in Figure 3.63, such levels were not present in the experiments.

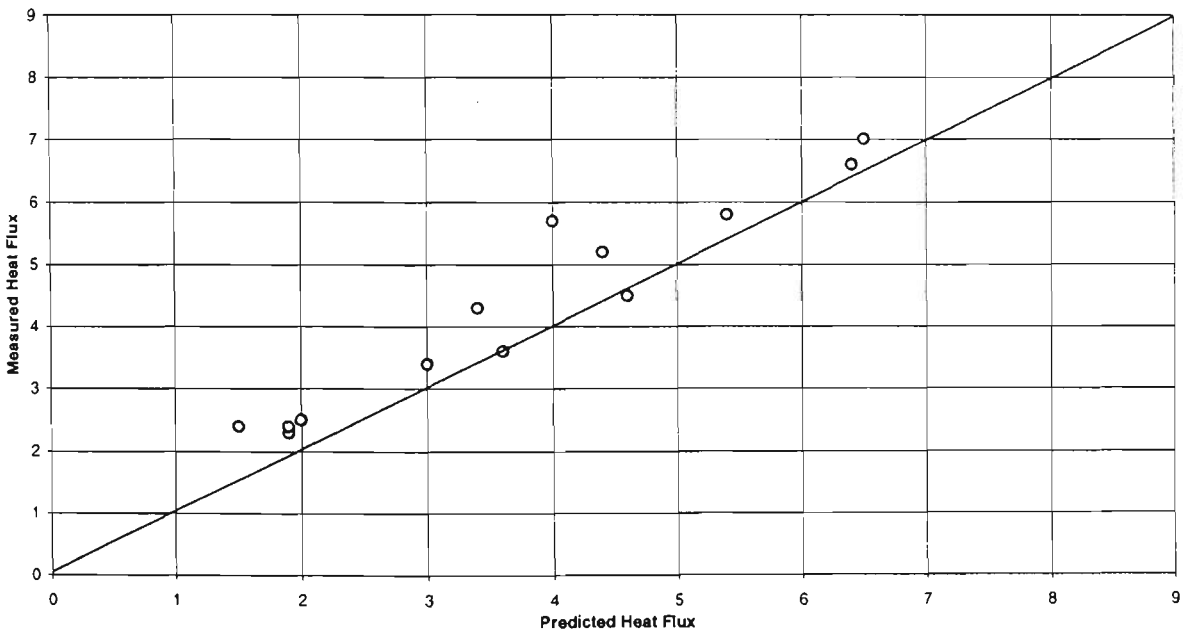

Figure 3.66 Measured versus predicted heat fluxes (kW/m^2)

As for the upper layer gas temperatures, the model tended to overestimate them, as shown in Figure 3.67. An explanation for this overprediction of temperatures was offered in Section 3.8.

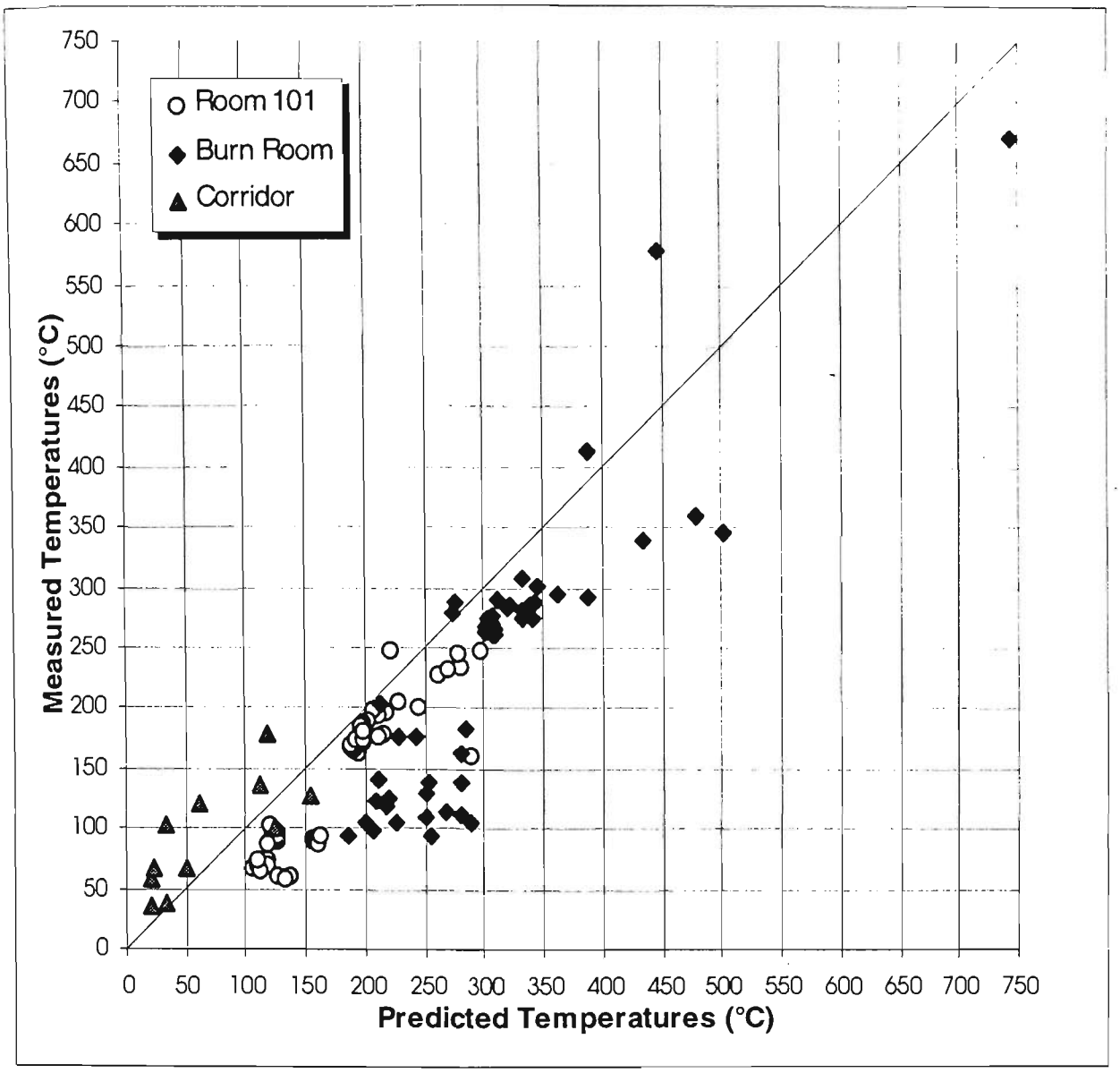

Figure 3.67 Measured versus predicted temperatures (°C)

The predicted and measured distributions of temperature, radiant flux, and carbon dioxide concentration are shown in Figure 3.68, Figure 3.69, Figure 3.70, and Figure 3.71. The comparisons are qualitative only, and are shown to demonstrate the context in which the predictions are made, to show the overall pattern of predictions.

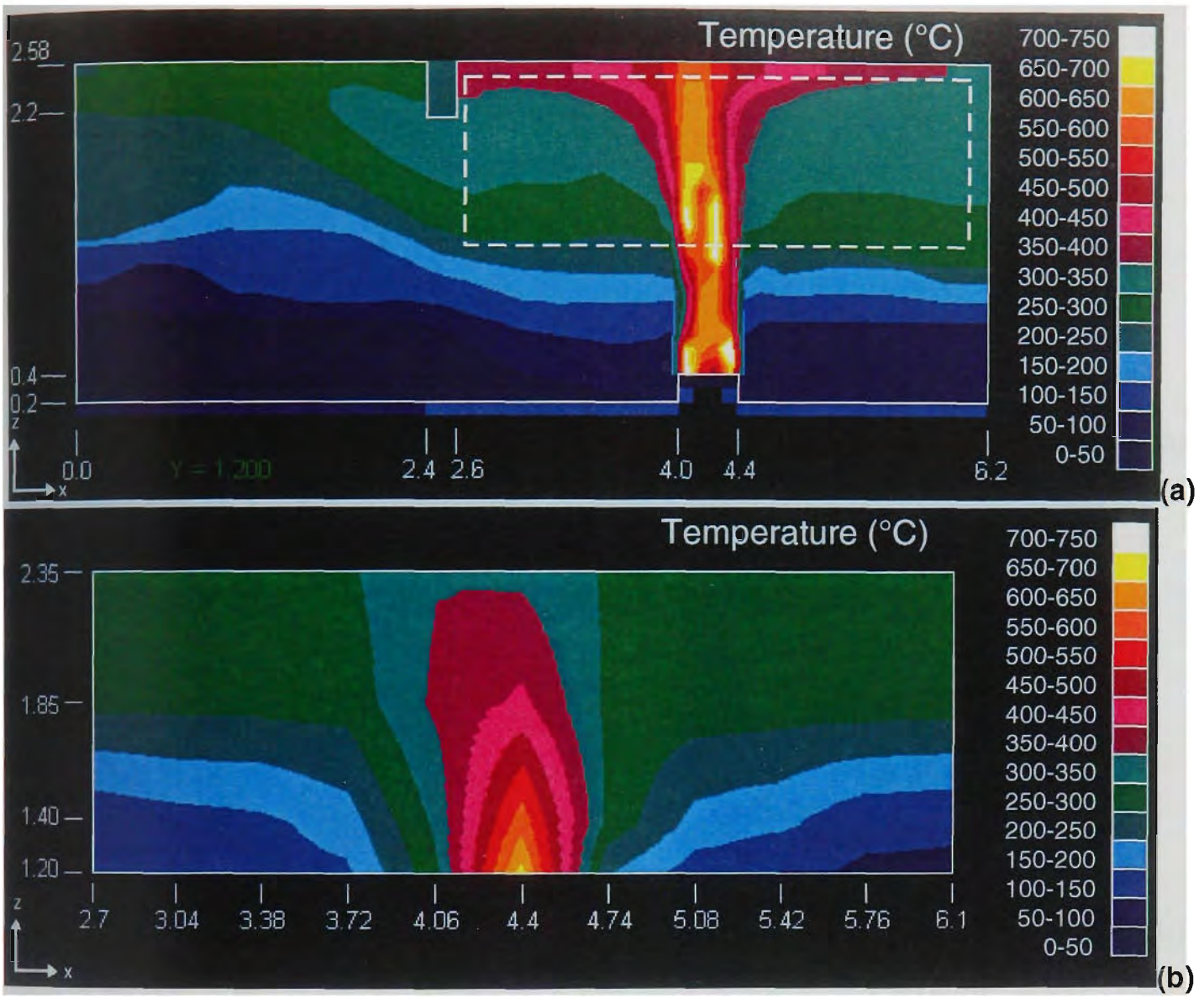

Figure 3.68 Predicted (a) and measured (b) temperatures along the centreline of the burn room

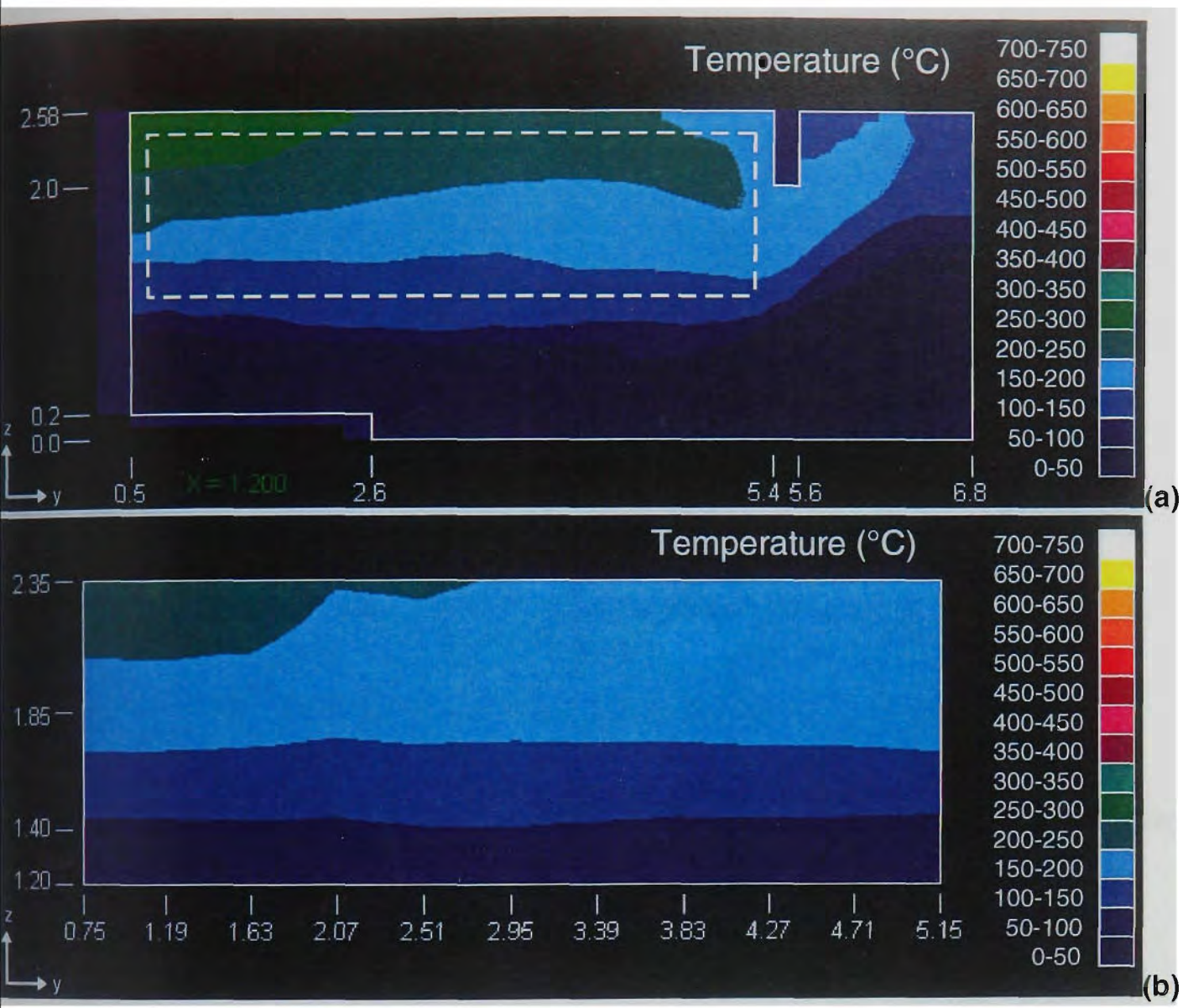

Figure 3.69 Predicted and measured temperatures along the centreline of the room 101

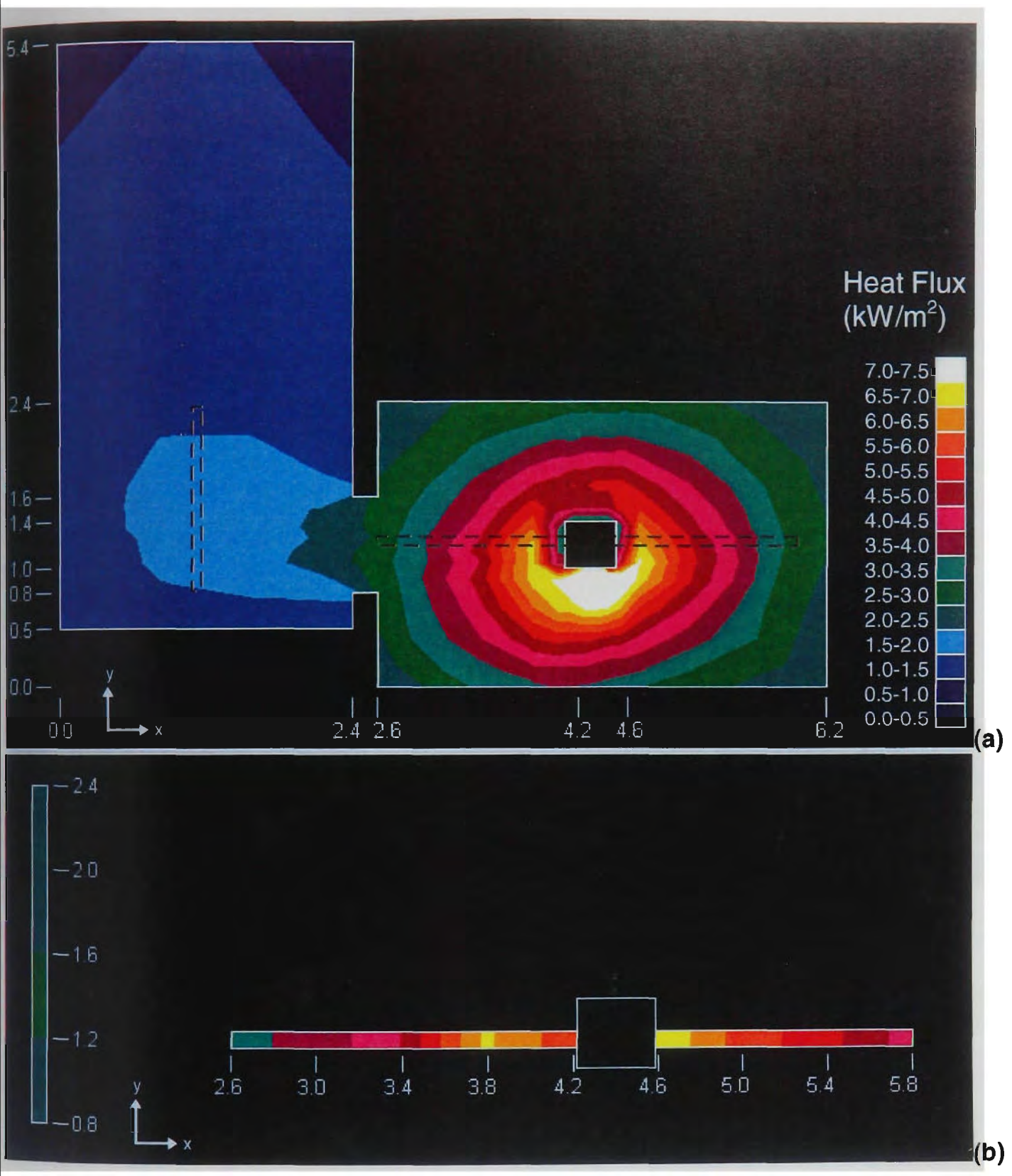

Figure 3.70 Predicted (a) and measured (b) heat fluxes at floor level

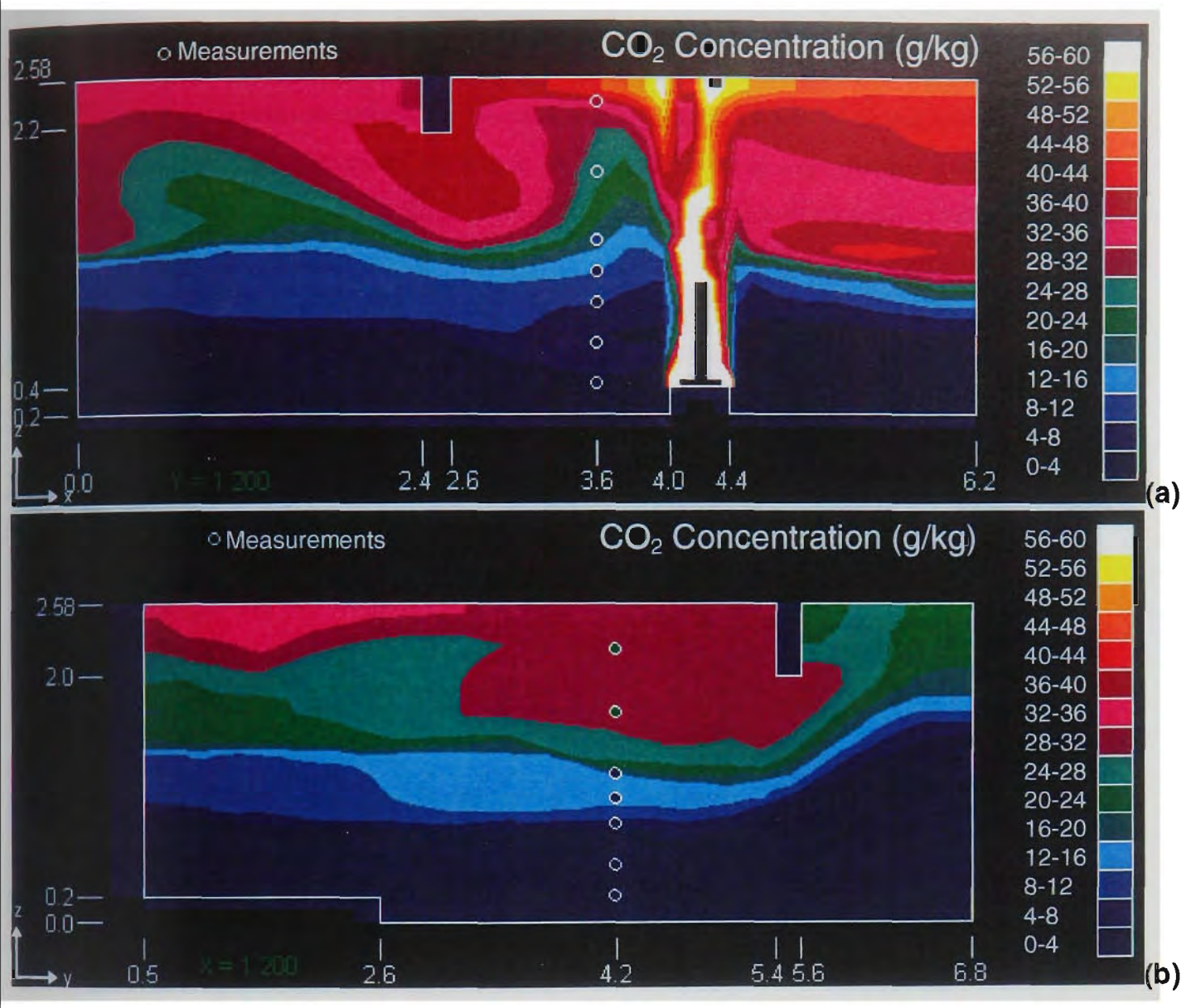

Figure 3.71 Predicted and measured carbon dioxide concentrations in (a) Burn room (b) Room 101

Despite the shortcomings mentioned previously, the predicted and measured data presented here are nevertheless in reasonable agreement. In particular, the radial pattern of the radiation contours at floor level around the fire plume, as shown in Figure 3.70, is an improvement over even earlier modelling results not presented here. This radial pattern was observed qualitatively in previous experiments performed at the EBFF.

Based on the results described here, it would appear that some additional improvement could be made. In particular, it was desirable that the grid be refined further to test whether the problem middle layer is an artefact of the grid spacing. It is also desirable that the predictions include Room 103. Since the room was part of the experiment, it should be included in the model. These observations were the motivation for carrying out the additional modelling presented in Sections 3.8 and 3.9 of this chapter.

3.12. CONCLUSIONS

The research into enclosure fire modelling, the results of which are presented in this chapter, was undertaken to improve previously identified discrepancies between experimentally measured radiant heat flux levels and predictions of the model CESARE-CFD. It was also undertaken to investigate the degree of numerical accuracy in the model and the results it produced.

Modifications were made to the radiation submodel of CESARE-CFD, which included spatially varying equations for the absorption coefficients of combustion products and a flux balance equation for calculating boundary temperatures. These modifications resulted in improved predictions of radiant flux to surfaces, and of temperatures in the room of fire origin, particularly in region of the fire plume, when compared to data obtained from a full-scale fire experiment.

Discrepancies still persist between experimental results and predicted results, and it is desirable to undertake future work to reduce the discrepancies further. The radiation predictions are sensitive to the ability of the overall CFD model to predict the stratification effect of enclosure fires, and the concentration of the radiatively interacting combustion products. Improvement of the CFD model prediction of these quantities and their distribution is necessary to improve the predictions of heat flux to surfaces and temperature distributions. While the equations used in the radiation model are somewhat simplistic, they are nevertheless sufficiently robust to demonstrate the justification of devoting a sizeable portion of computational resources to the modelling of radiation heat transfer in

enclosure fires. However, an extra degree of complexity may need to be included in the equations, such as polychromatic ray tracing, to further improve the radiation heat transfer predictions.

The numerical behaviour of the model was investigated to ensure that numerical errors were minimised. A grid refinement exercise was undertaken to test the grid independence of the solution. It was found that a truly grid independent solution is likely beyond the hardware resources available to the author, but that a solution sufficiently accurate for practical purposes may nevertheless be achieved with a grid of intermediate refinement.

The convergence of the solution for a variety of grid refinements was analysed. For the particular scenario modelled, residuals were found not to decrease indefinitely, but rather reach a limit. This limit was reached for all the results presented herein.

A sensitivity analysis was undertaken for five user-defined parameters of the CFD model for which the value was uncertain. Overall, the solution was found not to be sensitive to alterations to the values of the parameters, and that the default parameter values were found to be optimally chosen in most cases. However, there was sufficient variation in the predicted results, with alteration of the value of the parameters, to suggest that a more rigorous approach to their modelling (rather than setting them as a global constant) would further improve the modelling predictions.

4. COMBUSTION

4.1. AIMS

The overall aim of this thesis is to develop a flame spread model which is compatible with CFD models. The first stage in the development of a flame spread model is the consideration of the combustion behaviour of the fuel over which the flame is spreading. It is the combustion of the fuel which produces the flame, which in turn preheats the fuel surface ahead of the flame, which allows the flame to spread. While some approaches to flame spread endeavour to produce an empirical or analytical expression which will express the flame spread velocity as a function of fuel material properties and external conditions[73], the numerical approach to the modelling of flame spread presented in this thesis operates on the premise that if the ignition and combustion properties of a fuel are known, then by considering these properties individually for each element of a subdivided array of the fuel surface, the rate of flame spread is a corollary of individual ignitions of fuel surface elements. Similarly, the net heat and mass release of the fuel as a whole is taken to be the sum of the release rate of the individual elements. Thus, by examining the ignition and combustion properties of a collection of representative elements or units of fuel, an overall combustion and flame spread scenario may be modelled.

The aim of the research that is described in this chapter is to develop a numerical model to describe the ignition and combustion behaviour of fuels, to form the basis of a flame spread model described in later chapters. Essentially, the model will describe the behaviour of a single element, one of an array of cells which collectively form the entire solid fuel of the flame spread model described in later chapters. The modelling in this chapter focuses on the solid burning material, and any gas phase information required is determined by empirical methods. The model is developed in such a way that it depends on several material properties as input data, which can be derived from experiment.

The construction of the combustion model will be described in the next section, and the material properties required will be listed. Following this a description is given of the fuels considered throughout this thesis, namely two types of polyurethane foam, and the material properties required of the model that are already known or readily measured. Finally, a series of bench scale experiments that were performed to determine the remaining material properties required of the model are described.

4.2. THEORY OF COMBUSTION

Thermal degradation of a solid fuel is the precursor of most accidental enclosure fires, and many of the associated phenomena in such a conflagration, such as smouldering, flaming ignition, flame spread, and possible eventual flashover[74]. A fuel, in the technical sense, means any substance which may react chemically with an oxidant* in an exothermic manner, with the result that it produces heat as well as reaction products. Thus, elements and compounds such as sulphur, aluminium, methane, ethanol, and octane, for example, all technically fit this description. However, when considering the combustible materials typically present in enclosure fires, large molecular weight polymeric compounds are mainly being dealt with. These may be natural polymers such as cellulosic material (wood, paper, cotton) or proteins (wool, silk), or manufactured polymers such as plastics, foams, and synthetic fibres.

These large polymers, whether natural or synthetic, all possess a carbon "backbone", which accounts for the bulk of the fuel's mass. Attached to this backbone, in a typical polymer, are hydrogen atoms, hydrocarbon side chains and other functional groups which may contain oxygen and nitrogen, or less commonly sulphur, chlorine, and other halides. Hence, the main products formed in a chemical reaction with oxygen are carbon dioxide and water vapour, with lesser amounts of carbon monoxide, solid carbon in the form of soot, nitrogen and hydrogen cyanide, and various other products. The exact composition of the products will depend on the composition of the fuel, and the context of its burning, which includes factors such as flame temperature and the local concentration of oxygen.

4.2.1. Thermal Degradation of Solids

When heat is applied to a solid fuel, some of the heat will be responsible for raising the temperature of the solid, some of the heat will be re-emitted back to the surroundings, and some of the heat will go into breaking the chemical bonds in the long chain molecules of the solid and imparting sufficient energy to the molecular fragments to convert them to gaseous species, or volatiles. This latter effect is the thermal degradation, and the mechanism by which it occurs is different for each type of fuel. For some fuels such as polymethylmethacrylate (PMMA), most of the degradation occurs as a simple breaking up of the polymer into its constituent monomer, a liquid which becomes gaseous by the simple process of boiling. However, most fuels do not degrade quite so regularly,

* Typically gaseous oxygen in air, although many other substances may fit the definition of an oxidant

and tend rather to break at various locations throughout the polymer chain, usually forming intermediate compounds before producing volatiles. Sometimes a solid carbonaceous residue will remain after some of the lighter volatiles have evaporated, as is the case with many cellulosic fuels. Such fuels are referred to as charring, while fuels which do not show this tendency are referred to as non-charring fuels.

The rate at which a solid decomposes is an increasing function of temperature; the higher the temperature of the fuel, the more rapidly it will decompose. Like many chemical reactions, the kinetics of the reaction is assumed to obey an Arrhenius type relation. For a single step first-order reaction, the rate may be expressed

$$R_s = A \cdot \exp\left(-\frac{E}{RT_s}\right) \tag{4.1}$$

where R_s is the rate of decomposition of the solid, T_s is its temperature, and R is the universal gas constant. The two values characteristic of the reaction are the activation energy, E, and the pre-exponential constant, A. When decomposition is occurring by several mechanisms, there will be a separate activation energy and pre-exponential constant for each reaction. The reactions may occur in a single step, or in several steps. This study, however, does not go into any great detail in modelling the kinetics of decomposition, instead making the assumption that a single step global model is sufficiently accurate to model the decomposition of the fuels being dealt with. This approach has previously been found to sufficient for a variety of combustion and flame spread applications[28,75,76].

Treating the decomposition of the fuel as occurring in a single step obviously makes the process much simpler to model. Because only one reaction is occurring, it is a common practice to state that a given amount of heat will produce a given mass of volatiles (or equivalently, a given mass of volatiles produced will remove a given amount of heat). This is referred to as the heat of volatilisation, and it is generally an endothermic reaction.

4.2.2. Thermo-Gravimetric Analysis

Thermo-Gravimetric Analysis (TGA) is a method by which the chemical kinetics of thermal decomposition may be determined[77]. In simplest terms, a small sample (typically around 20 milligrams) of the material is placed on a fine balance, its temperature raised in a controlled fashion, and the mass of the sample recorded continuously as a function of time. The test may be

performed in a controlled atmosphere with a variety of compositions or in near vacuum conditions, depending on the specifications of the apparatus in question.

A small sample is used, as it can be heated uniformly throughout, with no appreciable time lag between heat being applied at a given temperature to the surface of the sample and the temperature at the centre of the sample rising to the temperature at the surface. Thus, thermal degradation will be uniform throughout the fuel sample. Once the sample is raised to a given temperature, the rate of mass loss is measured. This will be proportional to the amount of remaining mass i.e.

$$\frac{\partial m}{\partial t} = -R_s \cdot m \tag{4.2}$$

where R_s is the rate constant for solid composition, as given in Equation 4.1 for a first order reaction. The rate of mass loss is measured for a number of temperatures. If only one decomposition reaction is dominant, then according to a rearrangement of Equation 4.1 given by

$$\log\left(\frac{\dot{m}}{m}\right) = \log(R_s) = \log(A) - \frac{E}{RT} \tag{4.3}$$

it can be seen that a plot of $\log(R_s)$ versus $1/T$ will result in a series of points along a straight line with slope $-E/R$ and which intercepts the vertical axis at $\log(A)$.

If there is more than one reaction occurring at the same time (as is usually the case), then the points will not necessarily be linear, or may be linear over a number of segments with a particular reaction dominating at a given temperature. Also, there will be a delay in raising the sample to a given temperature. This may be avoided by the use of differential thermogravimetry (DTG). In this technique, the temperature of the sample is raised linearly with time, and the mass recorded continuously. The rate of mass loss is taken from the slope of the mass history, and divided by the mass history itself, to yield a time dependent reaction rate. Since the time dependence of the temperature is also known, Equation 4.3 can be rewritten with time t as a parameter

$$\log(R_s(t)) = \log\left(\frac{\dot{m}(t)}{m(t)}\right) = \log(A) - \frac{E}{R \cdot T(t)} \tag{4.4}$$

A plot of $\log(R_s(t))$ versus $1/T(t)$ will yield a continuous curve, with possibly one or more straight (or nearly straight) line segments. These segments result when a reaction dominates at a particular temperature range, and as this range is "traversed" in time by the rising temperature, the straight line segment will be parametrically traced according to Equation 4.4.

DTG was performed on two types of polyurethane foam, standard foam and a fire retarded foam, by researchers at CESARE. The results show that there appear to be many reactions occurring in the pyrolysis of polyurethane foam, but that two main reactions stand out. The overall results are given in Table 4.1. The columns show the fuel type, the composition of the atmosphere (pure nitrogen, pure oxygen, or a 20% oxygen/80% nitrogen mix), the temperature increase rate, and information for the first and second reaction peaks. The columns within the peak columns show temperature at which the peak occurs, the pre-exponential constant A, and the activation energy E. The values for the activation energy and particularly the pre-exponential factor are quite sensitive to the interpretation of the output data; depending on the chosen fit of the slope and intercept of the straight line segment in the data, the activation energy can vary by a factor of two or three, and the pre-exponential factor by several orders of magnitude (due to the factor appearing as $\log(A)$ in Equation 4.4). The figures given in the table therefore are taken as guidelines only for the modelling presented later in the thesis.

Table 4.1 Kinetic properties of polyurethane foams

Foam Type	Flow Gas	Temp. Ramp	1st Peak			2nd Peak		
		(°C/min)	T(°C)	A(s^{-1})	E(J/mol)	T(°C)	A(s^{-1})	E(J/mol)
Fire Ret.	N_2	15	270	6.6×10^{3}	59000	390	1.2×10^{13}	157000
Fire Ret.	N_2	30	270	5.4×10^{1}	47000	390	3.0×10^{9}	140000
Fire Ret.	N_2	50	270	7.3×10^{2}	56000	390	1.9×10^{8}	124000
Standard	N_2	30	280	2.5×10^{5}	79000	380	3.7×10^{12}	171000
Standard	N_2/O_2	30	240	2.1×10^{15}	168000	260	9.3×10^{15}	170000
Standard	O_2	30	240	7×10^{3}	160000	260	7.6×10^{16}	179000

4.2.3. Ignition

At some stage during the thermal degradation of a solid fuel, conditions may become suitable for the initiation of the exothermic reaction between the pyrolysis products and oxygen, a phenomenon referred to as ignition. Flaming ignition occurs in the gas phase, although it is strongly linked to the temperature of the solid fuel in the vicinity of the ignition point. The process of ignition by radiant heating has been outlined by Di Blasi[74] and is described briefly here. Upon exposure to a radiant heat flux, the fuel surface heats up and begins to release volatiles. The gas is heated by conduction from the hotter fuel surface. After a certain time, a combustible mixture of oxygen and volatiles is formed in the gas region above the surface. Unlike air, the volatiles may interact with the radiant

flux and absorb heat (and in doing so, block some of the radiation reaching the fuel surface). This absorption heats the fuel-air mixture further, to a point where self-ignition of the mixture may occur. Ignition of this type is known as autoignition, and generally requires high temperatures both within the gas and solid phases. If a small energetic source such as a spark or small flame is present in the fuel-air mixture, then ignition may occur at lower temperatures. The additional energy source is known as a pilot, and process known as piloted ignition.

So, for ignition to occur, two criteria need to be met. The pyrolysing surface must be supplying fuel vapours rapidly enough to maintain a flammable fuel-air mixture, and there must be sufficient temperature to initiate and maintain the reaction of the volatiles with air. Both these quantities relate back to the surface of the pyrolysing fuel itself, as indicated by the kinetics of decomposition given by Equation 4.1 which shows that increased mass loss occurs in tandem with increased solid fuel temperature. It is a common practice to assume that ignition occurs when the surface of the fuel reaches a critical temperature. While the concept of a surface ignition temperature remains somewhat controversial[78], few practical alternatives have been offered, so it is still the mainstay of many combustion and flame spread models[10,79,80,81].

Critical surface ignition temperature may be considered to be a basic material property which may be determined from appropriate experimental methods[82]. In practice, direct measurement of the surface temperature is very difficult to achieve. However, critical ignition temperature, whether piloted or auto, may be related to other fundamental material properties by the expression[58]

$$t_{ig} = \frac{\pi}{4}\frac{\Delta T_{ig}^2 (k\rho c_p)}{\dot{Q}_e''^2} \qquad (4.5)$$

where ΔT_{ig} is the temperature rise of the fuel surface above ambient or initial temperature, t_{ig} is the time to ignition of the material subjected to an applied external flux $\dot{Q}_e''$, and k is the conductivity, ρ the density, and c_p the thermal capacity of the fuel. The quantity $k\rho c_p$ is commonly referred to as the thermal inertia of the fuel. Flammable materials with a low thermal inertia, such as plastic foams, will ignite more rapidly than those with a higher thermal inertia.

In fact, Equation 4.5 only applies to fuels which are sufficiently "thick". A fuel is defined as thermally thick if its thickness, τ, satisfies the inequality[70]

$$\tau > 2\sqrt{\alpha t} \qquad (4.6)$$

where α is the thermal diffusivity of the solid, and t is the duration of heating. Also, Equation 4.5 is not valid when the value of the applied heat flux is close to the minimum heat flux required to ignite the fuel.

If the fuel does not satisfy Equation 4.6, it is described as being thermally thin. For thermally thin fuels, there will be no appreciable temperature difference between the two surfaces, so a "lumped thermal capacity" approach may be used[70]. The time to ignition in this case (taking into account convective heating) is given by

$$t_{ig} = \frac{\tau \rho c_p}{2h} \log\left(\frac{\dot{Q}_e''}{\dot{Q}_e'' - 2h\Delta T_{ig}} \right) \qquad (4.7)$$

where h is the heat transfer coefficient. The important parameter in this equation is the quantity $\tau\rho c_p$, which may be thought of as the product of the thermal capacity and the "mass per unit area" of the thermally thin solid. A comparison with the thermal inertia dependence for thermally thick fuels shows that while thick fuels depend on the thermal conductivity, k, thin fuels depend on the thickness, τ.

4.2.4. Combustion of Solid Fuels

For the decomposition reaction to proceed, there needs to be a continual input of heat to maintain the reaction. There are two main sources of heat in most situations. There is externally applied heat, and there is heat from the reaction of the volatiles themselves with oxygen. This may take the form of flaming combustion, whereby the volatiles are forced clear of the surface by the expansion pressure of the volatile formation, and reaction with air occurs via the turbulent mixing in the flaming region. Alternatively, glowing or smouldering combustion may occur at the surface of, or within, the porous char layer of charring fuels, where air must diffuse through to the active combustion region to react directly with the char. In either case, the heat released by the combustion of the volatiles is greater than the heat required to produce them, and this is usually sufficient to sustain the reaction.

Although combustion of the fuel (by definition) liberates energy, combustion will only be self sustaining if the feedback of heat from the combustion region back to the pyrolysing region of the fuel is greater than the heat losses occurring at this same region. For steady combustion, the heat from the flame will be in equilibrium with the losses. A simple balance equation can therefore be written[58].

$$\dot{m}'' L_v = \dot{Q}_f'' + \dot{Q}_e'' - \dot{Q}_{loss}'' \quad (4.8)$$

where $\dot{Q}_f''$ is the heat flux from the flame, $\dot{Q}_e''$ is the externally applied heat flux, $\dot{Q}_{loss}''$ is the heat lost from the surface (all these heat fluxes have units W/m^2), $\dot{m}''$ is the mass flux from the surface (kg/m^2s), and L_v is the latent heat of volatilisation (J/kg). The flame heat is the sum of the radiative and convective heat fluxes from the flame. The heat losses are a combination of heat conducted into the surface and re-radiated heat. Even for unsteady combustion, Equation 4.8 may be used to determine the instantaneous heat balance.

In order to consider Equation 4.8 in a more mathematically rigorous sense, the terms therein need to quantified. This requires a determination of the temperature of the surface, as the magnitude of the conduction, convection, and re-radiation heat fluxes which contribute to $\dot{Q}_{loss}''$ are all dependent on the surface temperature. The radiation heat transfer has been dealt with previously, with the surface re-radiation flux expressed by Equation 3.4.

Convection heat transfer is usually the most difficult factor to calculate in situations such as this, since it involves the movement of a fluid (air and combustion products), and its associated phenomena such as buoyancy, turbulence, and boundary layer effects. Accordingly, a full numerical solution of the effect is essentially an exercise in CFD modelling. However, basic expressions for the convective heat transfer are available for certain special cases[71], with the greatest simplification of all being that of a constant heat transfer coefficient. In this assumption, the heat transferred to the surface by convection is proportional to the temperature difference between the gas and the surface, with the constant of proportionality being the heat transfer coefficient, h. It is often taken to be a global constant, with a value for most situations of about 30 $kW/m^2 \cdot K$, although it may vary by orders of magnitude in some cases[71].

Like the convective heat transfer, the heat transfer from the flame as expressed by the term $\dot{Q}_f''$ in Equation 4.8 essentially depends on gas phase phenomena, and a full description of this term requires detailed numerical calculations. As is the case with convection, it is possible to make simplifications, such as to assume that $\dot{Q}_f''$ is a constant which is characteristic of the fuel in question, for a given configuration (usually horizontal, or pool fire configuration.) This may be determined from controlled, small scale tests. The constant heat assumption may be modified to take into account ambient oxygen concentration. For a higher concentration, the fuel will burn more rapidly and efficiently. This may be expressed[70]

$$\dot{Q}_f'' = \xi Y_{O_2} \quad (4.9)$$

Conduction of heat into the fuel is proportional to the temperature gradient at the surface, the value of which requires knowledge of the temperature profile in the fuel normal to the fuel surface. Pyrolysis of the fuel will result in mass loss. In the case of charring fuels, this will result in an overall density change in the char layer, while in non-charring fuels it results in an actual regression of the fuel surface. This must be taken into account in any model which attempts to calculate the internal fuel temperature.

There are essentially two methods for calculating the temperature distribution; a finite difference approach, and an integral method approach. The integral method simplifies the conduction problem by assuming a functional temperature profile and a heating depth. Quintiere et al[12] and Mogtaderi et al[83] assume a parabolic temperature profile, while Delichatsios et al[84,85] assume an exponential profile. This method therefore only needs to determine a relatively small number of unknowns associated with the boundary conditions, and despite its simplifications may yield reasonably accurate results[12,83,84,85]. These simplifications also make it a useful method for use in CFD combustion models, where computational resources are always limited[83]. One of the disadvantages of this method, however, is the fact that it is only designed to calculate the heat conduction normal to the surface, and cannot calculate the lateral heat conduction which is important in certain flame spread situations[86]. On the other hand, a finite difference method which solves the temperature distribution on a specified array of nodes may readily be expanded to three dimensions, and may more accurately determine the temperature profile within the fuel. The price paid for this accuracy and flexibility naturally enough is computation time.

What has been described here, while quite detailed, nevertheless only describes the basics of the theoretical nature of combustion of solid fuels. However, there is sufficient detail to form the basis of a workable solid-fuel combustion model, the formulation of which is described in the next section. The combustion properties of two fuels are required as input variables into the combustion model, and subsequently into flame spread models, and will be investigated in the following sections.

4.3. MODELLING OF COMBUSTION

Presented here is a model based on the surface heat balance equation (Equation 4.8), which takes into account the expressions for radiation, conduction, and convection which constitute the term $\dot{Q}''_{loss}$, and the Arrhenius expression for volatilisation of the fuel. It is similar to the model for combustion of PMMA developed by Steckler et al[87], except that in the model presented here,

surface temperature is calculated for all stages of the combustion, whereas the model of Steckler et al assumes vaporisation temperature of the PMMA. For now, the assumption will be made that the heat from the flame, $\dot{Q}_f''$ and the external radiation, $\dot{Q}_e''$ are known quantities, whether they be constants or time dependent. This model will later be included in a flame spread model which in turn will be incorporated into a CFD model, which will be responsible for the determination of these quantities by detailed simulation of the gas phase combustion processes. For the purposes of the model at this stage, $\dot{Q}_f''$ and $\dot{Q}_e''$ will be taken to be constants for the duration of the simulation. The temperature distribution within the fuel is calculated by the finite difference method, with a grid transformation to account for regression of the fuel surface as the combustion proceeds. The temperatures of the nodes are designated $T_0,\ldots,T_n$, the positions of the nodes $z_0,\ldots,z_n$, and the node spacing is given by $\Delta z_k = z_{k-1} - z_k$.

4.3.1. Surface Temperature

Surface temperature T_0, is calculated by considering a heat flux balance at the surface of the fuel. The surface is a mathematical construct which forms the boundary between solid phase and the gas phase. The conduction heat transfer at the surface is given by

$$\dot{q}''_{conduct} = -k \left.\frac{dT}{dz}\right|_{z=z_0} \tag{4.10}$$

where k is the conductivity of the fuel. The term on the right hand side of Equation 4.10 is the temperature gradient at the surface, evaluated at $z=z_0$. The gradient may be estimated by a linear temperature profile fit between the surface node and the first node beneath the surface; however, for improved accuracy, a parabolic fit between the surface temperature and the temperature of the first two nodes below the surface is chosen instead. This may be expressed by

$$\dot{q}''_{conduct} = -k \frac{(T_1 - T_0)(\Delta z_1 + \Delta z_2)^2 - (T_2 - T_0)\Delta z_1^{\,2}}{\Delta z_1 \Delta z_2 (\Delta z_1 + \Delta z_2)} \tag{4.11}$$

The reradiated flux from the surface is given by Equation 3.4 which for clarity is given again here

$$\dot{q}''_{reradiant} = \varepsilon \sigma T_0^4 \tag{4.12}$$

where ε is the emissivity of the fuel. The emissivity is also the fraction of the externally applied radiant heat, $\dot{Q}_e''$, which is absorbed by the surface. Convection to the surface from the flame is

incorporated in the term $\dot{Q}_f''$. Alternatively, if the temperature of the gas in contact with the surface, T_{gas}, is known, then the convective heat flux may be given as

$$\dot{q}''_{convect} = h(T_{gas} - T_0) \tag{4.13}$$

where h is the heat transfer coefficient.

Pyrolysis of the fuel is assumed to occur in an incremental layer close to the surface. This is a reasonable assumption for many fuels, at least in the initial stages of combustion, as the Arrhenius relation given by Equation 4.1 decreases rapidly with temperature due to the exponential nature of the function, and the temperature gradient itself is usually quite steep near the surface. It has been noted, however, that in some instances the pyrolysis rate may increase as combustion proceeds, even though the surface temperature remains unchanged[74]. This is due to the sub-surface fuel contributing to the gasification as the sub-surface temperature approaches the surface temperature. However, if the fuel is a poor conductor of heat and burns rapidly, as is the case with many foam polymers, this effect will be minimal, and the assumption of surface pyrolysis will hold. The effect is also less apparent at high heat fluxes than low heat fluxes[87]. The rate of pyrolysis of the fuel given by Equation 4.1 represents the mass flux of volatiles from the surface, which appears on the left hand side of Equation 4.8. Combining Equations 4.1, 4.8, 4.11, 4.12, and 4.13 results in the heat flux balance equation given by

$$\begin{aligned} L_v A \exp\left(\tfrac{-E}{R_u T_0}\right) &= \varepsilon \dot{Q}_r'' - \varepsilon\sigma T_0^4 + h(T_{gas} - T_0) \\ &+ T_0 k\left(\frac{(2\Delta z_1 + \Delta z_2)}{\Delta z_1(\Delta z_1 + \Delta z_2)}\right) - k\left(\frac{T_1(\Delta z_1 + \Delta z_2)}{\Delta z_1 \Delta z_2} - \frac{T_2 \Delta z_1}{\Delta z_2(\Delta z_1 + \Delta z_2)}\right) \end{aligned} \tag{4.14}$$

This may be rewritten

$$L_v A \exp\left(\frac{-E}{RT_0}\right) + aT_0^4 + bT_0 - c = 0 \tag{4.15}$$

where

$a = \varepsilon\sigma$

$$b = h + k\frac{(2\Delta z_1 + \Delta z_2)}{\Delta z_1(\Delta z_1 + \Delta z_2)}$$

$$c = \varepsilon \dot{Q}_r'' + hT_{gas} - k\left(\frac{T_1(\Delta z_1 + \Delta z_2)}{\Delta z_1 \Delta z_2} - \frac{T_2 \Delta z_1}{\Delta z_2(\Delta z_1 + \Delta z_2)}\right)$$

This equation cannot be solved analytically, so the solution is obtained numerically using the Newton-Raphson method. Ten iterations were found by the author to be sufficient for convergence, providing the initial guess of the temperature is within physical bounds*.

4.3.2. Conduction Within the Solid

Conduction of heat within the combustible solid is calculated by constructing a grid within the solid and calculating the temperatures at grid nodes using a finite difference method. The finite difference method begins by considering the one dimensional version of the general conservation equation, Equation 2.1, with heat the species being solved for in this equation. The equation is one-dimensional because lateral conduction of heat is not being considered, only conduction of heat normal to the surface†. Because a solid is being considered, there is no convective term, at least not for the movement of the bulk material, although some simulations allow for conduction heat transfer due to the production and movement of volatiles. For a non-porous, non-charring solid, convection can be ignored. Similarly, if the solid is opaque so that there is no penetration of radiation into the fuel, and there are no reactions taking place within the fuel, there will be no significant source term. Thus, in its simplest form, the resulting equation is the well known heat equation

$$\frac{\partial T}{\partial t} = \alpha \frac{\partial^2 T}{\partial z^2} \tag{4.16}$$

where α is the thermal diffusivity of the solid. For certain boundary conditions, such as a constant heat flux to the surface, this equation may be solved in closed form[88]. However, if the heating rate is transient, it is normally necessary to resort to numerical techniques. A common numerical approach is to use the finite difference method, a description of which may be found in many basic heat transfer texts [40,71]. A number of nodes is chosen throughout the depth of the fuel, and the following finite difference equation is solved for each node

$$\frac{T_k^{new} - T_k}{\Delta t} = \alpha \frac{2(\Delta z_k T_{k+1} - (\Delta z_k + \Delta z_{k+1})T_k + \Delta z_{k+1} T_{k-1})}{(\Delta z_k^2 \cdot \Delta z_{k+1} + \Delta z_k \cdot \Delta z_{k+1}^2)} \tag{4.17}$$

---

* i.e. greater than 0 K. In preliminary encodings of the model, a negative value of h occasionally appeared, which produced negative valued temperatures, which then lead to divergence (a problem subsequently remedied). An analysis of the complex dynamics of the equation revealed that provided both h and T are always positive, this equation will always converge to a (unique) solution.

† This assumption is justified in the context of considering combustion in an apparatus such as a Cone Calorimeter, where a uniform heat flux is applied at the top surface and minimal heat losses occur at the side of the fuel due to insulation. The more complex three dimensional heat conduction is considered for the case of a spreading flame in Chapter 5.

where T_k is the old temperature at the kth node, T_k^{new} is the temperature at the kth node after a timestep Δt, Δz_k is the distance between nodes k and k-1, and Δz_{k+1} is the distance between nodes k and k+1. The method is most accurate when the nodes are closely spaced where the temperature gradient is higher, which is usually close to the burning surface.

Equation 4.17 is known as the explicit method, since the new temperature can be calculated directly from the old temperatures. However, this can lead to numerical instabilities if the Fourier condition, given by

$$\frac{\alpha \Delta t}{\left(\min(\Delta z_1, \ldots, \Delta z_n)\right)^2} < \frac{1}{2} \tag{4.18}$$

is violated[71,40]. Hence, the unconditionally stable implicit method is often used instead. The old temperatures on the right hand side of Equation 4.17 are replaced with the new temperature at the same point, i.e.

$$\frac{T_k^{new} - T_k}{\Delta t} = \alpha \frac{2(\Delta z_k T_{k+1}^{new} - (\Delta z_k + \Delta z_{k+1}) T_k^{new} + \Delta z_{k+1} T_{k-1}^{new})}{(\Delta z_k^2 \cdot \Delta z_{k+1} + \Delta z_k \cdot \Delta z_{k+1}^2)} \tag{4.19}$$

The new temperatures are unknowns, so cannot be evaluated directly, but there are enough equations for all the nodes to solve the unknown temperatures simultaneously. The method used is the well known tri-diagonal matrix, or Thomas, algorithm[71]. However, before the setting up of the method is described, the regression of the surface needs to be accounted for.

If the solid surface is one which regresses as the combustion proceeds, a decision must be made for the method of dealing with the nodes. The node mesh may be made uniform, and each node removed from the calculation region as the surface regresses below it, or the grid may be allowed to "collapse" along with the surface. The latter method is chosen in this study, as it allows the retention of a fine grid close to the surface, and does not require checks for nodes removed from the calculation region.

The grid transformation proceeds as follows. Consider a sample of fuel undergoing combustion, whose burning surface is of unit area. One-dimensional conduction of heat occurs in the z-direction. The k+1 nodes within the fuel are initially at positions $z_1,\ldots,z_{k-1}$, with the node z_0 coinciding with the burning surface, and the node z_k coinciding with the surface opposite the burning surface at z=0. Thus, the fuel is initially of thickness z_0, and the mass of the sample is $M_0=\rho z_0$, where ρ is the density of fuel. Combustion of the fuel will result in a movement of the fuel surface towards the fixed opposite surface.

After undergoing combustion for some period of time, the thickness, z, and mass, M, of the sample is given by $M=\rho z$. The fraction burnt is therefore given by

$$F = \frac{M}{M_0} \tag{4.20}$$

The new positions of the nodes are given by $Fz_0,\ldots,Fz_n$. Since $z_n=0$, this node remains unchanged, which is desirable since it coincides with the fixed surface. Similarly, the node spacings are given by $F\Delta z_0,\ldots,F\Delta z_n$. The kth term as given by Equation 4.19 becomes

$$\begin{aligned}\frac{T_k^{new}-T_k}{\Delta t} &= \alpha\frac{2(F\Delta z_k T_{k+1}^{new}-(F\Delta z_k+F\Delta z_{k+1})T_k^{new}+F\Delta z_{k+1}T_{k-1}^{new})}{(F^2\Delta z_k^2\cdot F\Delta z_{k+1}+F\Delta z_k\cdot F^2\Delta z_{k+1}^2)} \\ &= \frac{\alpha}{F^2}\frac{2(\Delta z_k T_{k+1}^{new}-(\Delta z_k+\Delta z_{k+1})T_k^{new}+\Delta z_{k+1}T_{k-1}^{new})}{(\Delta z_k^2\cdot\Delta z_{k+1}+\Delta z_k\cdot\Delta z_{k+1}^2)}\end{aligned} \tag{4.21}$$

Rearranging gives the following expression

$$d_k = a_k T_{k-1}^{new} + b_k T_k^{new} + c_k T_{k+1}^{new} \tag{4.22}$$

where

$$\left.\begin{aligned} a_k &= -\frac{2\alpha\Delta t}{F^2}\frac{\Delta z_{k+1}}{(\Delta z_k^2\cdot\Delta z_{k+1}+\Delta z_k\cdot\Delta z_{k+1}^2)} = -\frac{2\alpha\Delta t}{F^2(\Delta z_k^2+\Delta z_k\cdot\Delta z_{k+1})} \\ b_k &= 1+\frac{2\alpha\Delta t}{F^2}\frac{(\Delta z_k+\Delta z_{k+1})}{(\Delta z_k^2\cdot\Delta z_{k+1}+\Delta z_k\cdot\Delta z_{k+1}^2)} = 1+\frac{2\alpha\Delta t}{F^2(\Delta z_k\cdot\Delta z_{k+1})} \\ c_k &= -\frac{2\alpha\Delta t}{F^2}\frac{\Delta z_k}{(\Delta z_k^2\cdot\Delta z_{k+1}+\Delta z_k\cdot\Delta z_{k+1}^2)} = -\frac{2\alpha\Delta t}{F^2(\Delta z_k\cdot\Delta z_{k+1}+\Delta z_{k+1}^2)} \\ d_k &= T_k \end{aligned}\right\} k=1,\cdots,n-1$$

The resulting series of equations may be written in matrix form, as follows

$$\begin{bmatrix} b_1 & c_1 & & & & & \\ a_2 & b_2 & c_2 & & & \varnothing & \\ & & \ddots & & & & \\ & & a_k & b_k & c_k & & \\ & & & & \ddots & & \\ & \varnothing & & & a_{n-2} & b_{n-2} & c_{n-2} \\ & & & & & a_{n-1} & b_{n-1} \end{bmatrix} \cdot \begin{bmatrix} T_1^{new} \\ T_2^{new} \\ \vdots \\ T_k^{new} \\ \vdots \\ T_{n-2}^{new} \\ T_{n-1}^{new} \end{bmatrix} = \begin{bmatrix} d_1 \\ d_2 \\ \vdots \\ d_k \\ \vdots \\ d_{n-2} \\ d_{n-1} \end{bmatrix} \tag{4.23}$$

All the constants lie along the central diagonal and the two diagonals either side, with the rest of the matrix filled with zeros (as represented by the null set, Ø)

Note that when $k=1$, T_0 is a known quantity which has been calculated from the surface heat flux balance. In this case, a_1T_0 can be subtracted from d_1 so that Equation 4.21, with $k=1$, is expressed with the terms b_1 and c_1 only. Similarly, a condition needs to be specified for the surface node at z_n.

A flux balance similar to the surface heat flux balance may be calculated to determine the temperature, or a constant temperature condition may be applied. In either case, the known temperature needs be subtracted as the term $c_{n-1}T_n$ from d_{n-1}. Alternatively, the perfectly insulated boundary condition may be specified instead. In this case, the heat transfer at the node z_n behaves as if there is a "mirror image" of the node z_{n-1} on the other side of the boundary, at z_{n+1}. This "virtual node" is has same temperature as its counterpart, and is the same distance from the boundary node. Thus, when Equation 4.21 is written for $k=n$, the two terms a_nT_{n-1} and c_nT_{n+1} are identical, and may be written as $2a_nT_{n-1}$. This necessitates an extra line in the matrix Equation 4.23 ($k=1,\ldots,n$ rather than $k=1,\ldots,n-1$) but the method is otherwise identical. Once the matrix is constructed and the coefficients established, solution of the matrix via the Thomas algorithm is straightforward[71].

The Thomas algorithm proceeds as follows. First, the leading diagonal of the matrix, consisting of the terms a_k, is eliminated. This is done by setting $\beta_1=b_1$, $\delta_1=d_1$, and recursively calculating the terms β_k and δ_k as follows

$$\left.\begin{aligned}\beta_k &= b_k - \frac{c_{k-1}a_k}{\beta_{k-1}} \\ \delta_k &= d_k - \frac{\delta_{k-1}a_k}{\beta_{k-1}}\end{aligned}\right\} k = 2,\cdots,n-1$$

The last line of the matrix now reads $\beta_{n-1}T_{n-1} = \delta_{n-1}$. Hence, the last temperature is determined by $T_{n-1} = \delta_{n-1}/\beta_{n-1}$, and the remaining temperatures evaluated by back substitution, which is achieved by the recursive calculation

$$T_k = \frac{\delta_k - c_kT_{k+1}}{\beta_k}, k = n-2,\cdots,1$$

Once all the node temperatures have been established regression of the fuel surface needs to be taken into account. If the mass flux from the surface is given by $\dot{m}''$, then after a time step Δt, the mass of the fuel sample will have decreased by $\dot{m}''\Delta t$. The new value for the remaining mass fraction as given by Equation 4.20 is

$$F_{new} = \frac{M - \dot{m}''\Delta t}{M_0} \qquad \textbf{(4.24)}$$

from which the new node positions may be established. However, the new positions will have slightly different temperatures to those calculated for the node positions at the beginning of the time step. The exceptions are the surface temperature, which is assumed to be maintained throughout the time step, and the opposite surface, which is invariant under the transformation. For the other nodes, the transformation will typically place them at a position between two old node locations.

Since the regression in one time step is generally smaller than even the fine node spacing near the burning surface, the new node will likely be near its old position. Hence, a simple linear interpolation of temperatures from the old node positions is used to determine the temperatures at the new node positions (parabolic and higher order interpolations are most likely unnecessary in such circumstances.)

This model was not intended to be constructed as a self contained model; it was developed as a component of a flame spread model, which is described in the next chapter. Consequently, no modelling results will be presented here; rather, a description of the modelling results as they pertain to flame spread is presented in the next chapter. The model has been described here in order to illustrate the combustion principles of the flame spread model in a more suitable context. To summarise this section, a list of the constants required of the model is given in Table 4.2.

Table 4.2 Constants required in the combustion and flame spread model

Symbol	Description	Units	Symbol	Description	Units
ρ	Density	kg/m^3	A	Pre-exponential constant	s^{-1}
k	Thermal conductivity	W/m·K	E	Activation energy	J/mol
c_p	Specific heat	J/kg·K	L_v	Latent heat of volatilisation	J/kg
ε	Emissivity	1	ΔH_c	Heat of combustion	J/kg
			$\dot{Q}''_f$	Heat flux from flame	W/m^2

4.4. COMBUSTION PROPERTIES OF FLEXIBLE POLYURETHANE FOAM

Presented here is a description of the thermal, physical and chemical properties of two types of polyurethane foam (PUF), a standard foam, and a fire retarded foam. These fuels are chosen to be used in the experimental component of this thesis as they are materials commonly encountered in domestic and commercial occupancies. They have been used at the EBBF in previous fire tests[8.52], so fuel samples were readily available to the author, as well as some relevant data from these previous tests. PUF also has the advantage of being homogenous and isotropic in composition with relatively simple combustion behaviour. This is in contrast to materials such as wood which, although a common building material, is generally non-uniform in composition and directional properties and burns in a complex fashion, and PMMA which, while it has simple uniform combustion properties and has been used extensively in previous flame spread research, is a somewhat uncommon building material.

4.4.1. Chemistry

The basic reaction in the formation of a generic polyurethane is the reaction of a diisocyanate with a diol, which may be written[89]

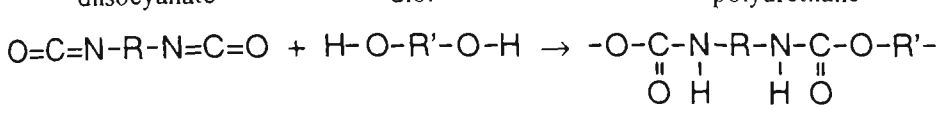

(4.25)

where R and R' are the organic molecules to which the functional groups (–O=C=N in the case of the diisocyanate, –OH in the case of the diol) are attached. In the manufacture of polyurethane foams (PUFs), the most commonly used diisocyanate is toluene diisocyanate (TDI), while the diol is most frequently a long chain polyether or polyester of high molecular weight, terminated at either end by a hydroxyl group[89]. The exact composition of the reactants, and the nature of the reaction (such as the degree of cross linking) is tailored for the requirements of the end product. Expansion of the polyurethane into a foam is achieved by the inclusion of a blowing agent in the reacting mixture. The agent is usually carbon dioxide formed from the reaction of the diisocyanate with water, or a low boiling point liquid such a chlorofluorocarbon, although the latter method has been largely abandoned due to the ozone depletion potential of chlorofluorocarbons.

4.4.2. Physical Properties

When polyurethane is expanded into a foam, the bulk of the foam's volume comprises the air occupying the foam cells. As a consequence, the density is very low compared to non-expanded polymers, and its thermal conductivity is quite similar to that of air, or in other words, polyurethane foam is a good insulator. This is because heat can only be conducted along the cell walls which, being thin, have a small cross-sectional area, and therefore can only conduct a small amount of heat. The combination of low density and low thermal conductivity makes the thermal inertia of PUFs particularly low, and therefore easy to ignite (see Equation 4.5) and subsequently combust.

Table 4.3. Physical properties of polyurethane foams

Material	AA23-130	ST32-80
Density ρ (kg/m^3)	23	32
Thermal Conductivity k (W/m· K)	0.036	0.038
Thermal Capacity c_p (J/kg· K)	1400	1400
Thermal Diffusivity α (m^2/s)	1.1×10^{-6}	8.5×10^{-7}
Thermal Inertia $k\rho c_p$ ($W^2\cdot s/m^4\cdot K^2$)	1200	1700

4.4.3. Thermal Properties

Polyurethane, like most organic polymers, is a combustible solid. The expansion of polyurethane into a foam decreases the density and thermal conductivity of the product, and consequently the thermal inertia, increasing its ignitability. Because of this increased fire hazard, many PUFs are manufactured with fire retardant chemicals as an additive. Common additives are phosphorous compounds, either as an unreactive compound in the diol-diisocyanate mix, or as a reactive phosphonate forming a copolymer with the other polymer constituents[90].

The first stage in the thermal degradation of polyurethane, commencing around 250°C, is the scission of the original diol-diisocyanate bond, resulting in the polymer reverting to its molten pre-polymerised state[77,89,90]. Polymerisation of the isocyanates to a more thermally stable compound may then occur, along with a thermo-oxidative reaction leading to char formation if pyrolysis occurs in an oxygenated atmosphere. At higher temperatures (around 400-600°C) breakdown of the polyisocyanates and char occurs.

Presence of a phosphorous containing fire retardant as a copolymer actually reduces the activation energy of the depolymerisation reaction, making the copolymer less thermally stable than the equivalent polymer without the phosphonate group. However, the fire retardant properties arise because the presence of the phosphorous compounds promotes the thermo-oxidative formation of the more thermally stable chars[77,90].

4.5. CONE CALORIMETER EXPERIMENTS ON POLYURETHANE FOAMS

4.5.1. Aims of the Cone Calorimeter Tests

This section describes a series of experiments that was performed on two types of flexible polyurethane foam, namely Dunlop AA23-130, a standard foam, and Dunlop ST32-80 "Stamina" foam, which contains a flame retardant additive. The aim of the experiments was to obtain basic thermophysical material properties of the two foams, to be used as input data for flame spread models. The primary data required are effective heat of combustion, heat of volatilisation, piloted ignition temperature, and autoignition temperature. Other data of secondary importance but nevertheless useful are histories of temperature within the fuel during combustion and flame temperature, the critical ignition flux for both piloted and non piloted ignition, and carbon dioxide, carbon monoxide and soot yields. Before proceeding with the experiments, however, it was necessary to investigate the suitability of the cone calorimeter as an apparatus capable of providing these data. Hence, this section also describes the standard test method for the cone calorimeter, and the feasibility of using the method to obtain the required data.

4.5.2. Feasiblity

A prototype cone calorimeter was first developed and described in 1982, and the basic principle has changed little since[91]. It was developed in response to the need for a bench scale engineering tool for measuring the rate of heat release of combustible items, as rate of heat release was becoming recognised as probably the most important variable influencing fire hazard[2]. Cone calorimetry is gaining acceptance as a standard method for assessing the fire hazard of materials, where it has the advantage of not only being able to pass/fail materials according to a criterion level but also, due to its quantitative nature, rank materials based on this same criterion[91]. Work is also being performed, with much success, in predicting the behaviour of full scale enclosure fires based on bench scale data, such as the EUREFIC project[92] which made predictions of flame spread and heat release in a room based on cone calorimeter tests of the lining materials, and a related project which correlated cone calorimeter data and time to flashover in a full scale enclosure[93]. Applications are not restricted to rate of heat release, and a cone calorimeter fitted with a Fourier Transform InfraRed (FTIR) spectrometer is capable of making real time measurements of rate of release, and composition of, toxic products of combustion[91,94].

In light of the success of research work performed with the cone calorimeter, it appeared to be a favourable method for exploring the parameters of the heat balance equation (Equation 4.8) in order to determine the heat of volatilisation and heat of combustion of the two types of foam used in this thesis. A few preliminary tests were undertaken with the cone calorimeter to assess the feasibility of the method, and to become familiar with the apparatus. However, the preliminary tests of polyurethane foam samples appeared to indicate that for the duration of the combustion of each sample, there was no obvious plateau in the heat release rate curve. As Equation 4.8 is most useful when steady burning of the fuel sample is attained at some stage in the cone calorimeter test, it was clear from these preliminary tests that careful consideration of the cone calorimeter combustion scenario is required in the interpretation of the data yielded from cone calorimetry tests.

The cone calorimeter testing of polyurethane has recently been investigated by Vanspeybroeck et al[95], who made some important observations regarding the burning of polyurethane foam in the cone calorimeter. Perhaps the most significant is that the heat flux produced by the cone decreases significantly with distance from the cone heater, down to 40% over the 50mm thickness of sample[95]. This is a problem for materials which melt readily, such as PUF, since the surface may regress significantly before ignition occurs. This leads to great uncertainty in estimating material properties such as critical ignition flux and surface ignition temperature. Vanspeybroeck et al chose to restrict the thickness of their samples to 25mm, to minimise errors caused by this effect[95]. Even this is a compromise, as there is a drop in heat flux even over the 25mm distance. One of the conclusions in their paper is that the cone calorimeter is an unsuitable method for determining the basic thermophysical material characteristics of polyurethane foam[95].

Another phenomenon which may be a factor is that observed by Orloff[15] in the modelling of thermal radiation from pool fires. It was found that the "collar" of the container in which the pool fire is burning is responsible for as much as 15% of the radiative feedback to the surface. This figure may be even greater so for the sample holder commonly used in cone calorimeter tests. What is occurring in this situation is that, as well as heat being radiatively transferred directly from the flame back to the surface, it is being transferred to the sides of the sample holder. Some will be reflected back to the surface of the fuel, although most will be absorbed by the sides of the sample holder, heating them up. This heat is then reradiated back to the flame and to the surface. The more the sample surface recedes, the more of the sample holder sides are exposed, and the greater the heat feedback to the fuel surface.

It is uncertain, at least before ignition, whether the radiative feedback from the sides of the sample holder to the fuel surface counteracts the drop in heat flux from the cone heater to the fuel surface

as the surface recedes. However, it is expected that after ignition, the heat from the flame should dominate the radiative heat transfer to the surface (except perhaps when the cone is operating at a high heat flux, say above 50 kW/m^2), so that the increasing radiative feedback from the holder sides is likely to be a greater effect than the decreasing cone radiation. Overall, it is not surprising, given the magnitude of the collar effect and the diminishing flux effect, that steady burning of foam samples in the cone calorimeter is not observed.

Indeed, it is surprising that steady burning of any fuel is observed. The key is the low density of the foam, and its rapidly regressing surface as it burns. The surface of a denser fuel burning with the same rate of mass loss as a foam will regress more slowly as it combusts. Since the holder feedback and diminishing cone radiation will not be changing significantly in magnitude over time, steady burning conditions may be readily attained. Some fuels do not even require the holder, and may burn as free-standing objects, provided some means of preventing the sides from igniting is implemented. Polyurethane foam, on the other hand, regresses swiftly as it burns, and its tendency to form molten products as it does so dictates the need for a sample holder.

Despite the lack of a steady burning interval for polyurethane foam tests in the cone calorimeter, it has been suggested that heat of volatilisation may be determined by measuring the peak rate of heat release for a variety of incident heat fluxes[96]. A plot of peak heat release rate versus external heat flux should reveal a linear relationship, the slope of the line being the quotient of the heat of combustion and heat of volatilisation[96]. So, despite the inherent difficulties described here, it still appeared possible to acquire the required data, namely heat of combustion and heat of volatilisation, from cone calorimeter tests, and it was decided to proceed with the series of experiments.

4.5.3. Cone Calorimeter Standard Test Method - ASTM E 1354

The Cone Calorimeter is rapidly gaining acceptance as a method for determining many basic material properties of combustibles. Its adoption as an ASTM standard test method[97] and an ISO standard test[98] is testimony to its usefulness. Described herein are the pertinent details of ASTM E 1354-94, which describes the Cone Calorimeter apparatus itself, and the use of the apparatus in compliance with the standard.

The test method itself is based on the observation that while most fuels possess a heat of combustion per unit mass which is unique to that fuel with a spread of values for a range of fuels,

the amount of heat released per unit mass of oxygen consumed shows markedly less variation between fuels. A value of 13100 kJ of heat released per kilogram of oxygen consumed is taken to be a good estimate for most common organic fuels.

The feature which gives the cone calorimeter its name is a cone shaped electrical heater capable of producing a uniform radiant flux across the surface of a fuel sample measuring up to 100×100mm (or 100mm diameter for circular samples). Irradiance levels up to 100 kW/m^2 may be produced, with a maximum variation of 2% across the fuel surface.

The calorimeter also features a load cell capable of continuously measuring the remaining mass of the fuel sample as combustion progresses. The requirement of the load cell is that it has a measuring range of 500g in 0.1g increments.

During combustion, the products are extracted at a known flow rate into a collection hood and duct arrangement. The products of combustion are sampled from the duct region, and the composition determined by chemical analysers. Oxygen analysis is mandatory for this method, and carbon dioxide and carbon monoxide are also commonly measured. Smoke obscuration may be measured by means of a helium-neon laser and silicon photodiode arrangement, with air purging to prevent soot depositing on the optics.

Fuel samples are prepared by wrapping them in a layer of aluminium foil, exposing one face, and placed in a purpose built sample holder. The sample is placed on the load cell at the commencement of the test, and ignition of the sample may occur by autoignition, or by piloted ignition by means of an electronic spark which is located 13mm above the sample surface. The samples may be tested either in a horizontal or vertical configuration. Some cone calorimeters have been constructed to operate in controlled atmospheres, so that samples may be tested in oxygen enriched or depleted atmospheres.

The heat release is calculated from the oxygen depletion using the following formula[97]

$$\dot{Q}(t) = 1.10 \frac{\Delta H_c}{r_0} C \sqrt{\frac{\Delta P}{T_e}} \frac{Y_{O_2}{}^0 - Y_{O_2}(t)}{1.105 - 1.5 Y_{O_2}(t)} \qquad \textbf{(4.26)}$$

where ΔH_c is the heat of combustion of the fuel, r_0 is the stoichiometric fuel-oxygen ratio, $Y_{O_2}{}^0$ the initial mole fraction of oxygen, and $Y_{O_2}(t)$ the mole fraction of oxygen at time t in the test. The flow rate is determined from the pressure difference, ΔP, across a bi-directional probe located in the

centre of the duct, and the flow temperature, T_e, at the oxygen sampling point. The calibration constant C is determined from a 5kW methane burn, which uses the value $\Delta H_c/r_0 = 12.54$ kJ/kg.

4.5.4. Experiments

Cone calorimeter experiments were performed with the cone calorimeter at the Division for Building, Construction and Engineering (Highett), CSIRO, on the Dunlop polyurethane foams AA23-130 and ST32-80. One series of experiments was performed in accordance with the standard ASTM E1354-94, while another series of experiments was performed with a slight variation on the standard, whereby thermocouples were placed within the fuel sample to measure temperature histories. As the thermocouples protruding from the sample holder redistributed load away from the load cell, mass readings would be unreliable in this series of experiments, so were not recorded. All samples were prepared in accordance with ASTM E1354-94; that is, each sample measured 100×100×50 mm, and was conditioned to moisture equilibrium at a temperature of 23±3°C and relative humidity of 50±5%. All samples were then wrapped on five sides with aluminium foil, shiny side inwards, exposing only a single 100×100 mm face, and placed in a sample holder which exposed 94×94 mm of this face, before testing.

The experiments were undertaken by the CSIRO technical officer responsible for the operation and maintenance of the cone calorimeter, with the assistance of the author in sample preparation. The author specified the irradiances levels at which the fuel samples were to be tested, the location of the thermocouples, and the extent of the mapping of the radiant heat flux distribution produced by the cone heater.

Samples were tested both with and without a pilot spark, to obtain data on piloted ignition and autoignition. The samples were tested at four irradiances; 10, 15, 25, and 35 kW/m^2, with three repeats at each irradiance level tested. A summary of cases tested (those which yielded useable data) is shown in Table 4.4, with nomenclature for test numbers which appear in later figures.

Table 4.4 Cases tested in the first series of cone calorimeter experiments

	AA23-130 (Test Series 105)		ST32-80 (Test Series 106)	
Irradiance	**Piloted**	**Non piloted**	**Piloted**	**Non piloted**
10 kW/m^2	E, F, G		E, F, G	
15 kW/m^2	A, B, C, D		A, C, D	
25 kW/m^2	P *	L, M, N *†		†
35 kW/m^2	R, T *	Q *	N, O, P *	K, L, M *

* mass loss unavailable † no ignition at 25 kW/m^2, so lower irradiances not tested

The data obtained from the standard experiments included rate of heat released (RHR), mass remaining, rate of mass loss, effective heat of combustion (EHC), specific extinction area, carbon dioxide and carbon monoxide concentrations. EHC is the quantity given by RHR divided by the rate of mass loss, while specific extinction area is a measure of the optical thickness of the smoke. These were all measured as a function of time, with the exception of the tests noted in Table 4.4. In these tests, it was discovered later that the load cell was malfunctioning, thus rendering the mass data invalid, and hence the EHC invalid as well. However, an average value for EHC may still be obtained from these tests, as the total mass was measured before the tests, and the total heat released may be obtained by a summation of the heat release data over the duration of the test.

Due to the instrument failure occurring in the first series of tests, a second series of tests was performed to repeat the lost data for standard foam, as well as extending the range of irradiances tested. The series of tests is shown in Table 4.5

Table 4.5 Cases tested in the second series of cone calorimeter experiments

Irradiance	**AA23-130 (Series 147)**	
	Piloted	**Non-Piloted**
25 kW/m^2	A25, B25, C25, D25	
35 kW/m^2	A35, B35, C35	D35, E35, F35
50 kW/m^2	D50, E50, F50	A50, B50, C50
70 kW/m^2		A70, B70, C70

In the experiments conducted with thermocouples, the samples were prepared in the same fashion as the standard method samples. Three 1.5mm diameter K-type MIMS thermocouples were placed along the central symmetry axis of the cone at heights 250mm, 120mm, and 25mm above the fuel surface (the latter corresponding to the height of the bottom edge of the cone heater). These were intended to measure flame temperature of the burning sample. Two thermocouples were inserted 30mm horizontally into the fuel at a depth of approximately 25mm. The depth was only

approximate, as due to the flexible nature of the foam, any twisting force on the thermocouple could displace its position within the foam*. The thermocouples were placed horizontally to minimise temperature gradients close to the tip which may compromise their accuracy in measurements (isotherms in the fuel are expected to be horizontal planes due to the geometry of the combustion scenario). Thermocouples of two different diameters were used in the fuel: a regular 1.5mm diameter MIMS, and a 1.0mm diameter MIMS. A sixth thermocouple was also recorded in the tests: in some tests, it was located within the experiment chamber where it recorded ambient temperature, and in some it was located at the centre of the base of the fuel sample. Positions of thermocouples are shown in Figure 4.1.

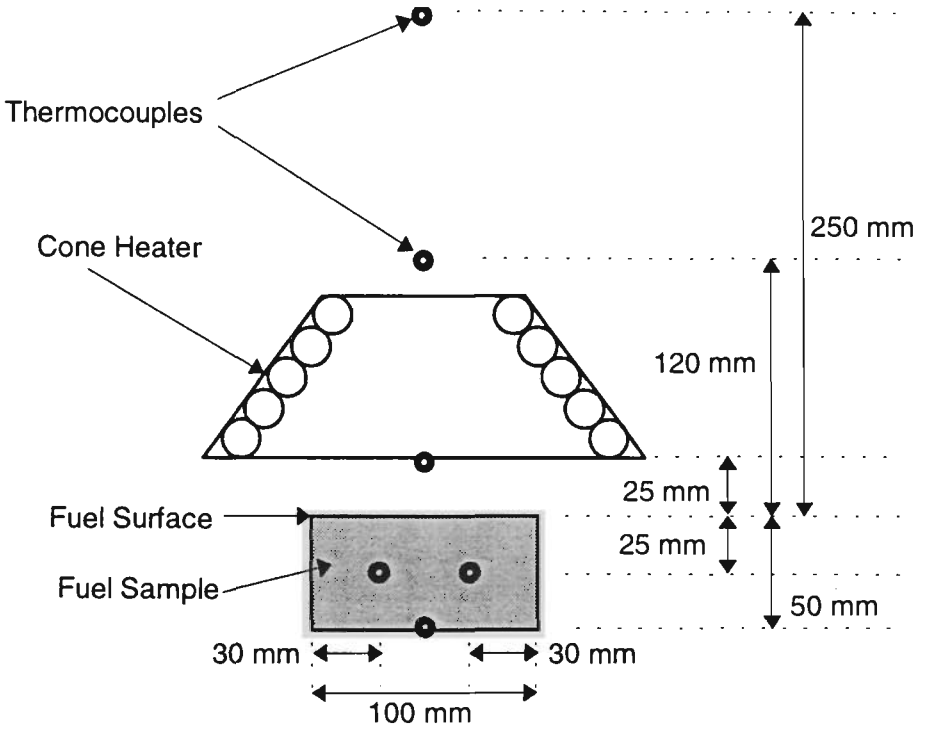

Figure 4.1 Position of thermocouples for cone calorimeter tests

As a preliminary exercise, the radiation from the cone heater was mapped in three dimensions, to investigate the findings of Vanspeybroeck et al[95] that the radiation drops with distance from the cone. The method undertaken to achieve this was to mark a piece of heat resistant tile with a grid, coat it with high emissivity paint, and position it on the load cell below the cone heater. This was to reduce the radiation reflected back to the cone. The heat flux meter normally used to confirm the cone heat flux setting was placed at the appropriate horizontal position above the painted tile. The distance between the flux meter and the cone was then adjusted to the desired height (an adjustment rail exists in the cone calorimeter apparatus which allows the cone heater itself to be raised and lowered). The cone heater was adjusted so that the heat flux meter read 25 kW/m^2 in the centre, at

* This is in contrast to rigid fuels such as wood, where the thermocouple may be accurately positioned by drilling a hole into the fuel.

a distance of 25mm below the cone heater. The flux was then read at six heights, namely at 25mm, 35mm, 45mm, 55mm ,65mm and 75mm below the cone heater. The flux was measured horizontally on a grid of 20mm increments, out to a distance of 60mm from the center on each side, for a total of 49 points on each horizontal plane. The meter was frequently returned to the central, 25mm height position, to that check the flux from the cone heater remained fixed at 25 kW/m^2. The mapping was done without the sample holder, since the metal mounting arm for the flux meter prevented positioning of the meter inside the holder.

The results of the heat flux map may be seen in Figure 4.2. At 25mm, corresponding to the surface of the fuel before any combustion or thermal degradation has taken place, it may be seen that the heat flux is quite uniform across the surface, and only decreased marginally at the points 60mm from the centre (most noticeable in the corners, which are at the greatest distance from the centre). As this is outside the sample area, this decrease is no cause for concern. However, at 35mm and 45mm below the cone heater, the flux is already dropping noticeably, and is decreasing more rapidly away from the centre. At 55mm, the flux at the centre is 20.3 kW/m^2, or 81% of the value at 25mm, dropping as low as 15 kW/m^2 in one corner of the central 80×80mm square, and even lower outside that. At 75mm below the cone, corresponding to the bottom of a standard 50mm thick sample, the flux is 16 kW/m^2 at the centre, and 10 kW/m^2 in one corner, which is respectively 64% and 40% of the surface flux. This not only confirms the reported decrease of radiant heat flux with vertical distance[95], but shows there is also an increasing non-uniformity in horizontal heat flux distribution.

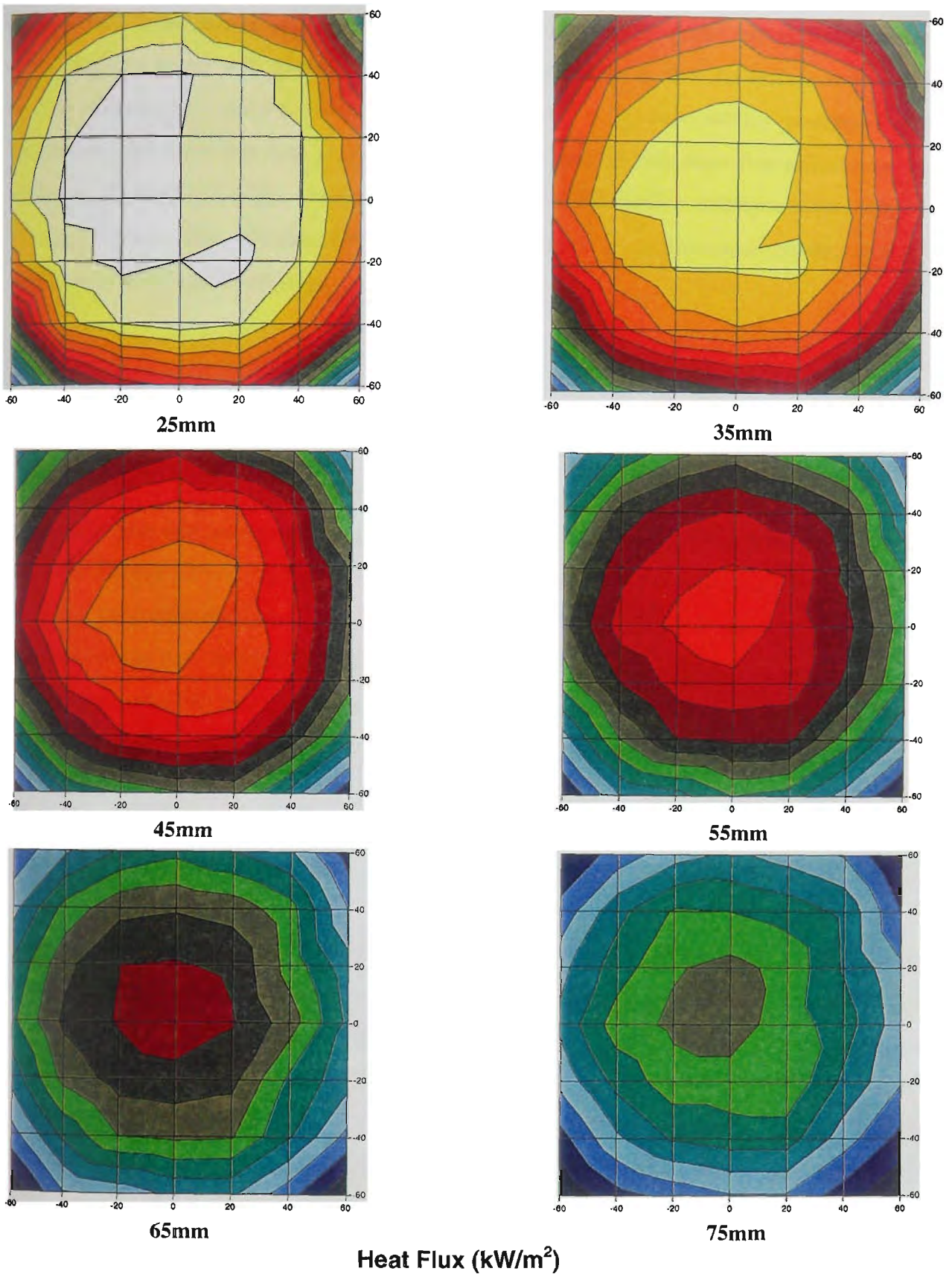

Figure 4.2 Radiation heat flux map beneath the Cone Calorimeter

An expected consequence of this heat flux distribution is that a sample undergoing combustion under the cone heater will pyrolyse more rapidly in the centre, so that the surface is expected to become increasingly concave as combustion progresses. A concave surface presents a greater surface area for mass loss than a planar surface, which may perturb mass flux calculations if the surface is assumed to be flat. Conduction of heat into the fuel surface no longer occurs only in the vertical direction. This will also affect any calculations based on experimental measurements if one dimensional combustion behaviour is assumed.

4.5.5. Results of Standard Tests

The results from two series of experiments are presented in this subsection. The first series of experiments was performed using imposed radiant fluxes in the range of 10kW/m^2 to 35kW/m^2. It was later discovered that the load cell had been malfunctioning in some of the tests, rendering the mass loss data unusable. Analysis of the remaining data was performed and certain trends noted, but it was found that the missing data was required to have greater confidence in the analysis. As a consequence, a second series of experiments was undertaken, to repeat the tests for which mass loss data was lost, and to extend the range of tested radiant heat fluxes up to 70kW/m^2.

4.5.5.1. First Series

Results for the 15kW/m^2 and 10kW/m^2 piloted ignition cone calorimeter tests on standard foam are shown in Figure 4.4 and Figure 4.5 respectively, while piloted ignition tests on retarded foam are shown in Figure 4.6. In all three figures, figure (a) shows the rate of heat release (RHR) as a function of time, figure (b) shows RHR as a function of the fraction of mass remaining, and figure (c) shows the effective heat of combustion (EHC) as a function of the fraction of mass remaining. Plotting these values as a function of mass remaining clarifies some of the trends in the data, particularly the EHC. At each end of the test, when mass loss rates are very small, the quotient of the heat release rate and mass loss rate is a very small number divided by a very small number, which produces an assortment of values of a range of magnitudes. Since this corresponds to the first few wisps of smoke at the start of the test, or the last few bubbles of tar at the end, such data is irrelevant for determining the combustion properties of the bulk of the fuel sample.

The tests at 10kW/m^2 and 15kW/m^2 irradiances were performed with the pilot spark in place above the fuel sample. Ignition occurred in a short space of time* for the 15kW/m^2 tests for both foams, and for the standard foam at 10kW/m^2. An unusual phenomena occurred for the retarded foam at this irradiance, as shown in Figure 4.3. Ignition occurred at about 40 seconds, and combustion proceeded for a further 10 seconds, producing a buildup of tarry products on the surface, after which the flames died down for a further 10-15 seconds, eventually extinguishing in two cases (Tests 106E and 106F) leaving a charred crust on the surface of the fuel. In these two cases, the fuel had regressed to approximately half its original depth in the centre (less in the corners), and lost approximately 15% of its original mass. However, in the third case (Test 106G), combustion continued, the flame appearing to eventually breach this crust, after which burning intensity increased again and combustion continued to completion.

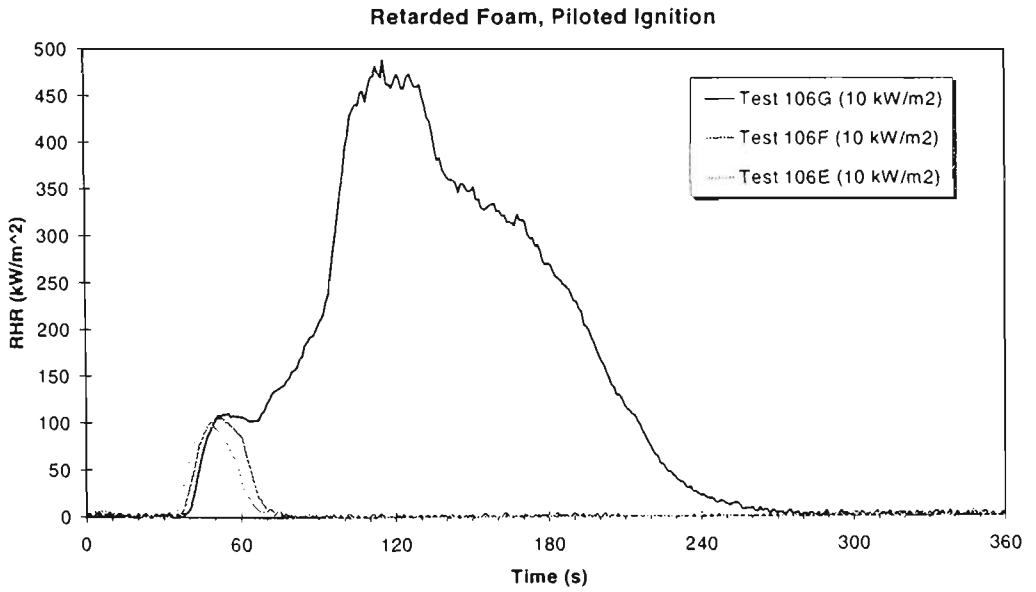

Figure 4.3 Rate of heat release of retarded foam at 10kW/m^2

Comparing this test at 10kW/m^2 (Test 106G) with the two tests at 15kW/m^2 (Tests 106A and 106D) in Figure 4.6(a), it can be seen that the RHR of the three samples shows quite different time histories, whereas when the RHR is plotted as a function of mass remaining, as shown in Figure 4.6(b), the histories are very similar. This suggests that the heat release behaviour of the fuel is dominated more by its combustion history than its heating history. In other words, while RHR is a temporal phenomenon ("rate" being the operative term), it is a material property of the fuel.

* As there was no shielding of the sample from the cone heater, ignition occurred as soon as the pilot spark was applied a few seconds after placement of the sample.

The effective heat of combustion (EHC) is shown in Figure 4.4(c), Figure 4.5(c) and Figure 4.6(c). In all three cases, it is a nearly linear function of fraction of mass, the value of which increases as the combustion progresses. This may be due to the tar and char having a higher heat of combustion than the more readily volatilised products of decomposition of the foam. As tar and char build up as combustion proceeds, they form a greater proportion of the remaining mass, so the amount of heat released per unit mass of remaining fuel will likewise increase.

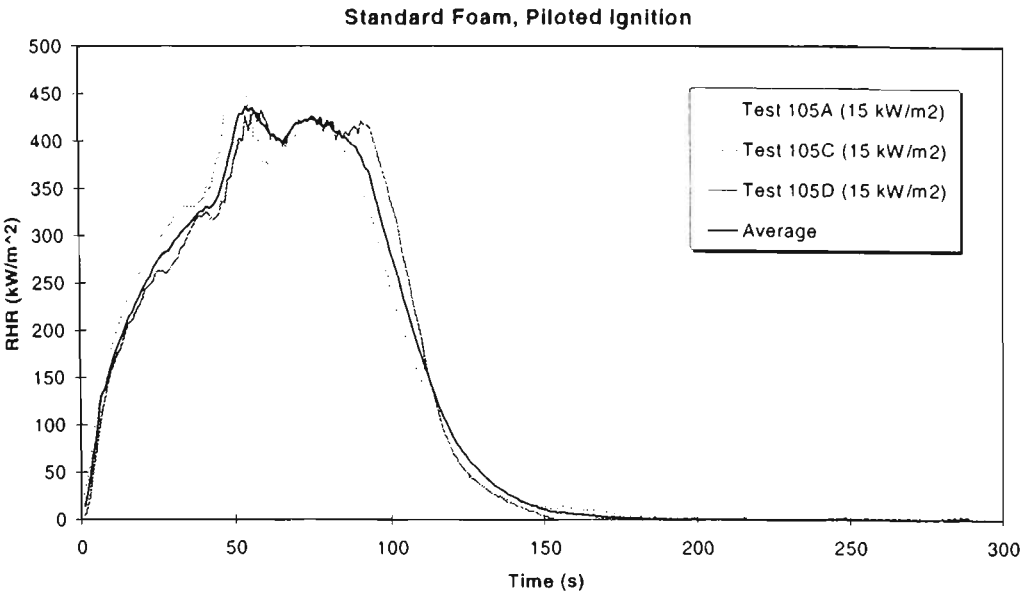

(a)

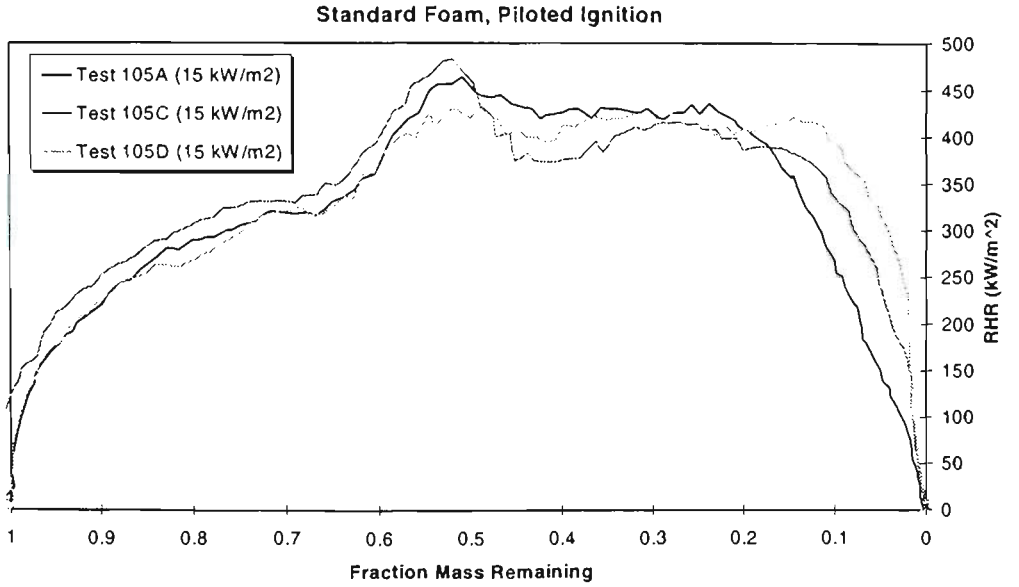

(b)

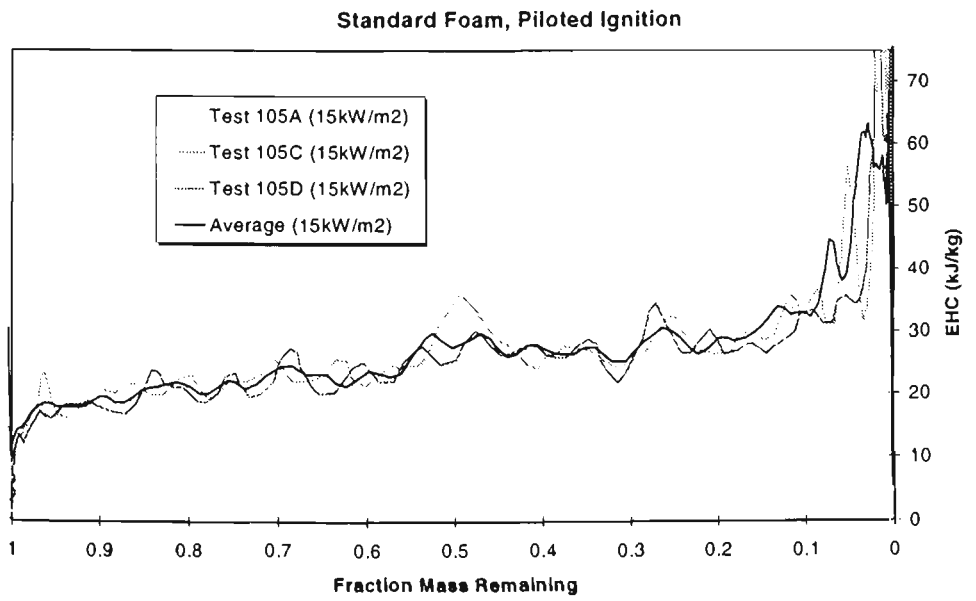

(c)

Figure 4.4 Results of 15 kW/m^2 cone calorimeter tests on standard foam

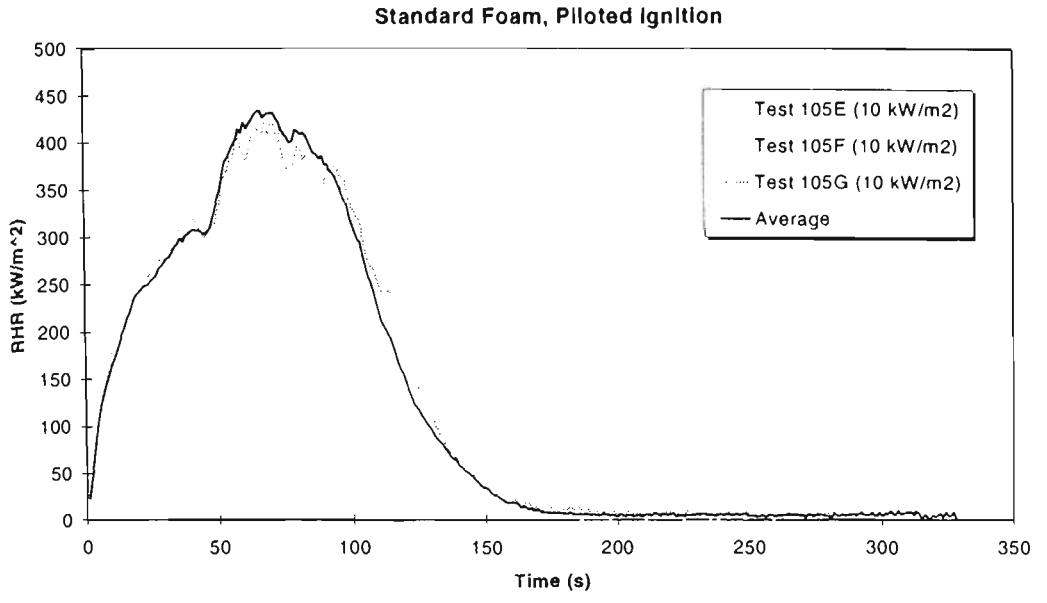

(a)

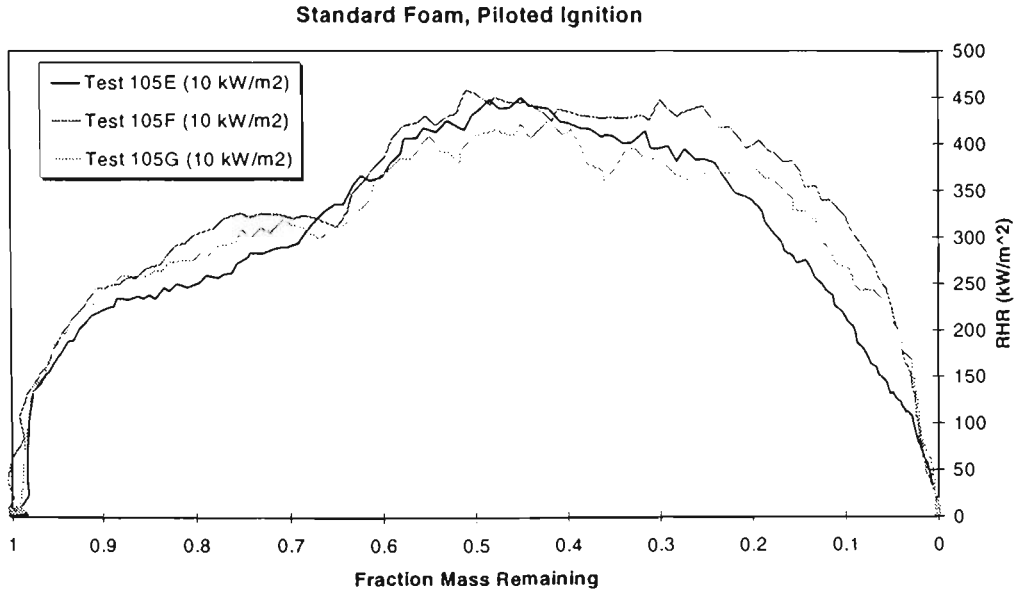

(b)

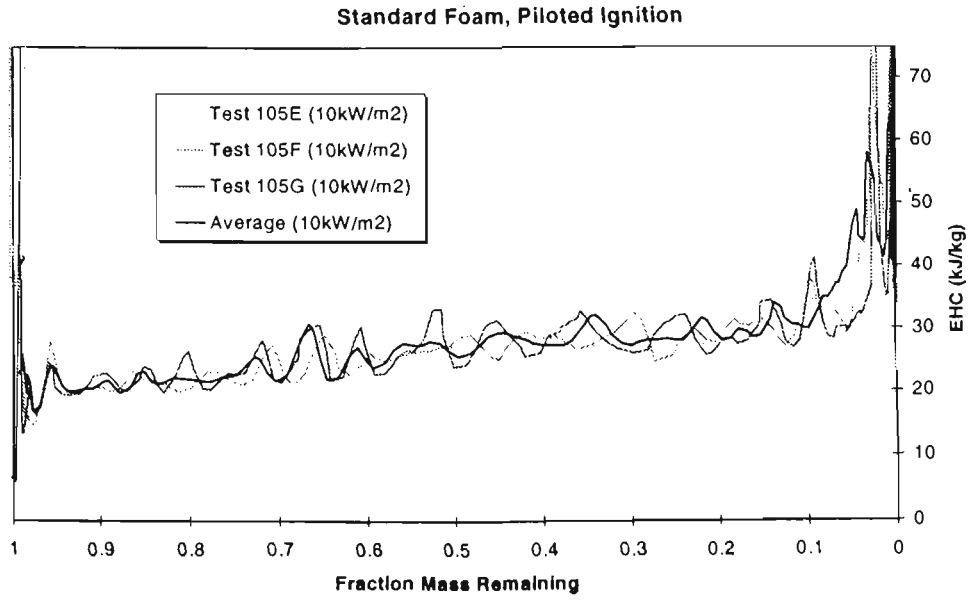

(c)

Figure 4.5 Results of 10 kW/m^2 cone calorimeter tests on standard foam

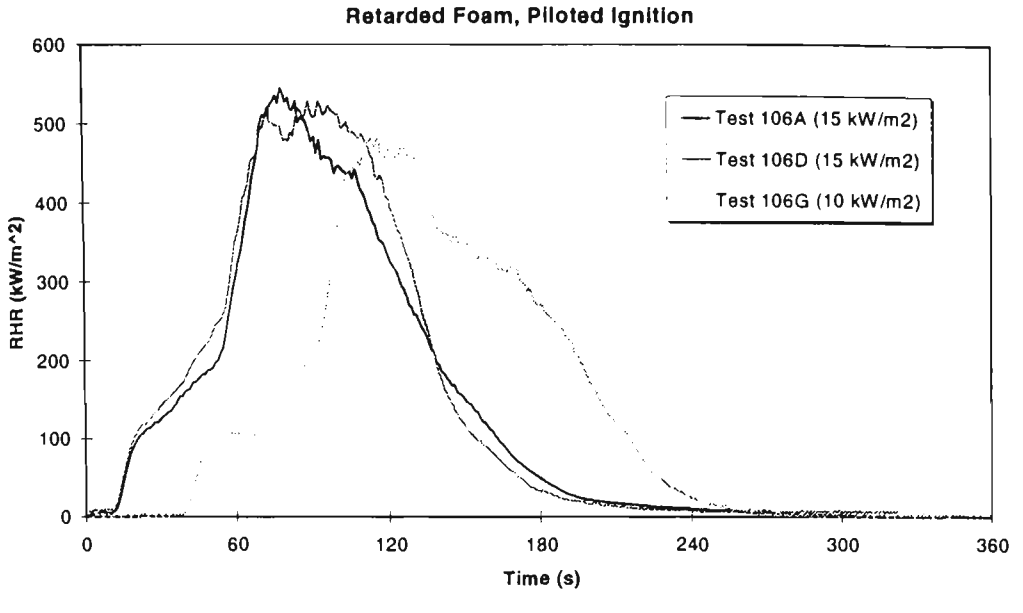

(a)

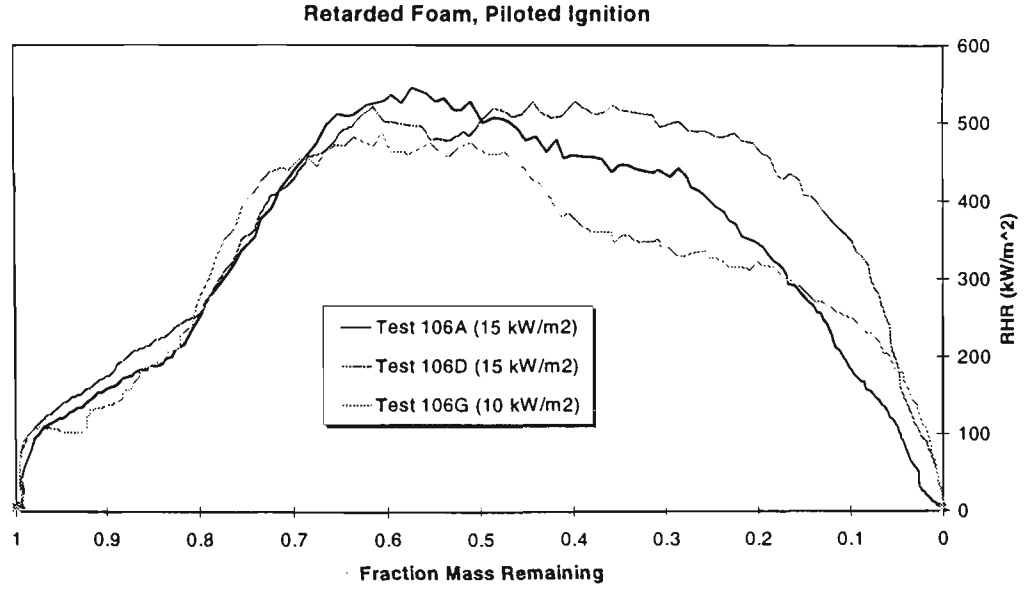

(b)

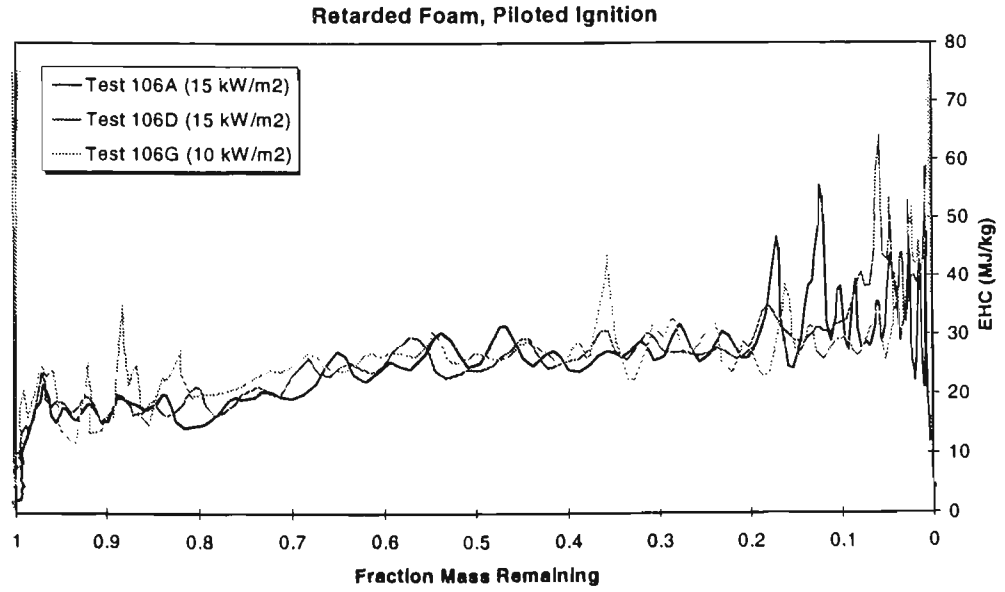

(c)

Figure 4.6 Results of cone calorimeter tests on retarded foam

4.5.5.2. Second Series

A second series of tests on standard polyurethane foam was performed with two aims: to repeat the experiments in the first series for which failure of the load cell resulted in no record of mass loss data, and to extend the range of tested values to higher irradiances, so as to provide extra data for linear fits of combustion quantities which depend on the applied heat flux. The second series differed from the first series only in that a water-cooled shield had been installed in the cone calorimeter, which can be placed between the cone heater and the sample, to prevent heating of the sample before the ignition spark is in place.

There are a few additional features of note in these tests. The higher heat fluxes (Figure 4.8, Figure 4.9, Figure 4.10, Figure 4.11, Figure 4.12), with corresponding high mass loss rates, resulted in a rather large amount of experimental noise in the readings of the mass load cell. This is most obvious in the graphs of heat release rate and effective heat of combustion plotted against the mass remaining. Since the mass remaining is subject to noise, the graphs are somewhat chaotic. The exception was the experiments conducted at 25 kW/m^2, which were mistakenly, although as it transpires, fortuitously, sampled at 5 second intervals rather than 1 second intervals. The resulting smoothing shows the trends in the data better.

As was determined in the first series of tests, non-piloted ignition does not occur at an irradiance of 25 kW/m^2, so this case was not tested. Also, the presence or absence of a pilot spark had little effect on the ignition time of the fuel at an irradiance of 50 kW/m^2 (ignition occurred at 2 seconds in both cases), so piloted ignition was not tested for an irradiance of 70 kW/m^2. It is interesting to note that ignition time actually *increased* as the irradiance increased from 50 to 70 kW/m^2. This surprising result may be due to the particularly rapid melting and regression of the fuel immediately the water-cooled shield was removed and the fuel exposed to the cone heater. As shown in Figure 4.2, the fuel surface would not need to regress far for the applied heat flux to have dropped to 50kW/m^2. However, a fuel sample with a layer of molten tar would be harder to ignite than a fresh sample, hence the increase in ignition time.

Rapid pyrolysis before ignition was also responsible for the short plateau at the beginning of the non-piloted 35kW/m^2 RHR versus mass remaining chart (Figure 4.9b). The graph shows that some 10% of the mass was lost before ignition occurred.

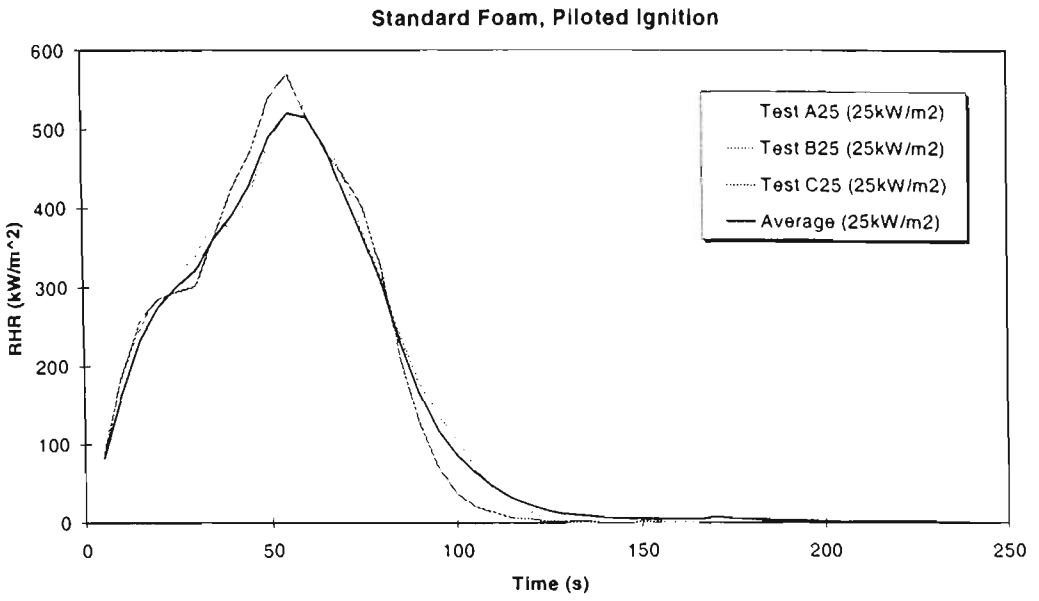

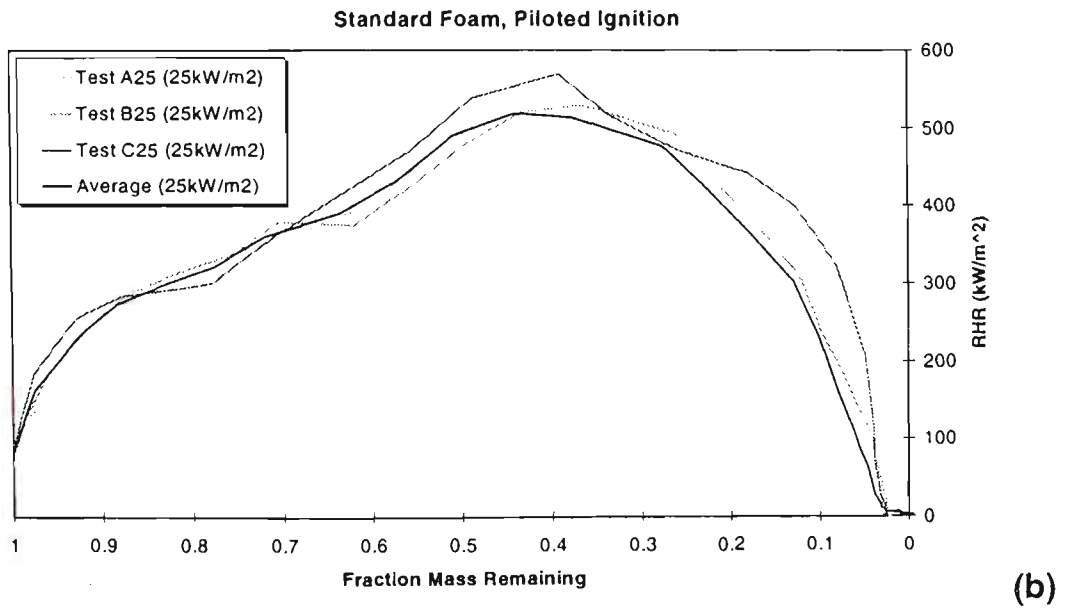

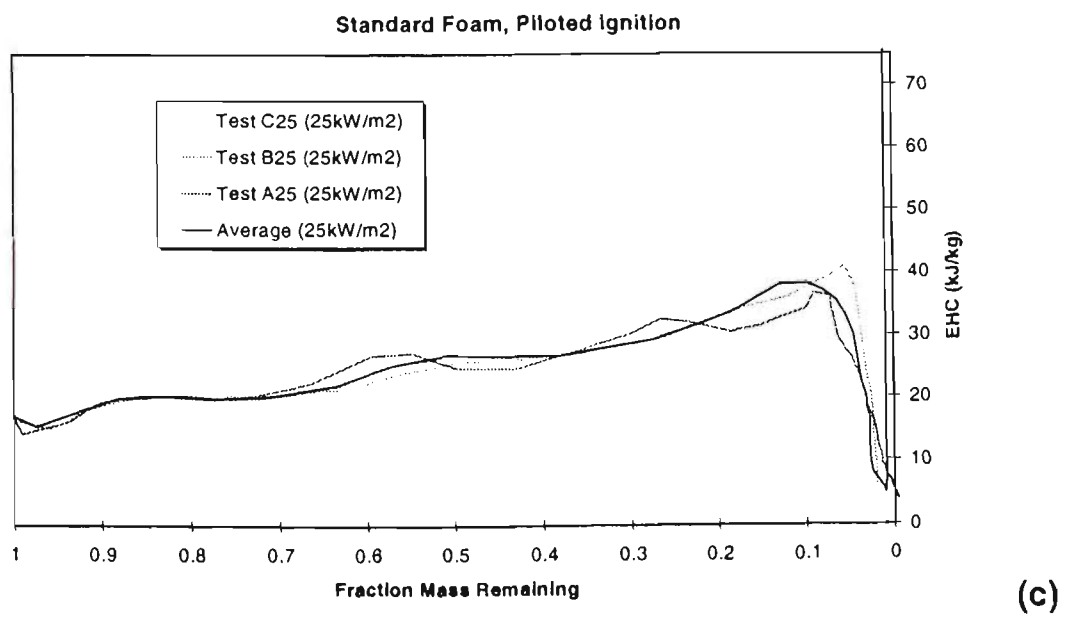

Figure 4.7 Results of 25 kW/m^2 piloted tests on standard foam

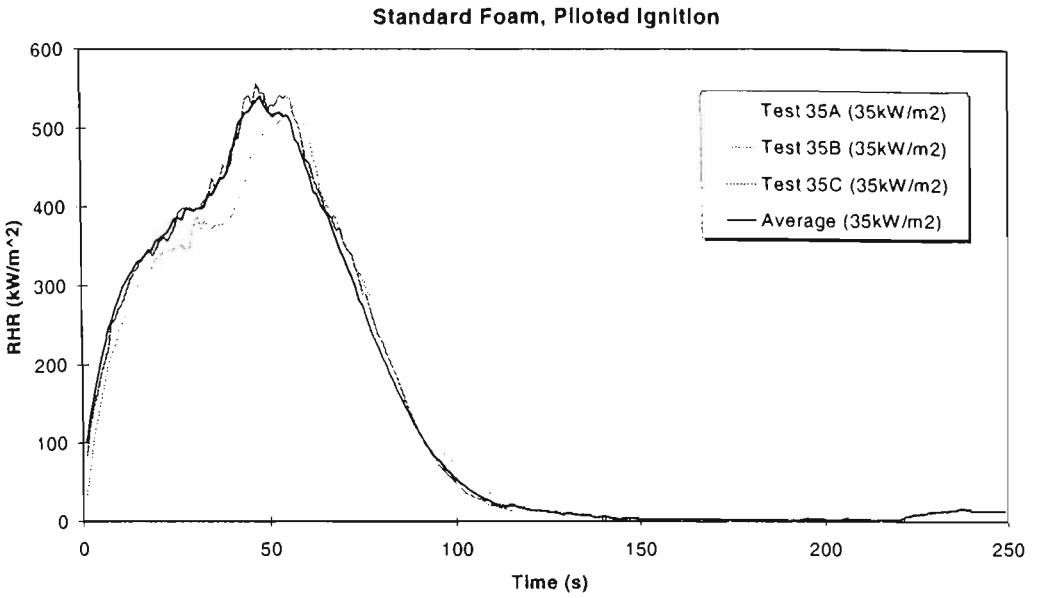

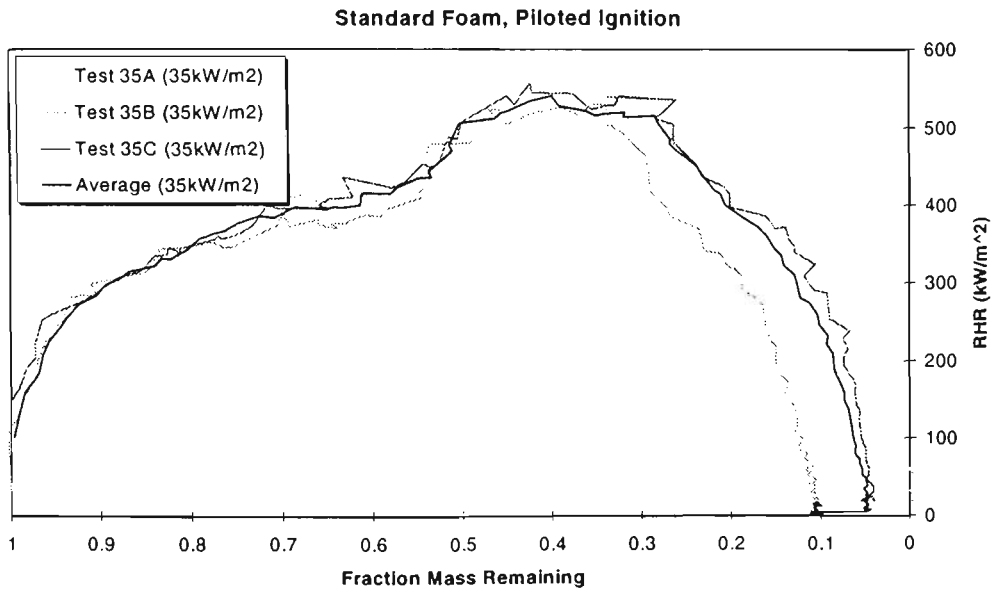

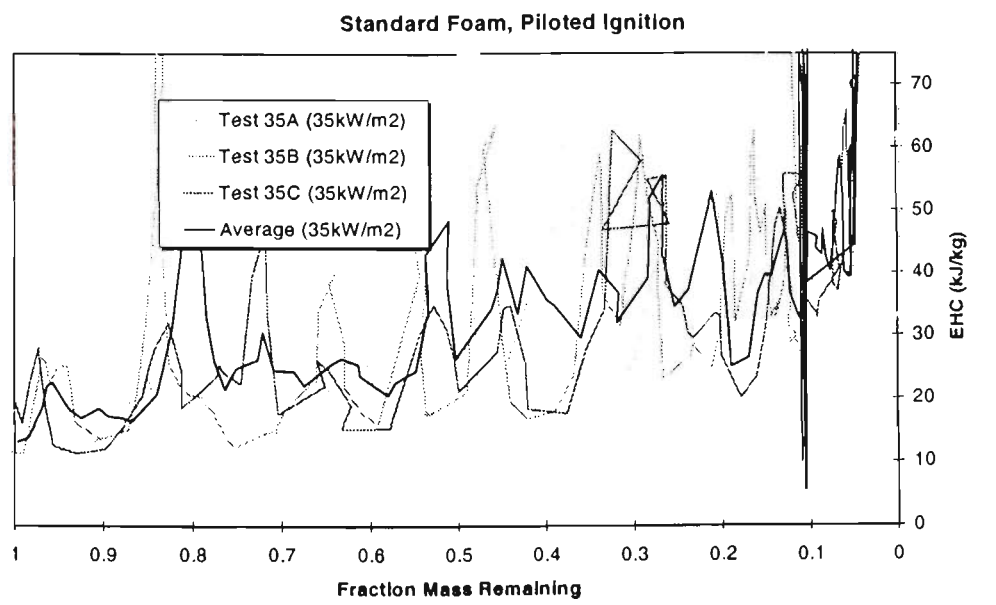

Figure 4.8 Results of 35 kW/m^2 piloted tests on standard foam

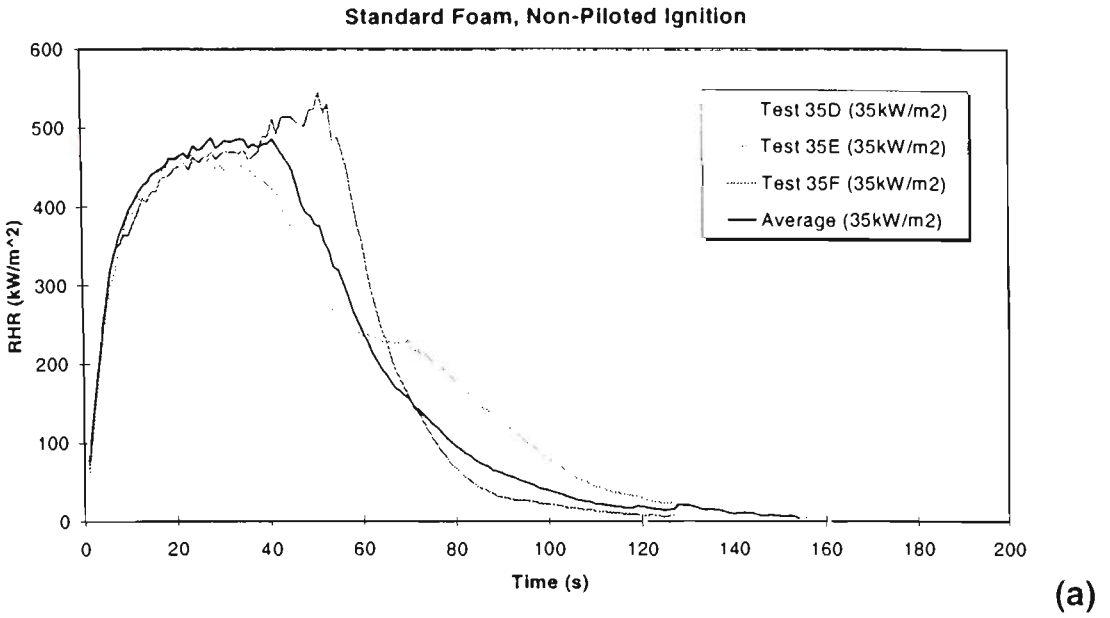

(a)

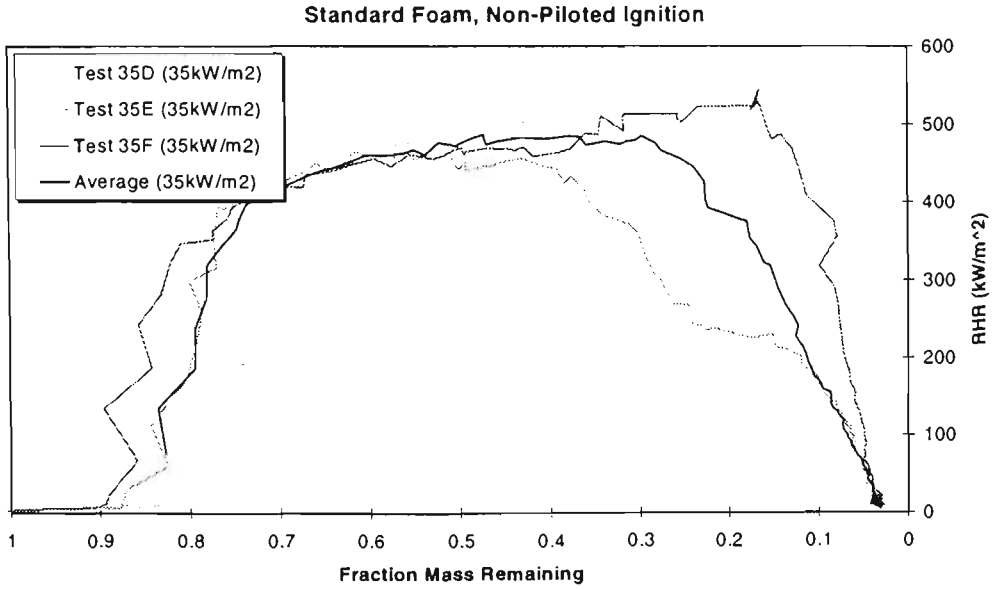

(b)

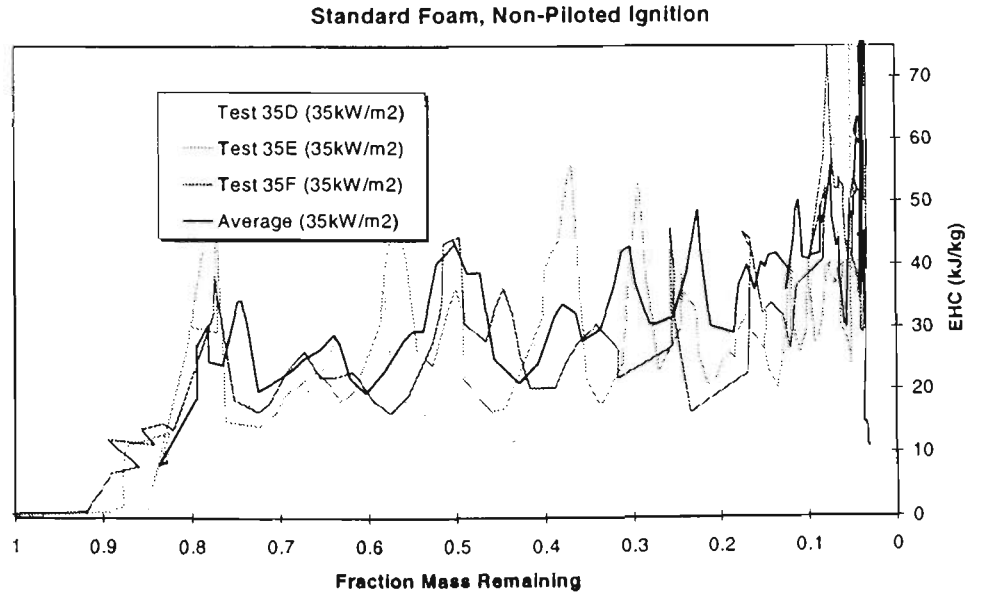

(c)

Figure 4.9 Results of 35 kW/m^2 non-piloted tests on standard foam

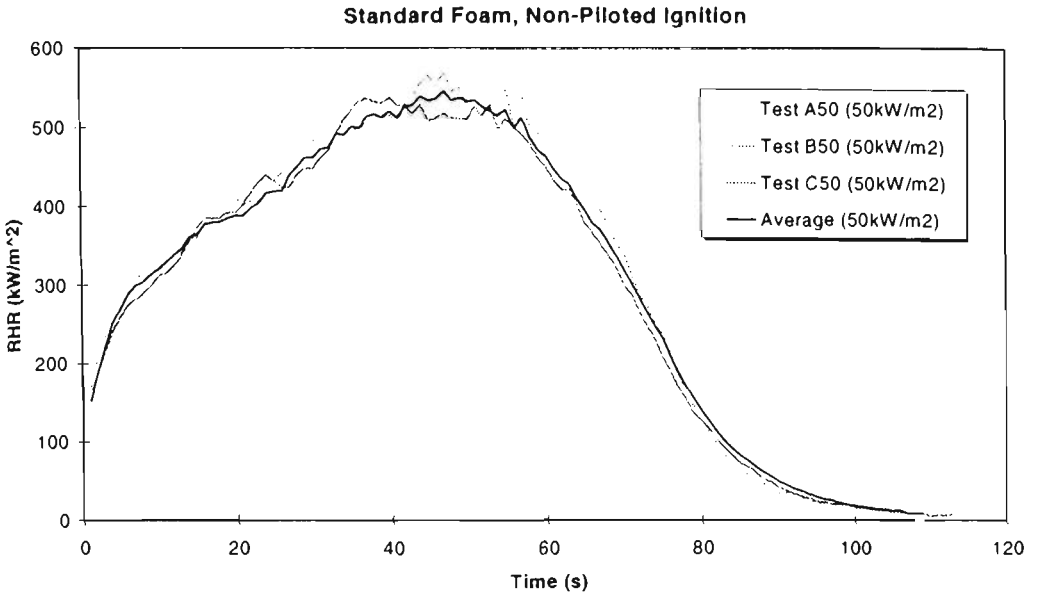

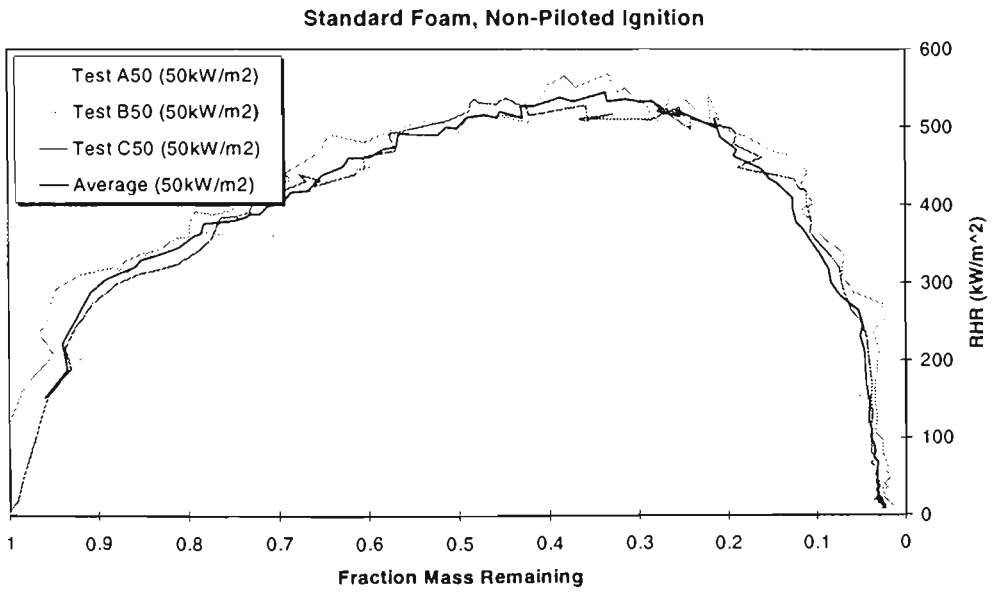

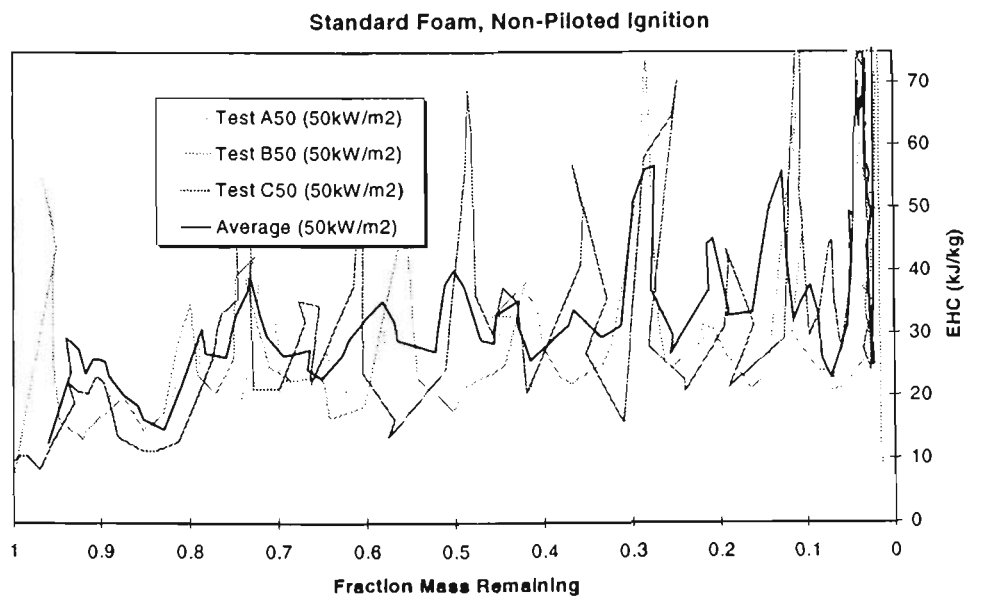

Figure 4.10 Results of 50 kW/m^2 non-piloted tests on standard foam

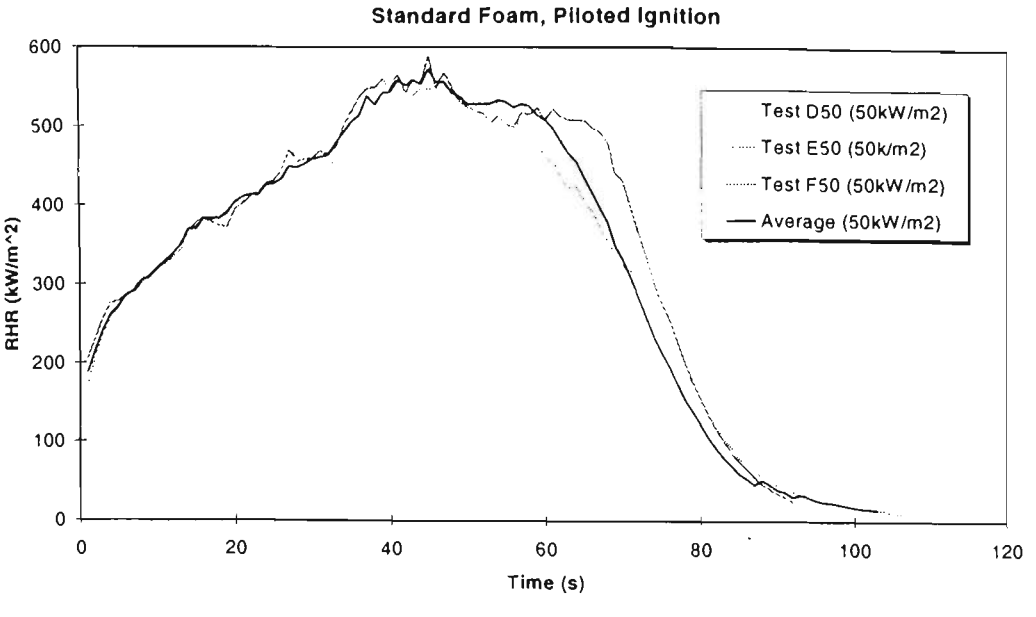

(a)

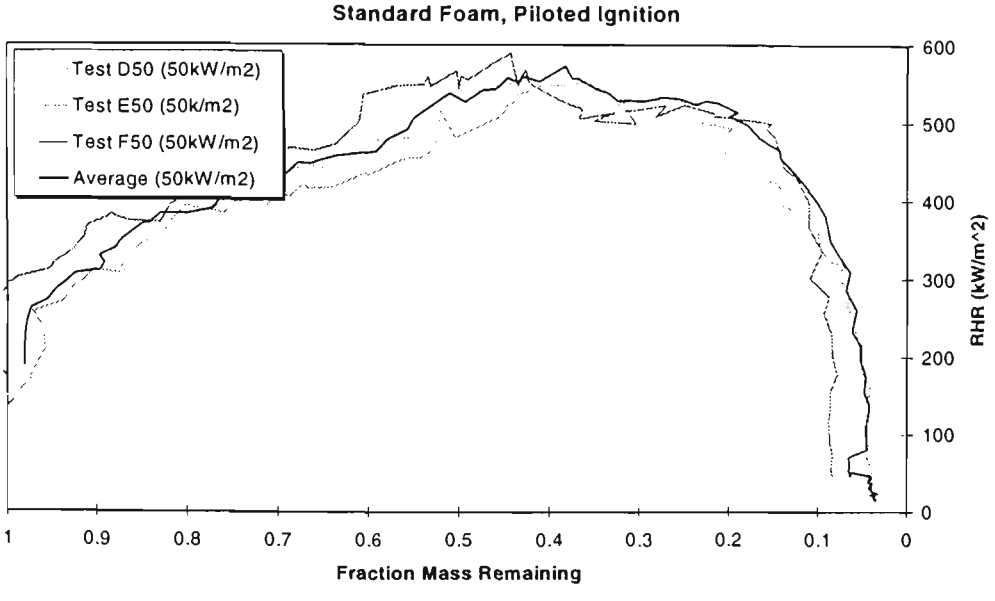

(b)

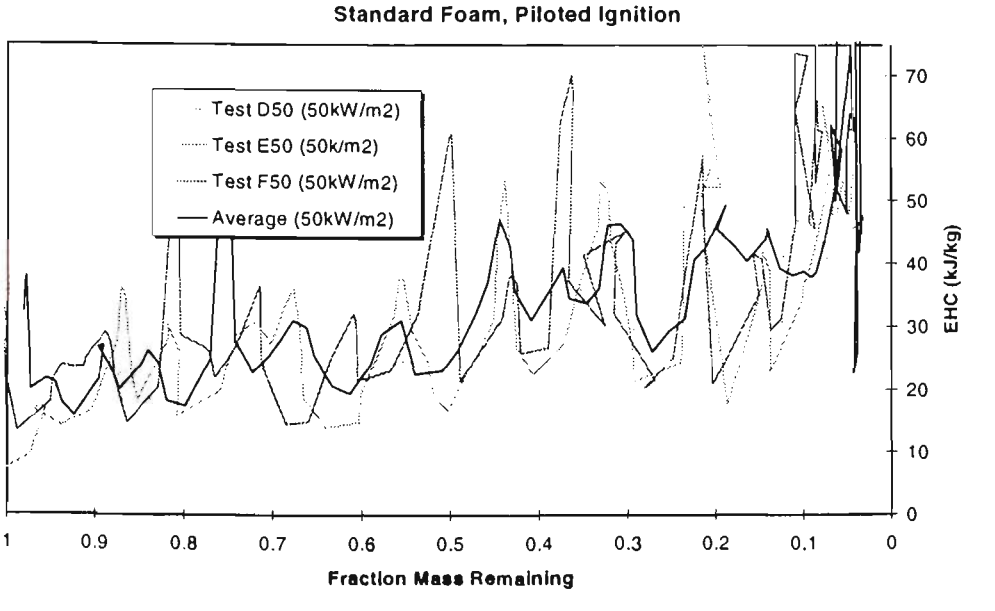

(c)

Figure 4.11 Results of 50 kW/m^2 piloted tests on standard foam

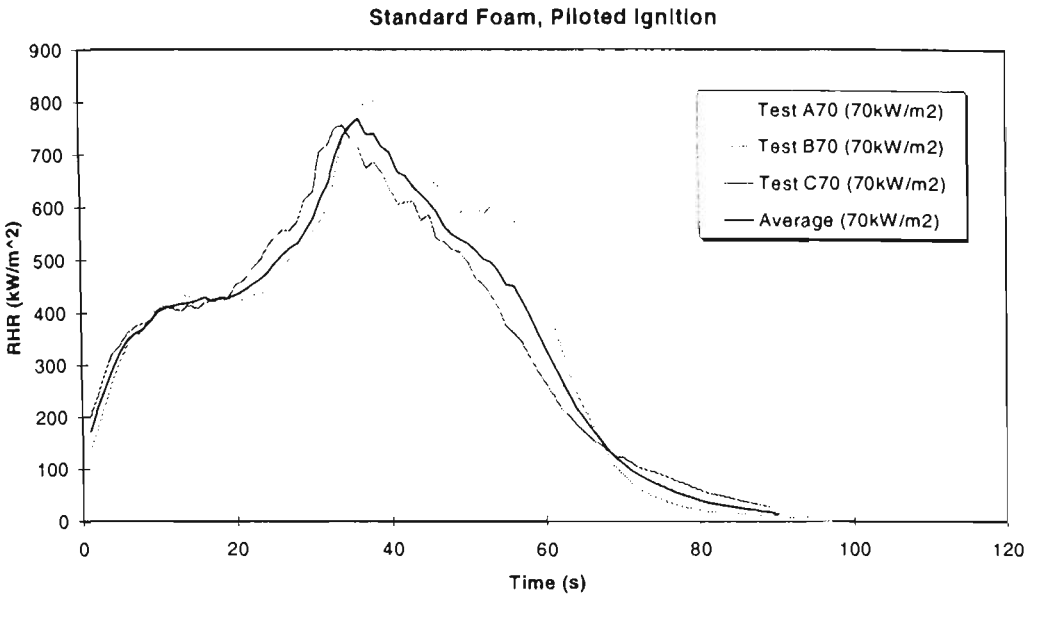

(a)

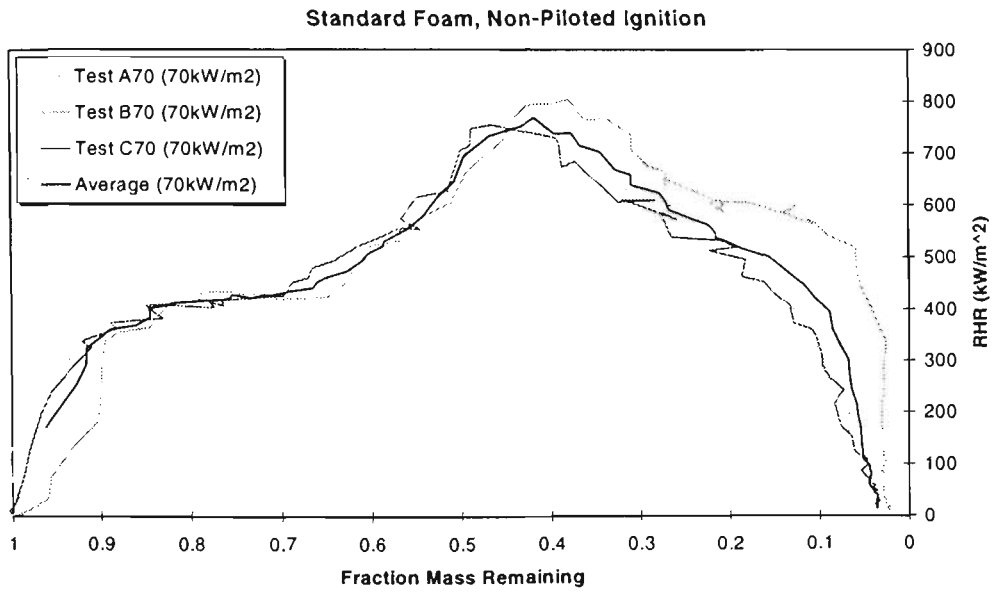

(b)

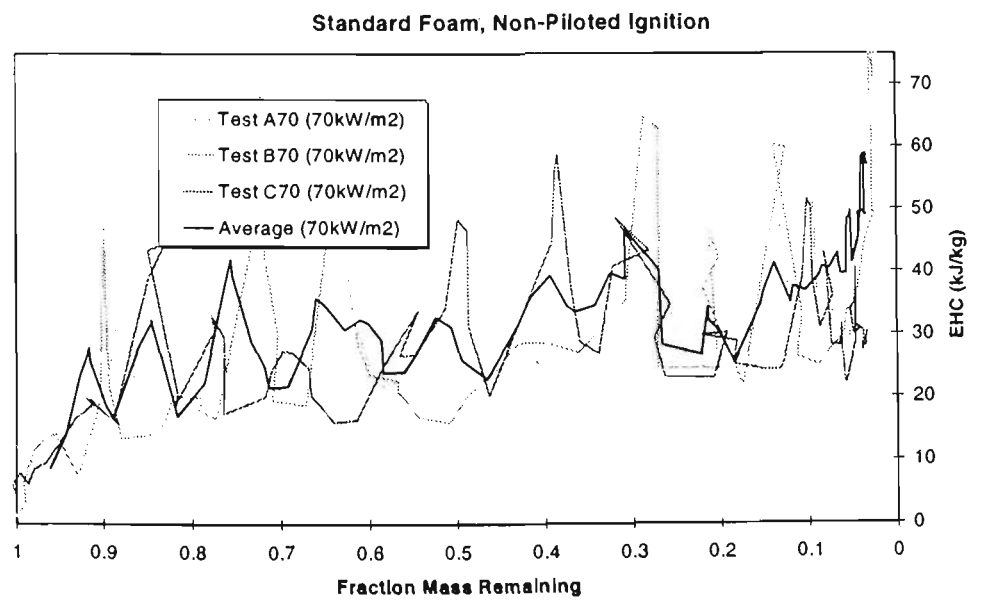

(c)

Figure 4.12 Results of 70 kW/m^2 non-piloted tests on standard foam

4.5.5.3. Analysis of Results

The average EHC is calculated by dividing the total heat released, as calculated by oxygen consumption, by the total mass loss. Values for tests of both standard and fire retarded foam are shown in Figure 4.13, including values for tests performed at 35kW/m^2 in which the load cell failed. Values for fire retarded foam range from 24 to 26 MJ/kg over all irradiances for piloted ignition, while for autoignition of the retarded foam, the values were much lower, around 16 to 18 MJ/kg. The explanation for this is that autoignition of these foams took some time; between 180 and 240 seconds after exposure to the radiant flux. By this time the samples were little more than a molten mess in the bottom of the holder, and a significant amount of mass had already been lost via pyrolysis without igniting and producing heat. As a consequence, when ignition eventually occurred, only the remaining mass released heat, so that the total heat released was less than if the entire mass had undergone combustion. This phenomenon was also observed to a lesser extent for the non-piloted tests of standard foam at 35kW/m^2. The ignition time for these tests was on average 30s, by which time a significant amount of fuel had already undergone pyrolysis.

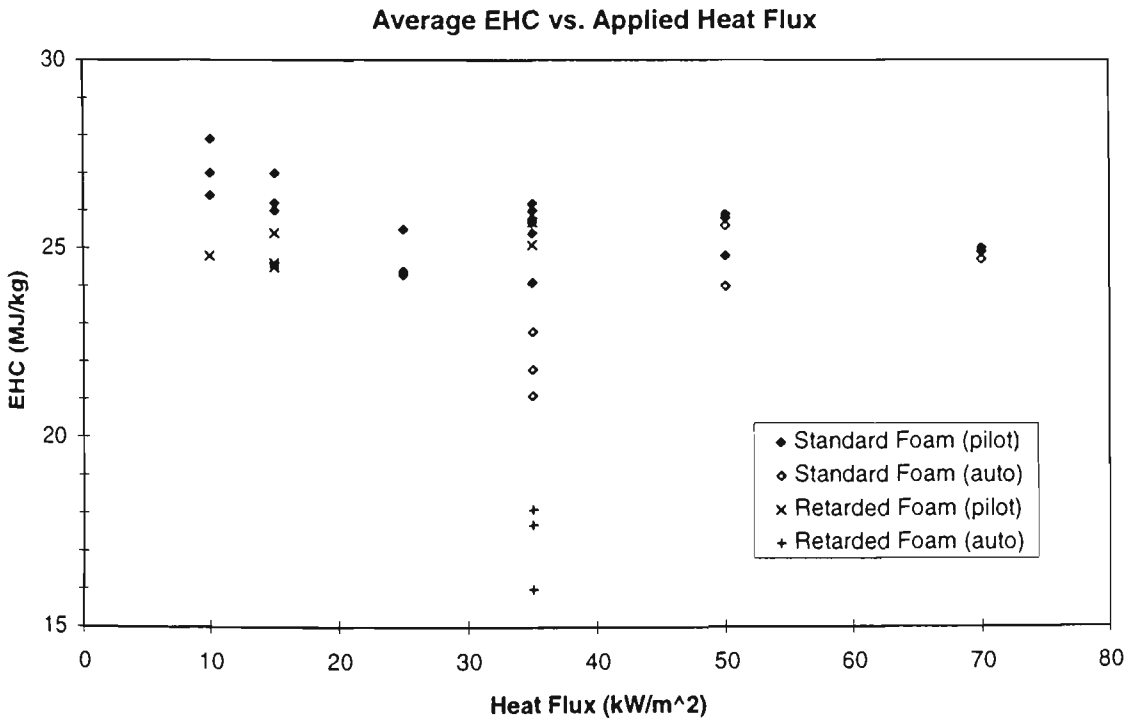

Figure 4.13 Average effective heat of combustion versus applied heat flux

The values of EHC for standard foam show a greater variance over the range of applied heat fluxes than do the values for fire retarded foam (ignoring the autoignition values of the latter). For piloted ignition, the value appears to decrease with increasing applied heat flux. This is somewhat puzzling, as the expectation would be that applying more heat would reduce heat lost from the

flame, and a hotter flame would produce more efficient combustion, resulting in increased values of EHC. A possible cause of the decrease is that the increased heat flux produces a higher flux of volatiles from the surface. The resulting flame may be fuel rich, and combustion therefore less efficient. Whatever the case may be, the heat of combustion is difficult to estimate accurately from the available data, since it appears to be dependent on the applied flux and burning conditions. Taking the average for all the tests results in a value of 25.7 MJ/kg for standard foam, and 25.1 MJ/kg for retarded foam.

As none of the RHR curves show any region of steady burning, the heat of volatilisation is calculated by considering the peak RHR. The peak RHR for the tests is shown in Figure 4.14. The retarded foam data shows no obvious linear relationship with applied heat flux, whereas a linear fit is shown for the standard foam. The solid line in Figure 4.14 shows the best fit as determined from linear regression. The gradient of this line is given[96] by $\Delta H_c/L_v$, where ΔH_c is taken to be the value 25.7 kJ/kg derived above. The slope of the solid line in Figure 4.14 is 4.71, which corresponds to a heat of volatilisation of 5.46 MJ/kg. This is considerably greater than the value of 1.22 MJ/kg given by Tewarson and Pion[70].

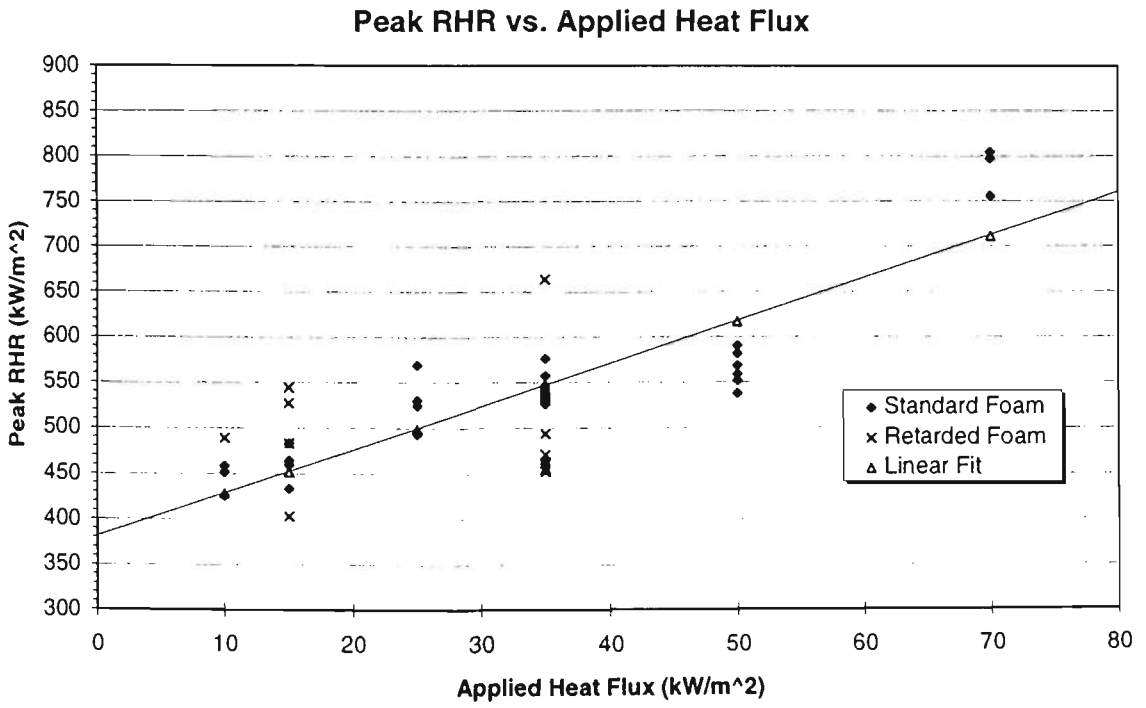

Figure 4.14 Peak rate of heat release versus applied heat flux

The peak heat release is a transient value, and therefore subject to experimental noise. Noting that the profile for rate of heat release versus mass remaining is similar for all irradiances, the value of RHR at key "milestones" in the mass loss history (rather than just at the peak) are examined in Figure 4.15. Each series corresponds to a particular fraction mass remaining value, from 0.1

through to 0.9 (1.0 and 0.0 naturally corresponding to zero). The average heat release rate for a given irradiance is plotted for each of the fraction mass remaining value. The results appear at a glance to show similar trends to the peak release rates.

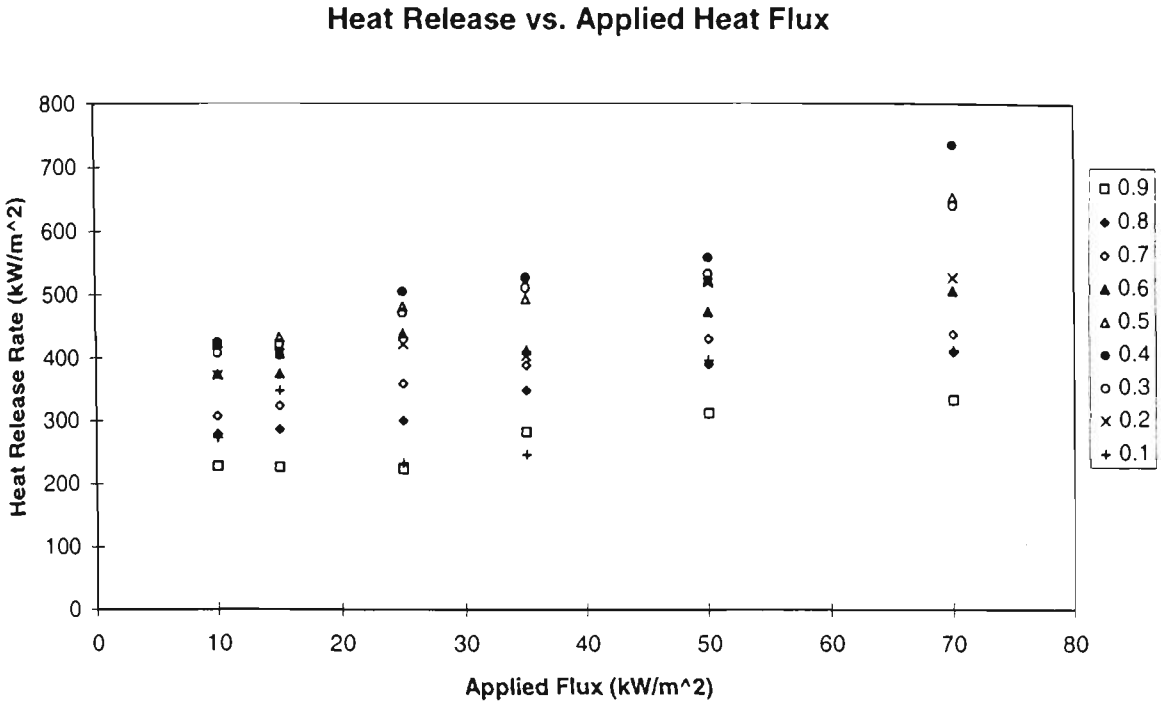

Figure 4.15 Heat release rate versus applied heat flux at various mass remaining values

Linear regression of each series leads to the chart shown in Figure 4.16. The open circles represent the slope of the regression lines, and therefore the relative value of the inverse of heat of volatilisation, as a function of mass remaining. The value of the slope is a little over 2 for most values, apart from a peak of almost 5 when a fraction of 0.4 of the mass of the fuel sample remains. These values correspond to a heat of volatilisation of around 10 MJ/kg for most of the burning history of the mass sample, dropping to around 4 MJ/kg at 0.4 mass remaining. Overall, the values of heat of volatilisation are even higher than that calculated using the peak heat release.

The intercepts of the regression lines are represented by the filled diamonds in Figure 4.16. These correspond to the theoretical RHR versus mass remaining curve for a sample subject to no external heat flux.

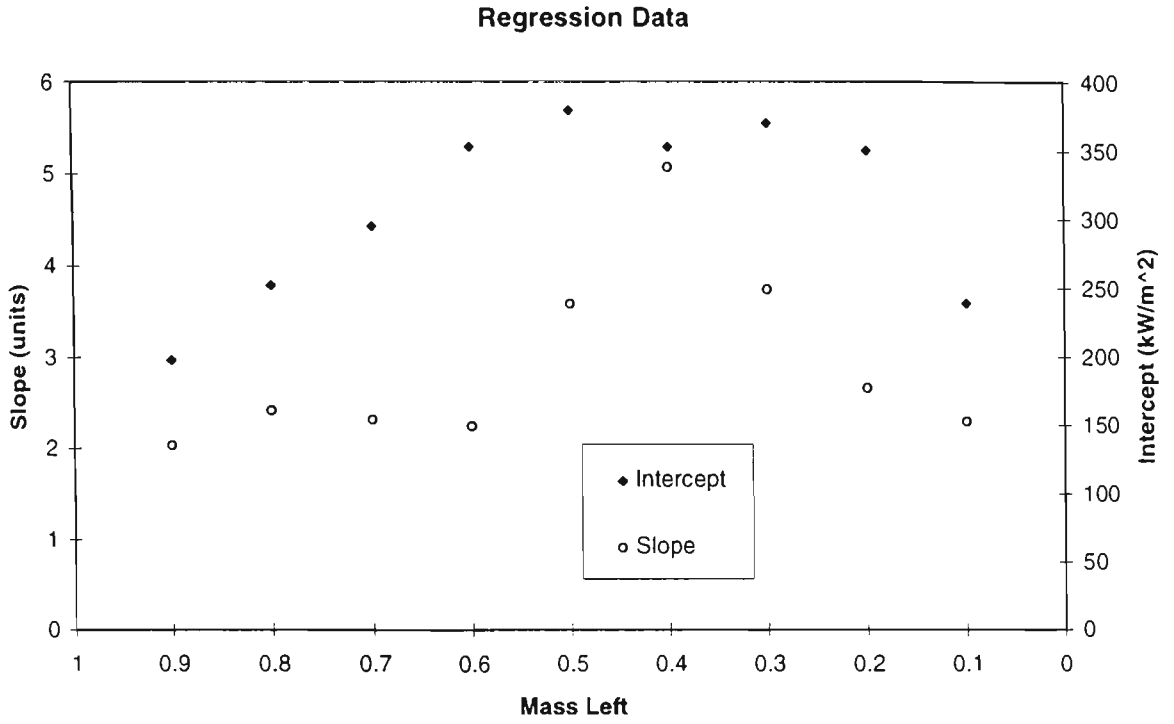

Figure 4.16 Regression data for the series shown in Figure 4.15

Tests without the pilot spark were performed on both foams at an irradiance of 25kW/m^2, but ignition did not occur in either instance. Similarly, neither fuels ignited with the pilot spark operating at an irradiance of 5 kW/m^2. A series of experiments was performed to determine the critical ignition flux for both types of fuel and both types of ignition. The critical flux was defined as the flux where two or three samples out of three ignited, and one or no samples out of three ignited at an irradiance 1kW/m^2 lower than the critical flux. A time limit for ignition was set at 600 seconds, after which the test was terminated and the fuel deemed to have not ignited. Adhering to these criteria, the critical flux for piloted ignition was found to be 7kW/m^2 for standard foam and 8kW/m^2 for fire retarded foam, while the respective limits for autoignition were 28kW/m^2 and 26kW/m^2. However, these figures cannot be given without some qualification.

In the vicinity of critical flux for piloted ignition at 7kW/m^2, relatively little vapour is given off by the fuel surface, and thermal degradation only becomes visibly obvious after several minutes. However, rather than being obvious over the whole surface, it first becomes noticeable directly beneath the pilot spark. This suggests that the spark may be responsible for locally increasing the heat input to the fuel surface, so that the true critical heat flux may be slightly higher. However, the effect is probably not major, and in any case, it is nearly impossible to introduce a heat source to fuel vapours which does not likewise impart heat to the fuel surface.

Of greater concern is the determination of critical flux for autoignition. At the more elevated heat flux in the vicinity of 26kW/m^2, the fuel undergoes significant melting and surface regression as well as volatilisation. By the time ignition occurs, the surface has often receded by a significant amount. Considering the changing heat flux as shown in Figure 4.2, this corresponds to quite a different flux to that at the surface of the virgin fuel. In the case of the fire retarded foam at 26kW/m^2, the situation was extreme. The fuel underwent thermal degradation and melting, and eventually reduced to a small amount of smouldering tar at the bottom of the holder. Then, between 540 and 600 seconds after application of the flux, this remaining tar ignited! There was only sufficient fuel remaining for a few seconds of combustion. What can be concluded from this particular test is uncertain, except to say that strictly adhering to a prescribed method can sometimes produce meaningless results. However, it is not clear how to better define the critical flux criterion for fuels such as polyurethane foam which readily melt and regress when exposed to a strong heat source. A shorter time limit, or a limit on surface regression, may better constrain the criteria so that a figure for critical heat flux may be stated with greater confidence.

Ignition times for each of the tests were recorded. It was anticipated that Equation 4.5 would be used to calculate the surface temperature rise, since thermal inertia of each foam is known, and externally applied heat flux and ignition time was readily measured. However, for the first series of tests, there was a delay between exposing the surface of the fuel to the heat flux and applying the pilot spark, as there was no shielding mechanism employed in these tests. For an irradiances of 35 kW/m^2, this delay time was significant, as the surface ignited very soon (within a few seconds) of the spark being brought into place. For the second series of tests, shielding of the sample was employed, and overall higher irradiances were tested. Ignition times were still found to be very short, and therefore subject to error in measurement. As noted earlier, for very high heat flux values, rapid surface regression due to melting and volatilisation actually delayed ignition.

At the other end of the scale, an irradiance of 10 kW/m^2 is too close to the critical heat flux (7 kW/m^2 for standard foam and 8 kW/m^2 for retarded foam) for the ignition time to be strictly useable. There is also the issue of surface regression and the subsequent variation in applied heat flux to take into account. Naively ignoring these factors, the figures for ΔT_{ig} as obtained from Equation 4.5 are around 2000K for piloted ignition of standard foam, and 1800K for piloted ignition retarded foam, which are significantly higher than the expected values of around 550K.[70] This is of some concern, and suggests that the methodology for measuring ignition time of polyurethane foam, and presumably other expanded thermoplastics, needs to be re-examined[99].

4.5.6. Results of Temperature Tests

In these tests, the aim is to obtain temperature data in the flame region for use in empirical combustion models, and within the fuel to verify the solid heat conduction submodel of the flame spread model. Thermocouples were used for this purpose as they are the most readily available and often used (and abused) instrument. However, there is always a degree of contentiousness about what exactly is being measured by a thermocouple, especially in situations of high radiant heat flux. This issue applies here, and there are a few other issues which were highlighted by these tests.

The first test was performed on a sample of retarded foam at an irradiance of 50 kW/m^2, without a pilot spark, and temperatures recorded at the locations shown in Figure 4.1. A temperature history of the six thermocouples for this test may be seen in Figure 4.17(a), with the temperature history for the actual duration of combustion of the sample shown in Figure 4.17(b). The recording of temperature commenced with the switching on of the cone heater, which reached its operational band by 500s. What is immediately apparent at this point is that the three thermocouples above the fuel surface read elevated temperatures, particularly the thermocouple 25mm above the fuel surface, level with the lower surface of the cone heater. This thermocouple read around 320°C, which is likely mostly due to direct radiant heating. Some heating of the air in the vicinity of the cone heater is also likely to have occurred, as the thermocouple at 250mm above the fuel surface, which does not receive direct radiation from the cone, also read elevated temperatures, in the vicinity of 90°C. At 1001s the fuel sample was placed on the load cell, and combustion proceeded until 1132s. Recording of temperature ceased at 1342s.

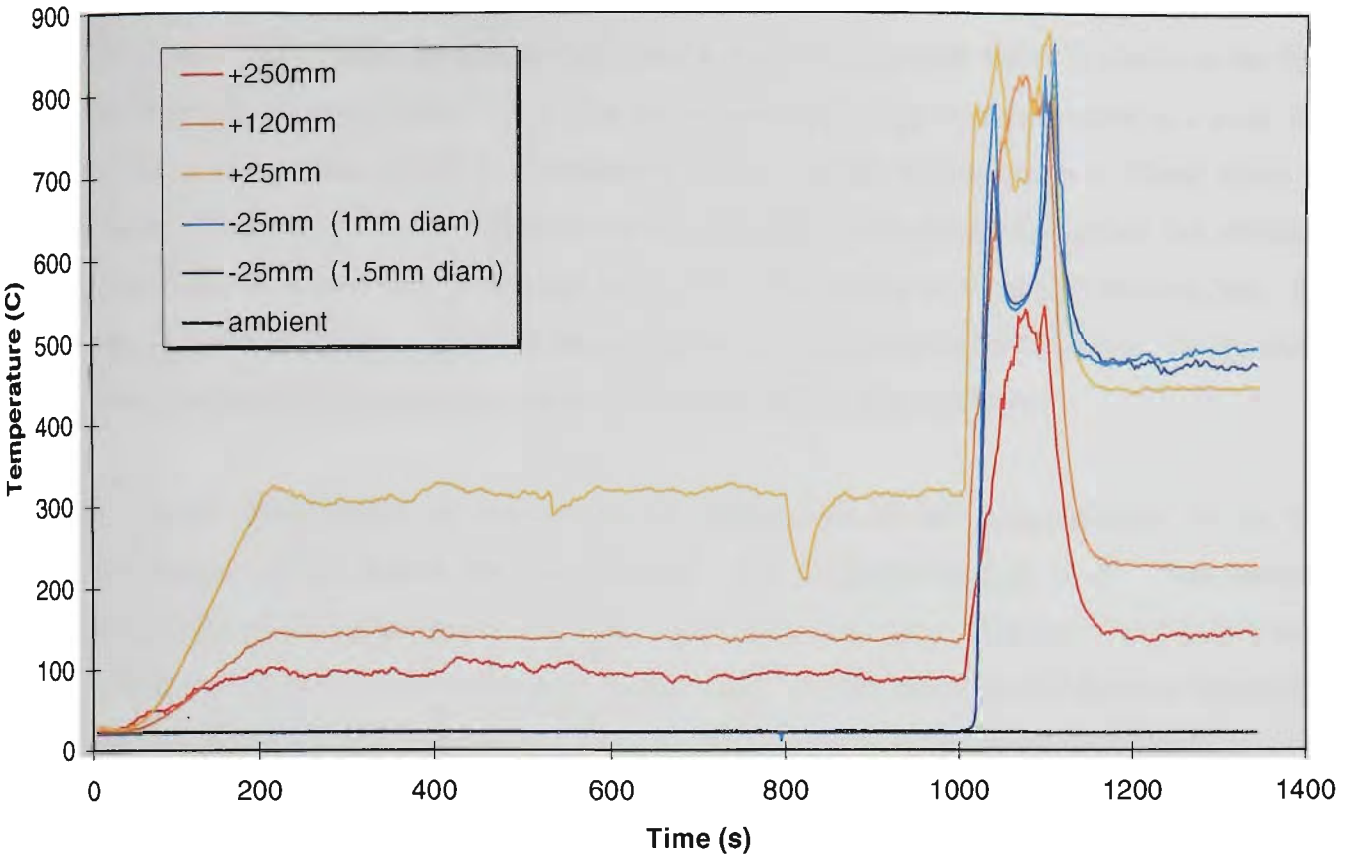

(a)

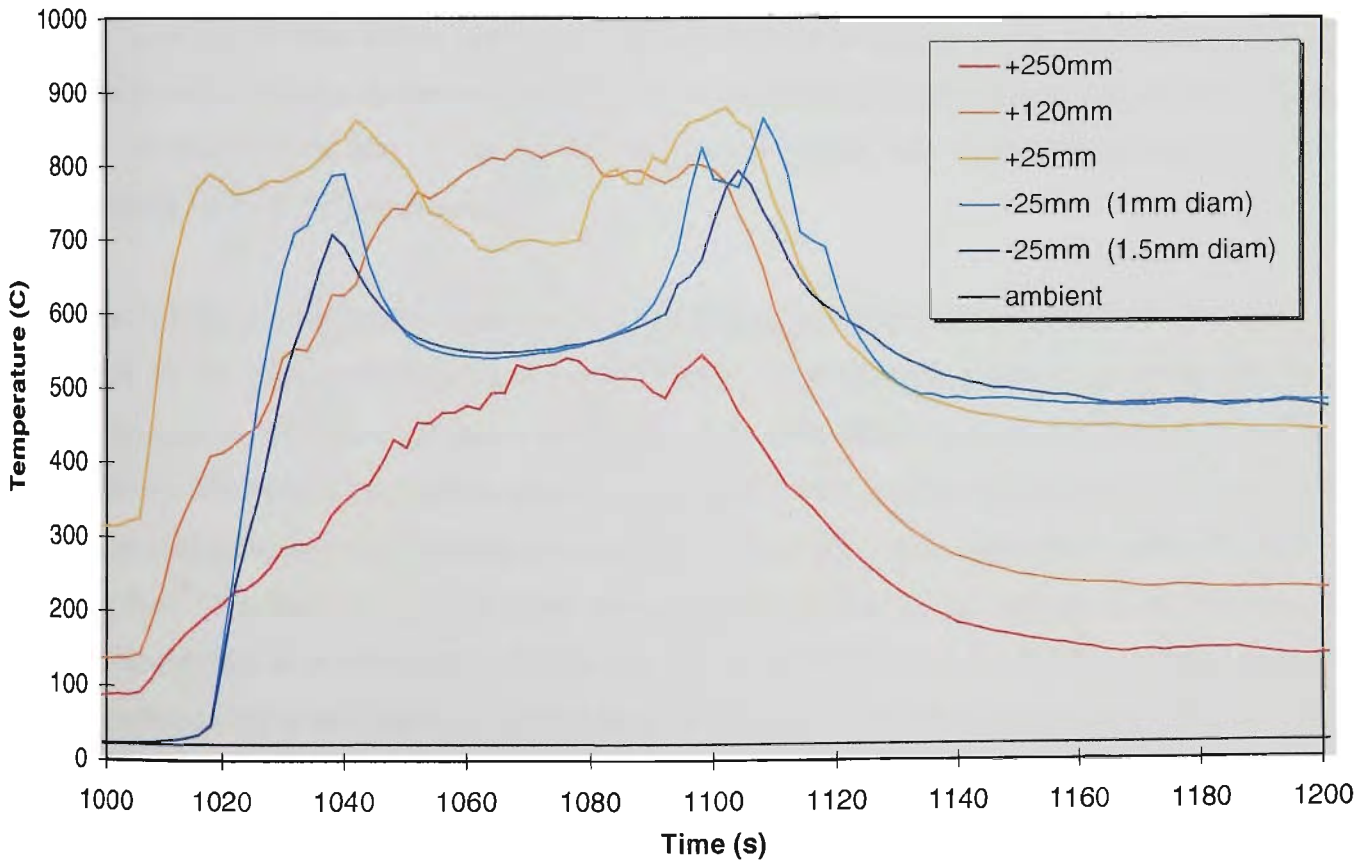

(b)

Figure 4.17 Temperature measurements for 50kW/m^2 autoignition test on fire retarded foam (a) combustion and non-combustion period (b) combustion period only

There are two phenomena of interest in the combustion portion of the test. The thermocouples at 120mm and 250mm above the fuel surface show a temperature profile which is similar to the RHR curves from the tests in Section 4.5.5, with the temperature rising in smooth curve to a peak, then decaying as combustion dwindles to extinction. However, the thermocouple at 25mm above the fuel surface, as well as the two thermocouples originally 25mm below the surface but obviously exposed soon after ignition, show a dip in the curve at the time of maximum burning rate. It is possible that these thermocouples are measuring the cool, fuel rich core of the flame, which extends above the surface at the time when volatilisation of the fuel is at a maximum.

The second phenomenon of interest is the comparison of the measurements of the two thermocouples 25mm below the fuel surface. The temperature plot of the 1mm diameter thermocouple shows higher peaks each side of the temperature dip, and a lower temperature in the dip, than does the 1.5mm thermocouple. It also shows a more rapid rise and decay in temperature either side of the peaks. This demonstrates a more rapid response to temperature fluctuations in the smaller diameter thermocouple.

After cessation of combustion, the thermocouple readings returned to steady values. However, the values are higher than before ignition. This is likely due to heating of the cone heater and other fittings and mountings by the test itself. Thus, in an extended combustion test, it is likely that the external radiant heat flux to the surface of the fuel sample may increase to a level above the specified value as the test proceeds.

A second and third test were performed on piloted ignition of fire retarded foam at an irradiance of 10kW/m^2, the results of which are shown in Figure 4.18. These two tests showed similar behaviour to the tests in Section 4.5.5 (see Figure 4.3), in that combustion ceased about 20 seconds after ignition. The sample was left in place for a further 2 minutes after cessation of burning. After removal, the sample was sectioned to examine the extent of thermal degradation within the fuel. It was found that there was a layer about 10mm thick below the burning surface which was affected by degradation, as evidenced by a brown coloration which faded away with depth. Heat may have been transferred to this depth by at least three methods, as the open cell structure of the fuel would have allowed diffusion of hot gas and penetration of radiation, as well as thermal conduction normally associated with the combustion of solid fuels.

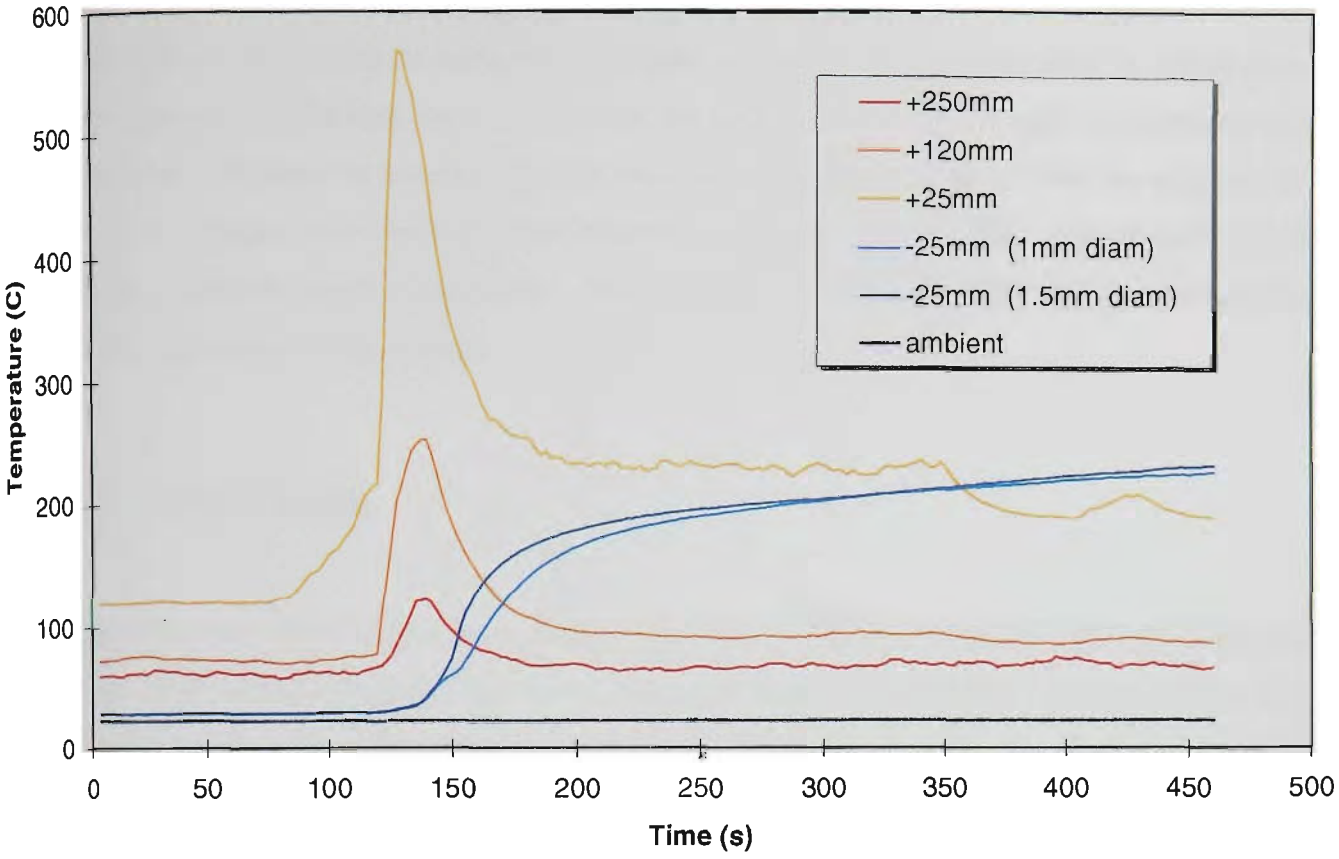

(a)

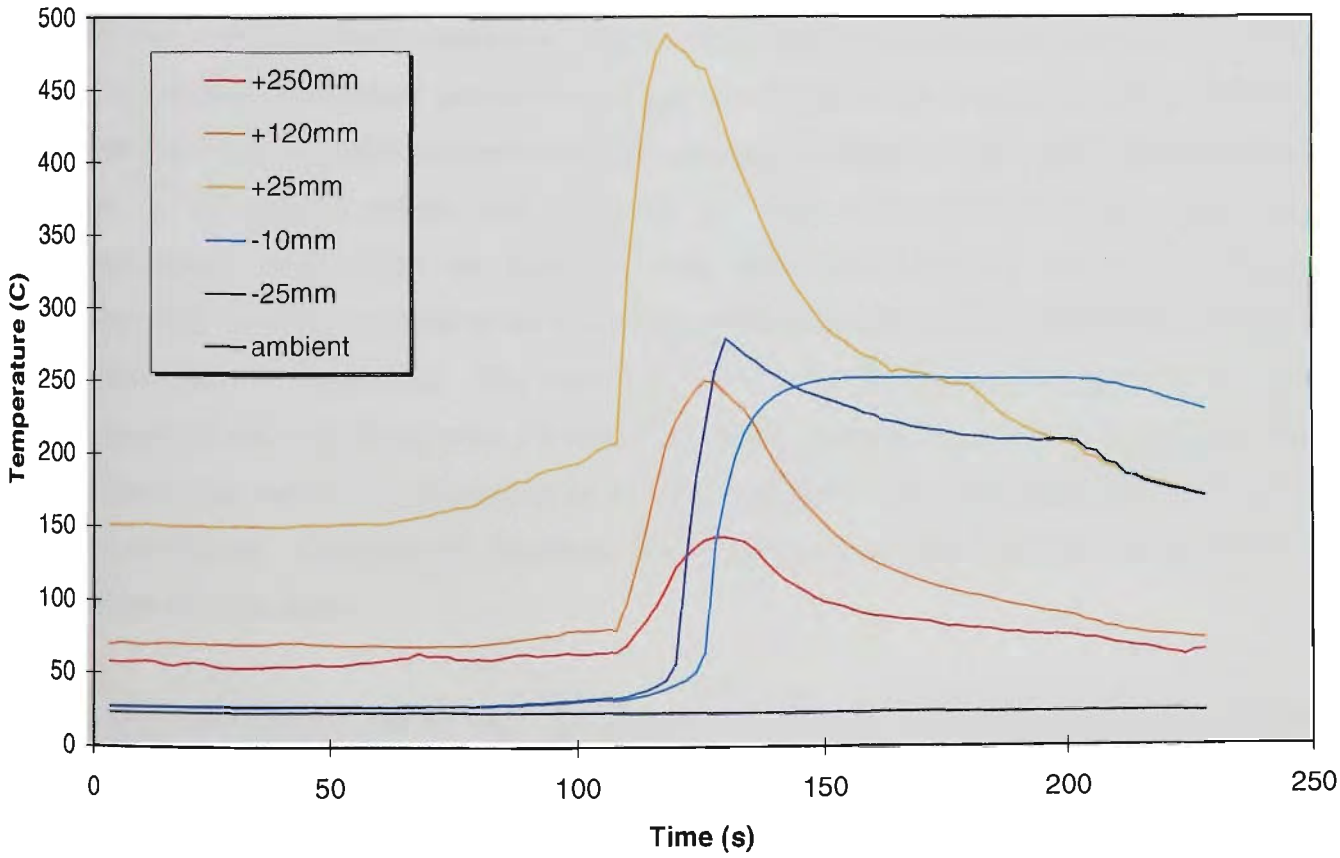

(b)

Figure 4.18 Temperature measurements for two 10kW/m^2 piloted tests on fire retarded foam

The location of the thermocouples was immediately apparent, as they had absorbed heat, presumably by penetration of radiation, and strongly degraded the foam in their vicinity. This calls into question the validity of using thermocouples to measure foam temperature in combustion, as thermocouples absorb heat more readily than the foam and are likely to read a temperature higher than would otherwise be present. Another issue uncovered by sectioning of the fuel was that, while the thermocouples were intended to be inserted at a depth of 25mm, they were in fact inserted at 32mm and 34mm depths respectively. Thus, not only is the temperature reading questionable, so too is the location of that reading.

4.6. CONCLUSIONS

The nature of combustion has been summarised, and a model was developed, although testing of the model and conclusions about its validity is discussed in later chapters. A large section of this chapter was devoted to describing cone calorimeter testing of polyurethane foam. These tests were conducted with the aim to determine the material properties for two types of foam. While reservations concerning the validity of the experimental procedures were identified, some of the aims were nevertheless achieved. In some cases, a value for the required material properties was obtained, with a degree of confidence, whereas other figures are clouded by uncertainty. The heat of combustion of standard polyurethane foam was found to be around 26 MJ/kg, and around 25 MJ/kg for fire-retarded polyurethane foam, although the figure in both cases appeared to depend both on the applied radiant heat flux, and the stage of combustion of the sample itself. Nevertheless, these values are expressed with some confidence, for two reasons: they are comparable to values reported in the literature, and the cone calorimeter is specifically designed to measure heat of combustion. The values for heat of volatilisation and critical surface ignition temperature were calculated to be 5.5 MJ/kg and 2000K respectively, but the methodology used to produce these values is considered to be unsuitable, and the values themselves are not stated with any confidence. Consequently, literature values will be used throughout the remainder of work presented in this thesis.

If cone calorimetry is to be used successfully to determine fundamental material combustion properties of polyurethane foam and other expanded thermoplastic polymers, then several issues need to be addressed, and overall experimental techniques need to be revised from a prescriptive standard method. In preparing foam samples, some means of doing away with the sample holder would help to reduce the heat feedback to the fuel surface from the holder. For instance, blocks of black PMMA burnt in the cone calorimeter as calibration runs, use a cardboard liner at the sides

which burns away as the surface regresses, yet remains in place long enough to prevent spillage of the liquid surface layer and the spread of combustion to the sample sides. Perhaps a container of some type of paper may be suitable for PUF samples. However, a series of experiments to find a suitable container is a project in itself, and beyond the scope of this thesis. Other factors to be addressed in the future include maintaining a steady heat flux as the surface of the fuel rapidly regresses, and the related issues of determining critical heat flux for autoignition and surface temperature at ignition. Such issues are not insurmountable, so there is no reason to suppose that cone calorimetry is incapable of determining fundamental material properties.

5. FLAME SPREAD

5.1. INTRODUCTION

The aim in this chapter is to construct a flame spread model which makes use of the combustion model presented in the previous chapter applied to an array of individual cells. As with the previous chapter, the focus is on heat transfer in the solid phase, with gas phase phenomena being modelled empirically.

There are several goals relevant to the construction of a flame spread model. The first stage in constructing the flame spread model is to develop a method of determining spread on an array. An investigation of cellular automata as a possible technique is presented here. The physics of flame spread is then examined to identify the physical aspects of flame spread which need to be addressed in the model.

Once the spread criteria and the physics have been identified, construction of the model is described. This includes the surface temperature and internal temperature calculations, taking into account three dimensional heat transfer as opposed to the one dimensional transfer described in the previous chapter (i.e. lateral heat transfer from cell to cell in the array), and the regression of the fuel, which will vary in amount from cell to cell. There also needs to be an empirical description of the fire plume above the fuel surface, as this is a major source of heat transferred to unburnt fuel elements. The configuration factor of the flame needs to be calculated, which means choosing a shape for the flame, and the temperature and emissivity need to be specified.

Modelling of a test case is undertaken, namely the radial spread of flame on the upper surface of a horizontal slab of fuel. A series of experiments were performed to provide data for comparison with the model. A "furniture calorimeter" was chosen for these tests over full-scale room tests at the EBFF, Fiskville, as the exhausting of the product gases reduces the radiative feedback from the hot gas layer, as would occur in a room test. Since the model developed in this chapter will not be considering feedback from the surroundings, this is a desirable feature of the furniture calorimeter. An additional factor for the choice was the increased accuracy of heat release rate data of the furniture calorimeter over the "door calorimeter" in place at the EBFF.

The model is executed with a set of previously used input parameters[11], and compared with the experimental results. A sensitivity analysis was performed on the model to identify the parameters which most affect the outcome of the modelling results.

5.2. PRELIMINARIES

Normally it would be customary in commencing a chapter about flame spread to begin by discussing the physics and chemistry of ignition and combustion, the mathematics of moving boundary problems, numerical techniques for solving the resulting equations, and so forth. So too in the development of a flame spread model itself, it would customary to begin with the fundamental physics and chemistry, and flame spread would follow as a natural consequence of solving the resulting equations. However, the model presented here, and hence the description of it, begins on a more fundamental level, by considering the phenomenon of spread itself.

5.2.1. The Phenomenon of "Spread"

This discussion begins by considering the question: what exactly is meant by "spread"? Firstly, it must apply to some "entity", be it substance, quality, or quantity, which may be a physical entity such as a flame, an animal or plant population, or a diffusing chemical species, or an abstract entity such as news, trends, or knowledge. Unless this entity is omnipresent or non-existent, consideration is being given unto a spatial distribution, whereby the entity is divided into regions of presence and absence, separated by one or several boundary regions. Similarly, unless this distribution is static for all eternity, it is a temporal as well as a spatial phenomenon, whereby the spatial distribution of the entity changes from one moment to the next. The changes may be considered to be of two types; creation and extinction, which occur at a finite distance from a boundary region, and propagation and recession, which are phenomena which occur at the boundary. (Alternatively, propagation and recession may respectively be considered to be creation and extinction which occur at an infinitesimal distance from the boundary rather than a finite distance.) In considering flame spread, the primary concern is with propagation effects, although creation (in this case, ignition) and extinction (burnout) are also taken into account.

The spatial and temporal distributions of this entity are seldom arbitrary, but generally follow set rules or criteria. Given a known spatial distribution at some point in time, the distribution at the next point in time is determined by the application of the rules. These rules may be totally

deterministic, so that the (unique) distribution is completely known (in theory) at any future time. Alternatively, there may be a probabilistic component to the rules, in which case there will a statistical spread of outcomes. In the case of a spreading flame, the physics of the scenario comprise the rules, and these will be discussed in a later section. The rules which govern the spread phenomena are seldomly applied arbitrarily to points in isolation. Rather, the points both within and between the regions are usually in contact or communication with each other. The likelihood of a point transferring from one state to another will depend on the state of neighbouring points, particularly if the point is near a boundary region.

As discussed in the overview, the aim is to construct a flame spread model which is compatible with CFD models, and is geometrically flexible. To be compatible with CFD models, it will most likely operate on a discrete grid, and will progress through time in a series of discrete time steps. For geometric flexibility, the most appropriate general purpose grid is a regular square lattice. The next section deals with perhaps the simplest set of rules for a two dimensional propagation phenomenon, that being of a cellular automaton operating on a regular square lattice.

5.2.2. Cellular Automata

Cellular automata modelling may be employed as a means of simplifying the calculations for a time marching physical process taking place on a discretised space. It has been used previously in fire spread modelling, both for large scale wildfire modelling[100], and for small scale turbulent combustion modelling.[101] The work presented herein describes a new application of cellular automata methods to intermediate scales, where the spatial grid size is of the order of millimetres, as opposed to metres for wildfires, and fractions of a millimetre for turbulent combustion.

A definition of a cellular automaton may be stated as follows[102]

A cellular automaton $<C,N>$ in n dimensions consists of an array C and a *neighbourhood function* $N: C \rightarrow 2^C$, where $C = c_{i_1 \cdots i_n}$, with $1 \leq i_j \leq r_j$, $r_j \in Z$, where $c_{i_1 \cdots i_n}$ are automata with identical programming. The neighbourhood of a cell consists of all other cells which interact with it.

This definition is best illustrated with a well known example, Conway's Life, invented by the mathematician John Conway in 1970[103]. A regular square array is considered (C in the above definition), with each cell in the array in one of two states, either "occupied" or "unoccupied" (1 or 0). The system is then allowed to evolve through a number of time steps, or "generations" by repeated applications, or iterations of the following neighbourhood function, N. The neighbourhood of a given cell is the eight cells immediately surrounding the cell; four at each edge, and four in each corner (see Figure 5.1), known as a Moore neighbourhood. If the cell is unoccupied, it will become occupied in the next generation if precisely three neighbouring cells are occupied. If a cell is occupied, it will remain occupied if two or three neighbouring cells are occupied, will "die out from overpopulation" (become unoccupied) in the next generation if four or more neighbours are occupied, and will "die of isolation" (become unoccupied) if it has only one or no neighbours. It turns out that these numbers (3 for "birth", 2 or 3 for "survival") are near critical to generate a rich variety of complex patterns when the neighbourhood function is repeatedly iterated; not too high to produce uniform growth, and not too low to produce rapid extinction.

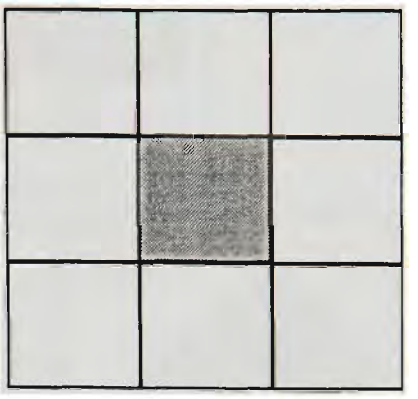

Figure 5.1 Moore neighbourhood of a cell

A variation of these rules may be used to at least qualitatively reproduce some of the behaviour witnessed in flame spread scenarios. If each cell is considered to be an element on the surface of a combustible surface, then a cell may either be burning or not burning. In the absence of any physical data, it is reasonable to presume (for the sake of the exercise) that once ignited, a cell will remain in that state for all future iterations (i.e. there is no extinction criterion). All that remains is to decide on a criterion which will ignite unignited cells. Again in the absence of physical data, such ignitions are expected to occur at the boundary between ignited and unignited regions. Hence, since a cell is fixed in space, the question being asked is at what point has the "spreading ignition front" reached the cell under consideration. This may be answered by considering the Moore neighbourhood of the cell, and stating that the cell will ignite when a certain number of neighbouring cells have ignited. This number will obviously be greater than zero. Also, if it is decided that n ignited neighbours are sufficient to cause ignition, then so too should any number between $n+1$ and 8 (implicit in this assumption is that the array is isotropic, i.e. that is there is no preferential weighting given to any of the neighbouring cells.)

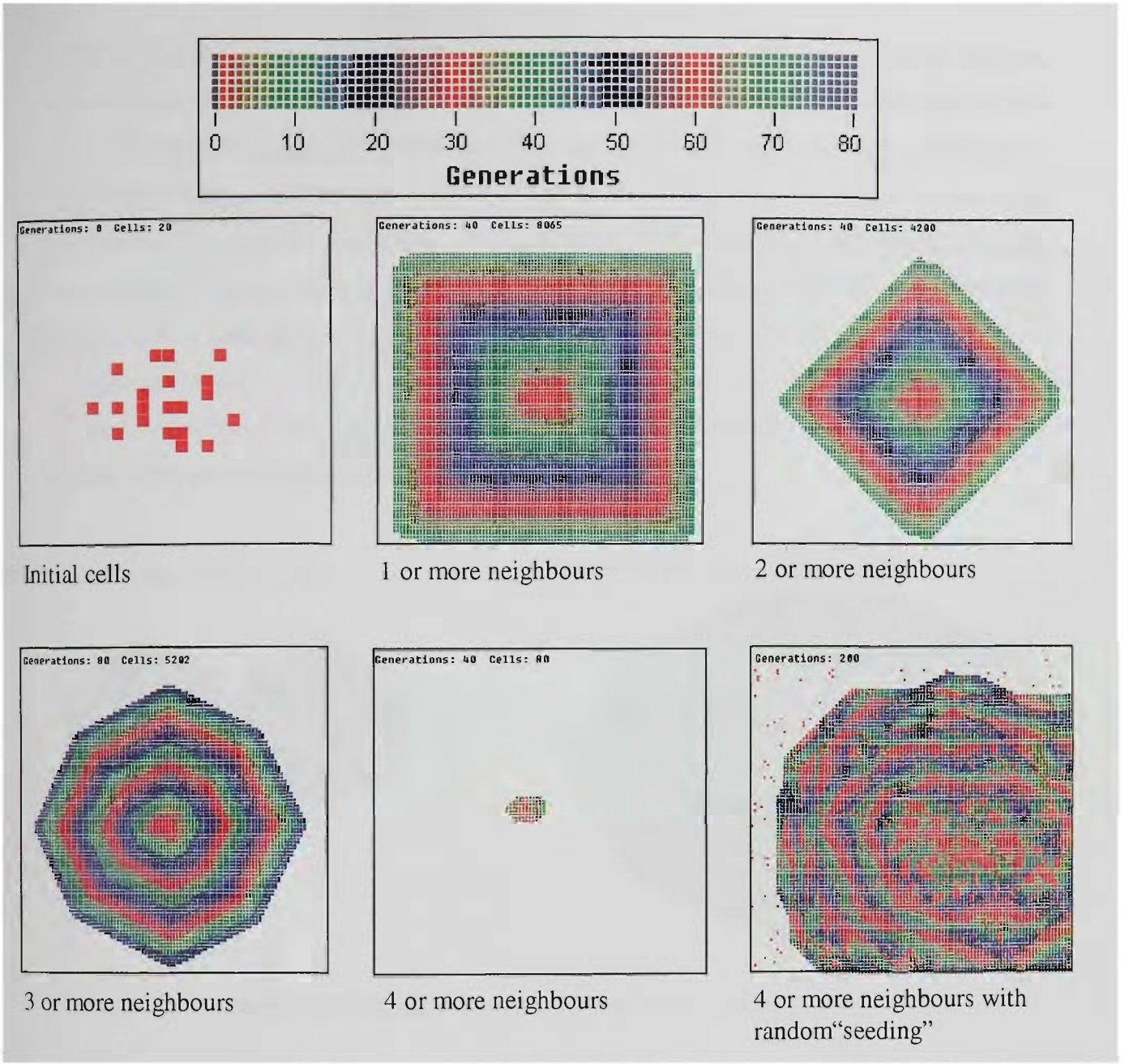

Figure 5.2 Spreading configurations for various "minimum neighbour" ignition criteria

By varying this minimum number n for a given arbitrary initial distribution, it may be shown that the optimum condition for producing realistic flame spread patterns is the condition that three or more neighbours be ignited (see Figure 5.2). One or more neighbours leads to rapid growth in a "square" configuration, which is obviously more rapid in the diagonal direction than in the axial direction, while two or more neighbours leads to rapid growth in a "diamond" configuration, which is more rapid in the axial direction than in the diagonal. Four or more neighbours will not spread, unless the region is "seeded" with numerous "spot flames". The stable configuration is an octagon, whereby unignited cells adjacent to the boundary have no more than three ignited neighbours, so further ignitions will not occur. Even if the surrounding regions are "seeded", spread is not radial, but transverse along each face, until a further "seed" is encountered.

In the case of three or more neighbours being ignited, the stable configuration is an octagon, with the eight vertices of the octagon lying on the axes and on the diagonals. This octagon will grow indefinitely, maintaining its shape as it does so. An octagon is a reasonable approximation to a circle, which is what would occur in a truly isotropic propagation scenario. Thus, using only a very simple cellular automaton, it is possible to mimic a uniform radial spread scenario. Another property of interest is if two growing octagons come in contact, the two concave regions formed near the point of contact will quickly "fill", and indeed become convex, to the point that a single larger octagon is eventually formed, as shown in Figure 5.3. This mimics the tendency for concave regions of a spreading flame front to spread more rapidly, due to the increased heating of the unburnt region bounded by the concave front.

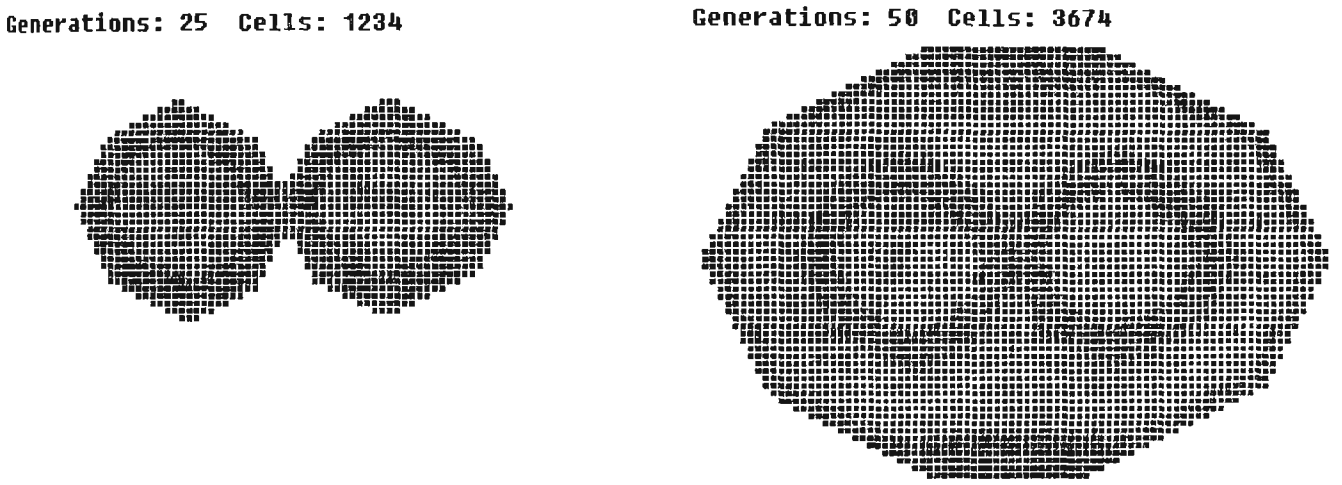

Figure 5.3 Merging of two burning regions into a single region

There are other properties of this particular cellular automaton which will be useful to explore at this stage. While it has been demonstrated that an octagon is the stable spreading configuration for this automaton, this configuration also represents a "speed limit" for propagation using these particular rules. If attention is paid to one of the axial vertices of the octagon, it is seen that the front advances in the axial direction by one cell every two generations (see Figure 5.4). Hence, in the direction of the axes, this limiting velocity is expressed

$$v_{\max} = 0.5\frac{\Delta x}{\Delta t} \qquad (5.1)$$

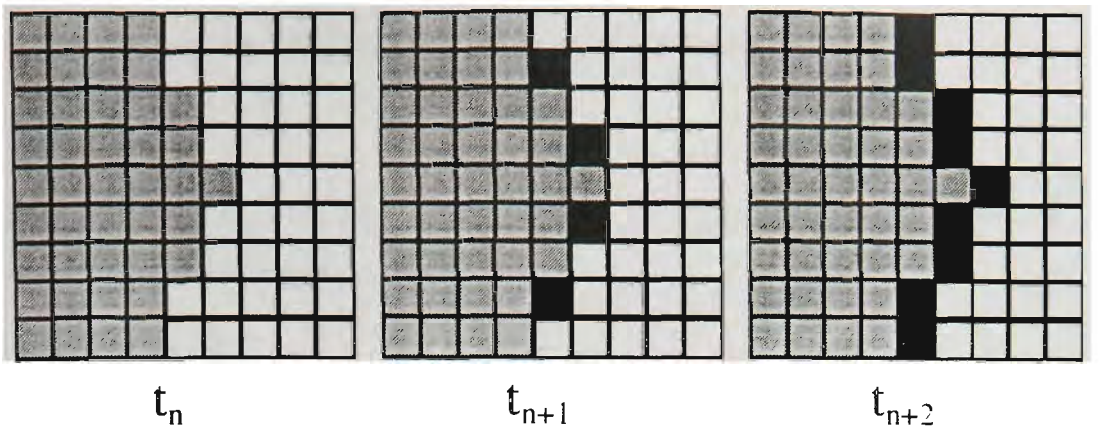

Figure 5.4 Limiting spread rate configuration

Since the array is not isotropic, spread is not radial and circular, so the limiting spread rate is not quite the same in all directions. Because it is not radial, the spreading direction is not perpendicular to the front in at all points, so it is difficult to determine the limiting spread rate in an arbitrary direction. However, the rate of change of area of the octagon is readily determined, and an equivalent limiting rate of radial spread may then be calculated if the octagon is approximated as a circle. The first step in this calculation is to construct a portion of the octagon as shown in Figure 5.5.

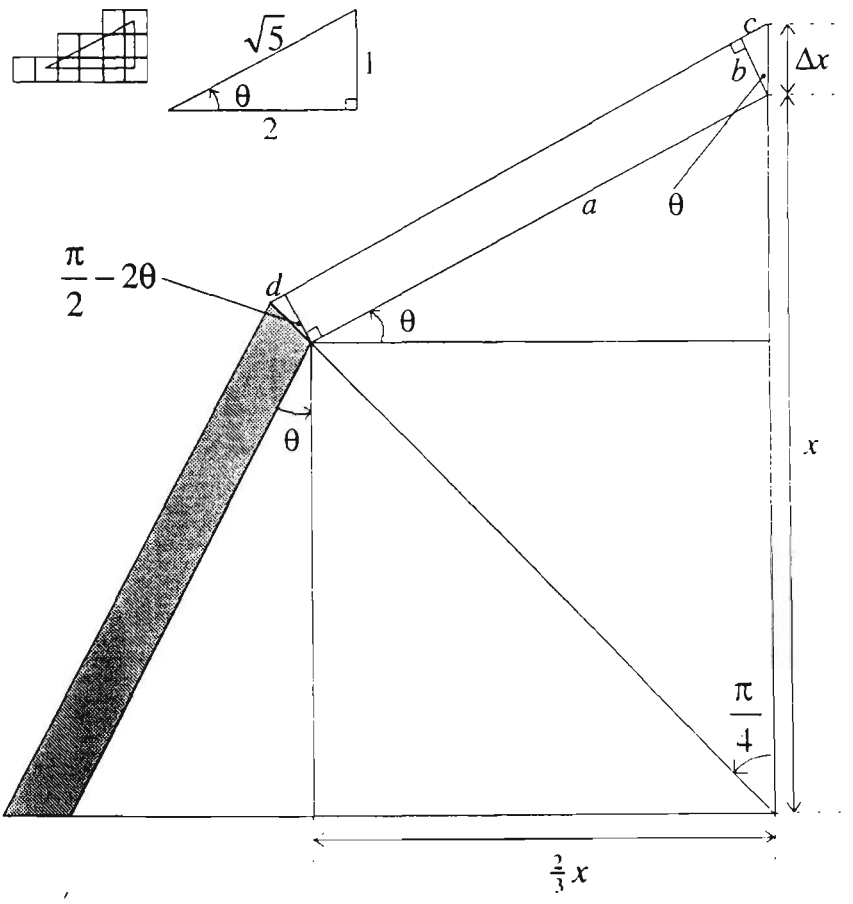

Figure 5.5 Geometry of the octagonal spread configuration

The area of the octagon is readily calculated by elementary geometry, and is given by

$$A = 4(2 \cdot \tfrac{1}{2} \cdot \tfrac{1}{3}x \cdot \tfrac{2}{3}x + \tfrac{2}{3}x \cdot \tfrac{2}{3}x) = \tfrac{8}{3}x^2 \tag{5.2}$$

To calculate the change in area, it is necessary to first calculate the lengths of sides a, b, c, and d. Again, by elementary trigonometry,

$$\begin{aligned} a &= \sqrt{(\tfrac{2}{3}x)^2 + (\tfrac{1}{3}x)^2} = \tfrac{\sqrt{5}}{3}x \\ b &= \Delta x \cos\theta = \tfrac{2}{\sqrt{5}}\Delta x \\ c &= \Delta x \sin\theta = \tfrac{1}{\sqrt{5}}\Delta x \\ d &= b\tan(\tfrac{\pi}{2} - 2\theta) = b\cot(2\theta) = b\frac{\cos^2\theta - \sin^2\theta}{2\sin\theta\cos\theta} = b\frac{(\frac{2}{\sqrt{5}})^2 - (\frac{1}{\sqrt{5}})^2}{2\frac{1}{\sqrt{5}}\frac{2}{\sqrt{5}}} = \frac{3}{4}b = \frac{3}{2\sqrt{5}}\Delta x \end{aligned} \tag{5.3}$$

The change in area is the eight times the sum of the shaded area in Figure 5.5, which is equal to the sum of the narrow rectangle and the two small triangles also shown, and is given by

$$\begin{aligned} \Delta A &= 8(a \cdot b + \tfrac{1}{2}b \cdot c + \tfrac{1}{2}b \cdot d) \\ &= 8(\tfrac{\sqrt{5}}{3}x \cdot \tfrac{2}{\sqrt{5}}\Delta x + \tfrac{1}{2} \cdot \tfrac{2}{\sqrt{5}}\Delta x \cdot \tfrac{1}{\sqrt{5}}\Delta x + \tfrac{1}{2} \cdot \tfrac{2}{\sqrt{5}}\Delta x \cdot \tfrac{3}{2\sqrt{5}}\Delta x) \\ &= 8(\tfrac{2}{3}x \cdot \Delta x + \tfrac{1}{5}\Delta x^2 + \tfrac{3}{10}\Delta x^2) \\ &= \tfrac{16}{3}x \cdot \Delta x + 4\Delta x^2 \end{aligned} \tag{5.4}$$

The "equivalent radius" of the octagon can be found by equating the area in Equation 5.2 with that of a circle

$$A = \tfrac{8}{3}x^2 \equiv \pi R^2 \Rightarrow R = \sqrt{\tfrac{8}{3\pi}}x \tag{5.5}$$

To find the "equivalent radial increment" the incremental area in Equation 5.4 is equated with the circular incremental area, and Equation 5.5 is substituted, to yield

$$\begin{aligned} \Delta A &= \tfrac{16}{3}x \cdot \Delta x + 4\Delta x^2 \equiv \pi(R + \Delta R)^2 - \pi R^2 \\ &\Rightarrow \tfrac{16}{3}\sqrt{\tfrac{3\pi}{8}}R \cdot \Delta x + 4\Delta x^2 = 2\pi R \cdot \Delta R + \pi \Delta R^2 \\ &\Rightarrow \frac{8}{3\pi}\sqrt{\frac{3\pi}{8}}\Delta x + \frac{2}{\pi R}\Delta x^2 = \Delta R + \frac{\Delta R^2}{2R} \\ &\Rightarrow \Delta R = \sqrt{\frac{8}{3\pi}}\Delta x + \frac{2}{\pi R}\Delta x^2 - \frac{\Delta R^2}{2R} \end{aligned} \tag{5.6}$$

From this, it can be seen that the radius increment is dependent on the size of the octagon. However, as the octagon increases in size (i.e. as $R \to \infty$), the last two terms in the last line of Equation 5.6 vanish. Hence, combining Equation 5.1 with Equation 5.6, an "average" isotropic propagation rate may be expressed as

$$v_{max} = 0.5\frac{\Delta R}{\Delta t} = \sqrt{\frac{2}{3\pi}}\frac{\Delta x}{\Delta t} \approx 0.4606\frac{\Delta x}{\Delta t} \tag{5.7}$$

What this value represents is an upper propagation limit for a spread model which utilises cellular automata techniques using this particular neighbourhood criterion. Naturally, in posing a flame spread problem employing such techniques, the parameters of the spread model should be carefully chosen to avoid encroaching on this limit. For instance, if the maximum "expected" flame spread rate is of the order of millimetres per second, then the grid size and time step should be chosen so that the limit given in Equation 5.7 is at least an order of magnitude larger than the expected maximum. Of course, this requires some foreknowledge of the flame spread problem, although if the limit is set to the order of metres per second, then this should be sufficient for most enclosure fires.

5.2.3. Modelling with Cellular Automata

What practical use are the observations of cellular automata properties to a real fire spread model? In fact, they help overcome a problem of a general model; that is, how is it known, in the absence of any geometrical assumptions, whether the flame front has reached an unignited cell? In the case of a radial spreading flame, it is known that the flame front will be circular, for an infinite planar flame it will be straight, for either horizontal or vertical flame spread. These cases reduce to one-dimensional flame spread, so that the position of the flame front may be inferred, even interpolated, between a cell which is alight and a cell which is not. However, for an arbitrary two-dimensional flaming surface region, this inference cannot be so easily made. It is important to know the position of the flame front, for as shall be seen later, there are important physical phenomena which are only significant close to the flame front.

For the moment, let us consider the most important phenomenon occurring at the flame front, that is, the ignition of unburnt cells which propagate the flame and add to the burning region. The state of the burning surface is being calculated every time step. Each cell is in one of three states, which are designated by a single integer; 0 for an unignited cell, 1 for and ignited cell, and -1 for a burntout cell. (The latter is chosen for convenience: for the purposes of calculating the ignition front, a burntout cell may be considered an ignited cell since, like an ignited cell, it cannot be "further" ignited. Thus when calculating the number of neighbouring cells ignited, the absolute values of the ignition state of the eight neighbours are added. Ignited and burntout cells will contribute 1, unignited cells will contribute 0.)

In order calculate the state of the system in the next time step, based on the previous time step, it is necessary to determine the number of cells which have satisfied the ignition criteria, and change the state of these cells from ignited to unignited. Leaving aside the physics for the moment, the required determination is whether an unignited cell has three or more neighbours. Now, the method which immediately springs to mind is to systematically check every surface cell, and count the number of neighbours which are ignited. However, this method can be time consuming. If a typical piece of solid fuel is, say, one metre by one metre, and a grid size of, say, five millimetres is being used (not an unreasonable situation) this involves adding up 8 neighbours for 40000 cells, a total of 320,000 calculations. It is then necessary to make the appropriate adjustments for each of these 40000 cells, which all takes time. It is possible, however, to reduce on the number of calculations.

For example, it is not necessary to consider cells which are already ignited. Nor is it necessary to consider any cells which do not have any neighbouring cells alight. Thus, it is only necessary to consider the unignited cells which have one or more neighbours ignited. This is achieved by keeping a list of unignited cells which have between one and eight ignited neighbours. For each time step, only this list of cells is systematically checked for the ignition criteria. If the criteria are satisfied, the cell is ignited, and it is removed from the list. Now, a newly ignited cell may advance into "virgin territory", thus bringing new cells into consideration. Therefore, every time a cell is ignited, a check must be made also of the eight neighbours. If a neighbour is ignited, nothing needs to be done. If it is unignited, a check must be made whether or not it is on the list. If it is listed, nothing needs to be done, but if not listed, it needs to be added to the list. Additionally, if an unignited neighbour is found to have seven ignited neighbours, then the cell from which the check is being made, a newly ignited cell, will be the eighth. It is reasonable to assume that a cell which is completely surrounded by burning cells should itself become ignited, so this neighbour shall become a newly ignited cell also.

Care must be taken in distinguishing for which timestep state of a particular cell is being considered. Consider for example if a sweep of the grid is performed in columns from left to right, and there is a region of ignited cells to the left. Cells one grid spacing to right of the ignited region may become ignited during a sweep of that column. The cells in the next column to the right are then considered. These cells will now have ignited neighbours, and they too may become ignited. And so on, all the way across the surface, potentially igniting cells which were remote from the ignited region one timestep previously. To avoid this situation, the ignition state of a cell is not actually changed until all the checks for potential ignitions have been made. If a cell is ignited, it is removed from the list and placed on a temporary list of "new ignitions" for that time step. Any unignited neighbours which were not on the list are added to the end of the list. Even though they

will be checked that timestep by the algorithm, they cannot become ignited because a check of ignited neighbours will show they have none. Only after all the cells on the list have been checked, the newly ignited cells have their state changed from 0 to 1. For clarity, this algorithm is illustrated by the flow chart in Figure 5.6.

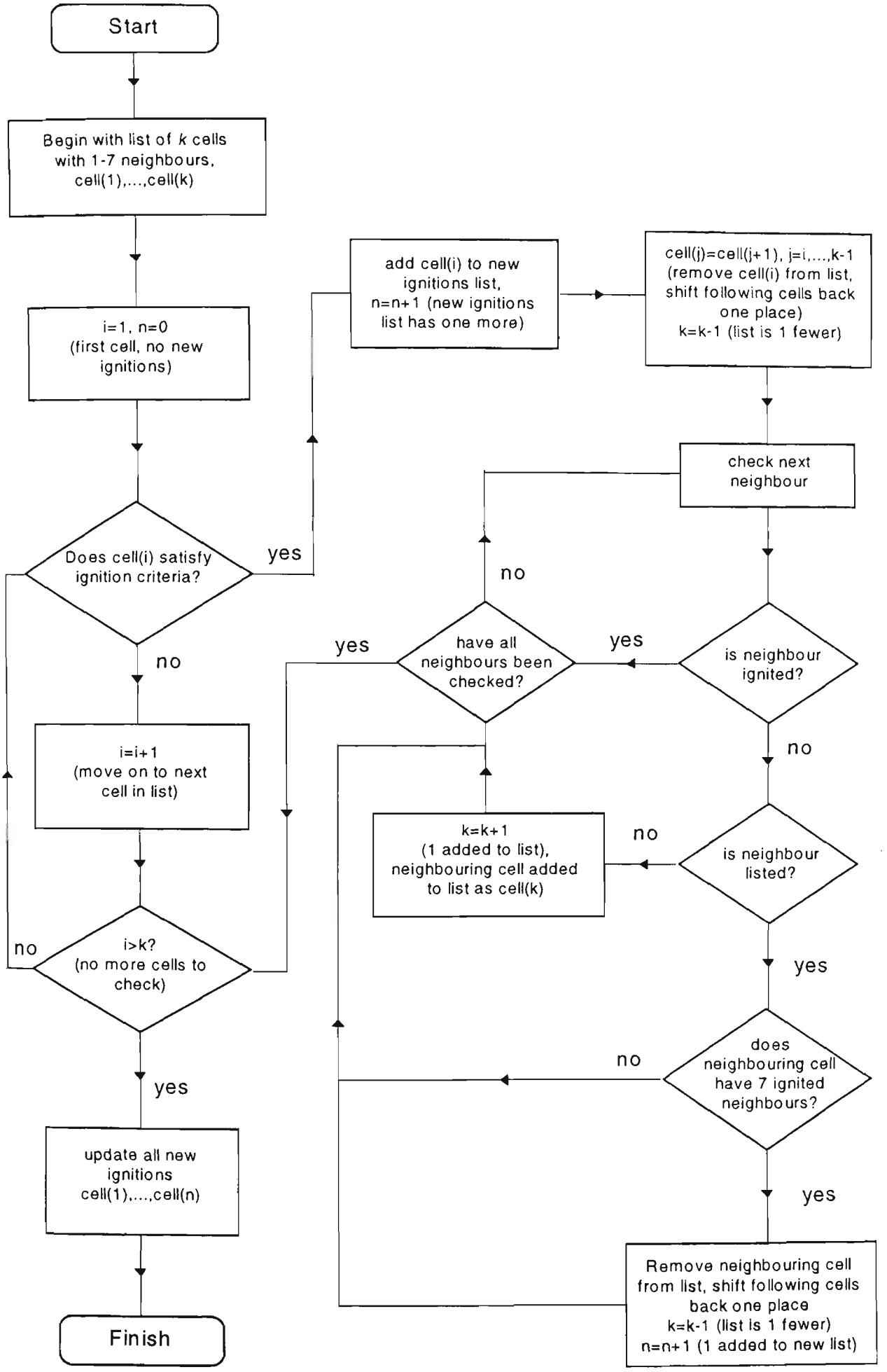

Figure 5.6 Flowchart for the cellular automata method of flame spread

5.2.4. Further observations on the cellular automata technique

In the previous section, a model for isotropic flame spread on a regular square grid array has been described. The isotropy is implicit in the fact that the eight neighbouring cells carry equal weighting. Of course, this need not necessarily be the case; indeed, the physics of the situation may be simplified further by assigning a different weighting to each of the eight cells. In a wildfire propagation and extinction model developed by Clarke et al[100], flame spread occurs by charting the course of "firelets" which originate from the fire centre. A firelet at a given cell will advance with a given probability into one of eight neighbouring cells. The base probability is 12.5% for each of the eight cells, but this is then weighted according to wind direction, slope, and fuel load (which may be reduced by previous burning.)

In building-fires, it is uncommon to encounter fuel loads that are as complex as wildland fuels, nor is it common to encounter slopes other than horizontal or vertical, or strong prevailing air movements, except perhaps when the fire has become well developed. Therefore, there appears to be little use for the stochastic methods of Clarke et al[100], as a full description of the physical geometry involved is feasible. However, where strong air movements do in fact prevail, there could be a case for consideration of a weighting factor. For instance, in vertical wall fires, the buoyancy of the flame induces a strong upward flow, which aids upward flame spread and resists downward flame spread. Thus, it is intuitive to presume that an unignited cell is more likely to be ignited by an ignited cell below it than by an ignited cell above it. Therefore, in constructing a cellular automata model for vertical flame spread, it is tempting to weight the neighbourhood function in favour of upward spread. However, there is a good physical reason that flame spreads more rapidly upwards than downwards, and that is that the flame and hot plume are directly impinging on the unburnt surface above the burning region, and rapidly heating it to ignition point. Thus, a cellular automata model which ignores this fact, or chooses to replace it with a number, can only be regarded as approximate at best.

Accordingly, physics must play an important role in a cellular automata flame spread model. The question to ask, therefore, is whether physics dominates the cellular automata behaviour, or vice-versa. Saïd and Borghi[101] used cellular automata techniques to simulate the spreading flamelet front in turbulent flames. They used a Von Neumann neighbourhood (the four cells adjoining the edges of the central cell) rather than a Moore neighbourhood in their simulations, and noted that the rate of propagation was almost twice as high for Moore neighbourhood compared with a Von Neumann neighbourhood. They also had difficulty simulating a circular propagation front (they postulated that a hexagonal grid may remedy the situation, although it was demonstrated earlier in this chapter

that three Moore neighbours on a square grid may be a suitable method). Overall, they reported a strong dependence of the propagation rate to the cellular automaton rules.

This problem has been addressed to some extent in section 5.2.2, where the limiting propagation rate for a given situation was described. If the physics determines that the true spread rate is less than this limit, then the model will be physics driven, and if the true spread rate is greater, the model will be automata driven. More specifically, if a cell with three or more ignited neighbours does not meet the physical requirements for ignition, it will not ignite, and the problem is physics driven, whereas if a cell meets the physical conditions but does not have three or more ignited neighbours, then the problem is automata driven.

Naturally, it is desirable to construct the problem for the model to be physics driven, as this will produce the most realistic predictions. However, as has been seen, cellular automata techniques still play an important role in a physically driven model in helping to determine propagation behaviour in the regions in the vicinity of the propagation front. The seemingly arbitrary choice of three or more ignited neighbours will at least preserve isotropy in the case where the automata rules become dominant. Attention will now be turned to the physical phenomena involved in flame spread.

5.3. THE PHYSICS OF FLAME SPREAD

The primary goal of this project is to develop a flame spread model which is compatible with CFD models, in particular for the application of such a model to the prediction of the behaviour of fire spread in full-scale enclosure fires. While it would be desirable to develop a model based completely on first principles, such a model is not likely feasible in view of the complexity of the problem. On the other hand, overuse of empirical assumptions is likewise undesirable, so a balance must be struck. What follows is an exploration of the literature accumulated in the area of flame spread, an identification of the important phenomena, and the choice of the methods most appropriate to this study.

5.3.1. Fundamentals

The phenomenon of flame spread has been studied for some time, and there are several review articles recently published which describe much of the research which has been undertaken in the

investigation of flame spread over solid[74,104], liquid[105], and wildland fuels[5]. In view of the discussion in section 5.2.1 on spread in general terms, a description will be given here in more definite terms how these concepts apply to the phenomenon of flame spread. A combustible fuel can be divided into two distinct regions, namely regions which are undergoing combustion, and regions which are not. The regions which are not undergoing combustion are of three types. Firstly, there is virgin fuel, where no combustion has taken place, the burnout region, where the fuel has undergone complete combustion, and regions where the burning fuel has been extinguished for some reason before complete combustion has occurred (and which potentially may become involved once again in the combustion process.) The focus in this study is with the first type of unburnt region, the virgin fuel, and its heating and subsequent involvement in the overall fire. It is also important here to make the distinction between the movement of the flame front laterally, as opposed to the movement of the flame front into the fuel due to regression of the burning fuel surface, which was discussed in Chapter 4.

Flame spread can only occur if there is some form of communication between the burning region and the unburnt region[78]. This invariably involves some form of heat transfer, and there are four main mechanisms by which this can occur, namely radiation, convection, conduction, and the movement of the burning fuel itself. The latter may take the form of drips from a burning thermoplastic material, or windblown embers from a wildfire, for example. Additionally, in considering the flame spread over solid fuels, there are two important components of the conduction to consider; conduction through the gas phase, and conduction through the solid phase. While it has been noted that in many instances some heat transfer mechanisms will make a negligible contribution in comparison with the others[78], a general purpose flame spread model should at least have the capability to calculate all possible modes of heat transfer, so that it is equipped to deal with any situation*.

It has been suggested[78] that all flame spread models solve, either explicitly or by implication, the fundamental flame spread equation, given by

$$\rho V \Delta h = q \qquad (5.8)$$

where V is the flame spread velocity, Δh is the enthalpy per unit mass required to raise the temperature of the unburnt fuel from ambient temperature to ignition point, ρ is the density of the fuel, and q is the net heat transferred to the fuel. There is a quantity which is in turn implied in this equation, and that is the surface ignition temperature. In these models, the approaching flame front

* For the purpose of modelling building-fires, flame spread by the movement of burning fuel will be ignored in this thesis.

increasingly heats the target fuel surface, at some point causing the fuel to release volatiles which feed the flame further, until the target surface ignites. Thus, the attainment of critical surface ignition temperature coincides with the arrival of the flame front. An exception to this scenario has been employed by Baroudi and Kokkala[106], whereby the flame is assumed to radiate a constant "average" flux to a certain distance from the flame, which is a function of its size and temperature. The time to ignition of the surface is determined experimentally by small scale testing of samples of this fuel at this same average flux. While this avoids the use of a surface ignition temperature, it uses assumptions and empirical data which are similarly debatable, and are not of the type of fundamental material properties being sought for the model.

Unless combustion occurs in a microgravity environment*, the buoyancy of the hot products of combustion will induce a flow, as the cool air moves in to fill the vacancy left by the rising products. Depending on the geometry of the situation, the flow may be in the opposite direction to the flame spread, or concurrent to it. In addition, there may be a forced flow present. The flame spread may be divided into two main types, opposed flow and wind aided flow. The two types may be further categorised, depending on the orientation of the surface and the nature of the flow[13].

5.3.2. Opposed Flow Flame Spread

Many analytical and numerical models have arisen in response to the problem of opposed flow flame spread, and by and large these focus on the phenomena occurring at the point of flame inception. Various techniques are employed in order to simplify the formulation and solution of the equations involved. In particular, the gas phase behaviour is often modelled with simple properties, such as an Oseen flow (constant velocity at all heights above the fuel surface) or a linear velocity profile with height. Another common technique is to have the reference frame for the solution move with the flame front rather than be fixed to the surface. This allows an analysis to be performed on the steady flame spread problem, that is, a flame front spreading with a constant velocity.

The combustion is modelled as a diffusion flame, with the flame spread rate therefore described as a continuous diffusion ignition[80]. An important consequence of such a detailed analysis is a description of the "triple flame" phenomenon, whereby the combustion zone has a premixed fuel rich boundary on the fuel side of the flame tip, a premixed fuel lean boundary on the flow side, and

* which is very rare in building-fires! However, by eliminating buoyancy forces, microgravity experiments provide much insight into the diffusive and radiative processes involved in combustion.[62]

a diffusion flame down the middle. The two outer or secondary fronts peter out downstream as the component which is in excess consumes the other, and the remainder diffuses inwards to the primary diffusion front. This analysis also allows for another alternative to the critical surface ignition temperature, and that is the critical surface mass flux. The flame front will have reached a point on the surface when the mass flux leaving the surface is high enough to satisfy the fuel lean combustion limit in the flow region immediately above this point[79]. However, since the mass flux is dependent on the kinetics of decomposition, which in turn is related to surface temperature, critical mass flux and critical temperature may be considered to be essentially equivalent.

The key finding arising from the study of opposed flow flame spread is that it is the gas phase conduction which is the primary forward heat transfer mechanism, at least close to the flame front. Radiative effects become more prominent as the fire size increases, and tend to dominate over gas phase conduction a short distance from the flame front. The role of forward solid phase conduction is a little ambiguous; Fernandez-Pello and Williams[86] did an analysis of opposed flow downward flame spread for the case where solid phase conduction is the dominant mode of heat transport, but it was later shown that such conditions would not arise except possibly in cases of low oxygen concentration, which probably would not support combustion anyway[104]. That is not to say that forward heat conduction is negligible, though, and since one dimensional conduction normal to the surface is significant and usually accounted for in a numerical calculation, the extension of the calculation to two or three dimensions to include forward heat conduction is generally not a problem.

5.3.3. Flow Assisted Flame Spread

Concurrent flow, or flow assisted, flame spread may be considered to be a study of what is occurring at the opposite end of the flame from an opposed flow flame front. Examples of concurrent flow flame spread include horizontal flow in a wind tunnel, upwards flame spread on a wall, or spread across a ceiling[13]. With flow assisted flame spread, the flame close to the pyrolysis region is in contact with the surface. Thus, the surface is strongly heated by radiated and convected heat flux directly from the flame to the fuel surface. Because of this, fuel ahead of the flame front will be rapidly heated to its ignition temperature, whereby it will be ignited by the impinging flame. This leads to a very rapid growth rate of the flame, leading to a further increase in the preheating of the fuel, with a corresponding increase in the flame spread rate.

For upwards flame spread, the spread rate has been found to be a function of flame height[78], which in turn is dependent on the length of the pyrolysis region[83,85]. This leads to a continuously growing, acceleratory mode of flame spread. While burnout at the lower, upstream edge of the flame will eventually limit the flame spread rate, this may not occur even in enclosures with very high ceilings.

The flame length is also proportional to pyrolysis length for horizontal wind-aided flow[17], although there are two distinct cases to consider. When the flame is small, it is constrained within the turbulent boundary layer of the flow region. As with upwards flame spread, heat transfer ahead of the pyrolysis region is by convection and conduction. However, once the flame has reached a certain size (dependent on the flow velocity), buoyancy forces begin to dominate, and the downstream portion of the flame stands up in a plume. Once this stage has occurred, radiation ahead of the flame becomes the dominant heat transfer mechanism[17].

5.3.4. Fire growth

The term "fire growth" pertains to those models which take into account the increase in heat output and flame size which often occur as a consequence of flame spread. While the analytical methods described above are useful in understanding the fundamental aspects of the flame spread phenomenon, they do not necessarily take into account the large scale aspects required of an engineering approach to predicting the effects of building-fires in general[104]. Many of the effects such as the "triple flame" phenomenon[104] will not be resolved on the coarse grids used in CFD models of full-scale fires in buildings. Likewise, an analytical solution which uses a moving reference frame fixed to the flame front will not be appropriate for such CFD models, as typically the fuel will be finite, and will have a definite fixed location with respect to the rest of the enclosure. In any case, Frey and Tien[107] found that numerical solution of the spreading flame was computationally easier with a reference frame fixed to the solid, as using a moving reference frame requires the spread rate to be initially guessed, and corrected after the solution has been computed. A solution which uses an assumption such as Oseen flow* will become somewhat redundant when a CFD model capable of predicting the flow field for itself is employed.

Atreya, in developing a model for horizontal radial flame spread over wood[79], makes the observation that while the gas phase phenomena near the flame foot are responsible for the

* "Oseen flow" refers to an assumption or approximation employed in the construction of fluid flow problems, whereby the velocity field of a fluid adjacent to a fixed surface is assumed to be uniform at all distances from the surface, from infinity to infinitesimally close to the surface.

propagation of the flame, it is the increasing radiative feedback from the flame region which is responsible for the *acceleratory* behaviour of the flame front. This is due to the increasing preheating rate of the unburnt fuel as the flame grows in size. Thus in large scale fires, the preheating of the fuel is dominated by the "far field" radiation emitted by the flame region. The gas phase conduction dominates close to the flame front, at a distance of the order of millimetres. In the model developed by Atreya[79], quite a detailed account is given of the radiant heat distribution from the flame, in comparison to the conducted heat which was reduced to a single exponential equation, two parameters of which were determined by experiment.

Upward flame spread models, such as that of Delichatsios et al[83], also exhibit fire growth characteristics. In this case, the radiation heat transfer from the flame is not "far field", as the flame is in contact with the surface. Acceleration in this case is due to the increasing flame length in contact with the unburnt surface.

5.4. THE FLAME SPREAD MODEL

This section describes the construction of a flame spread model incorporating the techniques of cellular automata model combined with the physics of heat transfer and flame spread. The aim at this stage of development is for the model to be largely self contained. Eventually the flame spread model is to be incorporated as a submodel into a larger CFD model. However, the encoding of CFD models, or submodels thereof, is a complex exercise, and the execution of the models time consuming.

If the flame spread model is to be developed initially to be stand alone, a choice needs to be made as to what flame spread mechanisms are to be included, and what empirical assumptions need to be made about factors external to the flame spread model. Since CFD models are designed to calculate fluid flow problems, the solid phase phenomena occurring in the stand alone model will be concentrated upon, and the gas phase modelling will be taken care of when the model is incorporated into the CFD model.

The problem chosen to model is the radial spread of flame over horizontal thermally thick thermoplastic fuels (such as polyurethane foam). This configuration is chosen for its isotropy; there is no preferred direction of flame spread. This is amenable to the isotropic cellular automata techniques developed earlier. It is also an easy configuration to perform experimentally, which will aid in the verification of the model. Flame spread rates are also easier to measure in this

configuration. It has been noted that for upwards flame spread, direct observation of the pyrolysis front is very difficult due to the fact that the flame obscures the location of the front[108].

Horizontal radial flame spread is in the category of opposed flow flame spread, with the dominant heat transfer mechanism being radiant heat flux from the buoyant plume, at least once the flame has reached a sufficient size. Flame conduction should also be included in a comprehensive model. However, this requires knowledge of the opposed flow velocity and the peak heat flux at the flame foot[79]. Atreya[79] avoided this problem by choosing the values which best conformed with an initial experimental result, and used these values for subsequent models. Baroudi and Kokkala[106] on the other hand compensate for it in the "effective heating range" of the flame. In the model presented here, the gas phase conduction is likewise ignored, but compensated for in the early stages of flame spread when the conduction is important by increasing the emissivity of the flame in this range, thus increasing the radiant component of the heat flux to the preheating fuel. Forward heat transfer is also accounted for in the solid phase. Solid phase conduction takes into account the regression of the fuel, as well as the varying degree of regression across the surface. The details of the model will now be described to a greater degree.

5.4.1. Surface Node Temperatures

The surface node temperatures are calculated by a similar technique as described in Section 4.3.1, that is, by a surface heat flux balance. In this case, the temperature is calculated for an array of points instead of just one, and there are two cases to consider: when the surface cell is combusting, and when the surface cell is in the preheating stage. Burnout is not considered, as there is no mass left in that particular element for heat transfer to be calculated for. In the combustion stage, the behaviour of the fuel element is as described in Section 4.3.1 for the one dimensional combustion problem, with a given total heat flux received from the flame. In the preheating stage, the gas temperature is taken to be ambient temperature, and radiant heat flux is transferred to the surface cell remotely via the flame. For this heat to be calculated, empirical models for the flame shape, temperature, and emissivity need to be made. Both preheating and combusting fuels may be subject to an externally applied radiant heat source as well.

Temperature within the fuel is indifferent to the combustion status of the surface, as is the radiant heat loss. Thus, in calculating the surface flux, the only difference between combusting and non-combusting fuel elements is the amount of radiant heat flux received.

5.4.2. Configuration Factor of the Flame

In order to calculate the far field radiation for the stand alone model, it is necessary to make some assumptions about the properties of the flame, particularly its size, shape, temperature, and emissivity. Since the assumption is that of radial spread of the flame in the horizontal orientation with no ambient drafts to bias the spreading direction, the flame region will have a circular base of known radius R. The height is determined from an empirical equation which gives the height of turbulent diffusion flames as a function of the flame radius and the heat release rate[109]. This equation may be written

$$H = 0.0145(\Delta H_c \dot{m}'')^{\frac{2}{5}} - 2.04R \qquad (5.9)$$

where the rate of heat release is a product of the heat of combustion, ΔH_c, and the rate of mass loss, $\dot{m}''$, and R is the radius of the flame at the base.

It is also necessary to know the shape of the flame, if the view factor is to be calculated, and the radiation heat transfer from the flame subsequently computed. There are at least two assumptions which have been made in the literature for doing this. Either a regular geometric shape such as a cone or cylinder is assumed, for which the configuration factor may be calculated using theoretical techniques (for example see Mudan[110]), or no assumption is made about the shape, but instead a parameter is introduced which is calculated empirically from experiment. The latter approach has been employed by Atreya[79] in developing a fire growth model for wood surfaces. Theoretical procedures were performed which resulted in a simple equation requiring one parameter, which was calculated to be equal to 1 for a cone, and 4 for a cylinder. A value of 2.5 was found to be the best fit for a sample of burning maple.

It was decided that in view of a lack of empirical flame shape data for polyurethane foams to choose a simple geometrical shape to model the flame, and to calculate the resulting view factor. However, bearing in mind the finding of Atreya that the shape is something between a cone and a cylinder, a hemi-ellipsoid was chosen as a possible candidate.

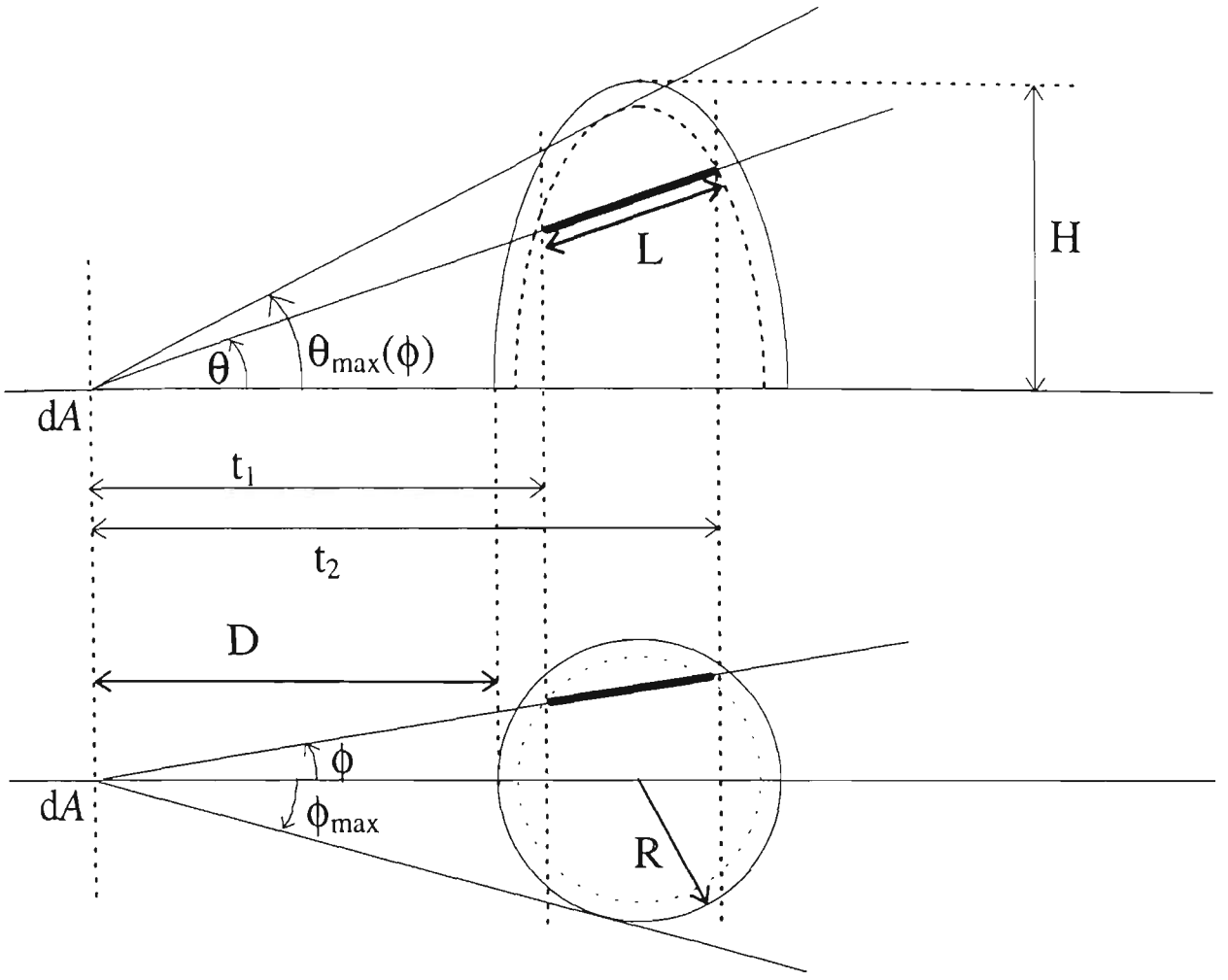

Figure 5.7 Construction of configuration factor

The geometry of the situation is shown in Figure 5.7 for a surface element located a distance D from the edge of a hemi-ellipsoid of radius R and height H. The distance to the centre of the hemi-ellipsoid is therefore $D+R$. The configuration factor of the hemi-ellipsoid is determined by similar methods as described in Section 3.3.2. However, rather than radiation being emitted diffusely from a surface, it is emitted from the depth of the flame. To find the configuration factor, an integration is performed using the heat flux per solid angle given by Equation 3.8, where the intensity is given by Equation 3.19. Therefore, the integral to be computed is

$$q = \frac{\sigma T^4}{\pi} \int_{\Omega} (1 - e^{-KL(\Omega)}) \sin(\theta) d\Omega \qquad (5.10)$$

where T is the temperature of the flame, K is the optical density per metre of the flame, and $L(\Omega)$ is the depth of the flame in the direction of the solid angle Ω. Substituting $d\Omega = \cos(\theta)\, d\theta d\phi$, and integrating over the "projected area" of the hemi-ellipsoid, the following equation is obtained

$$q = \frac{\sigma T^4}{\pi} \int_{\phi_{min}}^{\phi_{max}} \int_{0}^{\theta_{max}(\phi)} (1 - e^{-KL(\theta,\phi)}) \sin(\theta)\cos(\theta) d\theta d\phi \qquad (5.11)$$

By symmetry, $\phi_{min} = -\phi_{max}$ and the two halves of the hemi-ellipsoid are identical, so only half the shape need be integrated, and the result doubled. Hence, Equation 5.11 may be rewritten

$$q = \frac{\sigma T^4}{\pi} \int_0^{\phi_{max}} \int_0^{\theta_{max}(\phi)} (1 - e^{-KL(\theta,\phi)}) \sin(2\theta) d\theta d\phi \tag{5.12}$$

Note that the order of the integration is important. Integration is performed in the θ direction first, from 0 to a value which depends on the angle ϕ*. It is now necessary to determine the limiting angles ϕ_{max} and $\theta_{max}(\phi)$, and the path length $L(\theta,\phi)$. The limiting angle ϕ_{max} is easily determined by simple trigonometry by noting that a ray skimming the surface at this angle will be tangential to the base of the ellipsoid, so that the equation may be written

$$\phi_{max} = \sin^{-1}\left(\frac{R}{R+D}\right) \tag{5.13}$$

To find the other two limits, begin by expressing the Cartesian equation for the surface of the hemi-ellipsoid

$$z = \frac{H}{R}\sqrt{R^2 - (x^2 + y^2)} \tag{5.14}$$

A parametric equation for a ray emanating from the surface element dA in the direction $d\Omega$ may be expressed

$$\left.\begin{aligned} x &= \cos(\phi)t - (R+D) \\ y &= \sin(\phi)t \\ z &= t / \tan(\theta) \end{aligned}\right\} t \in [0,\infty) \tag{5.15}$$

To find where the ray intersects the ellipsoid, Equation 5.15 is substituted into Equation 5.14 and the resulting quadratic equation is solved for t. The two roots are given by the expressions

$$\begin{aligned} t_1 &= \frac{(D+R)\cos\phi - \sqrt{(D+R)^2\cos^2\phi - (\frac{R^2\tan^2\theta}{H^2}+1)(D^2+2DR)}}{(\frac{R^2\tan^2\theta}{H^2}+1)} \\ t_2 &= \frac{(D+R)\cos\phi + \sqrt{(D+R)^2\cos^2\phi - (\frac{R^2\tan^2\theta}{H^2}+1)(D^2+2DR)}}{(\frac{R^2\tan^2\theta}{H^2}+1)} \end{aligned} \tag{5.16}$$

These two roots are shown in Figure 5.7. The path length is now a straightforward calculation

$$L(\theta,\phi) = \frac{t_2 - t_1}{\cos\theta} = \frac{2\sqrt{(D+R)^2\cos^2\phi - (\frac{R^2\tan^2\theta}{H^2}+1)(D^2+2DR)}}{\cos\theta(\frac{R^2\tan^2\theta}{H^2}+1)} \tag{5.17}$$

---

* We could choose the dependence the other way around; the order is unimportant.

Terms inside the square root (the discriminant) determine the nature of the two roots, and hence the path length. When it is negative, the roots are non-real, corresponding to the case when the ray lies outside the hemi-ellipsoid, and when it is zero, the roots are identical and the path length is zero, corresponding to the case where the ray is tangential to the hemi-ellipsoid. This latter case occurs when $\theta = \theta_{max}(\phi)$, hence

$$(D+R)^2\cos^2\phi - \left(\frac{R^2\tan^2(\theta_{max}(\phi))}{H^2}+1\right)\cdot(D^2+2DR) = 0$$
$$\Rightarrow \theta_{max}(\phi) = \tan^{-1}\left(\frac{H}{R}\sqrt{\frac{(D+R)^2\cos^2\phi}{(D^2+2DR)}-1}\right) \qquad (5.18)$$

If Equations 5.13, 5.17, and 5.18 are substituted into Equation 5.12, the resulting integral is quite complicated, and cannot be solved in closed form. This is due to the algebraically complicated function in the exponential term introduced into the integral via the emissivity. However, a way around this is to assume that the overall flame is optically thick, and that an average emissivity may be determined by using the mean beam length, L_m, of the flame[79]. Thus, this average emissivity (a constant) may be brought out of the front of the integral. The terms remaining of the integral simply represent the projection of the hemi-ellipsoid onto the hemisphere surrounding the surface element. If the following nomenclature simplifications are made

$$s = \sin^{-1}\left(\frac{R}{R+D}\right)$$
$$a = \frac{H^2(D+R)^2}{R^2(D^2+2DR)} \qquad (5.19)$$
$$b = -\frac{H^2}{R^2}$$

then Equation 5.12 may be rewritten

$$q = \frac{\sigma T^4(1-e^{-KL_m})}{\pi}\int_0^s\int_0^{\tan^{-1}\left(\sqrt{a\cos^2\phi+b}\right)}\sin(2\theta)\,d\theta\,d\phi \qquad (5.20)$$

Somewhat remarkably, this integral has a closed form solution, and is given by

$$q = \frac{\sigma T^4(1-e^{-KL_m})}{\pi}\left[s - \frac{\tan^{-1}\left(\frac{\sqrt{(1+b)}\tan(s)}{\sqrt{(1+a+b)}}\right)}{\sqrt{(1+b)(1+a+b)}}\right] \equiv \sigma T^4(1-e^{-KL_m})F_{d1,2} \qquad (5.21)$$

where $F_{d1,2}$ is the view factor. While this equation is real valued for all H and R greater than or equal to zero, care should be taken in encoding this factor using standard programming languages (such as FORTRAN) as the value of b (-1 times the height to radius ratio) may be such that $1+b \leq 0$,

and hence the equation involves complex numbers or division by zero. However, the limit as b approaches -1 is defined and real valued so this limit can be used to avoid division by zero errors. When b is less than -1, the imaginary number i is taken out of the square root in both the numerator and denominator, the complex identity $\tan^{-1}(ix) = i\tanh^{-1}(x)$ is used, and then i is cancelled from numerator and denominator. Therefore, the configuration factor in Equation 5.21 for the three cases of b becomes

$$F_{d1,2} = \begin{cases} \frac{1}{\pi}\left(s - \frac{\tan^{-1}\left(\frac{\sqrt{(1+b)}\tan(s)}{\sqrt{(1+a+b)}} \right)}{\sqrt{(1+b)(1+a+b)}} \right) & b > -1 \\ \frac{1}{\pi}\left(s - \frac{\tan(s)}{a} \right) & b = -1 \\ \frac{1}{\pi}\left(s - \frac{\tanh^{-1}\left(\frac{\sqrt{-(1+b)}\tan(s)}{\sqrt{(1+a+b)}} \right)}{\sqrt{-(1+b)(1+a+b)}} \right) & b < -1 \end{cases} \tag{5.22}$$

For programming languages which do not have a built in function for $\tanh^{-1}$, the identity $\tanh^{-1}(x) = \frac{1}{2}\log(\frac{1+x}{1-x})$ is used. The third term in Equation 5.22 becomes

$$F_{d1,2} = \frac{1}{\pi}\left(s - \frac{\frac{1}{2}\log\left(\frac{\sqrt{(1+a+b)} + \sqrt{-(1+b)}\tan(s)}{\sqrt{(1+a+b)} - \sqrt{-(1+b)}\tan(s)} \right)}{\sqrt{-(1+b)(1+a+b)}} \right) \quad b < -1 \tag{5.23}$$

The mean beam length now needs to be accounted for. To find this, the beam length in the direction of the solid angle $d\Omega$ could be integrated over the same solid angle as in Equation 5.11, although again because of the intractable nature of the integral, it is only partly solvable in closed form, thus requiring numerical techniques to be determined fully. Instead, the approximation[79,71]

$$L_m \cong 3.6\frac{V_f}{A_b} \tag{5.24}$$

is used, where V_f is the volume of the flame, and A_b is the bounding surface area. For the hemi-ellipsoid, this is given by

$$L_m \cong 3.6\frac{\frac{2}{3}\pi R^2 H}{\frac{2}{3}\pi(2R^2 + H^2) + \pi R^2} = \frac{36R^2 H}{35R^2 + 10H^2} \tag{5.25}$$

Depending on the optical thickness of the flame, this approximation should produce emissivities close to unity for most cases except when the flame is small. This agrees with an earlier assumption that the flame is optically thick. Hence, the dominant geometric factor affecting the radiant heat flux is the view factor, or projected area, as given in Equation 5.22.

The radiant flux from the flame is now described by substituting Equation 5.25 into Equation 5.21. This may be expressed in its entirety

$$\dot{Q}''_{flame} = \frac{\sigma T_{flame}^4 (1 - e^{-K\frac{36R^2H}{35R^2+10H^2}})}{\pi} \left[\sin^{-1}\left(\frac{R}{R+D}\right) - \frac{\tan^{-1}\left(\frac{\sqrt{(1-\frac{H^2}{R^2})}\tan\left(\sin^{-1}\left(\frac{R}{R+D}\right)\right)}{\sqrt{\left(1+\frac{H^2}{(D^2+2DR)}\right)}} \right)}{\sqrt{\left(1-\frac{H^2}{R^2}\right)\left(1+\frac{H^2}{(D^2+2DR)}\right)}} \right] \qquad (5.26)$$

The total radiation received by a preheating surface element also includes the applied external radiation, $\dot{Q}''_{ext}$. The minimum value of this external radiation must be σT_{amb}^4 i.e. radiant heat due to the ambient temperature of the surroundings*. This externally applied radiation is assumed to emanate from the entire hemisphere above the surface element in question. However, a fraction of the hemisphere is occluded by the flame, namely the view factor of the flame, $F_{d1,2}$. Hence, the fraction of the applied external radiant flux incident upon the surface element is given by $(1 - F_{d1,2})\dot{Q}''_{ext}$. Also, the flame is not perfectly obscuring, so that a proportion of the external radiation will penetrated the flame region. This amount will be equal to $F_{d1,2} \cdot e^{-KL_m} \cdot \dot{Q}''_{ext}$. Hence, the total radiant flux falling on a surface element outside the flaming region is given by

$$\begin{aligned} \dot{Q}''_{total} &= \dot{Q}''_{flame} + (1 - F_{d1,2})\dot{Q}''_{ext} + (F_{d1,2} \cdot e^{-KL_m})\dot{Q}''_{ext} \\ &= \dot{Q}''_{flame} + [1 - F_{d1,2}(e^{-KL_m} - 1)]\dot{Q}''_{ext} \end{aligned} \qquad (5.27)$$

* It was discovered from preliminary numerical experiments that setting external radiation to zero resulted in cooling of the surface. This was due, as far as the model was concerned, to the surroundings effectively being at absolute zero.

5.4.3. Internal Nodes

In this model, the fuel is considered to be a regular rectangular slab. Combustion, and subsequent mass release is assumed to occur at one surface only (in this case, the upper surface.) Conduction within the fuel is calculated by solving the heat equation on an appropriately constructed grid. The fuel region is discretised with a regular square grid on the combustible surface, and an irregular grid in the direction normal to the surface. It is desirable that this grid be fine in the region of high temperature gradient, namely close to the surface. In order to maintain this fine region as the fuel regresses due to combustion, the grid "collapses" along with the fuel surface, as described in Chapter 4. Since the regression of the fuel varies across the surface, it is necessary to apply a grid transformation to restore orthogonality of the grid and make the depth of the fuel uniform. The transformation method is similar to that used previously by Singh and Thorpe.[111]

5.4.4. Grid Transformation

The analysis begins with the familiar heat conduction equation as given by Equation 4.16, this time in three dimensions. The coordinates x and y measure the directions parallel to the fuel surface, and z perpendicular to the fuel surface.

$$\frac{\partial T}{\partial t} = \alpha\left(\frac{\partial^2 T}{\partial x^2} + \frac{\partial^2 T}{\partial y^2} + \frac{\partial^2 T}{\partial z^2}\right) \tag{5.28}$$

The definition for the length, X, and width, Y, of the fuel is made, and the depth, F, where $F(x,y)$ is the local depth of the fuel at the point (x,y), which varies due to the local amount of combustion. The grid is then transformed to the unit cube via the following transformation:

$$\xi = \frac{x}{X}$$
$$\eta = \frac{y}{Y} \tag{5.29}$$
$$\zeta = \frac{z}{F}$$

The chain rule is applied to find the first spatial derivative of the temperature distributions.

$$\begin{aligned}\frac{\partial T}{\partial x} &= \frac{\partial T}{\partial \xi}\cdot\frac{\partial \xi}{\partial x}+\frac{\partial T}{\partial \eta}\cdot\frac{\partial \eta}{\partial x}+\frac{\partial T}{\partial \zeta}\cdot\frac{\partial \zeta}{\partial x}\\ &= \frac{\partial T}{\partial \xi}\cdot\frac{1}{X}+\frac{\partial T}{\partial \eta}\cdot 0+\frac{\partial T}{\partial \zeta}\cdot\frac{-z\cdot\frac{\partial F}{\partial x}}{F^2}\\ &= \frac{1}{X}\cdot\frac{\partial T}{\partial \xi}-\frac{z\cdot\frac{\partial F}{\partial x}}{F^2}\cdot\frac{\partial T}{\partial \zeta}\end{aligned} \tag{5.30}$$

Similarly,

$$\frac{\partial T}{\partial y} = \frac{1}{Y}\cdot\frac{\partial T}{\partial \eta}-\frac{z\cdot\frac{\partial F}{\partial y}}{F^2}\cdot\frac{\partial T}{\partial \zeta} \tag{5.31}$$

Also,

$$\begin{aligned}\frac{\partial T}{\partial z} &= \frac{\partial T}{\partial \xi}\cdot\frac{\partial \xi}{\partial z}+\frac{\partial T}{\partial \eta}\cdot\frac{\partial \eta}{\partial z}+\frac{\partial T}{\partial \zeta}\cdot\frac{\partial \zeta}{\partial z}\\ &= \frac{\partial T}{\partial \xi}\cdot 0+\frac{\partial T}{\partial \eta}\cdot 0+\frac{\partial T}{\partial \zeta}\cdot\frac{1}{F}\\ &= \frac{1}{F}\cdot\frac{\partial T}{\partial \zeta}\end{aligned} \tag{5.32}$$

Equations 5.30, 5.31, and 5.32 are differentiated again to find the second spatial derivatives

$$\begin{aligned}\frac{\partial^2 T}{\partial x^2} &= \frac{\partial}{\partial x}\left(\frac{\partial T}{\partial x}\right)\\ &= \frac{\partial}{\partial x}\left(\frac{1}{X}\cdot\frac{\partial T}{\partial \xi}-\frac{z\cdot\frac{\partial F}{\partial x}}{F^2}\cdot\frac{\partial T}{\partial \zeta}\right)\\ &= \frac{\partial}{\partial x}\left(\frac{1}{X}\cdot\frac{\partial T}{\partial \xi}\right)-\frac{\partial}{\partial x}\left(\frac{z\cdot\frac{\partial F}{\partial x}}{F^2}\right)\cdot\frac{\partial T}{\partial \zeta}-\frac{z\cdot\frac{\partial F}{\partial x}}{F^2}\cdot\frac{\partial}{\partial x}\left(\frac{\partial T}{\partial \zeta}\right)\\ &= \frac{\partial}{\partial \xi}\left(\frac{1}{X}\cdot\frac{\partial T}{\partial \xi}\right)\frac{\partial \xi}{\partial x}+\frac{\partial}{\partial \zeta}\left(\frac{1}{X}\cdot\frac{\partial T}{\partial \xi}\right)\frac{\partial \zeta}{\partial x}-\frac{\partial}{\partial x}\left(\frac{z\cdot\frac{\partial F}{\partial x}}{F^2}\right)\cdot\frac{\partial T}{\partial \zeta}-\frac{z\cdot\frac{\partial F}{\partial x}}{F^2}\left(\frac{\partial}{\partial \xi}\left(\frac{\partial T}{\partial \zeta}\right)\frac{\partial \xi}{\partial x}+\frac{\partial}{\partial \zeta}\left(\frac{\partial T}{\partial \zeta}\right)\frac{\partial \zeta}{\partial x}\right)\\ &= \frac{1}{X^2}\cdot\frac{\partial^2 T}{\partial \xi^2}+\frac{1}{X}\cdot\frac{\partial^2 T}{\partial \xi\partial \zeta}\cdot\frac{-z\cdot\frac{\partial F}{\partial x}}{F^2}-z\left(\frac{F^2\frac{\partial}{\partial x}\left(\frac{\partial F}{\partial x}\right)-\frac{\partial F}{\partial x}\frac{\partial}{\partial x}(F^2)}{(F^2)^2}\right)\cdot\frac{\partial T}{\partial \zeta}-\frac{z\cdot\frac{\partial F}{\partial x}}{F^2}\left(\frac{\partial^2 T}{\partial \xi\partial \zeta}\cdot\frac{1}{X}+\frac{\partial^2 T}{\partial \zeta^2}\cdot\frac{-z\cdot\frac{\partial F}{\partial x}}{F^2}\right)\\ &= \frac{1}{X^2}\cdot\frac{\partial^2 T}{\partial \xi^2}-\frac{1}{X}\cdot\frac{z\cdot\frac{\partial F}{\partial x}}{F^2}\cdot\frac{\partial^2 T}{\partial \xi\partial \zeta}-z\left(\frac{F^2\frac{\partial^2 F}{\partial x^2}-\frac{\partial F}{\partial x}\cdot 2F\cdot\frac{\partial F}{\partial x}}{F^4}\right)\cdot\frac{\partial T}{\partial \zeta}-\frac{1}{X}\cdot\frac{z\cdot\frac{\partial F}{\partial x}}{F^2}\cdot\frac{\partial^2 T}{\partial \xi\partial \zeta}+\left(\frac{z\cdot\frac{\partial F}{\partial x}}{F^2}\right)^2\frac{\partial^2 T}{\partial \zeta^2}\\ &= \frac{1}{X^2}\cdot\frac{\partial^2 T}{\partial \xi^2}-\frac{2}{X}\cdot\frac{z\cdot\frac{\partial F}{\partial x}}{F^2}\cdot\frac{\partial^2 T}{\partial \xi\partial \zeta}-z\left(\frac{F\frac{\partial^2 F}{\partial x^2}-2\left(\frac{\partial F}{\partial x}\right)^2}{F^3}\right)\cdot\frac{\partial T}{\partial \zeta}+\left(\frac{z\cdot\frac{\partial F}{\partial x}}{F^2}\right)^2\frac{\partial^2 T}{\partial \zeta^2}\end{aligned} \tag{5.33}$$

Similarly,

$$\frac{\partial^2 T}{\partial y^2} = \frac{1}{Y^2}\cdot\frac{\partial^2 T}{\partial \eta^2}-\frac{2}{Y}\cdot\frac{z\cdot\frac{\partial F}{\partial y}}{F^2}\cdot\frac{\partial^2 T}{\partial \eta\partial \zeta}-z\left(\frac{F\frac{\partial^2 F}{\partial y^2}-2\left(\frac{\partial F}{\partial y}\right)^2}{F^3}\right)\cdot\frac{\partial T}{\partial \zeta}+\left(\frac{z\cdot\frac{\partial F}{\partial y}}{F^2}\right)^2\frac{\partial^2 T}{\partial \zeta^2} \tag{5.34}$$

Also

$$\begin{aligned}\frac{\partial^2 T}{\partial z^2} &= \frac{\partial}{\partial z}\left(\frac{1}{F}\cdot\frac{\partial T}{\partial \zeta}\right)\\ &= \frac{\partial}{\partial \zeta}\left(\frac{1}{F}\cdot\frac{\partial T}{\partial \zeta}\right)\frac{\partial \zeta}{\partial z}\\ &= \frac{1}{F^2}\cdot\frac{\partial^2 T}{\partial \zeta^2}\end{aligned} \tag{5.35}$$

It is also necessary to express the partial derivatives of $F(x,y)$ in these co-ordinates. Now,

$$\frac{\partial F}{\partial x} = \frac{\partial F}{\partial \xi}\cdot\frac{\partial \xi}{\partial x} + \frac{\partial F}{\partial \eta}\cdot\frac{\partial \eta}{\partial x} + \frac{\partial F}{\partial \zeta}\cdot\frac{\partial \zeta}{\partial x} = \frac{1}{X}\cdot\frac{\partial F}{\partial \xi} \tag{5.36}$$

since F only varies in the x and y directions, i.e. $\frac{\partial F}{\partial \zeta} = 0$. Similarly,

$$\frac{\partial F}{\partial y} = \frac{1}{Y}\cdot\frac{\partial F}{\partial \eta}, \quad \frac{\partial^2 F}{\partial x^2} = \frac{1}{X^2}\cdot\frac{\partial^2 F}{\partial \xi^2}, \quad \frac{\partial^2 F}{\partial y^2} = \frac{1}{Y^2}\cdot\frac{\partial^2 F}{\partial \eta^2} \tag{5.37}$$

The heat equation may now be expressed in the new co-ordinates thus:

$$\begin{aligned}\frac{1}{\alpha}\frac{\partial T}{\partial t} &= \frac{1}{X^2}\frac{\partial^2 T}{\partial \xi^2} + \frac{1}{Y^2}\frac{\partial^2 T}{\partial \eta^2} - \left(\frac{2}{X^2}\frac{z\frac{\partial F}{\partial \xi}}{F^2}\right)\frac{\partial^2 T}{\partial \xi \partial \zeta} - \left(\frac{2}{Y^2}\frac{z\frac{\partial F}{\partial \eta}}{F^2}\right)\frac{\partial^2 T}{\partial \eta \partial \zeta}\\ &- \left(z\frac{F\left(\frac{1}{X^2}\frac{\partial^2 F}{\partial \xi^2} + \frac{1}{Y^2}\frac{\partial^2 F}{\partial \eta^2}\right) - 2\left(\frac{1}{X^2}\left(\frac{\partial F}{\partial \xi}\right)^2 + \frac{1}{Y^2}\left(\frac{\partial F}{\partial \eta}\right)^2\right)}{F^3}\right)\frac{\partial T}{\partial \zeta}\\ &+ \left(\frac{1}{F^2} + \left(\frac{z\frac{1}{X}\frac{\partial F}{\partial \xi}}{F^2}\right)^2 + \left(\frac{z\frac{1}{Y}\frac{\partial F}{\partial \eta}}{F^2}\right)^2\right)\frac{\partial^2 T}{\partial \zeta^2}\end{aligned} \tag{5.38}$$

5.4.5. Discretisation of the Heat Equation in the Transformed Co-ordinates

Since the surface is discretised in a regular fashion using a square grid, the familiar Finite Difference Method (FDM) may be employed in this situation to numerically calculate the terms $\frac{\partial^2 T}{\partial \xi^2}$, $\frac{\partial^2 T}{\partial \eta^2}$, $\frac{\partial F}{\partial \xi}$, $\frac{\partial F}{\partial \eta}$, $\frac{\partial^2 F}{\partial \xi^2}$, and $\frac{\partial^2 F}{\partial \eta^2}$ in the usual fashion[40], i.e.

$$\left.\frac{\partial F}{\partial \xi}\right|_{\substack{\xi=\xi_i \\ \eta=\eta_j}} = \frac{F(\xi_{i+1},\eta_j) - F(\xi_{i-1},\eta_j)}{2\Delta\xi}$$

$$\left.\frac{\partial F}{\partial \eta}\right|_{\substack{\xi=\xi_i \\ \eta=\eta_j}} = \frac{F(\xi_i,\eta_{j+1}) - F(\xi_i,\eta_{j-1})}{2\Delta\eta}$$

$$\left.\frac{\partial^2 F}{\partial \xi^2}\right|_{\substack{\xi=\xi_i \\ \eta=\eta_j}} = \frac{F(\xi_{i+1},\eta_j) + F(\xi_{i-1},\eta_j) - 2F(\xi_i,\eta_j)}{\Delta\xi^2}$$

$$\left.\frac{\partial^2 F}{\partial \eta^2}\right|_{\substack{\xi=\xi_i \\ \eta=\eta_j}} = \frac{F(\xi_i,\eta_{j+1}) + F(\xi_i,\eta_{j-1}) - 2F(\xi_i,\eta_j)}{\Delta\eta^2}$$

$$\left.\frac{\partial^2 T}{\partial \xi^2}\right|_{\substack{\xi=\xi_i \\ \eta=\eta_j}} = \frac{T(\xi_{i+1},\eta_j) + T(\xi_{i-1},\eta_j) - 2T(\xi_i,\eta_j)}{\Delta\xi^2}$$

$$\left.\frac{\partial^2 T}{\partial \eta^2}\right|_{\substack{\xi=\xi_i \\ \eta=\eta_j}} = \frac{T(\xi_i,\eta_{j+1}) + T(\xi_i,\eta_{j-1}) - 2T(\xi_i,\eta_j)}{\Delta\eta^2} \qquad \textbf{(5.39)}$$

Since the grid is regular in the ξ and η directions, these approximations are second order accurate[40].

In the direction normal to the surface (i.e. the ζ direction), it is desirable to have a fine grid spacing in the region of high temperature gradient, namely close to the surface. Further from the surface the grid spacing need not be as fine. This leads to a non-uniform grid spacing. If the *i*th node is denoted as ζ_i, with ζ_0 being the surface node and ζ_n the node at the opposite surface, then $\Delta\zeta_i$ is the grid spacing between ζ_{i-1} and ζ_i, and $\Delta\zeta_{i+1}$ is the grid spacing between ζ_i and $\Delta\zeta_{i+1}$ (see Figure 5.8).

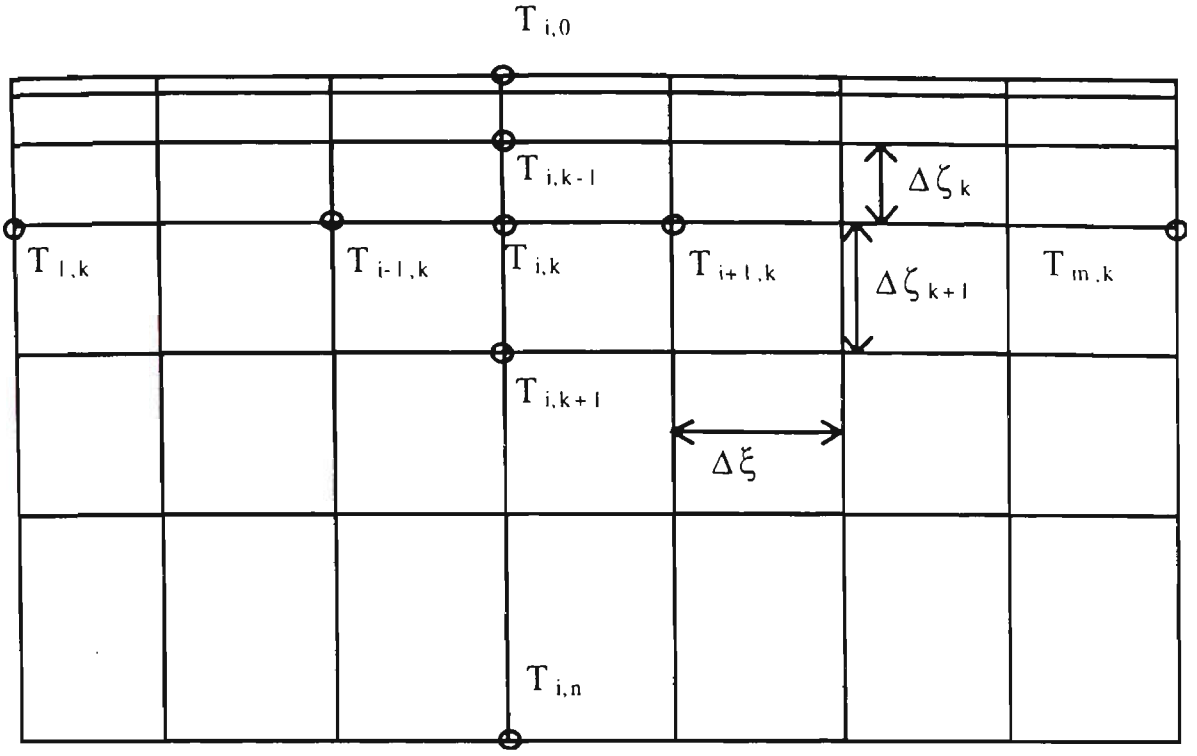

Figure 5.8 Node convention

Using this notation, the FDM for a non-uniform discretisation yields the following equations for $\frac{\partial T}{\partial \zeta}$ and $\frac{\partial^2 T}{\partial \zeta^2}$

$$\left.\frac{\partial T}{\partial \zeta}\right|_{\zeta=\zeta_k} = \frac{\Delta\zeta_k^2 T_{k+1} + (\Delta\zeta_{k+1}^2 - \Delta\zeta_k^2)T_k - \Delta\zeta_{k+1}^2 T_{k-1}}{(\Delta\zeta_k^2 \cdot \Delta\zeta_{k+1} + \Delta\zeta_k \cdot \Delta\zeta_{k+1}^2)}$$
$$\left.\frac{\partial^2 T}{\partial \zeta^2}\right|_{\zeta=\zeta_k} = \frac{2(\Delta\zeta_k T_{k+1} - (\Delta\zeta_k + \Delta\zeta_{k+1})T_k + \Delta\zeta_{k+1} T_{k-1})}{(\Delta\zeta_k^2 \cdot \Delta\zeta_{k+1} + \Delta\zeta_k \cdot \Delta\zeta_{k+1}^2)} \qquad \textbf{(5.40)}$$

It is also necessary to discretise the mixed derivatives, bearing in mind that the grid is non-uniform in the ζ direction. Begin with the Taylor expansion in two dimensions of the temperature distribution[112]

$$T(\xi_0 + \Delta\xi, \zeta_0 + \Delta\zeta) = T(\xi_0, \zeta_0) + \sum_{i=1}^{n} \frac{1}{i!}\left[\Delta\xi \cdot \frac{\partial}{\partial \xi} + \Delta\zeta \cdot \frac{\partial}{\partial \zeta}\right]^i T(\xi,\zeta)\Big|_{\substack{\xi=\xi_0 \\ \zeta=\zeta_0}} + O(n+1) \qquad \textbf{(5.41)}$$

Using the notation described above, the following four equations can be written

$$T_{i+1,k+1} = T_{i,k} + \Delta\xi\frac{\partial T}{\partial \xi} + \Delta\zeta_{k+1}\frac{\partial T}{\partial \zeta} + \frac{\Delta\xi^2}{2}\frac{\partial^2 T}{\partial \xi^2} + \Delta\xi\Delta\zeta_{k+1}\frac{\partial^2 T}{\partial \xi \partial \zeta} + \frac{\Delta\zeta_{k+1}^2}{2}\frac{\partial^2 T}{\partial \zeta^2} + O(3) \qquad \textbf{(5.42)}$$

$$T_{i+1,k-1} = T_{i,k} + \Delta\xi\frac{\partial T}{\partial \xi} - \Delta\zeta_k\frac{\partial T}{\partial \zeta} + \frac{\Delta\xi^2}{2}\frac{\partial^2 T}{\partial \xi^2} - \Delta\xi\Delta\zeta_k\frac{\partial^2 T}{\partial \xi \partial \zeta} + \frac{\Delta\zeta_k^2}{2}\frac{\partial^2 T}{\partial \zeta^2} + O(3) \qquad \textbf{(5.43)}$$

$$T_{i-1,k+1} = T_{i,k} - \Delta\xi \frac{\partial T}{\partial \xi} + \Delta\zeta_{k+1} \frac{\partial T}{\partial \zeta} + \frac{\Delta\xi^2}{2} \frac{\partial^2 T}{\partial \xi^2} - \Delta\xi\Delta\zeta_{k+1} \frac{\partial^2 T}{\partial \xi \partial \zeta} + \frac{\Delta\zeta_{k+1}^2}{2} \frac{\partial^2 T}{\partial \zeta^2} + O(3) \quad (5.44)$$

$$T_{i-1,k-1} = T_{i,k} - \Delta\xi \frac{\partial T}{\partial \xi} - \Delta\zeta_{k} \frac{\partial T}{\partial \zeta} + \frac{\Delta\xi^2}{2} \frac{\partial^2 T}{\partial \xi^2} + \Delta\xi\Delta\zeta_{k} \frac{\partial^2 T}{\partial \xi \partial \zeta} + \frac{\Delta\zeta_{k}^2}{2} \frac{\partial^2 T}{\partial \zeta^2} + O(3) \quad (5.45)$$

Subtracting Equation 5.43 from Equation 5.42, and Equation 5.45 from Equation 5.44 yields

$$T_{i+1,k+1} - T_{i+1,k-1} = (\Delta\zeta_{k+1} + \Delta\zeta_{k}) \frac{\partial T}{\partial \zeta} + \Delta\xi(\Delta\zeta_{k+1} + \Delta\zeta_{k}) \frac{\partial^2 T}{\partial \xi \partial \zeta} + \frac{(\Delta\zeta_{k+1}^2 - \Delta\zeta_{k}^2)}{2} \frac{\partial^2 T}{\partial \zeta^2} + O(3) \quad (5.46)$$

$$T_{i-1,k+1} - T_{i-1,k-1} = (\Delta\zeta_{k+1} + \Delta\zeta_{k}) \frac{\partial T}{\partial \zeta} - \Delta\xi(\Delta\zeta_{k+1} + \Delta\zeta_{k}) \frac{\partial^2 T}{\partial \xi \partial \zeta} + \frac{(\Delta\zeta_{k+1}^2 - \Delta\zeta_{k}^2)}{2} \frac{\partial^2 T}{\partial \zeta^2} + O(3) \quad (5.47)$$

Finally, Equation 5.47 is subtracted from Equation 5.46 and rearranged to give

$$\left.\frac{\partial^2 T}{\partial \xi \partial \zeta}\right|_{\substack{\xi=i \\ \zeta=k}} = \frac{T_{i+1,k+1} - T_{i+1,k-1} - T_{i-1,k+1} + T_{i-1,k-1}}{2\Delta\xi(\Delta\zeta_{k+1} + \Delta\zeta_{k})} \quad (5.48)$$

Similarly

$$\left.\frac{\partial^2 T}{\partial \eta \partial \zeta}\right|_{\substack{\eta=j \\ \zeta=k}} = \frac{T_{j+1,k+1} - T_{j+1,k-1} - T_{j-1,k+1} + T_{j-1,k-1}}{2\Delta\eta(\Delta\zeta_{k+1} + \Delta\zeta_{k})} \quad (5.49)$$

5.4.6. Boundary Conditions

Boundary conditions apply to two areas of the simulated fuel region. Firstly, in the usual location at the edges of the fuel, and secondly at cells adjacent to other cells which have burnt out and are no longer part of the calculation region. The discretised equations described above do not apply here, as they refer to cells which are outside the calculation region. A common way of dealing with this situation, which is used in this model, is to assume that the boundary is perfectly insulated. Effectively, this means that the temperature gradient at the boundary is zero, resulting in no heat flux being transferred across the boundary. Thus, heat transfer only occurs to or from cells still in the calculation region which are in contact with the cell in question.

For the mixed derivatives, Equation 5.41 is taken and expanded on one side of the central node only (this is done by taking $\Delta\xi = 0$, so that effectively the expansion is in the ζ direction only.) This results in the following "one-sided" discretisation equations

$$T_{i,k+1} = T_{i,k} + \Delta\zeta_{k+1}\frac{\partial T}{\partial \zeta} + \frac{\Delta\zeta_{k+1}^2}{2}\frac{\partial^2 T}{\partial \zeta^2} \tag{5.50}$$

$$T_{i,k-1} = T_{i,k} + \Delta\zeta_{k}\frac{\partial T}{\partial \zeta} + \frac{\Delta\zeta_{k}^2}{2}\frac{\partial^2 T}{\partial \zeta^2} \tag{5.51}$$

Subtracting Equation 5.51 from Equation 5.50 yields

$$T_{i,k+1} - T_{i,k-1} = (\Delta\zeta_{k+1} + \Delta\zeta_{k})\frac{\partial T}{\partial \zeta} + \frac{(\Delta\zeta_{k+1}^2 - \Delta\zeta_{k}^2)}{2}\frac{\partial^2 T}{\partial \zeta^2} \tag{5.52}$$

In turn Equation 5.52 is subtracted from Equation 5.46 and rearranged to give

$$\left.\frac{\partial^2 T}{\partial\xi\partial\zeta}\right|_{\substack{\xi=i\\ \zeta=k}} = \frac{T_{i+1,k+1} - T_{i+1,k-1} - T_{i,k+1} + T_{i,k-1}}{\Delta\xi(\Delta\zeta_{k+1} + \Delta\zeta_{k})} \tag{5.53}$$

Similarly

$$\left.\frac{\partial^2 T}{\partial\xi\partial\zeta}\right|_{\substack{\xi=i\\ \zeta=k}} = \frac{T_{i-1,k-1} - T_{i-1,k+1} - T_{i,k-1} + T_{i,k+1}}{\Delta\xi(\Delta\zeta_{k+1} + \Delta\zeta_{k})} \tag{5.54}$$

Similar expressions can also be derived for the η direction. Note that if Equation 5.53 is added to Equation 5.54, Equation 5.48 multiplied by 4 is obtained. This is useful to know in constructing the calculation procedure in the model. The separate contributions of each neighbour of the cell in the relevant direction is simply added, then divided by four if both neighbours are involved. (This saves on the condition checking in the routine; rather than check all four cases and use a separate discretisation equation for each, the contributions from both neighbours are added, so that the only check is whether both neighbours are involved.)

For the other terms, the insulated boundary condition may be simulated by considering a virtual node which is a "mirror image" of the boundary node in question, the "mirror" being the plane of the boundary. For example, if the node at (i,j) has no neighbour at i-1, then the discretised equation for $\frac{\partial^2 T}{\partial \xi^2}$ as given in Equation 5.39 results in the expression

$$\frac{\partial^2 T}{\partial \xi^2} = \frac{T_{i+1,j} - T_{i,j}}{\Delta\xi^2} \tag{5.55}$$

Similar expressions may be written for the other terms in Equation 5.39. Note that if both neighbours are absent, both sides of the cell are perfectly insulated and no heat should flow out of

the cell (in that direction, at least.) Indeed, if $T_{i,j}$ is also substituted for $T_{i+1,j}$ in Equation 5.55, the resulting expression is

$$\frac{\partial^2 T}{\partial \xi^2} = 0$$

as required.

5.4.7. Solution of the Discretised Equations

All the terms appearing in the heat equation for transformed coordinates, as given by Equation 5.38, have now been discretised. If the following definitions are made

$$P = \frac{1}{X^2}\frac{\partial^2 T}{\partial \xi^2} + \frac{1}{Y^2}\frac{\partial^2 T}{\partial \eta^2} - \left(\frac{2}{X^2}\frac{z\frac{\partial F}{\partial \xi}}{F^2}\right)\frac{\partial^2 T}{\partial \xi \partial \zeta} - \left(\frac{2}{Y^2}\frac{z\frac{\partial F}{\partial \eta}}{F^2}\right)\frac{\partial^2 T}{\partial \eta \partial \zeta}$$

$$Q = z\frac{F\left(\frac{1}{X^2}\frac{\partial^2 F}{\partial \xi^2} + \frac{1}{Y^2}\frac{\partial^2 F}{\partial \eta^2}\right) - 2\left(\frac{1}{X^2}\left(\frac{\partial F}{\partial \xi}\right)^2 + \frac{1}{Y^2}\left(\frac{\partial F}{\partial \eta}\right)^2\right)}{F^3} \qquad (5.56)$$

$$R = \frac{1}{F^2} + \left(\frac{z\frac{1}{X}\frac{\partial F}{\partial \xi}}{F^2}\right)^2 + \left(\frac{z\frac{1}{Y}\frac{\partial F}{\partial \eta}}{F^2}\right)^2$$

then, for clarity, Equation 5.38 may be rewritten

$$\frac{1}{\alpha}\frac{\partial T}{\partial t} = P - Q\frac{\partial T}{\partial \zeta} + R\frac{\partial^2 T}{\partial \zeta^2} \qquad (5.57)$$

Before a solution of the discretised equation is attempted, it should be noted that the problem is now three dimensional instead of the one dimensional, as was presented in Section 4.3.2, but that the problem remains of the collapsing grid in the z direction. (Even though the transformed grid does not strictly vanish, the quantity F appears in the denominator of most terms in the transformed equation, leading to divergence as F locally approaches 0.) Hence, an explicit solution of the finite difference equation will eventually lead to numerical instabilities. However, an implicit solution is not immediately forthcoming, as this would involve 15 unknowns on the right hand side of Equation 5.57, leading to a system of equations which is far more complex than the simple tridiagonal matrix, and therefore extremely laborious to calculate. An implicit method for three dimensions, the Alternating Direction Implicit (ADI) method, has been developed[51] for solving two and three dimensional problems. In this scheme, for three dimensions, the time step is divided into three parts, and the tridiagonal matrix solves the intermediate (or final) temperatures implicitly in one direction, using the initial (or previous intermediate) temperatures to calculate the terms

explicitly in the other two directions. In the three intermediate steps, each direction is solved once implicitly, and this yields an unconditionally stable solution.

However, the ADI method was not used here, for two main reasons. Firstly, the ADI method was developed for an orthogonal grid, meaning that there are only seven unknowns on the right hand side of the finite difference equation, requiring only a simple tridiagonal matrix to be solved implicitly in each direction. In the case of the transformed equation, the appearance of the mixed derivatives introduces four extra unknowns in each of the ξ and η directions, so that the implicit solution in either of these directions no longer involves only three unknowns, so the tridiagonal matrix method cannot be used. Secondly, the transformation itself introduces a degree of complexity, and correspondingly an increased calculation time, in order to model a phenomenon (forward solid phase conduction) which is seldom a dominant heat transfer mechanism, if indeed significant. The computational effort required for an implicit solution of the forward heat conduction would be disproportionate to the importance of the phenomena.

Fortunately, it is possible to avoid solving Equation 5.57 implicitly in three dimensions. Since the fuel does not collapse in the ξ and η directions, a judicious choice of grid spacings, $\Delta\xi$ and $\Delta\eta$, and time step, Δt, will ensure that explicitly calculating the terms $\frac{\partial^2 T}{\partial \xi^2}$, $\frac{\partial^2 T}{\partial \eta^2}$, $\frac{\partial^2 T}{\partial \xi \partial \zeta}$, and $\frac{\partial^2 T}{\partial \eta \partial \zeta}$ will not lead to instabilities. Therefore, the only terms which need to be solved for implicitly are $\frac{\partial T}{\partial \zeta}$ and $\frac{\partial^2 T}{\partial \zeta^2}$. Thus, the discretised version of Equation 5.57 (ignoring the i and j subscripts) may be written as

$$\frac{1}{\alpha}\frac{T_k - T_k^{old}}{\Delta t} = P - Q\frac{\Delta\zeta_k^2 T_{k+1} + (\Delta\zeta_{k+1}^2 - \Delta\zeta_k^2)T_k - \Delta\zeta_{k+1}^2 T_{k-1}}{(\Delta\zeta_k^2 \cdot \Delta\zeta_{k+1} + \Delta\zeta_k \cdot \Delta\zeta_{k+1}^2)} + R\frac{2(\Delta\zeta_k T_{k+1} - (\Delta\zeta_k + \Delta\zeta_{k+1})T_k + \Delta\zeta_{k+1} T_{k-1})}{(\Delta\zeta_k^2 \cdot \Delta\zeta_{k+1} + \Delta\zeta_k \cdot \Delta\zeta_{k+1}^2)} \quad (5.58)$$

Gathering terms,

$$\begin{aligned}
\frac{1}{\alpha}\frac{T_k - T_k^{old}}{\Delta t} - P &= \frac{-Q\Delta\zeta_k^2 + 2R\Delta\zeta_k}{(\Delta\zeta_k^2 \cdot \Delta\zeta_{k+1} + \Delta\zeta_k \cdot \Delta\zeta_{k+1}^2)} T_{k+1} \\
&+ \frac{-Q(\Delta\zeta_{k+1}^2 - \Delta\zeta_k^2) - 2R(\Delta\zeta_k + \Delta\zeta_{k+1})}{(\Delta\zeta_k^2 \cdot \Delta\zeta_{k+1} + \Delta\zeta_k \cdot \Delta\zeta_{k+1}^2)} T_k \\
&+ \frac{Q\Delta\zeta_{k+1}^2 + 2R\Delta\zeta_{k+1}}{(\Delta\zeta_k^2 \cdot \Delta\zeta_{k+1} + \Delta\zeta_k \cdot \Delta\zeta_{k+1}^2)} T_{k-1} \\
T_k^{old} + \alpha\Delta t \cdot P &= \alpha\Delta t \frac{Q\Delta\zeta_k - 2R}{\Delta\zeta_{k+1}(\Delta\zeta_k + \Delta\zeta_{k+1})} T_{k+1} \\
&+ \left(\alpha\Delta t \frac{Q(\Delta\zeta_{k+1} - \Delta\zeta_k) + 2R}{\Delta\zeta_k \cdot \Delta\zeta_{k+1}} + 1 \right) T_k \\
&+ \alpha\Delta t \frac{-Q\Delta\zeta_{k+1} - 2R}{\Delta\zeta_k(\Delta\zeta_k + \Delta\zeta_{k+1})} T_{k-1}
\end{aligned} \tag{5.59}$$

This is in the same form as Equation 4.22, i.e. $d_k = a_k T_{k-1}^{new} + b_k T_k^{new} + c_k T_{k+1}^{new}$ where

$$\left.\begin{aligned}
a_k &= \alpha\Delta t \frac{-Q\Delta\zeta_{k+1} - 2R}{\Delta\zeta_k(\Delta\zeta_k + \Delta\zeta_{k+1})} \\
b_k &= \alpha\Delta t \frac{Q(\Delta\zeta_{k+1} - \Delta\zeta_k) + 2R}{\Delta\zeta_k \cdot \Delta\zeta_{k+1}} + 1 \\
c_k &= \alpha\Delta t \frac{Q\Delta\zeta_k - 2R}{\Delta\zeta_{k+1}(\Delta\zeta_k + \Delta\zeta_{k+1})} \\
d_k &= T_k^{old} + \alpha\Delta t \cdot P
\end{aligned}\right\} k = 1, \cdots, n-1 \tag{5.60}$$

The solution is now straightforward. First, the terms Q and R from Equation 5.56 are evaluated, and the terms in P calculated explicitly from the previous temperatures. Then, the terms in Equation 5.60 are evaluated in terms of the calculated P, Q, and R. The surface node temperatures are calculated before the internal nodes, and hence are a known quantity in the equations. The surface node temperature and its coefficient, $a_1 T_{i,j,0}$, may be subtracted from d_1. The opposite surface is assumed to be perfectly insulated, which is equivalent to setting $c_n T_{n+1} = a_n T_{n-1}$, so that $a_n T_{n-1}$ is effectively replaced by $2a_n T_{n-1}$ in the last equation. The system of equations may be solved by the tridiagonal matrix algorithm as described in Section 4.3.2 to determine the internal node temperatures.

5.5. STRUCTURE OF THE MODEL

Described here is an overview of the model itself in its entirety. A flow chart of the process is shown in Figure 5.9.

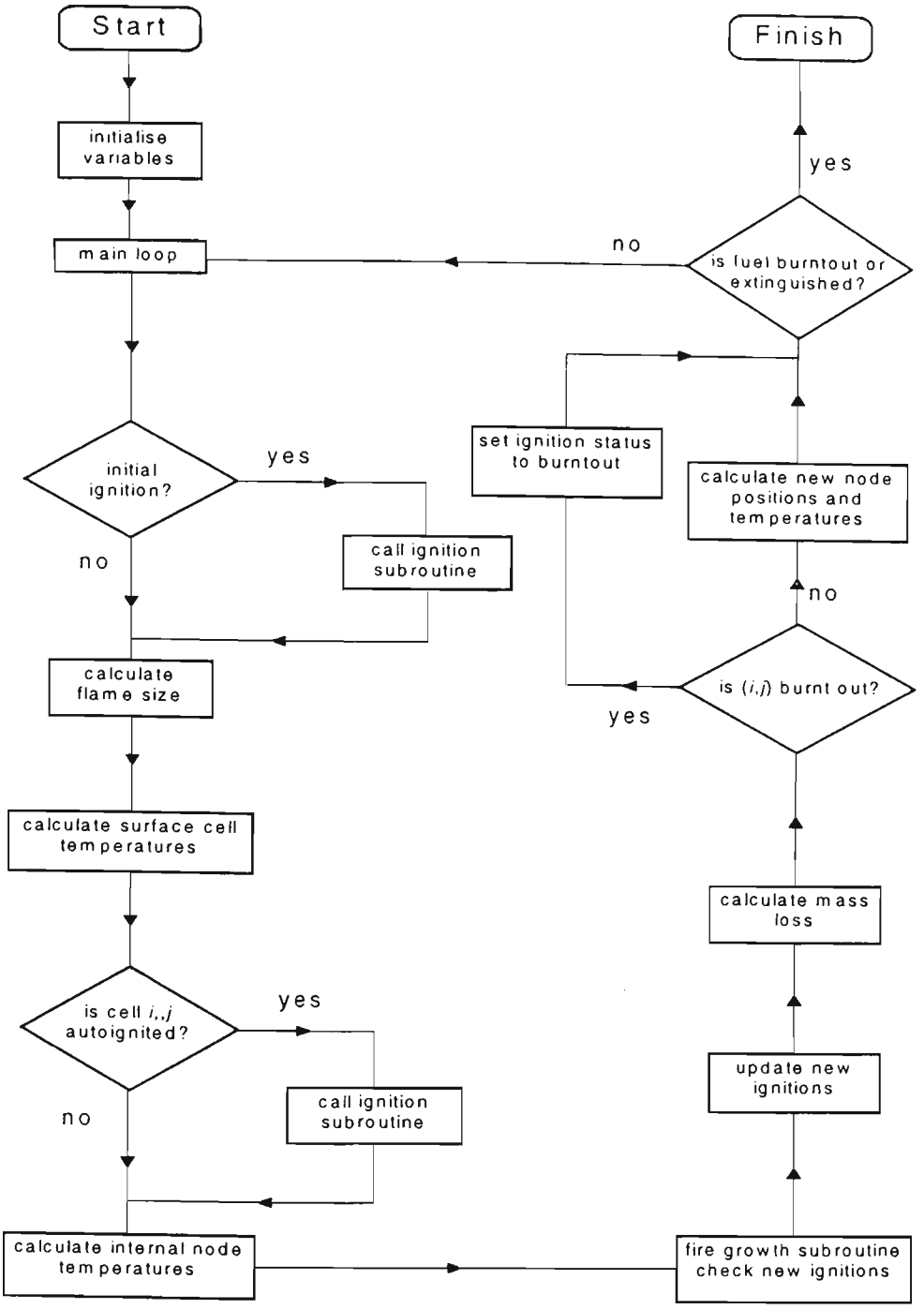

Figure 5.9 Flow chart for the stand-alone flame spread model

The model begins by reading in the material constants and other physical data which prevail throughout the run. These quantities are listed in the input file for the FORTRAN 77 program of the model, shown in Appendix A . The quantities include the fuel dimensions and grid spacings, fuel thermal properties, ignition temperatures, heat release and flame data, pyrolysis constants, ambient conditions, and solution methods. Temperature at all nodes is initially set to ambient temperature.

After initialisation of variables, the main iteration loop commences. The model allows for a preheat time period. If the model is in the preheat stage, the flame size and view factor routines are skipped, and the model proceeds directly to the temperature calculation routines. At the first iteration after the preheat period, a specified burning region is ignited. Each time a cell is ignited, the cellular automata subroutine described in Section 5.2.3 is executed, so that the unignited cells neighbouring ignited cells are accounted for.

If combustion has commenced, it is necessary to calculate the size of the flame. As described earlier, the flame is assumed to be hemi-ellipsoidal in shape. The base of the flame is therefore assumed to be circular. The equivalent diameter, D, of the base is calculated from the total area, A, of the ignited cells by the simple formula $D = 2\sqrt{\frac{A}{\pi}}$. For the purpose of calculating the diameter, burntout cells are considered to be ignited cells. The height is calculated from Equation 5.9. The heat release rate required in Equation 5.9 is equal to the sum of the pyrolysis rate for all cells multiplied by the heat of combustion. The pyrolysis rates are taken from the previous iteration (which are zero for the first iteration). If the height is found to be less than zero (as may be the case near burnout, when the diameter is large and the heat release rate low) the height is set to zero.

The next step in the routine is to calculate the surface temperature. The cells are all checked systematically. If a cell is burntout, the temperature calculation is skipped and the procedure moves on to the next cell. If a cell is unignited, the view factor of the flame is first calculated. The surface temperature of each cell is then calculated. The surface temperature is dependent on the pyrolysis rate and vice-versa, so that once the temperature is solved, the pyrolysis rate is likewise determined. A check is also made for autoignition at this stage, since a cell will ignite upon reaching critical autoignition temperature, regardless of the state of its neighbours. After the surface temperatures are calculated, the internal temperatures are all calculated.

Once all temperatures, both internal and surface, have been calculated, a check is made of cells for piloted ignition. As described in Section 5.2.3, only cells which are neighbouring ignited cells are checked. If such a cell in question satisfies the both criteria of being at pilot temperature and having three or more ignited neighbours, it is ignited. After all new ignitions have been determined, the ignition status of the newly ignited cells is updated.

The next stage is to calculate the mass loss from each cell. If the pyrolysis rate of the cell is less than the mass of the cell, then the cell's mass is reduced by the appropriate amount, the nodes shifted, and the temperatures at the new node positions calculated. If the pyrolysis rate is greater than the mass remaining, then the pyrolysis rate is reset to the remaining mass multiplied by the

time step, and the ignition status of the cell set to burntout. As each check is being made, the mass and pyrolysis rate of the cell is added to a total. If the total mass falls to zero, then the fuel has burnt to completion, and the program halts. Also, if the total pyrolysis rate falls below a certain value, after an initial ignition has taken place (i.e. after the preheat phase), then combustion is deemed to have ceased, and the program halts. Otherwise, data is written to output, the time step incremented, and the next iteration performed, until either burnout or extinguishment occurs.

5.5.1. Early Modelling Results

The early development of the model was first compared with a flame spread experiment conducted previously at the EBFF[8], in which a half-mattress of standard polyurethane foam measuring 940×950×150mm was ignited in the centre, and flame allowed to spread radially across the surface. Results of the model were presented elsewhere in a conference paper[11], which is included here in Appendix C. The effective diameter of the flame is shown in Figure 5.10, while the rate of mass loss is shown in Figure 5.11. Overall, there is good agreement in the experimental and modelling data, which is an encouraging outcome for the flame spread model. Values for the variables in the model were obtained, where available, from values for "typical" standard polyurethane foam[11]. The exceptions were the flame temperature and pre-exponential factor for the thermal degradation reaction, which were refined by trial and error running of the model.

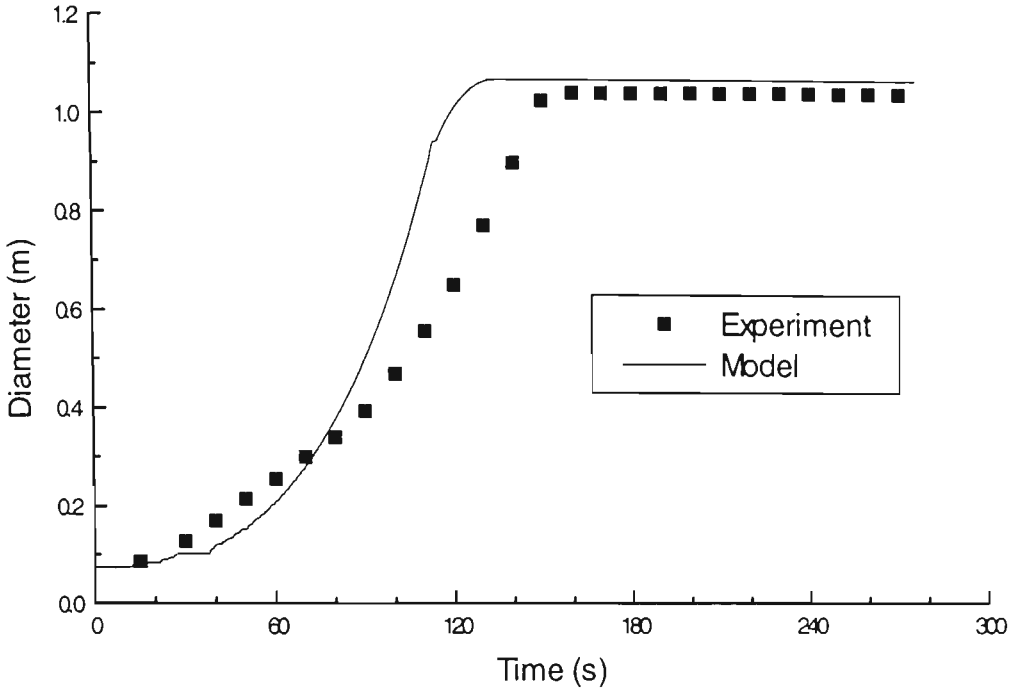

Figure 5.10 Effective flame diameter for half-mattress flame spread test

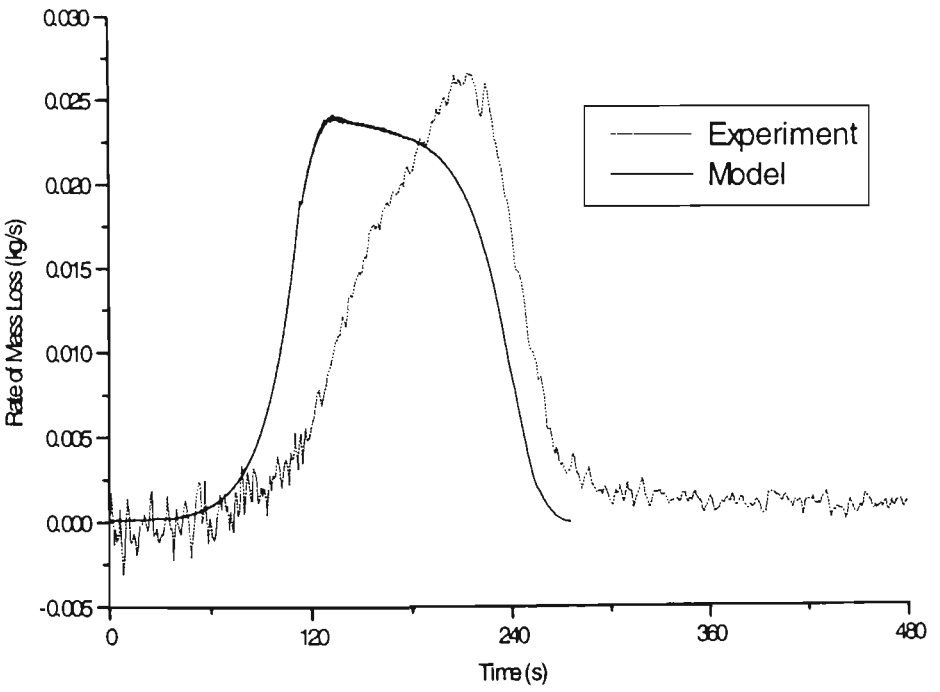

Figure 5.11 Mass loss rate for half-mattress flame spread test

The experiments themselves were not performed in an entirely suitable manner for validation of the stand-alone flame spread model. The half-mattress was open on the sides and lower surface, and placed on a wire rack which elevated it above the floor. When the fuel slab burned through in the middle, molten products flowed to floor level, forming a small pool fire below the slab. Also, upon reaching the edge of the surface, flame spread continued to the sides of the slab. As the stand-alone model assumes combustion only from the top surface and perfect insulation at the bottom and sides, this differs from the behaviour of the fuel slab in the experiments. Another factor is the combustion of the fuel slab occurred in a 2.4×3.6×2.4m room, which caused a buildup of hot products in the enclosure and likely increased heat feedback to the fuel surface, in turn causing an increase in mass loss and flame spread rates. However, the stand-alone flame spread model has only been constructed to consider a constant external heat flux, so this increasing heat feedback cannot be represented in the model.

The opportunity arose to perform a series of more precise and constrained experiments, which avoided the effects outlined above, and therefore was closer to the idealised situation encoded in the stand-alone flame spread model. This series of experiments is described in the next section.

5.6. FURNITURE CALORIMETER EXPERIMENTS

5.6.1. Aims

A series of experiments was performed in the furniture calorimeter at the Division for Building, Construction and Engineering (Highett), CSIRO. The aim of this series of experiments was to provide large scale flame spread, mass loss and heat release data for comparison and correlation with results obtained from the stand-alone flame spread model described in Section 5.4. The furniture calorimeter was chosen for these tests over full-scale room tests at the EBFF, Fiskville, as the exhausting of the product gases reduces the radiative feedback from the hot gas layer, as would occur in a room test. Since the stand alone model has no provision for a changing ambient radiation feedback, this is a desirable feature of the furniture calorimeter. An additional factor for the choice was the increased accuracy of heat release rate data of the furniture calorimeter over the "door calorimeter" [113] in place at the EBFF. While the door calorimeter has been shown to be quite accurate for steady state fires and large fires in small rooms, the method is not accurate for relatively small fires in large rooms due to accumulation of products within the room itself[113].

The tests were undertaken by the technical staff responsible for the operation and maintenance of the furniture calorimeter, with the assistance of the author. Preparation of the fuel sample and sample holder, and the location of the video camera for acquisition of visual data, were specified by the author.

5.6.2. Methods

The furniture calorimeter is an apparatus for measuring the heat release rate of large scale fires. It consists of a large hood with an area of 3m×3m which collects the products of combustion, and funnels them into a narrower fan-driven exhaust duct where various temperature and chemical analysis samplers reside. As with the cone calorimeter, heat release is calculated by the method of oxygen consumption[114]. Construction and operation of the hood conforms to the international standard test ISO-9705[114]. The hood is placed outside the compartment opening for room tests, but when being used for furniture tests, the combustible item is placed directly under the hood.

Three tests were performed on standard polyurethane foam slabs, measuring 560×560×100 mm, which were conditioned for 7 days at 25°C and 50% humidity. In each test, the slab was ignited in the centre with a small solid fuel tablet, and the radius and height of the flame, heat release rate, and mass loss were measured as a function of time. Heat release data were obtained from the continuous recording of oxygen concentration and flow rate through the exhaust duct. Flame spread was recorded by marking a 2cm grid on the surface of the foam and making a video recording of the flame spread for later analysis.

For Tests 1 and 3, the video camera was positioned approximately 3 metres from the centre of the foam slab with an elevation approximately 1.5 meters higher than the fuel surface. The foam slab was aligned so that one corner was aimed towards the video camera. For Test 2, the camera was positioned so that it was viewing one side of the slab, elevated such that the camera was almost level with the fuel surface*, so that the flame height could be measured. The camera was positioned 10 metres from the fuel slab to minimise parallax errors in measuring flame heights. A piece of steel mesh was placed near the slab, between the slab and the camera, to serve as a scale for height measurements. The spacing of the mesh grid was 100mm.

* The camera tripod was adjusted to its lowest, which was slightly higher than fuel level

Flame heights measured correspond to the persistent region of the flame. This is the region where flame may be observed 100% of the time (as opposed to the intermittent region, where flame may be observed only part of the time). The measurements were taken by video playback, noting the height after every 5 second interval of the test. The video was paused at the beginning of the time interval, and examined frame by frame throughout one second. The video was recorded at 25 frames per second, so this number of frames was examined. The flame height was recorded as the minimum height persistently visible over the one second interval.

The balance used to measure the mass of specimen could not be directly logged electronically to obtain the mass loss data. Therefore, the mass was recorded by directing a second video camera at the electronic display of the mass balance, and displaying the video picture as a frame within the main video of the burning fuel. Also superimposed on the main video was a timer recording the duration of the test. Mass loss as a function of time was later noted manually for 5 second intervals of the burning test by replaying the video.

5.6.3. Video Results

One full flame oscillation is shown in Figure 5.12 for Test 2 and Figure 5.15 for Test 3, with video stills obtained two frames apart, i.e. every 0.08s. The minimum typically occurred just after the "neck" of the flame was "pinched off" by vortex shedding, shown in Figure 5.13 for Test 2. The flame height as reported by Heskestad[109] refers to the height where the flame may be observed 50% of the time. As it is difficult to accurately measure this by visual means alone, the minimum height is used, noting that this will consistently underestimate the heights given by Heskestad. Also, at peak burning (150s), the top of the flame was frequently obscured by the calorimeter hood (Figure 5.14), increasing the difficulty of making height estimations at this point of the test.

While the testing of foams in the furniture calorimeter has its advantages over testing in a non-vented enclosure, a disadvantage manifested itself in the operation of these experiments. The operation of the hood extraction unit caused draughts in the vicinity of the flame. This had a marked effect particularly in the early stages of combustion of the specimens, when the flame was small and easily disturbed by air currents. While the spreading flame front appeared more or less circular, the circle centre was displaced progressively downwind of the initial ignition point, so that the spreading flame reached one edge of the fuel significantly earlier than the other. To make matters worse, the degree of displacement varied from test to test.

The growth of the fire from ignition to full surface involvement for Test 3 is shown in Figure 5.16 and Figure 5.17. This particular test burned the most symmetrically of the three tests conducted, although an asymmetry becomes apparent at around 90 seconds. As viewed from the video angle, there is a shift of the flame centre towards the back right-hand corner of the fuel slab, so that the spreading flame reached the back edge of the fuel before the front edge, and the right edge before the left edge. The third last frame in Figure 5.17, at t=135s, shows that the front-left corner is the last portion of the fuel surface to become involved in the fire. This was also true of Tests 1 and 2, which indicates that there was a prevailing air current present in the apparatus.

One of the suggested operating constraints on the furniture calorimeter is that the flow velocity under the hood should not exceed 0.4 m/s. The calorimeter was indeed operating within this constraint, as was reconfirmed with a hand-held anemometer after the experiments had taken place. So, while venting of the smoke and hot products produces a fire scenario which is simpler to model empirically in terms of heat feedback, the induced currents caused by venting reintroduces a degree of complexity back into the fire scenario. This series of tests shows that the flame is sensitive to currents of air whose velocity is lower than 0.4 m/s. While (initially) quiescent conditions are most desirable for modelling purposes, this is very difficult to achieve if forced ventilation is present.

t_0=106s

$t=t_0+0.08s$

$t=t_0+0.16s$

$t=t_0+0.24s$

$t=t_0+0.32s$

$t=t_0+0.40s$

$t=t_0+0.48s$

$t=t_0+0.56s$

Figure 5.12 Video stills of the oscilliating flame 106 seconds after ignition (Test 2)

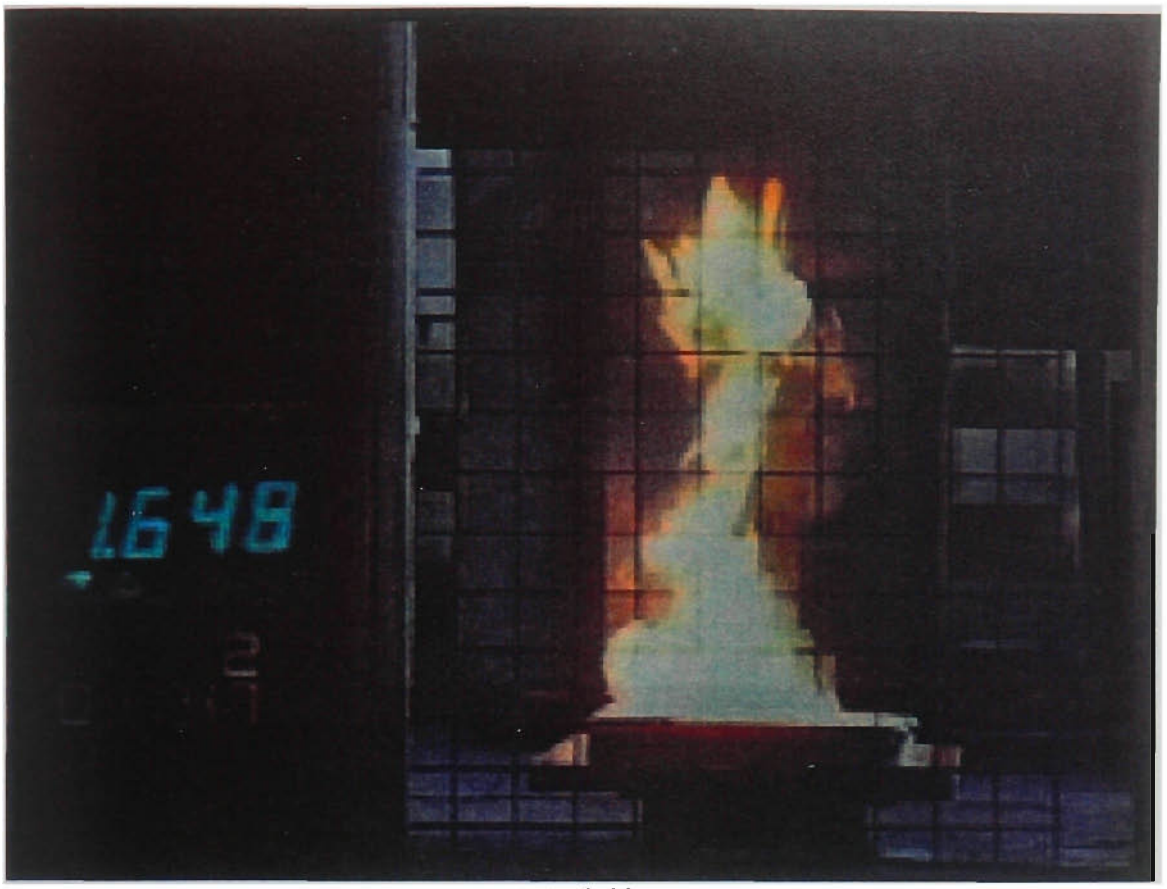

$t=t_0+0.44s$

Figure 5.13 Video still of the flame 106 seconds after ignition as the neck is "pinched off" (Test 2)

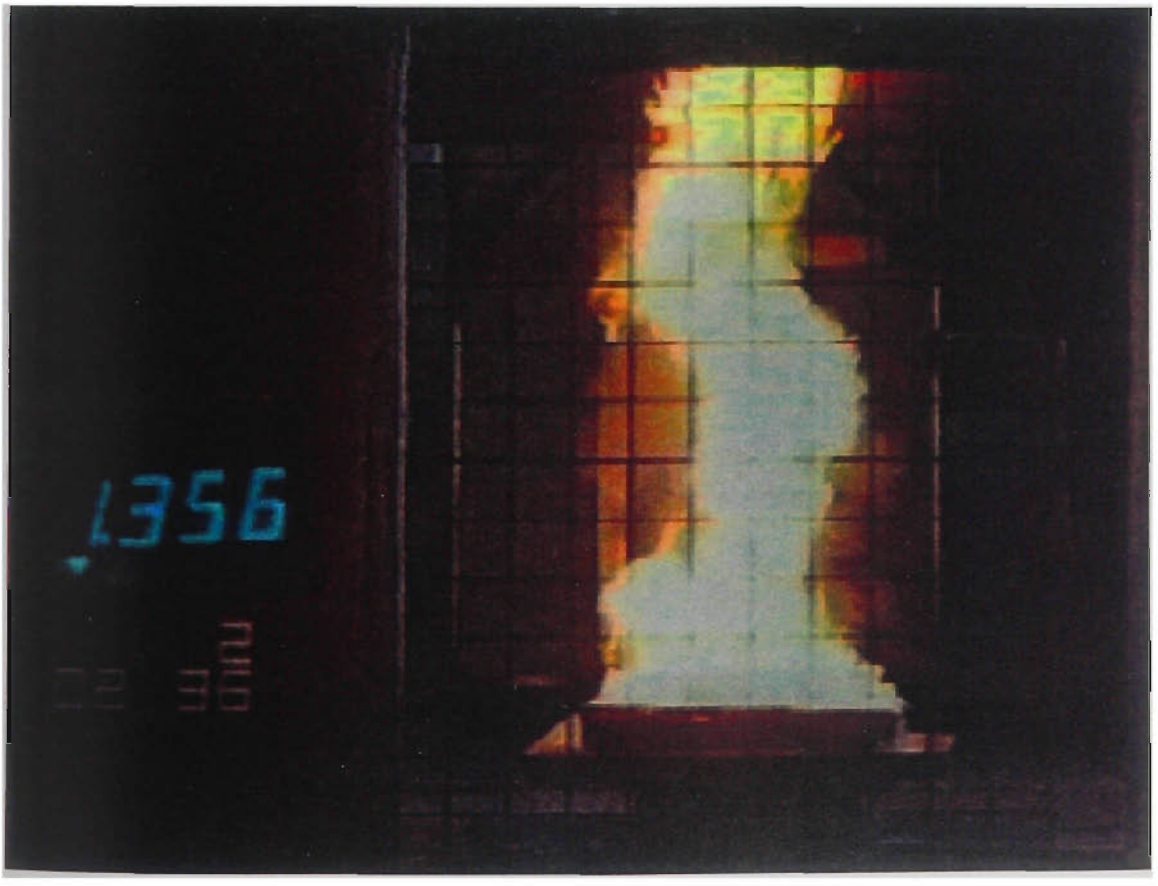

Figure 5.14 Flame at peak burning 156 seconds after ignition (Test 2)

t_0=90s	t_0+0.08s
t_0+0.16s	t_0+0.24s
t_0+0.32s	t_0+0.40s
t_0+0.48s	key

Figure 5.15 Video stills of the oscilliating flame 90 seconds after ignition (Test 3)

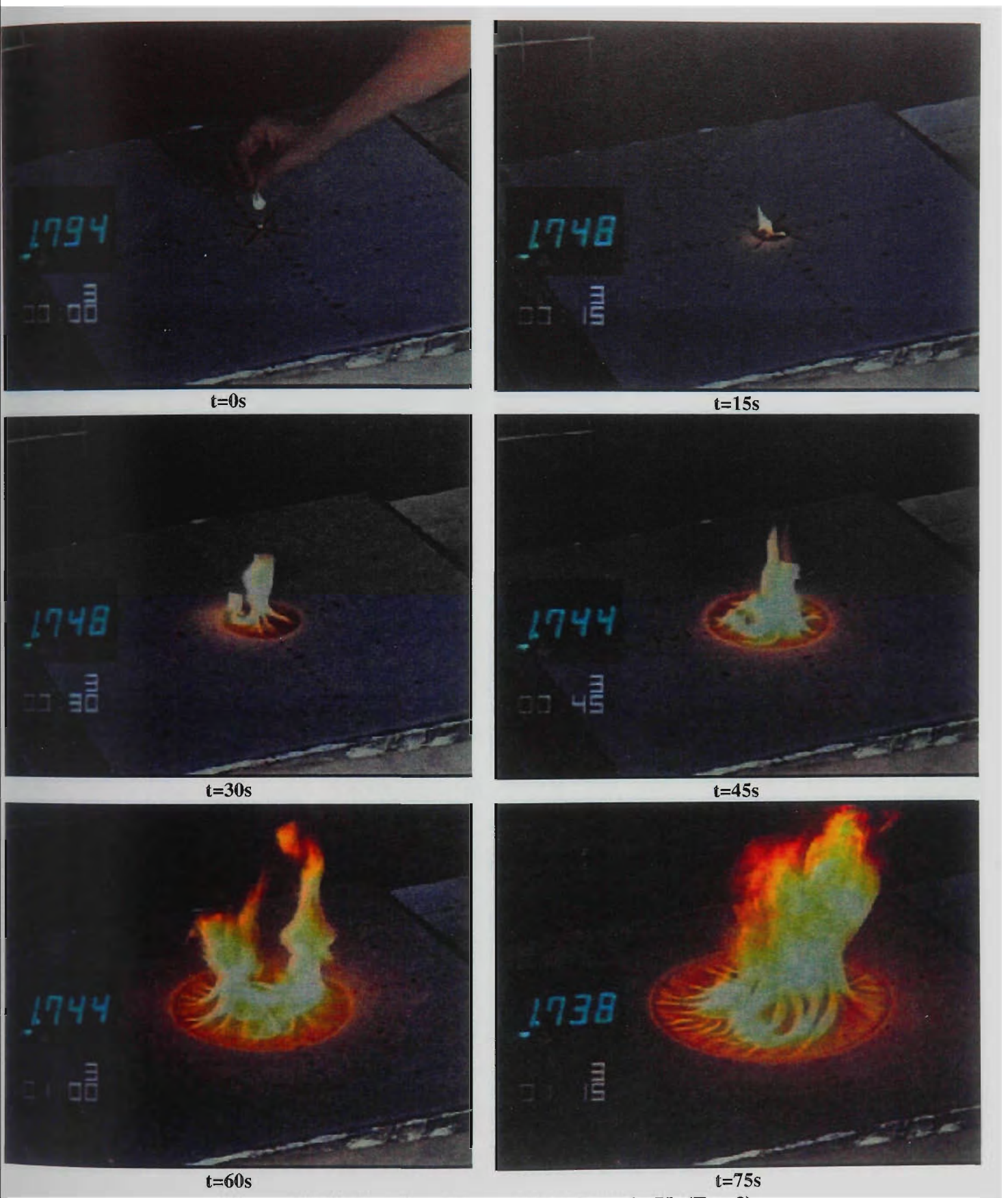

Figure 5.16 Video stills of the spreading flame 0s-75s (Test 3)

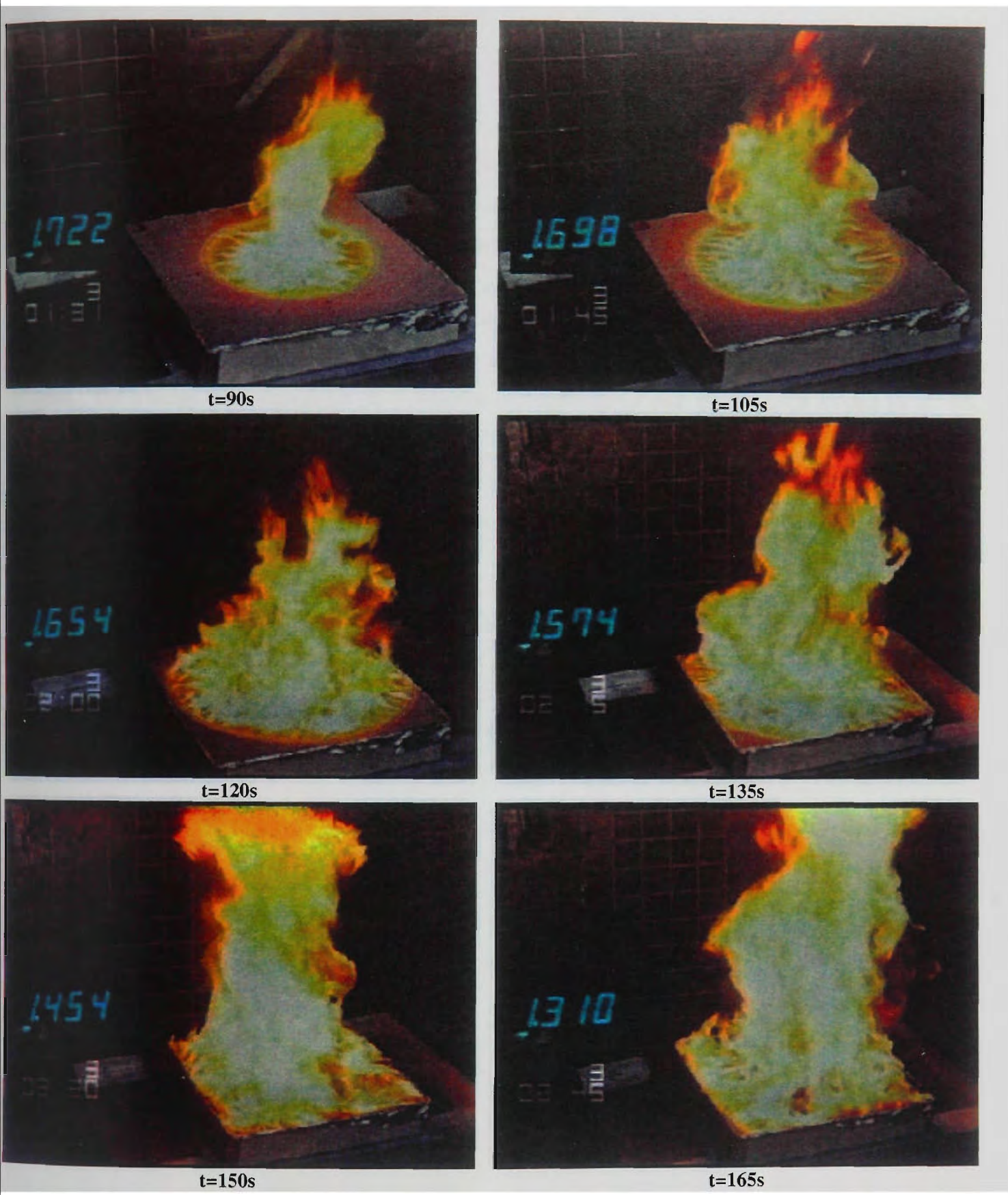

Figure 5.17 Video stills of the spreading flame 90s-165s (Test 3)

5.6.4. Experimental Results and Observations

The three tests showed good repeatability, so only the average values are shown here. The rate of mass loss (Figure 5.18) and rate of heat release (Figure 5.19) show similar profiles. This is reflected in the effective heat of combustion curve plotted as a function of mass remaining (Figure 5.21), which shows a slowly increasing value of 20-25 MJ/kg for the bulk of the mass. The curve profile is similar to that for the bench scale tests described in Chapter 4, with the same explanation applying to the phenomenon i.e. the buildup of tar and char products which have a higher heat of combustion. The uniformity of the EHC versus mass remaining curve, as compared with the time history as shown in Figure 5.20, is even more pronounced here than in the bench scale tests. The average EHC figures for the three tests, as calculated by total heat released divided by total mass lost, is 22.2, 22.2 and 22.7 MJ/kg. This is less than the values obtained by bench scale tests. This may be due to less efficient combustion within the larger fire plume.

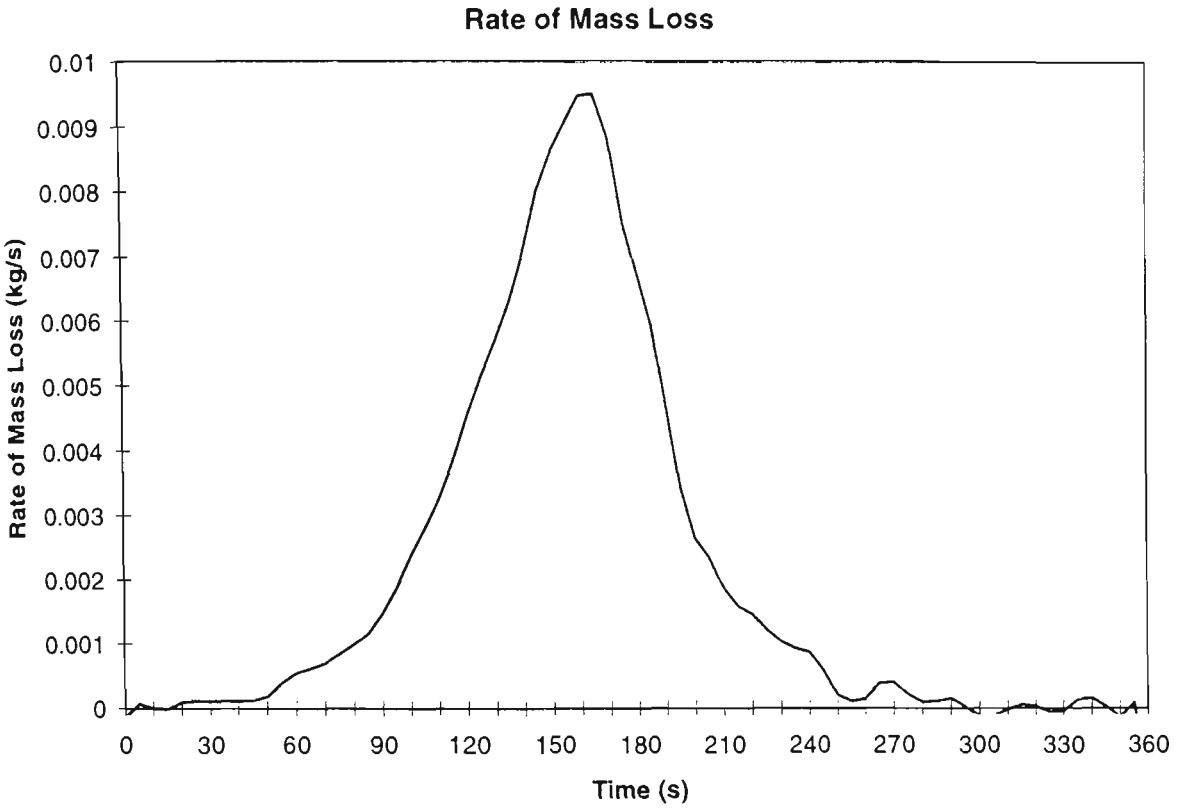

Figure 5.18 Average mass loss rate for the three tests

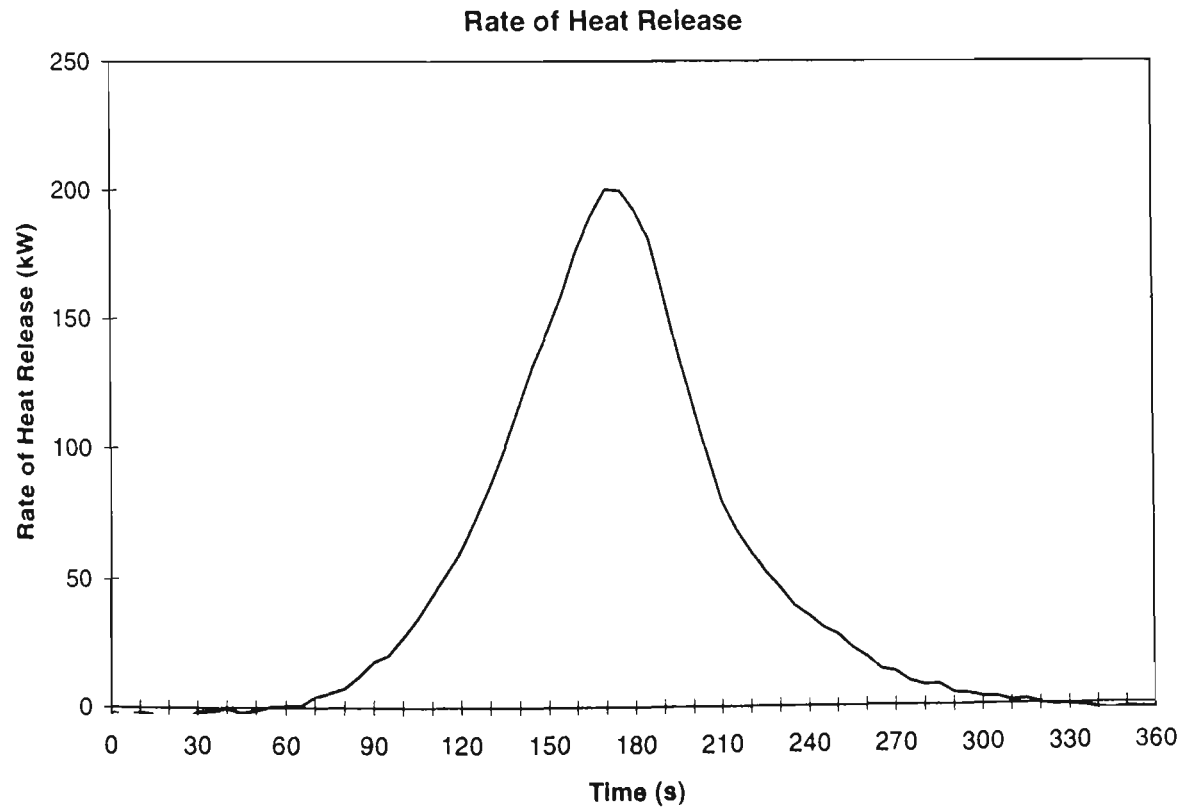

Figure 5.19 Average rate of heat release for the three tests

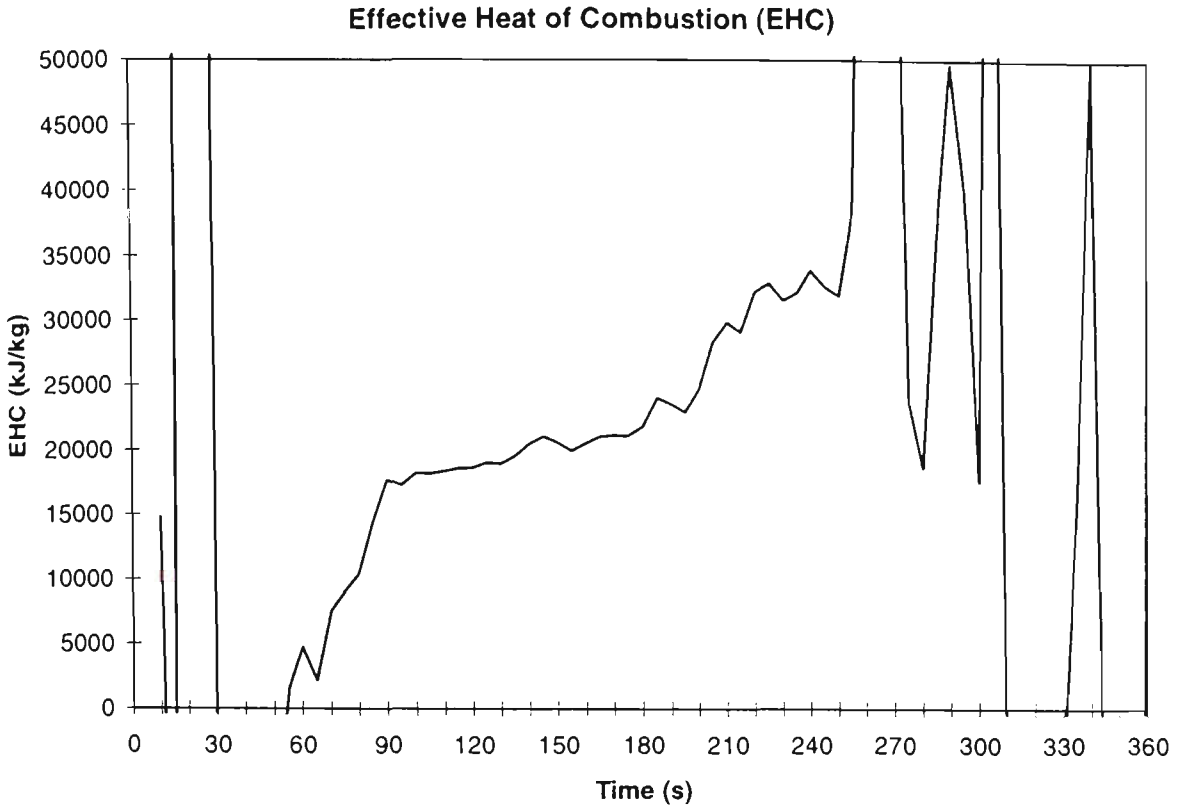

Figure 5.20 Average effective heat of combustion versus time for the three tests

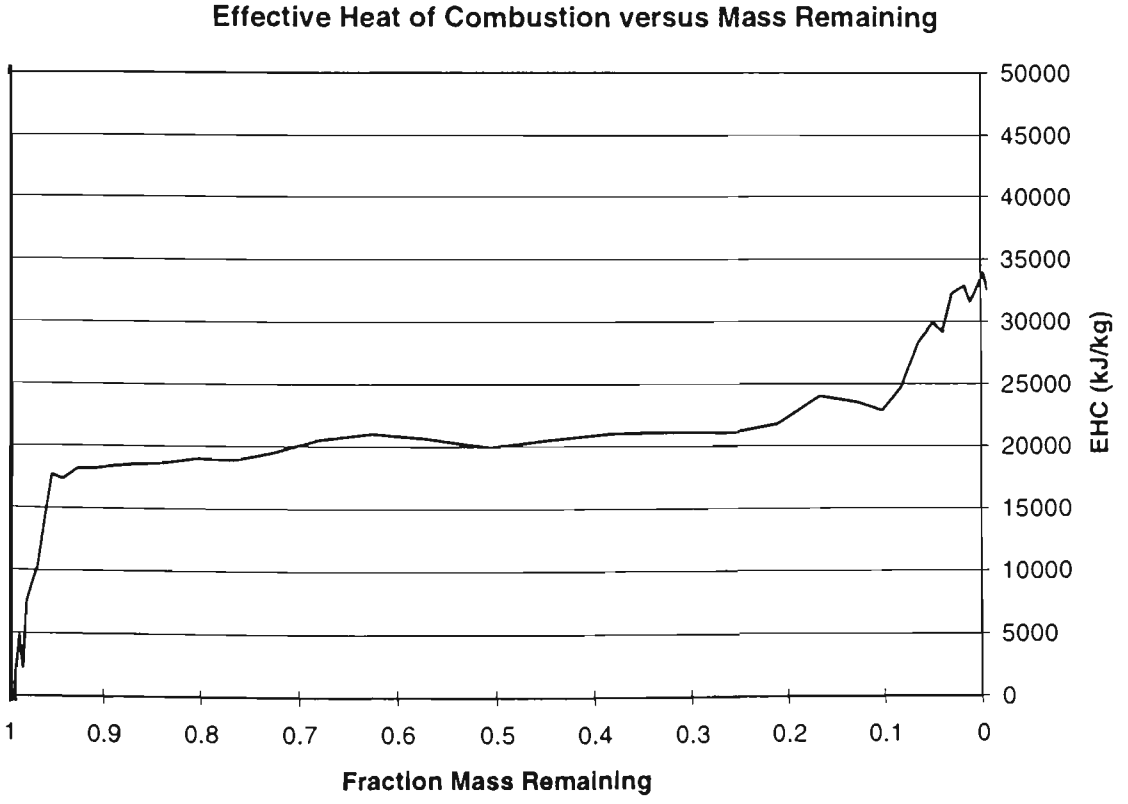

Figure 5.21 Average effective heat of combustion versus mass remaining for the three tests

Measured flame heights are shown in Figure 5.22, along with the theoretical flame heights calculated from Equation 5.9 using the measured diameter and the RHR in one instance, and the

measured rate of mass loss multiplied by the average EHC, 22.2MJ/kg, in the other. As expected, the measured flame heights are less than those calculated theoretically from the measured RHR, since the theoretical value is for the 50% intermittent height, not the minimum height. The measured height is further underestimated at peak burning, when the hood obscured the flame tip. The negative values of flame height are produced when Equation 5.9 is calculated for large flame diameters and low heat release rates, as occur at the end of fire tests.

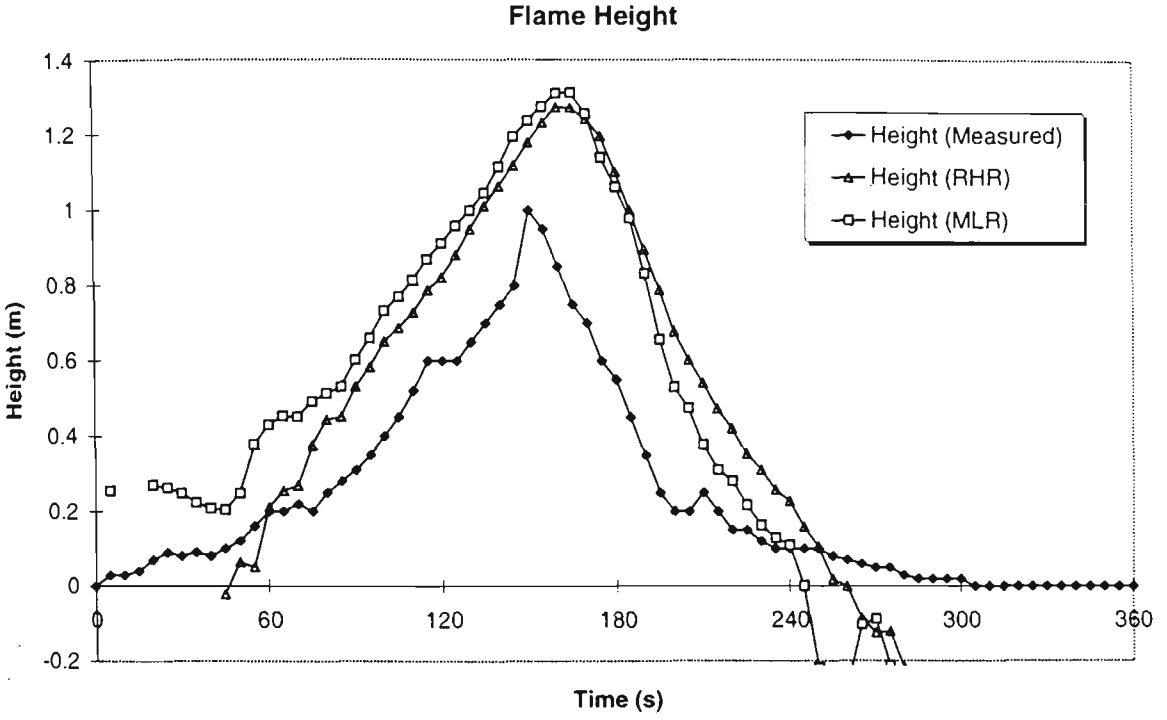

Figure 5.22 Measured and theroretical flame heights

5.7. MODELLING RESULTS

The model was compiled and executed on the same Sparc-10 used for the simulations presented earlier in Chapter 3. The fuel slab was discretised with a square surface grid, each surface element measuring 5mm×5mm. The initial burning region was the cells whose centre was within a circle of radius 35mm centred on the fuel slab's centre. The time step used in the simulation was 0.1 s, with 360 seconds of simulation time taking of the order of a few hours to execute. Three dimensional heat conduction within the fuel was considered in calculating fuel temperatures. Values of material constants used in the simulation are shown in Table 5.1, while values of gas phase constants are shown in Table 5.2.

Table 5.1 Material constants used in the stand-alone flame spread model

Symbol	Name	Value	Units	Reference
ρ	Density	23	kg m^{-3}	Table 4.3
k	Thermal Conductivity	0.036	W $m^{-1}K^{-1}$	Table 4.3
c_p	Thermal Capacity	1400	J $kg^{-1}K^{-1}$	Table 4.3
α	Thermal Diffusivity	1.12×10^{-6}	m^2s^{-1}	Table 4.3
L_v	Heat of Volatilisation	1.22×10^{6}	J kg^{-1}	Ref. 70
ΔH_c	Heat of Combustion	2.5×10^{7}	J kg^{-1}	Chapter 4
E	Activation Energy	1.25×10^{5}	J mol^{-1}	Ref. 90
A	Preexponential Constant	5×10^{7}	s^{-1}	
ε	Surface Emissivity	0.8	1	
T_{pilot}	Piloted Ignition Temperature	550	K	Ref. 70
T_{auto}	Autoignition Temperature	645	K	

Table 5.2 Gas phase parameters used in the stand-alone flame spread model

Symbol	Name	Value	Units	Reference
$T_{ambient}$	Ambient Temperature	298	K	—
T_{flame}	Flame Temperature	950	K	
ξ	Flame Heat Parameter	2.44×10^{5}	W m^{-2}	Ref. 70
Y_{O2}	Oxygen Concentration	0.2095	1	—
K	Flame Absorption Coefficient	1.0	m^{-1}	Ref. 106

The figures in Table 5.1 and Table 5.2 which are not referenced were derived from a combination of "guesstimates" and preliminary numerical experiments with the flame spread model. For instance, the surface emissivity was taken to be somewhere between carbon black (0.96), and non-metallic materials such as concrete (0.63), while the flame temperature and pre-exponential constant were taken for the best fit of data. Using the other parameters as input data, the surface temperatures were calculated using Equation 4.15, using the values of $8kW/m^2$ and $28kW/m^2$ which were the critical fluxes for piloted and non-piloted ignition determined in Chapter 4 for standard foam. The corresponding calculated temperatures 530K and 645K respectively. The former figure compares well with the figure given in Drysdale[70]. The autoignition temperature is probably not important to the situation being modelled here, as preliminary exercises show that ignition of cells only appears to occur due to piloted ignition.

The comparison of the simulated and measured flame diameter is shown in Figure 5.23. Overall, the comparison is reasonable, although there are a few features of the curve which deserve explanation. Early in the simulation (between 0s and 60s), the flame spreads in a series of jumps. This is an artefact of the cellular automata method. Early in the simulation, the ignition of one grid point represents a substantial size increase, proportionally, than later in the simulation. The theoretical spread rate is also slower in the early stages, so that several time steps may elapse before the front spreads from one cell to the next. There is also the issue of the three nearest neighbours criterion. For a circular flame front, some of the unignited cells adjacent to the front will have three or more ignited neighbours, and some will have two or less. For a circle whose radius is sufficiently large compared to the grid spacing, the circular front will resemble a straight line, and most unignited cells adjacent to the flame front the will have three or four ignited neighbours. Because of the slight convex curvature of the flame front, there will be a few adjacent cells with only two or one neighbours. Hence, a greater proportion of cells can potentially ignite by piloted means. On the other hand, early in the simulation when the flame radius is smaller, and the curvature is tighter, the number of cells adjacent the flame front with two or less ignited neighbours will be a proportionally larger. With less cells available to ignite by piloted means, it is expected that the flame spread will be somewhat disjointed.

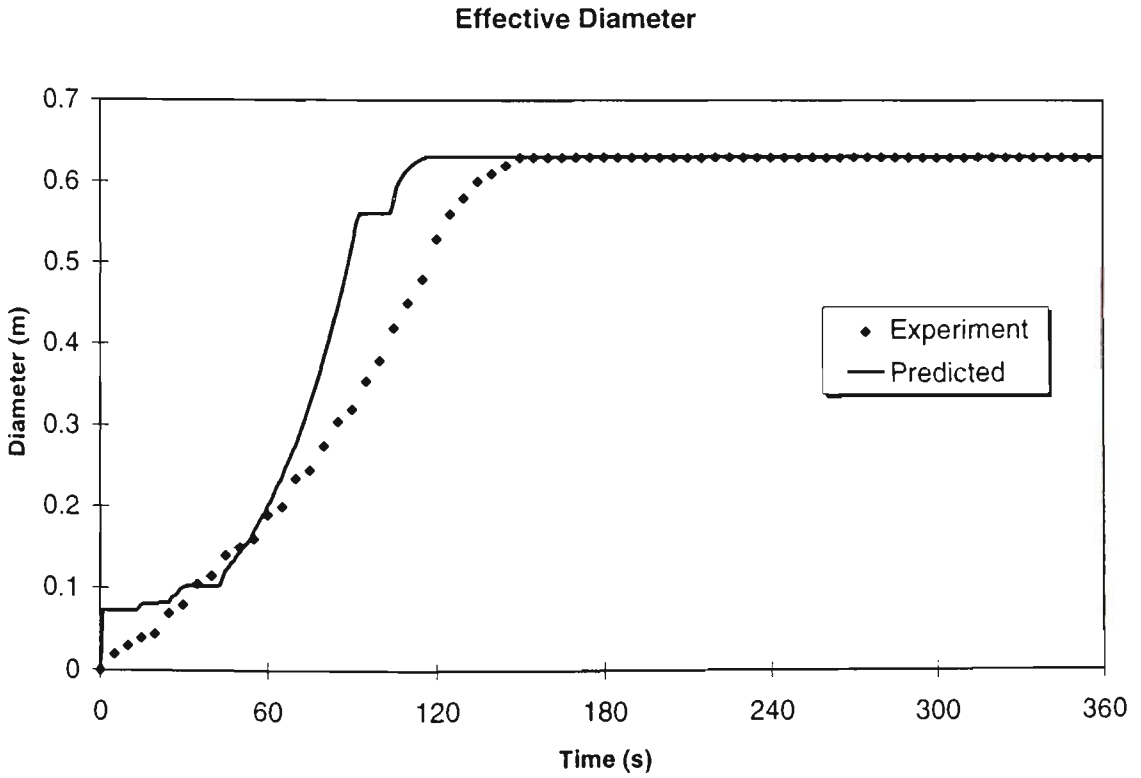

Figure 5.23 Predicted and measured flame diameter

After about 60s, the flame spread is much smoother, until the flame reaches a diameter of 0.56m. This corresponds to the circular flame reaching the edges of the square fuel slab, and marks a

transition within the model. While the flame diameter is less than 0.56m, there are two methods for determining the distance from unignited cells to the flame front for the purposes of calculating the radiation heat flux received from the flame. The first method is to assume that the flame front is circular, centred at the point of ignition. The diameter of this circle is calculated from its area, which is simply the sum of the area of all ignited and burntout cells. The distance of an ignited cell from this circular front is easily calculated, as this is simply the distance of the cell from the slab centre minus the circle diameter. However, when the area of ignited cells is such that the calculated circle is beyond the slab edges, the calculated distance of a cell from the flame front will be greater than the true distance. The second method for calculating distance is required in this instance. In Section 5.2.3 it was described how a list of unignited cells with between one and seven ignited neighbours is maintained by the model during execution, to reduce on checks within the program. This list is also employed here. If an unignited cell is on this list, then it is either 1 grid spacing or $\sqrt{2}$ grid spacings from the nearest ignited cell. Its distance from the flame front is assumed in this instance to be 1 grid spacing. If the cell is not listed, then the distance of from each of the listed cells is calculated, and the minimum taken. The distance from the flame front is taken to be this distance plus 1 grid spacing. (In the model, all unignited cells are checked, and if the cell concerned is listed, its distance from itself is zero, which is the minimum).

The second method may be used for the entire simulation if desired, but since systematically checking all listed cells is time consuming, the first method is used while it is still valid as it is much less computationally intensive. It is the transition from the first method to the second method which causes the short plateau in the graph when the diameter is 0.56m. Why this plateau occurs at all is still not clear, although it may be related to the fact that distances calculated by the first method may be less than one grid spacing in some instances, resulting in slightly greater view factors and correspondingly higher heating rates than if 1 grid spacing is a strict minimum, as is the case for the second method.

The features described above also manifest themselves in the calculated flame heights (Figure 5.25) and mass loss rate (Figure 5.24). The increased flame spread rate shown in Figure 5.23 results in earlier peaks in the flame height and mass loss rate, although the predicted peak value is close to the experimental peak value in both cases.

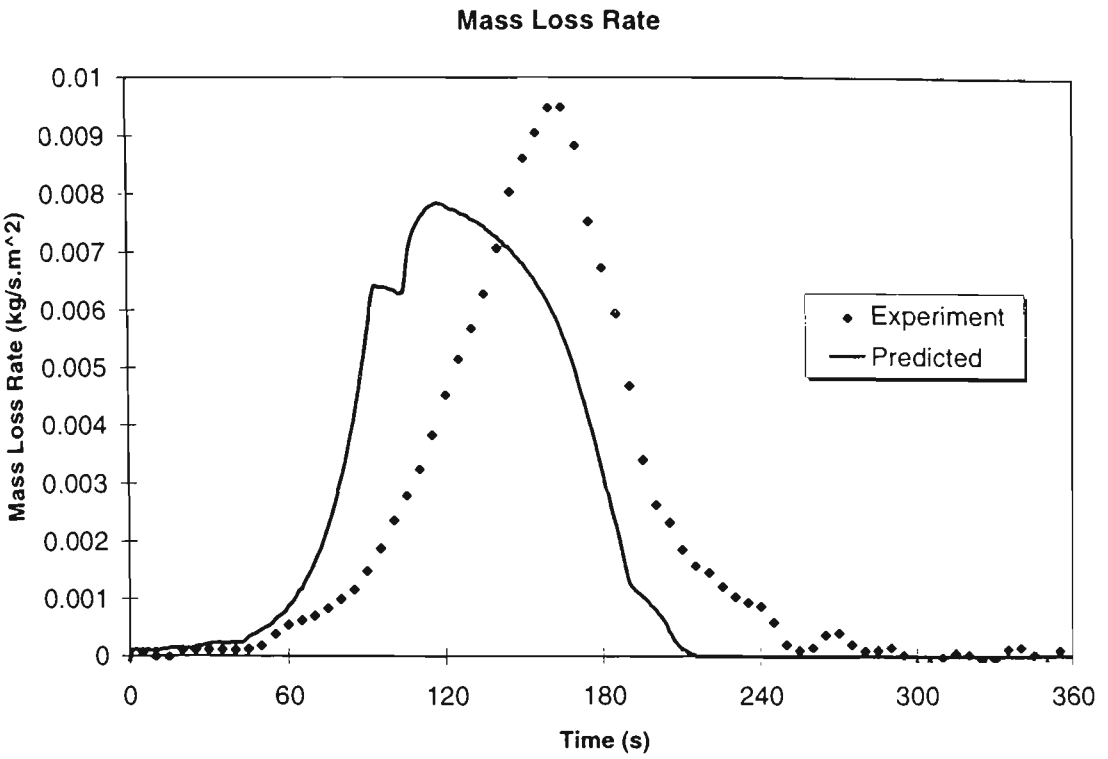

Figure 5.24 Predicted and measured mass loss rate

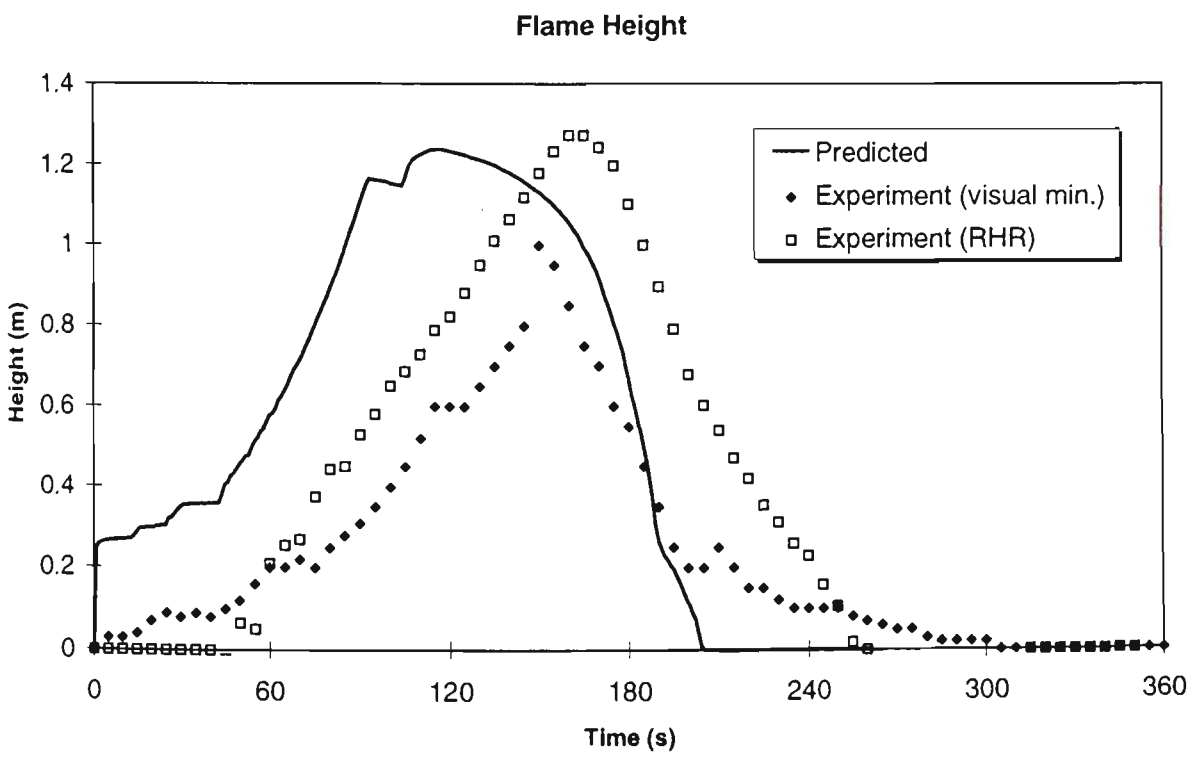

Figure 5.25 Predicted and measured flame height

5.8. SENSITIVITY ANALYSIS

In the development of the model, there was a significant amount of numerical experimentation involved in the fine tuning of the model, particularly with the variables for which no "typical" values were found in the literature or through experimentation, such as the pre-exponential constant in the Arrhenius equation for fuel decomposition. These numerical experiments showed that there was often a significant variation in the outcome of the model depending on the value of constants chosen. The exploration is formalised in this section, whereby the value of several key variables is systematically altered, and the model executed to test the outcome. Also discussed in the previous section was the presence of several numerical anomalies in the model which are products of the cellular automata method. In light of this, the effect of grid size and time step is also explored in this section. A summary of variables tested in this analysis, and the range of values, is listed in Table 5.3. The values in bold are the "default" or reference values. When one of the variables is altered, the values of the other variables listed in the table are the default value. The default values are those used in the modelling exercise presented in the previous section.

Grid Parameters		
Conduction Mode	Grid Size	Time Step
3-Dimensional	2.5 mm	0.05 s
1-Dimensional	**5 mm**	**0.1 s**
	10 mm	0.2 s
	20 mm	
Flame Parameters		
Flame Temperature	Flame Heat Coefficient ξ	Flame Absorption Coefficient
850 K	3.66×10^5 W/m^2	0.2 m^{-1}
900 K	3.0×10^5 W/m^2	**1 m^{-1}**
950 K	**2.44×10^5 W/m^2**	5 m^{-1}
1000 K	1.8×10^5 W/m^2	20 m^{-1}
1050 K		
Material Parameters		
Pre-exponential constant	Activation Energy	Piloted Ignition Temperature
5.0×10^6 s^{-1}	100 kJ/mol	525 K
5.0×10^7 s^{-1}	115 kJ/mol	**550 K**
1.0×10^8 s^{-1}	120 kJ/mol	575 K
5.0×10^8 s^{-1}	**125 kJ/mol**	
1.0×10^9 s^{-1}	140 kJ/mol	

Table 5.3 Variables tested in sensitivity analysis

5.8.1. Grid Parameters

The first of three grid parameters which was tested was the conduction mode. The default value used is three-dimensional (3D), and the other tested was one-dimensional (1D). In the one-dimension conduction mode, heat is assumed to be conducted from the surface into the depth of the fuel, but no conduction in the two directions parallel to the surface is considered. The results of the two cases is shown in Figure 5.26. Perhaps the most surprising aspect of the comparison is that the fire growth is more rapid for 1D case, with the plateaux in the diameter curve shorter in duration. What is intuitively expected is that the 3D case should be the more rapid, as heat is conducted through the solid ahead of the flame front, causing unignited cells to heat up to piloted ignition temperature more rapidly. What may be happening instead is that there is marginally less heat being lost from the cells in the flaming region. As a result, the temperature of these cells is greater,

resulting in increased mass loss and a larger flame. The resulting increase in flame radiation would compensate for any losses due to a lack of heat conducted from cells in the flame region. Another effect which may account for the result is that for 3D conduction, cells adjacent to the flame front are not only gaining heat from their ignited neighbours, but losing it to their unignited neighbours. If heat losses are more important than heat gains, then this would lead to more rapid growth for the 1D conduction case. Overall, though, there is little difference between the two curves.

This is in contrast to the second grid parameter tested, namely the grid size, where varying the value has a marked effect on the outcome. What is intuitively expected in this case is that for a finer grid, the flame spread should be much smoother, as each incremental "jump" of the flame front is less. This is indeed the case, as can be seen in Figure 5.27. The default value used is 5mm. Reducing the size to 2.5mm results in the flame spreading more rapidly, resulting in a more rapid rise in mass loss rate, which in turn contributes to the increasing heat feedback to the flame front. The plateau at the 0.56m diameter transition is practically non-existent. In contrast, increasing the grid size to 10mm results in a marked increase in the number and persistence of plateaux, which delays the spread rate, and the peak of the mass loss rate. It is also worth noting the decreasing trend in the mass loss rate during the 0.56m plateau. This is due to the burnout of cells and a corresponding decrease in mass loss rate while the size of the flame remains steady. The situation is even more extreme when a value of 20mm is taken. The initial flame area only increases by a few grid points, which all burn out by 130 seconds into the simulation, resulting in no further growth.

Overall, it appears the choice of grid size only affects the spread of flame in the initial phase of fire growth, to the point where it prevents spread for the 20mm grid case, and the transition phase when the flame reaches the edge of the slab. However, in the interim, where the flame is spreading from about 0.2m diameter to 0.56m diameter, grid size appears not to be limiting the ignition of cells, as evidenced by the flame diameter curves being parallel for the values examined. The failure of the model to predict well the flame spread in the early stage of the simulation is an aspect which requires closer attention in future development of the model. Whether the problem is due to an artefact of the cellular automata method, or an inadequacy of the modelled flame in the early stages, or a combination of both, cannot be concluded from the data presented here.

The third grid parameter tested is the time step, as shown in Figure 5.28. The trend here is quite apparent, with the shorter time step resulting in more rapid fire growth. Again, the trend is as intuitively expected. Consider a cell being heated in the growth stage of the fire. It is heated for one time step, after which its new temperature is determined. If the time step is halved, the same cell will receive heating at the same rate as before, but for half a timestep. The new temperature

and new heating rate is calculated, which will be slightly greater in the second timestep. After two half timesteps, the overall heating should be slightly more than for a full step at the lower heating rate. The cumulative result over many timesteps is a more rapid fire growth for a shorter time step. The same argument may be applied for a decaying heat release rate. Another factor which may occur in halving the time step, is ignitions occurring in the first half step rather than the second. This means that the mass loss rate from new ignitions will prevail longer than for old ignitions, resulting in the same increase in growth rate.

The flame diameter curves for timesteps of 0.05s and 0.02s show a very similar profile. The only difference is the shorter delay in the initial growth phase of the flame for the case where the timestep is 0.02s. This suggests that the effects described above only become significant when the time step becomes much greater than 0.1s. On the other hand, a timestep less than 0.05s will only be of benefit in overcoming the initial spread delay, since a smaller timestep will result in a greater number of iterations, and hence increased calculation time.

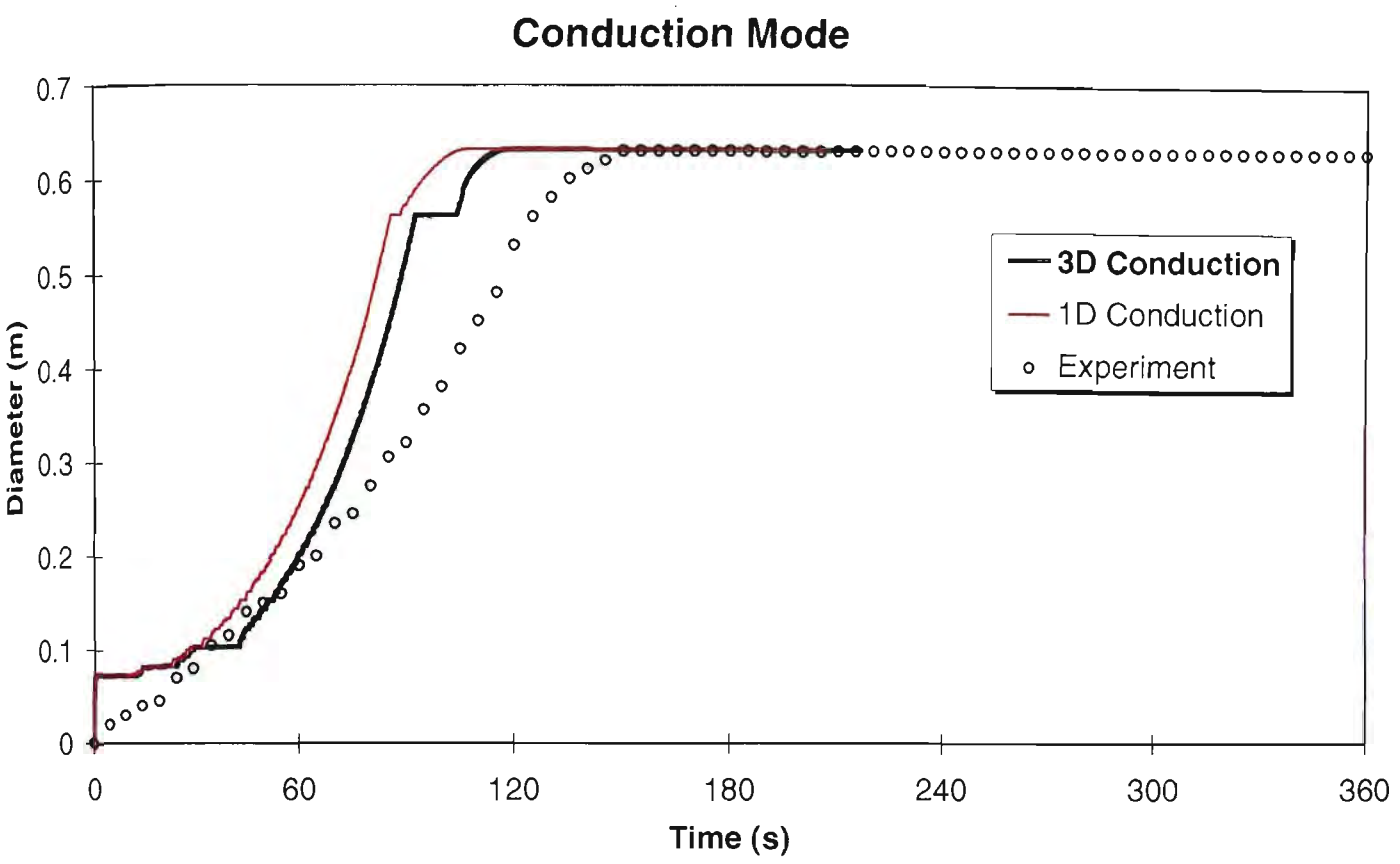

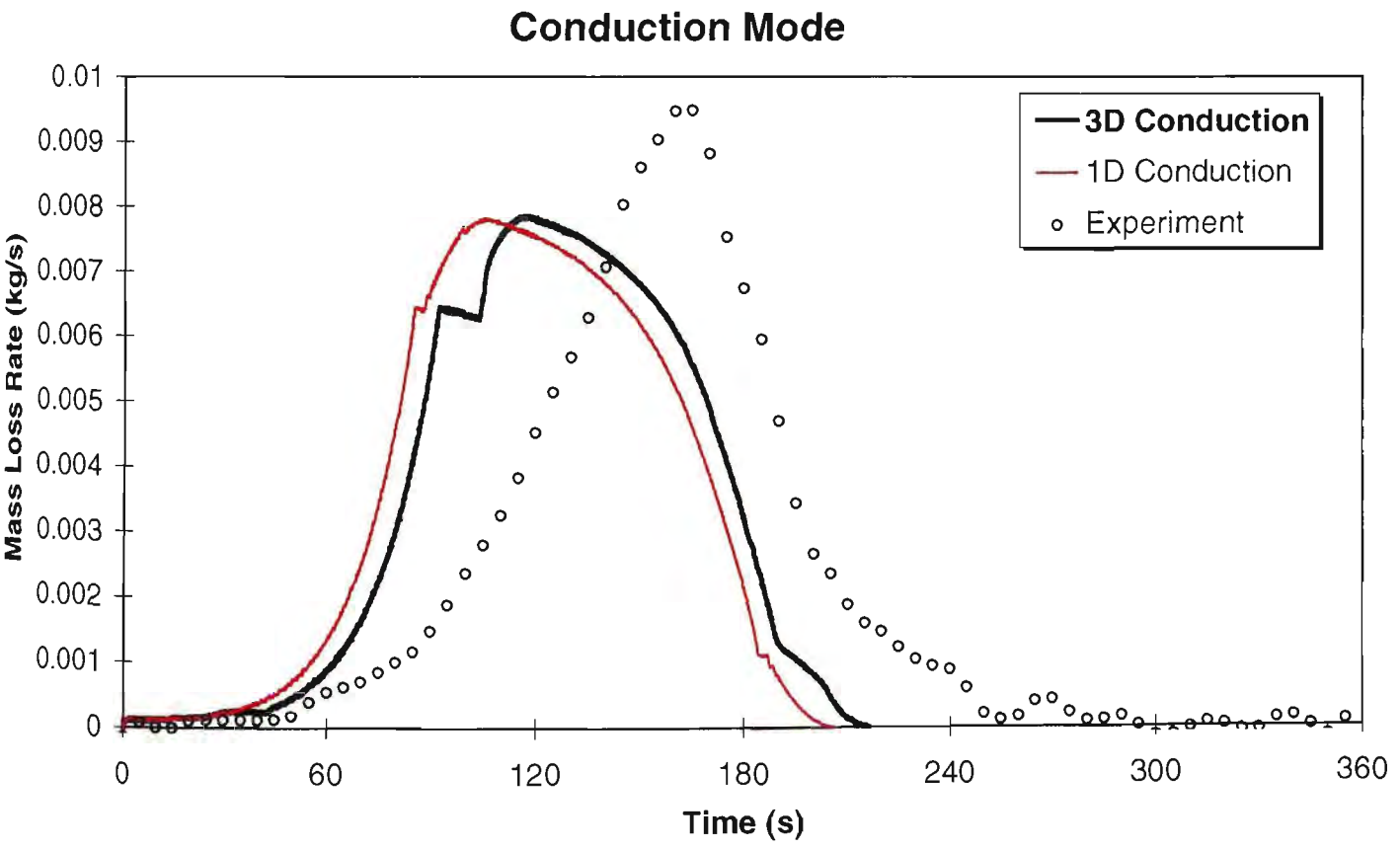

Figure 5.26 Flame spread and mass loss rate for varying conduction mode

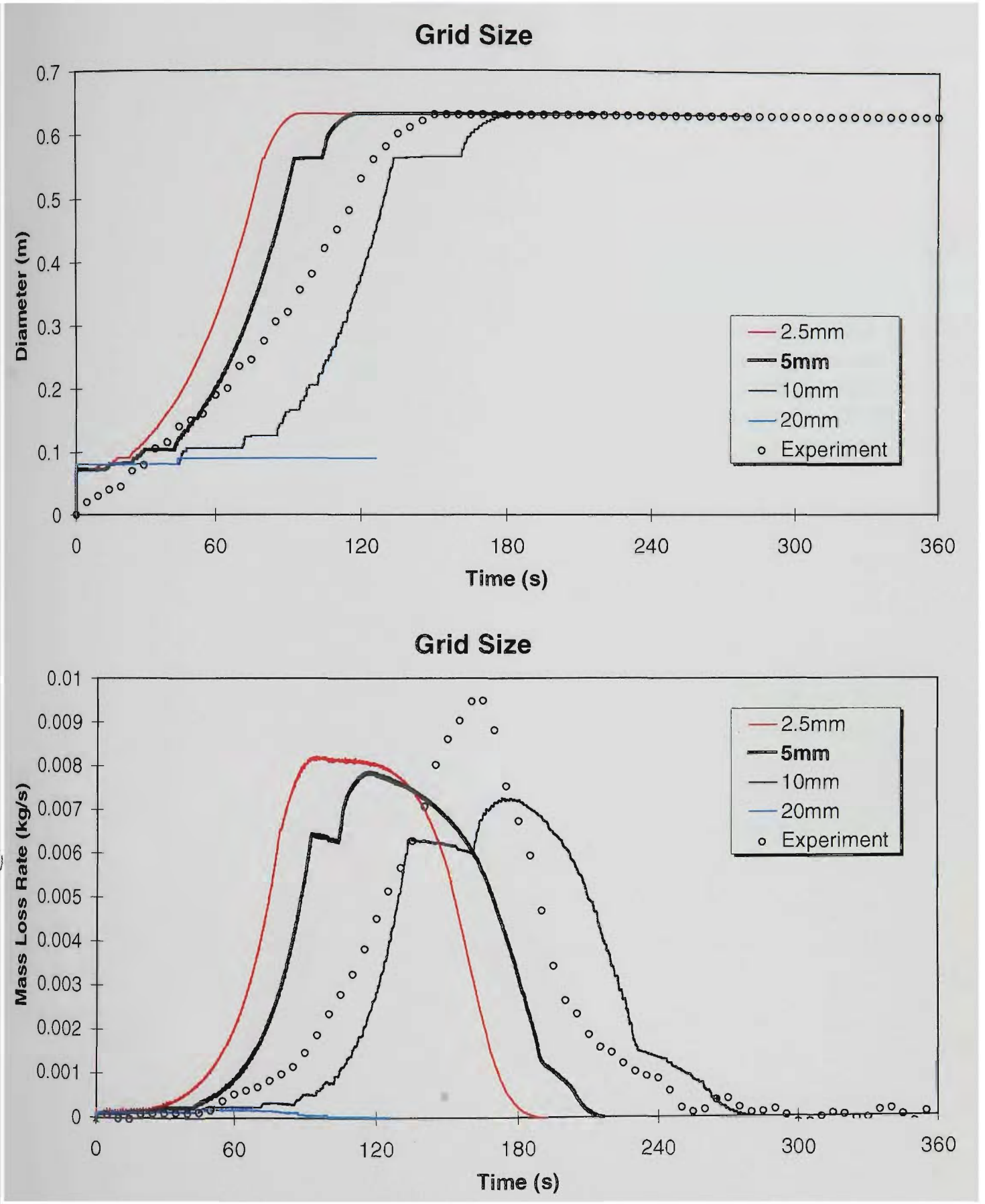

Figure 5.27 Flame spread and mass loss rate for varying grid size

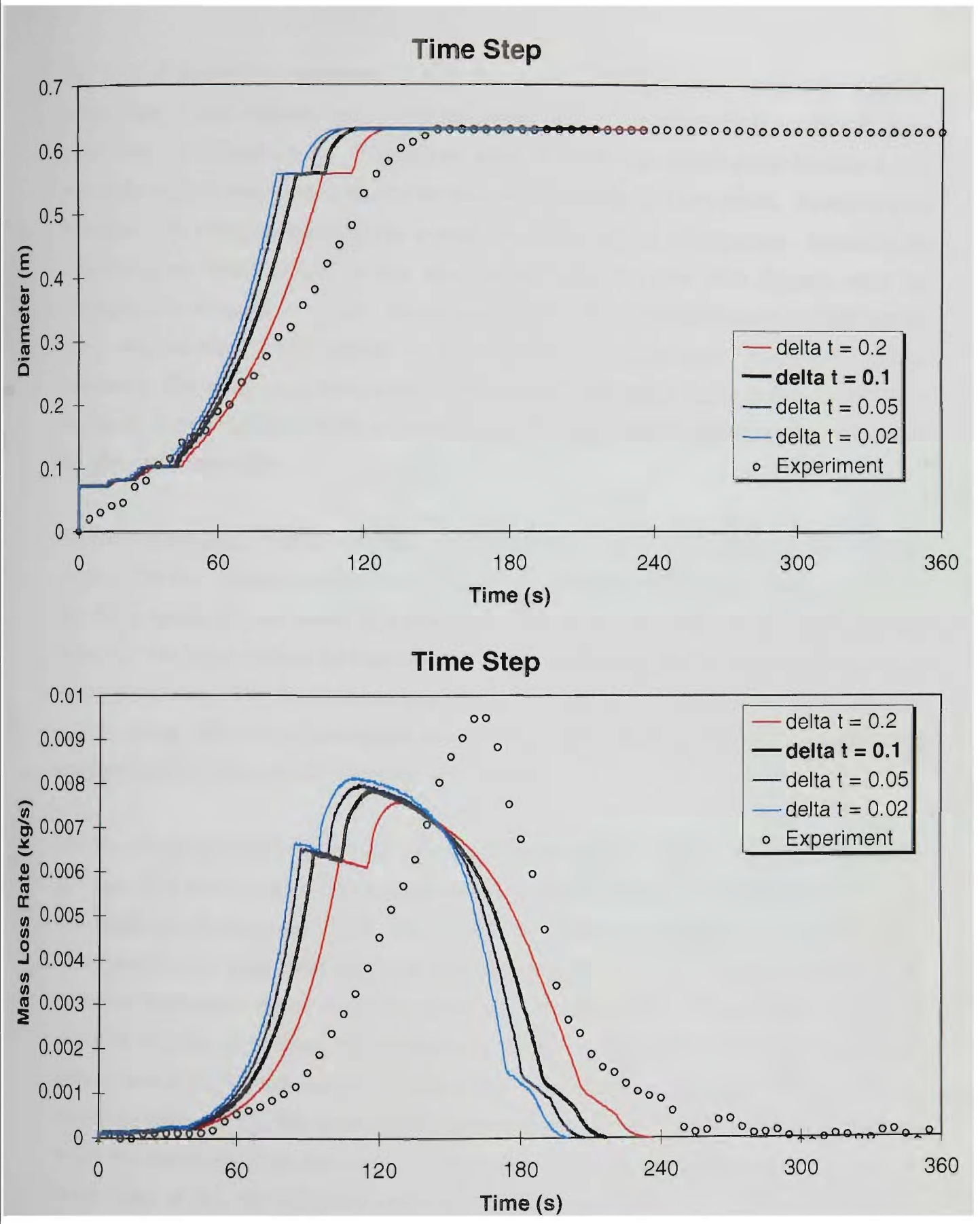

Figure 5.28 Flame spread and mass loss rate for varying time step

5.8.2. Flame Parameters

The first of three flame parameters tested was the flame temperature. In the real situation, temperature is not constant throughout the plume region, so pinpointing a value of flame temperature is difficult to do. The default value of 950K was chosen partly because it is a physically realistic value, but mainly on the basis that it produced the best results. As may be seen in Figure 5.29, changing this figure by a small amount has drastic consequences. Increasing the temperature to 1000K results in very rapid growth, which is even more dramatic when the temperature is increased to 1050K. On the other hand, reducing the temperature to 900K has the effect that the flame barely spreads at all. The mass loss rates show corresponding similar behaviour. The result is not unexpected, as the radiation heat output will be increased by 22% in raising the temperature from 950K to 1000K, due to the fourth power relationship between radiant heat flux and temperature.

The second parameter varied, the flame heat coefficient (or equivalently, the heat flux from the flame to the fuel surface), is a little more enigmatic. Increasing the value has very little effect on the flame spread rate, as shown in Figure 5.30. It does have an effect on the mass loss rate, however. For higher values, the heat feedback to the fuel is greater, resulting in higher mass loss rates, as expected. Why the corresponding increase in flame height, and therefore flame radiation, does not result in increased flame spread rates and hence affect the flame diameter is not clear. The expected trend is observed when the value is decreased.

The third flame parameter investigated was the flame absorption coefficient. The results, as shown in Figure 5.31, demonstrate one of the problems encountered in empirically modelling the flame for the stand-alone flame spread model. For a small flame, not only is the view factor small, but the mean pathlength is small, resulting in low flame emissivities, as given by Equation 3.18. As flame spread in the model is driven largely by radiation, a minimum value of 0.5 for flame emissivity is specified in order to increase flame radiation in the early stages of the simulation, when other effects, such as the low heating rate and the cellular automata effects discussed earlier, are already restricting flame spread. The sudden rapid increases shown in Figure 5.31 corresponds to the point where the calculated flame emissivity increases above 0.5. For the default value of 1.0 and the lower value of 0.2, the calculated emissivity never increases above 0.5, so both values show identical histories (the curve for 1.0 eclipses the curve for 0.2 in the chart). For the two cases where the emissivity does overcome this minimum, the increased radiant flux ahead of the flame increases the preheating of the fuel, and hence the flame spread rate, as expected. It is worth noting that the increase is sufficient to overcome the 0.56m plateau.

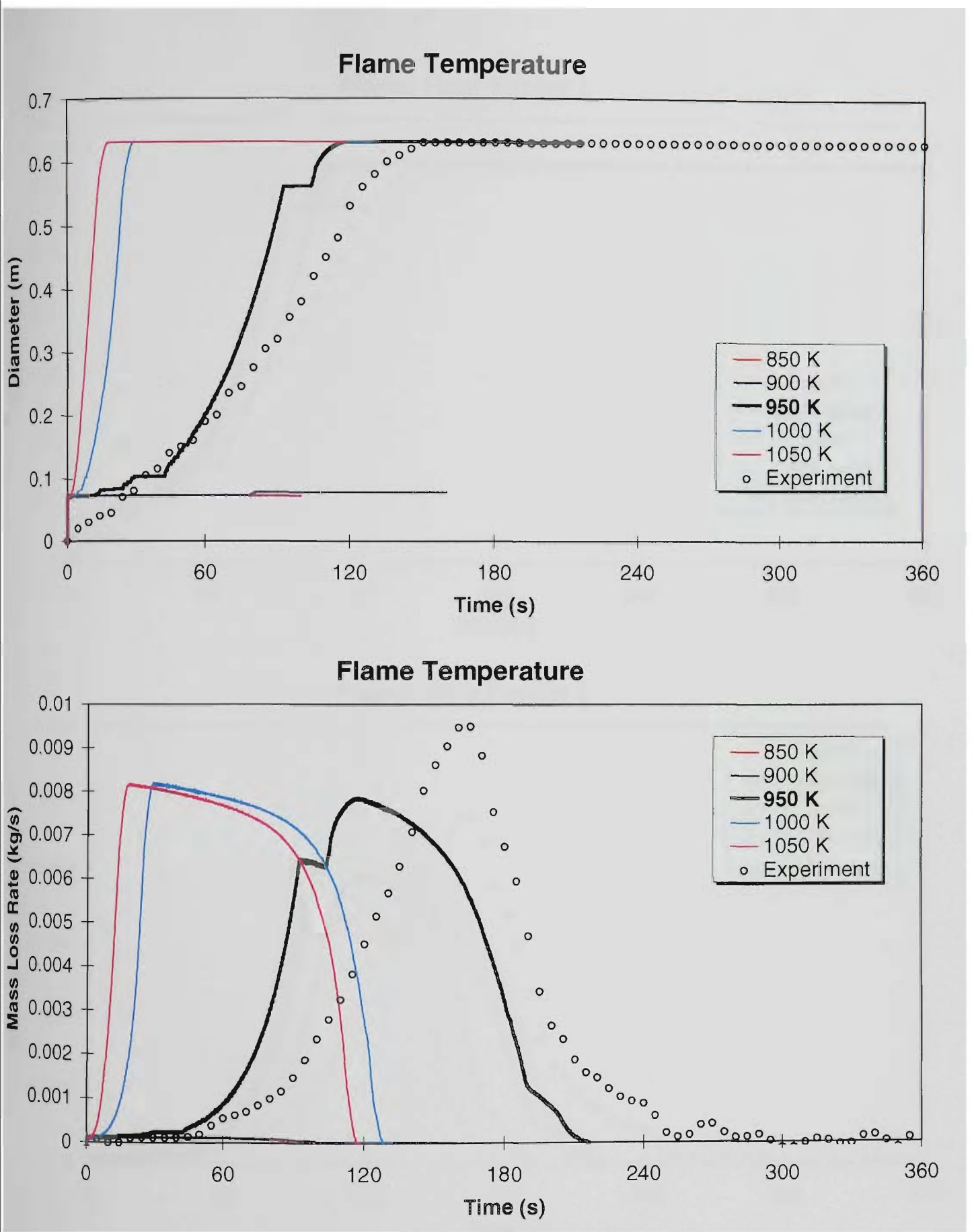

Figure 5.29 Flame spread and mass loss rate for varying flame temperature

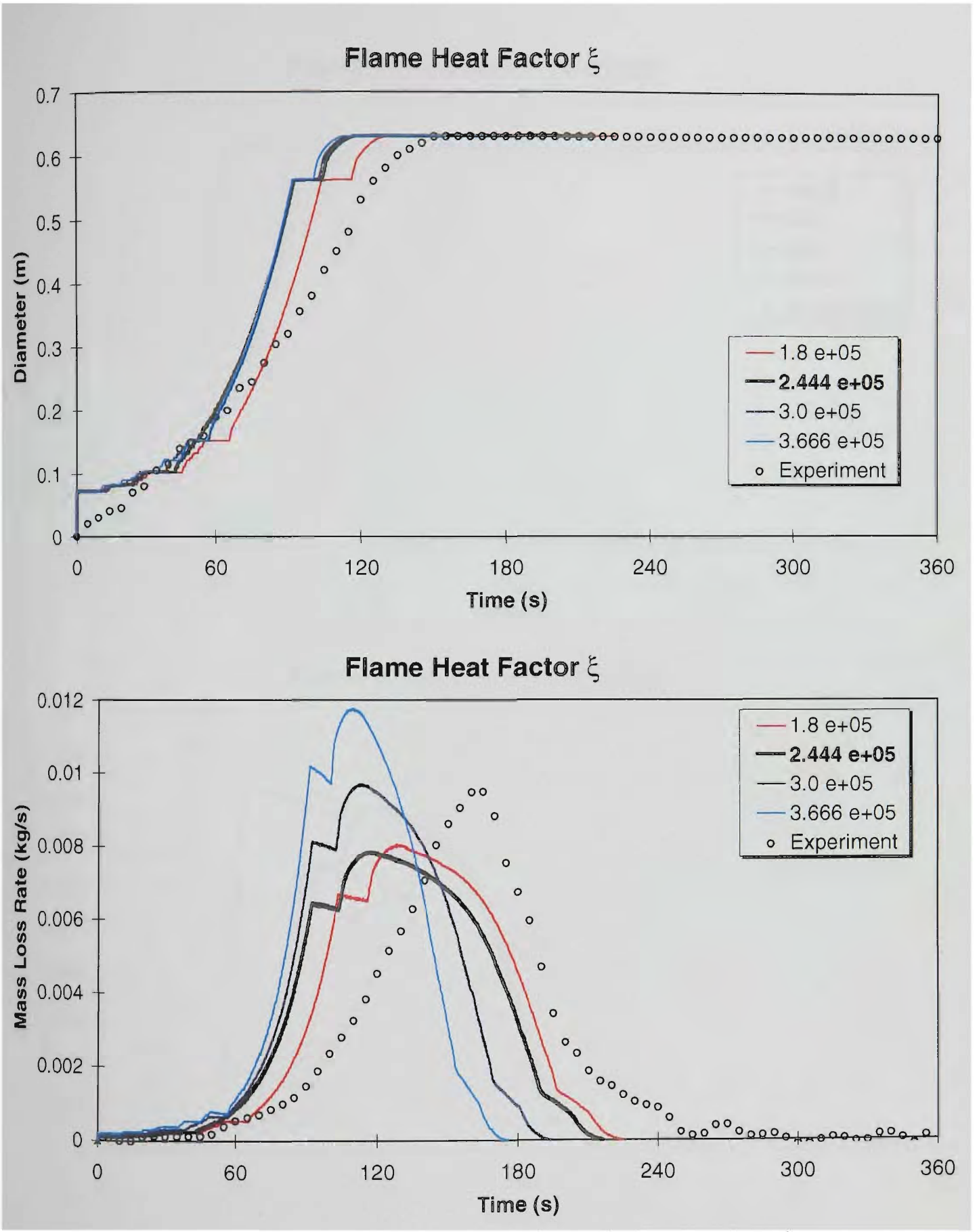

Figure 5.30 Flame spread and mass loss rate for varying flame heat factor ξ

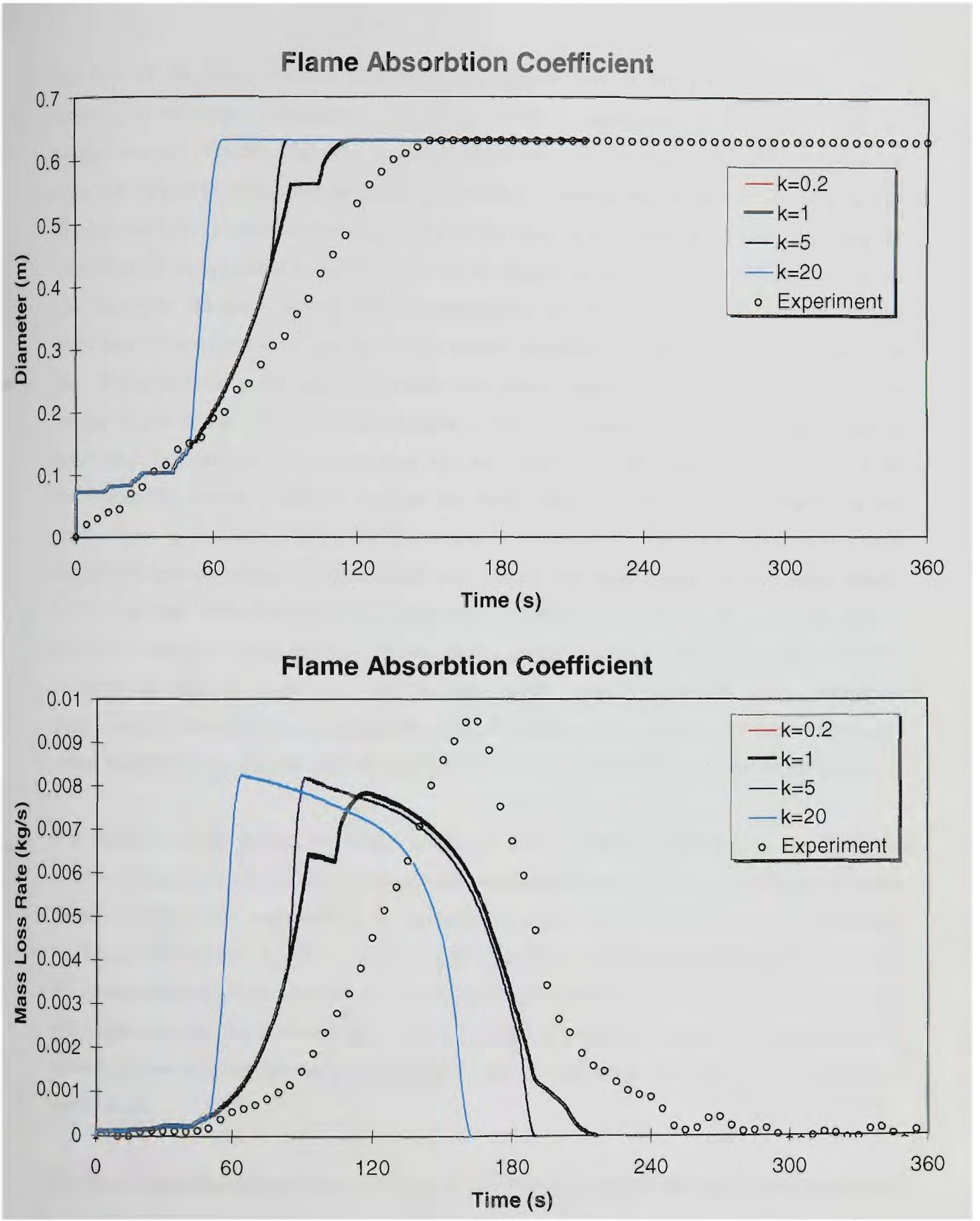

Figure 5.31 Flame spread and mass loss rate for varying flame absorbtion coefficient

5.8.3. Material Parameters

The first of the three material parameters investigated here is the pre-exponential constant appearing in the Arrhenius equation for fuel decomposition (Equation 4.1). As a quantity for this variable was not obtained, the value which produced the most realistic results was found through numerical experimentation with the model. The effect of altering this variable is complex, as fuel decomposition has a negative feedback effect on the value of the surface heat flux. Increasing the value of the pre-exponential factor increases the decomposition rate of the fuel, which increases the mass loss rate. However, increasing the decomposition rate also results in more heat lost through latent heat of volatilisation, causing a lower surface temperature, which decreases the mass loss rate. The actual rate is the point where these two effects balance. The result of this balance for various values of the pre-exponential constant is shown in Figure 5.32. Lower values result in lower mass loss rates as seen in the mass loss rate curves, but higher spread rates as seen in the flame diameter curves. This is because the lower mass loss rates result in higher surface temperatures, as less heat is being lost due to heat of volatilisation. The higher temperatures mean that piloted ignition temperature is reached more readily, and flame spread proceeds more rapidly. Lower mass loss rates also result in a broader and lower peak. A point worth noting in this series of tests is the range of values tested. The two values immediately higher and lower than the default value are an order of magnitude apart, yet show similar curves. However, another magnitude higher, and the flame does not spread at all. This shows that the pre-exponential constant is quite a robust variable, but only up to a point, after which it becomes remarkably sensitive to alteration.

The second variable tested, activation energy, is also a quantity appearing in the Arrhenius equation, so exhibits similar behaviour to the pre-exponential constant due to the negative feedback effects. Lowering the activation energy increases the mass loss rate, which increases the heat lost by heat of volatilisation, which lowers the calculated surface temperature, resulting in less ignitions. As shown in Figure 5.33, increasing the value above the default of 125 kJ/mol has only a minor effect, while decreasing it shows the same sharp transition, occurring between 120 kJ/mol and 115 kJ/mol, as seen with varying the pre-exponential constant. Below this transition, the flame does not spread at all.

The key to understanding this sharp transitional phenomenon may be seen by examining the third material parameter, critical surface ignition temperature, shown in Figure 5.34. Increasing the temperature from the default temperature of 550K to 575K results in no flame spread, while reducing it from 550K to 525K results in a greatly increased flame spread rate, and reduced time to peak mass loss rate. The cause of the critical point is due to the surface temperature as calculated

by the model. It is the nature of the Arrhenius equation that raising the temperature of the surface will not significantly increase decomposition, until a temperature in the vicinity of 500K is reached. At this point, decomposition becomes significant, and increasing the heat input to the surface results in increased mass loss rather than temperature rise. An increasingly larger heat input is required to raise the temperature any further. Thus, for the "typical" heat fluxes generated by the model, the surface temperature will lie within a relatively narrow range. For the default parameters, this temperature is somewhere in the vicinity of 575K. Thus, setting the critical surface ignition temperature to 525K results in surface elements readily igniting, and flame spread therefore rapid. Setting the critical temperature to 550K makes the surface elements less readily ignitable, but ignitable nevertheless. Setting the critical temperature to 575K results in very few cells reaching ignition temperature, as a great deal of heat input is required to raise temperature at this point. Flame spread therefore effectively ceases.

A similar situation arises when the critical temperature is fixed instead, and the pre-exponential constant and activation energy are altered. Altering these parameters alters the calculated surface temperature, and the temperature at which large increases in heat input result in small temperature rises. If this temperature is below the fixed critical ignition temperature, then spread will not occur.

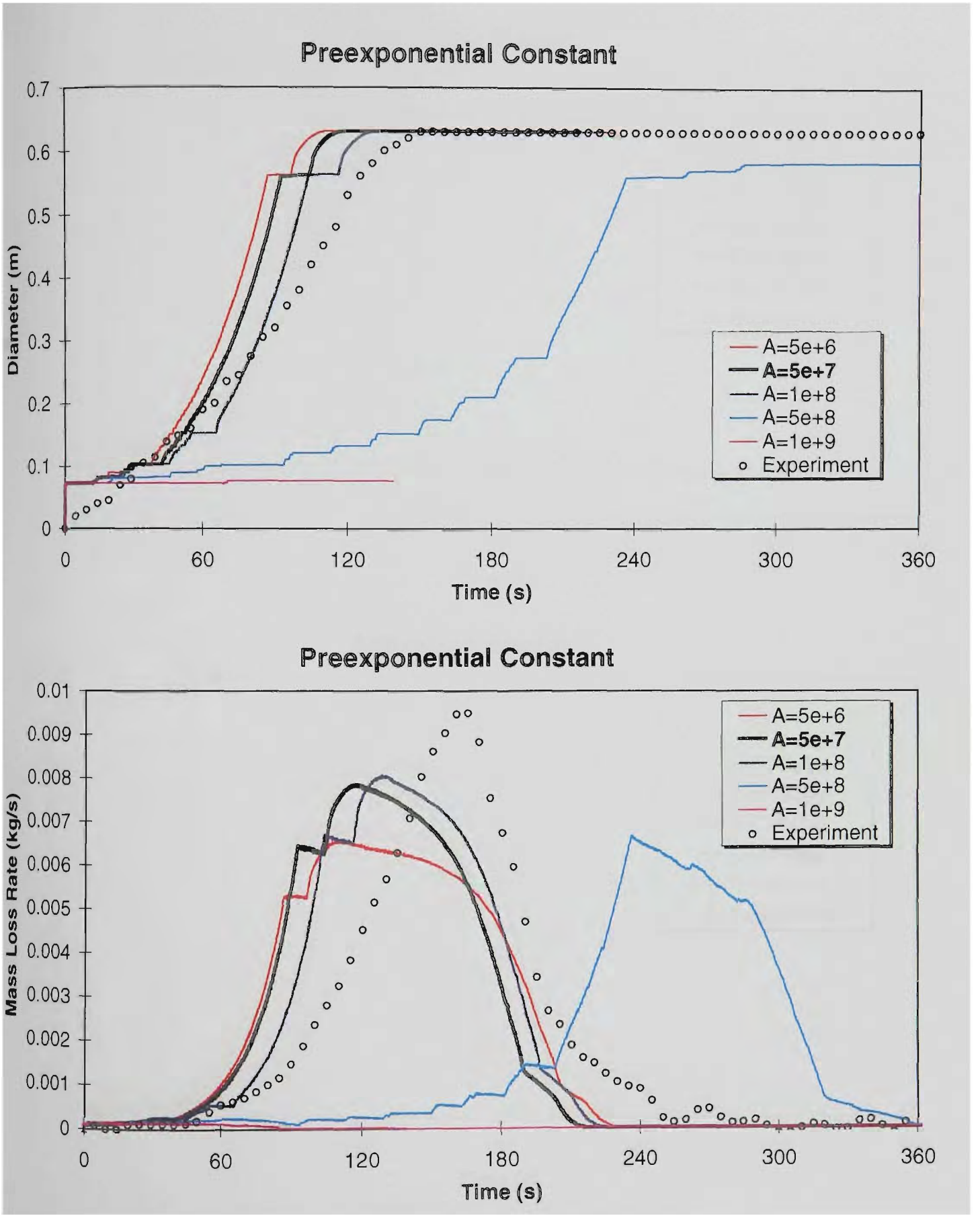

Figure 5.32 Flame spread and mass loss rate for varying pre-exponential constant

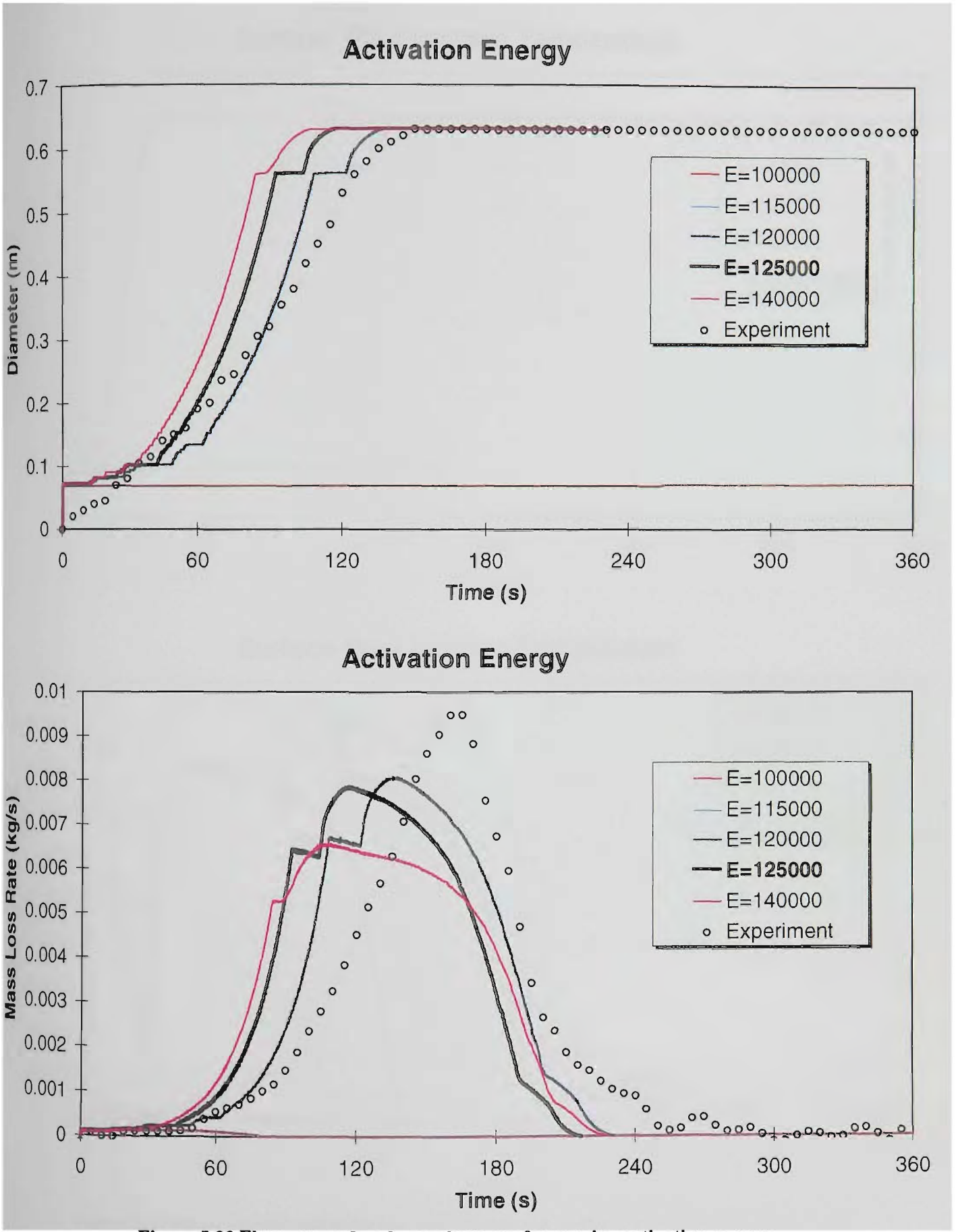

Figure 5.33 Flame spread and mass loss rate for varying activation energy

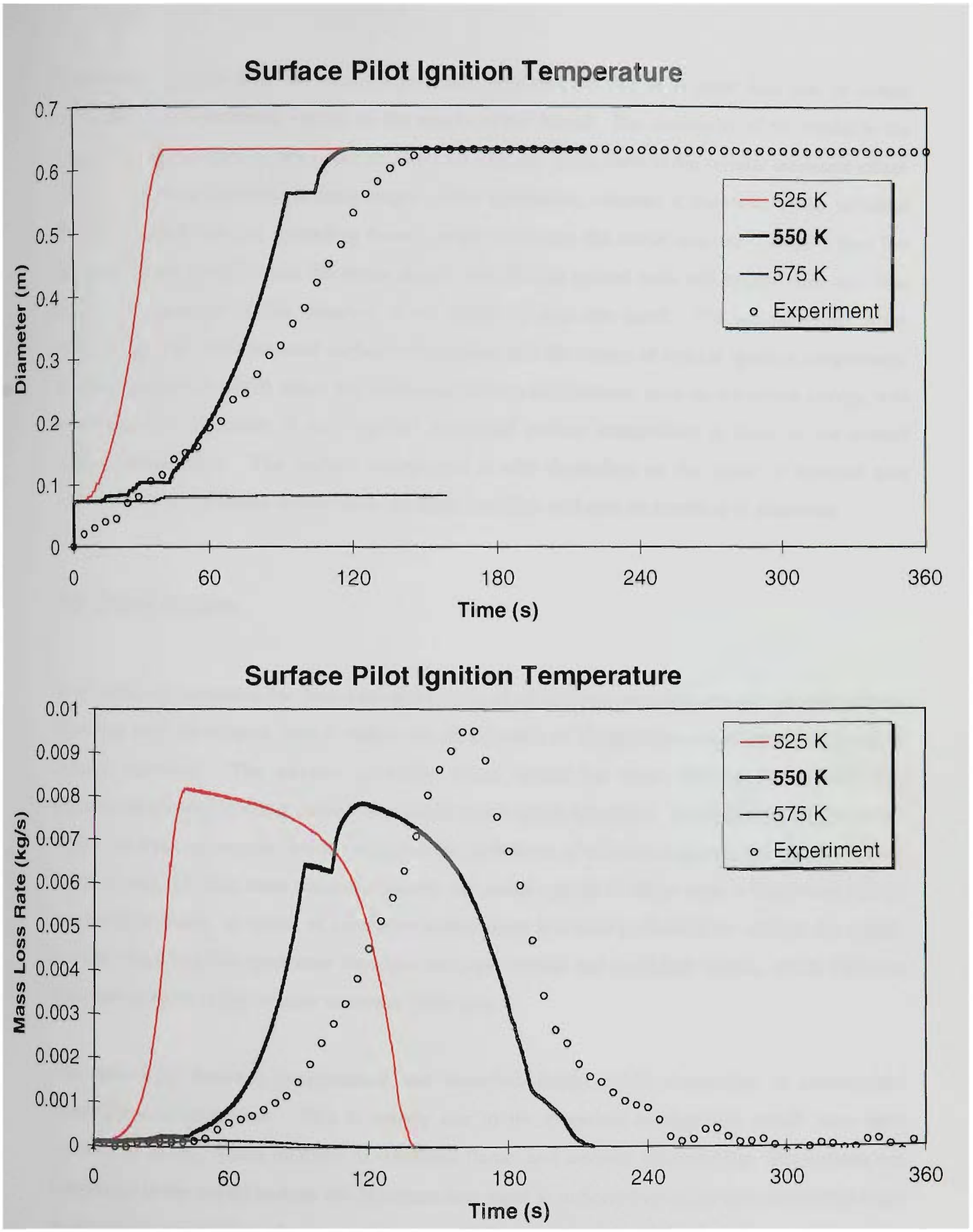

Figure 5.34 Flame spread and mass loss rate for varying surface pilot ignition temperature

5.8.4.Summary

Overall, it is evident from the analysis presented here that the choice of input data can, in certain instances, have a profound impact on the results of the model. The sensitivity of the model to the alteration of input data is dependent on two main effects. First, there is the cellular automata effect. There is a critical point in the early stages of the simulation, whereby if the value of the variables are chosen such that the spreading flame cannot overcome the initial discrete "jumps", then fire growth will not progress past the initial stages, and initially ignited cells will simply burn out. One of the key variables in this situation is the choice of grid size itself. The second effect is the relationship between computed surface temperature and the choice of critical ignition temperature. Material properties which affect the computed surface temperature, such as activation energy, will be sensitive to alteration if the "typical" computed surface temperature is close to the critical ignition temperature. The surface temperature is also dependent on the value of external heat sources, such as the flame temperature, so these variables will also be sensitive to alteration.

5.9. CONCLUSION

In this chapter, a method for determining the locus of an arbitrary two dimensional spreading flame front has been developed, which makes use of a branch of computational mathematics known as cellular automata. The physics governing flame spread has been investigated, and the key phenomena relating to flame spread over combustible solids identified. A stand-alone flame spread model has been developed, which combines the techniques of cellular automata with the physics of flame spread, and has been used to simulate the radial spread of flame over a horizontal slab of polyurethane foam. A series of controlled experiments has been performed to validate the model. Overall, there is good agreement between the experimental and modelled results, which indicates that there is merit in the cellular automata technique.

The correlation between experimental and modelled results, while reasonable, is nevertheless somewhat less than ideal. This is mainly due to the empirical assumptions which have been encoded in model, which describe an idealised flame, and ambient environment. Phenomena not considered in the model include the increased heat input to unburnt fuel at the foot of the flame due to gas phase conduction, the increasing opposed flow at the foot of the flame due to increasing entrainment of air into the growing flame, and the increasing heat feedback from the flame to the flaming fuel surface as the flame increases in size. These largely gas-phase phenomena may be rectified by modifying the empirical models to include a greater degree of sophistication. However,

such fine tuning is not within the scope of the project, as there are more powerful techniques available, namely those of computational fluid dynamics. This chapter has shown that the predictions of the solid-phase component of the flame spread model, including ignition, combustion, and mass loss rate, have been more than adequate, considering the empirical assumptions of the gas-phase components. Incorporation of the solid-phase model into a CFD model therefore appears to be feasible.

The cellular automata technique does have limitations, as revealed by the sensitivity analysis performed on the stand-alone flame spread model. For certain values of grid parameters and material constants, the method is fairly robust, but at other values, small changes in a parameter may have a large effect on the outcome of the model. It is important to be aware of this behaviour if the method is to be incorporated into a CFD model. Any inaccuracies or variations in the CFD model predictions will be magnified in the flame spread predictions if the flame spread model parameters are chosen in such a way that the overall model is sensitive. However, judicious construction of the model and choice of parameters will ensure that such problems are minimised.

6. FLAME SPREAD IN CFD

6.1. INTRODUCTION

The previous chapter demonstrated that it is possible to produce reasonably accurate results from an isolated flame spread model which makes only basic assumptions about the phenomena which are occurring in the gas phase. The approximations include the size, shape, temperature and optical thickness of the flame, and the constancy of such parameters as the external radiation heat flux, heat transfer coefficient, and direct heat flux from the flame to the burning surface. The inaccuracies in the stand-alone flame spread model can be largely attributed to these gas phase approximations, which are not flexible enough to adequately simulate the changing conditions occurring in the fire growth scenario.

CFD models on the other hand are concerned mostly with the simulation of gas phase phenomena occurring in a combustion scenario, and are also capable of calculating heat transfer from the gas phase to the boundaries. The CFD model requires that a fuel source is specified, to generate the heat and create the combustion scenario.

The aim of the work described in this chapter is to incorporate the solid phase component of the flame spread model* developed in earlier chapters into the field model CESARE-CFD. The solid phase model will calculate the temperature distribution within the fuel, and hence determine the rate of mass loss from the surface. This mass loss will appear as both a fuel mass source and enthalpy source in the CFD equations. In turn, the CFD model will calculate the combustion and heat transfer within the combustion region, and supply radiant and convective heat fluxes to the solid fuel surface. The process is not quite as straightforward as this, and the coupling necessary between the solid phase and gas phase models will be examined in greater detail.

In a recent paper, Nicolette, Tieszen and Moya[115] (hereafter referred to as NTM) discussed the necessary coupling between combustion and flame spread models, and general CFD fire models. Many of the points addressed in the NTM paper stem from a commonsense analysis of the problem; indeed, the author of this thesis independently reached similar conclusions in addressing several of the same points. Since the paper by NTM is non-specific with regards to the actual equations, this

* which hereafter is often referred to as the solid phase or solid fuel model, as distinct from the gas phase model, which the CFD model is often referred to as.

chapter will deal with the numerical methods required to merge the flame spread model with the field model CESARE-CFD.

NTM identified four major issues relating to the incorporation of a flame spread model into a fire field model. The first issue is the problem of tracking creeping (i.e. opposed flow) flame spread, which requires modelling of small scale phenomena, in a large enclosure. Since modelling of a large enclosure requires a coarse grid if computational resources are not to become prohibitive, it was proposed that a solution should track the creeping spread by empirical or other means on a subgrid of the CFD grid.

The second issue is how best to represent the fuel in the computational region; either as a solid object, or as a wall lining, and how to model the changing shape of the fuel as combustion progresses.

The third issue is the coupling of enthalpy and mass source terms was identified as being sensitive in field models; any imbalance will result in mass and energy no longer being conserved. This may be compounded by the variety of gaseous species produced by pyrolysis. The issue may be compound further if the time and heat flux dependence of the composition of pyrolysis products is taken into account.

The fourth issue is the choice of grid for the finite difference (or finite element) method used in both the flame spread and field models. NTM suggest a grid for the solid fuel which is refined at the surface near the flame front, and which moves with the front.

Recent advances in the incorporation of solid pyrolysis models into CFD models have been made, putting into practice some of the methods suggested by NTM. Novozhilov et al[116] incorporated a solid fuel pyrolysis model, which included one-dimensional heat transfer, chemical kinetics and surface regression, into a CFD model. This model was used to investigate fire extinguishment by direct cooling of the solid by water spray (as opposed to cooling of the fire plume region), so little additional information about the nature of the interaction of the solid and gaseous regions is given. Jia et al.[117] incorporated a simple thermal pyrolysis model into the model CFDS-FLOW3D, in order to investigate flashover and backdraft phenomena in a two-dimensional compartment with plywood linings. This model makes use of the concept of a pyrolysis temperature, whereby the fuel only undergoes pyrolysis once the pyrolysis temperature is reached. The assumption made about the solid-gas interactions are quite clearly defined in this instance; the solid does not melt or char, combustion gases leave the surface with zero initial velocity, and while the surface regresses due to

mass loss, this is assumed to have no impact on the gas motion near the solid. These features are similar to the assumptions made in the model presented in this thesis, and were shown to successfully reproduce the phenomena of interest, namely flashover and backdraft, on a qualititative level. However, no comparisons with experimental data were made, and the authors concede that the model is still in the developmental stage, and that quantitative data are required for validation.

6.2. THE CESARE-CFD FLAME SPREAD MODEL

6.2.1. Solid Fuel Embedding Method

The four issues raised by Nicolette et al[115], as described in the previous section, are dealt with to varying degrees in the method presented herein. In addressing the first issue, the need for a fine grid to model opposed flow flame spread was identified earlier in Chapter 5, and indeed the method chosen here is to construct a grid for the flame spread model which is finer than that used in the CFD model. The cellular automata techniques become useful in modelling the flame spread within the larger CFD grid cells. It was also identified in Chapter 5 that the solid fuel grid should be refined near the burning surface due to the high temperature gradient, which partly addresses the fourth issue listed above. For simplicity, moving grids at the flame front were avoided in the formulation of the solid combustion model. The only movement which was allowed for was the collapsing grid to maintain a refined region at the surface of the solid fuel.

Regarding the second issue, the fuel is modelled as an obstacle within the flow region, with combustion and mass loss occurring at one surface only. Although regression of the fuel surface is taken into account in the flame spread model, the fuel obstacle retains its shape in the flow region. The main reason for this is that CESARE-CFD operates on a fixed orthogonal grid. It is anticipated by the author that while the regression of the fuel surface is important to the heat conduction within the fuel, the effect will be negligible in terms of the large scale behaviour of the flow region. The behaviour of the flow region close to the fuel itself is, however, likely to be affected by the regression of the fuel surface, especially for expanded fuels such as polyurethane foam, which regress quite rapidly upon exposure to flame. The flame front will cause a zone of melt and surface regression, which will form a small "step" in the surface of the fuel. The air entrained by the plume will establish the usual boundary layer flow next to the unburnt solid surface. This flow may then be disrupted as it crosses the threshold of the step in the fuel, which in turn may affect the structure of the flame front. For denser fuels, especially charring ones, regression of the fuel is comparitively small, so this "step" effect is likely to be negligible. Hence, the assumption that the fuel surface

does not regress will be a reasonable valid approximation for such fuels. However, accounting for the regression for fuels such as polyurethane foam will introduce quite a degree of complexity, especially for the fixed orthogonal grid used in CESARE-CFD. Thus, the neglection of regression of the fuel surface in the flow region is used as a first approximation for the work presented here.

In regard to the third issue, the products of pyrolysis of the solid fuel are not modelled in any great detail in this model. The only properties of the gaseous fuel which are considered in CESARE-CFD are molecular weight and heat of combustion, both of which are average values, and constant throughout the execution of the model. In the absence of more appropriate data, the thermodynamic properties of methane are assumed to be sufficiently representative of the gaseous fuel. This assumption has been used with some success in past modelling of polyurethane combustion with CESARE-CFD[118]. The assumption is reasonable under the circumstances. The pyrolysis products of most solid fuels are variable in composition, and the constituents unknown. All that can be stated with confidence is that in the combustion reaction, the pyrolysis products will dissociate further into smaller, organic compounds such as methane. Another candidate for representation of the fuel could be acetylene, the precursor of soot formation[47]. In any case, the concentration of unburnt fuel is generally very small, except perhaps in the fire plume region, so its contribution to the thermodynamic properties of the fluid is expected to be minor.

6.2.2. Grid Embedding

Incorporation of the flame spread model in CESARE-CFD model requires embedding the flame spread grid as a subgrid of the CFD model's main flow grid, for reasons that were discussed previously. There are two issues to be considered here. First, quantities which are transferred from the fuel to the flow region need to be either summed or averaged, depending on the quantity. Secondly, quantities transferred from the flow region to the solid fuel need to be distributed over the solid region.

6.2.2.1. Transfer from Solid to Flow

Consider first transfer from the solid fuel to the flow region . The solid contributes gaseous fuel to the flow region, at a rate given by

$$\dot{m}'' = A \exp\left(\frac{-E}{RT}\right) \qquad (6.1)$$

where T is the temperature of the solid surface, which is calculated using Equation 4.15. This manifests itself as a mass source term in the flow cell immediately adjacent to the solid. Now, since the flow grid in general will be coarser than the solid grid, a flow cell adjacent to the solid surface will be in contact with several solid cells. The mass source in the flow cell will simply be the sum of the contributions from all the smaller solid cells with which it is in contact.

As well as mass, the vaporising solid contributes enthalpy to the flow region. The enthalpy of a unit mass of a gaseous species has a parabolic dependence on temperature T, and is given by the equation

$$h=b_2T^2+b_1T+b_0 \qquad (6.2)$$

The coefficients b_0, b_1, and b_2 used for the fuel in the model are those for methane (-735.0, 2.146, 0.0010804 respectively), for the reasons discussed above. The enthalpy contributed by a solid cell will be the product of the enthalpy per unit mass and the mass loss for that cell. It is assumed that temperature of the fuel gases leaving the surface is the same as the surface temperature of the solid cell. To calculate the total enthalpy contributed to a flow cell, a simple summation of the contributing solid cells is again sufficient.

However, the heat flux from the fuel surface to the flow region is another matter. The flow cell will receive radiated and conducted heat from the fuel surface, and since each surface cell in contact with the flow cell will, in general, be at a different temperature, the net contribution from all the cells is not immediately obvious. This is because the calculations for radiation and convection in the flow region involve a single surface temperature, but each component has a different temperature dependence. For example, if three quarters of the solid cells in contact with a flow cell are at a low temperature, and one quarter at a high temperature, a simple linear averaging of temperature will lead to a correct calculation of the convected heat flux (which is proportional to the linear temperature difference), but will underestimate the radiation heat flux, since the average of the fourth powers of temperatures will be greater than the fourth power of the average of the temperatures. Calculating the solid cell fluxes individually is a possibility, but transferring this information to the appropriate subroutines in CESARE-CFD poses some problem, given the structure of the program (although the problem is not insurmountable). As a first approximation, the following assumption is made.

For non-combustible surfaces in the rest of the modelled region, the surface grid coincides with the flow grid. The conducted, convected and radiated heat are dependent on the surface temperature, and are assumed to prevail uniformly across each surface element. The location of the surface node

itself is at the centre of the surface element. In view of this, an approximation for the surface temperature of the fuel surface is chosen to be that of the solid fuel element which coincides with the centre of the flow grid cell. This is expected to be a reasonable assumption for groups of solid cells of fairly uniform temperature (either all unignited, or all undergoing combustion), but may lead to some inconsistencies when the flame front is crossing the flow cell.

Apart from enthalpy and fuel mass, no other variables are transferred to the flow region. As in the study of Jia et al[117], the fuel is assumed to leave the surface with no velocity, so that no source term appears in the boundary momentum equation. Likewise, no turbulence quantities are introduced to the flow region at the solid surface. This assumption should not cause too much error for open cell foams or thermoplastics where there will be no buildup of internal pressure driving a surface flow. It may be a less accurate assumption for charring solids such as wood, where internal pressures develop and are sufficient to drive the fuel vapours from the surface with a non-zero velocity[79,119].

6.2.2.2. Transfer from Flow to Solid

The other transfer to consider is that from the flow region to the solid. The quantity transferred in this direction is heat flux, which is dependent largely on the properties of the flow cells in contact with the fuel surface. Now, an individual solid surface cell will be in contact with only one flow cell (if it is overlapping, then whichever flow cell the centre of the surface cell is in contact with may be taken to be the appropriate flow cell). The obvious choice of method for considering the heat transfer from the flow cell is to assume the properties of the flow cell, such as temperature, prevail at the surface point of interest.

However, in preliminary modelling exercises of the flame spread submodel incorporated in CESARE-CFD using the approach of uniformly prevailing flow cell properties revealed an inadequacy in this assumption. It was found that an "image" or "stamp" of the flow grid could be seen in the results from the solid submodel. Since the heat transfer values from the flow region were constant for whole blocks of solid grid cells, examination of values such as mass loss and surface temperature of the solid tended to likewise show whole blocks of cells with fairly uniform values, adjacent to blocks with uniform but different values. Some blurring occurred at the boundary between blocks, presumably due to conducted heat transfer within the solid. There are further complications with regards to this circumstance. If conditions for flame spread are favourable within one of these blocks, then such conditions will occur more or less simultaneously

at all cells within the block. Flame spread will progress rapidly across the block, limited only by the cellular automata restrictions, until the border with the next block is encountered.

Such a situation is undesirable, as it defeats the purpose of using a subgrid of the flow grid, which is to model phenomena whose mechanisms operate on smaller scale than resolved by the flow grid. If the behaviour of the subgrid is dominated by the large scale grid, then there is no gain in information. However, variables in the flow region are calculated on the assumption that the properties prevail uniformly over the control cell. While there is no more information than that available to the modeller, it is possible to extract further information by interpolating between the known values at the discrete flow cell nodes. The question arises as which interpolation method to use.

There are at least two simple interpolation methods, as identified by the author, and no doubt several other methods exist, although these are likely to be more complicated. The two simple methods will be described here, even though only one is actually used in the model. The quantity of interest distributed throughout the flow region is denoted ϕ. The surface cell under consideration is at (x,y), where x and y are coordinates in the two directions parallel to the fuel surface, and is in contact with a particular flow cell. The value of the quantity in the flow cell is denoted $\phi_{i,j}$, as calculated for the node located at (x_i,y_j). (In fact, the node is located in the middle of the flow cell cuboid, but its projection to the flow-fuel boundary places it in the middle of the boundary rectangle.) In general, each flow cell will have 8 neighbours likewise in contact with the surface, as shown in Figure 6.1.

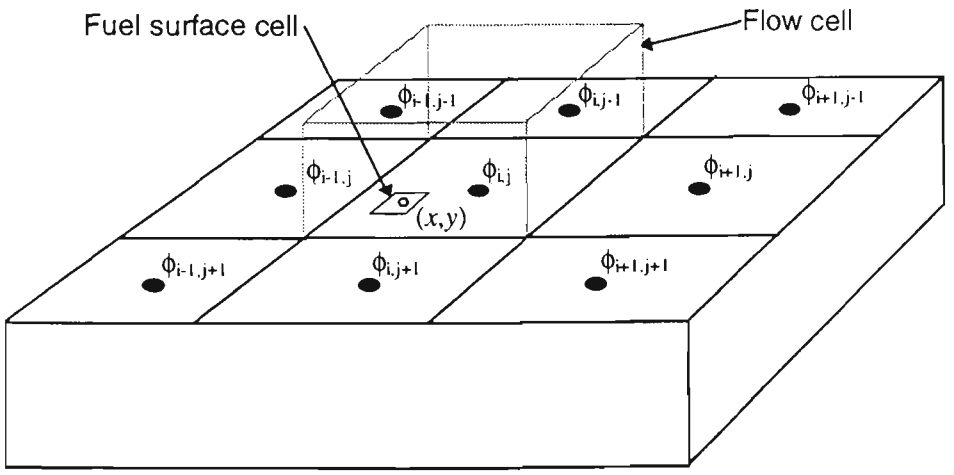

Figure 6.1 Flow cell neighbours

If the point at (x,y) coincides with the flow node, then the value of $\phi(x,y)$ is equal to $\phi_{i,j}$. If it is located a finite distance from the node, the value will be somewhere between $\phi_{i,j}$ and the value at the nearest neighbours.

The first interpolation method considered here is a paraboloidal curve fit. It is assumed that the profile of ϕ in the flow region may be expressed by the quadratic equation

$$\phi(x,y) = A(y-y_j)^2 + B(y-y_j) + C(x-x_i)^2 + D(x-x_i) + \phi_{i,j} \qquad \textbf{(6.3)}$$

The constants A, B, C, and D are determined by evaluating Equation 6.3 at locations where ϕ is known, namely the neighbouring flow nodes at (x_{i-1},y_j), (x_{i+1},y_j), (x_i,y_{j-1}), and (x_i,y_{j+1}). This results in four equations with four unknowns, which may be solved simultaneously.

There are three drawbacks to this method. Firstly, in general the resulting interpolated function $\phi(x,y)$ will not be continuous at flow cell boundaries. Secondly, simultaneous equations are inconvenient to solve. Thirdly, the method does not make use of the known values at the four corner neighbours.

The second method presented here is a linear interpolation method, which produces a continuous function with a single equation, and makes use of all 8 neighbours. The point at (x,y) will in general be located between four flow cell nodes, as shown in Figure 6.2.

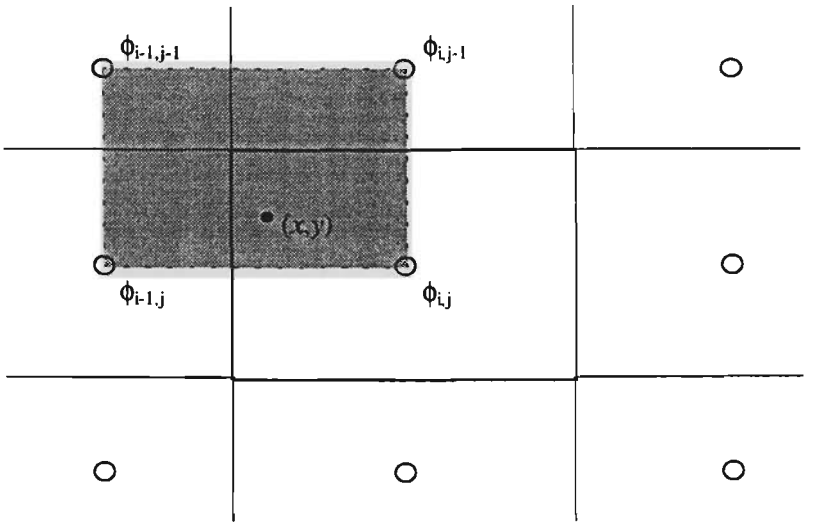

Figure 6.2 Linear interpolation method

The formula for linear interpolation in two dimensions is derived as follows. First, two intermediate values $\phi(x_{i-1},y)$ and $\phi(x_i,y)$ are determined by the usual linear interpolation method along the lines $x = x_{i-1}$ and $x = x_i$ respectively. The value at (x,y) is given by the linear interpolation between the two intermediate values. The resulting equation is given by

$$\phi(x,y) = \frac{(x_i-x)(y_j-y)\phi_{i-1,j-1} + (x_i-x)(y-y_{j-1})\phi_{i-1,j} + (x-x_{i-1})(y_j-y)\phi_{i,j-1} + (x-x_{i-1})(y_j-y)\phi_{i,j}}{(x_i-x_{i-1})(y_j-y_{j-1})} \qquad \textbf{(6.4)}$$

The linear interpolation method is used to determine the incident radiation flux distribution to the fuel surface from the surroundings, since the flux is calculated by the discrete transfer method for the flow nodes only. This method is also used to describe the local value of flow variables at the fuel surface.

There is likely to be some error associated with the interpolation method. The method assumes a linear profile between neighbouring flow cells, but then so does the finite difference method used in the calculations throughout the flow region. Hence, the error is expected to be of the same order as the finite difference method i.e. first order. The method does not take into account any weighting due to the relative sizes of neighbouring flow cells. Consequently, the method will produce the best results when the flow grid is uniformly spaced. The flow grid in the modelling presented later is refined in the region of the solid fuel, and is indeed uniform in this region.

The form of Equation 6.4 only directly applies when the solid fuel is in an "open" area i.e. the edges of the fuel surface are all adjacent to the flow region. This is the case for the modelling work described later; however, future applications will no doubt need to consider cases in which the solid fuel surface is adjacent to a wall or even another fuel surface (such as a chair arrangement or room corner fire). There are at least two options to choose from, and each option may well be best suited to different variables. The first option is that for the half cell between the centre of the flow cell and the boundary, the flow variable should prevail across the half cell. This is probably suitable for quantities such as the density and laminar viscosity of the fluid, as well as the radiant flux to the surface (in fact, a uniform value is already assumed for the incident surface radiant flux when there is no receiving surface beyond the edge of the fuel). Another option is that the variable be linearly interpolated with a fixed value at the wall (in some cases zero) across the half cell. This method is better suited to the temperature, which is known at the wall, and variables such as the turbulence kinetic energy which decreases to zero at the wall.

6.2.3. Convective Heat Transfer at the Gas-Solid Boundary

Most of the physics occurring at the boundary have been described in the previous section. All that remains is to determine the convective heat transfer to the surface. A model to calculate heat transfer from the flow region to the non-combustible boundaries has previously been encoded into CESARE-CFD. This is the wall-function method of Launder and Spalding[18] which was described in Section 2.4.6.1., and is given by the equation

$$\dot{Q}''_{wall} = \frac{C_p \rho C_\mu^{\frac{1}{4}} k_p^{\frac{1}{2}}}{\frac{\sigma_h}{\kappa} \log\left(\frac{E z_p C_\mu^{\frac{1}{4}} k_p^{\frac{1}{2}}}{\nu}\right)} (T_p - T_{wall}) \equiv h(T_p - T_{wall}) \qquad (6.5)$$

where h is the convective heat transfer coefficient, E is the wall roughness constant, equal to 9.0 for a smooth wall. The surface of polyurethane foam is quite rough, so a value of 1.0 was used in the modelling presented, as this produced a figure for h of the order of 10 kW/m^{2}K. Kumar and Cox[63] reported values of 0.568 for concrete walls and 0.064 for general brick walls, so the value for polyurethane foam may be lower still.

The local heat transfer coefficient for an element on the fuel surface is calculated by first linearly interpolating the flow variables in Equation 6.5, and then evaluating the equation. These flow variables are the fluid temperature, kinematic viscosity, turbulence kinetic energy, and density.

6.2.4. Initialisation of the Model

Computer modelling of an unsteady-state fire with CESARE-CFD is performed in two stages. First, the distribution of variables within the flow region needs to be "initialised" by solving a small steady state fire, whose heat release rate is typically of the order of a few kilowatts, and whose location is at the origin of initiation of the unsteady fire. Solution of the small steady state fire produces a distribution of the variables listed in Table 2.1, which serves as the starting point for the unsteady simulation. After convergence of the solution for this small steady-state fire has been attained, the unsteady state simulation is calculated by a forward marching time solution, using initial values of the variables in the steady state simulation as a starting point.

The stand-alone flame spread model is by its design an unsteady-state model, although like its more complex counterpart CESARE-CFD the forward marching time solution is calculated from an initial starting point. The starting point is an initially uniform ambient temperature for the solid fuel, a small area of which is ignited, optionally after a specified preheating time. However, incorporation of the flame spread model into the CFD model requires that the fuel slab be part of the steady-state initialisation process. This is due to the sensitivity of the coupling between the solid fuel and the flow region. Therefore, conditions need to be specified for the fuel during the steady-state phase of the modelling.

The preheating of the fuel is not an option likely to be used in the modelling of full-scale building-fires, where the problem of interest usually begins with the initiation of combustion. Hence, in this case the flame spread model will be initialised with a small ignited area.

For the steady state conduction of heat in an infinite slab of finite thickness and constant conductivity, the temperature distribution within the slab is a linear temperature profile between the two surfaces[70]. However, if an infinite slab which is initially at uniform temperature is instantaneously heated or cooled at one surface, it usually takes a long time (dependent on conductivity and thickness) for the temperature within the slab to assume an approximately linear profile (and theoretically an infinite time to exactly attain it.) For the flame spread model, the unsteady state will commence with the nearly instantaneous heating of a portion of the upper surface, with the rest of the fuel remaining approximately at ambient temperature. If heat conduction within the solid is allowed in the steady-state initialisation of the CFD model, the temperature distribution within the fuel will approach a linear one into the depth of the fuel, and radiating outwards from the ignition source as well. The result of this will be less conductive losses into the fuel and a greater preheating of the fuel ahead of the ignited region when the unsteady phase of the calculations commence, resulting in an increased combustion and flame spread rate. As a consequence, only surface temperatures are calculated for the flame spread model in the steady state, and the conduction into the fuel is ignored. Thus, at the commencement of the unsteady state, a localised region of the fuel surface will be at combustion temperature, and all temperatures within the fuel will be at ambient temperature.

Another issue to be addressed is the maintaining of a steady burning region on the fuel surface in the steady-state. The region of the surface designated as ignited must satisfy the criteria for ignition at the conclusion of the steady-state phase of calculations; that is, in the case of this model, the surface must be at least at the critical ignition temperature. If the criteria are not met, the flame spread scenario will not have been properly initiated, and flame spread may not occur. Indeed, combustion may even cease entirely, as insufficient fuel will be contributed to the flow region, resulting in less heat feedback.

In this model, maintenance of the ignition criteria is accomplished by prescribing a minimum heat flux to a fuel surface cell which has ignited. This value is the quantity $\dot{Q}''_{flame}$ that was used in the stand-alone model to model the heat flux received from the flame. In the flame spread model in CESARE-CFD, the sum of the radiation heat flux and the convected heat flux to the fuel surface is calculated (taking into account the linear interpolation described in the previous section.) If the total flux is less than $\dot{Q}''_{flame}$, then an appropriate adjustment is made to the heat transfer coefficient

to increase the convection heat flux, to the point where the sum of radiated and convected components is equal to $\dot{Q}''_{flame}$.

Despite the inclusion of a minimum flux to ensure no extinction in the steady-state phase of the calculations, a rapid drop in temperatures throughout the flow region frequently occurred soon after the commencement of the unsteady-state calculations, effectively causing extinction of the fire. This may be due to the somewhat artificial imposition of the minimum heat flux criterion. For this reason, the minimum flux criterion was retained in the flame spread model for the unsteady phase of the calculations.

6.3. A SIMPLE TEST CASE

In this section, a series of simple numerical experiments is described, which was devised to evaluate the validity of the assumptions made in the interfacing of the solid fuel model with the CFD model, as presented in the previous sections. The numerical experiments were not intended to make a correct prediction of the behaviour of the flow in the chosen geometry. Rather, the intention was to construct a reference flow region, which was interfaced with a variety of solid fuel grids, to test the robustness of the interface assumptions. Basically, a simulation was performed with given conditions and a given grid size for a solid fuel region. The grid size of the solid fuel was then refined by varying degrees, and changes to the solution, if any, were noted.

The numerical experiments were performed in a simple 1m×1m×1m flow region. A solid fuel slab with the thermophysical properties of polyurethane foam, measuring 1m×1m×0.1m was placed at the bottom of the flow region. The flow grid was originally set to 10×10×10 flow cells, all regularly spaced. This was altered to 11×11×10 so that a cell would coincide with the central symmetry lines along the x and y axes, rather than a cell boundary. After a few initial numerical experiments, the grid was refined close to the fuel surface in the vertical direction, to better model the heat transfer close to the solid surface. A vertical section of the grid for these exercises is shown in Figure 6.3. The radiation grid was set identical to the flow grid.

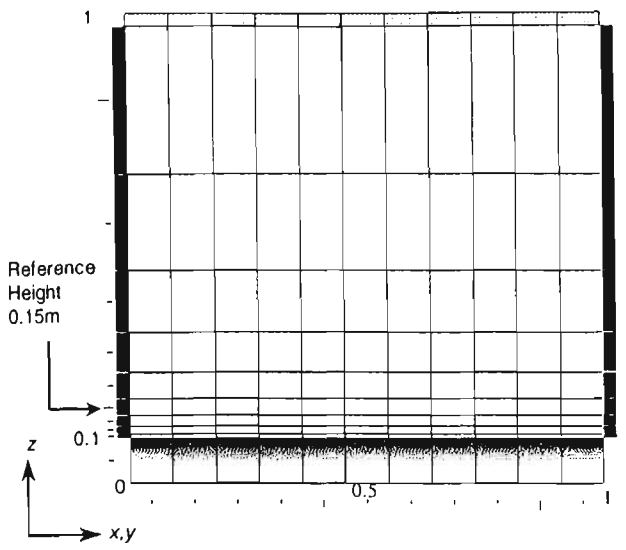

Figure 6.3 The flow grid used in the test cases

The four boundary walls were treated as solid walls having emissivity 0.9, while the ceiling was designated a balance port with emissivity 1.0. The temperatures of the walls and the flow region were initially set to ambient temperature, chosen to be 20°C. The temperature of the solid slab was initially set to a temperature of 40°C. Six divisions in the vertical direction were made in the fuel grid. These were made so each division was 1.5 times the thickness of the next division above.

Four grid refinements of the solid fuel in the horizontal direction were tested. The first refinement was an 11×11 grid, so that the solid surface cells were in a one-to-one correspondence with the flow cells. The second refinement was a 12×12 grid, which is slightly staggered with respect to the 11×11 flow grid. The third refinement was a 55×55 grid, whereby a 5×5 block of solid cells are in contact with each flow cell. The fourth refinement, used only in the third scenario described below, was a 110×110 grid, in which a 10×10 block of solid cells is in contact with each flow cell.

Three steady-state heat transfer scenarios were tested. The first was a simple heat conduction test. In this test, the velocity and turbulence calculations were switched off, so that the only heat transfer mechanisms in operation were conduction and radiation. In the second scenario, the velocity and turbulence calculations were included, but not fuel mixture fraction. The balance port was in operation, and the condition that the flow at the balance port is uniform was imposed. In the third scenario, fuel calculations were included. A rectangular section of the solid fuel measuring 0.2m×0.2m located in the centre was ignited, and a steady-state combustion initialisation performed. As the ignited section did not correspond to the grids used, a different effective combustion area and hence heat release rate were generated for the four grid refinements tested. The ceiling was designated a non-uniform balance port with maximum velocity 1m/s.

For all the simulations undertaken, temperatures were recorded along the three centrelines. The horizontal temperatures were recorded at a height equivalent to 0.05m above the solid surface (see Figure 6.3). This corresponds to the fourth flow cell above the surface. All tests were run for 1000 iterations, after which residuals had fallen below 10^{-4} m/s for velocity, 10^{-26} for mixture fraction, and 10^{-2} kJ/kg for enthalpy. This indicates a high degree of convergence, especially for mixture

fraction, when compared with the typical values quoted in Section 2.4.7. A full analysis of the convergence is described in a later subsection.

6.3.1. Conduction Results

The results of the experiments undertaken with conduction only (no velocity calculations) showed that for the three fuel grids tested, there was no difference in the calculated temperatures, at least to

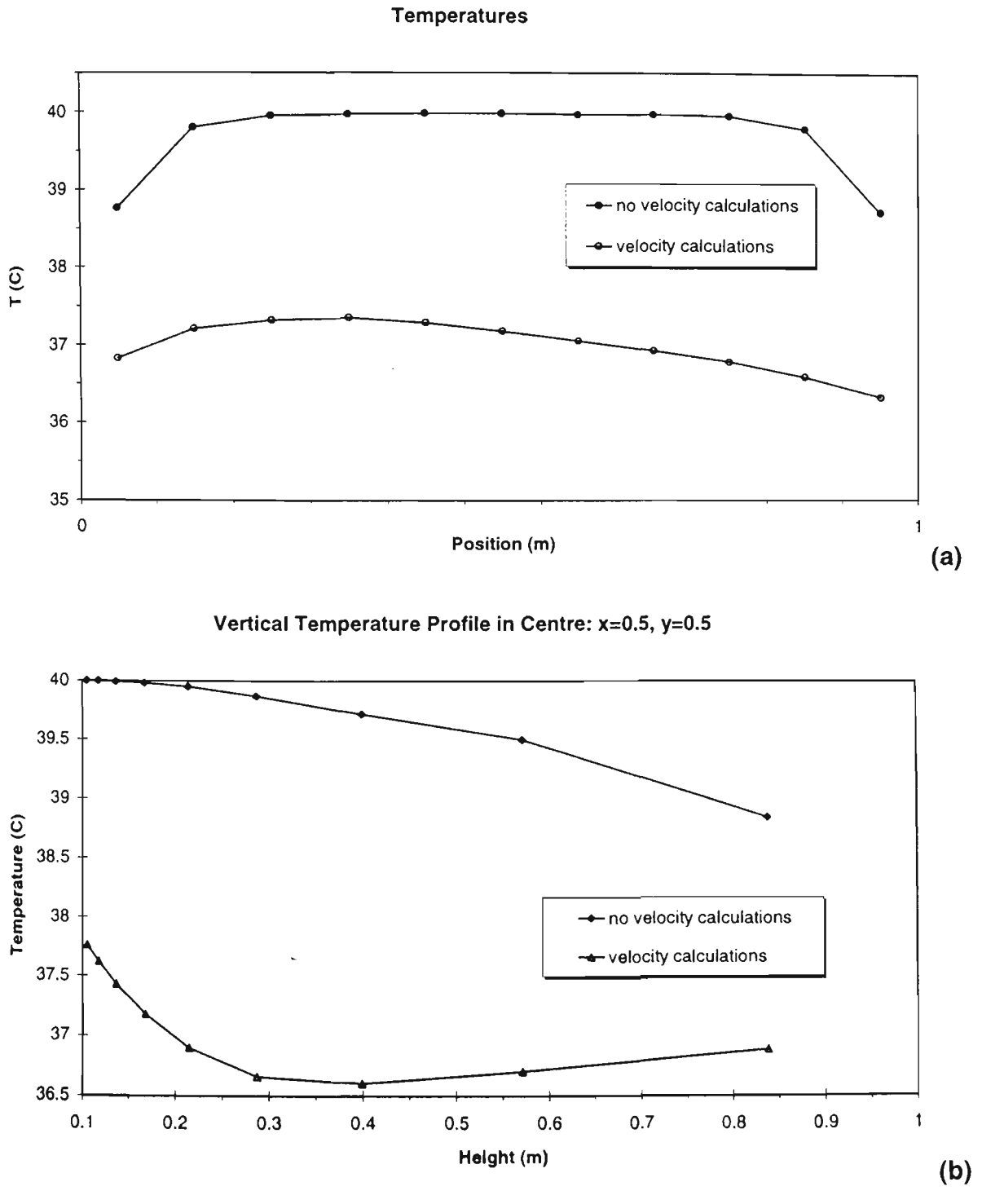

Figure 6.4 Temperature results of the first and second scenarios

two decimal places. What appears to be occurring is that because only the surface temperature was allowed to vary in the solid, the maintenance of the first sublayer at 40°C was sufficient to compensate for heat losses to the flow region. Because the surface temperature was maintained at 40°C, the flow layer adjacent the surface was likewise maintained at 40°C. Heat decreased vertically, and towards the boundary, as heat was lost to the walls and ceiling. Symmetry was maintained in the x and y directions, so that the temperature profiles in both directions are identical. As a result, only one set of results for the "no velocity" case is required to be displayed in each of Figure 6.4(a) and Figure 6.4(b), as the two curves coincide. The curve in the horizontal direction clearly shows the symmetry across the flow region, and the heat loss near the boundaries.

6.3.2. Conduction and Convection Results

As with the conduction only tests, the predicted temperature and velocity profiles were identical for the three grid refinements tested. The introduction of velocity flow decreased the temperature at the surface and hence throughout the flow region, as can be seen by comparing the "velocity" curves with the "no-velocity" curves in Figure 6.4(a) and (b). The x and y profiles were again identical, but in this case they were not symmetrical. What occurred when the velocity was included in the computation is that symmetry was broken, and a circulation pattern was established, whereby relatively cooler air descended in the corner x=1,y=1 and ascended in the corner x=0,y=0. The resulting flow was symmetrical about the plane x=y, with the result that the curves for the x and y directions again coincide. The profile in Figure 6.4(a) shows that the temperature is cooler towards x=1 and y=1, where the flow is descending.

The vertical temperature profile initially decreases with increasing distance from the surface, but then increases above z=0.4. This is a result of the circulating flow pattern carrying rising warm air across the top of the flow region. It is interesting to note that the flow temperature adjacent to the fuel surface is not at 40°C. This is because the flow is not stagnant; instead, descending cool air flows across the surface, keeping temperatures a few degrees below fuel temperature.

The "symmetry breaking" feature, leading to asymmetrical temperature profiles in what is a symmetrical flow region, requires some explanation. While a symmetrical flow pattern might theoretically be possible to generate (e.g. rising in the middle of the flow region, descending at the boundaries), such a pattern is analogous to a pencil balanced on a point. Just as a small perturbation will cause the pencil to fall one way or the other to a more stable configuration, a small perturbation in the flow calculations, such as truncation or roundoff (present in all computer

calculations to some degree), will cause the flow pattern calculations to converge to a more stable asymmetrical solution.

6.3.3. Conduction, Convection and Combustion Results

The four tests performed with the initialised combustion region showed greater variation in results. For the 11×11 grid, 9 cells were ignited, and the resulting calculated heat release rate was 20.43kW. Symmetry breaking caused the flame to be entrained towards the x=1 wall. For the 12×12 grid, 4 cells were ignited, resulting in a calculated heat release rate of 7.08kW. Symmetry breaking again caused the flame to lean towards the x=1 wall. The refinement of the 55×55 110×110 grids allowed the ignited area to be modelled more closely, as evidenced in the calculated heat release rates of 10.94kW and 10.92kW respectively. Symmetry breaking caused the flame in this instance to lean towards the x=0 wall. The temperature curves for both grids have very similar profiles. This suggests that there is little increase in error when the solid grid size is doubled from 110×110 to 55×55.

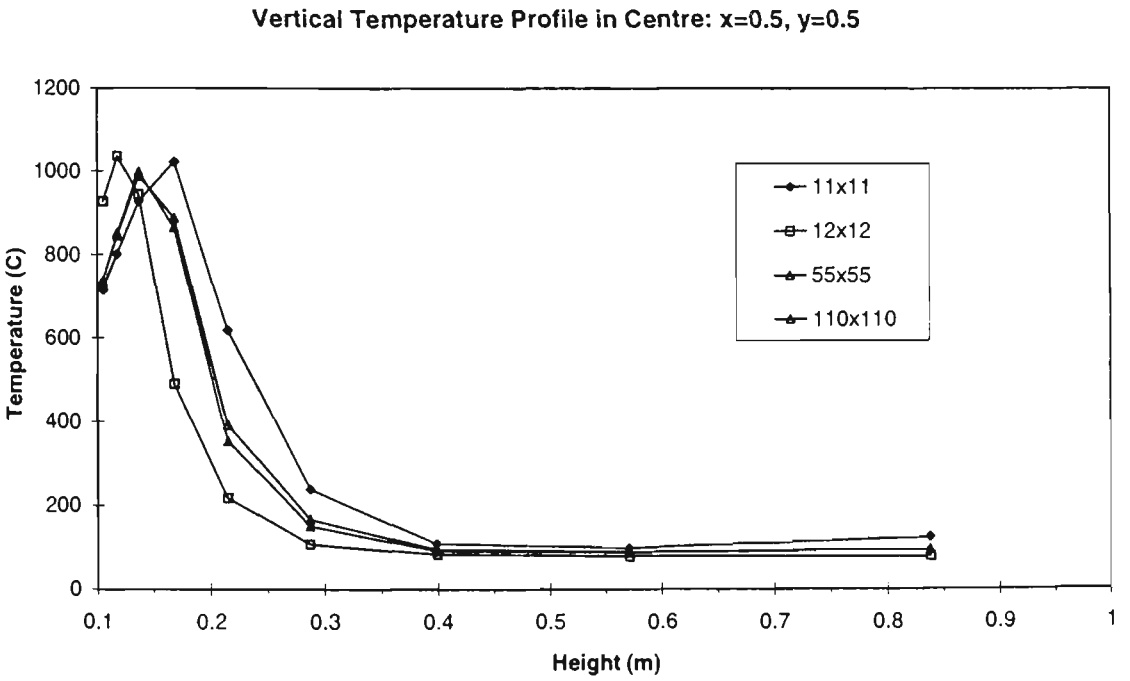

Figure 6.5 Temperature results of the third scenario: vertical direction

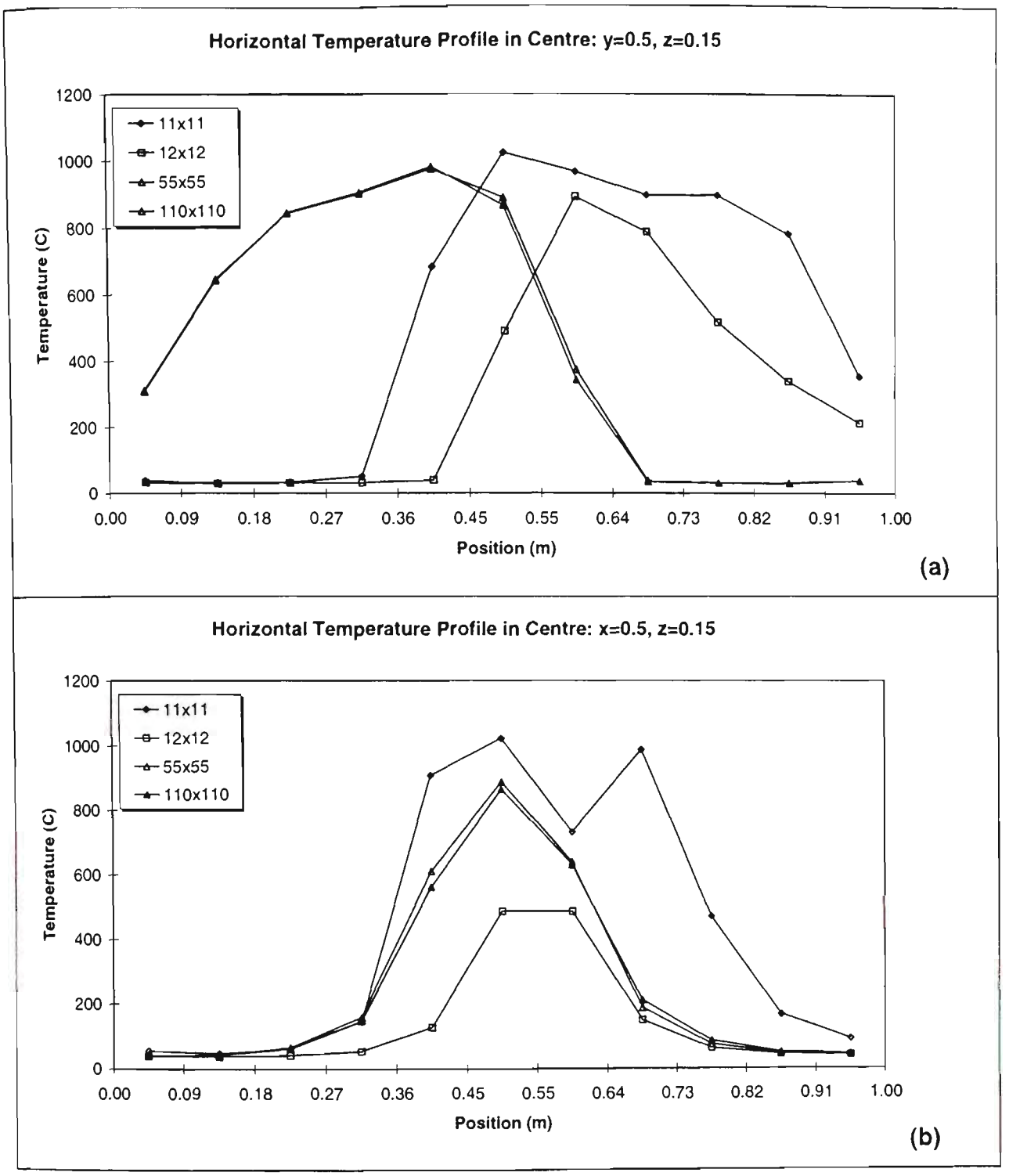

Figure 6.6 Temperature results of the third scenario: horizontal direction

6.3.4. Convergence Analysis

The simulation of the cubic enclosure, by virtue of its simple geometry and small number of grid nodes, converged very rapidly, particularly after 200 iterations. This is illustrated in Figure 6.7 for the velocity residuals, and Figure 6.8 for the residuals of other variables. Because of the large degree of convergence, the residual graphs are plotted using a logarithmic scale to illustrate the decreasing order of magnitude of convergence in the later stage of the simulation. Unlike the

200kW fires presented in Section 3.9.3, the fuel mixture fraction residuals follow the pattern of the other residuals (although the former is still of a much smaller magnitude than the others).

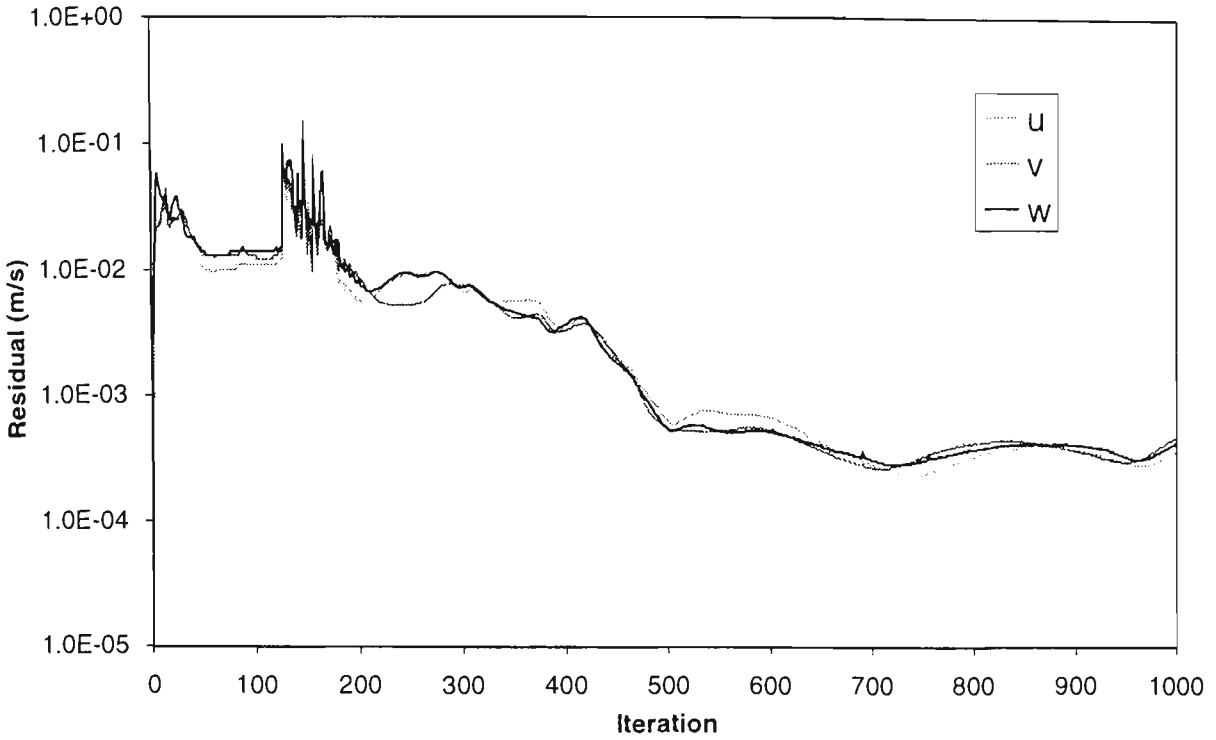

Figure 6.7 Velocity residuals for the flame spread test case simulation

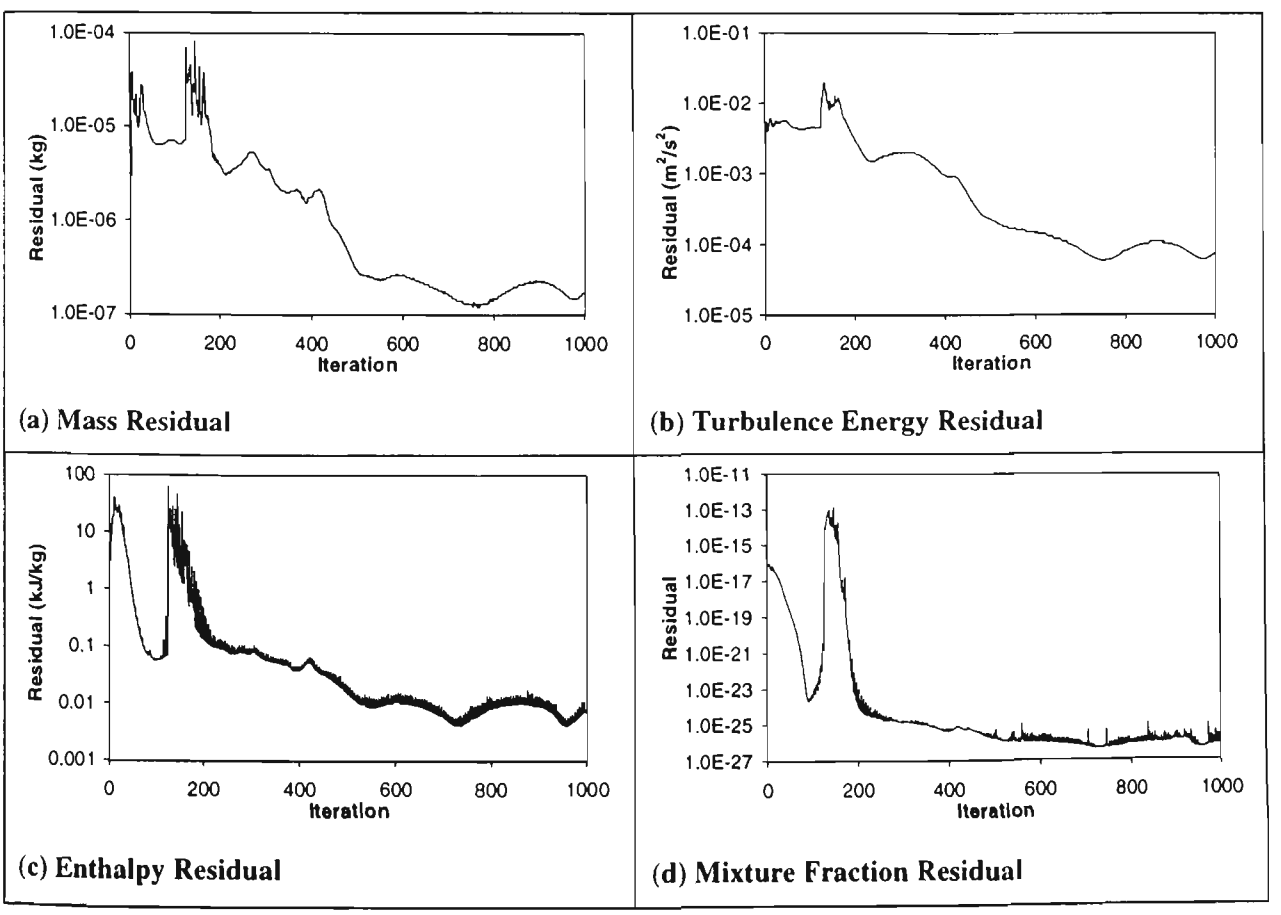

Figure 6.8 Residuals for the flame spread test case simulation

A feature of note in all residual charts is the initial decrease in residuals at the start of the simulation, followed by a rapid increase and plateau between 100 and 200 iterations. This increase may be due to a "symmetry breaking" phenomenon, described above. The sudden increase in residuals is a likely marker of the transition from a centrally rising plume to the adherence of the plume to one wall.

This transition is also highlighted in the energy balance chart shown in Figure 6.9. The balance between input and output energy is achieved early in the simulation, before being disrupted, and then restored. The fact that balance is achieved and is quite stable is further indication that an excellent degree of convergence has been attained for this particular scenario.

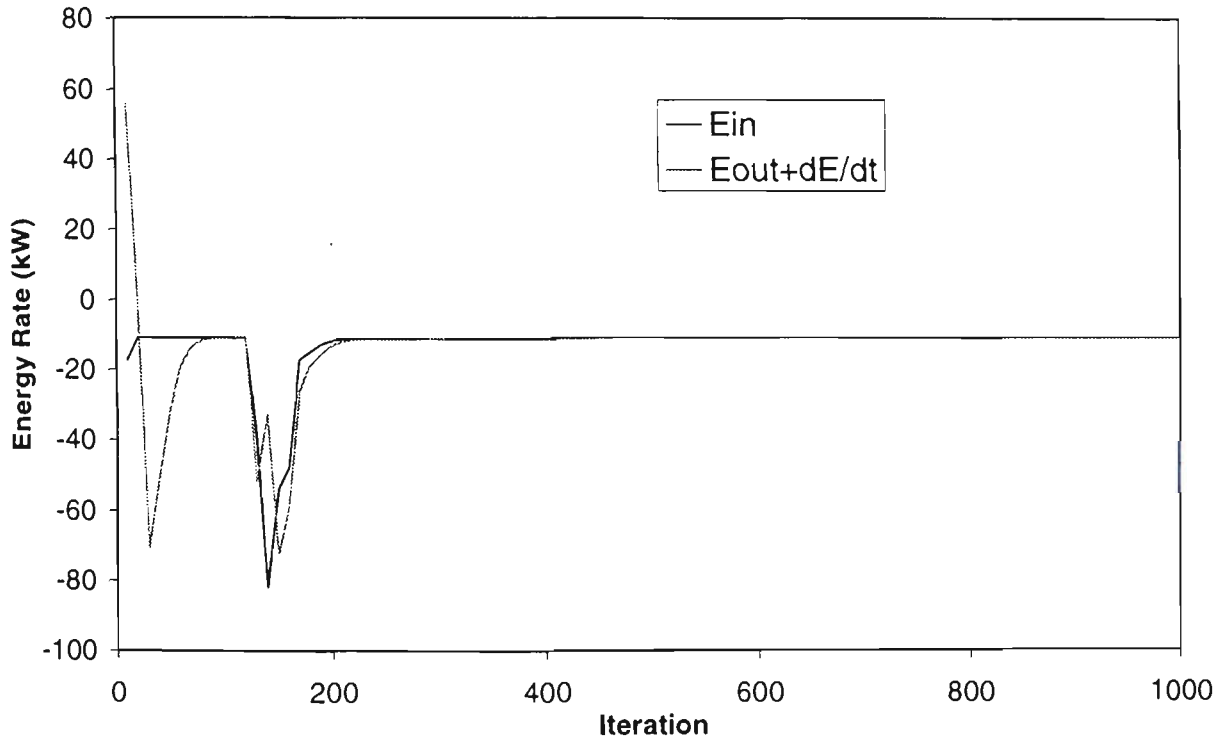

Figure 6.9 Energy balance residuals for the flame spread test case simulation

6.3.5. Concluding Remarks

The results of this series of experiments appear to indicate that if any errors are introduced into the model by the assumptions made in the previous section, the errors are not exacerbated by grid refinement or otherwise of the solid region. This does lead to some confidence in the overall solid embedding method. The results do highlight the need for a grid refinement to accurately model the fuel area and heat release rate of the solid. Obviously, the finer the grid, the more accurate will be the modelling, although this must be balanced against computational time. The results presented

here appear to indicate that a fivefold refinement of the solid grid relative to the flow grid should be sufficient to ensure acceptable accuracy, as a tenfold refinement does not significantly change the solution, at least for the simple geometry tested here. Additional testing in a variety of situations is required to verify this assertion.

6.4. EBFF FOAM SLAB EXPERIMENTS AND MODELLING

6.4.1. Experiments

A series of experiments was performed at the Experimental Building-Fire Facility to provide data on the burning of a polyurethane slab in a full-scale enclosure for comparison with the CESARE-CFD flame spread model. The primary aim of the experiment was to provide mass loss and visual flame data, including diameter and height, for combustion and flame spread over a slab of solid fuel, in a situation where heat feedback from the surroundings to the fuel surface was likely to be significant. It was therefore important to make a measurement of heat flux in the vicinity of the burning fuel, to complement the mass loss and flame spread data. As the experimental data is to be used for comparison with CFD model predictions, then acquisition of temperature, species concentration, and velocity data was likewise desirable.

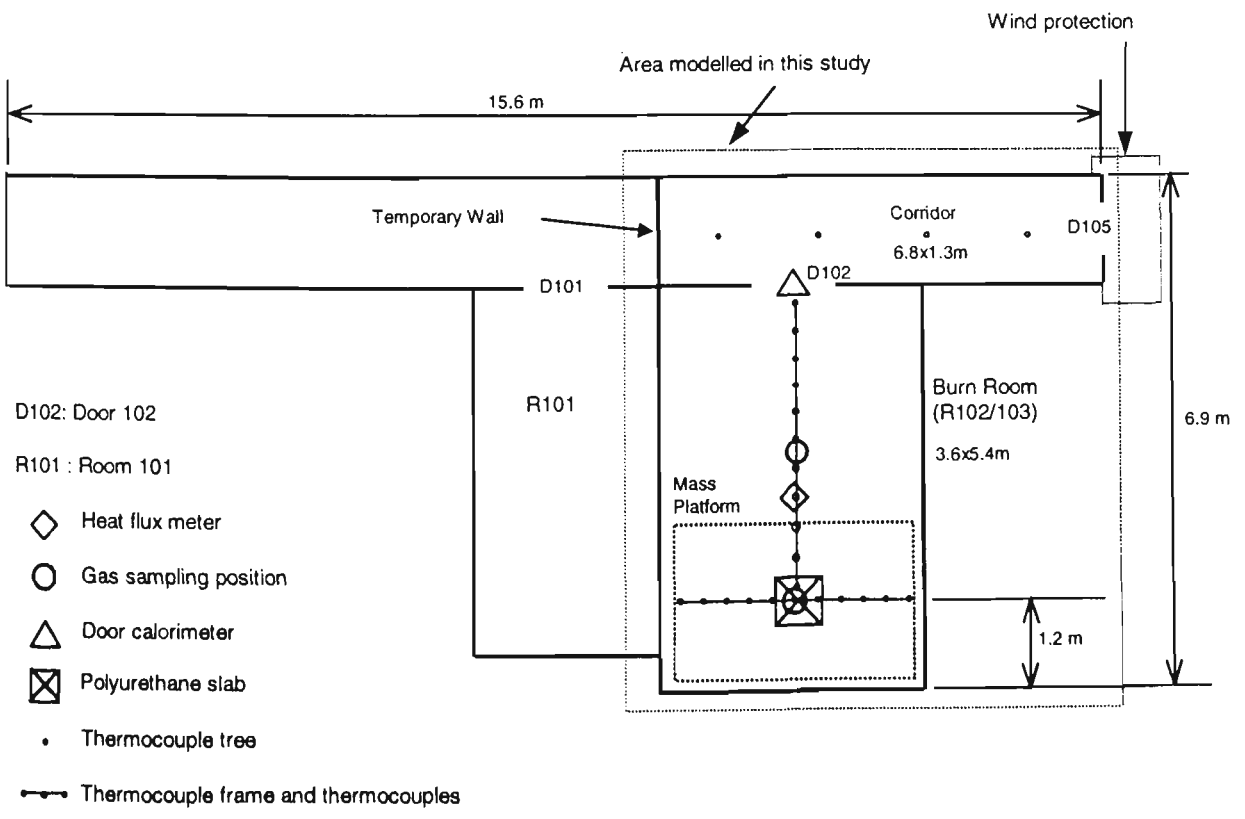

Figure 6.10 The portion of the Experimental Building-Fire Facility used in this study

The experiments took place on the ground floor only, in the section shown in Figure 6.10. The layout of the facility was altered from that used during the steady state experiments as described in Section 3.7, and was initially used for a series of sponsored experiments that were not related to this thesis. The wall between Rooms 102 and 103 was removed, creating a larger enclosure, with a window installed at the end of the room opposite the doorway. The doorway itself opened directly into the corridor, which was reduced in size due to the inclusion of a temporary wall. The floor of this enclosure comprises two mass loss platforms, only one of which was used in this series of experiments. The mass platform itself comprises a steel frame covered by a layer of 5mm compressed cement sheet, mounted on 3 XTRAN S1W load cells. The mass platform was capable of measuring a load of up to 75kg, with a measurement resolution of 15g.

With this new experimental configuration, a series of experiments was performed on standard cushion-sized slabs of polyurethane foam, measuring 560×560×100mm. The slabs were conditioned at 25°C, then wrapped in a layer of aluminium foil, with its shiny side facing inside, leaving the upper surface of the foam slab exposed, and placed horizontally in a specially constructed sample holder. The holder consisted of five pieces of fire-rated plasterboard, one bottom and four sides, sealed at the joints, and assembled so that the foam slab fitted snugly inside, flush with the top of the holder. This configuration was specified by the author, as the best approximation of the conditions assumed by the flame spread model; namely, no heat conduction at the sides and bottom of the fuel slab, and combustion occurring only at the upper surface. A grid was marked on the top surface of the foam slab, for visual measurement of flame size from video recordings. Ignition of the foam sample was achieved by the ignition of a small solid fuel tablet placed in the centre of the foam slab. Commencement of the experiment and data acquisition coincided with the ignition of the solid fuel tablet. Due to the rapid combustion characteristic of standard polyurethane foam, the duration of the burning of the cushion was five minutes. Data from the tests were recorded for an additional two minutes after burnout, or seven minutes in all. The standard polyurethane test was performed three times, while the fire retarded foam was tested only once. The three standard polyurethane foam tests are hereafter referred to as Tests 011A, 011B and 011C*. As will be seen in Section 6.5, the three experiments showed excellent repeatability. It was obvious from the single test of the retarded foam that its lack of combustibility would render any repetitions pointless. In this single test, the burning fuel tablet use to initiate the flame helped to burn a pit in the foam about 60mm in diameter at the point of ignition. Once the fuel tablet was consumed, a few feeble flames persisted for a short while without spreading any further, before eventually extinguishing.

* A convention in use at the EBFF.

A total of 86 MIMS thermocouples were used in this series of tests, along with two gas sampling tubes and a single heat flux meter. In addition, a "door calorimeter"[113] comprising 8 MIMS thermocouples, 8 gas sampling tubes and 8 velocity probes was located in the doorway. The door calorimeter has been used in previous work[113] to measure the heat release rate in the room of fire origin by using a principal of oxygen consumption similar to that used for the cone calorimeter and furniture calorimeter, described in earlier chapters. It has the advantage over methods which involve a collection hood to extract combustion products in that it has a minimal impact on the flow of combustion products beyond the enclosure of fire origin. The measuring devices are arranged with one velocity probe, one thermocouple, and one gas sampling tube at each of the eight heights 0.25, 0.5, 0.75, 1.0, 1.25, 1.5, 1.75 and 2.0m above the floor, for a doorway a little over 2m high. Unfortunately, two adjacent velocity probes in the upper level of the door calorimeter were malfunctioning in this series of tests, making estimation of rate of heat release from the data not feasible. It may have been possible to interpolate velocities if the malfunctioning probes were non-adjacent, but as they were, the gap to be interpolated is 0.75m, which is over one third of the door height.

The thermocouples were arranged in two-dimensional racks in the burnroom, and on vertical "trees" in the corridor, at the locations shown in Figure 6.10. Thermocouples were located at heights of 0.25, 0.65, 1.05, 1.25, 1.7, and 2.2m above floor level. Thermocouples in the corridor were at 0.5, 1.0, 1.5, and 2.0m above the floor. A heat flux meter was placed at floor level, facing upwards, near the edge of the mass loss platform, on the centreline of the burnroom. Two gas sampling tubes were located in the burnroom All measuring devices were fixed in location for the duration of the experiments.

All measurement devices were sampled at a rate of 1 Hz, and the voltage data recorded in binary form with a data logger set up on a 486 DX-4/100 PC. The voltage data were then converted to the appropriate physical quantities, and averaged over 25 points before analysis to filter out experimental noise.

Technical staff responsible for the operation of the EBFF undertook the experiments, with the assistance of the author. The author was responsible for the specification of the location the fuel samples, the heat flux meter, and video cameras for acquisition of visual data, and requested the installation of the temporary wall. The latter was introduced to create an enclosure with relatively simple geometry, which is better suited to accurate modelling. Preparation of the fuel samples was also undertaken by the author.

6.4.2. Modelling

The portion of the Experimental Building-Fire Facility shown in Figure 6.10 was the subject of a numerical modelling exercise undertaken with the flame spread model incorporated into the field model CESARE-CFD. The enclosure is modelled in the flow region with a 40×54×25 adaptive grid, which includes a refined region of 14×14 grid cells adjacent to the fuel slab. As the fuel slab measures 560×560 mm, this corresponds to a 40mm grid in the fine region. There are two refined regions in the vertical direction; adjacent to the upper surface of the fuel, and at the midplane of the enclosure, where it is anticipated the interface between the hot and cold interfaces will occur. The flow grid is shown in Figure 6.11.

The flame spread model discretises the fuel with a 5mm grid size, resulting in a 112×112 grid, and with 8 divisions in the fuel depth. Before surface regression, these divisions measured respectively from the surface downwards, 1mm, 2mm, 4mm, 8mm, 12mm, 18mm, 25mm, 30mm; the sum of which is the 100mm depth of the fuel. The kinetic and thermal properties of the standard polyurethane foam fuel are as given in Table 5.1 in Chapter 5.

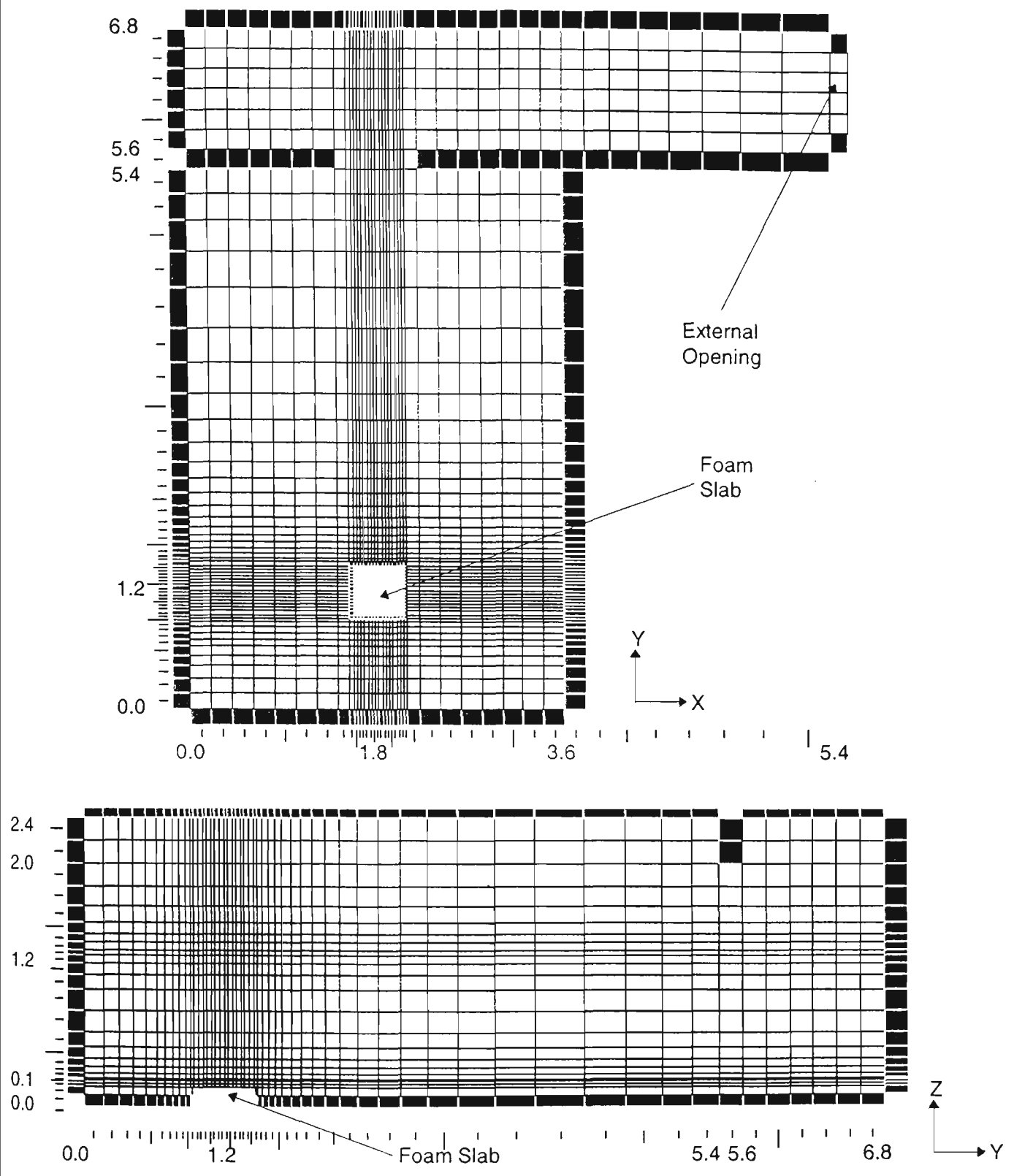

Figure 6.11 Flow grid used in this study

The steady-state initialisation of the flow region was performed in 2000 iterations, with the radiation subroutine executed once every five iterations of the flow region. The initial flame diameter was set to 0.06m. The residuals at the end of 2000 iterations were around 3×10^{-4} m/s for the velocity components, 10^{-5} for the fuel mixture fraction, 2×10^{-5} m^2/s^2 for the turbulence kinetic

energy, and 2×10^{-2} kJ/kg for enthalpy. These values were deemed to indicate sufficient convergence, in accordance with the discussions presented in Section 3.9.3.

After initialisation, the unsteady-state fire was modelled for 360 seconds simulation time, using a time step of 0.1s, a total of 3600 iterations. This was to ensure that the model included the burnout time, which occurred at around 300 seconds in the EBFF tests, and around 360 seconds in the furniture calorimeter tests presented in Chapter 5. The residuals remained at their low value at the beginning of the simulation, with little adjustment in the transition from steady-state to unsteady-state, probably due to the mass loss rate changing very little in the early stages. The residuals for fuel mixture fraction in particular then decreased quite rapidly, while the other residuals slowly decreased. After about 900 iterations (90 seconds in the simulation), the increasing mass loss rate and subsequent heat release rate began to exert an influence, and the residuals began to increase, peaking around the peak in heat release. The residuals at this stage were around 5×10^{-4} m/s for horizontal velocity components 2×10^{-3} m/s for the vertical velocity component, 10^{-5} for the fuel mixture fraction, and 0.3 kJ/kg for the enthalpy. After the peak heat release rate, the residuals again decreased to levels comparable to the beginning of the simulation. Overall, the residuals did not at any stage increase to a level that would suggest divergence of the solution.

6.5. COMPARISON OF EXPERIMENTAL AND MODELLED RESULTS

Of greatest interest in this research are the results for the flame spread across, and rate of mass loss of the solid fuel item undergoing combustion; accordingly these will be examined first. The effective diameter of the flame is shown in Figure 6.12. As mentioned previously, the effective diameter is calculated for a circle whose area is the same as the total area of the ignited cells, in the case of the flame spread model. In the experiment, the diameter was measured directly until the spreading circular front reached the edges of the square fuel slab (diameter 0.56m), after which the diameter was estimated, up to the equivalent diameter of 0.63m for a 0.56x0.56m square. In contrast to the tests performed in the furniture calorimeter at CSIRO, the measured flame spread was highly symmetrical about the point of ignition, suggesting that there was little influence of induced flow in the enclosure, at least until the flame had finished spreading and the fire had become well developed.

As can be seen from Figure 6.12, the predicted effective flame diameter failed to reach maximum possible diameter, nor was it predicted that the mass was totally consumed, as shown in Figure 6.13. Nevertheless, there is good agreement in the overall trends, which suggests that the

model is itself theoretically sound. The model shows the accelerating flame spread, and the timing of the peak mass loss rate corresponds well with the experimentally observed peak in the initial stages of the fire, as shown in Figure 6.14. It is the peak phase and the decay phase of the fire where the modelling results are in disagreement with experimental results. The model fails to predict the sharp peak at 180 seconds, instead predicting a lower, earlier peak with a more gradual decay.

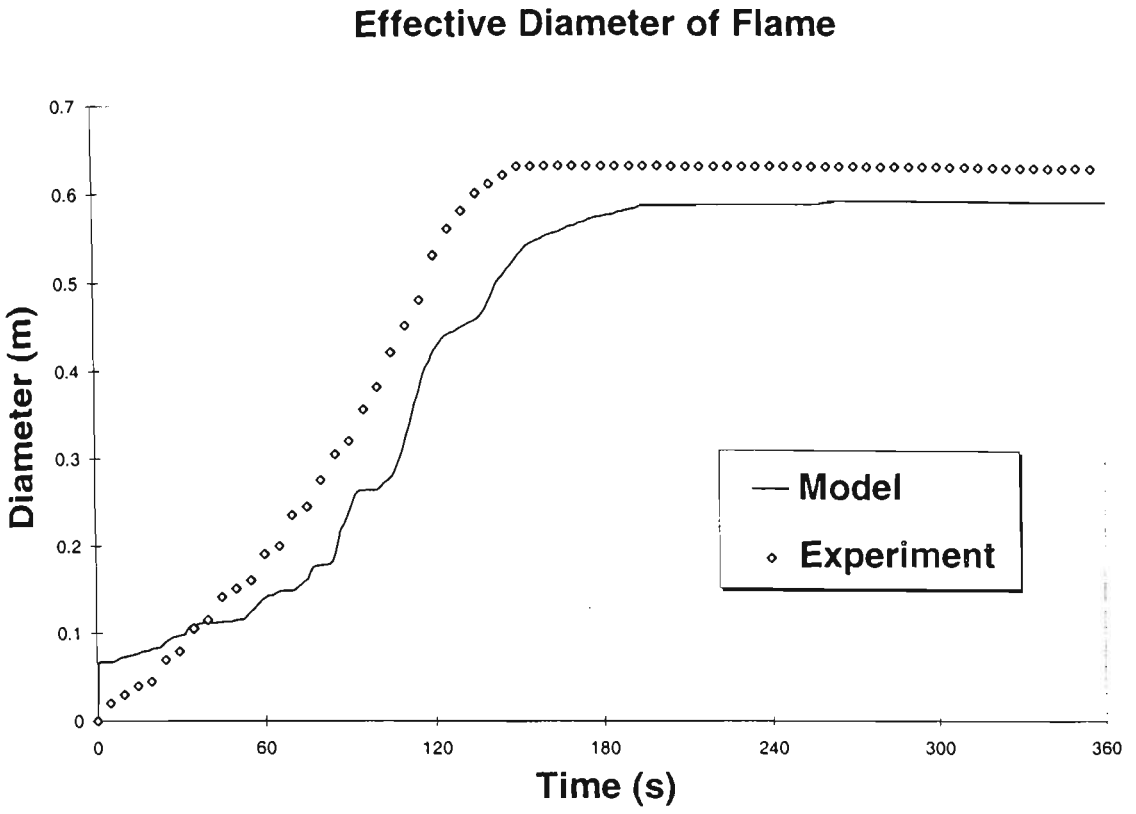

Figure 6.12 Effective diameter of flame

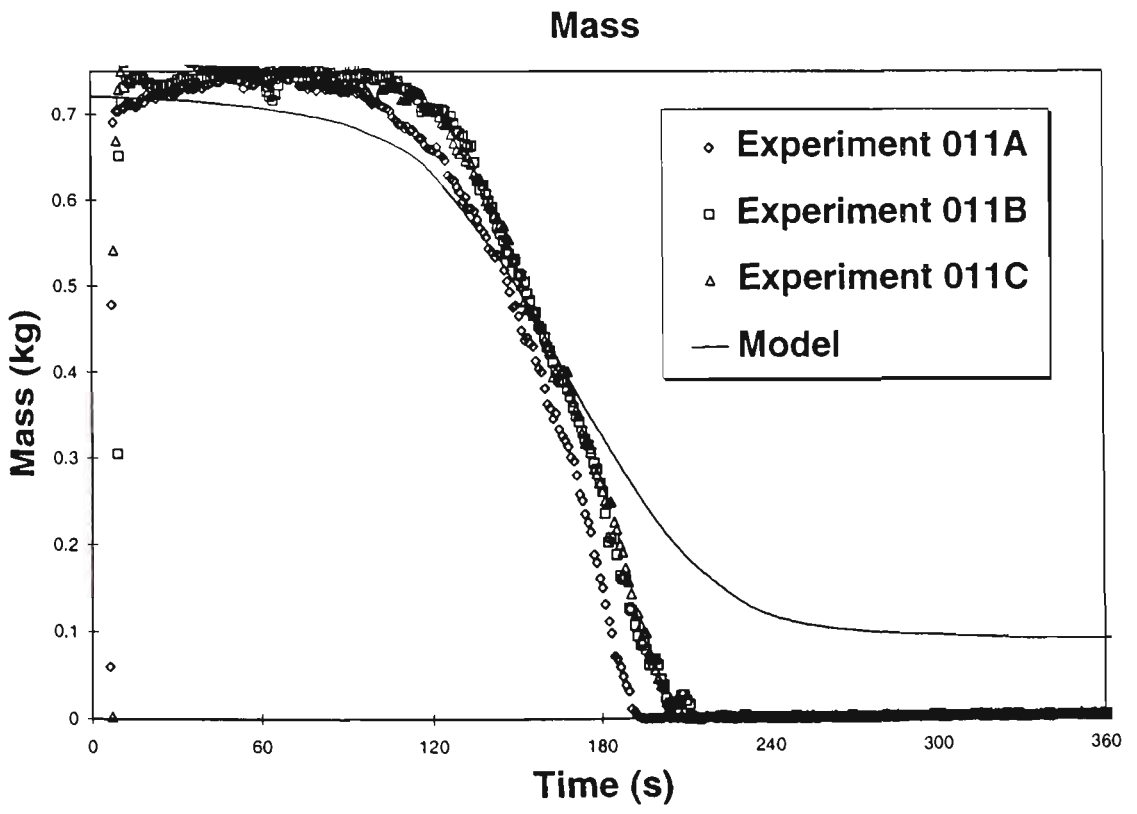

Figure 6.13 Total mass of fuel slab

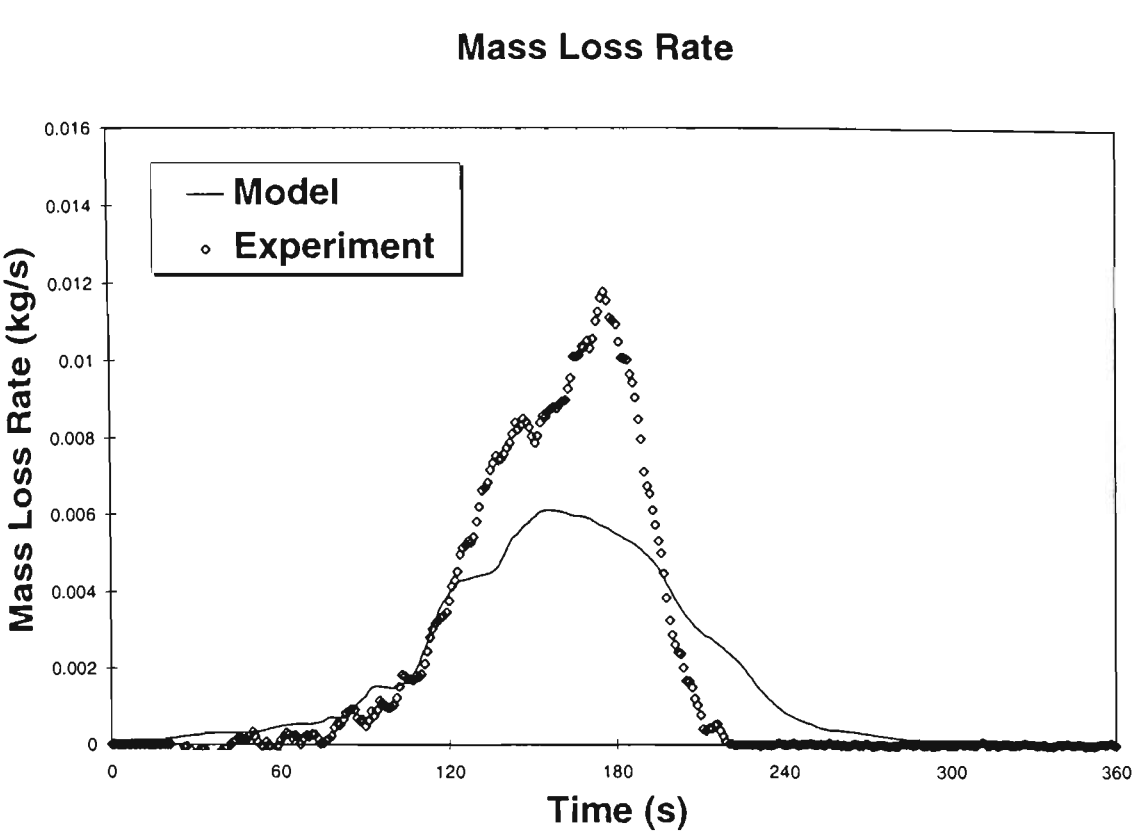

Figure 6.14 Mass loss rate of fuel

To understand the reasons for the discrepancy, it is necessary to examine the spreading flame in greater detail. In the model, as each ignition occurred, the grid reference of the ignited cell and the time of ignition was recorded, and likewise for the burnout of each cell. These are shown in Figure 6.15 and Figure 6.16. In these figures, early ignition and early burnout are shown in "warm" colours, while late ignition and late burnout are shown in "cool" colours. The light grey region in Figure 6.15 corresponds to cells which have not undergone ignition. Naturally, this region also appears in Figure 6.16, as cells which do not ignite cannot burnout. Examining the modelled ignition history reveals much information about how the model predicted the spreading flame.

Examining Figure 6.15, the initial burning region is clearly evident as the circular region at the centre of the fuel. The flame then spread towards the east (right in the figure), then radially in a relatively uniform fashion up until around 90 seconds. Between 90 and 120 seconds, the flame spread rapidly towards the south (downwards in the figure) and east, so rapidly in fact that a portion of the fuel failed to ignite before it was exposed to the cooler inner core of the flame. By this stage the fuel was beginning to burn out in the centre, as seen in Figure 6.16. Between 120 and 150 seconds, the flame spread rapidly in the westerly direction, while making little progress northwards, leaving a large portion of the northern edge of the fuel unignited. In the experiments, the flame had spread across the entire surface by this stage, with no apparent sign of central burnout, although

burnout was difficult to confirm visually until the flame had substantially died down. In the mass loss rate history shown in Figure 6.14, this is also the point where the predicted mass loss rate becomes noticeably less than the measured mass loss rate. In the time period between 150 and 180 seconds, the predicted flame makes some inroads north, but the increased burnout is reducing the heat output, and the mass loss rate is falling, whereas in the experiment it is continuing to increase rapidly to its peak value. After 180 seconds, the modelled flame continues to creep northwards, while burnout causes the flame to contract to the border of the unburnt northern portion of the fuel. This unburnt region continues to be a source of new ignitions and mass loss beyond 270 seconds of the simulation. In the experiment, however, the fuel has been almost totally consumed by 240 seconds, with only a few patches of burning tar in each corner of the holder. It appears, therefore, that the discrepancies in the mass loss rate and flame diameter curves can be largely attributed to the failure of the model to predict flame spread to the northern portion of the fuel between 120 and 150 seconds.

The unburnt region of the fuel in the simulation is defined by an almost straight line across the northern (top) portion of the fuel. This is the edge of the fuel which faces the doorway of the burn room, which provides a clue as to the nature of the feature. It is also no coincidence that this straight line, which corresponds to the coordinate j = 98, coincides with one of the cell boundaries of the CFD grid. In fact, closer examination of Figure 6.15 and Figure 6.16 reveals evidence of several such straight lines (the region near i,j=(30,70), for example), a phenomenon which was described in Section 6.2.2 and led to the inclusion of linear interpolation of flow variables in the flame spread model. The results here show that despite linear interpolation, there is still an "imprint" of the CFD grid on the flame spread grid. The northern portion of the fuel is the most dramatic example. It is likely that there is an important quantity which is uniform over the single row of CFD cells along the northern edge of the fuel, and which differs greatly from the uniform value over the next row of cells to the south. This discontinuity persists on the finer flame spread grid despite smoothing out by linear interpolation.

What appears to be causing this phenomenon is the establishment of a strong airflow pattern as combustion proceeds. The rising plume becomes increasingly pronounced, producing a ceiling jet which flows out of the upper half of the burn room opening, and in turn causing an increased flow of cool air through the lower half of the doorway. This flow continues unimpeded across the floor of the enclosure, until it encounters the fuel slab. It is then diverted upwards at the lip of the fuel, before being drawn across the surface of the fuel and into the rising plume. It is this diversion over the lip of the fuel which appears to be producing a current strong enough to oppose the spread of flame. More specifically, the heat transfer away from the surface of the cool air, as described by

Equation 6.5, is obviously sufficient to counteract the radiant heat flux to the surface (which at such proximity to the flame is surely quite substantial) and keep the surface temperature below even piloted ignition temperature. Ignition of some of the cells does eventually occur late in the simulation, when other regions have burnt out, flow velocities have decreased, and the small remaining flame is centred at the edge of the unburnt region. To illustrate the flow phenomenon, the modelled flow distribution at peak burning rate, 180 seconds after ignition, and the histories of some key locations are shown in Figure 6.17 and Figure 6.18 respectively. The region illustrated in Figure 6.17 is a section along the centreline of the burnroom, passing through the centre of the fuel slab and the doorway.

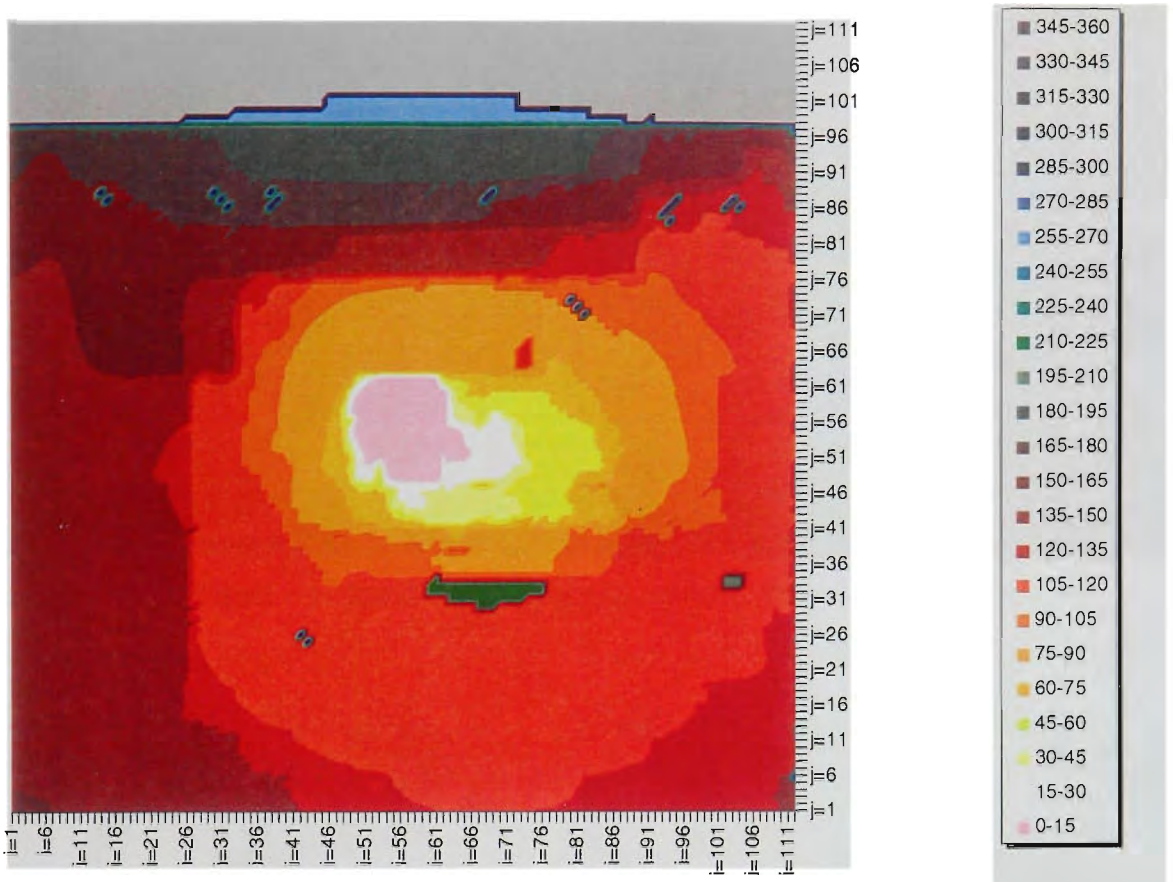

Figure 6.15 Time of ignition of cells (s)

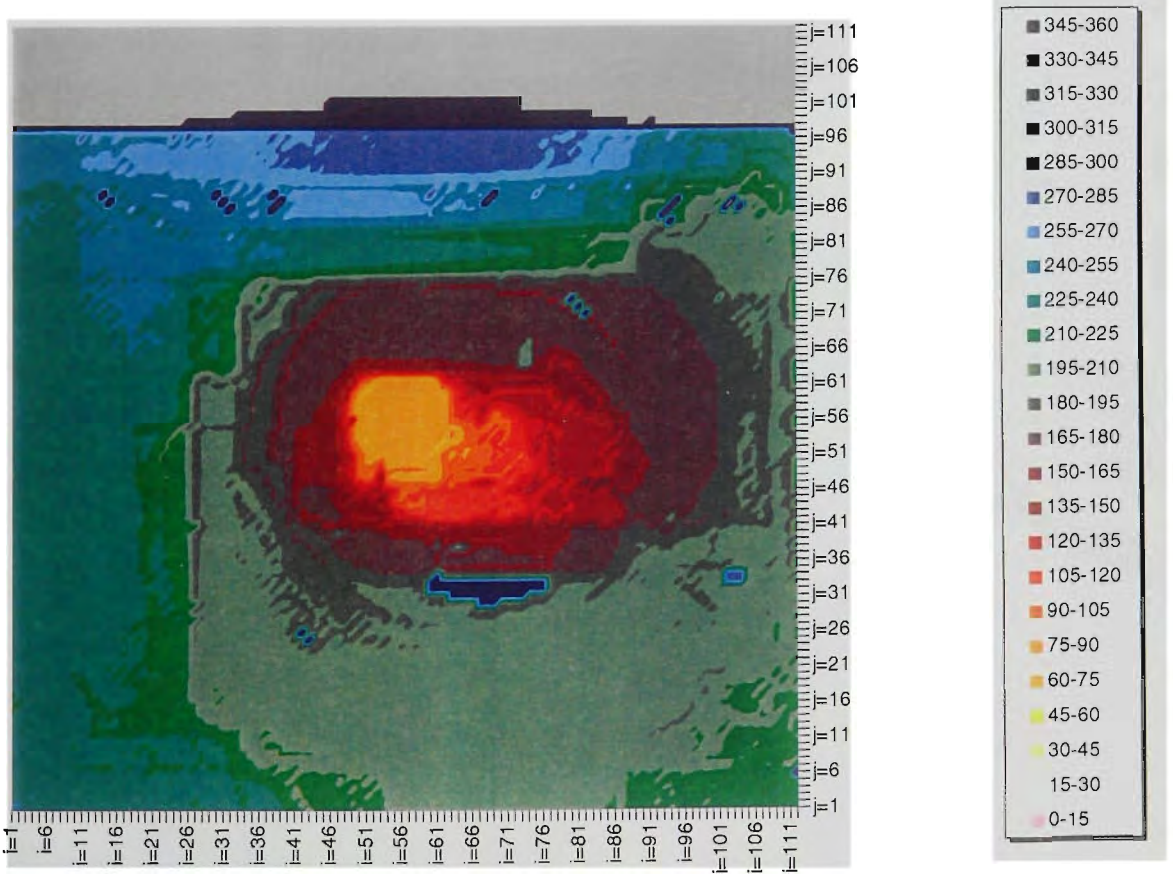

Figure 6.16 Time of burnout of cells (s)

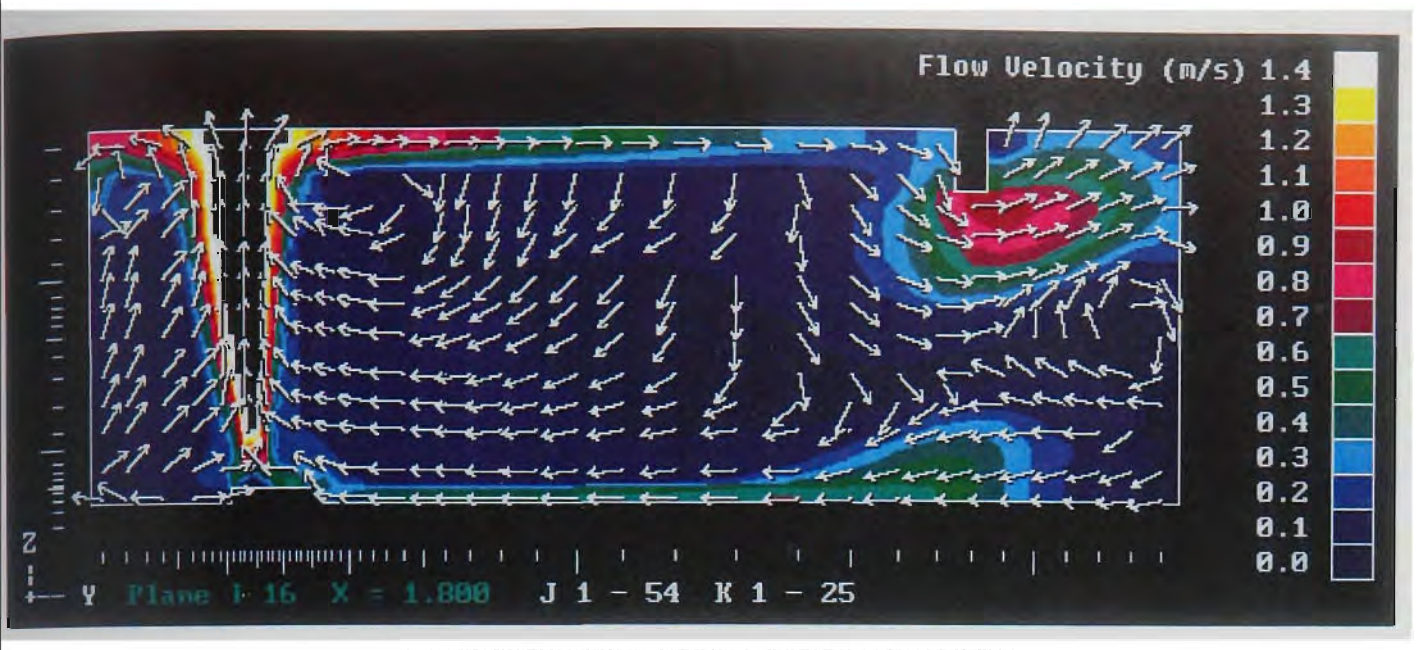

Figure 6.17 Velocity profile at peak burning (180s)

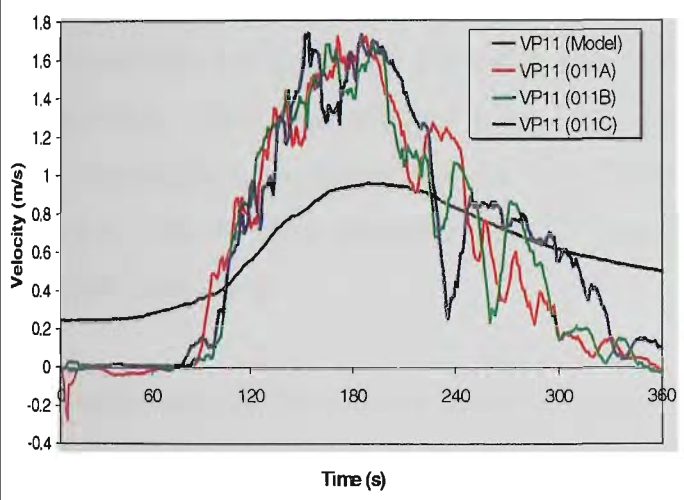

(a) Flow velocity out of doorway at 2.0m

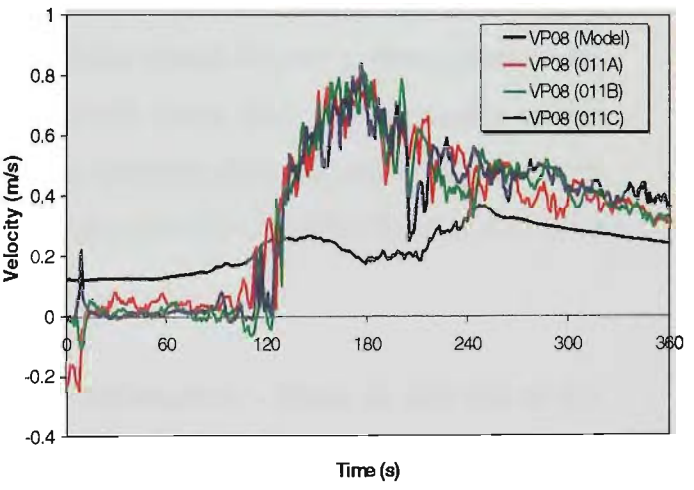

(b) Flow velocity out of door at 1.25m

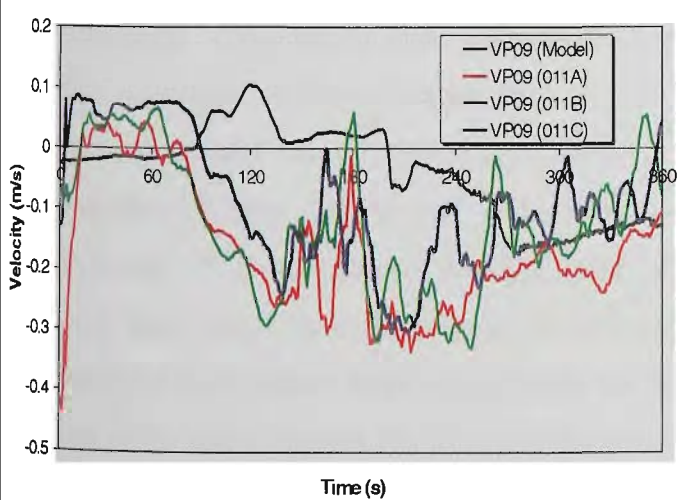

(c) Flow velocity out of doorway at 1.0m

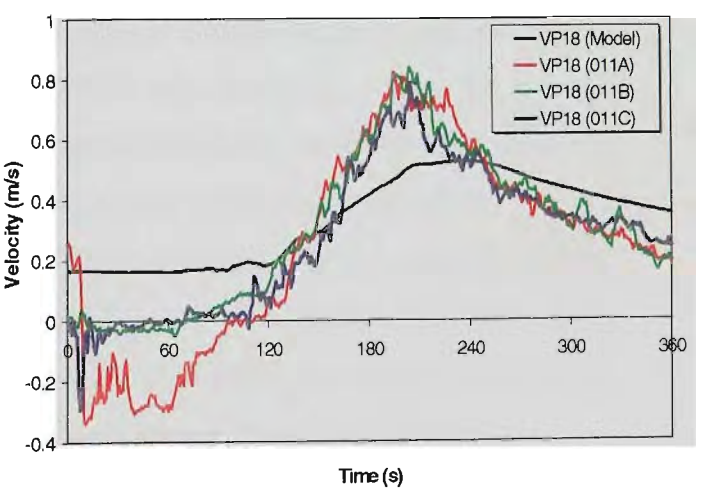

(d) Flow velocity into doorway at 0.25m

Figure 6.18 Velocity histories at four key locations

There are several phenomena of interest in Figure 6.17 and Figure 6.18. In the velocity profile, the magnitude of the velocity of the inflowing air is as high as 0.7 m/s close to the doorway, and 0.6 m/s over the lip of the fuel slab. Entrainment into the plume is greater on the door side of the plume than on the opposite wall side, causing the flame to lean towards the wall. This phenomenon was also observed visually in the EBFF experiments, although no quantitative measurements were made of velocity close to the fuel. A velocity of 0.6 m/s is a significant opposing flow, although it is reasonable to suppose such magnitudes may also have occurred in the experiment, at least at peak burning. A key factor in the experiment is that the flame had reached the edge of the fuel before 120 seconds of the test had elapsed, at which time the magnitudes of velocity were lower. In fact, the times for the circular flame front to reach each of the four edges all occurred within the 120-125 second time interval, which demonstrates that any entrainment and flow patterns created by the fire plume did not show any preferential direction up to this time. This conclusion stems from the furniture calorimeter results presented in Section 5.6. No flow velocities greater than 0.4m/s were measured in the vicinity of the fuel in this case, yet the flame spread showed a strong preferential direction. This suggests that a flow velocity of 0.6m will cause flame to noticeably spread preferentially in the direction of the flow. Thus, for flame spread to show no preferential direction up to 120s, the flow velocities were likely to be quite low; certainly less than 0.4m/s, and quite likely even lower.

Examination of the velocity histories reveals additional information. Flows in and out of the doorway were negligible in the first 90 seconds of the experiments*, and then began to increase noticeably, particularly after 120 seconds. In contrast, there is a significant flow in the simulation from the initial stages. This flow pattern is created by the steady state initialisation of the simulation. Consider the flow velocity into the room at height of 2.0m as shown in Figure 6.18(a). The magnitude of the simulated flow is approximately 0.25 m/s, increasing to 1.0 m/s at peak burning. Similar magnitude comparisons are shown in Figure 6.18(d) for the flow into the room at a height of 0.25m. This indicates that the initial flow rate is quite significant compared to the peak flow rate. This is a concern, considering the small heat output of the initial fire compared with the peak heat output, and is an issue which should be addressed in future model revisions. This predicted flow pattern helps explain why the flame spread in the simulation is toward the southern end of the slab (Figure 6.15), as this is the prevailing flow direction early in the simulation.

* apart from the first 10 seconds. The slab was ignited manually, and the "ignitor" (the author) exited the burn room by a window at the southern end of the room (which was closed after egress), as the doorway at the northern end was obstructed by gas sampling tubes and velocity probes. A through-flow was created by the open window and the external door at the end of the corridor, which persisted for the 5-10 seconds the ignitor was in the burn room.

The high velocity profile appears to caused by divergence of the balance port, a phenomenon which was discussed in Section 2.4.6.3. The maximum velocity was set at 2 m/s in both the initialisation and the unsteady simulation. As divergence causes the maximum velocity to be attained somewhere at the balance port during initialisation (in this case at floor level), then this is almost certainly the cause of the excessive velocity.

Some attempt has been made to redress these discrepancies, but it has been found that this is by no means a trivial exercise. The fundamental issue may be that the simulation and experimental results do not agree because the simulation was started as a steady-state solution. Hence, it is left as future work, and is discussed further in Section 6.7.

Histories of other variables are shown in the following figures. Selected temperature histories are shown in Figure 6.19 and Figure 6.20, while the concentrations of O_2 and CO_2 at selected locations are shown in Figure 6.21. Radiation heat flux to floor level is shown in Figure 6.22(a), alongside rate of mass loss (Figure 6.22(b), from Figure 6.14) to highlight the similarity in the profiles of the plots. Some similarity is expected, as the heat flux to the floor is dependent on the heat release rate, and the heat release rate is itself dependent on the mass loss rate.

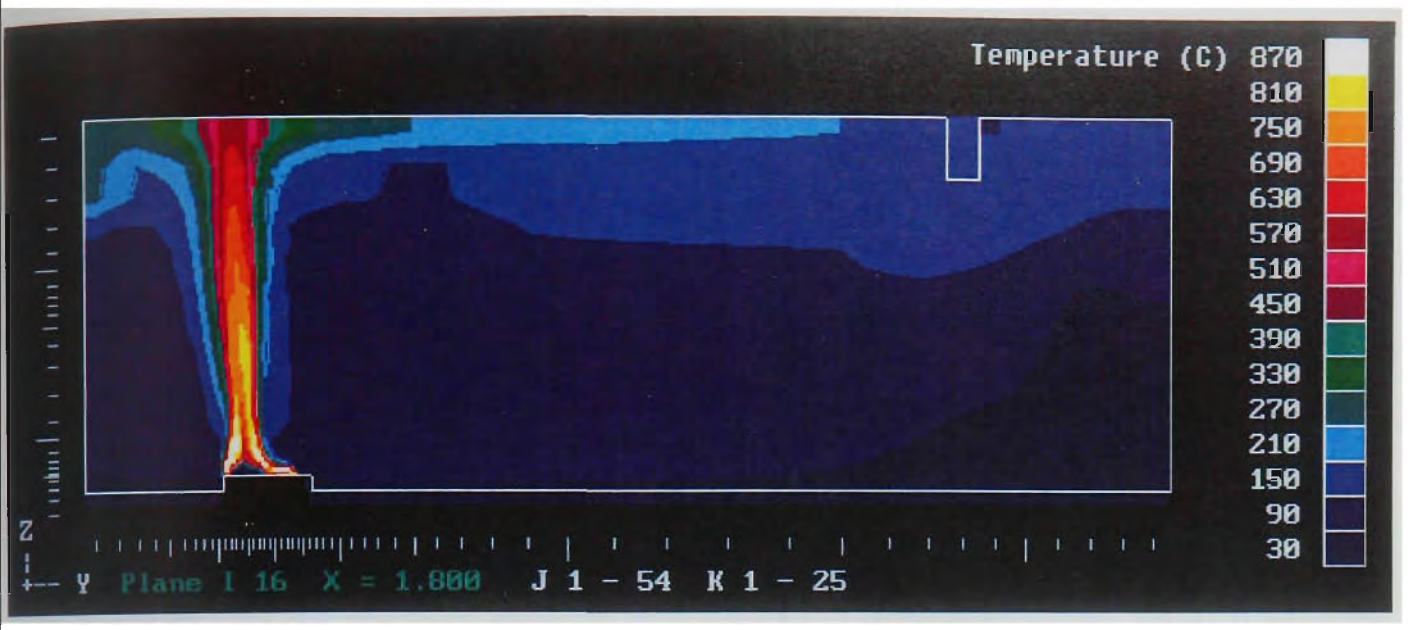

Figure 6.19 Predicted temperature profile at peak burning (180s)

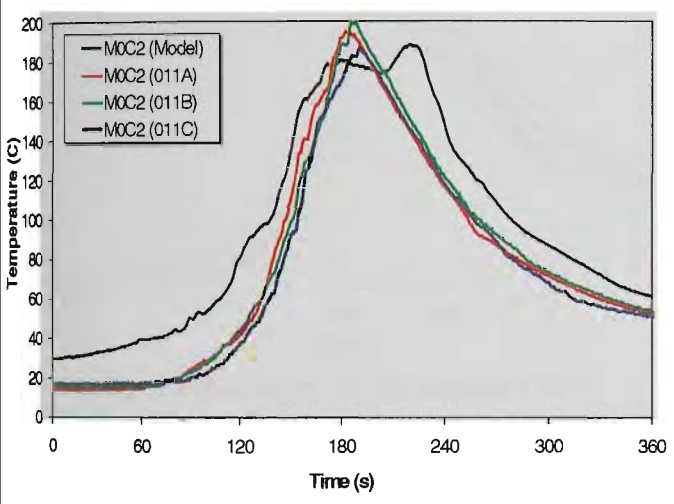

(a) Temperature above fuel slab at height 2.4m

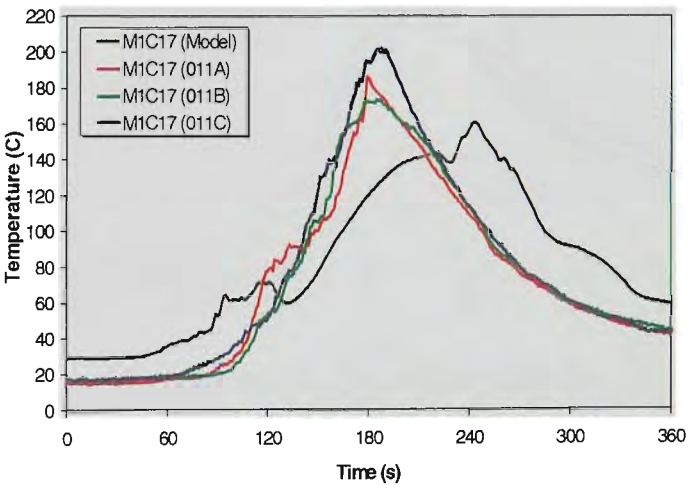

(b) Temperature above fuel slab front at height 1.9m

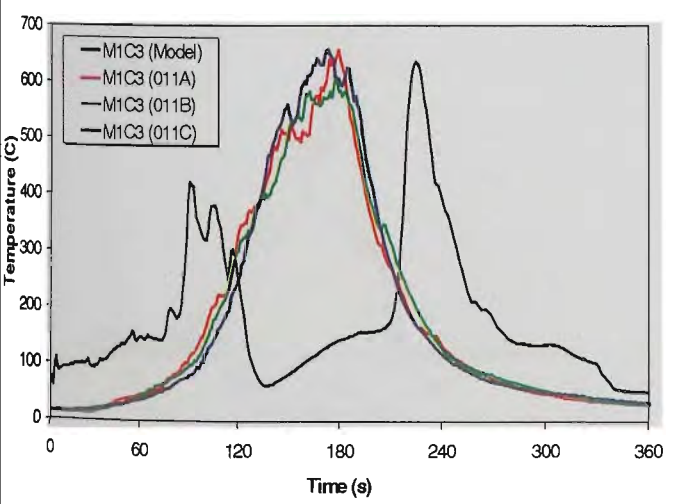

(c) Temperature above fuel slab at height 0.85m

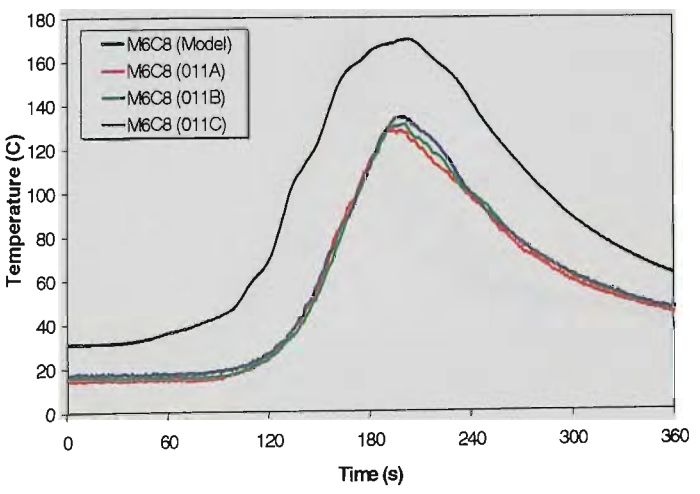

(d) Temperature in doorway at 2.0m

Figure 6.20 Temperature histories of four key locations

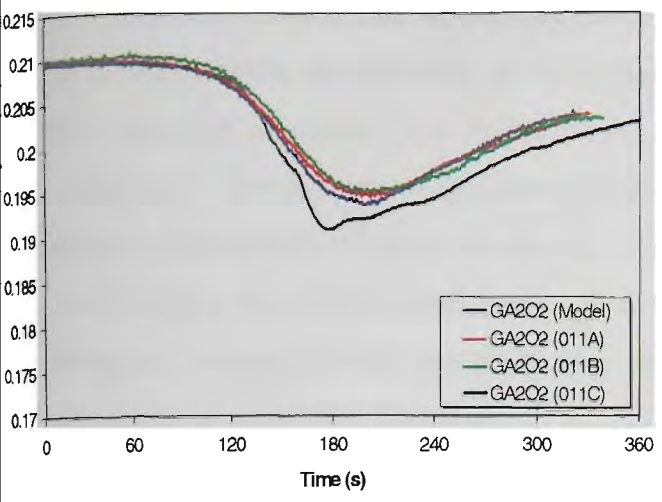

(a) O2 concentration in centre of room at height 1.9m

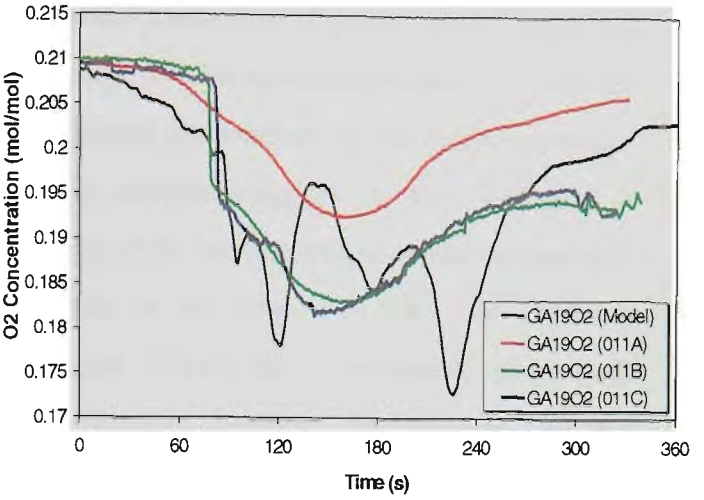

(b) O2 concentration above fuel slab at height 1.9m

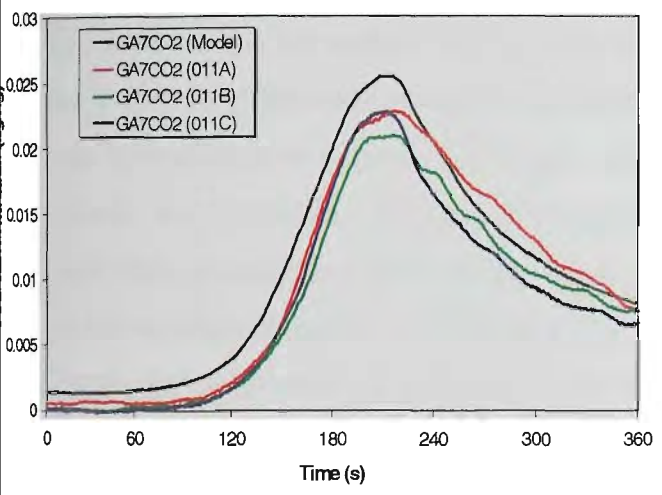

(c) CO2 concentration in doorway at height 1.75m

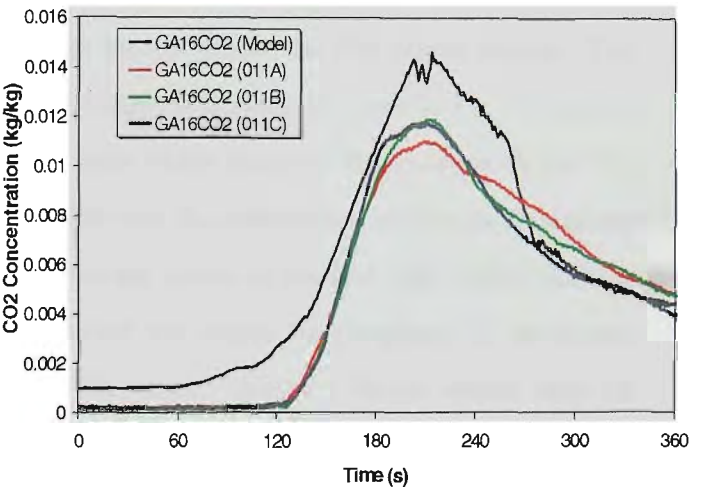

(d) CO2 concentration in doorway at height 1.0m

Figure 6.21 Species concentration at selected locations

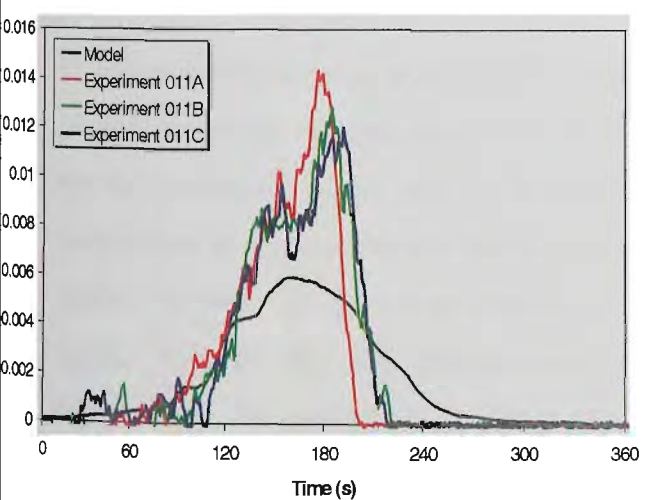

(a) Mass Loss Rate

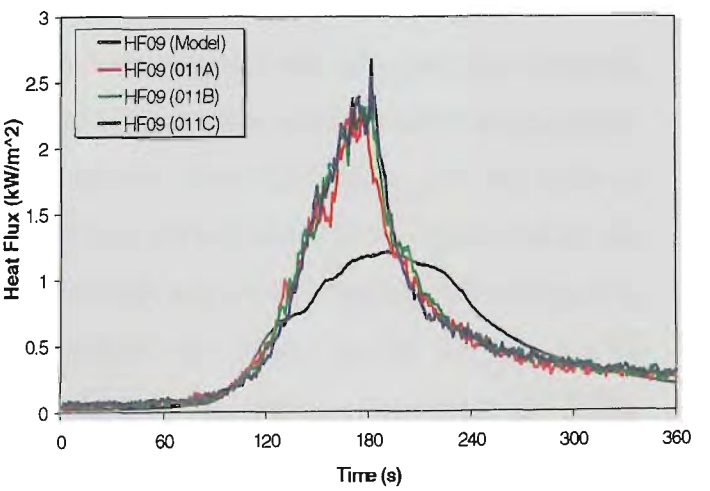

(b) Heat flux to floor centre

Figure 6.22 Mass loss and radiation heat flux histories

The simulated temperatures were recorded continuously for a selection of points, mostly clustered in the region above the fuel slab, or in the doorway as part of door calorimeter data. As with the flow velocities, the steady state initialisation created elevated temperatures at the beginning of the simulation. Overall, the temperatures were generally overpredicted, as is most apparent in Figure 6.20(d), which shows good agreement in the timing of the temperature peak, but consistently overestimates the temperature itself. Considering that in the simulation, the fuel was not completely consumed and the peak heat release lagged behind the experimental peak, such agreement is somewhat fortuitous. The temperature histories displayed by Figure 6.20(a) and Figure 6.20(b), are closer to what would be expected for a delayed and lower heat release peak.

Figure 6.20(c) shows least correlation with experimental data. This corresponds to a point above the centre of the fuel surface, which in the experiment is mostly within the fire plume region. The large drop in temperature at the time of maximum heat output at a point so close to the fire plume can be explained by a number of factors, although the most likely factor is the location of the fire plume. An examination of Figure 6.19 shows that at 180s into the simulation, the flame is bending noticeably towards the southern wall, and the points above the centre of the fuel slab, about halfway to the ceiling and where the point in question is monitored, are nearer the periphery of the flame, where the temperature is predicted to be lower than the core. Another factor which may be important is the cool core of the plume, which may be observed in Figure 6.19 just above the fuel surface. This is due to burnout of cells in the centre of the fuel, which no longer contribute a mass source to the flow region. However, this would only affect points close to the surface, and a return to higher temperatures, as occurs in Figure 6.20(c), would not occur for these points.

Experimental factors may also come into play. If it was to be assumed that the simulation correctly predicts the plume moving away from the thermocouples due to flow currents in the experiments, the thermocouples would still be heated by radiant transfer from the plume, and any drop in temperature as recorded by the thermocouple would be less pronounced than that predicted by the model. However, as there is no evidence of any temperature drop in the experimental results, it is highly probable that the thermocouple remained within the plume region throughout the experiments. Yet another possibility is that there is indeed a cool region in the core of the flame, although perhaps not as cool as predicted by the model, but that the temperature recorded by the thermocouple remains high because it is receiving radiation from the edge of the flame. This thermocouple heating phenomenon was observed in the cone calorimeter tests presented in Section 4.5.6.

Other data recorded in the experiments were species concentration in the doorway, and oxygen concentration within the enclosure. A sample of points is shown in Figure 6.21. Oxygen concentration shows excellent correlation between model and experiment in the centre of the enclosure, while above the fuel surface it shows quite a deal of fluctuation, again likely due to the movement of the plume throughout the simulation. Carbon dioxide concentration in the doorway likewise shows good correlation. Overall, there is a tendency for the model to over-predict both CO_2 concentration and O_2 depletion. However, like the temperatures, this is of some concern, since as the mass loss rate is underpredicted, it is expected that CO_2 concentrations should be likewise underpredicted as its source is the mass loss of the fuel. It is possible that this "extra" carbon may be produced by the steady-state initialisation of the simulation. A small fire allowed to burn for an extended period of time will build up a substantial layer of combustion products, even taking into account the high flow rates noted earlier. This would almost certainly produce a source of carbon in excess of the amount present early in the experiment.

The other quantity measured in these experiments was the radiant heat flux to the middle of the burn room floor, as shown in Figure 6.22. The heat flux is underpredicted as would be expected from the mass loss rate. Indeed, the curve for mass loss rate and radiation to the floor show very similar profiles, both for experiment and model, so much so that they appear to be directly proportional. To test this, a simple ratio of heat flux to mass loss rate is calculated and plotted, as

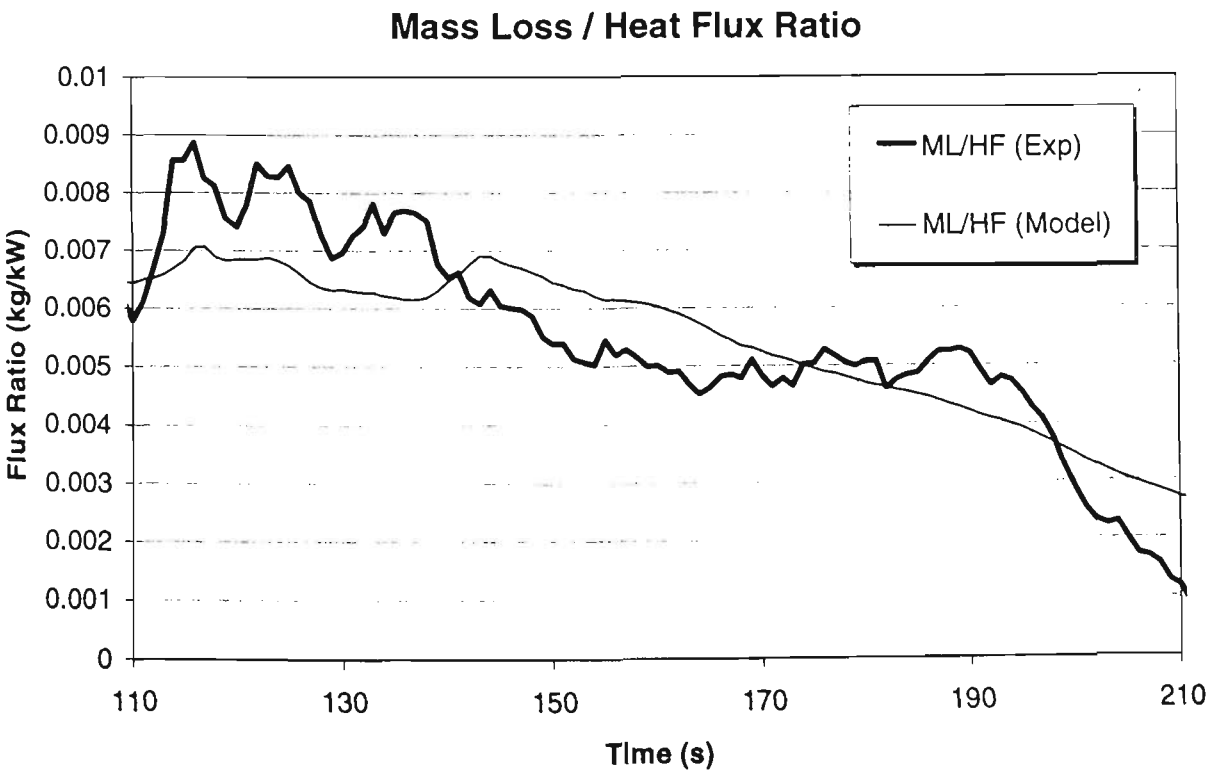

Figure 6.23 Mass loss rate to heat flux ratio

shown in Figure 6.23.

Figure 6.23 shows that for the peak combustion period between 120s and 210s, this ratio is quite steady at around 0.006 kg/kW, and that there is good agreement between model and experiment. In other words, the relatively poor prediction of radiative heat flux is a consequence of the poor prediction of mass loss rate, and hence rate of heat release of the fuel. If the mass loss rate were to have been predicted accurately, the ratio correlation suggests that the radiative heat transfer would likewise have been accurately predicted.

Many of the phenomena discussed above are apparent in the comparison of the measured and predicted data at the door calorimeter. The temperature data in Figure 6.24 shows that overall, the predicted temperatures are higher than the measured temperatures. As mentioned earlier, the timing of the temperature peaks are approximately the same for the measured and predicted temperatures. A subtle feature of note is that the measured peak temperature occurs later in the middle (around 1.0m to 1.25m) than in the top and bottom of the doorway, and that this is likewise observed in the predicted temperatures. Such a correlation is encouraging for the further development of model, because it indicates that despite the obvious discrepancies in the modelled results pointed out earlier, overall trends in fire growth in the enclosure are predicted well, and that further improvements of the model are likely to be concerned with detail rather than with fundamental overhauls.

The velocity data for the door calorimeter Figure 6.25 shows once again the elevated predicted velocities resulting from the initialisation phase of the simulation, and the reduced and delayed velocity peaks as compared to the measured peaks. A general trend which is demonstrated in both predicted and measured velocities is that peak velocity occurs earlier in the outflow region (top half of the doorway) than in the inflow region (bottom half of the doorway).

The oxygen concentration data shown in Figure 6.26 again shows the increased predicted oxygen depletion compared with the measured depletion. A feature of note in the oxygen concentration and temperature predictions is that there is a noticeable oxygen depletion and temperature increase in the lower layer. In contrast, the experiments show that the bottom layer remained nearly at ambient temperatures and oxygen concentrations for the duration of the test. It appears that the oxygen depletion and temperature are linked, so that the overprediction of the amount of fuel throughout the enclosure results in not only depleted oxygen, but elevated temperatures as well. Hence, it appears increasingly likely that many of the discrepancies reported in this section can ultimately be traced back to the initialisation of the model.

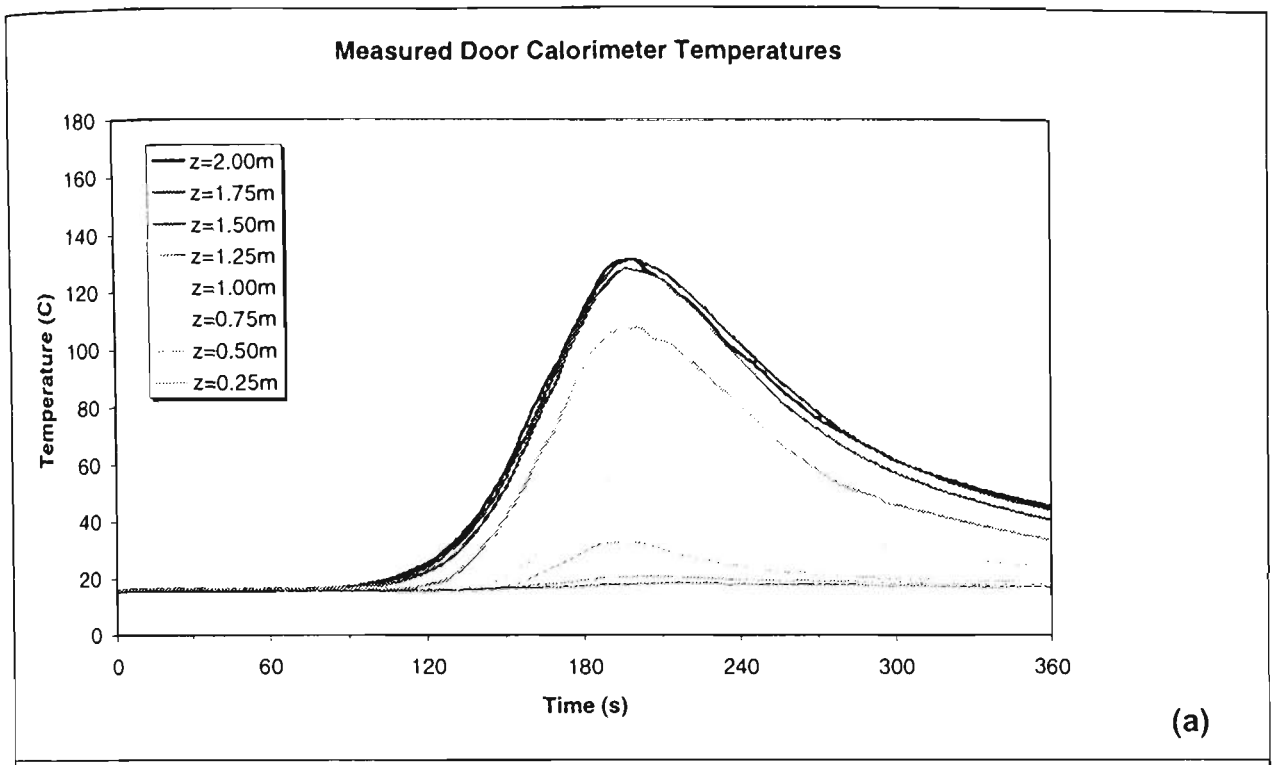

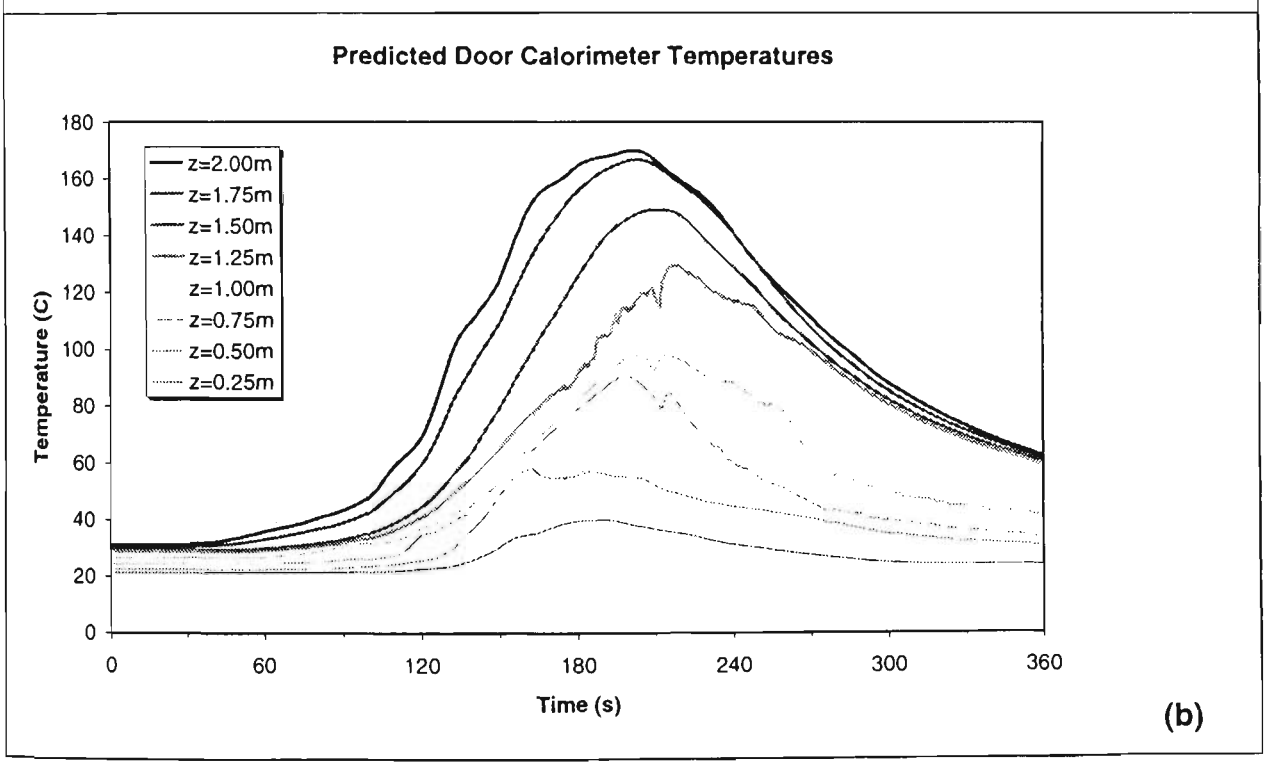

Figure 6.24 Measured (a) and predicted (b) temperatures at the door calorimeter

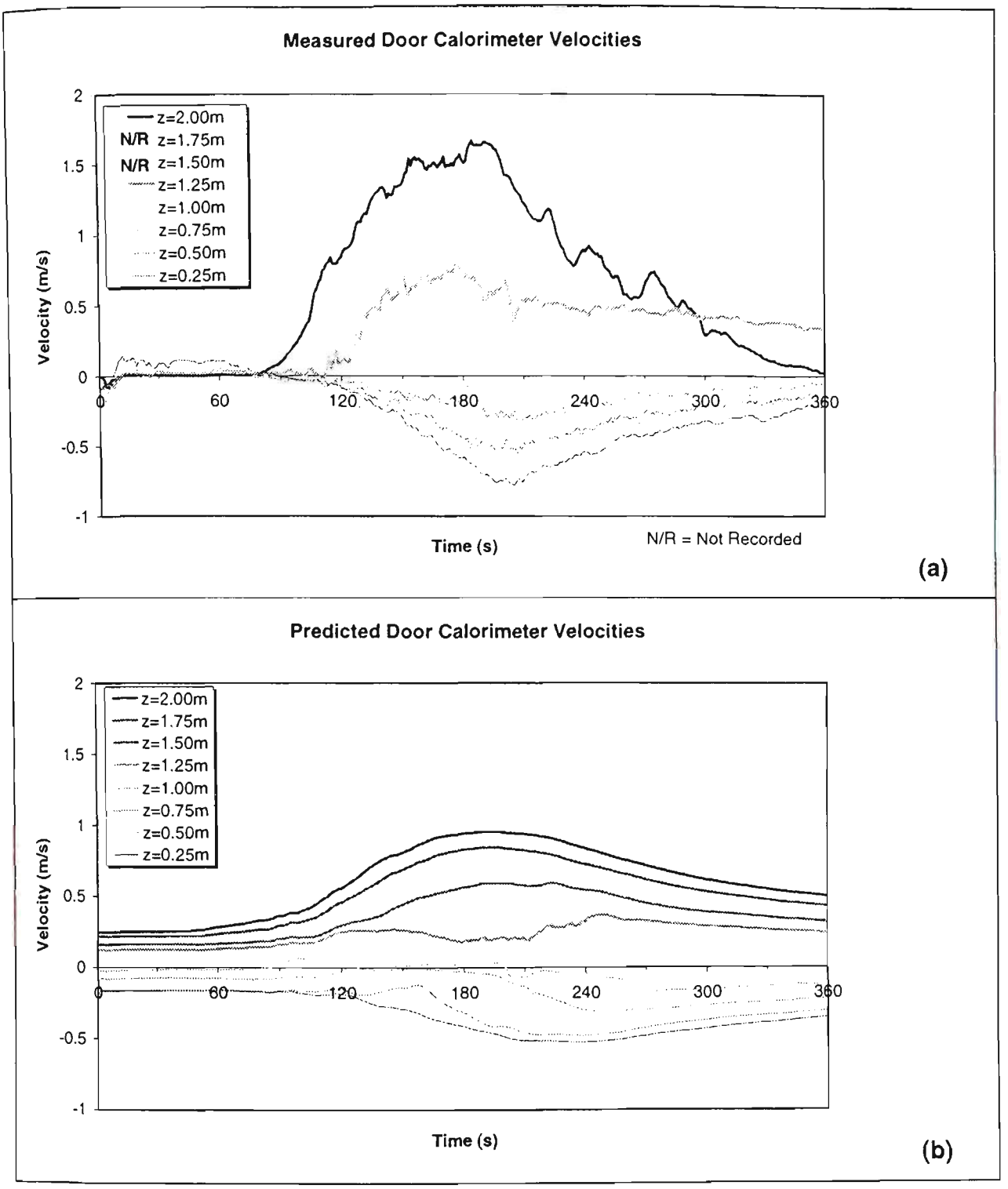

Figure 6.25 Measured (a) and predicted (b) velocities at the door calorimeter

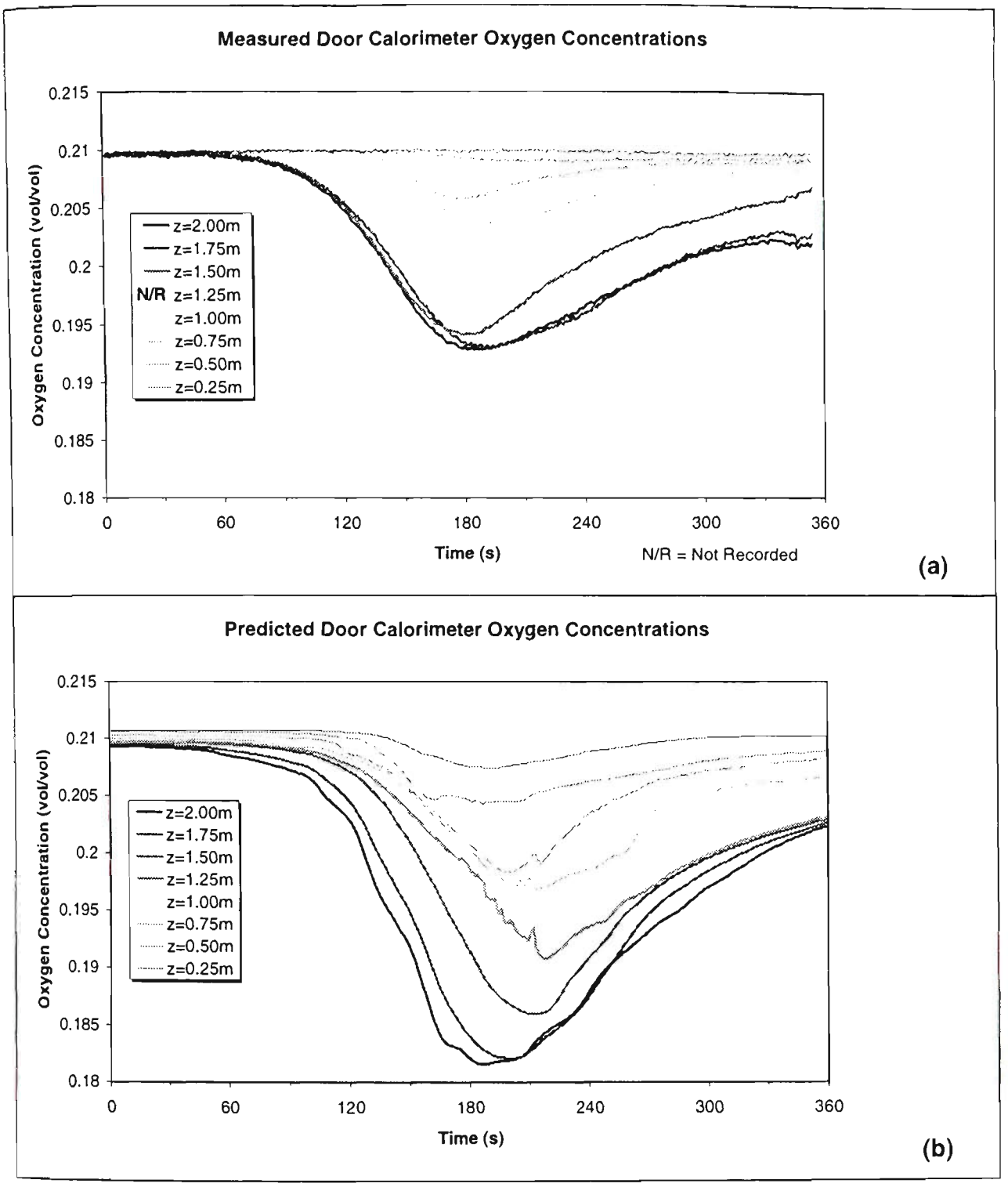

Figure 6.26 Measured (a) and predicted (b) oxygen concentrations at the door calorimeter

6.6. CONVERGENCE ANALYSIS

An analysis of the convergence of the model is presented here, using a scenario similar to the previous section* The mass loss peak in this scenario is higher and occurs more rapidly, but

* The original convergence data was lost due to a system failure. The data presented here is for an otherwise identical model with different material properties for the fuel, which results in a more rapid mass loss peak.

otherwise the results are suitable to demonstrate the trends in the residuals. The scenario analysed here differs from the other simulations for which convergence has been analysed previously in this work in that it is an unsteady simulation with a varying heat release rate. The scenario was initialised with a small steady fire for 2000 iterations. The simulation was then continued as an unsteady fire, for a total of 3600 additional iterations, each iteration corresponding to a timestep of 0.1s. The mass loss rate of the fuel is shown in Figure 6.29 (along with the energy balance for comparison), which is a close approximation of the heat release rate. The peak heat release rate occurs between 3200 and 4000 iterations (or between 120 and 200 seconds simulation time).

The velocity residuals are shown in Figure 6.27. The residuals are initially quite low, and do not vary significantly in the adjustment from the steady to the unsteady stage of the simulation. The residuals then increase by a significant amount when the rate of heat release dramatically increases after about 3200 iterations, reaching a maximum not long after the peak mass loss rate. The residuals then decrease and increase to a smaller peak around 200 iterations later, before decreasing somewhat again in a phase marked by rapid oscillation. At the point around the 4000 iteration mark where the mass loss rate decays rapidly, the residuals again increase, before decaying also, although not as rapidly as the mass loss rate. Overall, the response of the vertical velocity component is the most pronounced, showing the most exaggerated peaks. As noted earlier, as buoyancy is manifested in the vertical velocity component, the vertical component is more likely to be subject to

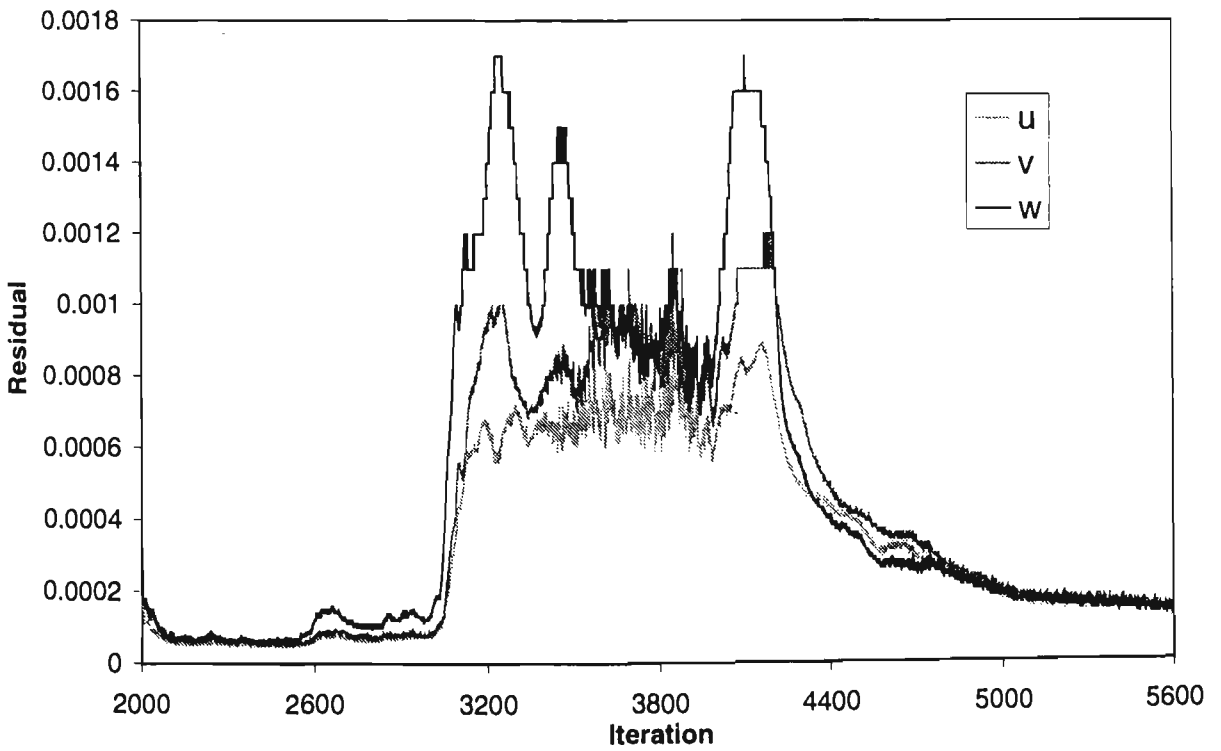

Figure 6.27 Velocity residuals for the full scale unsteady flame spread simulation

instabilities.

The residuals of other variables, shown in Figure 6.28, individually demonstrate particular features present in the velocity residuals. The mass residual (Figure 6.28a) does not show the peaks following the increase in the mass loss rate, but does show a slow decay rate after the decrease in mass loss rate. In contrast, the turbulence energy residual (Figure 6.28b) shows the peaks quite clearly, but also demonstrates a more rapid decay (with some "rebound"). Also, there is little evidence of any significant oscillatory behaviour during the plateau of the mass loss rate. While this last feature is not so significant in the turbulence energy residuals, it is the dominant feature in the enthalpy residuals (Figure 6.28c), which suggests that the high heat release rate is creating a degree of instability in the solution of the enthalpy equation. Overall, the behaviour of all these residuals is intuitive. It is not surprising that the enthalpy residuals are highest when the heat release rate is highest, while velocity residuals are expected to peak when the flow patterns are changing most rapidly, namely in the rapid growth and rapid decay phases of the mass loss rate. The residuals will stabilise for a relatively steady flow, as was seen in the previous subsection for the unsteady simulation of a constant heat release fire.

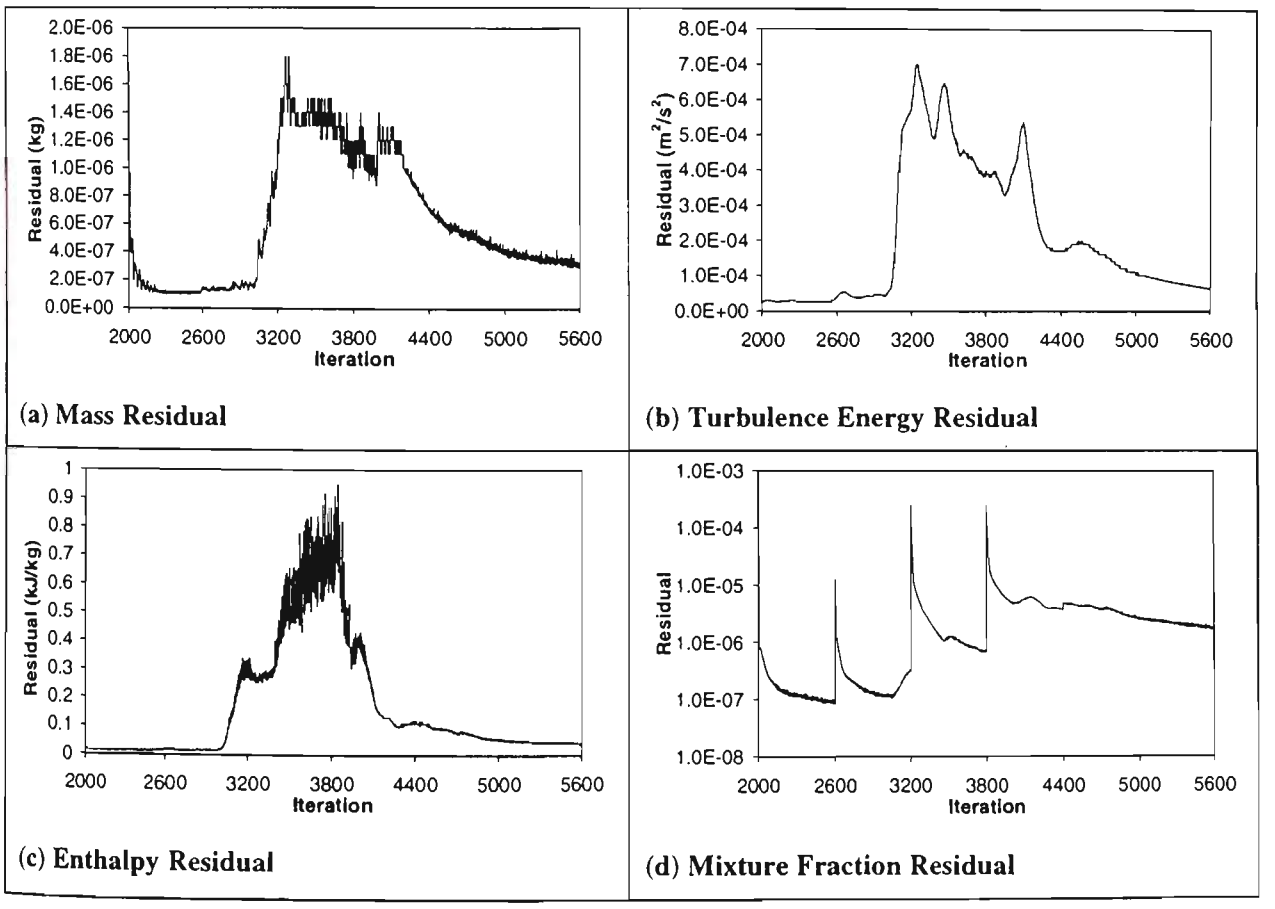

Figure 6.28 Residuals for the full scale unsteady flame spread simulation

The mixture fraction residuals in Figure 6.28(d) shows the overall rise in values seen in the other variable residuals, but the chart in this instance is dominated by spikes every 600 iterations. These are artefacts of the computer program, which resemble the spikes that occur when a steady

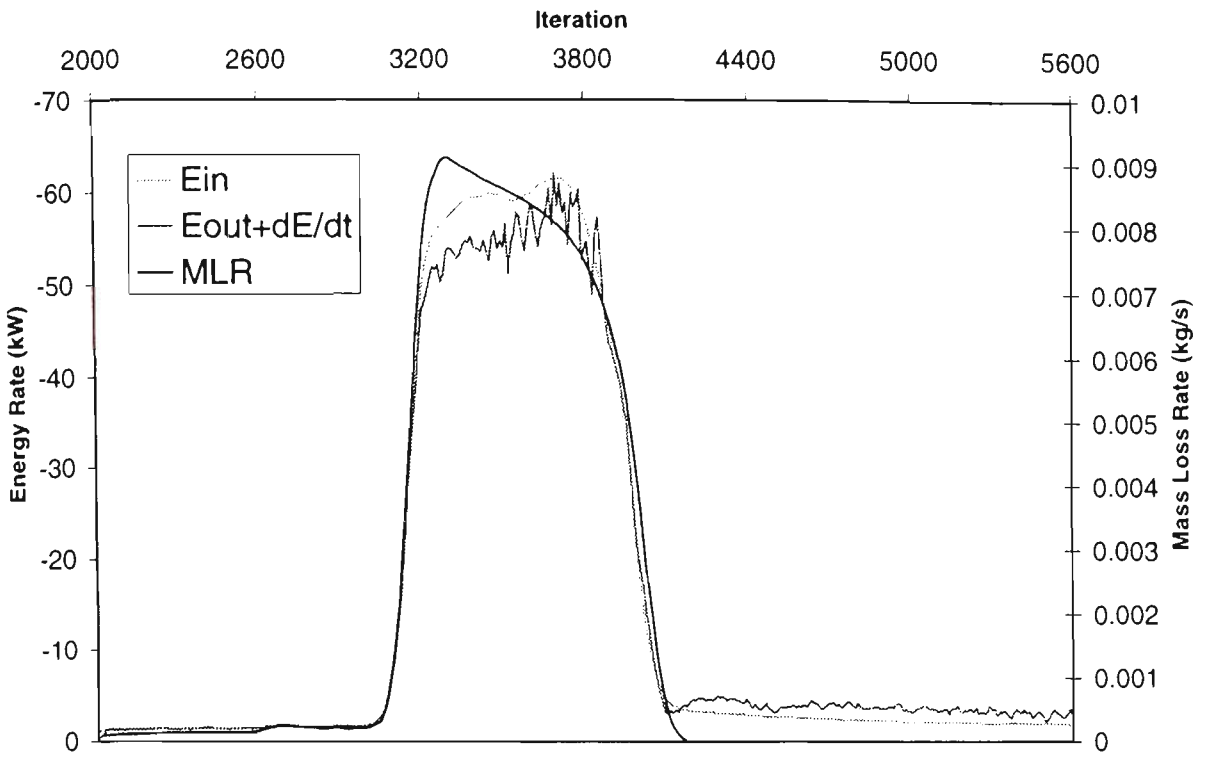

Figure 6.29 Energy balance residuals for the full scale unsteady flame spread simulation

simulation is restarted (see Figure 3.25d), and correspond to the iterations when information was output by the program. As these spikes do not manifest themselves in any of the other charts, it seems that their presence does not introduce any particular error or instability to the solution. The magnitude of the residuals reduces quickly after each peak, which may be a factor in reducing the impact on the rest of the variables.

The final chart considered in this section is the energy balance equation, shown in Figure 6.29. The energy balance (left axis) is plotted along with the mass loss rate (right axis), to illustrate how closely the former follows the latter. Indeed, this is to be expected, as the principal source of energy entering the system is heat released by combustion of the mass released. What is of greater interest, therefore, is the difference between the curves rather than the similarities.

The source of the input energy, E_{in}, is the burning of the fuel vapours which have been contributed to the flow region by the solid fuel. In the examples shown previously, the input energy is less prone to fluctuations than the sum of the output energy and energy change, and this example is no exception. The input energy follows the mass loss curve until just before the peak, where it falls below the mass loss rate. This may be due to incomplete combustion of the fuel, caused by ventilation controlled conditions (i.e. the fuel could only burn as quickly as oxygen was supplied to the enclosure). The opposite occurs shortly thereafter, whereby the input energy is greater than the mass loss rate, possibly due to unburnt fuel vapours undergoing combustion. The input energy then

follows the decay in the mass loss rate, but unlike the latter, does not vanish. A possible cause is the hot walls continuing to contribute energy to the flow region after the fuel is consumed.

The output energy follows the input energy and mass loss quite closely for most of the simulation. It begins to oscillate and fall away from both curves close to the peak mass loss rate. At this point, the balance is furthest from being attained, and it is likely connected to the fact that the enthalpy residuals show their greatest magnitude and variability at this point.

6.7. FUTURE IMPROVEMENTS

Several discrepancies in the model predictions have been highlighted in the previous section, each with its own particular cause. Rectification of the modelling results is therefore unlikely to be a trivial exercise. For example, in view of the sensitivity analysis of the flame spread model performed in Section 5.8, it may have been tempting to attempt to rectify the mass loss rate curve by adjusting the flame heat parameter to a higher value; however, this was not done. As shown in Figure 5.30, increasing the flame heat parameter resulted in the peak mass loss rate occurring earlier and with a greater magnitude, an effect which would be a desirable improvement on the CFD modelling results presented in this section. However, a higher flame heat parameter may also result in an earlier burnout of the cells which ignited earlier, so that the total number of cells simultaneously ignited at peak burning would actually be reduced. Also, changing an input parameter does not address the problem of the induced air flow preventing ignition of the northern portion of the fuel; indeed, a greater mass loss rate would likely induce a greater flow. In other words, if there are discrepancies in the model itself, then altering the input data will not necessarily improve the comparison between prediction and experiment. Satisfactory results are more likely to be achieved if the model discrepancies are themselves addressed.

Some preliminary work has been undertaken by the author in attempting to rectify some of the points resulting from the modelling exercise in the previous section, although at the time of writing, significant improvement on the results presented in the previous section has not been forthcoming. Some promising trends have nevertheless been identified. In particular, starting the model from ambient conditions rather than a small steady-state initialisation appears to avoid the initial buildup of combustion products and the establishment of an excessive fluid flow pattern. However, in order to avoid excessive oscillations early in the simulation, a large time step must be employed (say, 1 sec, rather than 0.1 sec). As this larger time step is not conducive to successful modelling with the flame spread model, as found in Chapter 5, the flame spread submodel must operate with a smaller

timestep. This may be done by iterating the flame spread subroutine several times per flow model iteration. Even with these measures, the residuals early in the simulation are quite high.

The divergence of flow at the balance port continues to prove a problematic aspect of the model. However, a recent modification by Fletcher et al.[39] to FURNACE shows some promise. They were investigating buoyant backflow in a ventilated tunnel, and required the possibility of backflow at the inlet port. Pressure was "anchored" to zero at the z=0 plane at a point outside the tunnel, and the external pressure set to

$$p(z) = a_g \int_0^z (\rho_{ref} - \rho) dz \qquad (6.6)$$

It was stated that without this correction, spurious flows develop due to vertical density gradients in the flow region[39]. As density gradients are present in all the modelling work presented here (a hot, low density layer above and a cool, high density region below), encoding of the correction given by Equation 6.6 may go some way towards rectification of the problem of divergence of flow velocity at the balance port.

Some further numerical experimentation has been performed with the kinetic parameters and other parameters governing the solid fuel model and cellular automata method. Similar trends are observed as were found in the stand alone model, in particular, choice of variables which were sufficient to cause spread early in the simulation tended to lead to excessive spread rates later in the simulation. Overall, there appear to be many parameters which are sensitive to methods employed here, and a full investigation of the effect of altering the parameters involves a substantial amount of additional work, as it involves the repeated execution of the CESARE-CFD flame spread model. While the results for the CFD flame spread model are an improvement on the results presented in Chapter 5, it appears there is still room for improvement. The nature of some of the assumptions may need to be re-evaluated, such as the heat flux from the solid to the gas, and the shape of the solid fuel in the flow region.

In addition to the refining the model for improving the predictions of the scenario investigated in this chapter, the broader scope of applications needs to be considered. Despite the flame spread model being developed to be applicable to any thermoplastic fuel in any orientation, it was only tested for one fuel in one orientation. Future validation exercises will need to incorporate many types of fuels, and of geometries other than horizontal radial spread. Other geometries would include vertical spread (upwards, downwards and lateral), horizontal planar (wind assisted and wind opposed), and even ceiling spread. The next stage would be to include multiple slabs so that

problems such as remote item ignition and combustion could be studied. Remote ignition of a second slab would be achieved by the autoignition of any of the surface cells due to the fire generated by the first slab. Subsequent spread of flame over the second item may then occur by a combination of autoignition and piloted ignition of cells, where applicable. In addition to situations where two slabs are physically separated, cases involving two slabs in contact could also be considered. For instance, two slabs placed vertically in a corner could be used to simulate a room corner fire, and a horizontal slab adjoining a vertical slab could mimic a chair configuration.

A significant future challenge would be to model flame spread across fuels with an extensive aspect, such as floor coverings and wall linings. The methods developed in this research to model thermoplastic fuels such as polyurethane foam may not be suitable to all types of fuel. Indeed, surface regression and even in-depth conduction of heat may not be necessary when considering, for example, plywood wall linings, where the fuel is thin and non-regressing. However, a CFD flame spread model incorporating cellular automata techniques needs only to accurately specify surface temperatures, surface mass loss rates, and piloted and non-piloted ignition criteria to be effective. For fuels as extensive as wall linings, some simplification of the fuel behaviour may be necessary to keep computer storage and calculation times to a minimum. Nevertheless, as flame spread is essentially a two-dimensional surface phenomenon, while fluid flow is a three-dimensional phenomenon, even large fuel loads should not significantly encumber calculations of full-scale fires. This is because the number of cells in the surface mesh is proportional to the square of the characteristic dimension of the enclosure, while the number of cells in the flow mesh is proportional to the cube of the characteristic dimension.

Further modifications of the CFD flame spread model are not addressed in this thesis, but instead are left as future work.

6.8. CONCLUSIONS

A flame spread model has been incorporated into a fire field model, and has been used to simulate an enclosure fire involving the combustion of a cushion sized slab of standard polyurethane foam. Discrepancies between experiment and modelling have been noted, and explanations have been proposed for several of the discrepancies. However, the results overall show good agreement, which is a favourable outcome for the methods adopted for flame spread modelling presented both in this chapter and throughout this thesis, and provides a solid foundation for further development of the model. In particular, the cellular automata method was found to be successful in predicting

the radial spread of flame from a central ignition point, although the findings presented here show that the method is sensitive to the physical data provided by the CFD model. One aspect in particular which had a major influence on the performance of the flame spread model was the prediction of air velocity in the vicinity of the fuel, which was unreasonably high, particularly in the initial stages of the simulation. This issue needs to be addressed in future work. A first step in rectification may be to incorporate the pressure correction at the balance port mentioned in Section 6.7. Likewise, refinement of the spread model is required, and further experimental work is desirable, particularly for other fuel configurations. These exercises are also left as future work.

7. CONCLUSIONS

7.1. GENERAL CONCLUSION

The aims described at the beginning of this thesis have been addressed throughout the body of the work, and each aim has been fulfilled to a degree. The primary aim of this research, namely the formulation of a CFD-compatible flame spread model, has been achieved. The flame spread model was incorporated into the model CESARE-CFD, and was applied to the special case of horizontal flame spread over a thermally thick thermoplastic solid fuel. Predictions were made not only for the flame spread rate over the fuel surface and the rate of mass loss of the fuel, but for the conditions within the enclosure in which the burning of the fuel was taking place. The predictions compared favourably with a series of full-scale experiments that were performed as part of this research.

The flame spread model was designed to be geometrically flexible, so that it may be used to model a variety of fire scenarios. The flexibility was achieved by incorporating cellular automata techniques into the methodology of the model. The application of these techniques in the context of modelling small-scale flame spread behaviour in a full-scale enclosure is a novel feature of the work presented in this thesis, and the results represent a contribution to the study of flame spread.

The task of developing a general flame spread model compatible with CFD models encompassed a broad range of topics, including radiation, combustion chemistry, flame spread and CFD modelling that were undertaken in conjunction with an extensive experimental program ranging from bench scale to full scale tests. As a result of the broad scope of the work presented in this thesis, many unresolved issues arose which could not be pursued in detail. Many of the unresolved issues are worthy of being researched in detail as part of future research projects.

7.2. SPECIFIC CONCLUSIONS

Several intermediate goals were achieved during the course of the research work presented in this thesis, and several further questions were raised, although not addressed in this work. These are summarised in the following section. A number of specific aims were identified in Section 1.2.2.

These are restated here, along with the conclusions and observations arising from the work undertaken in addressing the aims.

AIM: Identify which submodels encoded in CESARE-CFD, if any, yield inadequate predictions of physical quantities occurring in fire environments, and if possible to rectify these submodels.

- The formulation of the CESARE-CFD model was investigated and described and the solution methods found to be in accordance with standard methods.
- Preliminary modelling results indicated that there were deficiencies in the radiation submodel of CESARE-CFD.
- The submodel was modified to include a spatially varying grey gas absorption coefficient, the value of which is dependent on the local temperature and concentration of radiatively interacting species. Also included in the submodel was a routine to calculate the local temperature of the boundary walls, to more accurately predict the leaving intensity of thermal rays.
- A model to calculate soot distribution was required as an input to the modified radiation submodel. A 2% conversion of fuel to soot was employed in this study. A sensitivity analysis of the conversion amount found that the actual value is important in the fire plume, but that soot in fact only plays a minor role in regions remote from the plume.

AIM: Perform appropriate full-scale experiments to acquire data for comparison with model predictions, and investigate whether changes to the model result in improved predictions.

- Experiments involving a 200kW propane fire in a full-scale multi-room enclosure were performed. The experiments were designed to acquire the data most useful to the purpose of validation of the CFD model.
- CESARE-CFD was used to model the 200kW fire. The modifications to the radiation submodel were found to significantly improve the correlation between experiment and modelled results, not only for the prediction of radiant fluxes, but also for the prediction of flow variables in general. The improvement was particularly notable for temperatures in the fire plume, although there is room for further improvement in the predictions overall.
- The performance of the radiation submodel was found to be sensitive to data received from other submodels within CESARE-CFD, and vice-versa, particularly in regard to the distribution of product species. This highlights the need for accurate radiation predictions to successfully model enclosure fires. It also demonstrates that if the radiation predictions are to be improved

further, it will be necessary to scrutinise other submodels of the CFD model, as well as the radiation submodel itself.

- The model was tested to determine whether the solution was grid independent. A grid independent solution was not found, but the trends observed in the grid refinements tested indicated that accuracy was increasing with these refinements. Further grid refinement was beyond the capability of the available computer hardware.
- Comprehensive testing of the model was undertaken to determine the sensitivity of the solution to the variation of user-defined parameters. The proportion of fuel to soot conversion was found to be important only near the fire plume, while the velocity limit at the balance port was found to be important only in the room containing the port. Altering the oxygen limit for combustion had a radical effect for low limits, producing physically unrealistic results, which both justified and emphasised the choice of the values used in this study. Adjusting the wall heat transfer coefficient was found to have a noticeable but ambiguous affect on the predictions. Altering the heat of combustion had an expected effect on the results, and the effect was significant enough to recommend modification of the combustion model to incorporate local combustion efficiency as a worthwhile future exercise.
- During exercises undertaken to validate the radiation submodel, it was found that the model was unable to predict well the division between the hot and cold layers. The prediction errors were found to be lessened (but not eliminated) when a room that was not part of the main combustion product flow was removed from the calculation region. The presence of the room therefore appeared to be exacerbating the problem of layer mixing. This has important ramifications for the future use of CFD models as a fire safety tool.
- Modelling discrepancies appeared to be occurring in certain locations where insufficient data were obtained in the experiment to resolve the cause, in particular within, and at the opening to, a room which was not part of the main combustion product flow. It is recommended that such data be obtained in future experiments, to aid in improving model predictions. It is also recommended that modelling exercises be performed with a different model (such as one of the commercially available models) to test whether problem is an artefact of CESARE-CFD, or is common to other CFD models.
- Whilst the importance of accurately modelling radiation heat transfer was emphasised in the work, the computational costs of such accuracy may be prohibitive. The model adopted in this research uses the discrete transfer method to calculate radiation heat transfer. Monochromatic rays and a grey absorbing medium were assumed, to reduce the demand of computational resources. However, the difference in the spectra of absorbed and emitted radiation cannot be ignored, and a method for differentiating between the two needs to be considered. It was postulated that the changing spectral characteristics of the monochromatic beam as it was

tracked throughout the enclosure by the model may be represented by an "effective temperature". This would represent only one additional variable to the already tracked intensity. How the "effective temperature" would be calculated, its actual performance in a model, and even the validity of such an approach are all issues which could be the subject of future research.

AIM: Develop an ignition and combustion model that requires fundamental, experimentally derivable material properties. Acquire the required data for a selection of materials by a combination of bench-scale experiments and established literature values.

- A description of tests performed in the cone calorimeter with samples of polyurethane foam was given. These tests were conducted to determine the material properties of two types of foam, standard and fire retarded, for input into the flame spread model.
- The heats of combustion of the foams were determined, although the values in both cases appeared to depend both on the applied radiant heat flux, and the stage of combustion of the sample itself. An average value of heat of combustion was obtained for each foam, which was in agreement with values quoted in the literature.
- The values of the heat of volatilisation and critical surface ignition temperature were obtained, but the standard methodology used to produce the values appears to be questionable, and the values themselves are not stated with confidence.
- The cone calorimeter results were obtained using the approved standard method. This has been found by previous researchers to be questionable for fuels with physical properties similar to polyurethane foam. It was concluded that successful determination of fundamental material combustion properties of polyurethane foam would require a revision of the experimental techniques.
- In view of such shortcomings of the standard method, a method which avoids the problems of decreasing heat flux with distance from the cone heater (possibly by reducing sample thickness) and increasing heat feedback from the sample holder (possibly by developing a consumable sample holder such as thin paper) needs to be developed.

AIM: Develop a stand-alone flame spread model by combining the ignition and combustion model for an array of fuel cells in conjunction with spread criteria. Use empirical models and assumptions for the gas phase phenomena.

- An ignition and combustion model based on fundamental material properties was developed, and applied to an array of cells to form the basis of a stand-alone flame spread model. The

stand-alone model was developed to test the feasibility of using cellular automata techniques to model a spreading flame front of arbitrary shape across a flat solid-fuel surface.

- While the stand-alone model was developed to test the feasibility of using the methods of cellular automata for modelling flame spread without the cumbersome overheads of a full CFD simulation, this may not be the sole use of the stand-alone model. It may be possible to simplify the model further, so that its execution time is reduced (assuming one-dimensional heat conduction using an integral method for example). Such a model may be suitable for incorporation into a zone model, for example, so that heat release rate may be determined more accurately than a prescribed heat release rate. The possibilities of further development of the stand-alone model have not yet been fully explored.

AIM: Perform furniture calorimeter experiments to investigate the validity of the stand-alone flame spread model.

- The stand-alone flame spread model was used to produce a set of predicted results, which was compared with a series of full-scale experiments performed in a furniture calorimeter. It was found that there was a favourable comparison of the results, and this indicated that cellular automata techniques are suitable for fire spread modelling.
- Discrepancies between the results were largely attributed to the empirical flame models encapsulated in the flame spread model.
- A sensitivity analysis performed on the stand-alone flame spread model demonstrated that the model was quite robust within a certain range of input parameters, predicting reasonable spread rates. However, the results then underwent a transition from predicting reasonable spread rates to predicting no spread at all within a relatively small increment of input parameters.
- The sensitivity of the stand-alone flame spread model to certain parameters is a phenomenon to be wary of in incorporating the flame spread model into a CFD model, if the overall model is to remain robust. If care is not taken in choosing these parameters, it is possible that a combination of input parameters and flame characteristics predicted by the CFD model will result in no spread, or inaccurate spread rates.

AIM: Incorporate the flame spread model as a submodel of the field model CESARE-CFD.

- Incorporation of the flame spread model as a submodel of CESARE-CFD was achieved.
- Initial numerical experiments performed with an early version model revealed that the behaviour of the flame spread submodel was dominated by the larger behaviour of the flow

region. A linear interpolation of flow properties over the flame spread grid was introduced, which reduced the dominance of the flow properties.

- A series of simple test cases was performed with the updated version of the CFD flame-spread model, and the interpolation methods were found to be robust.

AIM: Investigate the validity of the combined CFD-flame spread model by comparing the predicted results with results obtained from a series of realistic full-scale experiments.

- A series of full-scale experiments involving a horizontal slab of fuel burning in a multi-room enclosure was performed. The scenario was simulated, and a comparison between predicted and experimental results was found to be reasonable.
- The radiation predictions in particular followed the predicted mass loss rate in a very similar manner to their respective measurements. This is further encouraging evidence of the effectiveness of the radiation modifications.
- It was found that the flame spread submodel was sensitive to the data received from other submodels in CESARE-CFD, and that greater attention needed to be paid to the interface between the two, particularly with regards to the heat transfer.

7.3. FUTURE WORK

The broad scope of the research described in this thesis, encompassing theoretical considerations, extensive numerical modelling work, and a comprehensive experimental program, resulted in the identification of a wide range of issues that are worthwhile research pursuits in their own right. The important issues are summarised as follows

- The assumption of monochromatic rays and grey media in the radiation submodel may be overly simplistic to capture the important subtleties of radiation heat transfer in an enclosure fire, such as the spectral difference between localised emission and absorption. However, adding complexity further burdens computational resources. A possible solution proposed by the author is to track the "effective temperature" of a monochromatic ray, which could conceivably capture the local emission and absorption characteristics of the absorbing medium without adding excessive computational burden.
- The CFD model did not predict well the sharp distinction between the hot and cool layers in a given fire scenario, but rather predicted a significant amount of mixing. Predicted layer mixing appeared to be particularly occurring in the vicinity of a room which was not part of the main

product flow, and for which limited experimental data was acquired. To either eliminate or confirm this locality as the source of layer mixing, two actions need to be performed:

- Acquire further experimental data to determine the flow pattern at the doorway to, and the temperature and product stratification within, the room in question.
- Model the scenario with other CFD models to determine whether the degree of layer mixing is an artefact of CESARE-CFD.

It has been suggested by an examiner of this thesis that mixing of the layers may be a consequence of using the k-ε turbulence model. An investigation of alternative turbulence models, and their effect on the diffusion of the two layers, is a significant area of future research.

- A sensitivity analysis of several parameters for which the values were uncertain indicated that improvements could be made to the model if these parameters were considered as local variables rather than global constants. In particular:
  - Higher soot formation in the fire plume may lead to improved temperature predictions in the plume.
  - The heat transfer coefficient was found to have a significant effect on overall predicted temperatures, so local calculation of the heat transfer coefficient should lead to improved predictions.
  - Globally reducing the heat of combustion from the stoichiometric value improved predicted temperatures. The effect could be formalised by considering a local value for the heat of combustion based on the local combustion efficiency.
- The ASTM standard test method for the Cone Calorimeter was found to be unsuitable for determining material properties other than heat of combustion for fuels such as polyurethane foam. To be more successful, a modification of the test method must avoid the problems of:
  - Decreasing heat flux with distance from the cone heater (possibly by using a thinner sample)
  - Increasing heat feedback from the sample holder (possibly by using a consumable sample holder such as thin paper).
- The stand-alone flame spread model was developed principally to test the feasibility of the cellular automata flame spread method, without the computational overheads of CFD. However, with further modifications and simplifications to decrease execution time, it may be suitable for applications such as incorporation into zone models to predict increasing heat release rate, rather than using a prescribed rate.
- The success of predictions with the combined CFD flame-spread model is largely attributable to the retention of the "minimum flux criterion", which was required to maintain combustion in the steady-state initialisation of a simulation, and to ensure smooth transition to the unsteady

phase of the solution. It is desirable to remove such empiricism from what is largely a deterministic model. A possible remedy is to include a fine grid in the flow region in the layer immediately adjacent to the fuel surface, which would resolve extra detail in the fuel-flow interface, and may lead to a spontaneous generation of the high heat flux predictions required to sustain combustion in the model.

- The problem of divergence in the current formulation of the balance port equations needs to be rectified. An alternative formulation involving a pressure correction based on the vertical density profile has been identified, but not implemented or tested. Implementation would serve several purposes:
  - The improvement of flow velocity predictions in the steady-state initialisation of transient flows.
  - The general improvement of the predictions of the conditions in the room containing the balance port.
  - The elimination of an empirical parameter in the model, namely the limiting balance port velocity.
- While the flame-spread model was formulated to be applicable to any thermoplastic fuel in any orientation, it was only tested for one fuel in one orientation. It is desirable to undertake further experimental and modelling work that would involve alternative fuel configurations, such as:
  - Vertical flame spread (upwards, downwards, lateral)
  - Horizontal spread (flow assisted planar, opposed flow planar, ceiling spread)
  - Multi-plane spread (chair or sofa configuration, corner fire)
  - Ignition of and flame spread over an item remote from initial burning item.
- A significant challenge is to model fuels with an extensive aspect, such as floor coverings or wall linings in a full-scale scenario. The techniques of surface regression and three-dimensional heat conduction in the solid used in this research for thermoplastic fuels would require in a significant proportion of computational resources to calculate the flame spread in such scenarios. However, these techniques may not be suitable or indeed necessary for such materials. Provided the surface temperatures, pyrolysis rates, and ignition criteria can be adequately determined and represented, the cellular automata techniques will be effective in modelling the flame spread. Consequently, a simpler model for fuel material behaviour would make modelling large fuel aspects possible. Additionally, as flame spread is a surface phenomenon, the number of cells is proportional to the square of the characteristic dimension of the modelled region, while the flow region is proportional to the cube of the characteristic dimension. Hence, increasing the dimensions or grid refinement of the modelled region will not proportionally increase the computational resources required to calculate flame spread, and in fact may decrease the proportion.

REFERENCES

1. BECK, V. R. "Fire Safety Design Using Risk Assessment Models: Developments in Australia", *Fire Safety Science - Proceedings of the Third International Symposium*, 1991, pp45-59

2. BABRAUSKAS, V. AND PEACOCK, R. D. "Heat Release Rate: The Single Most Important Variable in Fire Hazard", *Fire Safety Journal*, **18**, 1992 pp255-272

3. LUO, M. AND BECK, V. R., , "The Fire Environment in a Multi-Room Building-Comparison of Predicted and Experimental Results", *Fire Safety Journal*, **23**, 1994, pp413-438

4. GALEA, E., "On the Field Modelling Approach to the Simulation of Enclosure Fires", *Journal of Fire Protection Engineering*, **1**(1), 1989, pp11-22

5. WEBER, R. O. "Modelling Fire Spread Through Fuel Beds", *Progress in Energy and Combustion Science*, **17**, 1991, pp67-82

6. FRIEDMAN, R., "An International Survey of Computer Models for Fire and Smoke", *Journal of Fire Protection Engineering*, **4**(3), 1992, pp81-92

7. SIMCOX, S., WILKES, N. S. AND JONES, I. P. "Computer Simulation of the Flows of Hot Gases from the Fire at King's Cross Underground Station",*Fire Safety Journal*, **18**, 1992, pp49-73

8. LUO, M. AND BECK, V. R., "A Study of Non-Flashover and Flashover Fires in a Full-Scale Multi-Room Building", *Fire Safety Journal*, 1996, In Press.

9. TAKEDA, H. AND YUNG, D. "Simplified Fire Growth Models for Risk-Cost Assessment in Apartment Buildings", *Journal of Fire Protection Engineering*, **4** (2), 1992, pp53-66

10. DE RIS, J. N. "Spread of a Laminar Diffusion Flame", *Twelfth Symposioum (International) on Combustion*, 1969, pp241-252

11. FERNANDO, A. E. AND THORPE, G. R., "A Numerical Model for Horizontal Flame Spread over Combustible Solid Fuels", *Sixth Australasian Heat and Mass Transfer Conference*, University of New South Wales, Sydney, 1996, pp213-220

12. QUINTIERE, J. AND IQBAL, N. "An Approximate Integral Model for the Burning Rate of a Thermoplastic-like Material", *Fire and Materials*, **18**, 1994, pp89-98

13. JANSSENS, M., "Determining Flame Spread Properties from Cone Calorimeter Measurements, (a) General Concepts", *Heat Release in Fires*, edited by V. Babrauskas and S. J. Grayson, Elsevier Science Publishers Ltd., 1992, pp265-281

14. TEWARSON, A. AND OGDEN, S. D. "Fire Behaviour of Polymethylmethacrylate", *Combustion and Flame*, **89**, 1992, 237-259

15. ORLOFF, L. "Simplified Radiation Modelling of Pool Fires", *Eighteenth Symposium (International) on Combustion*, 1981, pp549-561

16. NOVOZHILOV, V., HARVIE, D. J. E., GREEN, A. R. AND KENT, J. H. "A Computational Fluid Dynamic Model of Fire Burning Rate and Extinction by Water Sprinkler", *Combustion Science and Technology*, to appear

17. APTE, V. B., BILGER, R. W., GREEN, A. R. AND QUINTIERE, J. G. "Wind Aided Turbulent Flame Spread and Burning Over Large-Scale Horizontal PMMA Surfaces", *Combustion and Flame*, **85**, 1991, pp169-184

18. LAUNDER, B. E. AND SPALDING, D. B. "The Numerical Computation of Turbulent Flows", *Computer Methods in Applied Mechanics and Engineering*, **3**, 1974, pp269-289

19. PATANKAR, S. V. *Numerical Heat Transfer and Fluid Flow*, McGraw Hill, NY, 1980

20. KUMAR, S., GUPTA, A. K., AND COX, G. "Effects of Thermal Radiation on the Fluid Dynamics of Compartment Fires", *Fire Safety Science - Proceedings of the Third International Symposium*, 1991, pp345-354

21. HADJISOPHOCLEOUS, G. V. AND CACAMBOURAS, M. "Computer Modeling of Compartment Fires", *Journal of Fire Protection Engineering*, **5**(2), 1993, pp39-52

22. KERRISON, L., MAWHINNEY, N., GALEA, E. R., HOFFMAN, N. AND PATEL, M. K. "A Comparison of Two Fire Field Models with Experimental Room Fire Data", *Fire Safety Science - Proceedings of the Fourth International Symposium*, 1994, pp161-172

23. BABRAUSKAS, V., Letter to the Editor, *Journal of Fire Protection Engineering*, **5** (1), 1993, p35

24. FLETCHER, D. F., SHORE, N. A., HAYNES, B. S., SOLA, A. A., JOSEPH, S. D., "CFD Modelling of Flow in a Gasifier", *The Australian Symposium on Combustion and the Fourth Australian Flame Days*, University of Adelaide, 1995, Session A6, pp13-18

25. WITT, P. J. AND PERRY, J. H., "Prediction of the Hydrodynamic Behaviour and Outlet Gas Composition of a Fluidised Bed Coal Gasifier", *The Australian Symposium on Combustion and the Fourth Australian Flame Days*, University of Adelaide, 1995, Session A6, pp1-6

26. RAVICHANDRAN, M. AND GOULDIN, F. C., "Numerical Simulation of Incinerator Overfire Mixing", *Combustion, Science and Technology*, **85**, 1992, pp165-185

27. BOYD, R. K. AND KENT, J. H. "Three Dimensional Furnace Computer Modelling", *Twenty-first Symposium (International) on Combustion*, 1986, pp265-274

28. YUEN, R., YEOH, G. H., CASEY, R., CHANDRASEKARAN, V., DE VAHL DAVIS, G. AND LEONARDI, E., "Three-Dimensional Numerical Prediction of Burning Wood in a Cone Calorimeter", *Proceedings of the International Conference on Fire Research and Engineering*, Orlando, USA, 1995, pp223-228

29. LOCKWOOD, F. C. AND MALALASEKERA, W. M. G. "Fire Computation: The Flashover Phenomenon", *Twenty-Second Symposium (International) on Combustion*, 1988, pp1319-1328

30. COX, G. AND KUMAR, S., "Field Modelling of Fire in Forced Ventilated Enclosures", *Combustion, Science and Technology*, **52**, 1987, pp7-23

31. THAN, C. H. AND SAVILONIS B. J. "Modelling Fire Behaviour in an Enclosure with a Ceiling Vent", *Fire Safety Journal*, **20**, 1993 pp255-272

32. CHOW, W. K. AND LEUNG, W. M. "Solid-wall Boundary Effect on a Building Fire Field Model", *Combustion, Science and Technology*, **71**, 1990, pp77-93

33. KERRISON, L., GALEA, E. R., HOFFMAN, N. AND PATEL, M. K. "A Comparison of a FLOW3D Based Fire Field Model with Experimental Room Fire Data", *Fire Safety Journal*, **23**, 1994, pp387-411

34. CHOW, W. K. "Combustion Effect on a Building Fire Field Model", *4th International Symposium Transport Phenomena in Heat and Mass Transfer*, Sydney, Australia, 1991, pp1274-1285

35. STECKLER, K. D., QUINTERE, J. G., AND RINKINEN, W. J. "Flow Induced by Fire in a Compartment", *NBSIR 82-2520*, National Bureau of Standards, USA, 1982

36. LEWIS, M. J., MOSS, M. B. AND RUBINI, P. A. "CFD Modelling of Combustion and Heat Transfer in Compartment Fires", *Fire Safety Science - Proceedings of the Fifth International Symposium*, 1997, pp463-474

37. ISENBERG, J. AND DE VAHL DAVIS, G. "Finite Difference Methods in Heat and Mass Transfer", *Topics in Transport Phenomena*, Edited by Chaim Gutfinger, John Wiley & Sons, Ch. 5

38. APTE, V. R., GREEN, A. R., AND KENT, J. H. "Pool Fire Plume Flow in a Large-Scale Wind Tunnel", *Fire Safety Science - Proceedings of the Third International Symposium*, 1991, pp425-434

39. FLETCHER, D. F., KENT, J. H. APTE, V. R., AND GREEN, A. R. "Numerical Simulations of Smoke Movement from a Pool Fire in a Ventilated Tunnel", *Fire Safety Journal*, **23**, 1994, pp305-325

40. MINKOWYCZ, W. J., SPARROW, E. M., SCHNEIDER, G. E. AND PLETCHER, R. H. *Handbook of Numerical Heat Transfer*, John Wiley and Sons, New York, 1988

41. GLEICK, J., *Chaos: Making a New Science*, Macdonald and Co. Ltd, London, 1988

42. WILCOX, D. C. *Turbulent Modeling for CFD*, DWC Industries, La Canada 1993

43. CHUKKAPALLI, G. AND TURAN, Ö. F. "Structural Parameters and Prediction of Adverse Pressure Gradient Turbulent Flows: An Improved k-ε Model", *Transactions of the ASME Journal of Fluids Engineering*, **117**, Sep 1995, pp424-432

44. KUO, K. K. *Principles of Combustion*, John Wiley and Sons, Singapore, 1986

45. TSUCHIYA, Y. "Chemical Modelling of Fire Gases", *Journal of Fire Sciences*, **13**, May/Jun 1995, pp214-223

46. GOTTUK, D. T., ROBY, R. J., PEATROSS, M. J. AND BEYLER, C. L. "Carbon Monoxide Production in Compartment Fires", *Journal of Fire Protection Engineering*, **4**(4), 1992, pp133-150

47. GOLDBERG, E. D. *Black Carbon in the Environment*, John Wiley and Sons, New York, 1985

48. MAGNUSSEN, B. F. AND HJERTAGER, B. H. "On Mathematical Modelling of Turbulent Combustion with Special Emphasis on Soot Formation and Combustion", *Sixteenth Symposium (International) on Combustion*, 1977, pp719-729

49. LOCKWOOD, F. C. AND NAGUIB, A. S. "The Prediction of the Fluctuations in the Properties of Free, Round-Jet, Turbulent, Diffusion Flames", *Combustion and Flame*, **24,** 1975, pp109-124

50. BILGER, R. W. "Computational Field Models in Fire Research and Engineering" *Fire Safety Science - Proceedings of the Fourth International Symposium*, 1993, pp95-110

51. DOUGLAS, J. AND RACHFORD, H. H. "On the numerical Solution of Heat Conduction in Two and Three Space Variables", *Transactions of the American Mathematical Society*, **3**, 1956, pp421-439

52. LUO, M. AND BECK, V. R. "Smouldering Fire in a Full-Scale Building: Prediction and Experiment", *The Australian Symposium on Combustion and the Fourth Australian Flame Days*, University of Adelaide, 1995, Session C3, pp7-12

53. KENT, J. H. *FURNACE Version 5.0*, Department of Mechanical and Mechatronic Engineering, University of Sydney, NSW Australia, 1992

54. BEYLER, C. L. "Major Species Production by Diffusion Flames in a Two-layer Compartment Fire", *Fire Safety Journal*, **10**, 1986, pp47-56

55. LOCKWOOD, F. C. AND SHAH, N. G. "A New Radiation Method For Incorporation in General Combustion Prediction Procedures", *Eighteenth Symposium (International) on Combustion*, 1981, pp1405-1414

56. ZHAO, L., "Computational Study of Radiation and Mixed Convection in Enclosures", *PhD Thesis*, University of New South Wales, Sydney, Australia, 1997

57. HENKES, R. A. W. M., "Natural-Convection Boundary Layers", *PhD Thesis*, Delft University, Delft, The Netherlands, 1990

58. TEWARSON, A. "Flammability Parameters of Materials: Ignition, Combustion and Fire Propagation", *Journal of Fire Sciences*, **12**, July/August, 1994, pp329-356

59. SIBULKIN, M., KULKARNI, A. K. AND ANNAMALAI, K. "Effects of Radiation on the Burning of Vertical Fuel Surfaces", *Eighteenth Symposium (International) on Combustion*, 1981, pp611-617

60. BHATNAGAR, S. K., VARSHNEY, B. S., MOHANTY, B. AND AGARWAL, C. P. "Steady Flame Spread Rate Measurement at Discrete Levels of External Radiant Heat Flux", *Twenty-Third Symposium (International) on Combustion*, 1990, pp1693-1699

61. HASEMI, Y., YOSHIDA, M., NOHARA, A. AND NAKABAYASHI T. "Unsteady-State Upward Flame Spreading Velocity along Vertical Combustible Solid and Influence of External Radiation on the Flame Spread", *Fire Safety Science - Proceedings of the Third International Symposium*, 1991, pp197-206

62. BHATTACHARJEE, S. AND ALTENKIRCH, R. A. "Radiation-Controlled, Opposed-Flow Flame Spread in a Microgravity Environment", *Twenty-Third Symposium (International) on Combustion*, 1990, pp1627-1633

63. KUMAR, S. AND COX, G. "Radiation and Surface Roughness Effects in the Numerical Modelling of Enclosure Fires", *Fire Safety Science - Proceedings of the Second International Symposium*, 1997, pp851-860

64. CHANG, L. C., YANG, K. T., AND LLOYD, J. R. "Radiation-Natural Convection Interactions in Two-Dimensional Complex Enclosures", *Journal of Heat Transfer*, **105**, Feb 1983, pp89-95

65. FUSEGI, T., FAROUK, B. AND KUWAHARA, K. "3-D Natural Convection-Radiation Interactions in a Cube Filled with Gas-Soot Mixtures", *Fire Safety Science - Proceedings of the Third International Symposium*, 1991, pp365-374

66. GRAY, W. A. AND MULLER, R. *Engineering Calculations in Radiative Heat Transfer*, Permagon Press, 1974

67. HOTTEL, H. C. AND SAROFIM, A. F. *Radiative Transfer*, McGraw-Hill, 1967

68. GRAY, W. A., KILHAM, J. K. AND MULLER, R. *Heat Transfer from Flames*, Paul Elek Scientific Books, 1976

69. TIEN, C. L., LEE, K. Y. AND STRETTON, A. J. "Radiation Heat Transfer", *SPFE Handbook of Fire Protection Engineering*, 1988, section 1, pp93-106

70. DRYSDALE, D. D., *An Introduction to Fire Dynamics*, John Wiley and Sons Ltd., 1985

71. HOLMAN, J. P., *Heat Transfer, Fifth Edition*, McGraw-Hill Inc., 1981

72. FERNANDO, A. E. AND LUO, M., "Modelling of Radiative Heat Transfer in Full-scale Building-Fires.", *Australian Symposium on Combustion and Fourth Flame Days*, University of Adelaide, Adelaide, Australia, 1995, ppC3-13-18

73. QUINTIERE, J. G. "Surface Flame Spread", SPFE Handbook of Fire Protection Engineering, 1988, section 1, pp360-367

74. DI BLASI, C., "Modelling and Simulation of Combustion Processes of Charring and Non-charring Solid Fuels", *Progress in Energy and Combustion Science*, **19**, 1993, pp77-104

75. OHKI, Y. AND TSUGÉ, S. "On the Flame Spreading over a Polymer Surface", *Combustion, Science and Technology*, **9**, 1974, pp1-12

76. DI BLASI, C., CONTINILLO, G., CRESCITELLI, S. AND RUSSO, G. "Numerical Simulation of Opposed Flow Flame Spread over a Thermally Thick Solid Fuel" *Combustion Science and Technology*, **54**, 1987, pp25-36

77. REICH, L. AND LEVI, D. W. "Dynamic Thermogravimetric Analysis in Polymer Degradation", *Macromol. Rev.*, **1**, pp173-275

78. WILLIAMS, F. A. "Mechanisms of Fire Spread", *Sixteenth Symposium (International) on Combustion*, 1976, pp1281-1294

79. ATREYA, A. "Fire Growth on Horizontal Surfaces of Wood", *Combustion Science and Technology*, **39**, 1984, pp163-194

80. MCALEVY, R. F. III AND MAGEE, R. S. "The Mechanism of Flame Spreading over the Surface of Igniting Condensed-Phase Materials", *Twelfth Symposioum (International) on Combustion*, 1969, pp215-227

81. WICHMAN, I. S. AND WILLIAMS, F. A., "A Simplified Model of Flame Spread in an Opposed Flow along a Flat Surface of a Semi-Infinite Solid", *Combustion Science and Technology*, **32**, 1983, pp91-123

82. DELICHATSIOS, M. A. "Basic Polymer Material Properties for Flame Spread", *Journal of Fire Sciences*, **11**, Jul/Aug 1993, pp287-295

83. MOGHTADERI, B., NOVOZHILOV, V., FLETCHER, D. F. AND KENT, J. H. "An Integral Model for the Pyrolysis of Solid Fuels", *Australian Symposium on Combustion and Fourth Flame Days*, University of Adelaide, Adelaide, Australia, 1995, ppC4-1-6

84. DELICHATSIOS, M. M., MATHEWS, M. K. AND DELICHATSIOS, M. A., "An Upward Fire Spread and Growth Simulation", *Fire Safety Science: Proceedings of the Third International Symposium*, 1991, pp207-216

85. DELICHATSIOS, M. A. AND SAITO, K., "Upward Fire Spread: Key Flammability Properties, Similarity Solutions and Flamability Indices", *Fire Safety Science: Proceedings of the Third International Symposium*, 1991, pp217-226

86. FERNÁNDEZ-PELLO, A. AND WILLIAMS, F. A. "A Theory of Laminar Flame Spread Over Flat Surfaces of Solid Combustibles", *Combustion and Flame*, **28**, 1977, 251-277

87. STECKLER, K. D., KASHIWAGI, T., BAUM, H. R., AND KANEMARU, K. "Analytical Model for Transient Gasification of Noncharring Thermoplastic Materials", *Fire Safety Science: Proceedings of the Third International Symposium*, 1991, pp 895-904

88. CARSLAW, H. S. AND JAEGER, J. C. *Conduction of Heat in Solids*, 2nd Edition, Oxford University Press, 1959

89. WOODS, G., *Flexible Polyurethane Foams; Chemistry and Technology*, Applied Science Publishers, Barking, England, 1982

90. CHANG, T. C., SHEN, W. S., CHIU, Y. S. AND HO, S. Y., "Thermo-oxidative Degradation of Phosphorus-containing Polyurethane", *Polymer Degradation and Stability*, **49**, 1995, pp353-360

91. BABRAUSKAS, V. "Ten Years of Heat Release Research with the Cone Calorimeter", *Heat Release and Fire Hazard: Proceedings of the First Japan Symposium*, Tsukuba, Japan, May 1993, Volume III, pp1-8

92. KARLSSON, B. "Models for Calculating Flame Spread on Wall Lining Materials and the Resulting Heat Release Rate in a Room", *Heat Release and Fire Hazard: Proceedings of the First Japan Symposium*, Tsukuba, Japan, May 1993, Volume II, pp25-44

93. ÖSTMAN, B. A.-L. AND TSANTARIDIS, L. D. "Correlations Between Cone Calorimeter Data and Time to Flashover in the Room Fire Test", *Heat Release and Fire Hazard:*

Proceedings of the First Japan Symposium, Tsukuba, Japan, May 1993, Volume III, pp37-44

94. KALLONEN, R. AND MIKKOLA, E. "Burning Characteristics and Toxicity Data for Some Products Used in Buildings", *Heat Release and Fire Hazard: Proceedings of the First Japan Symposium*, Tsukuba, Japan, May 1993, Volume III, pp9-14

95. VANSPEYBROECK, R., VAN HEES, P., AND VANDEVELDE, P., "Combustion Behaviour of Polyurethane Flexible Foams under Cone Calorimetry Test Conditions", *Fire and Materials*, **17**, 1993, pp 155-166

96. QUINTIERE, J. G. "A Simulation Model for Fire Growth on Materials Subject to a Room-Corner Test", *Fire Safety Journal*, **20**, 1993 pp313-339

97. ASTM E 1354-90 "Standard Test Method for Heat and Visible Smoke Release Rates for Materials and Products Using an Oxygen Consumption Calorimeter" *ASTM Fire Test Standards, 4th Edition*, ASTM, Philadelphia PA, 1993 pp968-984

98. ISO 5660 "Fire Tests - Reaction to Fire - Rate of Heat Release from Building Products" ISO TC91/SC-1/WG5/DOC N116, 1990

99. FERNANDO, A. E., LEONARD, J., WEBB, A., BOWDITCH, P. AND DOWLING, V. "Experimental Derivation of Material Combustion Properties for Flame Spread Models", *Fire and Materials 2001, 7th International Conference*, 2001, pp315-326.

100. CLARKE, K. C., BRASS, J. A. AND RIGGAN P. J. "A Cellular Automaton Model of Wildfire Propagation and Extinction", *Photogrammetric Engineering and Remote Sensing*, **60** (11), 1994, pp1355-1367

101. SAÏD, R. AND BORGHI, R. "A Simulation with a 'Cellular Automaton' for Turbulent Combustion Modelling", *Twenty-Second Symposium (International) on Combustion*, 1988, pp569-577

102. GREEN, D. G. "Emergent Behaviour in Biological Systems", *Complex Systems from Biology to Computation*, ed. Green, D. and Bossomaier, T., IOS Press, 1993, pp24-35

103. GARDNER, M. "The Fantastic Combinations of John Conway's New Solitaire Game 'Life'", *Scientific American*, October, 1970

104. WICHMAN, I. S., "Theory of Opposed-Flow Flame Spread", *Progress in Energy and Combustion Science*, **18**, 1992, pp553-593

105. ROSS, H. D. "Ignition and Flame Spread over Laboratory-Scale Pools of Pure Liquid Fuels", *Progress in Energy and Combustion Science*, **20**, 1994, pp17-63

106. BAROUDI, D. AND KOKKALA, M., "Flame Spread and Heat Release Rate Model for a Burning Mattress", *Interflam '96*, 1996, pp37-46

107. FREY, A. E. JR. AND T'IEN, J. S. "A Theory of Flame Spread over a Solid Fuel Including Finite-Rate Chemical Kinetics", *Combustion and Flame*, **36**, 1979, pp263-289

108. HASEMI, Y., YOSHIDA, M. AND YASUI, N. "Upward Flame Spread Along Vertical Charring Materials: Model, Model Verification and Application to the Evaluation of Material Fire Safety Performance", *Heat Release and Fire Hazard: Proceedings of the First Japan Symposium*, Tsukuba, Japan, 1993, Vol II, pp45-54

109. HESKESTAD, G., "Luminous Heights of Turbulent Diffusion Flames", *Fire Safety Journal*, **5**, 1983, pp103-108

110. MUDAN, K. S., "Geometric View Factors for Thermal Radiation Hazard Assessment", *Fire Safety Journal*, **12**, 1987, pp89-96

111. SINGE, A. K. AND THORPE, G. R. "A Grid Generation Technique for Numerical Modelling Heat and Moisture Movement in Peaked Bulks of Grain", *Journal of Food Process Engineering*, **16**, 1993, pp127-145

112. ATKINSON, K. E. *An Introduction to Numerical Analysis, Second Edition*, John Wiley and Sons, New York, 1989

113. HE, Y., LUO, M. AND BECK, V. R. "Oxygen Consumption Calorimetry in Room Fire Test", *The Australian Symposium on Combustion and the Fourth Australian Flame Days*, University of Adelaide, 1995, Session C3, pp1-6

114. ISO-9705 "Fire Test - Full-scale Room Tests for Surface Products".

115. NICOLETTE, V. F., TIESZEN, S. R., MOYA, J. L. "Interfacing Materials Models with Fire Field Models", *41st International SAMPE Symposium*, March 24-28, 1996

116. NOVOZHOLOV, V., MOGHTADERI, B. AND KENT, J. H. "Extinguishment of Burning Solid Materials by a Water Spray", *Sixth Australasian Heat and Mass Transfer Conference*, Sydney, Australia, 1996, pp249-256

117. JIA, F., GALEA, E. R. AND PATEL, M. K. "The Prediction of Fire Propagation in Enclosure Fires", *Fire Safety Science: Proceedings of the Fifth International Symposium*, 1997, pp 439-450

118. LUO, M. AND BECK, V. R., "Effects of Air-Handling System on Fire Spread in a Full-Scale Building", *Sixth Australasian Heat and Mass Transfer Conference*, University of New South Wales, Sydney, 1996, pp241-248

119. YUEN, R., CASEY, R., DE VAHL DAVIS, G. LEONARDI, E., YEOH, G. H., CHANDRASEKARAN, V. AND GRUBITS, S. J. "Thermophysical Properties for a Three-Dimensional Pyrolysis Model for Wood", *Sixth Australasian Heat and Mass Transfer Conference*, Sydney, Australia, 1996, pp257-268

Appendix A STAND-ALONE FLAME SPREAD MODEL

SPREAD.IN

```
Fuel grid
.............................................
0.94     <= fuel length (m)
0.95     <= fuel width  (m)
0.15     <= fuel depth  (m)
0.005    <= grid square size (m)
6        <= number of fuel depth divisions
-----------------------------------------------
Length of each depth division (m) (kfuel reqd, total = fuel depth)
.....................................................
0.001 0.005 0.010 0.030 0.045 0.059
-----------------------------------------------
Fuel properties
.........................................
23.0     <= density      (kg/m^3)
0.038    <= conductivity  (W/m.K)
1400.0   <= thermal capacity (J/kg.K)
0.80     <= fuel emissivity  (no dim.)
-----------------------------------------------
ignition properties
.........................................
550.     <= piloted ignition temperature (K)
715.     <= autoignition temperature (K)
-------------------------------------------------------
Combustion properties
.....................................................
1.22e+06 <= heat of volatilisation (J/kg)  L_v
2.44e+07 <= heat of combustion of volatiles (J/kg) H_c
2.444e+05 <= xi  (xi*oxyconc = Q"_f (W/m^2) )
24300    <= heat lost from surface (W/m^2)  Q"_e
950.     <= flame temperature (K)
1.0      <= flame absorption coefficient (m^-1)
-------------------------------------------------------
Ambient Conditions
.....................................................
0.       <= external heat flux   (W/m^2)
0.2095   <= local oxygen concentration  (vol. fract.)
298.15   <= ambient temperature (K)
-----------------------------------------------
Arrhenius Pyrolysis constants
.....................................................
5.0e+07  <= preexponential constant (kg/s.m^2)
125000.0 <= activation energy (J/mol)
-------------------------------------------------------
Program Parameters
.........................................
0.1      <= time step (s)
0.0      <= preheat time (s)
-----------------------------------
centre of flame initiation (m)
initial radius (m)
.................................
0.47   0.475
0.035
-----------------------------------
Monitor point ( i  j )
Fixed depth temperature zout (m)
.........................
90       90
0.1
----------------------
Number of steps per fleft.dat output
```

```
.........................
600
-----------------------------------------------------------
Conduction mode:                1 = 1D conduction
(default=2)                     2 = 3D near flame front only
                                3 = 3D conduction at all points
Method:                         0 = implicit in z-direction
(default=0)                     1 = explicit everywhere
Upwind Differencing:0 = no
(default=0)                     1 = yes
.............................................................
3       <=  mode
0       <=  method
1       <=  upwind
```

SPREAD.F

```
c=======================================================================
c
c                STAND-ALONE FLAME SPREAD MODEL
c
c                (C) 1995,1996,1997  Anthony Fernando
c
c=======================================================================

        program firespread

        include 'spread.inc'

        parameter(maxijfuel = 40000)
        parameter(maxkfuel  = 10    )

        integer ignite(maxijfuel)
        complex statnew(maxijfuel),stat17(maxijfuel)

        dimension t(maxijfuel*(maxkfuel+1)),
     >       tnew(maxijfuel*(maxkfuel+1)),
     >       fuelmass(maxijfuel),pyro(maxijfuel),znode(maxkfuel+1),
     >       znold(maxkfuel+1),znnew(maxkfuel+1),deltaz(maxkfuel),
     >       aimp(maxkfuel),bimp(maxkfuel),cimp(maxkfuel),
     >       dimp(maxkfuel)
c    >       ,ignite(maxijfuel)
c    >       ,statnew(maxijfuel),stat17(maxijfuel)

        pi=4.*atan(1.)
        sigma=5.67e-08
        unigas=8.31441

c----------------Read fuel dimensions from spread.in-----------------

        open(unit=25,file='spread.in',status='old')
        infile=25
        call findots(infile)
        read (25,*) fuelx
        read (25,*) fuely
        read (25,*) fuelz
        read (25,*) grid
        read (25,*) kfuel
        if(kfuel.gt.maxkfuel)then
          write(*,*)'kfuel must be less than or equal to ',maxkfuel
          goto 999
        endif
        ifuel=fuelx/grid
        jfuel=fuely/grid

        open(unit=24,file='spread.dat',status='new')
        write(24,*)'time(s) diam(m) height(m) mass(kg) frac-burnt ignite'
        open(unit=28,file='temps.dat',status='new')
        open(unit=27,file='fleft.dat',status='new')

        call spreadinit(t,tnew,fuelmass,pyro,ignite,deltaz,znode)

        call SPREAD(t,tnew,fuelmass,pyro,ignite,deltaz,znode,
     >          znold,znnew,statnew,stat17,aimp,bimp,cimp,dimp)

999     end

c=======================================================================

        subroutine spreadinit(t,tnew,fuelmass,pyro,ignite,deltaz,
     >          znode)

        include 'spread.inc'
```

```
      dimension t(ifuel,jfuel,0:kfuel),tnew(ifuel,jfuel,0:kfuel),
     >     fuelmass(ifuel,jfuel),pyro(ifuel,jfuel),deltaz(kfuel),
     >     znode(0:kfuel)
      integer ignite(ifuel,jfuel)

c-------------------------read in constants----------------------

      infile=25

c---------read in fuel depths------

      call findots(infile)
      read (25,*,err=998) (deltaz(i),i=1,kfuel)

      call findots(infile)
      read (25,*) density
      read (25,*) conduct
      read (25,*) capacity
      read (25,*) emiss
      call findots(infile)
      read (25,*) pilottemp
      read (25,*) autotemp
      call findots(infile)
      read (25,*) hvol
      read (25,*) hcomb
      read (25,*) xi
      read (25,*) qlost
      read (25,*) flametemp
      read (25,*) flamek
      call findots(infile)
      read (25,*) qext
      read (25,*) oxyconc
      read (25,*) ambtemp
      call findots(infile)
      read (25,*) preexp
      read (25,*) actenergy
      call findots(infile)
      read (25,*) tstep
      read (25,*) preheat
      call findots(infile)
      read (25,*) centrex, centrey
      read (25,*) radinit

c---------------output parameters-----------
      call findots(infile)
      read (25,*) iout,jout
      read (25,*) zout
      call findots(infile)
      read (25,*) lsteps

c----------------calculation method----------
      call findots(infile)
      read (25,*) mode3d
      read (25,*) method
      read (25,*) modeup

      close(unit=25,status='keep')

      z=0.
      znode(0)=fuelz
      do 20 i=1,kfuel
      z=z+deltaz(i)
      znode(i)=fuelz-z
20    continue
      if(abs(1-(fuelz/z)).gt.0.001)then
      write(*,*)'grid entered incorrectly'
      goto 999
      endif
```

```
      print*,'fleft.dat will be written to every ',
     >    lsteps*tstep,' seconds'

      alpha=conduct/(density*capacity)
      cellm=grid**2.*fuelz*density

c-----------------------------------------------------------------------
c     Initialise dimensional variables
c-----------------------------------------------------------------------

      do 50 i=1,ifuel
      do 50 j=1,jfuel

      ignite(i,j)=0
      fuelmass(i,j)=cellm
      pyro(i,j)=0.

      do 50 k=0,kfuel

      t(i,j,k)=ambtemp
      tnew(i,j,k)=ambtemp

50    continue

      return

998   print*,'error reading data'
999   stop
      end

c=======================================================================

      subroutine SPREAD(t,tnew,fuelmass,pyro,ignite,deltaz,znode,
     >          znold,znnew,statnew,stat17,aimp,bimp,cimp,dimp)

      include 'spread.inc'

      dimension t(ifuel,jfuel,0:kfuel),tnew(ifuel,jfuel,0:kfuel),
     >     fuelmass(ifuel,jfuel),pyro(ifuel,jfuel)
      integer ignite(ifuel,jfuel)
      dimension deltaz(kfuel),znode(0:kfuel),znold(0:kfuel),
     >     znnew(0:kfuel),aimp(kfuel),bimp(kfuel),cimp(kfuel),
     >     dimp(kfuel)
      complex statnew(ifuel*jfuel),stat17(ifuel*jfuel)
      logical pilot


      time=0.
      burntime=0.
      pilot=.true.
      lft=0

      qamb=sigma*ambtemp**4.
      if(qamb.gt.qext)then
        qext=qamb
      endif

c-----------------------------------------------------------------------
c     Main iteration loop
c-----------------------------------------------------------------------

10    ntotnew=0

      if((time.ge.preheat).and.pilot) then
        pilot=.false.
        call fstart(ignite,statnew,stat17)
      endif
```

```
      call flamesize(ignite,pyro,diam,height)

      call surfacebal(ignite,t,deltaz,pyro,diam,height,tnew,
     >     statnew,stat17,fuelmass)

      call bodybal(t,deltaz,znode,fuelmass,tnew,statnew,stat17,
     >     ignite,aimp,bimp,cimp,dimp)

      call firegrowth(ignite,tnew,statnew,stat17)

      if(ntotnew.eq.0)goto 80
      do 70 n=1,ntotnew
      i=real(statnew(n))
      j=aimag(statnew(n))
      ignite(i,j)=1
70    continue

80    call massloss(ignite,pyro,fuelmass,totalmass,totalpyro,
     >       znode,deltaz,t,tnew,znold,znnew)

      write(24,'(1x,f7.3,1x,f9.6,1x,f7.4,1x,
     >                    f9.6,1x,f5.4,1x,i2)'),
     >  time,diam,height,totalmass,
     >  fuelmass(iout,jout)/cellm,
     >  ignite(iout,jout)
      print'(1x,f6.2,1x,f6.3,1x,f6.3,1x,f6.3,
     >                                1x,f5.4,1x,i2)',
     >  time,diam,height,totalmass,
     >  fuelmass(iout,jout)/cellm,
     >  ignite(iout,jout)

      if(fuelmass(iout,jout)*znode(0)/cellm.lt.zout)then
        tout=flametemp
      else
        do 777 k=1,kfuel
          if((fuelmass(iout,jout)*znode(k-1)/cellm.ge.zout).and.
     >      (fuelmass(iout,jout)*znode(k)/cellm.lt.zout))then
            tout=((fuelmass(iout,jout)*znode(k-1)/cellm-zout)*
     >      t(iout,jout,k) +
     >       (zout-fuelmass(iout,jout)*znode(k)/cellm)*
     >      t(iout,jout,k-1))/
     >       (deltaz(k)*fuelmass(iout,jout)/cellm)
          endif
777     continue
      endif

      write(28,'(12(1x,f8.2))'),(t(iout,jout,k),k=0,kfuel),tout
      print'(12(1x,f8.2))',(t(iout,jout,k),k=0,kfuel),tout

      if(totalmass.le.0.0)then
        print*,'fuel consumed after ',burntime,' seconds of burning'
        goto 999
      elseif((totalpyro.le.0.000000015).and.(.not.pilot).and.
     >     (burntime.gt.0.))then
        print*,'burnt out without spreading further after',
     >   burntime,' seconds of burning'
        goto 999
      endif
      time=time+tstep
      lft=lft+1
      if(lft.eq.lsteps)then
        lft=0
        print*,'Writing to fleft.dat'
        do 100 i=1,ifuel
          write(27,'(200(1x,f5.3))'),(fuelmass(i,j)/cellm,j=1,jfuel)
100     continue
        write(27,*),' '
      endif
      if(.not.pilot)burntime=burntime+tstep
```

```
        go to 10

999     print*,'program finished'

        return
        end

c=======================================================================

        subroutine findots(infile)

        character*7 chr,spec
        data spec/'.......'/

12      read (infile,'(3x,a7)',end=13) chr
        if (chr.ne.spec) goto 12
        return

13      write(*,*)'string not found',spec
        stop
        end

c=======================================================================

c-----------------------------------------------------------------------
c       This subroutine calculates the effective diameter height
c       of the flame given the pyrolysis rate (and hence heat
c       release rate) and ignited area
c-----------------------------------------------------------------------

        subroutine flamesize(ignite,pyro,d,h)


        include 'spread.inc'

        integer ignite(ifuel,jfuel)
        dimension pyro(ifuel,jfuel)

        area=0.
        pyrolysis=0.

        do 70 i=1,ifuel
        do 70 j=1,jfuel

        pyrolysis=pyrolysis+pyro(i,j)/tstep
        if(iabs(ignite(i,j)).eq.1)then
          area=area+grid**2.
        endif

70      continue

        d=sqrt(4.*area/pi)
        h=0.23*(hcomb*pyrolysis/1000)**0.4 - 1.02*d
        if (h.le.0.)then
          h=0.
        endif
        return
        end


c=======================================================

c-------------------------------------------------------
c       This subroutine calculates the internal temperature
c       distribution of the fuel
c-------------------------------------------------------

        subroutine bodybal(t,dz,znode,fuelm,tnew,statnew,stat17,
     >    ignite,aimp,bimp,cimp,dimp)
```

```
      include 'spread.inc'

      dimension t(ifuel,jfuel,0:kfuel),tnew(ifuel,jfuel,0:kfuel)
      dimension dz(kfuel),znode(0:kfuel)
      dimension fuelm(ifuel,jfuel)
      dimension aimp(kfuel),bimp(kfuel),cimp(kfuel),dimp(kfuel)

      integer ignite(ifuel,jfuel)

      complex statnew(ifuel*jfuel),stat17(ifuel*jfuel)

      logical threed,listed

      do 100 i=1,ifuel
      do 100 j=1,jfuel

      frac=fuelm(i,j)/cellm
      f=frac*znode(0)

      if(frac.le.(0.001))then
        do 111 k=1,kfuel
        tnew(i,j,k)=tnew(i,j,0)
111     continue
        goto 100
      endif

      if(mode3d.eq.1)then
        threed=.false.
        goto 19
      elseif(mode3d.eq.3)then
        threed=.true.
        goto 19
      else
        threed=.false.
      endif

      listed=.false.

      if(ntot17.eq.0)goto 15
      kount=0
10    kount=kount+1
      if(kount.gt.ntot17)goto 15
      front=abs(i-real(stat17(kount)))+abs(j-aimag(stat17(kount)))
      if(front.le.2.)then
        listed=.true.
        goto 18
      endif
      goto 10

15    if(ntotnew.eq.0)goto 18
      kount=0
16    kount=kount+1
      if(kount.gt.ntotnew)goto 18
      front=abs(i-real(statnew(kount)))+abs(j-aimag(statnew(kount)))
      if(front.le.2.)then
        listed=.true.
        goto 18
      endif
      goto 16

18    if(listed)threed=.true.

19    do 90 k=1,kfuel

      if(.not.threed)goto 20

c---------- i direction ------------------------------------
```

```
c---------- i = 1  ---------------------------------

        if(i.eq.1)then
          if(ignite(i+1,j).eq.-1)then
            d2tdxi2=0.
            d2tdxidzeta=0.
          else
            d2tdxi2=(t(i+1,j,k)-t(i,j,k))/grid**2.
            if(k.eq.kfuel)then
              d2tdxidzeta=0.
            else
              d2tdxidzeta=
     >        (t(i+1,j,k+1)-t(i,j,k+1)-t(i+1,j,k-1)+t(i,j,k-1))
     >          *znode(0)/(grid*(dz(k)+dz(k+1)))
            endif
          endif
          dfdx=(4.*fuelm(i+1,j)-3.*fuelm(i,j)-fuelm(i+2,j))
     >           *znode(0)/(2.*cellm*grid)
          d2fdx2=(2.*fuelm(i,j)-4.*fuelm(i+1,j)+2.*fuelm(i+2,j))
     >           *znode(0)/(3.*cellm*grid**2.)

c--------- i = ifuel  ----------------------

        elseif(i.eq.ifuel)then
          if(ignite(i-1,j).eq.-1)then
            d2tdxi=0.
            d2tdxidzeta=0.
          else
            d2tdxi2=(t(i-1,j,k)-t(i,j,k))/grid**2.
            if(k.eq.kfuel)then
              d2tdxidzeta=0.
            else
              d2tdxidzeta=
     >        (t(i,j,k+1)-t(i-1,j,k+1)-t(i,j,k-1)+t(i-1,j,k-1))
     >         *znode(0)/(grid*(dz(k)+dz(k+1)))
            endif
          endif
          dfdx=(4.*fuelm(i-1,j)-3.*fuelm(i,j)-fuelm(i-2,j))
     >           *znode(0)/(2.*cellm*grid)
          d2fdx2=(2.*fuelm(i,j)-4.*fuelm(i-1,j)+2.*fuelm(i-2,j))
     >           *znode(0)/(3.*cellm*grid**2.)

c------- generic i ---------------------------

        else
          if(ignite(i-1,j).eq.-1)then
            dleft=0.
          else
            dleft=1.
          endif
          if(ignite(i+1,j).eq.-1)then
            dright=0.
          else
            dright=1.
          endif

          d2tdxi2=(dleft*(t(i-1,j,k)-t(i,j,k))+dright*
     >                        (t(i+1,j,k)-t(i,j,k)))/grid**2.

          if(k.eq.kfuel)then
            d2tdxidzeta=0.
          else
            d2tdxidzeta=
     >    (dright*(t(i+1,j,k+1)-t(i,j,k+1)-t(i+1,j,k-1)+t(i,j,k-1))
     >   +dleft*(t(i-1,j,k-1)-t(i,j,k-1)-t(i-1,j,k+1)+t(i,j,k+1)))
     >          *znode(0)/(grid*(dz(k)+dz(k+1)))
            if((dleft.eq.1.).and.(dright.eq.1.))then
              d2tdxidzeta=d2tdxidzeta/2.
            endif
```

```
          endif
          dfdx=(fuelm(i+1,j)-fuelm(i-1,j))*znode(0)/(2.*cellm*grid)
          d2fdx2=(fuelm(i+1,j)+fuelm(i-1,j)-2.*fuelm(i,j))*znode(0)
     >       /(cellm*grid**2.)
        endif

c------------- j direction -------------------------

c------------- j = 1  ------------------------

        if(j.eq.1)then
          if(ignite(i,j+1).eq.-1)then
            d2tdeta2=0.
            d2tdetadzeta=0.
          else
            d2tdeta2=(t(i,j+1,k)-t(i,j,k))/grid**2.
            if(k.eq.kfuel)then
              d2tdetadzeta=0.
            else
              d2tdetadzeta=
     >         (t(i,j+1,k+1)-t(i,j,k+1)-t(i,j+1,k-1)+t(i,j,k-1))
     >             *znode(0)/(grid*(dz(k)+dz(k+1)))
            endif
          endif
          dfdy=(4.*fuelm(i,j+1)-3.*fuelm(i,j)-fuelm(i,j+2))
     >          *znode(0)/(2.*cellm*grid)
          d2fdy2=(2.*fuelm(i,j)-4.*fuelm(i,j+1)+2.*fuelm(i,j+2))
     >          *znode(0)/(3.*cellm*grid**2.)

c--------- j = jfuel  -------------------

        elseif(j.eq.jfuel)then
          if(ignite(i,j-1).eq.-1)then
            d2tdeta2=0.
            d2tdetadzeta=0.
          else
            d2tdeta2=(t(i,j-1,k)-t(i,j,k))/grid**2.
            if(k.eq.kfuel)then
              d2tdetadzeta=0.
            else
              d2tdetadzeta=
     >         (t(i,j,k+1)-t(i,j-1,k+1)-t(i,j,k-1)+t(i,j-1,k-1))
     >             *znode(0)/(grid*(dz(k)+dz(k+1)))
            endif
          endif
          dfdy=(4.*fuelm(i,j-1)-3.*fuelm(i,j)-fuelm(i,j-2))
     >          *znode(0)/(2.*cellm*grid)
          d2fdy2=(2.*fuelm(i,j)-4.*fuelm(i,j-1)+2.*fuelm(i,j-2))
     >          *znode(0)/(3.*cellm*grid**2.)

c--------- generic j --------------

        else
          if(ignite(i,j-1).eq.-1)then
            dleft=0.
          else
            dleft=1.
          endif
          if(ignite(i,j+1).eq.-1)then
            dright=0.
          else
            dright=1.
          endif

          d2tdeta2=(dleft*(t(i,j-1,k)-t(i,j,k))+dright*
     >                        (t(i,j+1,k)-t(i,j,k)))/grid**2.

          if(k.eq.kfuel)then
            d2tdetadzeta=0.
```

```
          else
            d2tdetadzeta=
     >     (dright*(t(i,j+1,k+1)-t(i,j,k+1)-t(i,j+1,k-1)+t(i,j,k-1))
     >    +dleft*(t(i,j-1,k-1)-t(i,j,k-1)-t(i,j-1,k+1)+t(i,j,k+1)))
     >          *znode(0)/(grid*(dz(k)+dz(k+1)))
            if((dleft.eq.1.).and.(dright.eq.1.))then
              d2tdetadzeta=d2tdetadzeta/2.
            endif
          endif
          dfdy=(fuelm(i,j+1)-fuelm(i,j-1))*znode(0)/(2.*cellm*grid)
          d2fdy2=(fuelm(i,j+1)+fuelm(i,j-1)-2.*fuelm(i,j))*znode(0)
     >         /(cellm*grid**2.)
        endif

        dkx = d2tdxi2 - znode(k)*frac*dfdx*d2tdxidzeta/f**2.
        dky = d2tdeta2 - znode(k)*frac*dfdy*d2tdetadzeta/f**2.

20      if(method.eq.1)then

c---------begin--explicit--method---------

        if(k.eq.kfuel)then
          dtdzeta=(t(i,j,k)-t(i,j,k-1))*znode(0)/dz(k)
          d2tdzeta2=2.*(t(i,j,k-1)-t(i,j,k))*znode(0)**2.
     >      /dz(k)**2.
        else
          dtdzeta=(dz(k)**2.*t(i,j,k+1)+(dz(k+1)**2.-dz(k)**2.)
     >      *t(i,j,k)-dz(k+1)**2.*t(i,j,k-1))*znode(0)
     >      /(dz(k)*dz(k+1)*(dz(k)+dz(k+1)))
          dtdzetapos=(t(i,j,k)-t(i,j,k-1))*znode(0)/dz(k)
          dtdzetaneg=(t(i,j,k+1)-t(i,j,k))*znode(0)/dz(k+1)
          d2tdzeta2=2.*(dz(k)*t(i,j,k+1)-(dz(k)+dz(k+1))
     >      *t(i,j,k)+dz(k+1)*t(i,j,k-1))*znode(0)**2.
     >      /(dz(k)*dz(k+1)*(dz(k)+dz(k+1)))
        endif

        if(.not.threed)then
          d2tdx2=0.
          d2tdy2=0.
          goto 30
        endif

        fcx=(znode(k)*frac*(f*d2fdx2-2.*dfdx**2.)/f**3.)
        if(modeup.eq.1)then
          if(fcx.le.0.0)then
            dtdzeta=dtdzetaneg
          else
            dtdzeta=dtdzetapos
          endif
        endif
        d2tdx2 = dkx + (znode(k)*frac*dfdx/f**2.)**2.*d2tdzeta2 -
     >    fcx*dtdzeta

        fcy=(znode(k)*frac*(f*d2fdy2-2.*dfdy**2.)/f**3.)
        if(modeup.eq.1)then
          if(fcy.le.0.0)then
            dtdzeta=dtdzetaneg
          else
            dtdzeta=dtdzetapos
          endif
        endif
        d2tdy2 = dky + (znode(k)*frac*dfdy/f**2.)**2.*d2tdzeta2 -
     >    fcy*dtdzeta

30      dtdt = ( d2tdx2 + d2tdy2 + d2tdzeta2/f**2. ) * alpha
        tnew(i,j,k) = t(i,j,k) + tstep * dtdt

        if((tnew(i,j,k).gt.tnew(i,j,0)).and.
     >                              (tnew(i,j,0).gt.ambtemp))then
```

```
          tnew(i,j,k)=tnew(i,j,0)
        endif

c------------end---explicit---method--------------
        else
c------------initialise--implicit--variables-------

        if(.not.threed)then
          big1=0.
          big2=0.
        else
          big1=znode(k)**2.*(dfdx**2.+dfdy**2.)/f**2.
          big2=znode(k)*(f*(d2fdx2+d2fdy2)-2.*(dfdx**2.+dfdy**2.))
     >           /(2.*f**2.)
        endif

        if(k.eq.kfuel)then
          aimp(k)=-2.*alpha*tstep*(1./frac**2.+big1)/dz(k)**2.
          bimp(k)=1.+2*alpha*tstep*(1./frac**2.+big1)/dz(k)**2.
          goto 99
        endif

        if(modeup.eq.1)then
          if(big2.gt.0.)then
            ak=(dz(k+1)+dz(k))
            bk=dz(k+1)
            ck=0.
          else
            ak=0.
            bk=-dz(k)
            ck=-(dz(k)+dz(k+1))
          endif
        else
          ak=dz(k+1)
          bk=(dz(k+1)-dz(k))
          ck=-dz(k)
        endif

          aimp(k)=-2.*alpha*tstep*(1./frac**2.+big1+ak
     >      *big2)/(dz(k)*(dz(k)+dz(k+1)))
          bimp(k)=1.+2.*alpha*tstep*(1./frac**2.+big1+bk
     >      *big2)/(dz(k)*dz(k+1))
          cimp(k)=-2.*alpha*tstep*(1./frac**2.+big1+ck
     >      *big2)/(dz(k+1)*(dz(k)+dz(k+1)))

99      dimp(k)=t(i,j,k) + alpha*tstep*(dkx+dky)

c--------------end--implicit--initialisation------
        endif

90      continue

        if(method.eq.1)goto 100

c-------------calculate--temperatures--implicitly--------

        dimp(1)=dimp(1)-aimp(1)*tnew(i,j,0)

        do 92 k=2,kfuel
          bimp(k)=bimp(k) - cimp(k-1)*aimp(k)/bimp(k-1)
          dimp(k)=dimp(k) - dimp(k-1)*aimp(k)/bimp(k-1)
92      continue

        tnew(i,j,kfuel)=dimp(kfuel)/bimp(kfuel)

        do 94 k=kfuel-1,1,-1
          tnew(i,j,k)=(dimp(k)-cimp(k)*tnew(i,j,k+1))/bimp(k)
94      continue
```

```
100     continue

        return
        end

c=======================================================================

c-----------------------------------------------------------------------
c       This subroutine calculates the surface temperature distribution
c       of the fuel
c-----------------------------------------------------------------------

        subroutine surfacebal(ignite,t,dz,pyro,diam,h,tnew,
     >      statnew,stat17,fuelm)

        include 'spread.inc'

        dimension t(ifuel,jfuel,0:kfuel),tnew(ifuel,jfuel,0:kfuel)
        integer ignite(ifuel,jfuel)
        dimension pyro(ifuel,jfuel),dz(kfuel),fuelm(ifuel,jfuel)
        complex statnew(ifuel*jfuel),stat17(ifuel*jfuel)

        double precision a,b,c,y,z

        eps=1.0e-6

        do 120 i=1,ifuel
        do 120 j=1,jfuel

        call convect (i,j,hconv)

        if((ignite(i,j).eq.-1).or.(fuelm(i,j).le.0))then
          goto 120
        elseif(ignite(i,j).eq.0)then
          call flamerad(i,j,diam,h,statnew,stat17,psi)
          q=(1.-psi)*qext+psi*sigma*flametemp**4.0
        elseif(ignite(i,j).eq.1)then
          q=qext+xi*oxyconc/emiss
          hconv=0.
        endif

        a=emiss*sigma

c--------linear temperature profile conduction------------

c       b=hconv+(conduct*cellm/(fuelm(i,j)*dz(1)))
c       c=emiss*q+hconv*ambtemp+(conduct*t(i,j,1)*cellm/
c    >            (fuelm(i,j)*dz(1)))
c
c---------parabolic temperature profile conduction--------
        b=hconv+(conduct*cellm/fuelm(i,j))*(2.*dz(1)+dz(2))/
     >            (dz(1)*(dz(1)+dz(2)))
        c=emiss*q+hconv*ambtemp+(conduct*cellm/fuelm(i,j))
     >     *(t(i,j,1)*(dz(1)+dz(2))/(dz(1)*dz(2))-
     >       t(i,j,2)*dz(1)/(dz(2)*(dz(1)+dz(2))))

        y=t(i,j,0)

10      z=y-(a*y**4.+b*y-c+preexp*hvol*exp(-actenergy/(unigas*y)))/
     >      (4.*a*y**3.+b+preexp*hvol*actenergy/(unigas*y**2.)*
     >       exp(-actenergy/(unigas*y)))
        if(abs(z-y).ge.eps)then
          y=z
          goto 10
        else
          tnew(i,j,0)=z
        endif

        pyro(i,j)=grid**2.*tstep*preexp*exp(-actenergy
```

```
     >        /(unigas*tnew(i,j,0)))

         if((t(i,j,0).ge.autotemp).and.(ignite(i,j).eq.0))then
           call checklist(i,j,ignite,statnew,stat17)
         endif

120      continue

         return
         end

c=======================================================================

c-----------------------------------------------------------------------
c        This subroutine calculates the view factor of the flame as seen
c        from a surface element a distance d from the flame
c-----------------------------------------------------------------------

         subroutine flamerad(i,j,diam,h,statnew,stat17,psi)

         include 'spread.inc'

         complex statnew(ifuel*jfuel),stat17(ifuel*jfuel)

         r=diam/2.
         if(r.le.0.0) r=1.0e-06
         if((diam.lt.grid*ifuel).and.(diam.lt.grid*jfuel))then
           d=((centrex-((i-0.5)*grid))**2.+
     >       (centrey-((j-0.5)*grid))**2.)**0.5 - r
           if(d.le.0.0)then
             psi=0.5
             goto 888
           endif
         else
         d=sqrt((i-real(stat17(1)))**2.+(j-aimag(stat17(1)))**2.)
     >        *grid
         if(ntot17.le.1)then
           d=d+grid
           goto 20
         endif
         do 11 n=2,ntot17
         d=min(sqrt((i-real(stat17(n)))**2.+(j-aimag(stat17(n)))**2.)
     >        *grid,d)
11       continue
         d=d+grid

         endif

20       z=asin(r/(r+d))
         a=h**2.*(d+r)**2./(r**2.*(d**2.+2.*d*r))
         b=-h**2./r**2.
         if(b.gt.-1.)then
           y=sqrt((1.+a+b)*(1.+b))
           psi=(1./pi)*(z-atan((1.+b)*tan(z)/y)/y)
         elseif(b.lt.-1.)then
           y=sqrt((1.+a+b)*(-1.-b))
           psi=(1./pi)*(z-0.5*log((sqrt(1.+a+b)+sqrt(-1.-b)*tan(z))/
     >          (sqrt(1.+a+b)-sqrt(-1.-b)*tan(z)))/y)
         elseif(b.eq.1)then
           psi=(1./pi)*(z-tan(z)/a)
         endif

         if(psi.gt.1.)psi=1
         if(psi.lt.0.)psi=0.

         beamlength=(36.*r**2.*h)/(35.*r**2+10.*h**2.)
         flamemiss=max(0.5,1.-exp(-flamek*beamlength))
         psi=psi*flamemiss
```

```
888     return
        end

c=================================================================

c-----------------------------------------------------------------
c       This subroutine calculates the heat transfer coefficient at
c       the surface of the fuel (allowance was made for a position
c       dependent value, but a global constant was only ever used)
c-----------------------------------------------------------------


        subroutine convect(i,j,h)

        h=10.0

        return
        end

c=================================================================

c-----------------------------------------------------------------
c       This and subsequent subroutines calculate the number of new
c       ignitions
c-----------------------------------------------------------------

        subroutine firegrowth(ignite,t,statnew,stat17)

        include 'spread.inc'

        integer ignite(ifuel,jfuel)
        dimension t(ifuel,jfuel,0:kfuel)
        complex statnew(ifuel*jfuel),stat17(ifuel*jfuel)

        if(ntot17.le.0)goto 20

        m=1

11      i=real(stat17(m))
        j=aimag(stat17(m))
        if((t(i,j,0).lt.pilottemp).or.(t(i,j,0).ge.autotemp))then
          m=m+1
          goto 10
        endif
        call neighbors(ignite,i,j,n,statnew,stat17)
        if(n.ge.3)then
          call checklist(i,j,ignite,statnew,stat17)
        else
          m=m+1
        endif

10      if(m.le.ntot17)goto 11

20      return
        end

c=================================================================

        subroutine checklist(i,j,ignite,statnew,stat17)

        include 'spread.inc'

        integer ignite(ifuel,jfuel)
        complex statnew(ifuel*jfuel),stat17(ifuel*jfuel)

        if((i.lt.1).or.(i.gt.ifuel).or.(j.lt.1).or.(j.gt.jfuel))then
          print*,
     >    'Warning: attempted to ignite cell outside region (skipped)'
          goto 999
```

```
      endif

      ntotnew=ntotnew+1
      statnew(ntotnew)=cmplx(i,j)

      if(ntot17.le.0)goto 20
      call remlist(ignite,i,j,statnew,stat17)

20    do 10 l=-1,1
      do 11 m=-1,1

      if((l.eq.0).and.(m.eq.0))goto 11

      il=i+l
      jm=j+m

      if((il.eq.0).or.(il.eq.ifuel+1).or.(jm.eq.0).or.
     >   (jm.eq.jfuel+1))goto 11
      if(iabs(ignite(il,jm)).eq.1)goto 11

      call neighbors(ignite,il,jm,n,statnew,stat17)

      if(n.eq.0)then
        call addlist(ignite,il,jm,statnew,stat17)
      elseif(n.ge.7)then
        call remlist(ignite,il,jm,statnew,stat17)
      endif

11    continue
10    continue

999   return
      end

c=====================================================================

      subroutine neighbors(ignite,i,j,n,statnew,stat17)

      include 'spread.inc'

      integer ignite(ifuel,jfuel)
      complex statnew(ifuel*jfuel),stat17(ifuel*jfuel)

      n=0

      if(i.eq.1)goto 11
      if(j.eq.1)goto 13
      n=n+iabs(ignite(i-1,j-1))
13    n=n+iabs(ignite(i-1,j))
      if(j.eq.jfuel)goto 11
      n=n+iabs(ignite(i-1,j+1))
11    if(j.eq.1)goto 14
      n=n+iabs(ignite(i,j-1))
14    if(j.eq.jfuel)goto 10
      n=n+iabs(ignite(i,j+1))
10    if(i.eq.ifuel)goto 20
      if(j.eq.1)goto 16
      n=n+iabs(ignite(i+1,j-1))
16    n=n+iabs(ignite(i+1,j))
      if(j.eq.jfuel)goto 20
      n=n+iabs(ignite(i+1,j+1))

20    return
      end

c=====================================================================

      subroutine addlist(ignite,i,j,statnew,stat17)
```

```
      include 'spread.inc'

      complex statnew(ifuel*jfuel),stat17(ifuel*jfuel)
      complex check
      logical listed

      check=cmplx(i,j)
      listed=.false.

      if(ntot17.eq.0)goto 11
      do 10 m=1,ntot17
      if(stat17(m).eq.check)then
        listed=.true.
      endif
10    continue

11    if(ntotnew.eq.0)goto 17
      do 15 m=1,ntotnew
      if(statnew(m).eq.check)then
        listed=.true.
      endif
15    continue

17    if (.not.listed) then
        ntot17=ntot17+1
        stat17(ntot17)=check
      endif

      return
      end

C=======================================================================

      subroutine remlist(ignite,i,j,statnew,stat17)

      include 'spread.inc'

      complex statnew(ifuel*jfuel),stat17(ifuel*jfuel)
      complex check
      logical listed

      check=cmplx(i,j)
      listed=.true.

      do 10 m=1,ntot17
      if((listed).and.(stat17(m).eq.check))then
        listed=.false.
      endif

      if (.not.listed) then
        stat17(m)=stat17(m+1)
      endif

10    continue

      if (.not.listed) then
        stat17(ntot17)=cmplx(0.,0.)
        ntot17=ntot17-1
      endif

      return
      end

C=======================================================================

      subroutine massloss(ignite,pyro,fuelmass,total,totalp,
     >      znode,deltaz,t,tnew,znold,znnew)

      include 'spread.inc'
```

```
      dimension pyro(ifuel,jfuel),fuelmass(ifuel,jfuel),
     >     t(ifuel,jfuel,0:kfuel),tnew(ifuel,jfuel,0:kfuel),
     >     znode(0:kfuel),deltaz(kfuel),
     >     znold(0:kfuel),znnew(0:kfuel)
      integer ignite(ifuel,jfuel)

      total=0.
      totalp=0.

      do 10 i=1,ifuel
      do 10 j=1,jfuel

      if(ignite(i,j).eq.-1)goto 10

      t(i,j,0)=tnew(i,j,0)
      t(i,j,kfuel)=tnew(i,j,kfuel)

      do 11 n=0,kfuel
      znold(n)=fuelmass(i,j)*znode(n)/cellm
11    continue

      oldfuel=fuelmass(i,j)

      if(fuelmass(i,j).gt.pyro(i,j))then
        fuelmass(i,j)=fuelmass(i,j)-pyro(i,j)
      else
        pyro(i,j)=fuelmass(i,j)
        fuelmass(i,j)=0.
        ignite(i,j)=-1
      endif
      total=total+fuelmass(i,j)
      totalp=totalp+pyro(i,j)

      if(ignite(i,j).eq.-1)then
        do 12 n=1,kfuel
        t(i,j,n)=tnew(i,j,0)
12      continue
        pyro(i,j)=0.
        goto 10
      endif

      do 20 n=1,kfuel-1
      znnew(n)=fuelmass(i,j)*znode(n)/cellm
      do 20 k=n,kfuel-1
      if((znnew(n).le.znold(k)).and.(znnew(n).gt.znold(k+1)))then
      t(i,j,n)=((znnew(n)-znold(k+1))*cellm/
     >          (oldfuel*deltaz(k+1)))*tnew(i,j,k)
     >          +((znold(k)-znnew(n))*cellm/
     >          (oldfuel*deltaz(k+1)))*tnew(i,j,k+1)
      endif

20    continue
10    continue

      return
      end

C=====================================================================

      subroutine fstart(ignite,statnew,stat17)

      include 'spread.inc'

      integer ignite(ifuel,jfuel)
      complex statnew(ifuel*jfuel),stat17(ifuel*jfuel)

      print*,'igniting'
```

```
        i=centrex/grid
        j=centrey/grid
        ip=(centrex+radinit)/grid
        im=(centrex-radinit)/grid
        jp=(centrey+radinit)/grid
        jm=(centrey-radinit)/grid

        do 10 m=im,ip
        do 10 n=jm,jp
        if(sqrt((m-i)**2.+(n-j)**2.)*grid.le.radinit)then
          call checklist(m,n,ignite,statnew,stat17)
        endif
10      continue

c       k=i+1
c       l=i-1
c       m=j+1
c       n=j-1
c       call checklist(k,j,ignite,statnew,stat17)
c       call checklist(l,j,ignite,statnew,stat17)
c       call checklist(i,m,ignite,statnew,stat17)
c       call checklist(i,n,ignite,statnew,stat17)

        return
        end

c=======================================================================
```

SPREAD.INC

```
        common/fuelgrid/ifuel,jfuel,kfuel,tstep
     >         ,grid,cellm,fuelz,preheat
        common/fuelprops/density,conduct,capacity,emiss,alpha
        common/ignition/pilottemp,autotemp
        common/combust/hvol,hcomb,xi,qlost,flametemp,flamek
        common/ambient/qext,oxyconc,ambtemp
        common/parameters/pi,sigma
        common/iglist/ntotnew,ntot17
        common/flamecentre/centrex,centrey,radinit
        common/arrhenius/preexp,actenergy,unigas
        common/monitor/iout,jout,zout,lsteps
        common/conduct/mode3d,method,modeup
```

Appendix B CFD FLAME SPREAD MODEL

SPREAD.IN

```
Length of each depth division (m) (kfuel reqd, total = fuel depth)
.....................................................
0.001  0.002 0.004  0.008 0.012  0.018  0.025  0.030
-----------------------------------------------
Fuel properties
.....................................
23.0     <= density       (kg/m^3)
0.038    <= conductivity  (W/m.K)
1400.0   <= thermal capacity (J/kg.K)
0.80     <= fuel emissivity  (no dim.)
1.0      <= roughness constant (no dim.) =9.0 for smooth surface
-----------------------------------------------
ignition properties
.....................................
400.     <= pyrolysis temperature (K)
510.     <= piloted ignition temperature (K)
715.     <= autoignition temperature (K)
-----------------------------------------------------
Combustion properties and Arrhenius constants
.................................................
1.22e+06  <= heat of volatilisation (J/kg)  L_v
2.444e+05 <= xiflame (xiflame*oxyconc = Q"_f (W/m^2) )
5.0e+08   <= preexponential constant (kg/s.m^2)
125000.0  <= activation energy (J/mol)
-----------------------------------------------------------
Program Parameters
.....................................
0.0      <= preheat time (s)
-----------------------------------
Monitor point ( iout  jout )
.........................
56       56
-----------------------
Number of steps per fuelleft.dat output
.......................
300
-----------------------------------------------------------
Conduction mode:                1 = 1D conduction
(default=2)                     2 = 3D near flame front only
                                3 = 3D conduction at all points

Method:                         0 = implicit in z-direction
(default=0)                     1 = explicit everywhere

Upwind Differencing:0 = no
(default=0)                     1 = yes
.....................................................
3        <=  mode
0        <=  method
1        <=  upwind
-----------------------------------
flame initiation: region bounded by rectangle iigmin,iigmax,jigmin,jigmax
shape: 0 = rectangle, 1 = ellipse inscribed in rectangle
zmin     zmax        ymin       ymax       <==  nwallslb = 1 or 2
xmin     xmax        zmin       zmax       <==  nwallslb = 3 or 4
xmin     xmax        ymin       ymax       <==  nwallslb = 5 or 6
.............................................................
1.765   1.835   1.165   1.235
1          <=shape
```

SPREAD.F

```
c=======================================================================
c
c                    Flame Spread Subroutine
c                (C) 1996,1997  Anthony Fernando
c
c========1=========2=========3=========4=========5=========6==========72


      subroutine SPREADINIT(tempf,tnew,fuelmass,pyro,ignitef,deltaz,
     >    znode,smssrt,nfuelport,nfuelrad,mfports,mftot,mcell,
     >    statnew,stat17,unsteady)

      include 'dimens.inc'
      include 'files.inc'
      include 'spread.inc'
      include 'radgrid.inc'
      include 'gridcom.inc'
      include 'params.inc'
      include 'fuel.inc'

     dimension tempf(ifuel,jfuel,0:kfuel),tnew(ifuel,jfuel,0:kfuel),
     >     fuelmass(ifuel,jfuel),pyro(ifuel,jfuel),deltaz(kfuel),
     >     znode(0:kfuel),smssrt(maxplane)
      integer ignitef(ifuel,jfuel),nfuelport(ifuel,jfuel),
     >     nfuelrad(ifuel,jfuel,4),mfports(maxplane,3),
     >     mcell(0:nir+1,0:njr+1,0:nkr+1)
      complex statnew(ifuel*jfuel),stat17(ifuel*jfuel)
      logical pilot,burntout,unsteady

      open(unit=inspread, file='spread.in', status='old')
c---------read in fuel depths------
      call findmoredots
      read (inspread,*,err=666) (deltaz(i),i=1,kfuel)
c---------read in fuel properties-----
      call findmoredots
      read (inspread,*) density
      read (inspread,*) conduct
      read (inspread,*) capacity
      read (inspread,*) emiss
      read (inspread,*) elogf
      call findmoredots
      read (inspread,*) pyrotemp
      read (inspread,*) pilottemp
      read (inspread,*) autotemp
      call findmoredots
      read (inspread,*) hvol
      read (inspread,*) xiflame
      read (inspread,*) preexpf
      read (inspread,*) actenergyf
      call findmoredots
      read (inspread,*) preheat

c---------------output parameters----------
      call findmoredots
      read (inspread,*) iout,jout
      call findmoredots
      read (inspread,*) lsteps

c----------------calculation method----------
      call findmoredots
      read (inspread,*) mode3d
      read (inspread,*) method
      read (inspread,*) modeup
```

```
        zt=0.
        znode(0)=fuelz
        do 20 i=1,kfuel
        zt=zt+deltaz(i)
        znode(i)=fuelz-zt
20      continue
        if(abs(1-(fuelz/zt)).gt.0.001)then
          write(*,*)'grid entered incorrectly'
          stop
        endif

        alphaf=conduct/(density*capacity)
        cellm=grid**2.*fuelz*density

        print*,'fuelleft.dat will be written to every ',
     >     lsteps*tstep,' seconds'
        burntime=0.
        pilot=.true.
        burntout=.false.
        lft=0
c-----------------------------------------------------------------------
c       Initialise dimensional variables
c-----------------------------------------------------------------------

        do 50 i=1,ifuel
        do 50 j=1,jfuel

        ignitef(i,j)=0
        fuelmass(i,j)=cellm
        pyro(i,j)=0.

        do 50 k=0,kfuel

        tempf(i,j,k)=Tambnt
        tnew(i,j,k)=Tambnt

50      continue

c-----------------------------------------------------------------------
c       assign fuel cells to port cells
c-----------------------------------------------------------------------

        if(nwallslb.eq.1)then
         call RECTPORT(nwallslb,1,xfmax,yfmin,zfmin,xfmax,yfmax,zfmax,
     >    mfports,mftot,x,y,z,xu,yv,zw,ni,nj,nk,iregn,iport)
        elseif(nwallslb.eq.2)then
         call RECTPORT(nwallslb,1,xfmin,yfmin,zfmin,xfmin,yfmax,zfmax,
     >    mfports,mftot,x,y,z,xu,yv,zw,ni,nj,nk,iregn,iport)
        elseif(nwallslb.eq.3)then
         call RECTPORT(nwallslb,1,xfmin,yfmax,zfmin,xfmax,yfmax,zfmax,
     >    mfports,mftot,x,y,z,xu,yv,zw,ni,nj,nk,iregn,iport)
        elseif(nwallslb.eq.4)then
         call RECTPORT(nwallslb,1,xfmin,yfmin,zfmin,xfmax,yfmin,zfmax,
     >    mfports,mftot,x,y,z,xu,yv,zw,ni,nj,nk,iregn,iport)
        elseif(nwallslb.eq.5)then
         call RECTPORT(nwallslb,1,xfmin,yfmin,zfmax,xfmax,yfmax,zfmax,
     >    mfports,mftot,x,y,z,xu,yv,zw,ni,nj,nk,iregn,iport)
        elseif(nwallslb.eq.6)then
         call RECTPORT(nwallslb,1,xfmin,yfmin,zfmin,xfmax,yfmax,zfmin,
     >    mfports,mftot,x,y,z,xu,yv,zw,ni,nj,nk,iregn,iport)
        else
          print*,'incorrect value for nwallslb ',nwallslb
          stop
        endif

        do 60 n=1,mftot
          smssrt(n)=0.
          ic=mfports(n,1)
          jc=mfports(n,2)
```

```
          kc=mfports(n,3)
          if((nwallslb.eq.1).or.(nwallslb.eq.2))then
            ifmin=int((zw(kc-1)-zfmin)/grid)
            ifmax=int((zw(kc)-zfmin)/grid)
            jfmin=int((yv(jc-1)-yfmin)/grid)
            jfmax=int((yv(jc)-yfmin)/grid)
          elseif((nwallslb.eq.3).or.(nwallslb.eq.4))then
            jfmin=int((zw(kc-1)-zfmin)/grid)
            jfmax=int((zw(kc)-zfmin)/grid)
            ifmin=int((xu(ic-1)-xfmin)/grid)
            ifmax=int((xu(ic)-xfmin)/grid)
          elseif((nwallslb.eq.5).or.(nwallslb.eq.6))then
            ifmin=int((xu(ic-1)-xfmin)/grid)
            ifmax=int((xu(ic)-xfmin)/grid)
            jfmin=int((yv(jc-1)-yfmin)/grid)
            jfmax=int((yv(jc)-yfmin)/grid)
          endif
        do 60 i=ifmin,ifmax
        do 60 j=jfmin,jfmax
          nfuelport(i,j)=n
60      continue

c-----------------------------------------------------------------------
c       assign cells to radiation grid
c-----------------------------------------------------------------------

        if((nwallslb.eq.1).or.(nwallslb.eq.3).or.(nwallslb.eq.5))
     >  then
          iup=0
        else
          iup=1
        endif

        do 70 i=1,ifuel
        do 70 j=1,jfuel
          if((nwallslb.eq.1).or.(nwallslb.eq.2))then
            if(nwallslb.eq.1)then
              xf=xfmax
            else
              xf=xfmin
            endif
            yf=yfmin+(j-0.5)*grid
            zf=zfmin+(i-0.5)*grid

            call RCELL(ir,xf,iup,xvr,nir)
            call PCELL(jr,yf,yvr,njr,0)
            jr=jr-1
            call PCELL(kr,zf,zvr,nkr,0)
            kr=kr-1
            call RCELL(mr,yf,1,yvr,njr)
            call RCELL(nr,zf,1,zvr,nkr)

            if(mr.eq.jr)then
              jp=0
            else
              jp=1
            endif

            if(nr.eq.kr)then
              kp=0
            else
              kp=1
            endif

            ma=mcell(ir,jr-1+jp,kr-1+kp)
            mb=mcell(ir,jr-1+jp,kr+kp)
            mc=mcell(ir,jr+jp,kr-1+kp)
            md=mcell(ir,jr+jp,kr+kp)
```

```
elseif((nwallslb.eq.3).or.(nwallslb.eq.4))then
  if(nwallslb.eq.3)then
    yf=yfmax
  else
    yf=yfmin
  endif
  xf=xfmin+(i-0.5)*grid
  zf=zfmin+(j-0.5)*grid

  call PCELL(ir,xf,xvr,nir,0)
  ir=ir-1
  call RCELL(jr,yf,iup,yvr,njr)
  call PCELL(kr,zf,zvr,nkr,0)
  kr=kr-1
  call RCELL(lr,xf,1,xvr,nir)
  call RCELL(nr,zf,1,zvr,nkr)

  if(lr.eq.ir)then
    ip=0
  else
    ip=1
  endif

  if(nr.eq.kr)then
    kp=0
  else
    kp=1
  endif

  ma=mcell(ir-1+ip,jr,kr-1+kp)
  mb=mcell(ir+ip,jr,kr-1+kp)
  mc=mcell(ir-1+ip,jr,kr+kp)
  md=mcell(ir+ip,jr,kr+kp)

elseif((nwallslb.eq.5).or.(nwallslb.eq.6))then
  if(nwallslb.eq.5)then
    zf=zfmax
  else
    zf=zfmin
  endif
  xf=xfmin+(i-0.5)*grid
  yf=yfmin+(j-0.5)*grid

  call PCELL(ir,xf,xvr,nir,0)
  ir=ir-1
  call PCELL(jr,yf,yvr,njr,0)
  jr=jr-1
  call RCELL(kr,zf,iup,zvr,nkr)
  call RCELL(lr,xf,1,xvr,nir)
  call RCELL(mr,yf,1,yvr,njr)

  if(mr.eq.jr)then
    jp=0
  else
    jp=1
  endif

  if(ir.eq.lr)then
    ip=0
  else
    ip=1
  endif

  ma=mcell(ir-1+ip,jr-1+jp,kr)
  mb=mcell(ir+ip,jr-1+jp,kr)
  mc=mcell(ir-1+ip,jr+jp,kr)
  md=mcell(ir+ip,jr+jp,kr)

endif
```

```
      if((ma.le.0).and.(mb.le.0).and.(mc.le.0).and.(md.le.0))then
        print*,'fuel cell does not coincide with rad grid',
     >    xf,yf,zf
        stop
      endif

      nfuelrad(i,j,1)=ma
      nfuelrad(i,j,2)=mb
      nfuelrad(i,j,3)=mc
      nfuelrad(i,j,4)=md

70    continue

      if(.not.unsteady)then
        call fstart(ignitef,statnew,stat17)
        do 111 n=1,ntotnew
          i=real(statnew(n))
          j=aimag(statnew(n))
          ignitef(i,j)=1
111     continue
        ratemin=preexpf*exp(-actenergyf/(unigas*autotemp))*grid**2.
        totalmass=ntotnew*ratemin
        print*,'Initial mass flow rate (kg/s) ',totalmass
        print*,'Initial heat release rate (kW)',totalmass*coalspecen
      endif

      return

666   print*,'error reading spread data'
      stop
      end

c=======================================================================

      subroutine findmoredots
      include 'files.inc'

      character*7 chr,spec
      data spec/'.......'/

12    read (inspread,'(3x,a7)',end=13) chr
      if (chr.ne.spec) goto 12
      return

13    write(*,*)'string not found',spec
      stop
      end

c=======================================================================

      subroutine SPREAD(tempf,tnew,fuelmass,pyro,ignitef,deltaz,
     >    znode,znold,znnew,statnew,stat17,aimp,bimp,cimp,dimp,
     >    nfuelport,nfuelrad,smssrt,mftot,mfports,
     >    f,g,h,tflow,u,v,w,te,smap,shp,sup,svp,swp,den,
     <      vo2,visclam,cellptemp,partconc,qfp,deltime,time,totmass,
     <   totgasrel,ptogasenth,mcell,fuelend,unsteady,flashover)

      include 'dimens.inc'
      include 'gridcom.inc'
      include 'locdim.inc'
      include 'fluids.inc'
      include 'fuel.inc'
      include 'params.inc'
      include 'radgrid.inc'
      include 'spread.inc'

     dimension u(ijkp2), v(ijkp2), w(ijkp2), shp(ijkp2), smap(ijkp2)
     dimension sup(ijkp2),svp(ijkp2),swp(ijkp2),cellptemp(ijkp2),
```

```
     <          partconc(ijkp2)

      dimension  qfp(ncdim),
     > f(id1:id2,jd1:jd2,kd1:kd2),te(id1:id2,jd1:jd2,kd1:kd2),
     > g(id1:id2,jd1:jd2,kd1:kd2),den(id1:id2,jd1:jd2,kd1:kd2),
     > tflow(id1:id2,jd1:jd2,kd1:kd2),visclam(id1:id2,jd1:jd2,kd1:kd2),
     > h(id1:id2,jd1:jd2,kd1:kd2),mcell(0:nir+1,0:njr+1,0:nkr+1),
     > vo2(id1:id2,jd1:jd2,kd1:kd2)

c     integer*2 block(id1:id2,jd1:jd2,kd1:kd2)
      integer mfports(maxplane,3)
      logical fuelend,unsteady,flashover

         dimension tempf(ifuel,jfuel,0:kfuel),tnew(ifuel,jfuel,0:kfuel),
     >        fuelmass(ifuel,jfuel),pyro(ifuel,jfuel),smssrt(maxplane)
         integer ignitef(ifuel,jfuel),nfuelport(ifuel,jfuel),
     >        nfuelrad(ifuel,jfuel,4)
         dimension deltaz(kfuel),znode(0:kfuel),znold(0:kfuel),
     >       znnew(0:kfuel),aimp(kfuel),bimp(kfuel),cimp(kfuel),
     >       dimp(kfuel)
         complex statnew(ifuel*jfuel),stat17(ifuel*jfuel)
         logical pilot,burntout

c        save timeend

c-----------------------------------------------------------------------
c       Main iteration loop
c-----------------------------------------------------------------------

c-------steady state-------------------------------------------------

         if(.not.unsteady)then
           do 20 i=iigmin,iigmax
           do 20 j=jigmin,jigmax
             smssrt(nfuelport(i,j))=0.
20         continue

c          ratemin=preexpf*exp(-actenergyf/(unigas*autotemp))*grid**2.

         call surfacebal(ignitef,tempf,deltaz,pyro,tnew,
     >        statnew,stat17,fuelmass,tflow,qfp,nfuelrad,nfuelport,
     >       h,den,visclam,te,vo2,mfports,mftot,unsteady)

           do 30 i=iigmin,iigmax
           do 30 j=jigmin,jigmax
             if(ignitef(i,j).eq.1)then
             smssrt(nfuelport(i,j))=smssrt(nfuelport(i,j))+pyro(i,j)
             endif
30         continue

           call BRNSLB(u,v,w,tflow,sup,svp,swp,smap,shp,cellptemp,
     <          partconc,smssrt,totgasrel,ptogasenth,mftot,mfports)
           goto 999
         endif

c-----------------------------------------------------------------------

10       ntotnew=0

         if((time.ge.preheat).and.pilot) then
           pilot=.false.
           call fstart(ignitef,statnew,stat17)
         endif

         call surfacebal(ignitef,tempf,deltaz,pyro,tnew,
     >        statnew,stat17,fuelmass,tflow,qfp,nfuelrad,nfuelport,
     >       h,den,visclam,te,vo2,mfports,mftot,unsteady)

         call bodybal(tempf,deltaz,znode,fuelmass,tnew,statnew,stat17,
```

```
     >       ignitef,aimp,bimp,cimp,dimp)

        call firegrowth(ignitef,tnew,statnew,stat17)

        if(ntotnew.eq.0)goto 80
        do 70 n=1,ntotnew
        i=real(statnew(n))
        j=aimag(statnew(n))
        ignitef(i,j)=1
        write(30,*),i,j,time
70      continue

80      call massloss(ignitef,pyro,fuelmass,totalmass,totalpyro,
     >          znode,deltaz,tempf,tnew,znold,znnew,
     >           nfuelport,smssrt,mftot,time)

        call BRNSLB(u,v,w,tflow,sup,svp,swp,smap,shp,cellptemp,
     <   partconc,smssrt,totgasrel,ptogasenth,mftot,mfports)

        areaig=0.
        do 90 i=1,ifuel
        do 90 j=1,jfuel
        if(iabs(ignitef(i,j)).eq.1)then
          areaig=areaig+grid**2.
        endif
90      continue

        write(29,'(1x,f7.3,1x,f9.6,1x,
     >                      f9.6,1x,f5.4,1x,i2)'),
     >    time,areaig,totalmass,
     >    fuelmass(iout,jout)/cellm,
     >    ignitef(iout,jout)
        print'(1x,f6.2,1x,f6.3,1x,f6.3,1x,f5.4,1x,i2)',
     >    time,areaig,totalmass,
     >    fuelmass(iout,jout)/cellm,
     >    ignitef(iout,jout)

        write(28,'(11(1x,f8.2))'),(tempf(iout,jout,k),k=0,kfuel)
c       print'(11(1x,f8.2))',(tempf(iout,jout,k),k=0,kfuel)

        if(burntout)goto 999
        if(totalmass.le.0.0)then
          print*,'fuel consumed after ',burntime,' seconds of burning'
          burntout=.true.
          goto 999
        elseif((totalpyro.le.0.).and.(.not.pilot).and.
     >       (burntime.gt.0.))then
          print*,'burnt out without spreading further after',
     >     burntime,' seconds of burning'
          burntout=.true.
          goto 999
        endif
        lft=lft+1
        if(lft.eq.lsteps)then
          lft=0
          print*,'Writing to fuelleft.out'
          do 100 i=1,ifuel
            write(27,'(500(1x,f5.3))'),(fuelmass(i,j)/cellm,j=1,jfuel)
100       continue
          write(27,*),' '
        endif
        if(.not.pilot)burntime=burntime+tstep

999     return
        end

c=======================================================================

        subroutine bodybal(t,dz,znode,fuelm,tnew,statnew,stat17,
```

```
     >    ignitef,a,b,c,d)

          include 'spread.inc'
          include 'params.inc'

          dimension t(ifuel,jfuel,0:kfuel),tnew(ifuel,jfuel,0:kfuel)
          dimension dz(kfuel),znode(0:kfuel)
          dimension fuelm(ifuel,jfuel)
          dimension a(kfuel),b(kfuel),c(kfuel),d(kfuel)

          integer ignitef(ifuel,jfuel)

c         double precision dfdx,d2tdxi2,d2fdx2,d2tdxidzeta,dfdy,
c    >     d2tdeta2,d2fdy2,d2tdetadzeta,dtdzeta,d2tdzeta2,
c    >     dtdzetapos,dtdzetaneg,d2tdx2,d2tdy2,dtdt

          complex statnew(ifuel*jfuel),stat17(ifuel*jfuel)

          logical threed,listed

          do 100 i=1,ifuel
          do 100 j=1,jfuel

          frac=fuelm(i,j)/cellm
          f=frac*znode(0)

          if(frac.le.(0.001))then
            do 111 k=1,kfuel
            tnew(i,j,k)=tnew(i,j,0)
111         continue
            goto 100
          endif

          if(mode3d.eq.1)then
            threed=.false.
            goto 19
          elseif(mode3d.eq.3)then
            threed=.true.
            goto 19
          else
            threed=.false.
          endif

          listed=.false.

          if(ntot17.eq.0)goto 15
          kount=0
10        kount=kount+1
          if(kount.gt.ntot17)goto 15
          front=abs(i-real(stat17(kount)))+abs(j-aimag(stat17(kount)))
          if(front.le.2.)then
            listed=.true.
            goto 18
          endif
          goto 10

15        if(ntotnew.eq.0)goto 18
          kount=0
16        kount=kount+1
          if(kount.gt.ntotnew)goto 18
          front=abs(i-real(statnew(kount)))+abs(j-aimag(statnew(kount)))
          if(front.le.2.)then
            listed=.true.
            goto 18
          endif
          goto 16

18        if(listed)threed=.true.
```

```
19      do 90 k=1,kfuel-1


        if(.not.threed)goto 20

c---------- i direction ------------------------------------

c---------- i = 1  ----------------------------------

        if(i.eq.1)then
          if(ignitef(i+1,j).eq.-1)then
            d2tdxi2=0.
            d2tdxidzeta=0.
          else
            d2tdxi2=(t(i+1,j,k)-t(i,j,k))/grid**2.
            if(k.eq.kfuel)then
              d2tdxidzeta=0.
            else
              d2tdxidzeta=
     >         (t(i+1,j,k+1)-t(i,j,k+1)-t(i+1,j,k-1)+t(i,j,k-1))
     >           *znode(0)/(grid*(dz(k)+dz(k+1)))
            endif
          endif
c         dfdx=(4.*fuelm(i+1,j)-3.*fuelm(i,j)-fuelm(i+2,j))
c    >           *znode(0)/(2.*cellm*grid)
          dfdx=znode(0)*(fuelm(i+1,j)-fuelm(i,j))/(cellm*grid)
c         d2fdx2=(2.*fuelm(i,j)-4.*fuelm(i+1,j)+2.*fuelm(i+2,j))
c    >           *znode(0)/(3.*cellm*grid**2.)
          d2fdx2=znode(0)*(fuelm(i+1,j)-fuelm(i,j))/(cellm*grid**2.)

c--------- i = ifuel  ----------------------

        elseif(i.eq.ifuel)then
          if(ignitef(i-1,j).eq.-1)then
            d2tdxi=0.
            d2tdxidzeta=0.
          else
            d2tdxi2=(t(i-1,j,k)-t(i,j,k))/grid**2.
            if(k.eq.kfuel)then
              d2tdxidzeta=0.
            else
              d2tdxidzeta=
     >         (t(i,j,k+1)-t(i-1,j,k+1)-t(i,j,k-1)+t(i-1,j,k-1))
     >           *znode(0)/(grid*(dz(k)+dz(k+1)))
            endif
          endif
c         dfdx=(4.*fuelm(i-1,j)-3.*fuelm(i,j)-fuelm(i-2,j))
c    >           *znode(0)/(2.*cellm*grid)
          dfdx=znode(0)*(fuelm(i-1,j)-fuelm(i,j))/(cellm*grid)
c         d2fdx2=(2.*fuelm(i,j)-4.*fuelm(i-1,j)+2.*fuelm(i-2,j))
c    >           *znode(0)/(3.*cellm*grid**2.)
          d2fdx2=znode(0)*(fuelm(i-1,j)-fuelm(i,j))/(cellm*grid**2.)

c------- generic i ---------------------------

        else
          if(ignitef(i-1,j).eq.-1)then
            dleft=0.
          else
            dleft=1.
          endif
          if(ignitef(i+1,j).eq.-1)then
            dright=0.
          else
            dright=1.
          endif

          d2tdxi2=(dleft*(t(i-1,j,k)-t(i,j,k))+dright*
     >                        (t(i+1,j,k)-t(i,j,k)))/grid**2.
```

```
          if(k.eq.kfuel)then
            d2tdxidzeta=0.
          else
            d2tdxidzeta=
     >     (dright*(t(i+1,j,k+1)-t(i,j,k+1)-t(i+1,j,k-1)+t(i,j,k-1))
     >    +dleft*(t(i-1,j,k-1)-t(i,j,k-1)-t(i-1,j,k+1)+t(i,j,k+1)))
     >          *znode(0)/(grid*(dz(k)+dz(k+1)))
            if((dleft.eq.1.).and.(dright.eq.1.))then
              d2tdxidzeta=d2tdxidzeta/2.
            endif
          endif
          dfdx=(fuelm(i+1,j)-fuelm(i-1,j))*znode(0)/(2.*cellm*grid)
          d2fdx2=(fuelm(i+1,j)+fuelm(i-1,j)-2.*fuelm(i,j))*znode(0)
     >       /(cellm*grid**2.)
        endif

c------------- j direction -------------------------

c------------- j = 1  ------------------------

        if(j.eq.1)then
          if(ignitef(i,j+1).eq.-1)then
            d2tdeta2=0.
            d2tdetadzeta=0.
          else
            d2tdeta2=(t(i,j+1,k)-t(i,j,k))/grid**2.
            if(k.eq.kfuel)then
              d2tdetadzeta=0.
            else
              d2tdetadzeta=
     >         (t(i,j+1,k+1)-t(i,j,k+1)-t(i,j+1,k-1)+t(i,j,k-1))
     >             *znode(0)/(grid*(dz(k)+dz(k+1)))
            endif
          endif
c         dfdy=(4.*fuelm(i,j+1)-3.*fuelm(i,j)-fuelm(i,j+2))
c    >          *znode(0)/(2.*cellm*grid)
          dfdy=znode(0)*(fuelm(i,j+1)-fuelm(i,j))/(cellm*grid)
c         d2fdy2=(2.*fuelm(i,j)-4.*fuelm(i,j+1)+2.*fuelm(i,j+2))
c    >          *znode(0)/(3.*cellm*grid**2.)
          d2fdy2=znode(0)*(fuelm(i,j+1)-fuelm(i,j))/(cellm*grid**2.)

c--------- j = jfuel  --------------------

        elseif(j.eq.jfuel)then
          if(ignitef(i,j-1).eq.-1)then
            d2tdeta2=0.
            d2tdetadzeta=0.
          else
            d2tdeta2=(t(i,j-1,k)-t(i,j,k))/grid**2.
            if(k.eq.kfuel)then
              d2tdetadzeta=0.
            else
              d2tdetadzeta=
     >         (t(i,j,k+1)-t(i,j-1,k+1)-t(i,j,k-1)+t(i,j-1,k-1))
     >             *znode(0)/(grid*(dz(k)+dz(k+1)))
            endif
          endif
c         dfdy=(4.*fuelm(i,j-1)-3.*fuelm(i,j)-fuelm(i,j-2))
c    >          *znode(0)/(2.*cellm*grid)
          dfdy=znode(0)*(fuelm(i,j-1)-fuelm(i,j))/(cellm*grid)
c         d2fdy2=(2.*fuelm(i,j)-4.*fuelm(i,j-1)+2.*fuelm(i,j-2))
c    >          *znode(0)/(3.*cellm*grid**2.)
          d2fdy2=znode(0)*(fuelm(i,j-1)-fuelm(i,j))/(cellm*grid**2.)

c--------- generic j --------------

        else
          if(ignitef(i,j-1).eq.-1)then
```

```
          dleft=0.
        else
          dleft=1.
        endif
        if(ignitef(i,j+1).eq.-1)then
          dright=0.
        else
          dright=1.
        endif

        d2tdeta2=(dleft*(t(i,j-1,k)-t(i,j,k))+dright*
     >                        (t(i,j+1,k)-t(i,j,k)))/grid**2.

        if(k.eq.kfuel)then
          d2tdetadzeta=0.
        else
          d2tdetadzeta=
     >    (dright*(t(i,j+1,k+1)-t(i,j,k+1)-t(i,j+1,k-1)+t(i,j,k-1))
     >   +dleft*(t(i,j-1,k-1)-t(i,j,k-1)-t(i,j-1,k+1)+t(i,j,k+1)))
     >         *znode(0)/(grid*(dz(k)+dz(k+1)))
          if((dleft.eq.1.).and.(dright.eq.1.))then
            d2tdetadzeta=d2tdetadzeta/2.
          endif
        endif
        dfdy=(fuelm(i,j+1)-fuelm(i,j-1))*znode(0)/(2.*cellm*grid)
        d2fdy2=(fuelm(i,j+1)+fuelm(i,j-1)-2.*fuelm(i,j))*znode(0)
     >        /(cellm*grid**2.)
      endif

      dkx = d2tdxi2 - 2.*znode(k)*frac*dfdx*d2tdxidzeta/f**2.
      dky = d2tdeta2 - 2.*znode(k)*frac*dfdy*d2tdetadzeta/f**2.

20    if(method.eq.1)then

c---------begin--explicit--method---------

        if(k.eq.kfuel)then
          dtdzeta=(t(i,j,k)-t(i,j,k-1))*znode(0)/dz(k)
          d2tdzeta2=2.*(t(i,j,k-1)-t(i,j,k))*znode(0)**2.
     >      /dz(k)**2.
        else
          dtdzeta=(dz(k)**2.*t(i,j,k+1)+(dz(k+1)**2.-dz(k)**2.)
     >      *t(i,j,k)-dz(k+1)**2.*t(i,j,k-1))*znode(0)
     >      /(dz(k)*dz(k+1)*(dz(k)+dz(k+1)))
          dtdzetapos=(t(i,j,k)-t(i,j,k-1))*znode(0)/dz(k)
          dtdzetaneg=(t(i,j,k+1)-t(i,j,k))*znode(0)/dz(k+1)
          d2tdzeta2=2.*(dz(k)*t(i,j,k+1)-(dz(k)+dz(k+1))
     >      *t(i,j,k)+dz(k+1)*t(i,j,k-1))*znode(0)**2.
     >      /(dz(k)*dz(k+1)*(dz(k)+dz(k+1)))
        endif

c       if((i.eq.iout).and.(j.eq.jout).and.(k.eq.1))then
c         write(26,'(1x,e10.3,1x,e10.3,1x,e10.3,1x,e10.3,1x,e10.3,
c    >              1x,e10.3,1x,e10.3,1x,e10.3,1x,e10.3,1x,e10.3)'),
c    >               dfdx,d2tdxi2,d2fdx2,d2tdxidzeta,
c    >               dfdy,d2tdeta2,d2fdy2,d2tdetadzeta,
c    >               dtdzeta,d2tdzeta2
c         print'(1x,e10.3,1x,e10.3,1x,e10.3,1x,e10.3,1x,e10.3,
c    >              1x,e10.3,1x,e10.3,1x,e10.3,1x,e10.3,1x,e10.3)',
c    >               dfdx,d2tdxi2,d2fdx2,d2tdxidzeta,
c    >               dfdy,d2tdeta2,d2fdy2,d2tdetadzeta,
c    >               dtdzeta,d2tdzeta2
c       endif

        if(.not.threed)then
          d2tdx2=0.
          d2tdy2=0.
          goto 30
        endif
```

```
        fcx=(znode(k)*frac*(f*d2fdx2-2.*dfdx**2.)/f**3.)
        if(modeup.eq.1)then
          if(fcx.le.0.0)then
            dtdzeta=dtdzetaneg
          else
            dtdzeta=dtdzetapos
          endif
        endif
        d2tdx2 = dkx + (znode(k)*frac*dfdx/f**2.)**2.*d2tdzeta2 -
     >    fcx*dtdzeta

        fcy=(znode(k)*frac*(f*d2fdy2-2.*dfdy**2.)/f**3.)
        if(modeup.eq.1)then
          if(fcy.le.0.0)then
            dtdzeta=dtdzetaneg
          else
            dtdzeta=dtdzetapos
          endif
        endif
        d2tdy2 = dky + (znode(k)*frac*dfdy/f**2.)**2.*d2tdzeta2 -
     >    fcy*dtdzeta

30      dtdt = ( d2tdx2 + d2tdy2 + d2tdzeta2/f**2. ) * alphaf
        tnew(i,j,k) = t(i,j,k) + tstep * dtdt

        if((tnew(i,j,k).gt.tnew(i,j,0)).and.
     >                              (tnew(i,j,0).gt.Tambnt))then
          tnew(i,j,k)=tnew(i,j,0)
        endif

c------------end---explicit---method--------------
        else
c------------initialise--implicit--variables-------

        if(.not.threed)then
          big1=0.
          big2=0.
        else
          big1=znode(k)**2.*(dfdx**2.+dfdy**2.)/f**2.
          big2=znode(k)*(f*(d2fdx2+d2fdy2)-2.*(dfdx**2.+dfdy**2.))
     >          /(2.*f**2.)
        endif

c       if(k.eq.kfuel)then
c         a(k)=-2.*alphaf*tstep*(1./frac**2.+big1)/dz(k)**2.
c         b(k)=1.+2*alphaf*tstep*(1./frac**2.+big1)/dz(k)**2.
c         goto 99
c       endif

        if(modeup.eq.1)then
          if(big2.gt.0.)then
            ak=(dz(k+1)+dz(k))
            bk=dz(k+1)
            ck=0.
          else
            ak=0.
            bk=-dz(k)
            ck=-(dz(k)+dz(k+1))
          endif
        else
          ak=dz(k+1)
          bk=(dz(k+1)-dz(k))
          ck=-dz(k)
        endif

          a(k)=-2.*alphaf*tstep*(1./frac**2.+big1+ak
     >      *big2)/(dz(k)*(dz(k)+dz(k+1)))
          b(k)=1.+2.*alphaf*tstep*(1./frac**2.+big1+bk
```

```
     >       *big2)/(dz(k)*dz(k+1))
             c(k)=-2.*alphaf*tstep*(1./frac**2.+big1+ck
     >       *big2)/(dz(k+1)*(dz(k)+dz(k+1)))

99       d(k)=t(i,j,k) + alphaf*tstep*(dkx+dky)

c--------------end--implicit--initialisation------
         endif

90       continue

         if(method.eq.1)goto 100

c-------------calculate--temperatures--implicitly--------

         d(1)=d(1)-a(1)*tnew(i,j,0)
         d(kfuel-1)=d(kfuel-1)-c(kfuel-1)*tnew(i,j,kfuel)

         do 92 k=2,kfuel-1
           b(k)=b(k) - c(k-1)*a(k)/b(k-1)
           d(k)=d(k) - d(k-1)*a(k)/b(k-1)
92       continue

         tnew(i,j,kfuel-1)=d(kfuel-1)/b(kfuel-1)

         do 94 k=kfuel-2,1,-1
           tnew(i,j,k)=(d(k)-c(k)*tnew(i,j,k+1))/b(k)
94       continue

100      continue

         return
         end

c=======================================================================

         subroutine surfacebal(ignitef,t,dz,pyro,tnew,
     >       statnew,stat17,fuelm,tflow,qfp,nfuelrad,nfuelport,
     >       h,den,visclam,te,vo2,mfports,mftot,unsteady)

         include 'dimens.inc'
         include 'gridcom.inc'
         include 'locdim.inc'
         include 'fluids.inc'
         include 'radgrid.inc'
         include 'spread.inc'
         include 'params.inc'

         dimension t(ifuel,jfuel,0:kfuel),tnew(ifuel,jfuel,0:kfuel),
     >     tflow(id1:id2,jd1:jd2,kd1:kd2),qfp(ncdim),
     >     h(id1:id2,jd1:jd2,kd1:kd2),te(id1:id2,jd1:jd2,kd1:kd2),
     >     den(id1:id2,jd1:jd2,kd1:kd2),vo2(id1:id2,jd1:jd2,kd1:kd2),
     >     visclam(id1:id2,jd1:jd2,kd1:kd2)
         integer ignitef(ifuel,jfuel),nfuelrad(ifuel,jfuel,4),
     >     mfports(maxplane,3),nfuelport(ifuel,jfuel)
         dimension pyro(ifuel,jfuel),dz(kfuel),fuelm(ifuel,jfuel)
         complex statnew(ifuel*jfuel),stat17(ifuel*jfuel)

         double precision a,b,c,yn,zn
         logical unsteady

         epsil=1.0e-6

         iup=0
         jup=0
         kup=0
         if(nwallslb.eq.1)then
           ds=x(mfports(1,1)+1)-xu(mfports(1,1))
           iup=1
```

```
        elseif(nwallslb.eq.2)then
          ds=xu(mfports(1,1))-x(mfports(1,1))
          iup=-1
        elseif(nwallslb.eq.3)then
          ds=y(mfports(1,2)+1)-yv(mfports(1,2))
          jup=1
        elseif(nwallslb.eq.4)then
          ds=yv(mfports(1,2))-y(mfports(1,2))
          jup=-1
        elseif(nwallslb.eq.5)then
          ds=z(mfports(1,3)+1)-zw(mfports(1,3))
          kup=1
        elseif(nwallslb.eq.6)then
          ds=zw(mfports(1,3))-z(mfports(1,3))
          kup=-1
        endif

        do 120 i=1,ifuel
        do 120 j=1,jfuel

        ic=mfports(nfuelport(i,j),1)+iup
        jc=mfports(nfuelport(i,j),2)+jup
        kc=mfports(nfuelport(i,j),3)+kup

        if((ignitef(i,j).eq.-1).or.(fuelm(i,j).le.0))then
          do 77 k=0,kfuel
          tnew(i,j,k)=tflow(ic,jc,kc)
77        continue
          goto 120
        endif

        if((.not.unsteady).and.(ignitef(i,j).ne.1))goto 120


      if((nwallslb.eq.1).or.(nwallslb.eq.2))then
        zf=zfmin+(i-0.5)*grid
        yf=yfmin+(j-0.5)*grid
        call interpol(den,nwallslb,zf,yf,z,y,kc,jc,ic,denf)
        call interpol(te,nwallslb,zf,yf,z,y,kc,jc,ic,tef)
        call interpol(visclam,nwallslb,zf,yf,z,y,kc,jc,ic,visf)
        call interpol(tflow,nwallslb,zf,yf,z,y,kc,jc,ic,gastemp)
        call interpol(h,nwallslb,zf,yf,z,y,kc,jc,ic,hf)
c       call interpol(vo2,nwallslb,zf,yf,z,y,kc,jc,ic,vo2f)
      elseif((nwallslb.eq.3).or.(nwallslb.eq.4))then
        xf=xfmin+(i-0.5)*grid
        zf=zfmin+(j-0.5)*grid
        call interpol(den,nwallslb,xf,zf,x,z,ic,kc,jc,denf)
        call interpol(te,nwallslb,xf,zf,x,z,ic,kc,jc,tef)
        call interpol(visclam,nwallslb,xf,zf,x,z,ic,kc,jc,visf)
        call interpol(tflow,nwallslb,xf,zf,x,z,ic,kc,jc,gastemp)
        call interpol(h,nwallslb,xf,zf,x,z,ic,kc,jc,hf)
c       call interpol(vo2,nwallslb,xf,zf,x,z,ic,kc,jc,vo2f)
      elseif((nwallslb.eq.5).or.(nwallslb.eq.6))then
        xf=xfmin+(i-0.5)*grid
        yf=yfmin+(j-0.5)*grid
        call interpol(den,nwallslb,xf,yf,x,y,ic,jc,kc,denf)
        call interpol(te,nwallslb,xf,yf,x,y,ic,jc,kc,tef)
        call interpol(visclam,nwallslb,xf,yf,x,y,ic,jc,kc,visf)
        call interpol(tflow,nwallslb,xf,yf,x,y,ic,jc,kc,gastemp)
        call interpol(h,nwallslb,xf,yf,x,y,ic,jc,kc,hf)
c       call interpol(vo2,nwallslb,xf,yf,x,y,ic,jc,kc,vo2f)
      endif

c-----------------------------------------------
c    convective heat transfer coefficient
c-----------------------------------------------

        if(gastemp.lt.Tambnt)gastemp=Tambnt
        if(tef.le.0)tef=0.
```

```
        if(visf.eq.0.)then
          gamth=0.
          goto 22
        endif

        dk=denf*sqrt(tef)
        dlplus = dk*ds*cmu25/visf
        if (dlplus.le.11.63)then
          gamth = visf/prlam
        else
          gamth = dk*capc/(prh*alog(elogf*dlplus))
        endif
22      if(gastemp-298.15.eq.0.0)then
          hconv=0.
        else
          hconv=abs(gamth*hf/(gastemp-298.15))
        endif

c-------------------------------------------------------------
c       incident radiant heat flux
c-------------------------------------------------------------

        ma=nfuelrad(i,j,1)
        mb=nfuelrad(i,j,2)
        mc=nfuelrad(i,j,3)
        md=nfuelrad(i,j,4)

        if((ma.le.0).and.(mb.le.0).and.(mc.le.0))then
          q=qfp(md)
          goto 111
        elseif((ma.le.0).and.(mb.le.0).and.(md.le.0))then
          q=qfp(mc)
          goto 111
        elseif((ma.le.0).and.(mc.le.0).and.(md.le.0))then
          q=qfp(mb)
          goto 111
        elseif((mb.le.0).and.(mc.le.0).and.(md.le.0))then
          q=qfp(ma)
          goto 111
        endif

      if((nwallslb.eq.1).or.(nwallslb.eq.2))then
        if((ma.le.0).and.(mc.le.0))then
         q=((py(md)-yf)*qfp(mb)+(yf-py(mb))*qfp(md))/(py(md)-py(mb))
          goto 111
        elseif((ma.le.0).and.(mb.le.0))then
         q=((pz(md)-zf)*qfp(mc)+(zf-pz(mc))*qfp(md))/(pz(md)-pz(mc))
          goto 111
        elseif((mb.le.0).and.(md.le.0))then
         q=((py(mc)-yf)*qfp(ma)+(yf-py(ma))*qfp(mc))/(py(mc)-py(ma))
          goto 111
        elseif((mc.le.0).and.(md.le.0))then
         q=((pz(mb)-zf)*qfp(ma)+(zf-pz(ma))*qfp(mb))/(pz(mb)-pz(ma))
          goto 111
        else
          q=((pz(mb)-zf)*(py(mc)-yf)*qfp(ma)+
     >       (pz(mb)-zf)*(yf-py(ma))*qfp(mc)+
     >       (zf-pz(ma))*(py(mc)-yf)*qfp(mb)+
     >       (zf-pz(ma))*(yf-py(ma))*qfp(md))/
     >      ((pz(mb)-pz(ma))*(py(mc)-py(ma)))
          goto 111
        endif

       elseif((nwallslb.eq.3).or.(nwallslb.eq.4))then
        if((ma.le.0).and.(mc.le.0))then
         q=((pz(md)-zf)*qfp(mb)+(zf-pz(mb))*qfp(md))/(pz(md)-pz(mb))
          goto 111
        elseif((ma.le.0).and.(mb.le.0))then
         q=((px(md)-xf)*qfp(mc)+(xf-px(mc))*qfp(md))/(px(md)-px(mc))
```

```
          goto 111
        elseif((mb.le.0).and.(md.le.0))then
         q=((pz(mc)-zf)*qfp(ma)+(zf-pz(ma))*qfp(mc))/(pz(mc)-pz(ma))
          goto 111
        elseif((mc.le.0).and.(md.le.0))then
         q=((px(mb)-xf)*qfp(ma)+(xf-px(ma))*qfp(mb))/(px(mb)-px(ma))
          goto 111
        else
          q=((px(mb)-xf)*(pz(mc)-zf)*qfp(ma)+
     >       (px(mb)-xf)*(zf-pz(ma))*qfp(mc)+
     >       (xf-px(ma))*(pz(mc)-zf)*qfp(mb)+
     >       (xf-px(ma))*(zf-pz(ma))*qfp(md))/
     >      ((px(mb)-px(ma))*(pz(mc)-pz(ma)))
          goto 111
        endif

      elseif((nwallslb.eq.5).or.(nwallslb.eq.6))then
        if((ma.le.0).and.(mc.le.0))then
         q=((py(md)-yf)*qfp(mb)+(yf-py(mb))*qfp(md))/(py(md)-py(mb))
          goto 111
        elseif((ma.le.0).and.(mb.le.0))then
         q=((px(md)-xf)*qfp(mc)+(xf-px(mc))*qfp(md))/(px(md)-px(mc))
          goto 111
        elseif((mb.le.0).and.(md.le.0))then
         q=((py(mc)-yf)*qfp(ma)+(yf-py(ma))*qfp(mc))/(py(mc)-py(ma))
          goto 111
        elseif((mc.le.0).and.(md.le.0))then
         q=((px(mb)-xf)*qfp(ma)+(xf-px(ma))*qfp(mb))/(px(mb)-px(ma))
          goto 111
        else
          q=((px(mb)-xf)*(py(mc)-yf)*qfp(ma)+
     >       (px(mb)-xf)*(yf-py(ma))*qfp(mc)+
     >       (xf-px(ma))*(py(mc)-yf)*qfp(mb)+
     >       (xf-px(ma))*(yf-py(ma))*qfp(md))/
     >      ((px(mb)-px(ma))*(py(mc)-py(ma)))
          goto 111
        endif
        endif

c-------------------------------------------------------

111     a=emiss*stefboltz
c   convert kW to W
        q=q*1000.
        hconv=hconv*1000.

        if(ignitef(i,j).eq.1)then
          qmin=xiflame*.2095
          qf=emiss*q+hconv*(gastemp-t(i,j,0))
          if(qf.lt.qmin)then
            q=(qmin+hconv*(t(i,j,0)-gastemp))/emiss
          endif
        endif

c--------linear temperature profile conduction------------

c       b=hconv+(conduct*cellm/(fuelm(i,j)*dz(1)))
c       c=emiss*q+hconv*gastemp+(conduct*t(i,j,1)*cellm/
c    >             (fuelm(i,j)*dz(1)))

c---------parabolic temperature profile conduction--------

        if(unsteady)then
          b=hconv+(conduct*cellm/fuelm(i,j))*(2.*dz(1)+dz(2))/
     >             (dz(1)*(dz(1)+dz(2)))
          c=emiss*q+hconv*gastemp+(conduct*cellm/fuelm(i,j))
     >      *(t(i,j,1)*(dz(1)+dz(2))/(dz(1)*dz(2))-
     >        t(i,j,2)*dz(1)/(dz(2)*(dz(1)+dz(2))))
        else
```

```
          b=hconv+conduct/dz(1)
          c=emiss*q+hconv*gastemp+conduct*t(i,j,1)/dz(1)
        endif

c-------------------------------------------------------------

        yn=t(i,j,0)
        it=0
        if(yn.le.Tambnt)yn=Tambnt

10      if((yn.le.0).or.(yn.ge.2000))then
          print*,'warning: yn=',yn,' a,b,c =',a,b,c
          print*,'q,hconv,gastemp ',q,hconv,gastemp
          print*,'i,j,t0,t1,t2 ',i,j,t(i,j,0),t(i,j,1),t(i,j,2)
        endif
        zn=yn-(a*yn**4.+b*yn-c+preexpf*hvol*
     >     exp(-actenergyf/(unigas*yn)))/
     >      (4.*a*yn**3.+b+preexpf*hvol*actenergyf/(unigas*yn**2.)*
     >       exp(-actenergyf/(unigas*yn)))
        if(abs(zn-yn).ge.epsil)then
          yn=zn
          it=it+1
          if(it.le.30)then
            goto 10
          else
            tnew(i,j,0)=zn
            print*,'warning: surface temperature not converged ',i,j
          endif
        else
          tnew(i,j,0)=zn
        endif

        pyro(i,j)=grid**2.*tstep*preexpf*exp(-actenergyf
     >        /(unigas*tnew(i,j,0)))

c       a=(hconv+(conduct*cellm/(fuelm(i,j)*dz(1))))/(emiss*stefboltz)
c       b=(emiss*q+hconv*ambtemp+(conduct*t(i,j,1)*cellm/
c    >          (fuelm(i,j)*dz(1)))
c    >    -hvol*(pyro(i,j)/(tstep*grid**2.)) )/(emiss*stefboltz)
c       z=(27.*a**2.+sqrt(729.*a**4.+6912.*b**3.))**(1./3.)
c       y=-(2.**(7./3.)*b)/z + z/(3.*2.**(1./3.))
c       tnew(i,j,0)=(-sqrt(y)+sqrt(-y+2.*a/sqrt(y)))/2.

c------------opposite to burning surface losses---------------

        tnew(i,j,kfuel)=
     >    (conduct*t(i,j,kfuel-1)*cellm/(dz(kfuel)*fuelm(i,j)) +
     >     Clamda*Tambnt/wallthck) /
     >    (conduct*cellm/(dz(kfuel)*fuelm(i,j))+Clamda/wallthck)

        if(.not.unsteady)goto 120

        if((t(i,j,1).ge.autotemp).and.(ignitef(i,j).eq.0))then
          call checklist(i,j,ignitef,statnew,stat17)
        endif

120     continue

        return
        end

c=====================================================================

        subroutine interpol(phi,nwall,xf,yf,x,y,i,j,norm,phinter)

        include 'dimens.inc'
        include 'locdim.inc'

        dimension x(maxdim),y(maxdim)
```

```
      dimension phi(id1:id2,jd1:jd2,kd1:kd2)

      if(xf.gt.x(i))then
        i1=i
        i2=i+1
      else
        i1=i-1
        i2=i
      endif
      if(yf.gt.y(i))then
        j1=j
        j2=j+1
      else
        j1=j-1
        j2=j
      endif

      if((nwall.eq.1).or.(nwall.eq.2))then
        phinter=((x(i2)-xf)*(y(j2)-yf)*phi(norm,j1,i1)+
     >           (x(i2)-xf)*(yf-y(j1))*phi(norm,j2,i1)+
     >           (xf-x(i1))*(y(j2)-yf)*phi(norm,j1,i2)+
     >           (xf-x(i1))*(yf-y(j1))*phi(norm,j2,i2))/
     >           ((x(i2)-x(i1))*(y(j2)-y(j1)))
      elseif((nwall.eq.3).or.(nwall.eq.4))then
        phinter=((x(i2)-xf)*(y(j2)-yf)*phi(i1,norm,j1)+
     >           (x(i2)-xf)*(yf-y(j1))*phi(i1,norm,j2)+
     >           (xf-x(i1))*(y(j2)-yf)*phi(i2,norm,j1)+
     >           (xf-x(i1))*(yf-y(j1))*phi(i2,norm,j2))/
     >           ((x(i2)-x(i1))*(y(j2)-y(j1)))
      elseif((nwall.eq.5).or.(nwall.eq.6))then
        phinter=((x(i2)-xf)*(y(j2)-yf)*phi(i1,j1,norm)+
     >           (x(i2)-xf)*(yf-y(j1))*phi(i1,j2,norm)+
     >           (xf-x(i1))*(y(j2)-yf)*phi(i2,j1,norm)+
     >           (xf-x(i1))*(yf-y(j1))*phi(i2,j2,norm))/
     >           ((x(i2)-x(i1))*(y(j2)-y(j1)))
      endif

      return
      end

c=======================================================================

      subroutine firegrowth(ignitef,t,statnew,stat17)

      include 'spread.inc'

      integer ignitef(ifuel,jfuel)
      dimension t(ifuel,jfuel,0:kfuel)
      complex statnew(ifuel*jfuel),stat17(ifuel*jfuel)

      if(ntot17.le.0)goto 20

      m=1

11    i=real(stat17(m))
      j=aimag(stat17(m))
      if((t(i,j,1).lt.pilottemp).or.(t(i,j,1).ge.autotemp))then
        m=m+1
        goto 10
      endif
      call neighbors(ignitef,i,j,n,statnew,stat17)
      if(n.ge.3)then
        call checklist(i,j,ignitef,statnew,stat17)
      else
        m=m+1
      endif

10    if(m.le.ntot17)goto 11
```

```
20      return
        end

c=======================================================================

        subroutine checklist(i,j,ignitef,statnew,stat17)

        include 'spread.inc'

        integer ignitef(ifuel,jfuel)
        complex statnew(ifuel*jfuel),stat17(ifuel*jfuel)

        if((i.lt.1).or.(i.gt.ifuel).or.(j.lt.1).or.(j.gt.jfuel))then
          print*,
     >    'Warning: attempted to ignite cell outside region (skipped)'
          goto 999
        endif

        ntotnew=ntotnew+1
        statnew(ntotnew)=cmplx(i,j)

        if(ntot17.le.0)goto 20
        call remlist(ignitef,i,j,statnew,stat17)

20      do 10 l=-1,1
        do 11 m=-1,1

        if((l.eq.0).and.(m.eq.0))goto 11

        il=i+l
        jm=j+m

        if((il.eq.0).or.(il.eq.ifuel+1).or.(jm.eq.0).or.
     >    (jm.eq.jfuel+1))goto 11
        if(iabs(ignitef(il,jm)).eq.1)goto 11

        call neighbors(ignitef,il,jm,n,statnew,stat17)

        if(n.eq.0)then
          call addlist(ignitef,il,jm,statnew,stat17)
        elseif(n.ge.7)then
          call remlist(ignitef,il,jm,statnew,stat17)
          ntotnew=ntotnew+1
          statnew(ntotnew)=cmplx(il,jm)
        endif

11      continue
10      continue

999     return
        end

c=======================================================================

        subroutine neighbors(ignitef,i,j,n,statnew,stat17)

        include 'spread.inc'

        integer ignitef(ifuel,jfuel)
        complex statnew(ifuel*jfuel),stat17(ifuel*jfuel)

        n=0

        if(i.eq.1)goto 11
        if(j.eq.1)goto 13
        n=n+iabs(ignitef(i-1,j-1))
13      n=n+iabs(ignitef(i-1,j))
        if(j.eq.jfuel)goto 11
        n=n+iabs(ignitef(i-1,j+1))
```

```
11      if(j.eq.1)goto 14
        n=n+iabs(ignitef(i,j-1))
14      if(j.eq.jfuel)goto 10
        n=n+iabs(ignitef(i,j+1))
10      if(i.eq.ifuel)goto 20
        if(j.eq.1)goto 16
        n=n+iabs(ignitef(i+1,j-1))
16      n=n+iabs(ignitef(i+1,j))
        if(j.eq.jfuel)goto 20
        n=n+iabs(ignitef(i+1,j+1))

20      return
        end

c=======================================================================

        subroutine addlist(ignitef,i,j,statnew,stat17)

        include 'spread.inc'


        complex statnew(ifuel*jfuel),stat17(ifuel*jfuel)
        complex check
        logical listed

        check=cmplx(i,j)
        listed=.false.

        if(ntot17.eq.0)goto 11
        do 10 m=1,ntot17
        if(stat17(m).eq.check)then
          listed=.true.
        endif
10      continue

11      if(ntotnew.eq.0)goto 17
        do 15 m=1,ntotnew
        if(statnew(m).eq.check)then
          listed=.true.
        endif
15      continue

17      if (.not.listed) then
          ntot17=ntot17+1
          stat17(ntot17)=check
        endif

        return
        end

c=======================================================================

        subroutine remlist(ignitef,i,j,statnew,stat17)

        include 'spread.inc'

        complex statnew(ifuel*jfuel),stat17(ifuel*jfuel)
        complex check
        logical listed

        check=cmplx(i,j)
        listed=.true.

        do 10 m=1,ntot17
        if((listed).and.(stat17(m).eq.check))then
          listed=.false.
        endif

        if (.not.listed) then
```

```
          stat17(m)=stat17(m+1)
        endif

10      continue

        if (.not.listed) then
          stat17(ntot17)=cmplx(0.,0.)
          ntot17=ntot17-1
        endif

        return
        end

c=======================================================================

        subroutine massloss(ignitef,pyro,fuelmass,total,totalp,
     >       znode,deltaz,tf,tnew,znold,znnew,
     >           nfuelport,smssrt,mftot,time)

        include 'dimens.inc'
        include 'spread.inc'

        dimension pyro(ifuel,jfuel),fuelmass(ifuel,jfuel),
     >      tf(ifuel,jfuel,0:kfuel),tnew(ifuel,jfuel,0:kfuel),
     >      znode(0:kfuel),deltaz(kfuel),
     >      znold(0:kfuel),znnew(0:kfuel),
     >      smssrt(maxplane)
        integer ignitef(ifuel,jfuel),nfuelport(ifuel,jfuel)

        total=0.
        totalp=0.

        do 20 n=1,mftot
          smssrt(n)=0.
20      continue

        do 10 i=1,ifuel
        do 10 j=1,jfuel

        if(ignitef(i,j).eq.-1)goto 10

        tf(i,j,0)=tnew(i,j,0)
        tf(i,j,kfuel)=tnew(i,j,kfuel)

        do 11 n=0,kfuel
        znold(n)=fuelmass(i,j)*znode(n)/cellm
11      continue

        oldfuel=fuelmass(i,j)

        if(fuelmass(i,j).gt.pyro(i,j))then
          fuelmass(i,j)=fuelmass(i,j)-pyro(i,j)
        else
          pyro(i,j)=fuelmass(i,j)
          fuelmass(i,j)=0.
          ignitef(i,j)=-1
          write(35,*),i,j,time
        endif

        total=total+fuelmass(i,j)
        totalp=totalp+pyro(i,j)

        smssrt(nfuelport(i,j))=smssrt(nfuelport(i,j))
     >                                  +pyro(i,j)/tstep

        if(ignitef(i,j).eq.-1)then

          do 12 n=1,kfuel-1
          tf(i,j,n)=tnew(i,j,0)
```

```
12          continue

            pyro(i,j) = 0.0
            goto 10
          endif

          do 30 n=1,kfuel-1
          znnew(n)=fuelmass(i,j)*znode(n)/cellm
          do 30 k=n,kfuel-1
          if((znnew(n).le.znold(k)).and.(znnew(n).gt.znold(k+1)))then
          tf(i,j,n)=((znnew(n)-znold(k+1))*cellm/
     >           (oldfuel*deltaz(k+1)))*tnew(i,j,k)
     >           +((znold(k)-znnew(n))*cellm/
     >           (oldfuel*deltaz(k+1)))*tnew(i,j,k+1)
          endif

30        continue
10        continue

          return
          end

c=======================================================================

          subroutine fstart(ignitef,statnew,stat17)

          include 'spread.inc'
          include 'files.inc'

          integer ignitef(ifuel,jfuel)
          complex statnew(ifuel*jfuel),stat17(ifuel*jfuel)

          call findmoredots
          read(inspread,*) x1,x2,x3,x4
          read(inspread,*) ntype
          close(unit=inspread,status='keep')

          if(ntype.eq.1)then
            semii=(x2-x1)/2.
            centi=x1+semii
            semij=(x4-x3)/2.
            centj=x3+semij
          endif

          if((nwallslb.eq.1).or.(nwallslb.eq.2))then
            iigmin=(x1-zfmin)/grid+0.5
            iigmax=(x2-zfmin)/grid-0.5
            jigmin=(x3-yfmin)/grid+0.5
            jigmax=(x4-yfmin)/grid-0.5
          elseif((nwallslb.eq.3).or.(nwallslb.eq.4))then
            iigmin=(x1-xfmin)/grid+0.5
            iigmax=(x2-xfmin)/grid-0.5
            jigmin=(x3-zfmin)/grid+0.5
            jigmax=(x4-zfmin)/grid-0.5
          elseif((nwallslb.eq.5).or.(nwallslb.eq.6))then
            iigmin=(x1-xfmin)/grid+0.5
            iigmax=(x2-xfmin)/grid-0.5
            jigmin=(x3-yfmin)/grid+0.5
            jigmax=(x4-yfmin)/grid-0.5
          endif

          do 20 i=iigmin,iigmax
          do 20 j=jigmin,jigmax
            if(ntype.eq.1)then
              if((nwallslb.eq.1).or.(nwallslb.eq.2))then
                p=((i-0.5)*grid+zfmin-centi)**2./semii**2.
     >           +((j-0.5)*grid+yfmin-centj)**2./semij**2.
              elseif((nwallslb.eq.3).or.(nwallslb.eq.4))then
                p=((i-0.5)*grid+xfmin-centi)**2./semii**2.
```

```
     >          +((j-0.5)*grid+zfmin-centj)**2./semij**2.
              elseif((nwallslb.eq.5).or.(nwallslb.eq.6))then
                p=((i-0.5)*grid+xfmin-centi)**2./semii**2.
     >          +((j-0.5)*grid+yfmin-centj)**2./semij**2.
              endif
            endif
            if((ntype.eq.0).or.((ntype.eq.1).and.(p.le.1.)))then
              call checklist(i,j,ignitef,statnew,stat17)
              areaig=areaig+grid**2.
            endif
20        continue
          print*,'Initial area of ignited region (m^2) ',areaig

          return
          end

c=========================================================

      subroutine BRNSLB(u,v,w,t,sup,svp,swp,smap,shp,cellptemp,
     <    partconc,smssrt,totgasrel,ptogasenth,mftot,mfports)

      include 'dimens.inc'
      include 'gridcom.inc'
      include 'props.inc'
      include 'locdim.inc'
      include 'fuel.inc'
      include 'spread.inc'

      dimension smap(id1:id2,jd1:jd2,kd1:kd2),
     > shp(id1:id2,jd1:jd2,kd1:kd2),partconc(id1:id2,jd1:jd2,kd1:kd2),
     > sup(id1:id2,jd1:jd2,kd1:kd2),svp(id1:id2,jd1:jd2,kd1:kd2),
     > swp(id1:id2,jd1:jd2,kd1:kd2),cellptemp(id1:id2,jd1:jd2,kd1:kd2)

      dimension t(id1:id2,jd1:jd2,kd1:kd2),
     > u(id1:id2,jd1:jd2,kd1:kd2),v(id1:id2,jd1:jd2,kd1:kd2),
     > w(id1:id2,jd1:jd2,kd1:kd2),mfports(maxplane,3),smssrt(maxplane)

c     integer*2 block(id1:id2,jd1:jd2,kd1:kd2)

      call RELAX(sup,svp,swp,smap,shp,cellptemp,partconc)

        totgasrel = 0.0

        iup=0
        jup=0
        kup=0
        if(nwallslb.eq.1)then
        iup=1
        elseif(nwallslb.eq.2)then
        iup=-1
        elseif(nwallslb.eq.3)then
        jup=1
        elseif(nwallslb.eq.4)then
        jup=-1
        elseif(nwallslb.eq.5)then
        kup=1
        elseif(nwallslb.eq.6)then
        kup=-1
        endif

      do   200 n=1,mftot
      i = mfports(n,1)+iup
      j = mfports(n,2)+jup
      k = mfports(n,3)+kup

      qrates = smssrt(n)*(enth(1,5)*t(i,j,k)**2+enth(2,5)*t(i,j,k)
     <             + enth(3,5))
           shp(i,j,k)=shp(i,j,k) + qrates*urfshp
           smap(i,j,k)=smap(i,j,k) - smssrt(n)*urfsmap
```

```
200      continue

       ptogasenth = 0.

      do    111 k=1,nk
      do    111 j=1,nj
      do    111 i=1,ni
      totgasrel =totgasrel - smap(i,j,k)
      ptogasenth = ptogasenth + shp(i,j,k)
  111 continue
      do 112 k=1,nk
      do 112 j=1,nj
      do 112 i=1,ni
c     if(cellpnum(i,j,k).gt.0)then
c     cellptemp(i,j,k)=cellptemp(i,j,k)/partconc(i,j,k)
c     partconc(i,j,k)=partconc(i,j,k)/(sew(i)*sns(j)*sud(k))
c     else
      cellptemp(i,j,k)=t(i,j,k)
c     partconc(i,j,k)=0.0
c     endif
 112   continue

      return
      end
C=================================================================
```

SPREAD.INC

```
common/spreadconsts/ifuel,jfuel,kfuel,tstep,
     >    grid,cellm,fuelz,nwallslb,
     >    xfmin,xfmax,yfmin,yfmax,zfmin,zfmax,
     >    density,conduct,capacity,emiss,elogf,alphaf,
     >    pyrotemp,pilottemp,autotemp,
     >    hvol,xiflame,
     >    ntotnew,ntot17,
     >    preexpf,actenergyf,
     >    iout,jout,
     >    mode3d,method,modeup,
     >    burntime,pilot,lsteps,lft,burntout,
     >    iigmin,iigmax,jigmin,jigmax
```

Appendix C

A Numerical Model for Horizontal Flame Spread over Combustible Solid Fuels

Anthony Fernando and Graham Thorpe

Centre for Environmental Safety and Risk Engineering
Victoria University of Technology
Melbourne, Australia

ABSTRACT

A simplified numerical horizontal flame spread model for thermally thick fuels has been developed with the intention of being incorporated as a submodel of a larger Computational Fluid Dynamics (CFD) model, in order to make predictions of a burning fuel object in a full scale building fire. The model presented here is self contained, employing empirical models for the shape and size of the fire plume, and the combustion behaviour of the solid fuel in question.

The fuel surface is discretised on a regular rectilinear grid. Flame spread is determined by considering the ignition and combustion properties of each surface grid cell, with the spreading flame front modelled as a series of discrete ignitions. Physical factors considered in the model include surface temperature, flame heat radiation, three dimensional heat conduction within the solid, and mass loss from and subsequent regression of the fuel surface.

A series of full scale fire tests has been performed with slabs of standard polyurethane foam, and the flame diameter and rate of mass loss were measured. There is good agreement between the modelled and experimental results.

NOMENCLATURE

A	Preexponential constant (kg m^{-2}s^{-1})
c	Specific heat (J kg^{-1}K^{-1})
D	Distance from flame front (m)
E	Activation energy (J mol^{-1})
$F(x,y)$	Local depth of fuel (m)
h	Heat transfer coefficient (W m^{-2}K^{-1})
H	Flame height (m)
ΔH_c	Specific heat of combustion (J kg^{-1})
k	Conductivity (W m^{-1}K^{-1})
L_e	Mean beam length (m)
L_v	Latent heat of volatilisation (J kg^{-1})
$\dot{m}''$	Mass flux (kg m^{-2}s^{-1})
$\dot{q}''$	Heat flux (W m^{-2})
R_u	Universal gas constant (J mol^{-1}K^{-1})
R	Flame radius (m)
t	Time (s)
T_{gas}	Ambient gas temperature (K)
T_n	Temperature at nth fuel node (K)
v_{max}	Maximum flame velocity (m s^{-1})
Δx	Surface grid size (m)
Y_{O2}	Oxygen concentration fraction
Δz_n	nth fuel node separation distance (m)
x,y,z	Cartesian coordinates (m)
α	Thermal diffusivity (m^2 s^{-1})
ε	Emissivity
κ	Optical density (m^{-1})
ρ	Density (kg m^{-3})
σ	Stefan-Boltzmann constant (W m^{-2}K^{-4})
ϕ	Configuration factor of flame
χ	Flame heat constant (W m^{-2})
ξ,η,ζ	Transformed coordinates (m)

1. INTRODUCTION

The initiation and spread of fires in buildings is a serious threat to both life and property, and as such the investigation and understanding of the behaviour of building fires is an important avenue of research. The rate of release of heat from flammable materials has been identified as one of the most important factors that determine the hazard of a fire scenario (Babrauskas 1992). The heat release rate is itself dependent on other factors, in particular the combustion properties of the material, and the rate at which the material becomes involved

in combustion and contributes to the heat release, in other words, the flame spread rate.

Computer modelling is a valuable tool which may be used in the understanding of building fires as it is cheaper than full scale tests, and can potentially yield information about a wide variety of fire scenarios. In particular, Computational Fluid Dynamics (CFD) models are becoming increasingly widespread as a research tool (Galea, 1989) as high powered computers become cheaper and more readily accessible.

CFD modelling of full scale building fires has been a major aspect of the fire safety research at the Centre for Environmental Safety and Risk Engineering (CESARE), and a number of building fire scenarios have been successfully modelled in the past (Luo & Beck, 1994, 1996, Fernando & Luo, 1995). Current work is focusing on the problem of modelling flame spread and heat release.

Despite the increasing power of computers, CFD models still take considerable time to execute, some problems taking days to compute the solution. It is therefore practical that the developmental stage of the flame spread model be self contained, so that trial runs would not be burdened by the computation time required of CFD models. This paper describes the completed stand-alone spread model, and at the time of writing encoding in a CFD model is well under way.

The main aim to be met in the construction of the flame spread model is that it will be ultimately compatible with typical CFD models in existence. In keeping with the spirit of such models, the spread model should be based as much as possible on first principles. However, for the purposes of constructing a stand-alone model, certain empirical assumptions must be made. These assumptions will naturally not be required once incorporation of the spread model into a CFD model has been achieved.

In order for the flame spread model to be generally useful, the material properties used in the model must be experimentally available (Quintiere, 1994). This model follows the example of several other combustion and spread models (Quintiere 1994, Delichatsios et al 1991, Baroudi and Kokkala 1996, Tewarson 1994) in that the combustion behaviour is determined largely from bench scale tests, such as cone calorimetry and thermo-gravimetric analysis.

2. SPREAD MODEL

The fuel is taken to be a regular rectangular slab. Combustion, and subsequent release of mass is assumed to occur at one surface only (in this case, the upper surface.) The other surfaces are taken to be perfectly insulated in terms of both heat and mass loss. The flame spread is determined by considering the ignition and combustion properties of discrete elements on the fuel surface. Spread of flame therefore occurs as a series of discrete ignitions of fuel elements adjacent to the existing flame front.

Each element on the combustion surface is in one of three states; preheating, combusting, or burnt out. In the preheating stage, the element is heated remotely by radiation from the flame, and from external sources, with the amount of heat received dependent on the location of the point in question.

In the combusting stage, the element is assumed to receive a constant heat flux from the flame plus the external radiation. The rate of mass loss is given by the equation (Tewarson 1993)

$$\dot{m}'' = \frac{(\dot{q}''_{ext} + \dot{q}''_{flame} - \dot{q}''_{loss})}{L_v} \qquad (1)$$

where q_{ext} is the externally applied radiant flux, and q_{flame} is the sum of the radiative and convective components of heat transfer from the flame and q_{loss} the sum of heat losses under steady burning conditions. While steady burning seldom occurs under real fire conditions, this expression for the flame heat is nevertheless a useful one.

In the burnt out stage, the element is no longer a part of the calculation region, and neighbouring cells are treated as boundary cells.

2.1. Surface Node Temperature

The temperature at the surface is calculated by considering the heat flux balance at the surface. This balance takes into account radiant heat

flux to the surface both from the surroundings and directly from the flame, convective heat transfer to the surface, conduction of heat into the fuel, reradiation from the surface, and latent heat of vaporisation of the fuel. These factors are described below.

2.1.1. Conduction

The conduction heat flux at the surface is proportional to the temperature gradient at the surface. The gradient is approximated by a parabolic fit of the temperature of the surface node and the first two nodes below the surface. The conduction heat flux is therefore given by

$$\dot{q}''_{cond} = -k\left.\frac{\partial T}{\partial z}\right|_{z=0} = -k\frac{(T_1-T_0)(\Delta z_1+\Delta z_2)^2-(T_2-T_0)\Delta z_1^2}{\Delta z_1\Delta z_2(\Delta z_1+\Delta z_2)} \quad (2)$$

2.1.2 Convection

Convective heat transfer is a difficult phenomenon to model accurately. In this model, convective heating was modelled by the expression

$$\dot{q}''_{convect} = h(T_{gas} - T_0) \quad (3)$$

The heat transfer coefficient, h, is taken to be constant over the entire surface.

2.1.3. Heat of Volatilisation

The heat loss due to volatilisation of the solid fuel is given by the expression

$$\dot{q}'' = \dot{m}'' L_v \quad (4)$$

The mass flux of volatiles from the surface is assumed to obey the simple Arrhenius equation

$$\dot{m}'' = A\exp\left(\frac{-E}{R_u T_0}\right) \quad (5)$$

2.1.4. Radiation Heat Transfer

The re-radiant heat loss from the fuel is given by the expression

$$\dot{q}''_{rr} = \varepsilon\sigma T_0^4 \quad (6)$$

The radiant flux to the surface depends on whether the fuel element in question is undergoing combustion or not. If combustion is occurring, the flame radiant flux is given by

$$\dot{q}''_r = \chi Y_{O_2} + \dot{q}''_{ext} \quad (7)$$

If the fuel element is outside the flame region, then the flux to the surface is given by

$$\dot{q}''_r = \phi\sigma\varepsilon_{flame}T^4_{flame} + (1-\phi)\dot{q}''_{ext} \quad (8)$$

where ϕ is the view factor of the flame as seen from the surface element.

In calculating the view factor, it is a common practise to assume a cylindrical shape for the luminous portion of diffusion flames (Mudan 1987). However, it has been noted by Janssens (1992) that the factor for the shape is somewhere between that of a cylinder and a cone. So, we will use instead a hemi-ellipsoid to model the flame, with a circular base of radius R, and height H, with the surface element located a distance D from the edge of the flame. (Figure 1.)

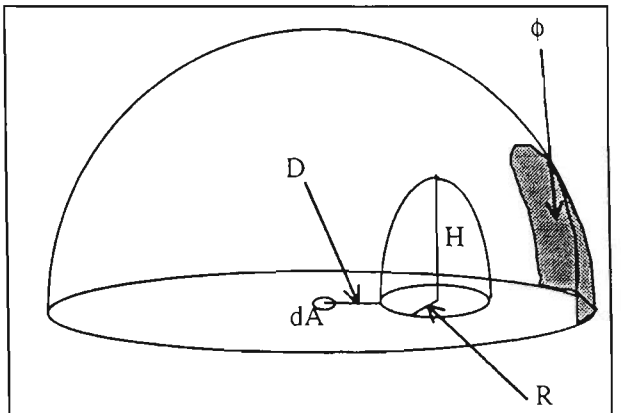

Figure 1 Configuration factor at surface element dA

The view factor is calculated by taking the projection of the hemi-ellipsoid onto the hemisphere surrounding the surface element, and assuming an average emissivity of the flame over this region. The resulting equation for the view factor is

$$\phi = \begin{cases} \dfrac{1}{\pi}\left(s - \dfrac{\arctan\left(\dfrac{\sqrt{(1+b)}\tan(s)}{\sqrt{(1+a+b)}}\right)}{\sqrt{(1+b)(1+a+b)}}\right) & b > -1 \\ \dfrac{1}{\pi}\left(s - \dfrac{\tan(s)}{a}\right) & b = -1 \\ \dfrac{1}{\pi}\left(s - \dfrac{\operatorname{arctanh}\left(\dfrac{\sqrt{-(1+b)}\tan(s)}{\sqrt{(1+a+b)}}\right)}{\sqrt{-(1+b)(1+a+b)}}\right) & b < -1 \end{cases}$$

where

$$s = \arcsin\left(\frac{R}{R+D}\right)$$

$$a = \frac{H^2(D+R)^2}{R^2(D^2+2DR)} \quad (9)$$

$$b = -\frac{H^2}{R^2}$$

The emissivity of the flame is given by the expression

$$\varepsilon_{flame} = 1 - \exp(-\kappa L_e) \quad (10)$$

where the mean beam length, L_e, is approximated by the equation for a general shape (Holman, 1981)

$$L_e \approx 3.6 \frac{\text{Vol}}{\text{S.Area}} \quad (11)$$

which for a hemi-ellipsoid is

$$L_e = 3.6 \frac{\frac{2\pi}{3} R^2 H}{\frac{2\pi}{3}(2R^2 + H^2) + \pi R^2} = \frac{36R^2 H}{35R^2 + 10H^2} \quad (12)$$

The luminous height for a turbulent diffusion flame is approximated by the expression (Heskestad 1983)

$$H = 0.0145(\Delta H_c \dot{m}'')^{\frac{2}{5}} - 2.04R \quad (13)$$

where the mass flux is calculated from equation (5).

2.1.5. Flux Balance Equation

By combining equations (2)-(13) we derive the equation for the surface flux balance

$$aT_0^4 + bT_0 + c + A\exp\left(\frac{-E}{R_u T_0}\right) = 0 \quad (14)$$

where

$$a = \varepsilon\sigma$$

$$b = h + k\frac{(2\Delta z_1 + \Delta z_2)}{\Delta z_1(\Delta z_1 + \Delta z_2)}$$

$$c = \varepsilon \dot{q}_r'' + hT_{gas} + k\left(\frac{T_1(\Delta z_1 + \Delta z_2)}{\Delta z_1 \Delta z_2} - \frac{T_2 \Delta z_1}{\Delta z_2(\Delta z_1 + \Delta z_2)}\right)$$

This equation is solved for the surface temperature, T_0, by Newton-Raphson's method, using the value from the previous iteration as the initial guess.

2.2. Internal Node Temperatures

Conduction within the fuel is analysed by solving the heat equation on an appropriately constructed grid. The fuel region is discretised with a regular square grid on the combustible surface, and an irregular grid in the direction normal to the surface. It is desirable that this latter grid be fine in the region of high temperature gradient, namely close to the surface. In order to maintain this fine region as the fuel regresses due to combustion, the grid "collapses" along with the fuel surface. Since the degree of regression of the fuel varies across the surface, we need to apply a grid transformation to restore orthogonality of the grid.

We begin with the familiar heat conduction equation

$$\frac{\partial T}{\partial t} = \alpha\left(\frac{\partial^2 T}{\partial x^2} + \frac{\partial^2 T}{\partial y^2} + \frac{\partial^2 T}{\partial z^2}\right) \quad (15)$$

We define the length, X, and width, Y, of the fuel, and the depth, F, where F(x,y) is the local depth at (x,y). We then transform the grid to the unit cube via the following transformation:

$$\xi = x / X$$
$$\eta = y / Y \quad (16)$$
$$\zeta = z / F$$

In these new co-ordinates, the terms in the heat equation (15) become

$$\frac{\partial^2 T}{\partial x^2} = \frac{1}{X^2}\frac{\partial^2 T}{\partial \xi^2} + \left(\frac{z\frac{\partial F}{\partial x}}{F^2}\right)^2 \frac{\partial^2 T}{\partial \zeta^2} - \left(\frac{1}{X}\frac{z\frac{\partial F}{\partial x}}{F^2}\right)\frac{\partial^2 T}{\partial \xi \partial \zeta} - \left(z\frac{F\frac{\partial^2 F}{\partial x^2} - 2(\frac{\partial F}{\partial x})^2}{F^3}\right)\frac{\partial T}{\partial \zeta}$$

$$\frac{\partial^2 T}{\partial y^2} = \frac{1}{Y^2}\frac{\partial^2 T}{\partial \eta^2} + \left(\frac{z\frac{\partial F}{\partial y}}{F^2}\right)^2 \frac{\partial^2 T}{\partial \zeta^2} - \left(\frac{1}{Y}\frac{z\frac{\partial F}{\partial y}}{F^2}\right)\frac{\partial^2 T}{\partial \eta \partial \zeta} - \left(z\frac{F\frac{\partial^2 F}{\partial y^2} - 2(\frac{\partial F}{\partial y})^2}{F^3}\right)\frac{\partial T}{\partial \zeta} \quad (17)$$

$$\frac{\partial^2 T}{\partial z^2} = \frac{1}{F^2}\frac{\partial^2 T}{\partial \zeta^2}$$

)

The new terms involving ξ, η, and ζ may now be discretised using the finite difference method (e.g. Holman 1990)

It is often customary to ignore lateral heat conduction, and consider conduction only normal to the burning surface. In this case, we only need consider the third term in equation (17). However, lateral conduction is an important factor close to the flame front, especially in the early stages of burning, when the flame is small and radiation heat transfer subsequently less dominant. In order to calculate three-dimensional conduction, we first solve the terms $\frac{\partial^2 T}{\partial \xi^2}$, $\frac{\partial^2 T}{\partial \eta^2}$, $\frac{\partial^2 T}{\partial \xi \partial \zeta}$, and $\frac{\partial^2 T}{\partial \eta \partial \zeta}$ explicitly, then solve the terms involving

$\frac{\partial^2 T}{\partial \zeta^2}$ and $\frac{\partial T}{\partial \zeta}$ implicitly, treating the former terms as source terms in the resulting equation. It is essential to solve the discretised equation implicitly in the z-direction, since the collapsing grid will eventually violate the Fourier condition for the explicit method, $\frac{\alpha \Delta t}{(\Delta z)^2} < 0.5$, regardless of what time step Δt is chosen.

Once the node temperatures have been determined, the surface regression due to mass loss as given by equation (5) is taken into account, and the new node positions are calculated. The temperature at these new positions is calculated by linear interpolation from the old node positions and temperatures.

2.3. Flame Front Location

Most flame spread models either calculate the spread rate explicitly (e.g. Baroudi and Kokkala 1996), or the position of the flame front is determined by interpolating between points which are undergoing combustion, and those which are not (e.g. Delichatsios, 1991). Both methods rely on assumptions about the geometry or configuration of the combustion taking place; for example, circular spread, horizontal planar spread, or vertical upward spread. The common concept shared by all these methods is that the arrival of the flame front coincides with the fulfilment a determining criterion, this normally being that the surface temperature has reached a critical value.

The model presented here differs from other models in that it does not explicitly calculate the flame front location or velocity. Spread occurs by a series of ignitions of surface elements, or cells, whose temperature has reached a critical temperature. This temperature does depend, though, on the ignition status of neighbouring cells. The term "neighbouring" refers to the eight cells on a square grid which surround the central square (Figure 2)

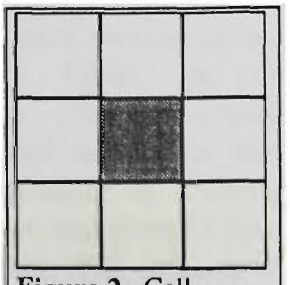

Figure 2. Cell neighbourhood

The model here considers two types of ignition, namely autoignition and piloted ignition. Autoignition occurs when the surface temperature of the fuel is raised to such a high value that the volatiles produced react spontaneously with oxygen in the air to initiate combustion. In the model, a cell will ignite if it reaches autoignition temperature, regardless of the state of neighbouring cells.

With piloted ignition, the volatiles are ignited by an external energy source such as a small flame (pilot) or electric spark, and the energy thus produced is sufficient to sustain combustion. (Prior to the attainment of the critical surface temperature required for piloted ignition, the volatiles may "flash", but combustion is not sustained.) Piloted ignition typically occurs at significantly lower temperatures than autoignition. In the case of a spreading flame, the pilot is provided by the flame front.

So, for piloted ignition in our model, we need to decide whether the flame front is in the vicinity of the cell in question when it has reached piloted ignition temperature. We treat the spreading flame as a cellular automaton, and impose the condition that for piloted ignition to occur, three or more neighbouring cells must be already ignited (Figure 3.)

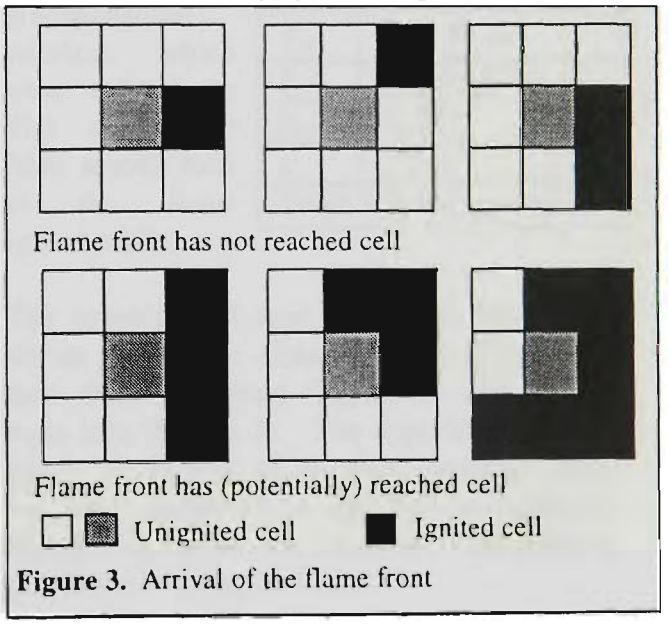

Figure 3. Arrival of the flame front

Naturally, there are both advantages and disadvantages to using this method. The main advantage is that no assumptions are made about the overall geometry of the fire spread scenario (other than those imposed by other aspects of the model). The method can mimic

both planar and radial spread. This makes it particularly useful for applications such as general purpose CFD models.

The main disadvantage is that the choice of grid size restrains the scale of the model's application. If the grid size is too large, spread to neighbouring cells may not occur, particularly if the true spread rate is quite small. Also, the grid may be too coarse to accurately represent fine detail, such as the initial stages of burning when the flame front is a small circle. There is also an upper limit on the spread rate, dependent on the grid size and the time step. If we consider a large region already at ignition temperature with some arbitrary ignited region, the shape of the flame front will quickly converge to an octagonal configuration, one corner of which is shown in Figure 4.

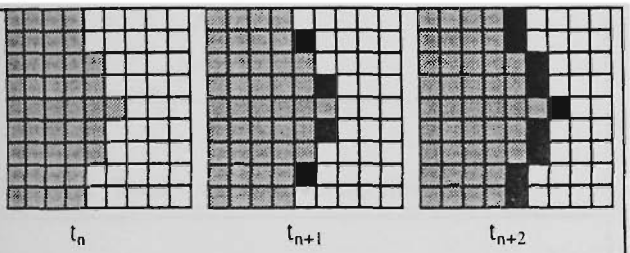

Figure 4. Limiting spread rate configuration

The limiting rate depends on direction. In the direction of the grid axes it is

$$v_{max} = 0.5\frac{\Delta x}{\Delta t} \tag{18}$$

while if we approximate the octagon as a circle, and calculate the changing radius from the rate of change of area, the limiting rate is

$$v_{max} = \sqrt{\frac{2}{3\pi}}\frac{\Delta x}{\Delta t} \approx 0.4606\frac{\Delta x}{\Delta t} \tag{19}$$

3. MODELLING AND EXPERIMENT

A series of experiments was conducted in a full scale multi-room building, involving the combustion of slabs of standard polyurethane foam, the details of which have been described elsewhere (Luo and Beck, 1996). In one scenario, a polyurethane slab measuring 940x950x150 mm was placed on an open wire frame on a balance platform, and flaming combustion was initiated in the centre of the slab with an electronic igniter. The diameter of the flame front and the total mass released were measured, along with large amount of data including temperature, gas composition, and radiant flux throughout the building. This test was performed twice, with both runs showing very similar spread rate and mass loss histories, indicating good repeatability.

Material properties for the polyurethane foam used in these tests is shown in Table 1. The density and conductivity were measured directly, while the others were taken from typical values in the literature for standard flexible polyurethane foam (Drysdale, 1985, Chang et al. 1995).

ρ	23 kg m^{-3}
k	0.038 W m^{-1}K^{-1}
c	1400 J kg^{-1}K^{-1}
α	1.18×10^{-6} m^{2}s^{-1}
L_v	1.22×10^{6} J kg^{-1}
ΔH_c	2.44×10^{7} J kg^{-1}
E	1.25×10^{5} J mol^{-1}
A	$L_v\times5\times10^{7}$

Table 1 Material properties

The model was executed using a time step of 0.1s, and a surface grid square size of 5mm, and an initial flame diameter of 70mm. Other parameters required by the model are shown in Table 2. Again, most values are from the literature (Drysdale, 1985, Baroudi, 1996) apart from those pertaining to ambient conditions. The exceptions are the flame temperature, and the preexponential constant, which were refined by trial and error from several runs of the flame spread model.

T_{pilot}	550 K
T_{auto}	715 K
T_{gas}	298.15 K
T_{flame}	950 K
$\dot{q}''_{ext}$	σT_{gas}^4 W m^{-2}
ξ	2.444×10^{5} W m^{-2}
Y_{O2}	0.2095
κ	1.0 m^{-1}

Table 2 Model parameters

The experimental and modelling results are shown below, for flame diameter (Figure 5), total mass consumed (Figure 6), and rate of mass loss (Figure 7). The experimental mass loss is an average of the two test runs, which was then smoothed by adjacent averaging of data points, before the derivative was taken to determine the mass loss rate.

Overall, the model shows good agreement with the experiments. However, it should be noted that the modelling results are somewhat sensitive to input data, particularly flame temperature.

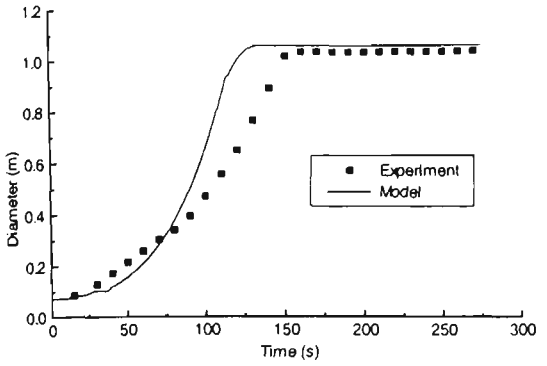

Figure 5. Diameter of flame versus time

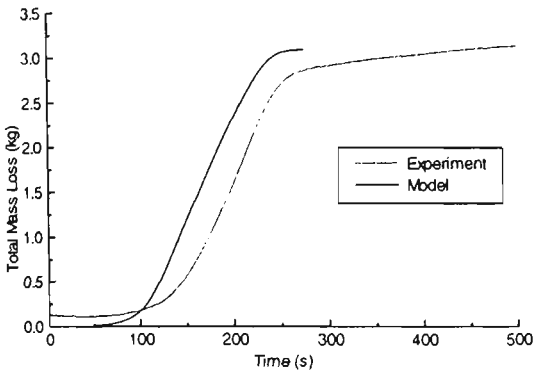

Figure 6. Total mass loss versus time

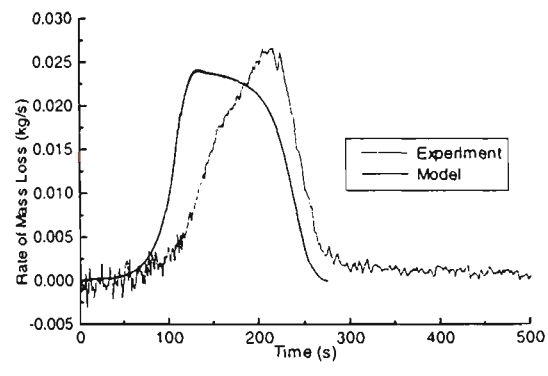

Figure 7. Rate of mass loss versus time

The spread rate is largely driven by the radiation from the flame, which is evident from Figure 5. The slope of the flame diameter curve becomes quite steep just before the flame front reaches the edge of the fuel. This is due to the increase in size of the flame, with corresponding increase in emissivity (equations (9) and (10)), resulting in higher radiant heat flux to the fuel surface.

Of course, by this reasoning we expect to see a similar phenomenon occurring in the experiment. In fact, we would expect it more so, considering that in the experiment we have increasing radiative feedback from the hot layer in the enclosure as the burning progresses (as opposed to the constant ambient radiation in the model). However, the increase in spread rate is markedly less in the experiments.

The most probable cause of this discrepancy is the lack of a comprehensive convection model in the flame spread model. It was observed in the experiment that once the flame diameter had reached approximately 0.4 m, the familiar oscillatory behaviour of turbulent diffusion flames commenced. Oscillations of the flame were accompanied by similar oscillations in the radial velocity of the entrained air. It could be clearly seen that with the strong inrushing phase of the oscillation, the flame front essentially halted, while in the relatively still phase in between, the flame front advanced by a noticeable increment. Taking this into account, we would therefore expect a slower spread rate in the experiment than predicted by the idealised still air convection of the model.

It should also be noted that this model idealises the combustion behaviour of the polyurethane foam. It is assumed in the model that surface regression is due solely to the production of volatiles. In fact, in the case of polyurethane foam, its open cell structure and its tendency to form a liquid tar before volatilising means that a considerable proportion of surface regression is due to melting rather than volatilisation. In relation to this, care should also be taken in the interpretation and use of fundamental material data obtained from small scale tests such as the cone calorimeter (Vanspeybroeck et al, 1993).

4. CONCLUSION

The model presented here has been shown to model with reasonable accuracy the spread rate and mass release of a simple fire scenario, despite the simplifications and assumptions present in the model. This indicates that the general ignition, combustion, and flame spread principles contained in the model are suitable for incorporation into a more complex fire model, such as a CFD model, which can model the fire environment more generally and with greater accuracy. This would produce a versatile fire growth and spread model of great value and use in fire safety engineering.

5. ACKNOWLEDGMENTS

This research is financially supported by Australian Research Council (ARC) Infrastructure Grants and an ARC Collaborative Research Grant which is conducted in association with BHP and the National Association of Forest Industries.

6. REFERENCES

Babrauskas, V., and Peacock, R. D., 1992, "Heat Release Rate: The Single Most Important Variable in Fire Hazard", *Fire Safety Journal*, **18**, pp 255-272

Baroudi, D., and Kokkala, M., 1996, "Flame Spread and Heat Release Rate Model for a Burning Mattress", *Interflam '96*, pp 37-46

Chang, T. C., Shen, W. S., Chiu, Y. S., and Ho, S. Y., 1995, "Thermo-oxidative Degradation of Phosphorus-containing Polyurethane", *Polymer Degradation and Stability*, **49**, pp 353-360

Delichatsios, M. M., Mathews, M. K., and Delichatsios, M. A., 1991, "An Upward Fire Spread and Growth Simulation", *Fire Safety Science: Proceedings of the Third International Symposium*, pp 207-216

Delichatsios, M. A., 1993, "Basic Polymer Material Properties for Flame Spread", *Journal of Fire Sciences*, **11**-Jul/Aug, pp 287-295

Drysdale, D. D., 1985, *An Introduction to Fire Dynamics*, John Wiley & Sons Ltd.

Fernando, A. E., and Luo, M., 1995, "Modelling of Radiative Heat Transfer in Full Scale Building Fires.", *Australian Symposium on Combustion and Fourth Flame Days*, University of Adelaide, Adelaide, Australia, pp C3-13-18

Galea, E., 1989, "On the Field Modelling Approach to the Simulation of Enclosure Fires", *Journal of Fire Protection Engineering*, **1**(1) pp 11-22

Heskestad, G., 1983, "Luminous Heights of Turbulent Diffusion Flames", *Fire Safety Journal*, **5**, pp 103-108

Holman, J. P., 1981, *Heat Transfer, Fifth Edition*, McGraw-Hill Inc.

Janssens, M., 1992, "Determining Flame Spread Properties from Cone Calorimeter Measurements, (a) General Concepts", *Heat Release in Fires*, edited by V. Babrauskas and S. J. Grayson, Elsevier Science Publishers Ltd., pp 265-281

Luo, M., and Beck, V. R., 1994, "The Fire Environment in a Multi-Room Building-Comparison of Predicted and Experimental Results", *Fire Safety Journal*, **23**, pp 413-438

Luo, M., and Beck, V. R., 1996, "A Study of Non-Flashover and Flashover Fires in a Full-Scale Multi-Room Building", *Fire Safety Journal*, In Press.

Mudan, K. S., 1987, "Geometric View Factors for Thermal Radiation Hazard Assessment", *Fire Safety Journal*, **12**, pp 89-96

Quintiere, J., and Iqbal, N., 1994, "An Approximate Integral Model for the Burning Rate of a Thermoplastic-like Material", *Fire and Materials*, **18**, pp 89-98

Steckler, K. D., Kashiwagi, T., Baum, H. R., and Kanemaru, K., 1991, "Analytical Model for Transient Gasification of Noncharring Thermoplastic Materials", *Fire Safety Science: Proceedings of the Third International Symposium*, pp 895-904

Tewarson, A., 1994, "Flammability Parameters of Materials: Ignition, Combustion, and Fire Propagation", *Journal of Fire Sciences*, **12**-Jul/Aug, pp 329-356

Vanspeybroeck, R., Van Hees, P., and Vandevelde, P., 1993, "Combustion Behaviour of Polyurethane Flexible Foams under Cone Calorimetry Test Conditions", *Fire and Materials*, **17**, pp 155-166

A CELLULAR AUTOMATA APPROACH TO CFD FLAME SPREAD MODELLING

ANTHONY FERNANDO
Centre for Environmental Safety and Risk Engineering
Victoria University of Technology, Melbourne, Australia

ABSTRACT

This paper focuses on the growth and spread stage of full-scale fires in enclosures, where a localised flame spreads across a single fuel item, increasing the heat release rate, thereby resulting in increased fire hazard. The development of a numerical model for fire spread over a solid fuel surface, and its integration into a CFD model, is described. The conflicting demands of resolving the small scale flame front phenomena while simultaneously accounting for the large-scale enclosure flow phenomena are addressed. The surface of the fuel is descretised with a regular square array, and flame spread occurs as a series of ignitions of surface elements. Ignition of an element is determined by a combination of critical surface ignition temperature and cellular automata techniques. Regression of the combusting fuel surface is modelled, with a fine grid retained at the fuel surface by allowing the grid to "collapse" with the surface. A grid transformation is applied to restore orthogonality of the collapsed grid, for simple computation of the heat equation. The flame spread model has been designed to be independent of geometry, although experimental validation exercises are carried out for radial spread over horizontal surfaces only. Predictions are made for the burning of a slab of polyurethane foam in a full-scale multi-room experimental building-fire facility. The predictions compare favourably with the experiments, indicating the broad validity of the methods used in flame spread model.

KEY WORDS: CFD, Field Modelling, Flame Spread, Fire Growth, Cellular Automata.

INTRODUCTION

Rate of heat release has been identified as an important factor in determining the fire safety hazard in an enclosure of a particular material. The heat release rate in an actual fire is in turn influenced by the conditions the material experiences, including the heat feedback from the surroundings, and the flame spread across the material which increases the area releasing heat. Computational fluid dynamics (CFD) modelling, or fire field modelling, is a useful tool to aid in predicting the possible fire hazard of a particular material. However, despite the continuing advancements in computer processing speed and storage capacity, fire field models still push the capabilities of computers to

their limits when modelling full-scale unsteady-state enclosure fires, due to the sheer number of calculations required. This is particularly true for a model which is attempting to simulate a large enclosure, in which both small and large scale phenomena are occurring, such as the progression of a flame front under the heating influence of a hot combustion product layer. In the past, modellers have tended to concentrate on one of the other of these phenomena; for example, if the enclosure as a whole is being modelled, then the heat release rate is often prescribed [1], and if flame spread is considered, then it is usually in the form of an empirical equation [2], or restricted to a special case, such as vertical spread up a wall. On the other hand, if flame spread is concentrated upon in detail, it is often in isolation, with conditions prescribed for the fire environment [3].

This paper describes the construction of a flame spread model in such a way that it operates in conjunction with a CFD model to predict full-scale fires involving flame spread across solid fuel objects. The flame spread model contributes heat and fuel volatiles to the gas phase, whereby the CFD model calculates combustion of the fuel vapours, and distributes the heat and products of combustion accordingly. At the same time, the CFD model calculates the heat feedback to the fuel surface within the flame spread model, in turn affecting the flame spread rate and rate of volatilisation of the fuel.

MODEL DESCRIPTION

Model Requirements

It has been shown previously [4] that it is possible to produce reasonably accurate results from an isolated flame spread model that makes only basic assumptions about the gas phase phenomena. Inaccuracies in the isolated flame spread model were largely attributed to these assumptions, which are not flexible enough to adequately simulate the changing conditions occurring in a fire growth scenario. Fire field models on the other hand are designed to simulate the gas phase phenomena occurring in a combustion scenario, given a heat or fuel source.

There are several requirements of such a flame spread submodel, which need to be taken into account if is to be generally compatible with a CFD model. For compatibility, the flame spread model will operate on a discrete grid. This means that unlike most analytical models of flame spread, the flame front will be characterised as advancing by a series of discrete jumps rather than continuously. The requirements of the flame spread model are basically threefold. Firstly, like CFD models, the flame spread model should be based as much as possible on first principles. Secondly, it must be geometrically flexible, so that it is capable of modelling a wide variety of flame spread scenarios. Thirdly, the fundamental material properties required for the model must be experimentally derivable [5].

In a recent paper, Nicolette et al. discussed the necessary coupling between combustion and flame spread models, and general CFD fire models [6]. While their analysis appears commonsense, the authors nevertheless provide a useful summary of the problem, and the essence of the analysis may be reduced to four main points.

The first point concerns the problem of tracking creeping (ie. opposed flow) flame spread, which requires modelling of small-scale phenomena, in a large enclosure. Since modelling of a large enclosure requires a coarse grid if computational resources are not to become prohibitive, it was proposed that a solution should track the creeping spread by empirical or other means on a subgrid

of the CFD grid. The second point concerns the representation of the fuel in the computational region, either as a solid object or a wall lining for example, and how to model the changing shape of the fuel as combustion progresses. Thirdly, the coupling of enthalpy and mass source terms was identified as being sensitive in field models. Any imbalance will result in mass and energy no longer being conserved. Hence, accurate coupling is important. The fourth point concerns the choice of grid for the finite difference (or finite element) method used in both the flame spread and field models. A suggestion was for a grid for the solid fuel which is refined at the surface near the flame front, and which moves with the front.

These four issues are dealt with to varying degrees in the method presented herein. The need for a fine grid to model opposed flow flame spread was previously identified by the author [4], and indeed the method chosen here is to construct a grid for the flame spread model which is finer than that used in the CFD model. The flame spread within the larger CFD grid cells is modelled using a cellular automata techniques, explained later. The fuel is modelled as an obstacle within the flow region, with combustion and mass loss occurring at one surface only. Regression of the fuel surface is taken into account in the flame spread model, as a first approximation, the fuel obstacle retains its shape in the CFD model, mainly because the CFD model presented here operates on a fixed orthogonal grid. The author anticipates that while the regression of the fuel surface is important to the heat conduction within the fuel, the effect will be negligible in terms of the large-scale behaviour of the flow region. The products of pyrolysis of the solid fuel are not modelled in any great detail. The only property of the gaseous fuel considered here is heat of combustion, which is assumed constant throughout the execution of the model. The thermodynamic properties of methane are assumed to be sufficiently representative of the gaseous fuel. This assumption has been used with some success in past modelling of polyurethane combustion [2,7].

The CFD Flame Spread Model

The field model CESARE-CFD has been developed in recent years at the Centre for Environmental Safety and Risk Engineering (CESARE) to model a number of fire experiments which have been performed at the Centre's Experimental Building-Fire Facility (EBFF) [7,8]. It is a modified version of the field model FURNACE, originally developed by Boyd and Kent to model coal fired furnaces and pool fires [9]. The model solves the Navier-Stokes and general conservation equations in three dimensions, with the pressure-momentum equations being solved by the SIMPLER algorithm. The standard k-ε model is used to calculate turbulence, incorporating additional equations to account for turbulence induced by buoyant flows. The quantities solved, and the values for the exchange coefficients and source terms for these quantities are described elsewhere [7].

The combustion of the fuel is modelled by computing the local fuel mixture fraction, then reacting the fuel with the air. The local combustion rate is governed by the local mixing rate of fuel with air. When the local oxygen concentration falls below a specified value (typically in the region of 5-10%), combustion is assumed not to occur. A simple empirical equation is used to calculate the composition of combustion products [7]. Radiation heat transfer is calculated using the discrete transfer method [10]. As the radiation calculations are particularly time consuming, the calculations are performed on a coarser grid than used for the flow variables, and performed once for every five iterations of the flow region calculations.

The grid itself, both in the flow subroutine and in the radiation subroutine, is rectilinear, with cell boundaries perpendicular to one of the three Cartesian axes. Since most enclosures in architecture are rectilinear, particularly those associated with domestic and office buildings, the rectilinear grid

is quite adequate for such applications. The grid spacing in each of the three directions may be specified, so that the grid may be refined in required regions, for instance in regions where high temperature gradients are expected.

The Cellular Automata Flame Spread Technique

Most flame spread models either calculate the spread rate explicitly [11], or the position of the flame front is determined by interpolating between points which are undergoing combustion, and those which are not [12]. Such models rely on assumptions about the geometry or configuration of the combustion taking place. In most cases, these models share the concept that the arrival of the flame front coincides with the fulfilment a determining criterion, usually the attainment by the surface of a critical temperature. The model presented here differs from these other models in that it does not explicitly calculate the flame front location or velocity. Spread occurs by a series of ignitions of surface elements, or cells, whose temperature has reached a critical temperature. This temperature does depend, though, on the ignition status of neighbouring cells. The term "neighbouring" refers to the eight cells on a square grid which surround the central square.

The model presented here considers two types of ignition, namely autoignition and piloted ignition. Autoignition of a cell will occur when the surface temperature of the cell is raised to a sufficiently high value, independent of the ignition status of neighbouring cells. Piloted ignition of a cell may occur at a temperature significantly lower than that for autoignition. In the case of a spreading flame, the pilot is provided by the flame front. For piloted ignition in this model, it is necessary to decide whether the flame front is in the vicinity of the cell in question. The spreading flame is treated as a cellular automaton, and the condition imposed that for piloted ignition to occur, three or more neighbouring cells must be already ignited, as shown in Figure 1. The three or more neighbour criterion is chosen because, in the absence of other physical criteria, this will lead to a roughly circular spreading flame front [4].

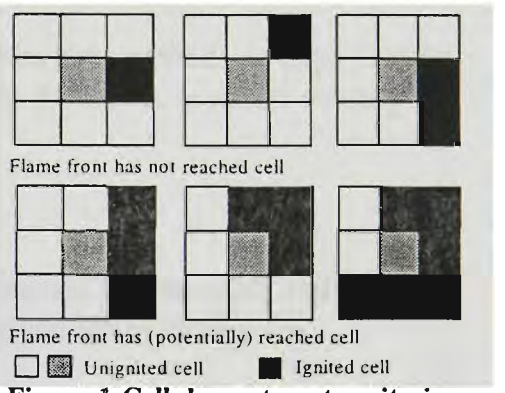

Figure 1 Cellular automata criterion for the arrival of the flame front.

Solid Pyrolysis Model

The fuel is taken to be a regular rectangular slab. Combustion and mass loss is assumed to occur at one surface only. The other surfaces are assumed to be perfectly insulated in terms of both heat and mass loss. The flame spread is determined by considering the ignition and combustion properties of discrete elements on the fuel surface, with spread occurring as a series of discrete ignitions of fuel elements adjacent to the existing flame front, as described above.

Each element on the combustion surface is in one of three states; preheating, combusting, or burnt out. In the preheating stage, the element is heated remotely by radiation from the flame and external sources. In the burnt out stage, the element is no longer a part of the calculation region, and neighbouring cells are treated as boundary cells. In the combusting stage, the element is assumed to receive at least a minimum heat flux total from the flame and external radiation, for reasons discussed later. The rate of mass loss, $\dot{m}''$, is given by the simplified equation for steady combustion [13]

$$\dot{m}'' = \frac{\dot{q}''_{flame} + \dot{q}''_{external} - \dot{q}''_{loss}}{H_v} \qquad (1)$$

where $\dot{q}''_{flame}$ is the heat flux from the flame, $\dot{q}''_{external}$ is the externally applied flux, $\dot{q}''_{loss}$ is the radiation and conduction losses, and H_v is the latent heat of volatilisation. While steady burning seldom occurs under real fire conditions, this expression for the flame heat is nevertheless useful for describing the instantaneous heat balance at the surface.

The temperature at the surface, T_0, is calculated by considering the heat flux balance at the surface. This balance takes into account the incident radiant heat flux to the surface, $\dot{q}''_{external}$, convective heat transfer to the surface, $\dot{q}''_{convect}$, conduction of heat into the fuel, $\dot{q}''_{conduct}$, reradiation from the surface, $\dot{q}''_{rr}$, and latent heat of volatilisation of the fuel. The conduction heat flux at the surface is proportional to the temperature gradient at the surface, as given by

$$\dot{q}''_{conduct} = -k\left.\frac{\partial T}{\partial z}\right|_{z=0} \tag{2}$$

The gradient is approximated by a parabolic fit of the temperature of the surface node and the first two nodes below the surface. Convective heating is modelled by the expression

$$\dot{q}''_{convect} = h(T_{gas} - T_0) \tag{3}$$

The heat transfer coefficient, h, is calculated using the wall function method, as described by Launder and Spalding [14]. The mass flux of volatiles from the surface is assumed to obey the simple Arrhenius equation

$$\dot{m}'' = A\exp\left(\frac{-E}{RT_0}\right) \tag{4}$$

where E is the activation energy and A the pre-exponential constant for the fuel, and R is the universal gas constant. The re-radiant heat loss from the fuel is given by the expression

$$\dot{q}''_{rr} = \varepsilon\sigma T_0^4 \tag{5}$$

Equations 2-5 are substituted back into Equation 1, to derive an expression for the surface temperature, T_0, which is solved using the Newton-Raphson method. Once surface temperatures are solved, the interior temperatures are solved by the tri-diagonal matrix algorithm, using the surface temperature as a boundary condition. Regression of the fuel surface is taken into account by means of a grid transformation, details of which appear elsewhere [4].

Grid Embedding

Incorporation of the flame spread model in the CFD model requires embedding the flame spread grid as a subgrid of the CFD model's main flow grid. There are two issues to be considered here. First, quantities which are transferred from the fuel to the flow region need to be either summed or averaged, depending on the quantity. Secondly, quantities transferred from the flow region to the solid fuel need to be distributed over the solid region.

Consider first transfer from the solid fuel to the flow region. The solid contributes gaseous fuel to the flow region. This manifests itself as mass and enthalpy source terms in the flow cell immediately adjacent to the solid. Since the flow grid will in general be coarser than the solid grid, a flow cell adjacent to the solid surface will be in contact with several solid cells. The source terms in the flow cell will simply be the sum of the contributions from all the solid cells with which it is in contact. The heat flux from the fuel surface to the flow region must be treated differently. The flow cell will receive radiated and conducted heat from the fuel surface, and since each surface cell in contact with the flow cell will, in general, be a different temperature, the net contribution from all the cells is not a straightforward calculation. As a first approximation, the

fuel surface temperature of is chosen to be that of the solid fuel element which coincides with the centre of the flow grid cell.

The other transfer to be considered is heat flux from the flow region to the solid, which is dependent largely on the properties of the flow cells in contact with the fuel surface. An individual solid surface cell will be in contact with only one flow cell, so the obvious choice is to assume the properties of the flow cell prevail at the surface point of interest. However, preliminary modelling exercises using this approach revealed that an "image" of the flow grid could be seen in the results for the solid submodel, due to similar conditions prevailing over blocks of solid cells. Such a situation is undesirable, as it defeats the purpose of using a subgrid of the flow grid, which is to model phenomena whose mechanisms operate on smaller scale than resolved by the flow grid. If the behaviour of the subgrid is dominated by the large scale grid, then there is no gain in information.

Further information about the flow region may be extracted by interpolating between the known values at the discrete flow cell nodes. A simple linear interpolation method is used here, as it is in agreement with the assumed piecewise linear profile between flow nodes used in the derivation of the CFD equations. The quantity of interest distributed throughout the flow region is denoted ϕ. The surface cell under consideration is at (x,y), where x and y are coordinates in the two directions parallel to the fuel surface, and is in contact with a particular flow cell. The value of the quantity in the flow cell is denoted $\phi_{i,j}$, as calculated for the node located at (x_i,y_j). In general, each flow cell will have 8 neighbours likewise in contact with the surface, as shown in Figure 2.

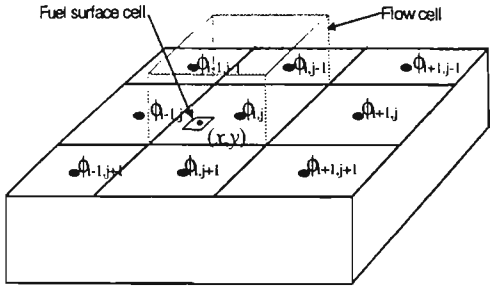

Figure 2 Flow cell neighbours

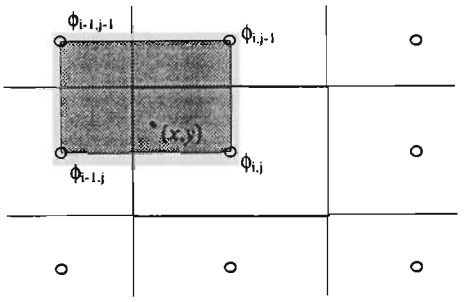

Figure 3 Linear interpolation method

If the point at (x,y) coincides with the flow node, then the value of $\phi(x,y)$ is equal to $\phi_{i,j}$. If it is located a finite distance from the node, the value will be somewhere between $\phi_{i,j}$ and the value at the nearest neighbours.. The point at (x,y) will in general be located between four flow cell nodes, as shown in Figure 3. The linear interpolation method produces a continuous function with a single equation in two dimensions, and for the example in Figure 3 is given by

$$\phi(x,y)=\frac{(x_i-x)(y_j-y)\phi_{i-1,j-1}+(x_i-x)(y-y_{j-1})\phi_{i-1,j}+(x-x_{i-1})(y_j-y)\phi_{i,j-1}+(x-x_{i-1})(y_j-y)\phi_{i,j}}{(x_i-x_{i-1})(y_j-y_{j-1})} \quad (6)$$

The linear interpolation method is used to determine the incident radiation flux distribution to the fuel surface from the surroundings, since the flux is calculated by the discrete transfer method for the flow nodes only. This method is also used to describe the local values of the flow variables at the fuel surface. These are used to calculate the convective heat transfer to the surface, using the wall-function method. The local heat transfer coefficient for an element on the fuel surface is calculated by first linearly interpolating the flow variables that appear in the wall function equation, and then evaluating the equation.

Initialisation of the Model

Computer modelling of an unsteady-state fire with the CFD model used here is performed in two stages. First, the distribution of variables within the flow region is "initialised" by solving a small steady state fire located at the origin of initiation of the unsteady fire. After convergence of the solution for this small steady-state fire has been attained, the unsteady state simulation is calculated by a forward marching time solution. The flame spread model is by design an unsteady-state model, with the forward marching time solution being calculated from an initial starting point. The starting point is an initially uniform ambient temperature for the solid fuel, a small area of which is ignited. However, incorporation of the flame spread model into the CFD model requires that the fuel be part of the steady-state initialisation process, due to the sensitivity of the coupling between the solid fuel and the flow region. Therefore, conditions need to be specified for the fuel during the steady-state phase of the modelling.

For the steady state conduction of heat in an infinite slab of finite thickness and constant conductivity, the temperature distribution within the slab is a linear temperature profile between the two surfaces. However, it usually takes a long time (dependent on conductivity and thickness) for the temperature within the slab to assume an approximately linear profile. For the flame spread model, the unsteady state will commence with the nearly instantaneous heating of a portion of the upper surface, with the rest of the fuel remaining approximately at ambient temperature; a situation which reflects reality. As a consequence, only surface temperatures are calculated for the flame spread model in the steady state, and the conduction into the fuel is ignored.

Another issue to be addressed is the maintaining of a steady burning region on the fuel surface in the steady-state. The region of the surface designated as ignited must satisfy the criteria for ignition at the conclusion of the steady-state phase of calculations; that is, in the case of this model, the surface must be at least at the critical ignition temperature. If the criteria are not met, the flame spread scenario will not have been properly initiated, and flame spread may not occur. Indeed, combustion may even cease entirely, as insufficient fuel will be contributed to the flow region, resulting in less heat feedback. Maintenance of the ignition criteria is accomplished by prescribing a minimum heat flux to a fuel surface cell that has ignited. This value is the quantity $\dot{q}''_{flame}$ which appears in Equation 1.

Despite the inclusion of a minimum flux to ensure no extinction in the steady-state phase of the calculations, a rapid drop in temperatures throughout the flow region frequently occurred soon after the commencement of the unsteady-state calculations, effectively causing extinction of the fire. This may be due to the somewhat artificial imposition of the minimum heat flux criterion. For this reason, the minimum flux criterion was retained in the flame spread model for the unsteady phase of the calculations.

FOAM SLAB EXPERIMENTS AND MODELLING

Experiments

A series of experiments was performed at the EBFF to provide data on the burning of a polyurethane slab in a full-scale enclosure for comparison with the CESARE-CFD flame spread model. The experiments took place in the section of the ground floor shown in Figure 4.

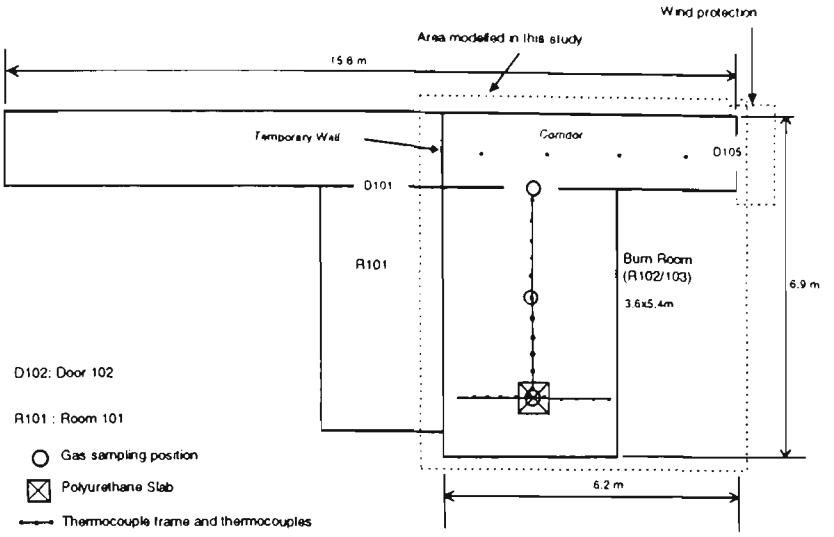

Figure 4 The portion of the Experimental Building-Fire Facility used in this study

The layout of the facility comprised a large enclosure connected to the outside via a doorway and corridor, with a window measuring installed at the end of the room opposite the doorway. The floor of the burn room comprised two mass loss platforms, only one of which was required for these experiments.

A series of experiments were performed on standard cushion-sized slabs of polyurethane foam, measuring 560×560×100mm, wrapped in a layer of aluminium foil, and placed horizontally in a holder consisting of five pieces of fire-rated plasterboard (one bottom and four sides, sealed at the joints) assembled so that the foam slab fitted snugly inside, flush with the top of the holder. A grid was marked on the top surface of the foam slab, for visual measurement of flame size from video recordings. Ignition of the foam sample was achieved by the ignition of a small solid fuel tablet placed in the centre of the foam slab. The test was performed three times, with the three tests showing excellent repeatability. An array of thermocouples, gas sampling tubes, velocity probes, and a heat flux meter were used to record a variety of physical quantities at a variety of locations throughout the enclosure in each test.

Modelling

The portion of the Experimental Building-Fire Facility shown in Figure 4 was the subject of a numerical modelling exercise undertaken with the CFD flame spread model. The enclosure is modelled in the flow region with a 40×54×25 adaptive grid, which includes a refined region of 14×14 grid cells adjacent to the fuel slab. As the fuel slab measures 560×560 mm, this corresponds to a 40mm grid in the fine region. There are two refined regions in the vertical direction; adjacent to the upper surface of the fuel, and at the midplane of the enclosure, where it is anticipated the interface between the hot and cold interfaces will occur.

Table 1 Properties of Polyurethane Foam

ρ	23 kg/m^3
k	0.038 W/m·K
c	1400 J/kgK
L_v	1.22×10^6 J/kg
ΔH_c	2.27×10^7 J/kg
E	1.25×10^5 J/mol
A	$L_v\times1\times10^8$
T_{pilot}	550 K
T_{auto}	715 K

The flame spread model discretises the fuel with a 5mm grid size, resulting in a 112×112 grid, and with 8 divisions in the fuel depth, increasing in size from the surface to the depth. The kinetic and thermal properties of the standard polyurethane foam fuel are as given in Table 1. The density and conductivity were measured directly, while the others were taken from typical values in the literature for standard flexible polyurethane foam [13,15], except for the pre-exponential constant, which was determined by trial and error in previous work [4].

The steady-state initialisation of the flow region was performed in 1000 iterations. The initial flame diameter was set to 0.06m. After initialisation, the unsteady-state fire was modelled for 360 seconds simulation time, using a time step of 0.1s, which results in a total of 3600 iterations. This was to ensure that the model included the burnout time, which occurred at around 300 seconds in the EBFF tests.

RESULTS

The results are shown for the flame spread across the solid fuel item. The effective diameter of the flame is shown in Figure 5. The effective diameter is calculated for a circle whose area is the same as the total area of the ignited cells, in the case of the flame spread model. In the experiment, the diameter was measured directly until the spreading circular front reached the edges of the square fuel slab (diameter 0.56m), after which the diameter was estimated, up to the equivalent diameter of 0.63m for a 0.56×0.56m square.

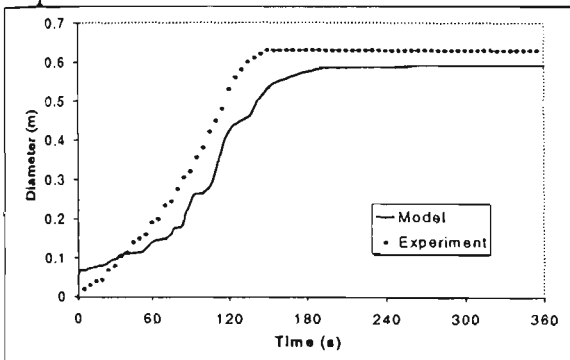

Figure 5 Effective diameter of flame

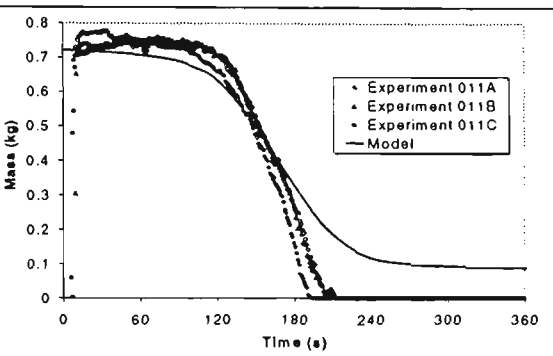

Figure 6 Total mass of fuel slab

As can be seem from Figure 5, the predicted effective flame diameter failed to reach maximum possible diameter, nor was it predicted that the mass was totally consumed, as shown in Figure 6. Nevertheless, there is reasonable agreement in the overall trends, which suggests that the model is itself reasonable. The model shows the accelerating flame spread, and the timing of the peak mass loss rate corresponds well with the experimentally observed peak in the initial stages of the fire, as shown in Figure 7(a). It is the peak phase and the decay phase of the fire where the modelling results are in disagreement with experimental results. The model fails to predict the sharp peak at 180 seconds, instead predicting a lower, earlier peak with a more gradual decay.

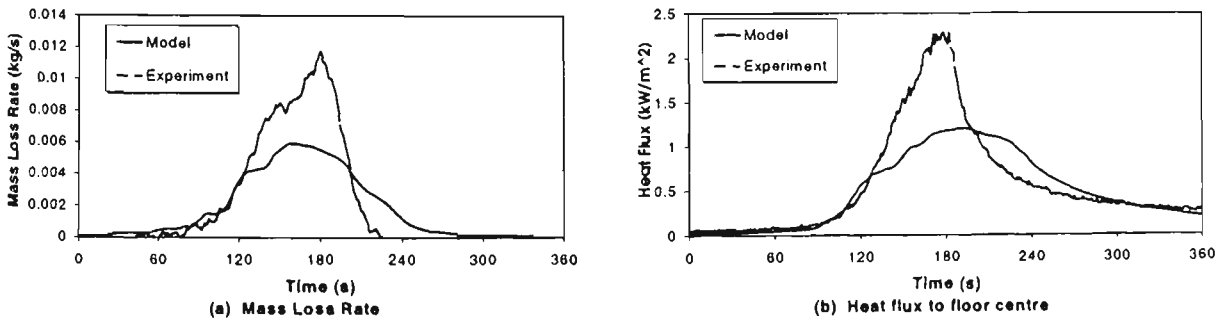

Figure 7 Mass loss and radiation heat flux histories

To understand where the discrepancies are occurring, it is helpful to examine the predictions of the spreading flame in greater detail. The time of ignition of each cell was recorded, and is shown in Figure 8. The light region at the top of Figure 8 corresponds to cells which have not undergone ignition. The initial burning region is the circular region at the centre of the fuel. The flame then

spreads radially in a relatively uniform fashion up until around 90 seconds, after which it spreads more rapidly to the south (downwards in the figure) and east, while making little progress northwards, leaving a large portion of the northern edge of the fuel unignited. The flame had spread across the entire surface by 150s. The model also predicted burnout in the centre at around 120s, whereas the experiments, with no apparent sign of central burnout, although burnout was difficult to confirm visually. Figure 7(a) shows that this is the point where the predicted mass loss rate becomes noticeably less than the measured mass loss rate. It appears that the discrepancies in the mass loss rate and flame diameter curves can be largely attributed to the failure of the model to predict flame spread to the northern portion of the fuel between 120 and 150 seconds.

The unburnt region of the fuel in the simulation is defined by an almost straight line across the northern (top) portion of the fuel. This is the edge of the fuel which faces the doorway of the burn room. The straight line coincides with one of the cell boundaries of the CFD grid. In fact, close examination of Figure 8 reveals evidence of several such straight lines, a phenomenon which was mentioned earlier and led to the inclusion of linear interpolation of flow variables in the flame spread model. The results here show that despite linear interpolation, there is still an "imprint" of the CFD grid on the flame spread grid, of which the northern portion of the fuel is the most dramatic example.

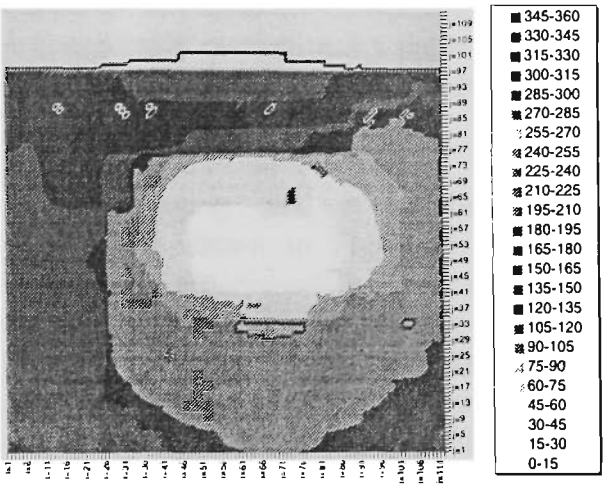

Figure 8 Time of ignition of cells

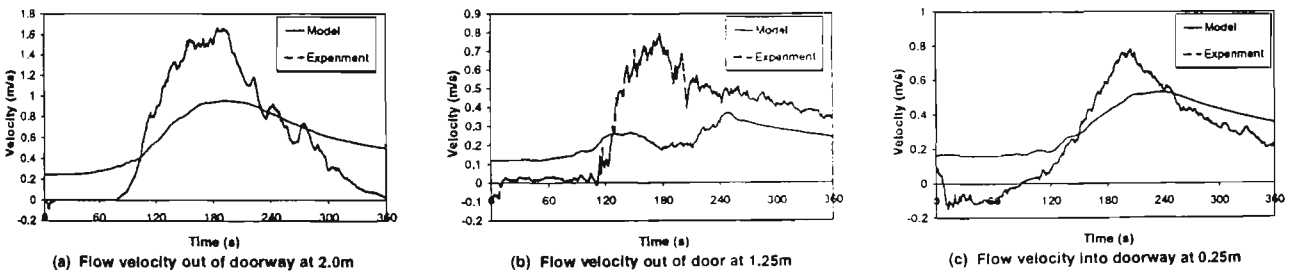

(a) Flow velocity out of doorway at 2.0m (b) Flow velocity out of door at 1.25m (c) Flow velocity into doorway at 0.25m

Figure 9 Velocity histories

What appears to be causing this predicted phenomenon is the establishment of a strong airflow pattern as combustion proceeds, characterised by the flow of cool air through the lower half of the doorway, across the floor of the burnroom, up the lip of the fuel and across the surface of the fuel, and into the rising plume. This current appears to be strong enough to oppose the spread of flame, or at least to transfer sufficient heat away from the surface to keep the surface temperature below even piloted ignition temperature. In the experiment is, the flame reached each of the four edges within the 120-125 second time interval, indicating that any entrainment and flow pattern created by the fire plume did not show any strong preferential direction up to this time. Examination of the velocity histories in Figure 9 reveals additional information. In the experiment, flows in and out of the doorway were negligible in the first 90 seconds of the experiments and then began to increase noticeably, particularly after 120 seconds. In contrast, there is a significant flow in the simulation from the initial stages, which helps explain the bias to the south in the flame spread simulation. This flow pattern is created by the steady state initialisation of the simulation, and is an issue that will be addressed in future model revisions.

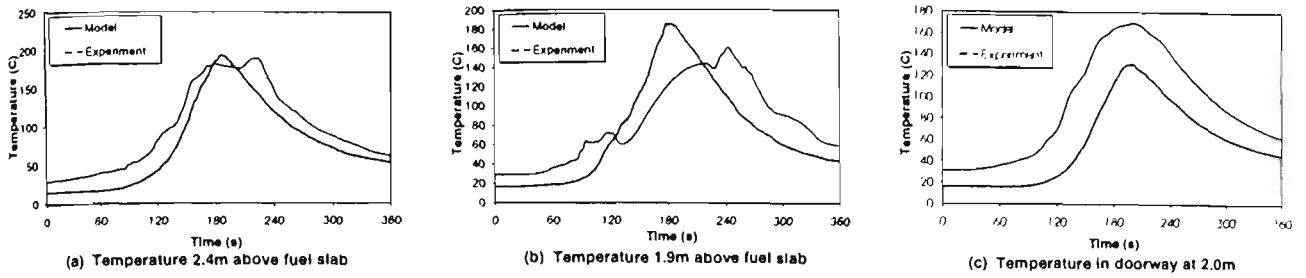

Figure 10 Temperature histories

Temperature histories are shown in Figure 10. As with the flow velocities, the steady state initialisation created elevated temperatures at the beginning of the simulation. Overall, the temperatures were generally overpredicted, as is most apparent in Figure 10(c), which shows good agreement in the timing of the temperature peak, but consistently overestimates the temperature itself. The temperature histories shown Figure 10(a) and Figure 10(b) again show the delayed and lower peak exhibited by the mass loss rate.

Other data recorded were species concentration in the doorway, and in addition oxygen concentration within the enclosure. A sample of points is shown in Figure 11. Oxygen concentration shows excellent correlation between model and experiment in the centre of the enclosure, while above the fuel surface it shows quite a deal of fluctuation, most likely due to the movement of the plume throughout the simulation. Carbon dioxide concentration in the doorway likewise shows good correlation. Overall, there is a tendency for the model to over-predict both CO_2 concentration and O_2 depletion. However, since the mass loss rate is underpredicted, it is expected that CO_2 concentrations should be likewise underpredicted as its source is the mass loss of the fuel. The "extra" carbon is probably an artefact of the steady-state initialisation.

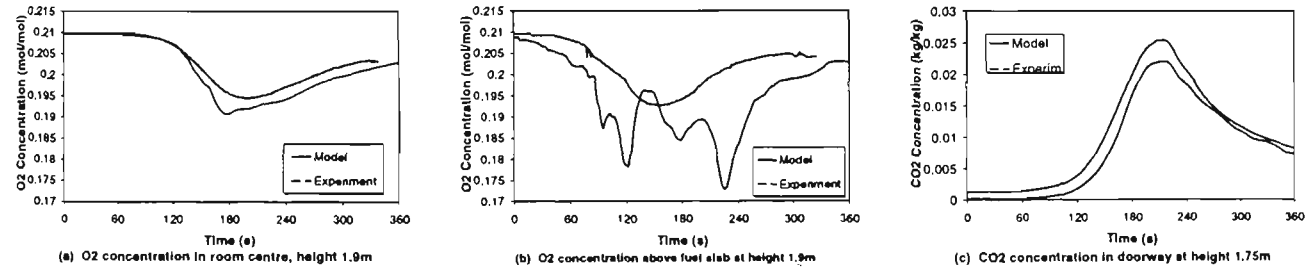

Figure 11 Species concentration at selected locations

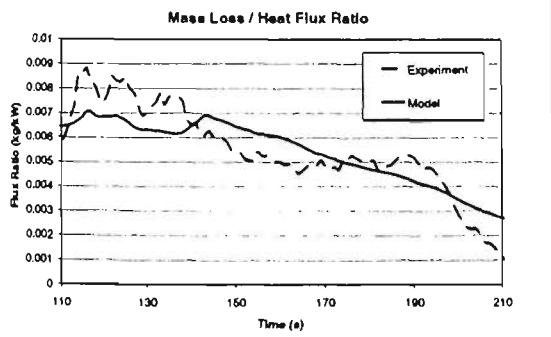

Figure 12 Mass loss rate to heat flux ratio

The other quantity measured in these experiments was the radiant heat flux to the middle of the burn room floor, as shown in Figure 7(b). The heat flux is underpredicted as would be expected from the mass loss rate. Indeed, the curve for mass loss rate and radiation to the floor show very similar profiles, both for experiment and model, so much so that they appear to be directly proportional. To test this, a simple ratio of heat flux to mass loss rate is calculated and plotted, as shown in Figure 12. This figure shows that for the peak combustion period between 120s and 210s, the ratio is quite steady at around 0.006 kg/kW, and that there is good agreement between model and experiment. In other words, the relatively poor prediction of radiative heat flux is a consequence of the poor prediction of mass loss rate, and hence rate of heat release of the fuel. If the mass loss rate were to have been predicted accurately, the ratio correlation suggests that the radiative heat transfer would likewise have been accurately predicted.

CONCLUSIONS

A flame spread model has been incorporated into a fire field model, and has been used to simulate an enclosure fire involving the combustion of a cushion sized slab of standard polyurethane foam. Discrepancies between experiment and modelling have been noted, and an explanation proposed for several of the discrepancies. However, the results overall show reasonably good agreement, which is a favourable outcome for the methods adopted for flame spread modelling presented in this paper. In particular, the cellular automata method is successful in predicting the radial spread of flame from a central ignition point, although the findings presented here show that it is sensitive to the physical data provided by the CFD model. Further refinement of the spread model is required, and further experimental work is desirable, particularly for other fuel configurations. These exercises are also left as future work.

REFERENCES

1 Hadjisophocleous, G. V. and Cacambouras, M. "Computer Modelling of Compartment Fires", Journal of Fire Protection Engineering, **5** (2), 39-52, 1993

2 Luo, M. and Beck, V. R. "Effects of Air-Handling System on Fire Spread in a Full-Scale Building", Sixth Australasian Heat and Mass Transfer Conference, 241-248, 1996

3 Di Blasi, C., Continello, G., Crescitelli, S. and Russo, G. "Numerical Simulation of Opposed Flow Flame Spread over a Thermally Thick Solid Fuel", Combustion Science and Technology, **54**, 25-36, 1987

4 Fernando, A. E. and Thorpe, G. R., "A Numerical Model for Horizontal Flame Spread over Combustible Solid Fuels", Sixth Australasian Heat and Mass Transfer Conference, 213-220, 1996

5 Quintiere, J. and Iqbal, N. "An Approximate Integral Model for the Burning Rate of a Thermoplastic-like Material", Fire and Materials, **18**, 89-98, 1994

6 Nicolette, V. F., Tieszen, S. R., Moya, J. L. "Interfacing Materials Models with Fire Field Models", 41st International SAMPE Symposium, March 24-28, 1996

7 Luo, M. and Beck, V. R., "A Study of Non-Flashover and Flashover Fires in a Full-Scale Multi-Room Building", Fire Safety Journal, 1996.

8 Luo, M. and Beck, V. R., "The Fire Environment in a Multi-Room Building-Comparison of Predicted and Experimental Results", Fire Safety Journal, **23**, 413-438, 1994

9 Boyd, R. K. and Kent, J. H. "Three Dimensional Furnace Computer Modelling", Twenty-first Symposium (International) on Combustion, 265-274, 1986

10 Lockwood, F. C. and Shah, N. G. "A New Radiation Method For Incorporation in General Combustion Prediction Procedures", Eighteenth Symposium (International) on Combustion, 1405-1414, 1981

11 Baroudi, D., and Kokkala, M., "Flame Spread and Heat Release Rate Model for a Burning Mattress", Interflam '96, 37-46, 1996

12 Delichatsios, M. M., Mathews, M. K., and Delichatsios, M. A., "An Upward Fire Spread and Growth Simulation", Fire Safety Science: Proceedings of the Third International Symposium, 207-216, 1991

13 Drysdale, D. D., An Introduction to Fire Dynamics, John Wiley and Sons Ltd., 1985

14 Launder, B. E. and Spalding, D. B. "The Numerical Computation of Turbulent Flows", Computer Methods in Applied Mechanics and Engineering, **3**, 269-289, 1974

15 Chang, T. C., Shen, W. S., Chiu, Y. S., and Ho, S. Y. "Thermo-oxidative Degradation of Phosphorus-containing Polyurethane", Polymer Degradation and Stability, **49**, 353-360, 1995

EXPERIMENTAL DERIVATION OF MATERIAL COMBUSTION PROPERTIES FOR FLAME SPREAD MODELS

Anthony Fernando
CESARE, Victoria University of Technology, Australia
Justin Leonard, Alex Webb, Paul Bowditch & Vince Dowling
Department of Building and Construction Engineering, CSIRO, Australia

ABSTRACT

With increasing computational resources becoming more readily available, there is a trend to incorporate more complex and fundamental combustion properties into fire growth and spread models[1]. Properties of the fuel which may be required in a combustion model include conductivity, specific heat, density, heat of combustion, rate of heat release per unit area, latent heat of volatilisation, and surface ignition temperature. Decomposition of the fuel may be modelled using an Arrhenius equation, in which case activation energy and the pre-exponential constant are also required. Flame spread across the fuel is another factor which may be required by some models, although previous work has shown that flame spread arises as a consequence of modelling a series of ignitions over a fuel surface, using only the aforementioned material properties[2].

Previous work involving flame spread modelling and large scale experiments[1,2] used a standard, non-flame retarded polyurethane foam as a fuel, chosen for its regular combustion behaviour and its frequent use in everyday furnishings. This paper examines the experimental methods used to obtain material data necessary for input into the computer models, focusing principally on the Cone Calorimeter, using the ASTM standard method[3], but also discussing Thermo-Gravimetric Analysis and other small scale methods. While it was possible do derive a reliable value for heat of combustion from the Cone Calorimeter results, it was difficult to determine other material properties required for the combustion models. This is likely a result of following the standard method, and variations to the standard are identified which may enhance the possibility of extracting the other material data from the results. In particular, Cone Calorimeter experiments performed in reduced oxygen environment show promise in identifying pyrolysis rates as a function of applied radiant flux, without the variable influence of the presence of a flame.

INTRODUCTION

Mathematical and computational modelling is a comparatively safe and inexpensive method of gaining insight into the behaviour of fire and fire related phenomena. With computational resources becoming both increasingly powerful and less expensive, the opportunity arises to make models increasingly more complex, and incorporate theoretical or fundamental principles, rather than rely on empirical models and equations derived from experiment. This paper describes the experimental and modelling program which culminated in the development of a Computational Fluid Dynamics (CFD) model incorporating a solid fuel flame spread and fire growth model along with its existing combustion and mass transport equations. The experimental program that accompanied the development of the model incorporated both bench-scale and full-scale tests. Aspects of all the experiments are described to some degree herein, although the focus will be on a series of Cone Calorimeter experiments that were performed on a type of standard polyurethane foam, that is, without fire retarding additives.

The motivation for developing the CFD flame spread model is to further develop the potential of such models to be used as a fire safety tool, particularly for enclosure fires. An important factor in determining the fire safety hazard in an enclosure of a particular material is the Rate of Heat Release (RHR)[4]. The heat release rate in an actual enclosure fire itself has many influences, but these may be grouped into two main categories. Firstly, there are those that relate to the material properties of the fuel undergoing combustion, such as heat of combustion, thermal inertia, and rate of decomposition. Secondly, there are those that relate to the nature of the fire itself, such as the conditions prevailing in the enclosure, the area of the material burning, and even the orientation of the material. This second category is the most variable, and it is these factors which need to be controlled or constrained in a modelling and experimental program. For instance, if the response to the material to a given imposed heat flux or oxygen concentration is known, then given the conditions in a particular fire scenario, an estimate of the burning behaviour of that material should be readily forthcoming. Also, the heat release rate of a material is proportional to the burning area, so that knowing the rate at which the area is increasing, namely the flame spread rate, will aid in prediction of the burning area at a future time.

The material investigated in this study is a standard polyurethane foam (PUF). The material was chosen for its isotropic material properties and fairly uniform combustion properties, which make it relatively easy to model (as opposed to wood, for instance), and for the fact that it is a commonly occurring material in real enclosures (as opposed to materials such as PMMA).

MODELLING

CFD modelling of fire, otherwise known as fire field modelling, is a method that can yield much detail about the conditions prevailing in the enclosure being modelled. Such models require a heat and mass source, namely the burning item, as a boundary condition to the equations being solved. Often, this source is prescribed[5], and does not respond to the conditions prevailing in the modelled enclosure. However, for accuracy, the burning item should respond to the conditions prevailing in the enclosure, as predicted by the model, and generate an appropriate heat and mass source accordingly. The model should therefore predict both the combustion response and the fire spread rate. Examples of fundamental flame spread modelling exist, but in such cases the flame spread is concentrated upon in detail in isolation, with conditions prescribed for the fire environment[6].

A CFD fire model was previously developed[7] in which a simple combustion model was combined with a flame spread model, where the flame spread rate was a function of the received heat flux at the flame front. The model produced some useful results, but was limited by assumptions about the geometry of the flame spread, namely that the burning surface was horizontal, circular, and spreading radially. Also, the rate of flame spread used an empirical function, relying on measurements in a particular configuration and material, under a variety of imposed heat fluxes[8].

In order to overcome geometric and empirical assumptions, a more fundamental approach to the modelling of the flame spread was devised. The surface of the fuel is divided into a fine square mesh. The state of each surface element is considered individually, and properties of each element considered include the surface temperature, internal temperature, mass loss rate, and mass remaining. Flame spread across the surface is not calculated explicitly. Instead, flame spread occurs as a consequence of individual surface elements igniting. The ignition criterion is based on surface temperature, and the method incorporates cellular automata techniques. Details of the model and the cellular automata techniques have been described previously by Fernando et al[1,2].

Because CFD modelling is computationally intensive, the flame spread model was developed as a stand-alone model first, then incorporated into the CFD model. The stand-alone model assumed a horizontal fuel surface, with the flame itself having a hemi-ellipsoidal shape with a circular base, and whose height was a function of the mass loss rate and burning diameter. The model was compared with two series of full-scale tests to verify that the flame spread modelling method was feasible. After the method was satisfactorily verified, the stand-alone model was incorporated into the CFD model,

and compared with another series of full-scale tests which were designed to extract additional data from the fire environment itself.

Thermal Degradation of Solids

Thermal degradation of a solid fuel is the precursor of combustion, and the initiation of most accidental enclosure fires[9]. When heat is applied to a solid fuel, some of the heat will be responsible for raising the temperature of the solid, some of the heat will be re-emitted back to the surroundings, and some of the heat will go into breaking the chemical bonds in the long chain molecules of the solid and imparting sufficient energy to the molecular fragments to convert them to gaseous species, or volatiles. This latter effect is the thermal degradation, and the mechanism by which it occurs is different for each type of fuel.

The rate at which a solid decomposes is an increasing function of temperature. Like many chemical reactions, the kinetics of the reaction is assumed to obey an Arrhenius type relation. For a single step first-order reaction, the rate may be expressed

$$R_s = A \cdot \exp\left(-\frac{E}{RT_s}\right) \qquad [1]$$

where R_s is the rate of decomposition of the solid, T_s is its temperature, and R is the universal gas constant. The two values characteristic of the reaction are the activation energy, E, and the pre-exponential constant, A. When decomposition is occurring by several mechanisms, there will be a separate activation energy and pre-exponential constant for each reaction. However, the model presented here makes the assumption that a single step global model is sufficiently accurate to model the decomposition of the fuel being dealt with. This approach has previously been found to sufficient for a variety of combustion and flame spread applications[10,11,12].

Treating the decomposition of the fuel as occurring in a single step obviously makes the process much simpler to model. Because only one reaction is occurring, it is a common practice to state that a given amount of heat will produce a given mass of volatiles (or equivalently, a given mass of volatiles produced will remove a given amount of heat). This is referred to as the heat of volatilisation, and it is generally an endothermic reaction.

Ignition

At some stage during the thermal degradation of a solid fuel, conditions may become suitable for the ignition of the fuel. Flaming ignition actually occurs in the gas phase, although it is strongly linked to the temperature of the solid fuel in the vicinity of the ignition point. The process of ignition by radiant heating has been outlined by Di Blasi[9]. It is a common practice to assume that ignition occurs when the surface of the fuel reaches a critical temperature. While the concept of a surface ignition temperature remains somewhat controversial[13], few practical alternatives have been offered, so it is still the mainstay of many combustion and flame spread models[14,15].

Critical surface ignition temperature may be considered to be a basic material property which may be determined from appropriate experimental methods[16]. In practice, direct measurement of the surface temperature is very difficult to achieve. However, critical ignition temperature, whether piloted or auto, may be related to other fundamental material properties by the expression[17]

$$t_{ig} = \frac{\pi}{4}\frac{\Delta T_{ig}^2 (k\rho c_p)}{\dot{Q}_e''^2} \qquad [2]$$

where ΔT_{ig} is the temperature rise of the fuel surface above ambient or initial temperature, t_{ig} is the time to ignition of the material subjected to an applied external flux $\dot{Q}_e''$, and k is the conductivity, ρ

the density, and c_p the thermal capacity of the fuel. Equation 2 only applies to fuels which are thermally thick, that is, if its thickness, τ, satisfies the inequality[18]

$$\tau > 2\sqrt{\frac{kt}{\rho c_p}} \qquad [3]$$

where t is the duration of heating. Also, Equation 2 is not valid when the value of the applied heat flux is close to the minimum heat flux required to ignite the fuel.

Combustion of Solid Fuels

For the decomposition reaction to proceed, there needs to be a continual input of heat to maintain the reaction. The two main sources of heat are externally applied heat, and heat from the reaction of the fuel volatiles themselves with oxygen. This may take the form of smouldering, glowing, or flaming combustion, and it is the latter that is of interest in this study. Although combustion of the fuel (by definition) liberates energy, combustion will only be self sustaining if the feedback of heat from the combustion region back to the pyrolysing region of the fuel is greater than the heat losses occurring at this same region. For steady combustion, the heat from the flame will be in equilibrium with the losses. A simple balance equation can therefore be written[17].

$$\dot{m}'' L_v = \dot{Q}_f'' + \dot{Q}_e'' - \dot{Q}_{loss}'' \qquad [4]$$

where $\dot{Q}_f''$ is the heat flux from the flame, $\dot{Q}_e''$ is the externally applied heat flux, $\dot{Q}_{loss}''$ is the heat lost from the surface, $\dot{m}''$ is the mass flux from the surface, and L_v is the latent heat of volatilisation. The flame heat is the sum of the radiative and convective heat fluxes directly from the flame. The heat losses are a combination of heat conducted into the surface and re-radiated heat. Even for unsteady combustion, Equation 4 may be used to determine the instantaneous heat balance.

In order to consider Equation 4 in a more mathematically rigorous sense, the terms therein need to quantified. This requires a determination of the temperature of the surface, as the magnitude of the conduction, convection, and re-radiation heat fluxes which contribute to $\dot{Q}_{loss}''$ are all dependent on the surface temperature. Conduction of heat into the fuel is proportional to the temperature gradient at the surface, given by the equation

$$\dot{q}_{conduct}'' = -k \left.\frac{dT}{dz}\right|_{z=z_0} \qquad [5]$$

where k is the conductivity of the fuel. The reradiated flux from the surface is given by

$$\dot{q}_{reradiant}'' = \varepsilon \sigma T_0^4 \qquad [6]$$

where ε is the emissivity of the fuel, which can be taken to be close to 1 when the fuel is undergoing combustion. The emissivity is also the fraction of the externally applied radiant heat, $\dot{Q}_e''$, which is absorbed by the surface. Convection to the surface from the flame is incorporated in the term $\dot{Q}_f''$. Alternatively, if the temperature of the gas in contact with the surface, T_{gas}, is known, the heat transferred to the surface by convection may be given by

$$\dot{q}_{convect}'' = h(T_{gas} - T_0) \qquad [7]$$

where h is the heat transfer coefficient, and T_{gas} and T_0 are the gas and surface temperatures respectively. Basic expressions for the convective heat transfer constant are available for certain special cases, and it is often taken to be a global constant[19].

Like the convective heat transfer, the heat transfer from the flame as expressed by the term $\dot{Q}_f''$ in Equation 4 essentially depends on gas phase phenomena. As is the case with convection, it is possible to make simplifications, such as to assume that $\dot{Q}_f''$ is a constant which is characteristic of the fuel in question, for a given configuration (usually horizontal, or pool fire configuration.) This may be determined from controlled, small-scale tests. The constant heat assumption may be modified to take into account ambient oxygen concentration. For a higher concentration, the fuel will burn more rapidly and efficiently. This may be expressed[18]

$$\dot{Q}_f'' = \xi Y_{O_2} \qquad [8]$$

Pyrolysis of the fuel will result in mass loss. In the case of charring fuels, this will result in an overall density change in the char layer, while in non-charring fuels it results in an actual regression of the fuel surface. This must be taken into account in any model which attempts to calculate the internal fuel temperature.

There are essentially two methods for calculating the temperature distribution; a finite difference approach, and an integral method approach. The integral method simplifies the conduction problem by assuming a functional temperature profile and a heating depth. Quintiere et al[20] and Mogtaderi et al[21] assume a parabolic temperature profile, while Delichatsios et al[22,23] assume an exponential profile. This method therefore only needs to determine a relatively small number of unknowns associated with the boundary conditions, and despite its simplifications may yield reasonably accurate results[20,21,22,23]. These simplifications also make it a useful method for use in CFD combustion models, where computational resources are always limited[21]. One of the disadvantages of this method, however, is the fact that it is only designed to calculate the heat conduction normal to the surface, and cannot calculate the lateral heat conduction which is important in certain flame spread situations[24]. On the other hand, a finite difference method which solves the temperature distribution on a specified array of nodes may readily be expanded to three dimensions, and may more accurately determine the temperature profile within the fuel. The price paid for this accuracy and flexibility naturally enough is computation time.

Combining Equations 1, 4, 5, 6, and 7 results in the heat flux balance equation given by

$$L_v A \exp\left(\frac{-E}{R_u T_0}\right) = \varepsilon \dot{Q}_r'' - \varepsilon\sigma T_0^4 + h(T_{gas} - T_0) - \frac{k}{\Delta z}(T_0 - T_l) \qquad [9]$$

This equation is solved numerically to give the surface temperature, T_0, from which the other quantities may be derived. The combustion model is similar to that developed by Steckler et al[25] for combustion of PMMA, except that in the model presented here, surface temperature is calculated for all stages of the combustion, whereas the model of Steckler et al assumes vaporisation temperature of the PMMA. The temperature distribution within the fuel is calculated by the finite difference method, with a grid transformation to account for regression of the fuel surface as the combustion proceeds. A summary of the constants required for the model is given in Table 1.

Table 1 Constants required in the combustion and flame spread model

Symbol	Description	Units	Symbol	Description	Units
ρ	Density	kg/m^3	A	Pre-exponential constant	s^{-1}
k	Thermal conductivity	W/m·K	E	Activation energy	J/mol
c_p	Specific heat	J/kg·K	L_v	Latent heat of volatilisation	J/kg
ε	Emissivity	1	ΔH_c	Heat of combustion	J/kg
T_{ig}	Ignition temperature	K	$\dot{Q}_f''$	Heat flux from flame	W/m^2

EXPERIMENTS

The material properties that both the stand-alone and the combined CFD flame spread model require were initially derived, where available, from literature values. These values were quoted for a material described simply as "polyurethane foam". However, the chemical composition and foam density varies considerably from sample to sample, depending on the particular manufacturers' specifications. Consequently, these values were subsequently determined, where possible, from cone calorimeter experiments on foam from a particular manufacturer. The method of operation of the cone calorimeter followed ASTM standard E 1354-90. Basic physical properties of the foam as provided by the manufacturer are: density 23 kg/m^3, thermal conductivity 0.036 W/m· K, and thermal capacity 1400 J/kg· K.

Thermo-Gravimetric Analysis

Thermo-Gravimetric Analysis (TGA) is a method by which the chemical kinetics of thermal decomposition may be determined[26]. In simplest terms, a small sample (typically around 20 milligrams) of the material is placed on a fine balance, its temperature raised in a controlled fashion, and the mass of the sample recorded continuously as a function of time. Once the sample is raised to a given temperature, the rate of mass loss will be proportional to the amount of remaining mass i.e.

$$\frac{\partial m}{\partial t} = -R_s \cdot m \qquad [10]$$

where R_s is the rate constant for solid composition, as given in Equation 1 for a first order reaction. The rate of mass loss is measured for a number of temperatures. If only one decomposition reaction is dominant, then according to a rearrangement of Equation 1 given by

$$\log\left(\frac{\dot{m}}{m}\right) = \log(R_s) = \log(A) - \frac{E}{RT} \qquad [11]$$

it can be seen that a plot of $\log(R_s)$ versus $1/T$ will result in a series of points along a straight line with slope $-E/R$ and which intercepts the vertical axis at $\log(A)$.

If there is more than one reaction occurring at the same time (as is usually the case), then the points will not necessarily be linear, or may be linear over a number of segments with a particular reaction dominating at a given temperature. Also, there will be a delay in raising the sample to a given temperature. This may be avoided by the use of differential thermogravimetry (DTG). In this technique, the temperature of the sample is raised linearly with time, and the mass recorded continuously. The rate of mass loss is taken from the slope of the mass history, and divided by the mass history itself, to yield a time dependent reaction rate. Since the time dependence of the temperature is also known, Equation 11 can be rewritten with time t as a parameter

$$\log(R_s(t)) = \log\left(\frac{\dot{m}(t)}{m(t)}\right) = \log(A) - \frac{E}{R \cdot T(t)} \qquad [12]$$

A plot of $\log(R_s(t))$ versus $1/T(t)$ will yield a continuous curve, with possibly one or more straight (or nearly straight) line segments. These segments result when a reaction dominates at a particular temperature range, and as this range is "traversed" in time by the rising temperature, the straight line segment will be parametrically traced according to Equation 12.

Preliminary DTG experiments were performed on a sample of polyurethane foam. There was insufficient data to confidently determine values of A and E from Equation 12, but the results did confirm that there are two main reactions occurring at around 270°C and 380°C respectively. The activation energy of the second peak was measured at around 170 kJ/mol, which is comparable to values quoted elsewhere[27,28].

Cone Calorimetry

In light of the success of past research work performed with the cone calorimeter, it appeared to be a favourable method for exploring the parameters of the heat balance equation (Equation 4) in order to determine the heat of volatilisation and heat of combustion of the foam used in this study. Also, by measuring the ignition times, the critical ignition temperature could be determined from Equation 2. A series of cone calorimeter experiments was performed in accordance with the standard ASTM E1354-94. All samples were prepared in accordance with standard. All samples were then wrapped on five sides with aluminium foil, shiny side inwards, exposing only a single 100×100 mm face, and placed in a sample holder which exposed 94×94 mm of this face, before testing. Samples were tested both with and without a pilot spark, to obtain data on piloted ignition and autoignition. The samples were tested at six irradiances; 10, 15, 25, 35, 50, and 70 kW/m^2. The data of interest obtained from the standard experiments were rate of heat released (RHR), mass remaining, rate of mass loss, and effective heat of combustion (EHC), given by RHR divided by the rate of mass loss. These were all measured as a function of time.

Ignition Tests

A series of experiments was performed to determine the critical ignition flux for both types of ignition. The critical flux was defined as the flux where two or three samples out of three ignited, and one or no samples out of three ignited at an irradiance $1kW/m^2$ lower than the critical flux. A time limit for ignition was set at 600 seconds, after which the test was terminated and the fuel deemed to have not ignited. Adhering to these criteria, the critical flux for piloted ignition was found to be $7kW/m^2$, and $28kW/m^2$ for autoignition. However, these figures cannot be given without some qualification. At $7kW/m^2$, initial discolouration of the sample occurs mainly beneath the pilot spark rather than uniformly across the surface, which suggests that additional energy is being supplied by the pilot, and that the critical flux is actually slightly higher. At $28kW/m^2$, there is significant melting and surface regression before ignition. Considering the changing heat flux with height (discussed in further detail below), the flux present at the surface at the actual moment of ignition will be significantly different from the flux at the virgin fuel surface.

Ignition times for each of the tests were recorded. It was anticipated that Equation 2 would be used to calculate the surface temperature rise, since thermal inertia of the foam is known, and externally applied heat flux and ignition time was readily measured. However, the ignition times were found to be very short, and therefore subject to error in measurement. For very high heat flux values, rapid surface regression due to melting and volatilisation occurred, and this actually delayed ignition.

At the other end of the scale, an irradiance of 10 kW/m^2 is too close to the critical heat flux (7 kW/m^2) for the ignition time to be strictly useable. There is also the issue of surface regression and the subsequent variation in applied heat flux to take into account. Naively ignoring these factors, the figure for ΔT_{ig} as obtained from Equation 2 is around 2000K for piloted ignition of standard foam, which is significantly higher than the expected value[18] of around 550K.

Combustion Tests

The mass loss as a function of time for a number of applied heat flux values is shown in Figure 1. As expected, the higher applied heat fluxes result in more rapid mass loss rates. Consequently, in order to compare the other quantities, heat release rate and effective heat of combustion, it is useful to plot them as a function of mass remaining rather than as a function of time. These charts are shown in Figure 2 and Figure 3 respectively. Also shown here in Figure 4, but discussed later, is the mass loss of the sample performed in an inert atmosphere (N_2) where no combustion took place. The same trend of increasing mass loss rate with increasing applies heat flux is demonstrated as with Figure 1.

Figure 1 Mass fraction remaining as a function of time.

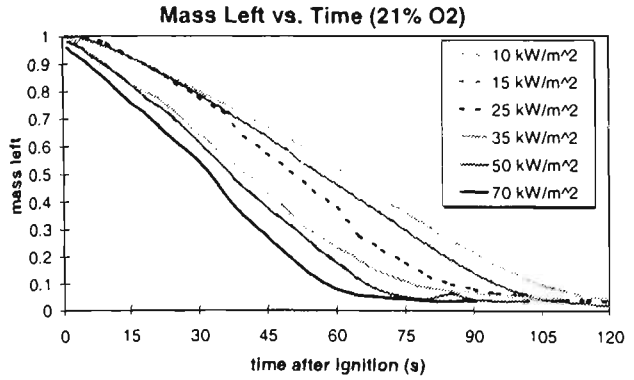

Figure 2 Rate of heat release as a function of mass remaining.

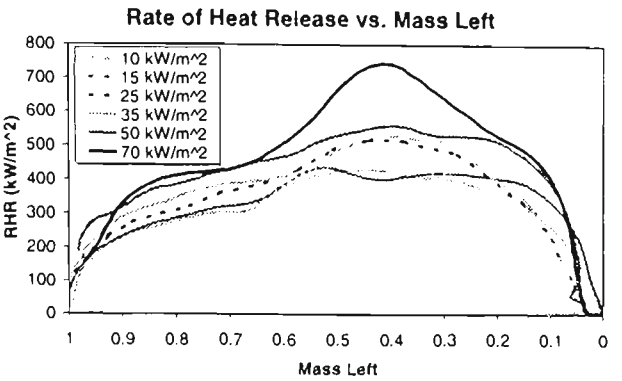

Figure 3 Effective heat of combustion as a function of mass remaining.

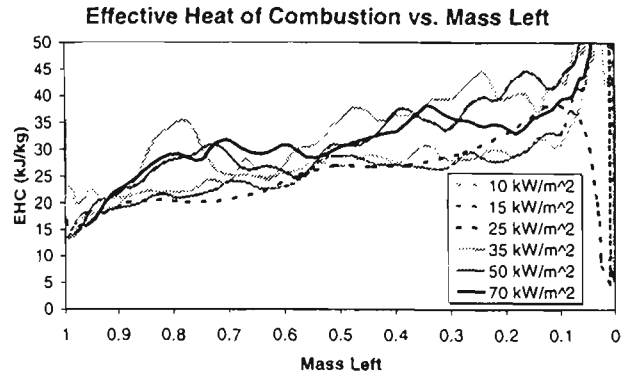

Figure 4 Mass fraction remaining as a function of time with no combustion.

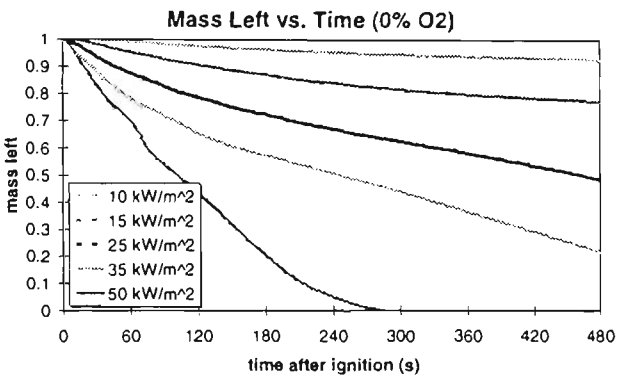

It is apparent from Figure 2 that for the duration of the combustion of each sample, there is no obvious plateau in the heat release rate curve. As Equation 4 is most useful when steady burning of the fuel sample is attained at some stage in the cone calorimeter test, it is clear that careful consideration of the cone calorimeter combustion scenario is required in the interpretation of the data yielded from these tests.

The cone calorimeter testing of polyurethane has been investigated previously by Vanspeybroeck et al[29]. An important finding is that the heat flux produced by the cone decreases significantly with distance from the cone heater, down to 40% over the 50mm thickness of sample. This is a problem for materials which melt readily, such as PUF, since the surface may regress significantly before ignition occurs. This leads to great uncertainty in estimating material properties such as critical ignition flux and surface ignition temperature. Vanspeybroeck et al chose to restrict the thickness of their samples to 25mm, to minimise errors caused by this effect. Even this is a compromise, as there is a drop in heat flux even over the 25mm distance. One of the conclusions in their paper is that the cone calorimeter is an unsuitable method for determining the basic thermophysical material characteristics of polyurethane foam.

As part of the work presented in this paper, the radiant flux was mapped as a function of the distance below the prescribed fuel surface height, and also laterally from the centre. Not only was it confirmed that the heat flux decreased with height below the surface, up to a 36% drop 50mm below the surface, but it was also found that the horizontal flux distribution became progressively less uniform with increasing depth. It was found that there was a 60% drop in the corner of the sample at 50mm depth. An expected consequence of this heat flux distribution is that a sample undergoing combustion under the cone heater will pyrolyse more rapidly in the centre, so that the surface is expected to become increasingly concave as combustion progresses. A concave surface presents a greater surface area for mass loss than a planar surface, which may perturb mass flux calculations if the surface is assumed to be flat.

Another phenomenon which may be a factor is that observed by Orloff[30] in the modelling of thermal radiation from pool fires. It was found that the "collar" of the container in which the pool fire is burning is responsible for as much as 15% of the radiative feedback to the surface. This figure may be even greater so for the sample holder commonly used in cone calorimeter tests. Overall, it is not surprising, given the combined effects of the sample holder reradiation and the diminishing flux with height, that steady burning of foam samples in the cone calorimeter is not observed.

Indeed, it is surprising that steady burning of any fuel is observed. The key issue is the low density of the foam, and its rapidly regressing surface as it burns. The surface of a denser fuel burning with the same rate of mass loss as a foam will regress more slowly as it undergoes combustion. Since the holder feedback and diminishing cone radiation will not be changing significantly in magnitude, at least over short time intervals, steady burning conditions may be readily attained. Some fuels do not even require the holder, and may burn as free-standing objects, provided some means of preventing the sides from igniting is implemented. Polyurethane foam, on the other hand, regresses swiftly as it burns, and its tendency to form molten products as it does so dictates the need for a sample holder.

Further Analysis of Cone Calorimeter Results

Despite the lack of a steady burning interval for polyurethane foam tests in the cone calorimeter, it has been suggested that heat of volatilisation may be determined by measuring the peak rate of heat release for a variety of incident heat fluxes[31]. A plot of peak heat release rate versus external heat flux should reveal a linear relationship, the slope of the line being the quotient of the heat of combustion and heat of volatilisation. So, despite the inherent difficulties described here, it is still possible to acquire the required data, namely heat of combustion and heat of volatilisation.

The average EHC is calculated by dividing the total heat released, as calculated by oxygen consumption, by the total mass loss. Values for both piloted and non-piloted tests of standard foam are shown in Figure 5. A phenomenon observed for the non-piloted tests at 35kW/m^2 is the significantly lower EHC, which is largely due to the lengthy ignition time. The ignition time for these tests was on average 30s, by which time a significant amount of fuel had already undergone pyrolysis.

Figure 5 Average effective heat of combustion versus applied heat flux

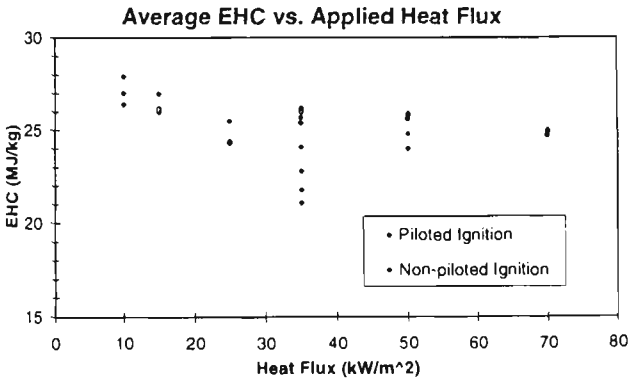

Figure 6 Peak rate of heat release versus applied heat flux

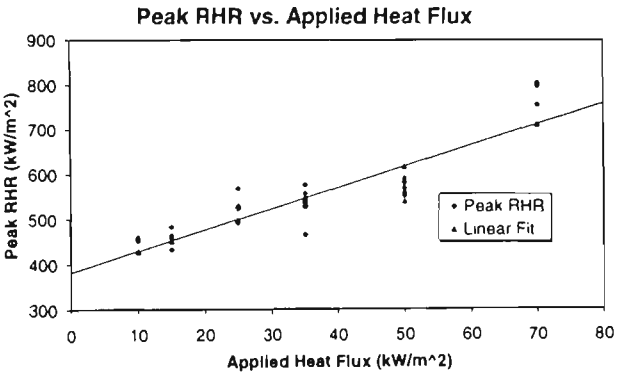

There is a significant variance in the values of EHC over the range of applied heat fluxes. For piloted ignition, the value appears to decrease with increasing applied heat flux. This is somewhat puzzling, as the expectation would be that applying more heat would reduce heat lost from the flame, and a hotter flame would produce more efficient combustion, resulting in increased values of EHC. A possible cause of the decrease is that the increased heat flux produces a higher flux of volatiles from the surface. The resulting flame may be fuel rich, and combustion therefore less efficient. Whatever the case may be, the heat of combustion is difficult to estimate accurately from the available data, since it appears to be dependent on the applied flux and burning conditions. Taking the average for all the tests results in a value of 25.7 MJ/kg for heat of combustion.

As none of the RHR curves show any region of steady burning, the heat of volatilisation is calculated by considering the peak RHR. The peak RHR for the tests is shown in Figure 6. The retarded foam data shows no obvious linear relationship with applied heat flux, whereas a linear fit is shown for the standard foam. The solid line in Figure 6 shows the best fit as determined from linear regression. The gradient of this line is given[11] by $\Delta H_c/L_v$, where ΔH_c is taken to be the value 25.7 kJ/kg derived above. The slope of the solid line in Figure 6 is 4.71, which corresponds to a heat of volatilisation of 5.46 MJ/kg. This is considerably greater than the value of 1.22 MJ/kg given by Tewarson and Pion[18], so some doubt must be cast on the figure experimentally derived here.

Controlled Atmosphere Tests

The uncertainty in the results presented so far is primarily due to the influence of the flame when the sample undergoes combustion. Controlled atmosphere tests offer the possibility of being able to quantify the influence of the flame. Typically, tests are performed in a reduced oxygen atmosphere due to the hazards associated with oxygen enrichment. A series of tests were performed in the same cone calorimeter, configured so that samples may undergo combustion in a controlled atmosphere. The additional tests presented here were performed in an atmosphere composed of 100% nitrogen. The mass loss rates were shown earlier in Figure 4. The figure shows the expected increase in mass loss rate with increased applied heat flux, as well as the decrease in mass loss rate as the sample pyrolyses. This latter effect is likely due to the combined effect of decreased flux as the sample surface recedes from the cone heater, and the increasing heat of volatilisation of the remaining sample as the more readily pyrolysed compounds are "boiled off".

In order to avoid some of the previously described uncertainty, analysis of the results is best performed on the earliest stage of the test, when the samples have undergone less than 5% mass reduction. The fuel surface at this point has not regressed significantly, so the applied surface flux is known, and conditions will not be changing significantly over such a relatively short time interval. The mass loss rates for the first 5% pyrolysis were averaged for the controlled atmosphere (0% O_2) tests as well as the ambient atmosphere (21% O_2) tests, and presented in Figure 7.

Figure 7 Mass loss rate versus applied heat flux for controlled and ambient atmospheres

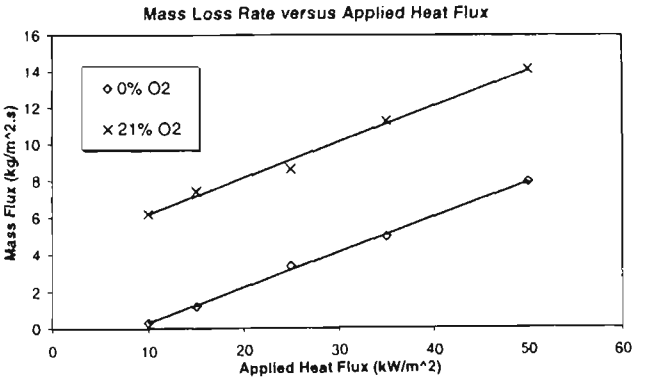

The chart demonstrates a clear linear trend of increasing mass loss rate with increased applied heat flux. The gradient of the linear trends is the inverse of the heat of volatilisation, which gives figures of 5.28 MJ/kg for controlled atmosphere, and 5.08 MJ/kg for ambient atmosphere, both of which are comparable to the figure derived earlier by consideration of peak heat release rates. The chart yields additional information: the 0% trend intercepts the x-axis at 8.2 kW/m^2, which implies that in the absence of a flame, this is the flux required to overcome heat losses and produce volatiles. This is consistent with the figure of 7 kW/m^2 for the critical flux for piloted ignition, and the hypothesis that the pilot flame may be providing additional energy. The 21% trend intercepts the x-axis at -21.4 kW/m^2, which, when subtracted from the 0% intercept, yields the flux produced by the flame, 29.6 kW/m^2. Naturally, for the reasons given above, this figure only applies at the initial stages of combustion, as the changing combustion conditions will alter the flame characteristics. Nevertheless, it is a useable figure for development of the combustion model.

CONCLUSIONS

A combustion model was developed and described, and cone calorimeter testing of polyurethane foam was undertaken to with the aim to determine the material properties of the foam for use with the model. While reservations concerning the validity of the experimental procedures were identified, some of the aims were nevertheless achieved, and reliable figures for some of the fundamental material properties were attained. The heat of combustion of standard polyurethane foam was found to be around 26 MJ/kg, although the figure appeared to depend both on the applied radiant heat flux, and the stage of combustion of the sample itself. Nevertheless, these values are expressed with some confidence, for two reasons: they are comparable to values reported in the literature, and the cone calorimeter is specifically designed to measure heat of combustion. The value for heat of volatilisation was calculated in three instances to be around 5.2 MJ/kg, which is encouraging for its internal consistency, but is greater than previously reported values. The calculation method for critical surface ignition temperature was found to be unsuitable for the experimental method chosen, so no reliable figure was derived here.

If cone calorimetry is to be used successfully to determine fundamental material combustion properties of polyurethane foam and other expanded thermoplastic polymers, then several issues need to be addressed, and overall experimental techniques need to be revised from a prescriptive standard method. In preparing foam samples, some means of doing away with the sample holder would help to reduce the heat feedback to the fuel surface from the holder. For instance, blocks of black PMMA burnt in the cone calorimeter as calibration runs, use a cardboard liner at the sides which burns away as the surface regresses, yet remains in place long enough to prevent spillage of the liquid surface layer and the spread of combustion to the sample sides. Perhaps a container of some type of paper may be suitable for PUF samples. Other factors to be addressed in the future include maintaining a steady heat flux as the surface of the fuel rapidly regresses, and the related issues of determining critical heat flux for autoignition and surface temperature at ignition. Such issues are not insurmountable, so there is no reason to suppose that cone calorimetry is incapable of determining fundamental material properties.

REFERENCES

1. FERNANDO, A. E. "A Cellular Automata Approach to CFD Flame Spread Modelling", *Fire Safety Science: Sixth International Symposium*, University of Poitiers, Poitiers, 1999, p625-636.
2. FERNANDO, A. E. AND THORPE, G. R., "A Numerical Model for Horizontal Flame Spread over Combustible Solid Fuels", *Sixth Australasian Heat and Mass Transfer Conference*, University of New South Wales, Sydney, 1996, pp213-220.
3. ASTM E 1354-90 "Standard Test Method for Heat and Visible Smoke Release Rates for Materials and Products Using an Oxygen Consumption Calorimeter" *ASTM Fire Test Standards, 4th Edition*, ASTM, Philadelphia PA, 1993 pp968-984.
4. BABRAUSKAS, V., AND PEACOCK, R. D., "Heat Release Rate: The Single Most Important Variable in Fire Hazard", *Fire Safety Journal*, **18**, 1992, pp255-272
5. HADJISOPHOCLEOUS, G. V. AND CACAMBOURAS, M. "Computer Modelling of Compartment Fires", *Journal of Fire Protection Engineering*, **5 (2)**, 1993, pp39-52
6. DI BLASI, C., CONTINELLO, G., CRESCITELLI, S. AND RUSSO, G. "Numerical Simulation of Opposed Flow Flame Spread over a Thermally Thick Solid Fuel", *Combustion Science and Technology*, **54**, 1987, pp25-36.
7. LUO, M. AND BECK, V. R. "Effects of Air-Handling System on Fire Spread in a Full-Scale Building", *Sixth Australasian Heat and Mass Transfer Conference*, 1996, pp241-248.
8. QUINTIERE, J. G. "Surface Flame Spread", *SPFE Handbook of Fire Protection Engineering*, 1988, Section 1, pp360-367
9. DI BLASI, C., "Modelling and Simulation of Combustion Processes of Charring and Non-charring Solid Fuels", *Progress in Energy and Combustion Science*, **19**, 1993, pp77-104

10. YUEN, R., YEOH, G. H., CASEY, R., CHANDRASEKARAN, V., DE VAHL DAVIS, G. AND LEONARDI, E., "Three-Dimensional Numerical Prediction of Burning Wood in a Cone Calorimeter", *Proceedings of the International Conference on Fire Research and Engineering*, Orlando, USA, 1995, pp223-228
11. OHKI, Y. AND TSUGÉ, S. "On the Flame Spreading over a Polymer Surface", *Combustion, Science and Technology*, **9**, 1974, pp1-12
12. DI BLASI, C., CONTINILLO, G., CRESCITELLI, S. AND RUSSO, G. "Numerical Simulation of Opposed Flow Flame Spread over a Thermally Thick Solid Fuel" *Combustion Science and Technology*, **54**, 1987, pp25-36
13. WILLIAMS, F. A. "Mechanisms of Fire Spread", *Sixteenth Symposium (International) on Combustion*, 1976, pp1281-1294
14. DE RIS, J. N. "Spread of a Laminar Diffusion Flame", *Twelfth Symposioum (International) on Combustion*, 1969, pp241-252
15. ATREYA, A. "Fire Growth on Horizontal Surfaces of Wood", *Combustion Science and Technology*, **39**, 1984, pp163-194
16. DELICHATSIOS, M. A. "Basic Polymer Material Properties for Flame Spread", *Journal of Fire Sciences*, **11**, Jul/Aug 1993, pp287-295
17. TEWARSON, A. "Flammability Parameters of Materials: Ignition, Combustion and Fire Propagation", *Journal of Fire Sciences*, **12**, July/August, 1994, pp329-356
18. DRYSDALE, D. D., *An Introduction to Fire Dynamics*, John Wiley and Sons Ltd., 1985
19. HOLMAN, J. P., *Heat Transfer, Fifth Edition*, McGraw-Hill Inc., 1981
20. QUINTIERE, J. AND IQBAL, N. "An Approximate Integral Model for the Burning Rate of a Thermoplastic-like Material", *Fire and Materials*, **18**, 1994, pp89-98
21. MOGHTADERI, B., NOVOZHILOV, V., FLETCHER, D. F. AND KENT, J. H. "An Integral Model for the Pyrolysis of Solid Fuels", *Australian Symposium on Combustion and Fourth Flame Days*, University of Adelaide, Adelaide, Australia, 1995, ppC4-1-6
22. DELICHATSIOS, M. M., MATHEWS, M. K. AND DELICHATSIOS, M. A., "An Upward Fire Spread and Growth Simulation", *Fire Safety Science: Proceedings of the Third International Symposium*, 1991, pp207-216
23. DELICHATSIOS, M. A. AND SAITO, K., "Upward Fire Spread: Key Flammability Properties, Similarity Solutions and Flamability Indices", *Fire Safety Science: Proceedings of the Third International Symposium*, 1991, pp217-226
24. FERNÁNDEZ-PELLO, A. AND WILLIAMS, F. A. "A Theory of Laminar Flame Spread Over Flat Surfaces of Solid Combustibles", *Combustion and Flame*, **28**, 1977, 251-277
25. STECKLER, K. D., KASHIWAGI, T., BAUM, H. R., AND KANEMARU, K. "Analytical Model for Transient Gasification of Noncharring Thermoplastic Materials", *Fire Safety Science: Proceedings of the Third International Symposium*, 1991, pp 895-904
26. REICH, L. AND LEVI, D. W. "Dynamic Thermogravimetric Analysis in Polymer Degradation", *Macromol. Rev.*, **1**, pp173-275
27. WOODS, G., *Flexible Polyurethane Foams; Chemistry and Technology*, Applied Science Publishers, Barking, England, 1982
28. CHANG, T. C., SHEN, W. S., CHIU, Y. S. AND HO, S. Y., "Thermo-oxidative Degradation of Phosphorus-containing Polyurethane", *Polymer Degradation and Stability*, **49**, 1995, pp353-360
29. VANSPEYBROECK, R., VAN HEES, P., AND VANDEVELDE, P., "Combustion Behaviour of Polyurethane Flexible Foams under Cone Calorimetry Test Conditions", *Fire and Materials*, **17**, 1993, pp 155-166
30. ORLOFF, L. "Simplified Radiation Modelling of Pool Fires", *Eighteenth Symposium (International) on Combustion*, 1981, pp549-561
31. QUINTIERE, J. G. "A Simulation Model for Fire Growth on Materials Subject to a Room-Corner Test", *Fire Safety Journal*, **20**, 1993 pp313-339